



ALMA MATER STUDIORUM-UNIVERSITÀ DI BOLOGNA

DOTTORATO IN SCIENZE DELLA TERRA
XX° CICLO

SETTORE SCIENTIFICO DISCIPLINARE GEO/07

Titolo della Tesi

***Metamorfismo Ercinico di Bassa-Pressione: Evoluzione Tettonico-
Metamorfica del Complesso di Mandatoriccio
(Massiccio della Sila - Calabria)***

Presentata dal Dott. Antonio Langone

Coordinatore del dottorato:

Prof. William Cavazza

Relatori

Prof. Rottura A.

Prof. Caggianelli A.

Prof. Godard G.

Prof. Prosser G.

Esame finale anno 2008

A mia madre

ACKNOWLEDGMENTS

Ripercorrendo gli anni del dottorato devo ringraziare in primo luogo tutta la Famiglia Iozzi di Mandatoriccio. La Sig.ra Preziosa, il Sig. Saverio, Cataldo, Caterina e Giovanni mi hanno ospitato durante tutti i mesi di rilevamento geologico, mettendomi a disposizione la loro casa. Grazie di cuore per la vostra cordialità e generosità.

A Bologna ho avuto la fortuna di conoscere tanti colleghi validissimi e simpaticissimi: Roberto, Irene, Giovanna, Marta, Veronica, gli “Antoni”, e tanti altri; ai quali rivolgo i miei più sinceri ringraziamenti e auguri. Devo ringraziare i Dott. Gamberini Fabio e Mordenti Alceo per il loro prezioso contributo nella parte analitica. Un affettuoso grazie lo devo a Sonia, Alfonsa, Maria, Silvano ed Alceo per avermi considerato la loro “creatura”. Grazie di cuore.

Voglio ringraziare il Prof. Gaston Godard per avermi invitato e ospitato presso l’Istituto di Fisica del Globo di Parigi (IPJP) per circa un anno. Grazie a questo soggiorno a Parigi ho avuto il piacere di conoscere molti dottorandi e ricercatori. Voglio ringraziarli per avermi fatto conoscere la loro cultura e gli auguro tanto successo. Amel, Bruno, Nadia, Violaine e Zouhir vi ringrazio infinitamente.

Ringrazio infine il Dott. Braga R. e il Professor Calanchi N. per aver fatto una revisione molto attenta e dettagliata del presente lavoro di tesi. Li ringrazio per i suggerimenti proposti circa il contenuto e la forma del testo.

ABSTRACT

Low-pressure/high-temperature (LP/HT) metamorphic belts are characterised by rocks that experienced abnormal heat flow in shallow crustal levels ($T > 600\text{ }^{\circ}\text{C}$; $P < 4\text{ kbar}$) resulting in anomalous geothermal gradients ($60\text{--}150\text{ }^{\circ}\text{C/km}$). The abnormal amount of heat has been related to crustal underplating of mantle-derived basic magmas or to thermal perturbation linked to intrusion of large volumes of granitoids in the intermediate crust. In particular, in this latter context, magmatic or aqueous fluids are able to transport relevant amounts of heat by advection, thus favouring regional LP/HT metamorphism. However, the thermal perturbation consequent to heat released by cooling magmas is responsible also for contact metamorphic effects. A first problem is that time and space relationships between regional LP/HT metamorphism and contact metamorphism are usually unclear. A second problem is related to the high temperature conditions reached at different crustal levels. These, in some cases, can completely erase the previous metamorphic history. Notwithstanding this problem is very marked in lower crustal levels, petrologic and geochronologic studies usually concentrate in these attractive portions of the crust. However, only in the intermediate/upper-crustal levels of a LP/HT metamorphic belt the tectono-metamorphic events preceding the temperature peak, usually not preserved in the lower crustal portions, can be readily unravelled.

The Hercynian Orogen of Western Europe is a well-documented example of a continental collision zone with widespread LP/HT metamorphism, intense crustal anatexis and granite magmatism. Owing to the exposure of a nearly continuous cross-section of the Hercynian continental crust, the Sila massif (northern Calabria) represents a favourable area to understand large-scale relationships between granitoids and LP/HT metamorphic rocks, and to discriminate regional LP/HT metamorphic events from contact metamorphic effects. Granulite-facies rocks of the lower crust and greenschist- to amphibolite-facies rocks of the intermediate-upper crust are separated by granitoids emplaced into the intermediate level during the late stages of the Hercynian orogeny. Up to now, advanced petrologic studies have been focused mostly in understanding P-T evolution of deeper crustal levels and magmatic bodies, whereas the metamorphic history of the shallower crustal levels is poorly constrained. The Hercynian upper crust exposed in Sila has been subdivided in two different metamorphic complexes by previous authors: the low- to very low-grade Bocchigliero complex and the greenschist- to amphibolite-facies Mandatoriccio complex. The latter contains favourable mineral assemblages in order to unravel the tectono-metamorphic evolution of the Hercynian upper crust.

The Mandatoriccio complex consists mainly of metapelites, meta-arenites, acid metavolcanites and metabasites with rare intercalations of marbles and orthogneisses. Siliciclastic metasediments show a static porphyroblastic growth mainly of biotite, garnet, andalusite, staurolite and muscovite, whereas cordierite and fibrolite are less common. U-Pb ages and internal features of zircons suggest that the protoliths of the Mandatoriccio

complex formed in a sedimentary basin filled by Cambrian to Silurian magmatic products as well as by siliciclastic sediments derived from older igneous and metamorphic rocks.

In some localities, metamorphic rocks are injected by numerous aplite/pegmatite veins. Small granite bodies are also present and are always associated to spotted schists with large porphyroblasts. They occur along a NW-SE trending transcurrent cataclastic fault zone, which represents the tectonic contact between the Bocchigliero and the Mandatoriccio complexes. This cataclastic fault zone shows evidence of activity at least from middle-Miocene to Recent, indicating that brittle deformation post-dated the Hercynian orogeny.

P-T pseudosections show that micaschists and paragneisses of the Mandatoriccio complex followed a clockwise P-T path characterised by four main prograde phases: thickening, peak-pressure condition, decompression and peak-temperature condition. During the thickening phase, garnet blastesis started up with spessartine-rich syntectonic core developed within micaschists and paragneisses. Coevally (340 ± 9.6 Ma), mafic sills and dykes injected the upper crustal volcanoclastic sedimentary sequence of the Mandatoriccio complex. After reaching the peak-pressure condition (≈ 4 kbar), the upper crust experienced a period of deformation quiescence marked by the static overgrowths of S_2 by Almandine-rich-garnet rims and by porphyroblasts of biotite and staurolite. Probably, this metamorphic phase is related to isotherms relaxation after the thickening episode recorder by the Rb/Sr isotopic system (326 ± 6 Ma isochron age). The post-collisional period was mainly characterised by decompression with increasing temperature. This stage is documented by the andalusite+biotite coronas overgrown on staurolite porphyroblasts and represents a critical point of the metamorphic history, since metamorphic rocks begin to record a significant thermal perturbation. Peak-temperature conditions (≈ 620 °C) were reached at the end of this stage. They are well constrained by some reaction textures and mineral assemblages observed almost exclusively within paragneisses. The later appearance of fibrolitic sillimanite documents a small excursion of the P-T path across the And-Sil boundary due to the heating. Stephanian U-Pb ages of monazite crystals from the paragneiss, can be related to this heating phase. Similar monazite U-Pb ages from the micaschist combined with the lack of fibrolitic sillimanite suggest that, during the same thermal perturbation, micaschists recorded temperatures slightly lower than those reached by paragneisses. The metamorphic history ended with the crystallisation of cordierite mainly at the expense of andalusite. Consequently, the Ms+Bt+St+And+Sill+Crd mineral assemblage observed in the paragneisses is the result of a polyphasic evolution and is characterised by the metastable persistence of the staurolite in the stability fields of the cordierite. Geologic, geochronologic and petrographic data suggest that the thermal peak recorded by the intermediate/upper crust could be strictly connected with the emplacement of large amounts of granitoid magmas in the middle crust. Probably, the lithospheric extension in the relatively heated crust favoured ascent and emplacement of granitoids and further exhumation of metamorphic rocks.

After a comparison among the tectono-metamorphic evolutions of the different

Hercynian crustal levels exposed in Sila, it is concluded that the intermediate/upper crustal level offers the possibility to reconstruct a more detailed tectono-metamorphic history. The P-T paths proposed for the lower crustal levels probably underestimate the amount of the decompression. Apart from these considerations, the comparative analysis indicates that P-T paths at various crustal levels in the Sila cross section are well compatible with a unique geologic scenario, characterized by post-collisional extensional tectonics and magmas ascent.

INDEX

I - INTRODUCTION	I
1 - GEOLOGICAL SETTING	
1.1 - CALABRIA-PELORITANI TERRANE	1
1.2 - SILA MASSIF	3
1.3 - BOCCHIGLIERO AND MANDATORICCIO COMPLEXES	4
1.4 - STUDIED AREAS	5
1.4.1 - Mandatoriccio-Umbriatico area	6
1.4.2 - Cropalati-Caloveto area	12
2 – PETROGRAPHY AND MICROSTRUCTURES OF ROCKS OF THE MANDATORICCIO COMPLEX	
2.1 - METAVOLCANITES	15
2.2 - AMPHIBOLITES	15
2.3 - METAPELITES AND META-ARENITES	18
2.3.1 - Micaschists and paragneisses	20
2.3.1.1 - Micaschists	20
2.3.1.2 - Paragneisses	27
2.3.2 - Spotted schists with large porphyroblasts	33
3 - MINERAL CHEMISTRY IN THE MAIN ROCK TYPES OF THE MANDATORICCIO COMPLEX	
3.1 - AMPHIBOLITES	38
3.2 - MICASCHISTS	40
3.3 - PARAGNEISSES	44
4 - METAMORPHIC EVOLUTION OF THE MANDATORICCIO COMPLEX	
4.1 - DEFORMATION-CRYSTALLISATION HISTORY	50
4.2 - REACTION HISTORY	51
4.3 - PRESSURE-TEMPERATURE ESTIMATES	62
4.3.1 - An overview of available methods	62
4.3.2 - Thermodynamically calculated phase-relations	63
4.3.2.1 - Chemical system	64
4.3.2.2 - Effective-bulk-rock composition	65
4.3.2.3 - P-T phase diagrams of rocks	67
4.3.2.4 - P-T phase diagrams of reaction domains	73
4.3.2.4.1 - Staurolite-consuming reaction	74
4.3.2.4.2 - Cordierite-producing reaction	78
4.3.3 - P-T paths	79
4.3.4 - Comparison with conventional thermobarometry	84

5 - GEOCHRONOLOGY	
5.1 - GEOCHRONOLOGIC BACKGROUND	87
5.2 - NEW GEOCHRONOLOGIC DATA	89
5.2.1 - Dating methods	89
5.2.2 - <i>In-situ</i> U-Th-Pb zircon ages	91
5.2.2.1 - Paragneiss	91
5.2.2.2 - Meta-sill	93
5.2.2.3 - Porphyritic dyke	94
5.2.3 - <i>In-situ</i> U-Th-Pb monazite ages	95
5.2.3.1 - Paragneiss	95
5.2.3.2 - Micaschist	97
5.2.4 – Interpretation of the U-Th-Pb ages	98
5.2.4.1 - The Early Palaeozoic sedimentary sequence	98
5.2.4.2 – The Hercynian evolution	98
 6 - P-T-t PATHS AND TECTONO-METAMORPHIC MODELS	
6.1 - P-T-t PATH AND TECTONO-METAMORPHIC MODEL OF THE HERCYNIAN INTERMEDIATE/UPPER CRUST	100
6.1.1 - Comparison with P-T-t paths followed by other crustal levels	102
6.1.2 - Implications for the crustal scale tectono-metamorphic model	105
6.1.3 - Palaeogeographical implications	106
 7 – SUMMARY AND CONCLUSIONS	108
 REFERENCES	111
 LIST OF TABLES	124
 APPENDIXES	
1 - Langone <i>et al.</i> (2006)	125
2 - XRF whole-rock analyses	126
3 - Analytical and imaging techniques	129
4 - Mass balance calculations and composition of reaction domains	236
5 - Effective-Bulk-Composition (EBC) calculations	243
6 - Liotta <i>et al.</i> (submitted)	246
7 - Geochronologic dating	247

I – INTRODUCTION

Low-pressure/high-temperature (LP/HT) metamorphic belts are characterised by rocks that experienced abnormal heat flow in shallower crustal levels ($T > 600\text{ }^{\circ}\text{C}$; $P < 4\text{ kbar}$; *e.g.* Thompson & England, 1984) resulting in anomalous geothermal gradients ($60\text{--}150\text{ }^{\circ}\text{C/km}$). These particular metamorphic belts are very common throughout the world (Miyashiro, 1961; Hietanen, 1967; Carmichael, 1978) and have been observed in different geodynamic settings such as: magmatic arcs (Oxburgh & Turcotte, 1971; Barton & Hanson, 1989; Okudaira, 1996); subduction zones (Miyazaki & Okumura, 2002); continental collision zones (England & Thompson, 1984); continental collision zones with additional mantle thermal pulse (Bodorkos *et al.*, 2002); thermal subsidence following rifting (Sandiford *et al.*, 1998). Apart from the geodynamic setting, the abnormal amount of heat has been related to crustal underplating of mantle-derived basic magmas (Thompson, 1981 and Thompson & England, 1984) or to thermal perturbation linked to intrusion of huge volume of granitoids in the intermediate crust (Lux *et al.*, 1986; De Yoero *et al.*, 1990; 1991). In particular, in this latter thermal model magmatic or aqueous fluids can transmit important amounts of heat by advection during metamorphism. For these reasons, low-pressure metamorphic belts are often associated to huge masses of granitoids (De Yoero *et al.*, 1991; Vilà *et al.*, 2007). The thermal perturbation linked to these magmatic bodies is responsible for the regional LP/HT metamorphism and causes also contact metamorphic effects resulting in a complex metamorphic evolution. The major problems are related to the high temperature conditions reached by the different crustal levels. LP/HT metamorphic conditions could completely reset the previous metamorphic history making very difficult the P-T-t reconstructions. Notwithstanding this problem is very marked in lower crustal levels, petrologic and geochronologic studies usually concentrate in these attractive portions of the crust. Probably, the intermediate/upper-crustal levels of a LP/HT metamorphic belt are the key areas in order to unravel the tectono-metamorphic events preceding the LP/HT one, usually not preserved in the lower crustal portions.

The Hercynian Orogen of Western Europe is a well-documented example of a continental collision zone with widespread LP/HT metamorphism, intense crustal anatexis and granite magmatism (*e.g.* Pin & Vielzeuf, 1983).

In particular, the Hercynian massifs exposed in Calabria (Southern Italy) provide a classical example of LP/HT regional metamorphism (*e.g.* Graessner & Schenk, 1999) and granite magmatism (*e.g.* Rottura *et al.*, 1990; Ayuso *et al.*, 1994) documenting an important thermal event whose origin and geodynamic significance are still a matter of debate (*e.g.* Schenk, 1984; Graessner & Schenk, 2001; Acquafredda *et al.*, 2006; Caggianelli *et al.*, 2007).

Owing the exposure of a nearly continuous cross-section through the Hercynian continental crust, the Sila massif (northern Calabria) represents a favourable area in order to understand the large scale relationships between granitoids and LP/HT metamorphic

rocks, and offers also the possibility to discriminate regional LP/HT metamorphic events from contact ones. All the crustal levels trend on average northwest-southeast, with granulite-facies rocks, of the lower crust, in the southwest and greenschist- to amphibolite-facies rocks, of the intermediate-upper crust, in the northeast. Metamorphic rocks of these two crustal levels are separated by granitoids emplaced into the intermediate crust during the late stages of the Hercynian orogeny. The exposure of different crustal levels represents an interesting open-air laboratory for geologists and offers the possibility to unravel the tectono-metamorphic evolution of the entire crust. Up to now, advanced petrologic studies have been focused mostly in understanding deeper crustal levels and magmatic bodies. The Hercynian upper crust exposed in Sila has been subdivided by previous authors in two different metamorphic complexes: the low to very-low grade Bocchigliero complex and the greenschist- to amphibolite-facies Mandatoriccio complex.

The low metamorphic conditions of the Bocchigliero complex and the occurrence of typical low-pressure metamorphic assemblages exclusively in the Mandatoriccio complex led to concentrate petrologic and geochronologic studies on the Mandatoriccio complex.

Despite the previous studies, the tectono-metamorphic evolution of the Mandatoriccio complexes is still poorly constrained. Moreover, ages of protoliths of the Mandatoriccio complex are still unknown. Previous works (*e.g.* Acquafredda *et al.*, 1994a) consider the Mandatoriccio complex as part of an ancient basement (*e.g.* Ordovician), source of the Bocchigliero Palaeozoic sequence. In addition, chronological relationships between LP/HT metamorphism and granitoid intrusions are not well established.

This study integrates petrographic and structural field data, microstructural observations, whole-rock geochemistry, electron microprobe mineral analyses, mineral equilibrium calculations and P–T estimates to get a better understanding of the metamorphic evolution of the intermediate-upper crust (*i.e.* Mandatoriccio complex) exposed in Sila. To this end, major attention has been paid to porphyroblast-bearing rocks showing garnet+biotite+muscovite+andalusite+staurolite±cordierite±fibrolite assemblage. These rocks contain important information on the relationships between deformation and porphyroblast growth. Isotopic dating of metamorphic and magmatic rocks allowed to complete the tectono-metamorphic scenario of the intermediate-upper crust deciphering the time relationships between metamorphism and granite emplacement in the crust.

Integrating the petrologic and geochronologic data, the time-space relationships among regional metamorphism, deformation and magmatism through the crustal section have been constrained.

The thesis has been subdivided into seven chapters.

The first chapter contains a brief description of major geological aspects of the Calabria-Peloritani terrane with particular attention to the Sila massif. After an overview of main structural and lithologic features of the Bocchigliero and Mandatoriccio complexes, new geological maps and structural data will be discussed.

The second chapter has been dedicated to the petrographic and microstructural

description of major rock types of the Mandatoriccio complex. Rocks have been subdivided into three types on the basis of their protolith: acid metavolcanites, amphibolites and metapelites/meta-arenites. Protoliths have been determined petrographically and by whole-rock chemical analyses.

The third chapter contains a detailed study of the chemical composition of the rock-forming minerals suited for petrologic and geochronologic studies.

The fourth chapter deals with the metamorphic evolution of the Mandatoriccio complex. On the basis of microstructures, petrography and mineral chemistry a reconstruction of the deformation-crystallisation history has been proposed. In particular, microstructural and petrographic analyses lead to recognise relative sequence of mineral growth and different mineral generations, whereas mineral chemistry highlighted the possible compositional differences between various generations of minerals. Deformation-crystallisation history represents the starting point for the reconstruction of the tectono-metamorphic evolution. This chapter contains a thorough treatment of the observed and inferred metamorphic reactions that have been illustrated in chemographic diagrams. Observed reactions have been balanced using matrix calculations, whereas inferred reactions have been reconstructed mainly by chemographic diagrams.

A large part of this chapter has been dedicated to the pressure-temperature estimates and to the reconstructions of the P-T trajectories. P-T conditions have been mainly determined using phase diagrams calculated for a fixed bulk-rock composition (or isochemical phase diagrams, or P-T pseudosections). After petrographic and microstructural analyses, P-T pseudosections have been considered the more appropriate method for constraining the P-T evolution of the analysed rock types at least for two major reasons: 1) petrographic analyses revealed that rocks are garnet-free or garnet-poor, hindering the use of classical techniques for P-T determinations (conventional thermobarometry and Gibbs method); 2) the P-T pseudosections show the stability fields of mineral assemblages resulting very helpful to depict prograde and retrograde evolution of the rocks on the basis of reconstructed reaction history.

P-T estimates obtained with isochemical sections have been compared with P-T conditions determined by conventional thermobarometry.

The fifth chapter has been addressed to the geochronologic aspects relative to the magmatic and metamorphic rocks outcropping in Sila. After a complete overview of the existing geochronologic data, new U-Pb analyses on zircon and monazite have been discussed. Radiometric ages, combined with petrologic studies, can be used in order to decipher the time relationships between magmatic and metamorphic events. To this end, after structural and petrologic studies three samples have been selected. A fibrolite-bearing paragneiss has been considered the most appropriate sample for dating the metamorphic evolution. A porphyritic dike has been selected to constrain the time of the end of the magmatic activity, since it represents the latest magmatic product cross-cutting the older granitoids. Isotopic analyses have been performed also on a basic meta-sill sub-concordant

with respect to the main regional schistosity of micaschists and paragneisses of the Mandatoriccio complex. In this case, U-Pb zircon data provide geochronologic constraints on the protolith and on the metamorphic evolution.

The **sixth** chapter has been dedicated to the reconstructions of the tectono-metamorphic history. P-T trajectories (Chapter 4) and radiometric ages (Chapter 5) have been used to model the tectono-metamorphic evolution of the Mandatoriccio complex. Reconstructed P-T paths for the Hercynian upper crust have been compared with those of other Hercynian crustal levels outcropping in the Sila massif. Finally, the tectono-metamorphic model has been discussed on the basis of existing palaeogeographical reconstructions.

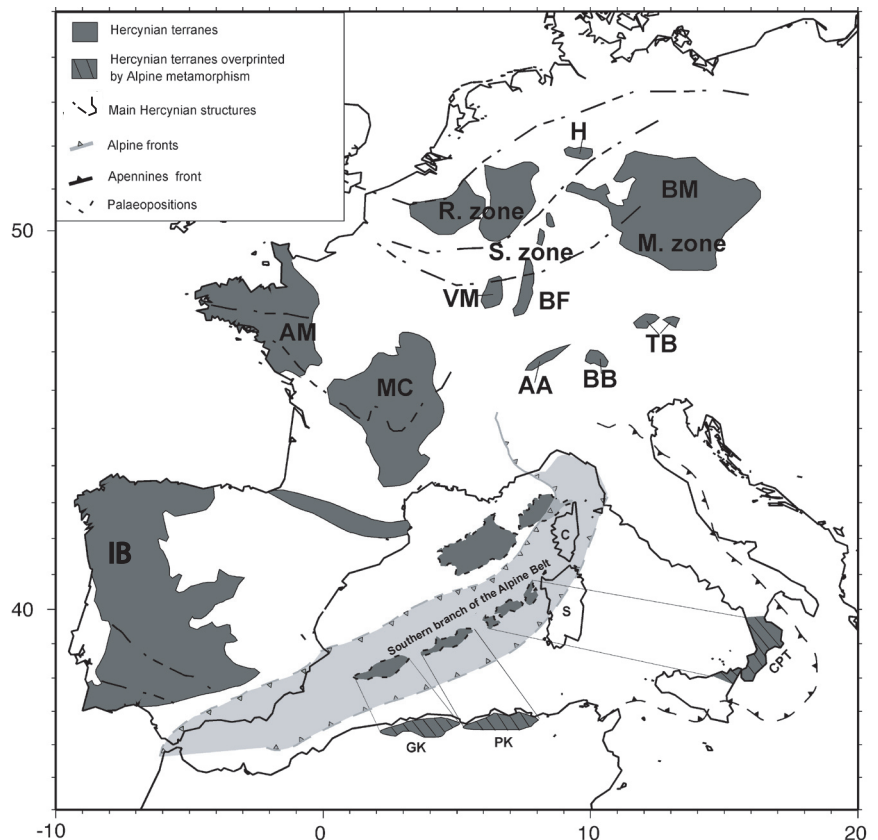
The **seventh** chapter resumes the major results of the present work.

CHAPTER 1 - GEOLOGICAL SETTING

1.1 – CALABRIA-PELORITANI TERRANE

The Calabria-Peloritani terrane consists of a nappe-structured belt located between the NW-SE trending southern Apennines and E-W trending Maghrebides (Amodio-Morelli *et al.*, 1976). It is built up of metamorphic and igneous rocks of the Hercynian continental crust partially involved in the Alpine orogeny, oceanic-derived rocks with local high-pressure\ low-temperature metamorphism and metasedimentary rocks of Apennine pertinence (Bonardi *et al.*, 2001 and references therein). In particular, the Calabria-Peloritani terrane represents a fragment of the European Hercynian chain, also known as the European Variscan chain. This mountain belt, that extended in Permian time from the Caucasus and Urals in Europe to the Appalachian and Ouachita Mountains in America (Matte, 2002), in central Europe it is now recognisable from Spain to Poland. Generally, in the proposed reconstructions the European Variscan belt assumes a sinuous form characterised by two major arcs, the Ibero-Armorican arc, to the southwest, and the Bohemian arc, to the northeast (**Fig. 1.1**). Almost complete sections of the European Hercynian belt are visible

Fig. 1.1: simplified geologic map of European Hercynian Massifs (modified from Carrigan *et al.*, 2005) and of the southern branch of the Alpine Belt (modified after Langone *et al.*, 2006). IB=Iberian Massif, AM=Armorica Massif, MC=Massif Central, VM=Vosges Massif, BF=Black Forest Massif, AA=Aar Batholith, BB=Bernina Batholith, TB=Tauern Batholith, BM=Bohemian Massif, H=Harz Massif, M. zone=Moldanubian zone, R. zone=Rhenehercynian Zone. C=Corse, S=Sardinia, GK=Grande Kabylie, PK=Petite Kabylie, CPT=Calabria-Peloritani terrane.



in Portugal, in Spain and in France (Matte, 2002) whereas some fragments (*e.g.* Calabria-Peloritani terrane, Kabyles, Corse and Sardinia) are dispersed in the peri-Mediterranean regions, in the Alpine chain *sensu stricto* and in the Carpathians (**Fig. 1.1**). Pre-Triassic

palaeogeographical reconstruction of the Hercynian orogens has been complicated by later (Triassic to recent) tectonic events (*e.g.* Alpine orogeny, Western Mediterranean evolution, Apennine orogeny). This is the case of the Calabria-Peloritani terrane drifted in the present position by the combined effects of the opening of the western Mediterranean basins (*e.g.* Liguro-Provençal and Tyrrhenian basins) and the Apennine orogeny, since the Oligocene (Alvarez *et al.*, 1974). Alpine and post-Oligocene tectono-metamorphic evolution of the Calabria-Peloritani terrane has been treated in a special paper (Langone *et al.*, 2006; **Appendix 1**). A consequence of this geological evolution is a regional crustal exhumation (Schenk, 1980; Thomson, 1994; Caggianelli *et al.*, 2000; Festa *et al.*, 2003) with a tilting of about 40–45° that favoured the exposure of nearly complete Hercynian crustal sections (**Fig. 1.2**; Dubois, 1976; Schenk, 1980), almost unaffected by later tectono-metamorphic events.

In the latter, granulite-facies metamorphic rocks of the lower crust are separated from greenschist- to amphibolite-facies metamorphic rocks of the upper crust by a thick sheet of late-Hercynian granitoids (around 290 Ma, Borsi & Dubois, 1968; Ayuso *et al.*, 1994).

According to some authors (Schenk, 1980; Graessner & Schenk, 1999), a single low-pressure/high-temperature (LP/HT) metamorphic event was responsible for the present structure of the Hercynian crust.

Peak metamorphic conditions estimated for the migmatitic paragneisses of the lower crust ($P = 4–6$ kbar and $T = 740–770$ °C; Graessner & Schenk, 2001) are in good agreement with low-pressure conditions found in the European Hercynian belt (Vielzeuf & Pin, 1989). Graessner *et al.* (2000) dated the age of the metamorphic peak at 300–304 Ma by U-Pb method on monazite. According to Caggianelli & Prosser (2002) peak metamorphism in migmatitic paragneisses can be related to the heat released by thick granitoid sheets intruded in the intermediate continental crust. Emplacement of granitoids was also responsible for low-pressure metamorphism of the upper crustal rocks, largely recognised in the Sila (Borghi *et al.*, 1992), Serre (Colonna *et al.*, 1973) and Aspromonte Massifs (Graessner & Schenk, 1999; **Fig. 1.2**).

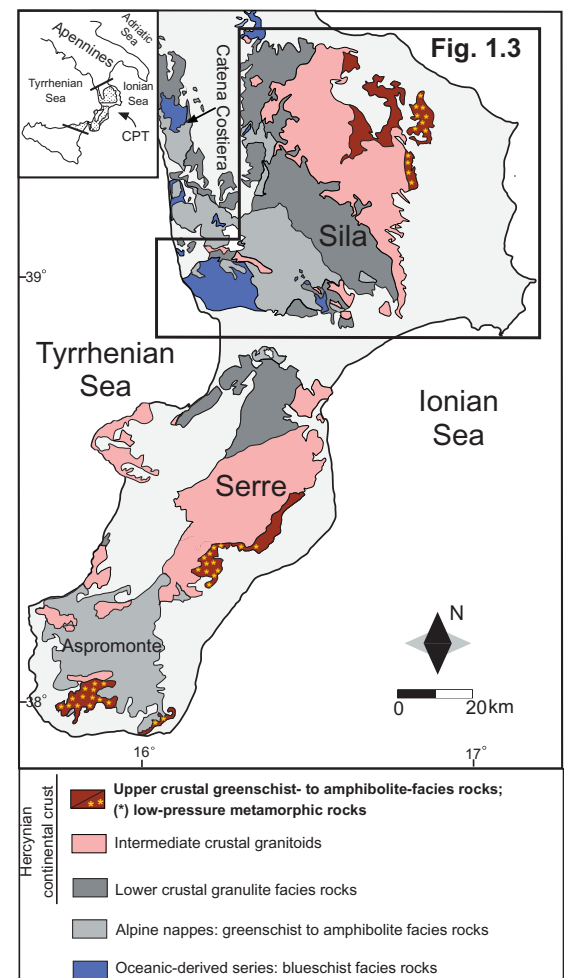


Fig. 1.2: geological sketch map showing metamorphic and magmatic rocks exposed in Calabria.

1.2 –SILA MASSIF

In northern Calabria (Sila and Catena Costiera, **Figs. 1.2, 1.3**) the Hercynian crustal complexes are covered by Meso-Cenozoic sedimentary rocks and tectonically overlie oceanic-derived series related to the Jurassic rifting (Rossetti *et al.*, 2001). In turn, continental- and oceanic-derived metamorphic rocks overlie sedimentary rocks of the Apenninic units (**Figs. 1.3a, b**).

The Hercynian crustal section occupies the highest structural position (**Fig. 1.3b**), with different crustal levels mainly striking NW-SE (**Fig. 1.3a**), resulting in a NE-SW metamorphic gradient.

The lower crust (**Fig. 1.3c**), with a thickness of about 7 km, consists mainly of migmatitic paragneisses with minor metabasites and marbles (Dubois, 1971; Lorenzoni & Zanettin-Lorenzoni, 1983; Graessner & Schenk, 2001). Towards higher crustal levels, high-grade rocks show a gradational contact (*i.e.* a migmatitic border zone) with the late-Hercynian intrusions. Plutonic rocks, referred to as the Sila batholith (Ayuso *et al.*, 1994), have an overall thickness of about 7–9 km (Caggianelli & Prosser, 2001; **Fig. 1.3c**) and have calc-alkaline affinity. They are represented by tonalite, granodiorite, monzogranite and leucogranite (Messina *et al.*, 1991), moving from deeper to shallower crustal levels.

Towards the upper crust, granitoids intruded low- to medium-grade metamorphic rocks ascribed to two distinct complexes. These complexes have been reported for the first time by De Vivo *et al.* (1978) and identified as Bocchigliero and Mandatoriccio complexes by Gurrieri *et al.* (1978). These complexes outcrop in eastern Sila (Ionian side), with an average NW-SE trend, and are bounded to the west by late-Hercynian granitoids (**Fig. 1.3a**). Towards the Ionian coast, the middle-Miocene/Pleistocene transgressive sedimentary succession (Selli, 1957; Ogniben, 1962) generally covers the Hercynian basement rocks. Locally, the pre-Alpine basement preserves its Mesozoic sedimentary cover distinguished in an Upper Triassic(?)–Upper Liassic Longobucco sequence and a Lower Liassic–Lower Cretaceous Caloveto group (Magri *et al.*, 1965, Young *et al.*, 1986, Santantonio & Teale, 1987).

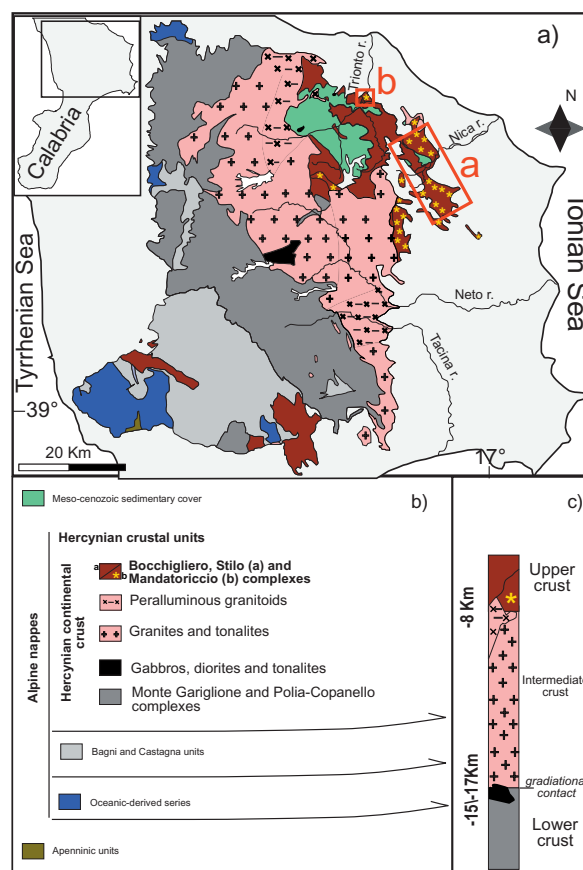


Fig. 1.3: simplified geological map (a) and tectonic scheme (b) of the Sila massif. c) Schematic column of the Hercynian continental crust. Modified after Ayuso *et al.* (1994); Graessner *et al.* (2000). Red boxes indicate the location of studied areas: a) Mandatoriccio-Umbriatico area; b) Cropolati-Caloveto area.

1.3 – BOCCHIGLIERO AND MANDATORICCIO COMPLEXES

The Bocchigliero complex is mainly composed of Ordovician to Siluro-Devonian phyllites, meta-sandstones, meta-conglomerates with minor metavolcanic rocks of andesitic to rhyolitic composition (Acquafredda *et al.*, 1988; 1991; 1994a; 1994b). These rocks recorded low to very low-grade metamorphism that allowed to local preservation of several primary sedimentary features and Cambrian to Devonian fossils such as Acritarchs (Bouillin *et al.*, 1984; 1987). The occurrence of roughly well-preserved fossils suggests that peak thermal conditions do not exceeded 300-350 °C, whereas celadonitic content of phengite analysed in a slate by Borghi *et al.* (1992) indicates pressures in excess of 4-4.5 kbar. The main metamorphism has been dated at 330±4 Ma (Rb-Sr whole rock isochron) by Acquafredda *et al.* (1991).

The Mandatoriccio complex consists mainly of metapelites, meta-arenites, metavolcanites and metabasites with rare intercalations of marbles and orthogneisses (Acquafredda *et al.*, 1988; 1991). Mica-rich lithologies show a static porphyroblastic growth mainly of biotite, garnet, andalusite, staurolite and muscovite whereas cordierite and fibrolite are less common (Lorenzoni & Zanettin-Lorenzoni, 1979; Borghi *et al.*, 1992; Palumbo, 1995).

The tectono-metamorphic evolution of the Mandatoriccio complex is still under debate. At least three different interpretations based on microstructural, petrologic and geochronologic data are reported in the literature (**Fig. 1.4**).

Lorenzoni & Zanettin-Lorenzoni, (1979) proposed a five-stage metamorphic history characterized by four regional metamorphic events, followed by a contact metamorphism (**Fig. 1.4**).

	pre-Cambrian - Ordovician				Carboniferous
	pre-Hercynian (Cadomian ?)				Hercynian
	Syntectonic ①	②	Static ③	④	Contact ⑤
Lorenzoni & Zanettin-Lorenzoni (1979)					
Acquafredda et al. (1991; 1992; 1994)	Syntectonic ①	Syntectonic ②	Static ③		Syntectonic ④
Borghi et al. (1992)					Syntectonic ① Static ② Syntectonic ③

Fig. 1.4: schematic diagram showing different tectono-metamorphic evolutions of the Mandatoriccio complex proposed by previous authors.

Alternatively, the metamorphic evolution proposed by Acquafredda *et al.*, (1992) consists of two earlier syntectonic events in greenschist-facies conditions followed by a static thermal event in amphibolite-facies conditions (**Fig. 1.4**). All these events (Ordovician) pre-date the Hercynian orogeny during which basement rocks experienced weak dynamic greenschist-facies retrogression. According to Acquafredda *et al.* (1992), geochronologic data (326±6 Ma; Rb-Sr whole rock isochron) could be related to this latter event that is comparable and coeval with the main event recorded in the Bocchigliero complex (330±4

Ma, Acquafredda *et al.*, 1991). Following their previous works (Acquafredda *et al.*, 1991; 1992), Acquafredda *et al.* (1994a) suggested that static thermal metamorphism of the Mandatoriccio complex could be coeval with volcanic products observed in the Palaeozoic sequence of the Bocchigliero complex. Consequently, the Mandatoriccio complex may be considered as the pre-Hercynian (pre-Cambro-Ordovician) metamorphic basement of the Bocchigliero complex. The total absence of clasts consisting of metamorphic rocks of the Mandatoriccio complex within the Palaeozoic sequence of the Bocchigliero complex led Acquafredda *et al.* (1994) to suppose that the Mandatoriccio complex did not constitute the primary clastic source of Palaeozoic sequence of the Bocchigliero complex, probably because it was located at greater depths. Following this interpretation, during the Hercynian orogeny the Palaeozoic sequence was detached from its original basement, which is now totally absent in the Sila massif.

Borghi *et al.*, (1992) proposed a polyphase monocycle tectono-metamorphic evolution characterized by an earlier syntectonic event in greenschist-facies conditions, followed by a higher-temperature/lower-pressure static event in the amphibolite-facies conditions (**Fig. 1.4**) during which thermal peak (550-600 °C) was reached. Metamorphic history ended with a regional low-pressure/low-temperature pervasive retrogression. In this monocyclic evolution, Carboniferous ages (326±6 Ma) obtained by Acquafredda *et al.* (1992) suggested a Hercynian age of the metamorphism in the Mandatoriccio complex.

Summarising, previous work gave strongly controversial results on the origin and the tectono-metamorphic evolution of the Mandatoriccio complex. Consequently, a detailed petrologic and geochronologic characterisation is needed to unravel the genesis and the evolution of this metamorphic complex.

1.4 - STUDIED AREAS

Geological mapping and sampling have been performed in selected areas of the eastern Sila Massif (**Fig. 1.3**) in order to make a detailed petrographic characterisation of the Mandatoriccio complexes and to unravel the relationships between plutonic and metamorphic rocks. To this end, two different areas have been selected on the basis of existing geological maps of Calabria (1:25000; Burton, 1971) and previous works (Lorenzoni *et al.*, 1978; Lorenzoni & Zanettin-Lorenzoni, 1979; 1983, Bouillin *et al.*, 1984; Acquafredda *et al.*, 1988; 1991; Borghi *et al.*, 1992; Caggianelli & Prosser, 2001).

Major attention has been dedicated to a large area situated between Mandatoriccio and Umbriatico villages (**Fig. 1.3**) that encompasses most of the outcropping Mandatoriccio complex. Consequently, this area resulted particularly interesting firstly for the reconstructions of the original relationships between metamorphic and granitoid rocks and secondary for the petrographic characterisation of the Mandatoriccio complex.

The area situated between Cropalati and Caloveto villages (**Fig. 1.3**) has been selected because the studied metamorphic complex is in contact with a small granitoid body and low-grade metamorphic rocks of the Bocchigliero complex.

1.4.1 - Mandatoriccio-Umbriatico area

In this large area, metamorphic rocks of the Mandatoriccio and Bocchigliero complexes (Figs. 1.3; 1.5) are exposed.

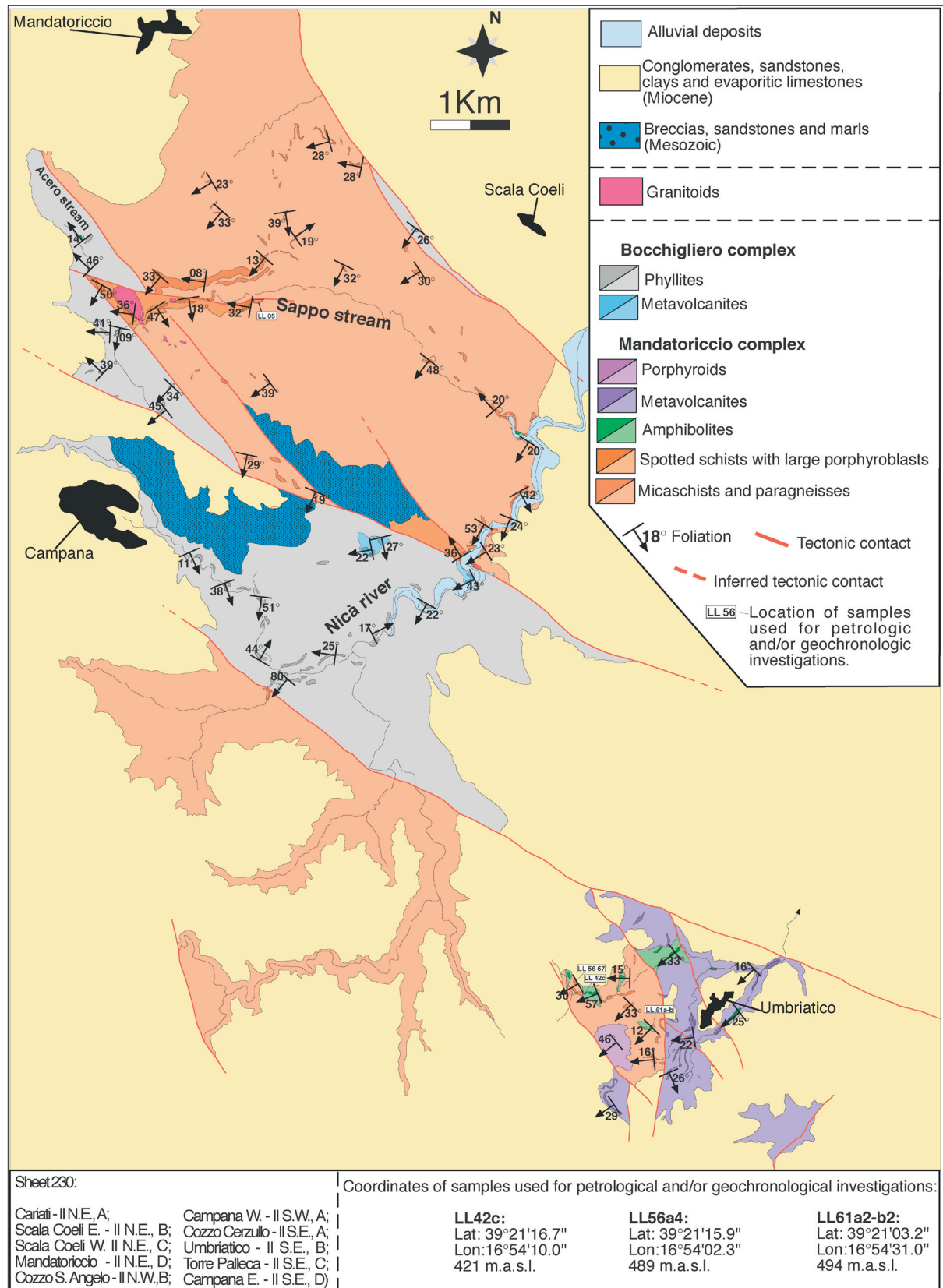


Fig. 1.5: geological sketch map of the Mandatoriccio-Umbriatico areas, based on original 1:10000 mapping, showing location of samples used for petrological and/or geochronologic investigations. Darker tonalities refer to outcrops.

Medium-grade metamorphic rocks of the Mandatoriccio complex show lithologic variations moving from southeast (Umbriatico village area) toward northwest (Sappo stream area).

Southeastern area (Umbriatico village).

The southeastern area (Umbriatico village) is characterised by:

- a) the prevalence of metavolcanites and metabasites (**Fig. 1.6a**) with respect to micaschists and paragneisses;
- b) the absence of granitoid bodies and the abundance of aplite and pegmatite veins that cross cut basement rocks (**Fig. 1.6b**);
- c) the occurrence of garnet-bearing micaschists and paragneisses.

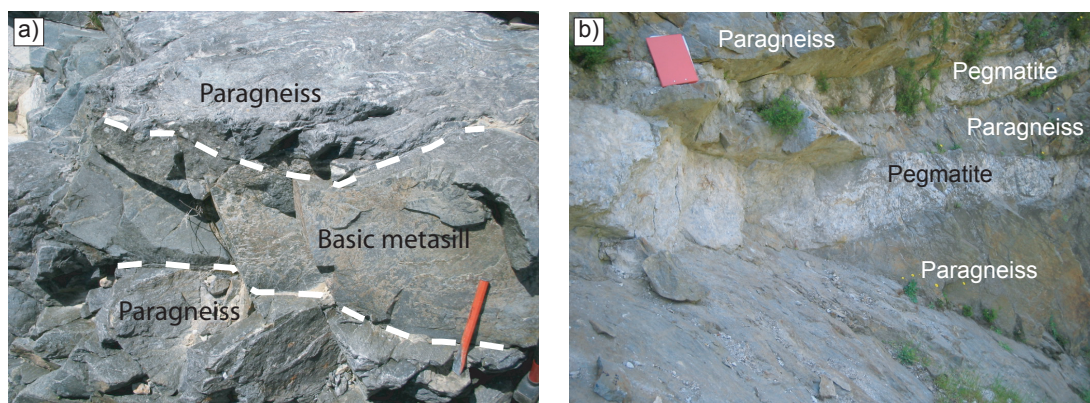


Fig. 1.6a, b: a) basic meta-sill within paragneisses in the Umbriatico village area; b) pegmatite veins crosscutting paragneisses in the Umbriatico village area.

Metavolcanites show a porphyroclastic texture, locally with augen aspect, and consist of large crystals of feldspar imbedded in quartz+mica-rich layers. The latter define the main S_2 regional foliation. Locally, porphyroids with blastoporphyrict texture have been observed.

Amphibolites occur as schistose rocks, with large amphibole crystals, and as fine-grained dark green rocks, with a gneissic appearance. Amphibolites have been observed chiefly as lenses interlayered within metavolcanites, micaschists and paragneisses.

Garnet-bearing micaschists and paragneisses are confined only in a small area located east-northeast of the Umbriatico village. These rocks are characterised by compositional layering in which white mica-rich domains define the S_2 regional foliation. Small biotite crystals without any preferred orientation are also recognisable on the foliation planes. Relics of an earlier foliation (S_1) have been rarely observed within microlithons.

Structural data measured in the Mandatoriccio complex around the Umbriatico village are shown in **Figs. 1.7a-c**. The main regional S_2 foliation strikes mainly from N-S to NW-SE with gentle and moderate dips toward the W-SW and the E-NE (**Fig. 1.7a**). Mineralogical lineations have been observed mainly on foliation planes of the metabasites.

They are defined by a weak alignment of quartz and plagioclase crystals and show shallow plunges toward NW and SE (**Fig. 1.7a**). Foliation planes are overprinted by well-developed crenulations with axes of microfolds oriented mainly NW-SE with low plunge angles (**Fig. 1.7a**). A similar orientation has been observed for the axes of major folds (**Fig.**

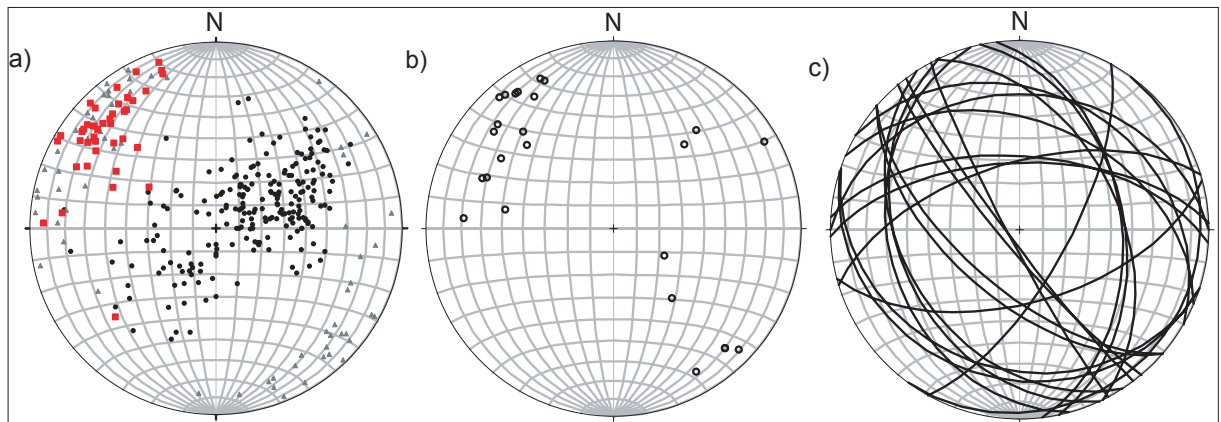


Fig. 1.7: equal area projection (lower hemisphere) of structural data from the Umbriatico village area. a) Poles of 215 foliation planes (black circles); 62 mineral lineations (triangles); 45 crenulation lineations (red boxes). b) 24 axes of major kink folds. c) 22 great circles of fault planes.

1.7b) with a kink geometry (**Fig. 1.8a**), observed mainly near cataclastic bands (**Fig. 1.8b**). Metamorphic rocks are intensely affected by brittle deformation characterised by well-developed fine-grained cataclasites that in some cases consist of fault breccia and gouge (**Fig. 1.8b**). Brittle fault planes are mainly oriented N 140° (**Fig. 1.7c**) and can be followed along strike for several meters in the field. Basement rocks are covered by conglomerates, arenites and clays of the middle-late Miocene transgressive sedimentary succession (Selli, 1957; Ogniben, 1962).

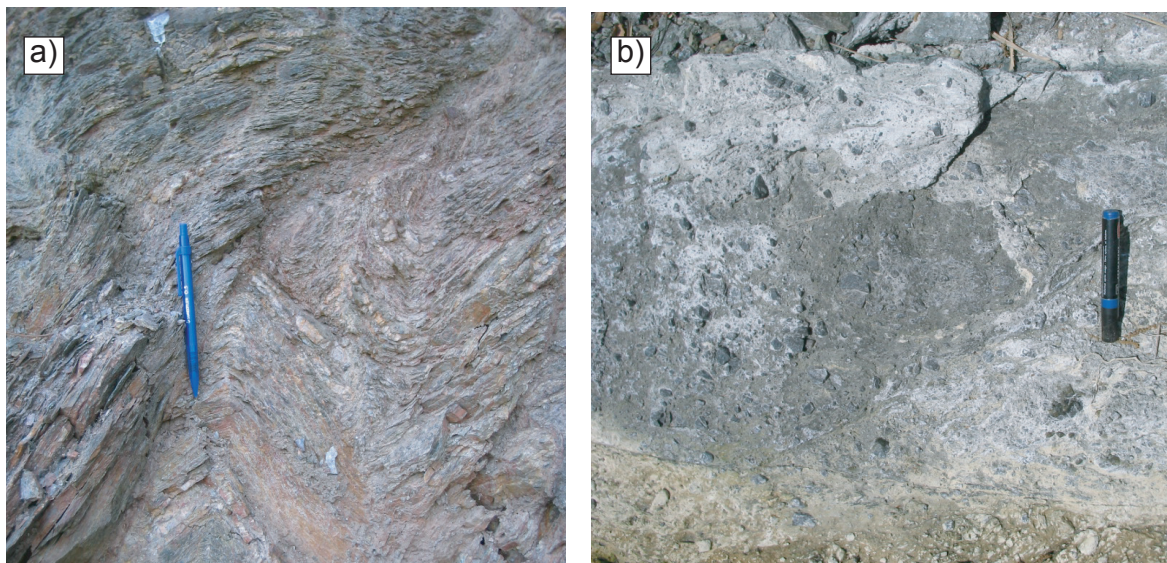


Fig. 1.8a, b: kink fold on a metavolcanite (a); fault breccia and fine-grained cataclasite derived from a metavolcanite (b).

Northwestern area (Sappo stream area).

As mentioned above, toward northwest structural and lithologic features of the Mandatoriccio complex are different. In the area comprised between Mandatoriccio, to the north, Scala Coeli, to the northeast, and Campana, to the southwest, micaschists and paragneisses are the dominant rock types (**Fig. 1.5**). Pegmatite and aplite veins are rare, whereas small granitoid bodies have been observed in several localities (*e.g.* Acero stream, Sappo stream, and Nicà river, **Figs. 1.5, 1.9a, b**). Granitoids, which are affected by intense brittle deformation (**Fig. 1.9b**), contain mafic enclaves (**Fig. 1.9b**) and are always associated to spotted schists with large porphyroblasts (**Fig. 1.9c**). These latter are characterised by biotite spots and large porphyroblasts of andalusite or cordierite undistinguishable at macroscopic scale. Commonly, the large porphyroblasts show cusped terminations. Spots and large porphyroblasts are imbedded in a fine grained white-mica-rich matrix.

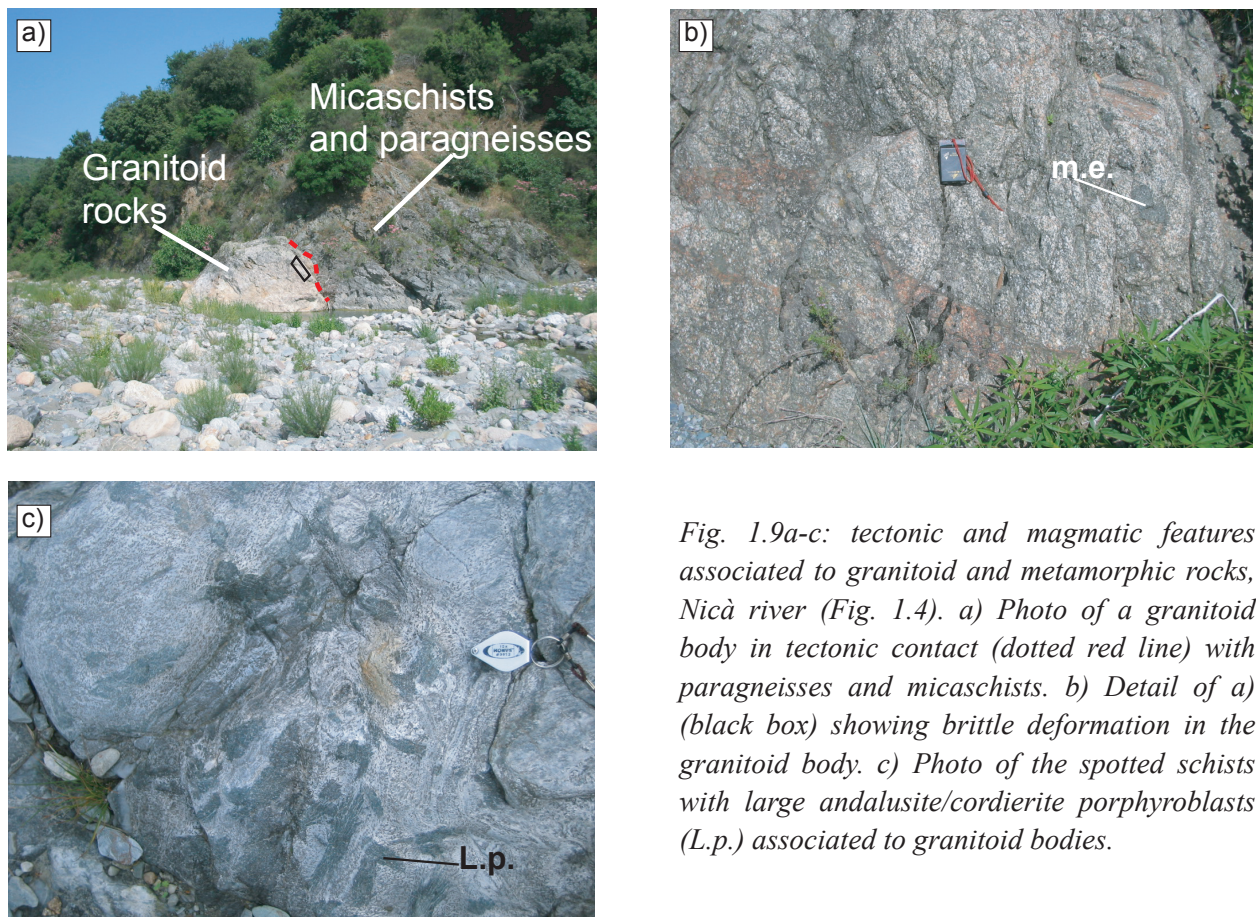


Fig. 1.9a-c: tectonic and magmatic features associated to granitoid and metamorphic rocks, Nicà river (Fig. 1.4). a) Photo of a granitoid body in tectonic contact (dotted red line) with paragneisses and micaschists. b) Detail of a) (black box) showing brittle deformation in the granitoid body. c) Photo of the spotted schists with large andalusite/cordierite porphyroblasts (L.p.) associated to granitoid bodies.

Micaschists and paragneisses are well-exposed along the SS 181 Silana road that connects Mandatoriccio and Campana villages and along the Sappo stream. They are characterized by well-developed compositional layering with alternating quartz- and mica-rich levels. Quartz veins and layers are frequent and in some cases show evidence of boudinage. Rarely, metavolcanites and amphibolites have been found along the Nicà river.

Structural data relative to Mandatoriccio complex outcropping in the northwestern area (Sappo stream area) are shown in **Figs. 1.10a-c**. Foliation planes strike from N-S to NW-SE and dip mainly toward the SW (**Fig. 1.10a**). Crenulations are oriented NW-SE with gentle plunges toward NW and SE (**Fig. 1.10a**). Axes of major folds observed near the main cataclastic bands show scattered orientation (**Fig. 1.10b**). Cataclastic bands have been largely observed during field work; they are related to faults striking broadly N120° and N160° with moderate to high dip angles (**Fig. 1.10c**). Brittle deformations have affected mainly micaschists and paragneisses and in some cases produced fine grained cataclastic bands. Metamorphic rocks are locally covered by marly or arenaceous red limestones of probable Jurassic age, and by middle- to upper-Miocene arenites.

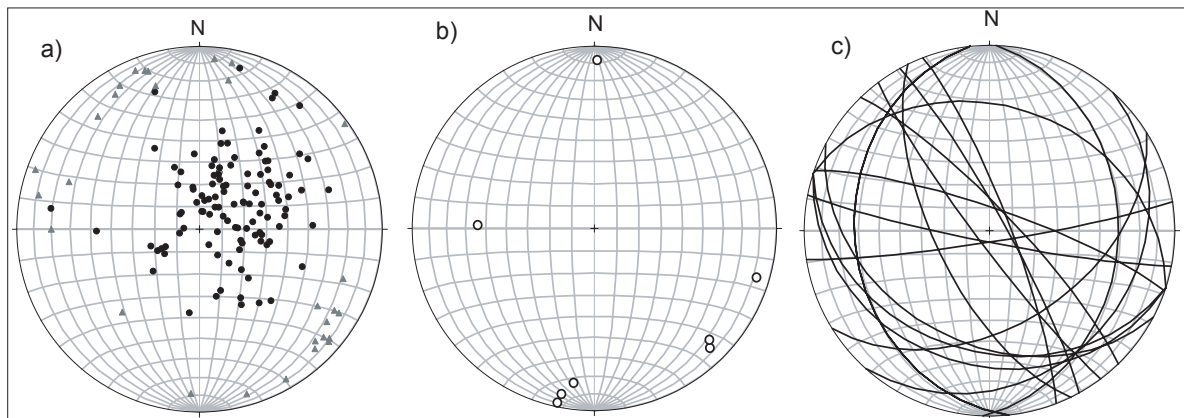


Fig. 1.10a-c: equal area projection (lower hemisphere) of structural data from the Mandatoriccio village area. a) Poles of 112 foliation planes; 29 crenulation lineations (triangles). b) 8 axes of major kink folds. c) 17 great circles of fault planes.

In the central and northwestern sector of the area (**Fig. 1.5**), the Bocchigliero complex is well exposed and consists mainly of phyllites with minor metabasites, metavolcanites, marbles and orthogneisses. Generally, in these low-grade rocks a regional S_2 foliation, preceded by an early S_1 schistosity (**Fig. 1.11a**), has been recognised. Relics of the S_0 foliation have been rarely observed. Phyllites and other low-grade rocks are strongly affected by brittle shear zones showing well-developed S-C shear bands (**Fig. 1.11b**).

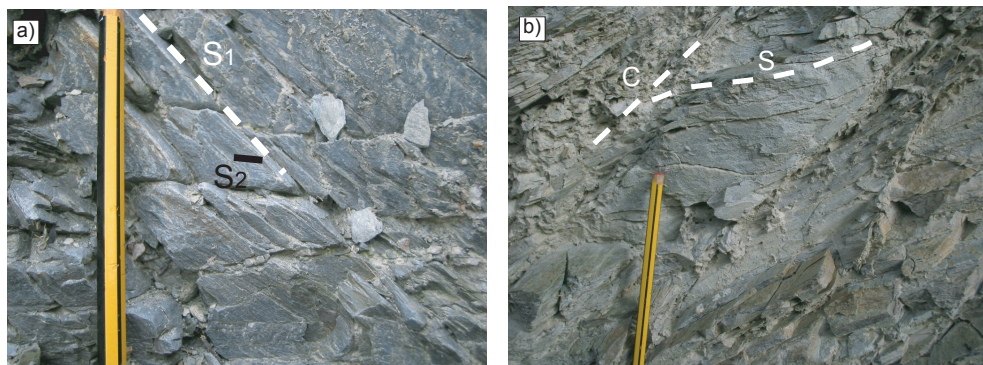


Fig. 1.11a-b: major features of the phyllites of the Bocchigliero complex. a) relationships between S_1 and S_2 foliations (Acero stream); b) S-C shear bands.

Structural data relative to phyllites of the Bocchigliero complex are shown in **Figs. 1.12a-b**. Poles to foliation planes show a weak clustering in the northeast quadrant indicating that planes dip mainly to the SW (**Fig. 1.12a**). Crenulation lineations are mainly oriented NW-SE with low angles of dip. Two axes of major folds are oriented coherently with crenulations, whereas other two axes show a nearly north-south orientation (**Fig. 1.12a**). Generally, fault planes are oriented NW-SE with moderate dips toward SW (**Fig. 1.12b**).

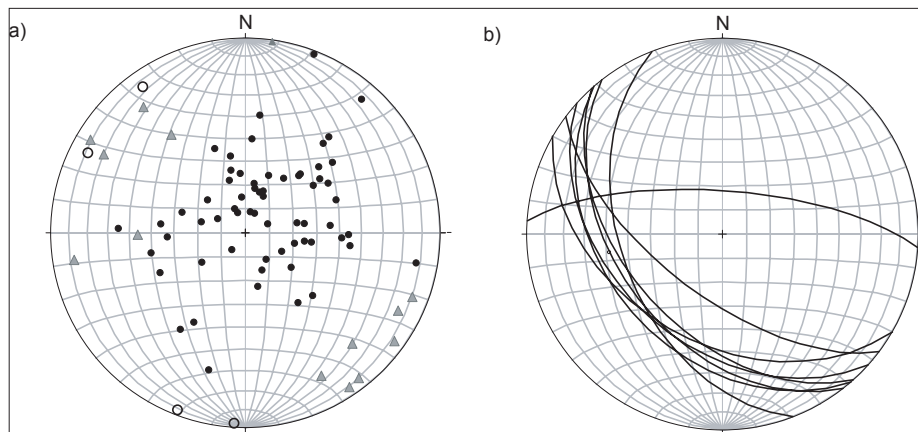


Fig. 1.12a-b: equal area projection (lower hemisphere) of structural data. a) Poles of 64 foliation planes (black circles); 14 crenulation lineations (grey triangles); 4 axes of major folds (empty circles). b) Great circles of 8 fault planes.

In the Sappo stream area, the Palaeozoic sequence of the Bocchigliero complex and, in minor extent, the metamorphic rocks of the Mandatoriccio complex show a Mesozoic sedimentary cover (**Figs. 1.5; 1.13a; 1.13b**). Metamorphic rocks are covered by red marly or arenaceous limestones of Jurassic age (Lias), rarely containing ammonites and angular clasts of phyllites (**Fig. 1.13c**). In turn, metamorphites and Mesozoic sediments are widely covered by middle- to upper-Miocene arenites and conglomerates (**Figs. 1.5; 1.13a**).



Fig. 1.13a-c: a) phyllites of the Bocchigliero complex and its Meso-Cenozoic sedimentary cover. View from the Campana village (Fig. 1.4) looking toward southeast. Black square indicates location of b) illustrating a detail of a). c) Red marly or arenaceous limestones with angular clasts of phyllites.

The tectonic contact between the Bocchigliero and the Mandatoriccio complexes has been observed in different localities in the studied area (*e.g.* the Nicà river, the Sappo and Acero streams). The two metamorphic complexes are always separated by thick bands of grey cataclasites mainly oriented NW-SE (**Fig. 1.5**). Brittle deformation affects plutonic rocks observed along the tectonic contact. However, contrary to the observations of Lorenzoni & Zanettin-Lorenzoni (1979) and Borghi *et al.* (1992), the tectonic contact is never intruded by granitoids, indicating that brittle deformation post-dated the Hercynian orogeny.

Field work revealed that cataclastic bands can be subdivided in two generations. The first generation is oriented about N160° and is sutured by Miocene deposits (**Fig. 1.5**), whereas the second generation trends about N120° and affects also the Miocene sedimentary cover (**Fig. 1.5**). Following Van Dijk *et al.* (2000), in the studied area a NW-SE trending oblique transcurrent fault zone, identified as the San Nicola-Rossano Fault Zone (SRFZ), can be recognised. According to Van Dijk *et al.* (2000), this fault zone was active at least from middle-Miocene to Recent and can be linked to the collision of the Calabria-Peloritani terrane with the Apennine chain.

1.4.2 – Cropalati-Caloveto area

Studied outcrops are located mainly along a segment of the Trionto river that separates Caloveto from Cropalati villages (**Figs. 1.3; 1.14a**). In this small area phyllites of the Bocchigliero complex prevail with respect to metasedimentary rocks of the Mandatoriccio complex. In particular, the latter consists only of schists with porphyroblastic texture (spotted schists with large porphyroblasts) outcropping near the bridge of the S.S Silana (km 11-12) and along the south-eastern bank of the Trionto river. The large porphyroblasts are randomly oriented and show a dark-grey/dark-green colour and are surrounded by light-grey white-mica-rich matrix. On a macroscopic scale the composition of the large porphyroblasts is not recognisable and texturally these porphyroblasts seem to be compatible both with andalusite and cordierite. On the foliation planes small biotite spots are also visible. A small body of granitoid rocks outcrops in the north-western bank of the Trionto river. Phyllites and spotted schists with large porphyroblasts show foliation planes gently dipping toward SE (**Fig. 1.14b**), whereas measured crenulations are oriented NW-SE with shallow plunge angles (**Fig. 1.14b**).

The tectonic contact between Bocchigliero and Mandatoriccio complexes is not exposed and the juxtaposition seems to be related to brittle faults developed during Alpine-Apennine deformation. Metamorphic rocks are covered by sandstones of middle- to upper-Miocene age and turbidite sandstones of Oligocene-Aquitania age (Paludi formation; Zuffa & De Rosa, 1978; Bonardi *et al.*, 2005).

Petrographic and petrologic studies have been performed only on spotted schists with large porphyroblasts, in order to define the significance and the metamorphic evolution of

these rocks (cf. 2.3.2).

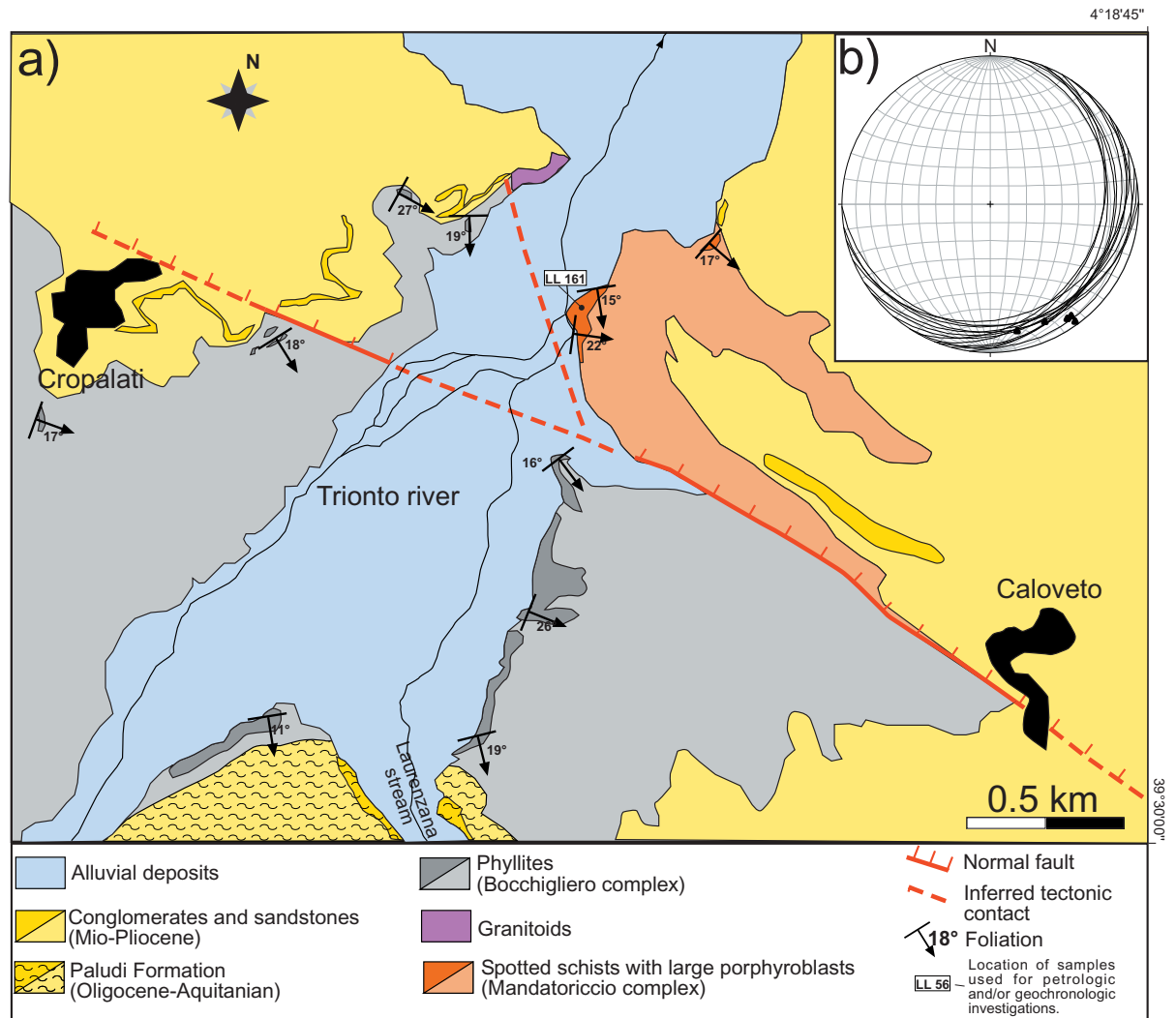


Fig. 1.14a, b: a) geological sketch map of the Cropalati-Caloveto area, based on original 1:10000 mapping (Cropalati - I.S.W., C - S.230). Darker tonalities refer to outcrops. b) Equal area projection (lower hemisphere) of 25 foliation planes (great circles) and 5 crenulation lineations (triangles).

CHAPTER 2 – PETROGRAPHY AND MICROSTRUCTURES OF ROCKS OF THE MANDATORICCIO COMPLEX

Petrographic and microstructural analyses have been focused on main rock types of the Mandatoriccio complex.

Firstly, these analyses resulted very helpful to define protoliths, mineral assemblages and parageneses; secondary, they have been fundamental in order to recognise reaction textures and to reconstruct relationships between deformation and crystallisation. Different generations of minerals have been also constrained by chemical microanalyses, whereas protoliths of interesting samples have been well established by whole-rock chemical analyses.

Metapelitic rocks are of particular importance for petrographic, microstructural and petrologic investigations because they sensibly develop a wide range of distinctive minerals in response to changes in P-T conditions. In addition, metapelitic rocks are very able to record and preserve different deformational events and, for these reasons, they are very useful to reconstruct the tectono-metamorphic history. However, metapelites, or more generally metamorphic rocks, that have experienced medium- to high-temperature metamorphic events recorded only limited information about preceding thermal stages. These information are mainly related to mineralogy and chemical composition of inclusions in porphyroblasts, chemical zoning of porphyroblasts, pseudomorphs and other reaction textures. On the other hand, morphology of inclusion trails in porphyroblasts (Zwart, 1962; Bell & Rubenach, 1983; Lang & Dunn, 1990), relationships between inclusion trails and external or matrix foliation can be analysed to unveil deformation paths.

Petrographic and microstructural analyses have been performed combining observations provided by optical microscope with BSE (Back Scattered Electrons) images and X-ray element maps acquired with a SEM (Scanning Electron Microscope). Microdomains of reaction and zoned crystals have been studied almost exclusively using classified images obtained from X-ray element maps (**Appendix 3**). In some cases, reaction textures occupy a large portion of the analysed thin sections. Therefore, it has been necessary to make a mosaic of X-ray maps to cover a significant portion or the entire reaction texture. Smaller X-ray maps have been acquired to point out chemical zoning of petrologic interesting mineral phases such as garnet, staurolite, biotite and cordierite. RGB (Red Green Blue) images constructed using X-ray maps relative to Ca, Fe and Mn distribution have highlighted compositional zoning of garnet. Mg has been ignored due to its low abundance in garnet crystals. X-ray maps have been also acquired to unravel chemical variation of porphyroblasts related to reactions. Compositional changes of the outer parts have been also used in the mass balance calculations in order to define mineral reactions.

Petrographic and microstructural studies, performed with optical and electron

microscope, have been preliminary for planning microprobe analyses. In particular, RGB maps and classified images of reaction domains revealed major phases involved in the reactions, whereas X-ray element maps resulted essential to select the best chemical profile through zoned crystals, such as garnet.

2.1 - METAVOLCANITES

They include leucocratic schists and gneisses with porphyroclastic texture of volcanic origin (rhyolites, dacites, Acquafredda *et al.*, 1988, 1991). Porphyroclasts, mainly represented by feldspars, biotite, quartz-feldspar aggregates, quartz-biotite aggregates and quartz aggregates, are surrounded by alternating mica- and quartz-rich layers. In some cases, large porphyroclasts are very abundant conferring an augen texture to the rocks. Mica- and quartz-rich layers define the main regional foliation (S_2) and contain microlithons in which it is possible to recognise an early crenulated foliation (S_1) defined by quartz, plagioclase, biotite and muscovite. Apatite, epidote, zircon, opaques and rarely garnet are present as accessory phases. Biotite and muscovite are particularly abundant in metarhyolites and are chiefly present as small plates. Porphyroclasts of biotite have been also recognised and are characterised by sigmoidal shapes and lobed contours more pronounced in quartz-rich layers. Locally, biotite crystals are partially or totally replaced by chlorite. Porphyroclasts of plagioclase and K-feldspar can reach significant dimension (up to 4 mm), they have euhedral to sub-euhedral habit with rounded contours and can show twinning and exsolution lamellae. Biotite, muscovite and epidote can be present as inclusions. Often, feldspars are cloudy because entirely replaced by very-fine-grained alteration products.

Locally, a weak mylonitic fabric characterised by undulose extinction of feldspar and quartz, deformation bands and subgrain boundaries of quartz has been recognised.

2.2 - AMPHIBOLITES

In this section are described amphibole-bearing rocks with schistose or gneissic fabric. Amphibolitic schists can be also subdivided in granolepidoblastic and porphyroblastic schists. Amphibolites are very abundant in the southeastern part of the studied area, around the Umbriatico village (**Fig. 1.5**). Generally, they are present as lenses, with thickness of about some meters, interlayered and sub-concordant with micaschists and paragneisses. They preserve a clear Hercynian metamorphic fabric and they are overprinted by later micro-folding events. These rocks are characterised by a fine-grained assemblage of plagioclase, quartz, and amphibole. In minor extent, biotite, opaques, titanite, zircon, and apatite occur. Chlorite has been recognised as retrograde product whereas calcite forms later veins. Generally, titanite occurs around Fe-Ti oxides. Porphyroblastic-amphibolite schists are characterised by large amphibole crystals with near sigmoidal shapes. Commonly, the amphibole porphyroclasts show static overgrowths that crosscut the S_2 foliation (**Fig. 2.1a**) and they are characterised by pressure shadows composed of quartz, plagioclase and small

crystals of amphibole. Compositional bands composed of amphibole-rich layers and Pl+Qtz-rich layers are commonly observed. Amphibole occurs as euhedral or subhedral grains and is commonly elongated with its crystallographic c -axes in the direction parallel to the foliation (S_2). Locally, amphibole is oriented perpendicularly with respect to S_2 schistosity (**Fig. 2.1b**). The studied porphyroblastic-amphibolite schists contain limited information about

deformation-crystallisation relationships. Two textural generation of amphibole have been found in these rocks. Small crystals aligned parallel to the foliation and porphyroclasts wrapped by the foliation show evidence of pre- to syntectonic growth (Amph I, **Figs. 2.1a, b**). Unfortunately, porphyroclasts do not contain a large variety of

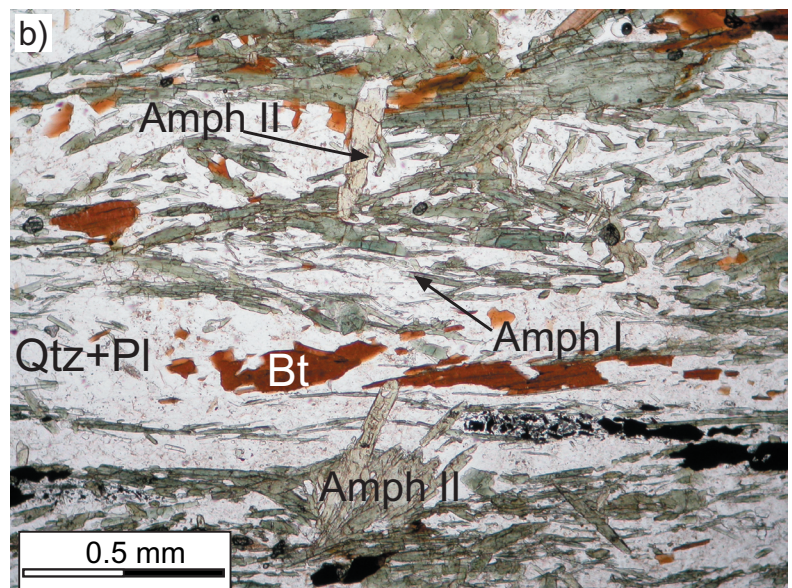
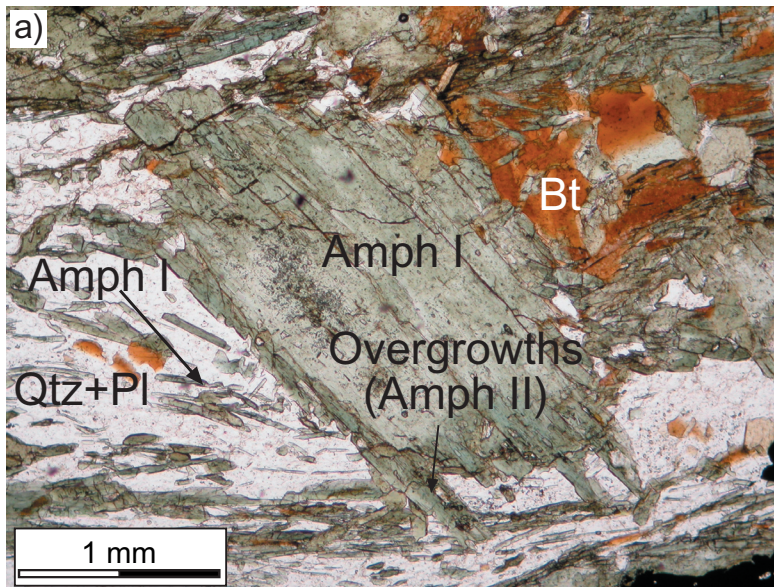


Fig. 2.1a, b: plane-polarised light microphotographs of amphibolites. a) Amphibole porphyroblast (Amph I) with overgrowths (Amph II) that crosscut foliation planes; b) amphibole crystals perpendicular to foliation planes.

inclusions and therefore they are not very helpful for microstructural analyses. Only small straight aligned opaque inclusions can be found in porphyroblasts and, generally, they are oriented at high angle with respect to the external foliation, without evidence of continuity. Amphibolites recorded a post-tectonic crystallisation event highlighted by new amphibole crystals and overgrowths around old porphyroclasts that cross cut S_2 schistosity (Amph II **Figs. 2.1a, b**).

Whole-rock analyses (**Table 1** in **Appendix 2**) suggest that most amphibolites fall within the field of basic rocks (**Fig. 2.2a**) with dominant basaltic composition (**Figs. 2.2b, c**).

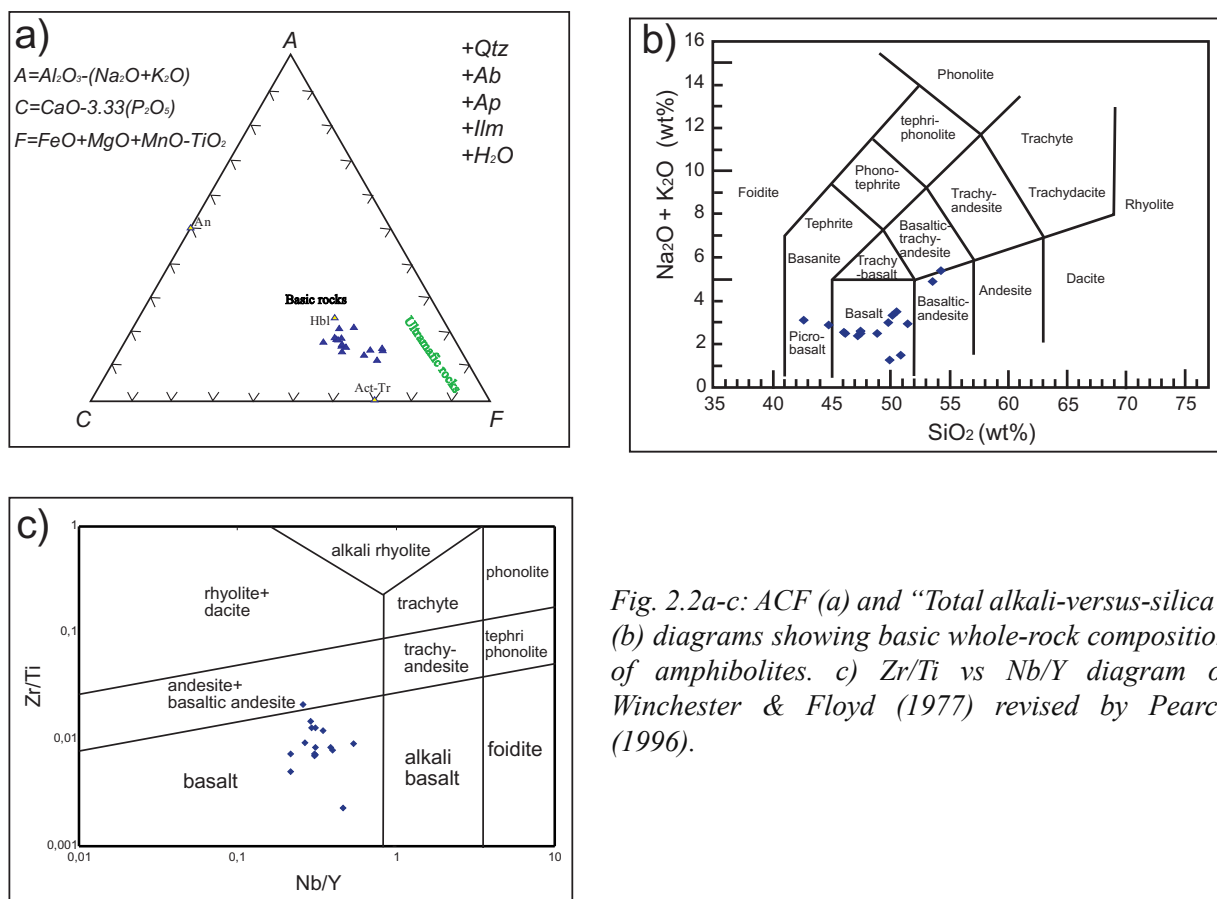


Fig. 2.2a-c: ACF (a) and “Total alkali-versus-silica” (b) diagrams showing basic whole-rock composition of amphibolites. c) Zr/Ti vs Nb/Y diagram of Winchester & Floyd (1977) revised by Pearce (1996).

2.3 - METAPELITES AND META-ARENITES

Samples have been classified following macroscopic, microscopic and chemical features.

Major element composition of representative samples (**Table 2** in **Appendix 2**) have been used to classify rocks using the diagram proposed by Herron (1988), based on $\text{SiO}_2/\text{Al}_2\text{O}_3$ and $\text{Fe}_2\text{O}_3/\text{K}_2\text{O}$ ratios and CaO concentration in rocks (**Fig. 2.3**). A large part of analysed samples falls in the field of shales with almost constant values of $\text{Fe}_2\text{O}_3/\text{K}_2\text{O}$ and variable $\text{SiO}_2/\text{Al}_2\text{O}_3$ ratios (**Fig. 2.3**), only a typical quartz+plagioclase-rich layer of paragneiss (LL61a2) differs significantly from other samples. Following Herron (1988) classification, studied rocks are noncalcareous ($\text{CaO} < 4\%$) except for three cases (LL42b, LL80, LL122) with CaO slightly higher than 4% (**Table 2** in **Appendix 2**). Chemical compositions and protoliths are comparable with those relative to rocks ascribed at the same metamorphic complex outcropping northwards with respect to the studied areas, obtained by Caggianelli & Prosser (2001, Fig. 10.5a).

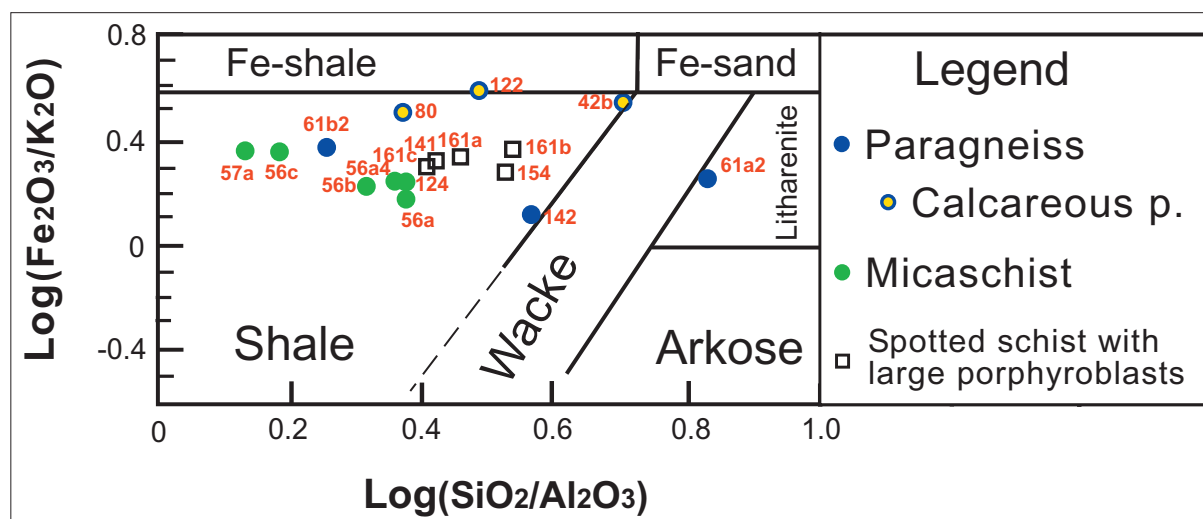


Fig. 2.3: chemical classification diagram proposed by Herron (1988) for clastic terrigenous sediments here used to infer protoliths of siliciclastic metasediments.

Molar proportions obtained from major element concentrations have been used to represent the relationships between rock compositions and mineral assemblages, in classical triangular diagrams (**Figs. 2.4a-d**). ACF, A'KF and AFM diagrams show that paragneiss compositions are scattered, confirming heterogeneous appearance observed in the field. Micaschists and schists with static growth make two different clusters in the field of shales. In particular, porphyroblastic rocks show a more Al-rich trend with respect to micaschists. On the basis of chemical analyses and macroscopic features, siliciclastic metasediments have been subdivided in three main groups: micaschists, paragneisses and spotted schists with large porphyroblasts. Detailed petrographic and microstructural analyses have been focussed on these three rock types.

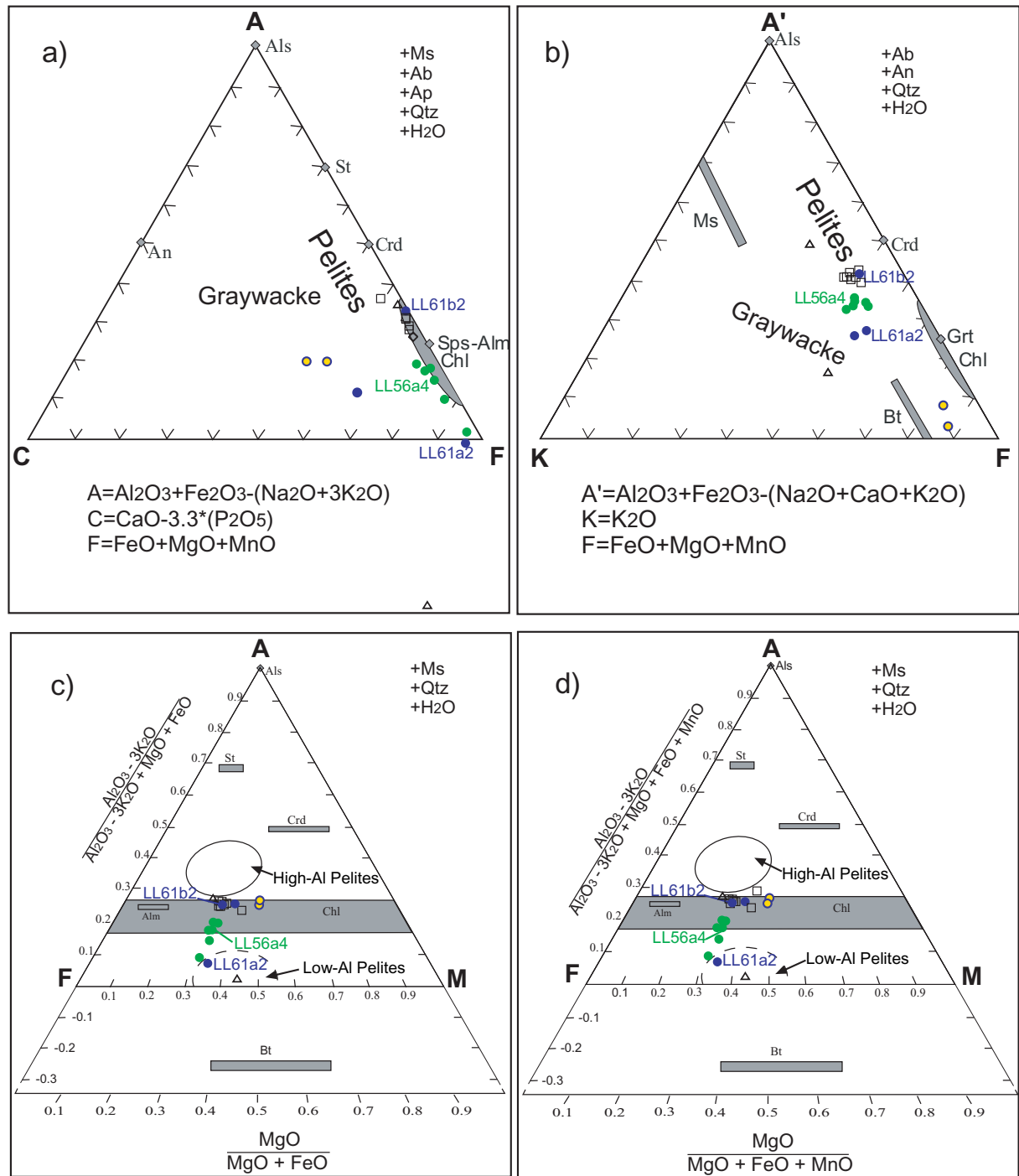


Fig. 2.4a-d: chemographic diagrams of whole rock compositions (Table 2-Appendix 2) and representative theoretical compositions of some interesting phases. In the diagrams are specified only samples used for P-T calculations. For symbols, see legend in Fig. 2.3. In ACF diagram (a) are highlighted calcareous lithologies whereas A'KF is very helpful to discriminate aluminous metasediments. AFM projections (c, d) indicate that a large part of samples fall between low-Al pelite and high-Al pelite fields (field positions after Spear, 1993). The addition of MnO in the AFM projection (d) do not changes significantly the position of whole-rock compositions with respect to classical AFM projection (c).

2.3.1 - Micaschists and paragneisses

Micaschists and paragneisses have been differentiated mainly on the basis of macroscopic and field observations. Micaschists have a well-pronounced schistosity characterised by large biotite flakes. These rocks show a medium grain size differently from paragneisses that are characterised by a matrix with a fine grain size and a gneissic layering. Biotite-rich layers alternating with quartz+plagioclase-rich layers outline the latter. Micaschists and paragneisses are composed of quartz, muscovite, biotite and plagioclase. Garnet, andalusite and staurolite have been founded as porphyroblasts, whereas ilmenite, titanite, apatite and tourmaline are present as accessory phases. Fibrolitic sillimanite and cordierite porphyroblasts occur exclusively within paragneisses outcropping in few localities (**Fig. 1.5**). The larger mineral assemblages Qtz+Ms+Bt+Pl+Grt+St+And and Qtz+Ms+Bt+Pl+Grt +St+And±Crd±Fib (mineral abbreviation are listed in **Table 3** of **Appendix 3**) are typical of micaschists and paragneisses, respectively. These rocks outcrop in the southeastern part of the studied area, around the Umbriatico village (**Fig. 1.5**). Northwestward, a Qtz+Ms+Bt+Pl+St+And assemblage has been recognised only in a cataclastic paragneiss (LL05) sampled in the Sappo stream, near the Mandatoriccio village (**Fig. 1.5**).

2.3.1.1 - Micaschists

Micaschists are mainly composed of biotite, muscovite, quartz, andalusite, plagioclase, garnet and staurolite. Minor amounts of chlorite, apatite, tourmaline, zircon, monazite and oxides have been observed. Rarely, staurolite contains inclusions of corundum (LL57). These rocks show a porphyro-lepidoblastic texture characterised by the presence of biotite, garnet, staurolite and andalusite porphyroblasts set in a mica-rich matrix.

Garnet. Euhedral to anhedral small (diameter < 3mm) crystals of garnet generally show a turbid inclusion-rich core surrounded by almost inclusion-free rims (**Fig. 2.5a**). Cores contain both solid and fluid inclusions. These latter, easily recognisable because of their continuous Brownian motion, are responsible for the turbid aspect (**Fig. 2.5a**).

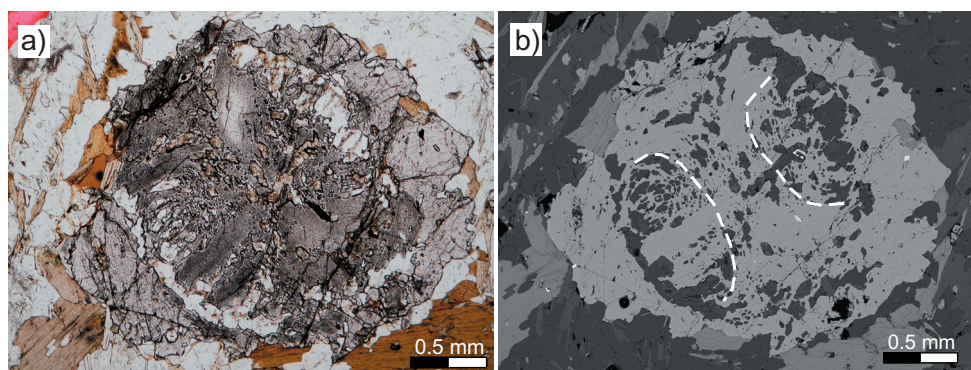


Fig. 2.5a, b: plane-polarised light microphotograph (a) and BSE-images (b) of garnet (LL56a1) showing inclusion-rich turbid core; inclusion-free rims. BSE-image emphasizes ∇C inclusion pattern indicating section cuts parallel to, and containing, the rotation axis of garnet (Barker, 1990).

Solid inclusions have different nature being represented by quartz, biotite, plagioclase, muscovite, ilmenite, and minor, chlorite, tourmaline, zircon, monazite, and K-feldspar. Most examined garnet crystals show evidence of syntectonic growth. Curved inclusion trails, strain shadows and deflected external foliation around porphyroblasts are the main features used to define this stage of growth. During syntectonic development of garnet, earlier stages of crenulation cleavage have been preserved in the core of crystals as sigmoidal or curved inclusion patterns (**Figs. 2.5a, b**; Bell & Rubenach, 1983). Often, almost inclusion-free rims surround syntectonic cores. In some cases, these rims are very narrow (few microns). Generally, inclusion-free rims overgrew mica-rich layers that, in turn, have been mimetically replaced by andalusite porphyroblasts (**Figs. 2.6a, b**).

In some samples, garnet crystals have an oval shape and are inclusion-free. Rarely, they are completely or partially enclosed in staurolite porphyroblasts (**Fig. 2.6c**). In these cases, a thin shell of andalusite separates garnet from the outer staurolite.

In several samples, garnet appears completely or partially pseudomorphosed by biotite, white mica, quartz and plagioclase aggregates (**Fig. 2.6d**). The degree of the replacement could be variable in the same sample and, generally, is a function of the matrix composition around garnet. In fact, crystals in mica-rich layers are more commonly replaced than those surrounded by quartz and plagioclase. This microstructure is often associated to reactions developed during retrograde metamorphism.

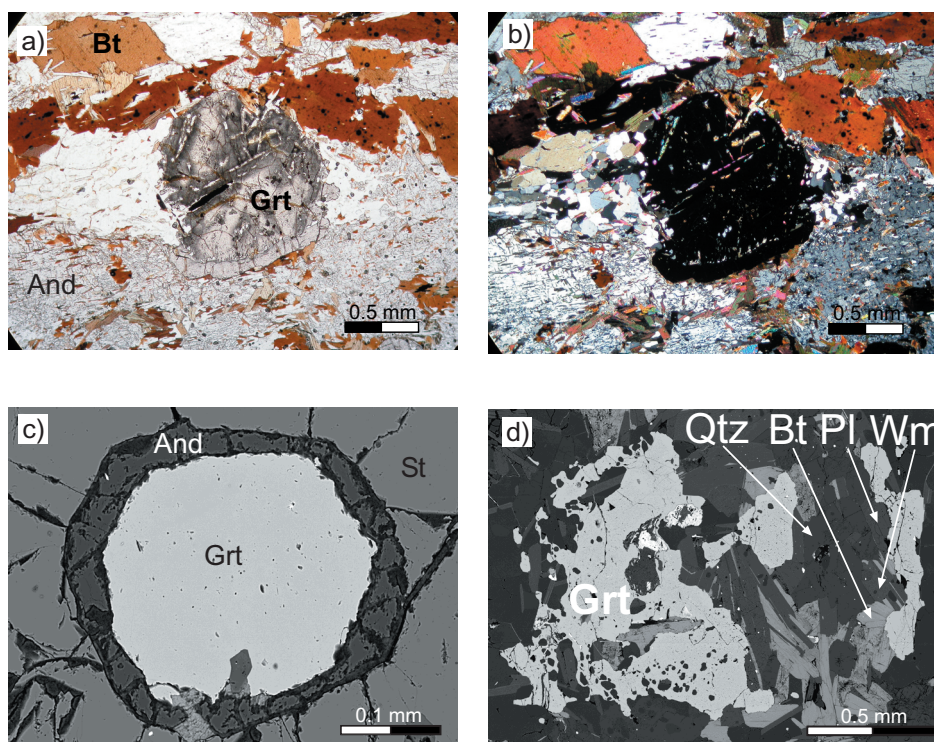


Fig. 2.6a-d: plane-polarised light (a) and crossed-polarised light (b) microphotographs of garnet crystal with inclusion-free static rims overgrew on mica-rich layers subsequently replaced by andalusite porphyroblasts (LL56b). c) BSE-image of small garnet included in staurolite. d) BSE images showing partially pseudomorphosed garnet.

X-ray maps showed that most garnet crystals have common chemical features. In order to obtain information about chemical zoning of garnet, maps relative to Ca, Fe and

Mn distributions have been combined to construct RGB images. Generally, garnet show a compositional zoning characterised by Fe increase from core to rims and antithetic distribution of Mn and Ca (**Figs. 2.7a-d**). Mg concentration is very low and compositional zoning is less visible. This pattern of chemical zoning could be explained with a fractional crystallisation model of garnet growth (Spear, 1993). Generally, the outer parts of rims (only few microns) show an inverse zoning pattern (**Figs. 2.7a, c**) that could be interpreted as consequence of diffusion during retrogression.

Actually, Ca-distribution has a more complex pattern. Generally, grossular component is very low but some crystals have sectors and/or cores with high-Ca content compared with remaining garnet portions (**Figs. 2.7b, d**). X-ray maps of several garnets show that these higher-Ca portions are always associated to plagioclase-inclusion rich crystals. Instead, porphyroblasts devoid of Ca-rich zones are characterised by low abundance of plagioclase inclusions and of plagioclase grains in the surrounding matrix (**Figs. 2.7a, c**). Patchy distribution of Ca could be considered as resulting from the absorption of anorthitic plagioclase during garnet growth, whereas the presence of grossular-rich cores with sharp limits could be ascribed to inherited pre-tectonic grossular-rich grains.

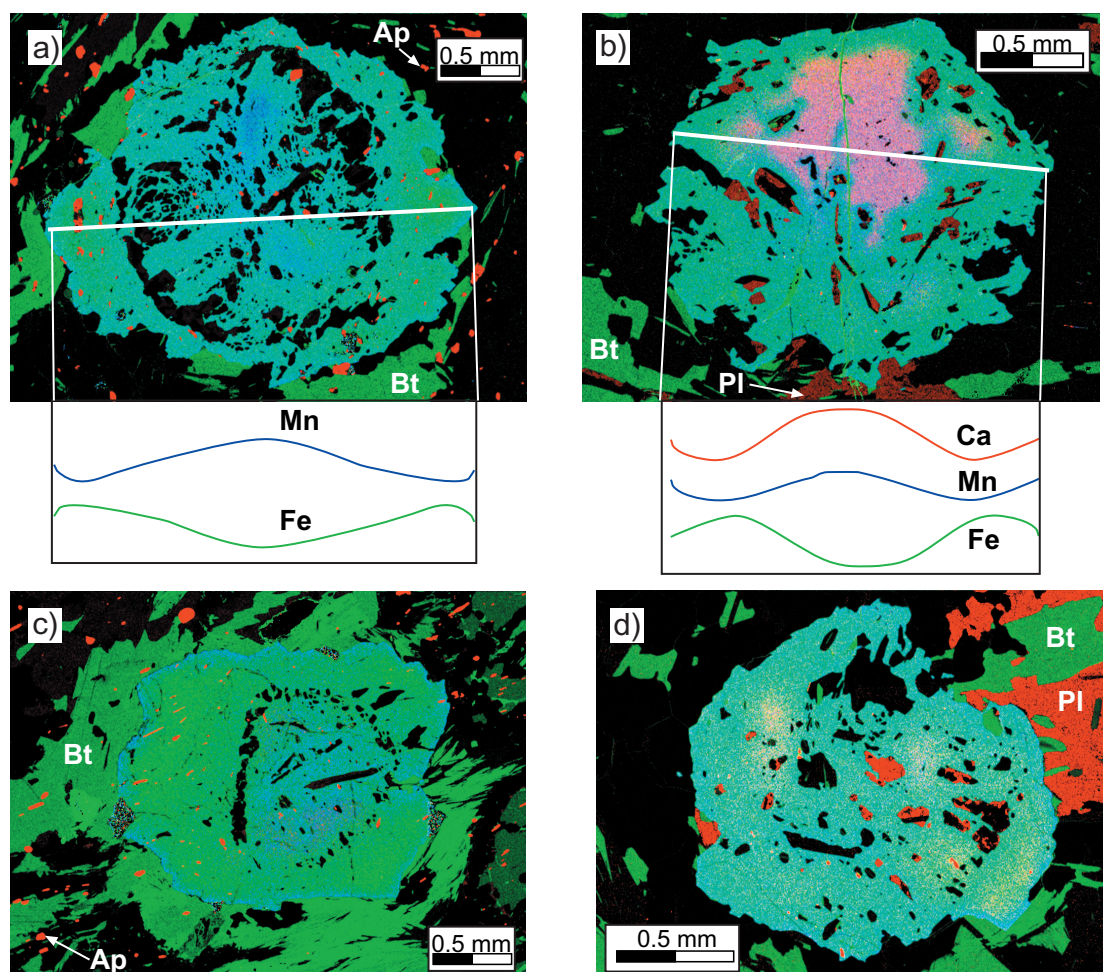


Fig. 2.7a-d: RGB images of garnet crystals relative to Ca (Red), Fe (Green) and Mn Blue) distribution, respectively (LL56). a) and b) contain also two schematic profiles. See text for explanations.

Biotite. In all the samples, it is possible to recognise at least three main textural generations of biotite. Small inclusions of biotite in garnet and medium sized lepidoblasts oriented along the main foliation (S_2) crystallised during the D_2 deformation (Bt I). The second generation (Bt II) is represented by large porphyroblast, up to 5 mm in length, crystallised after D_2 deformation as documented by the orientation of their cleavages perpendicular or oblique to S_2 (**Fig. 2.8**). Often, biotite porphyroblasts

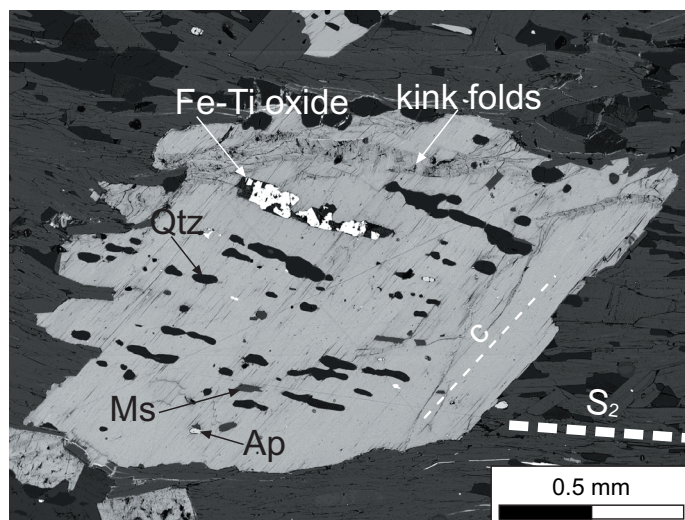


Fig. 2.8: BSE-image of biotite porphyroblast mimetically overgrew on mica-rich layer showing inclusions trails parallel to S_2 foliation and cleavages (C) oblique to schistosity (LL56a3). Kink folds of the cleavages are also visible.

(Bt II) grew mimetically over muscovite-rich layers and contain remnants of muscovite, quartz, plagioclase, oxides, tourmaline, apatite and monazite that are aligned and continuous with external foliation. A later generation of biotite (Bt III) could be represented by small crystals intergrown with andalusite replacing staurolite porphyroblasts.

A later deformational event (D_3), in lower greenschist facies, is recognisable mainly in biotite porphyroblasts (Bt II). D_3 produced kinking and/or deflection of cleavage planes, accompanied by partial chloritisation.

Staurolite. It is typically represented by large porphyroblast; more rarely, it occurs as small relict crystals (**Figs. 2.9a-d**). Porphyroblasts are oriented with their basal section perpendicular to the main foliation (S_2). Weakly developed inclusion trails are sub-parallel with external foliation. Inclusions are mainly represented by Fe-Ti oxides and in minor amount by apatite, quartz, plagioclase, chlorite, tourmaline, zircon and garnet. Only in a silica-poor domain of the LL57 sample (**Figs. 2.10a-b**), a staurolite porphyroblast contains small relicts of corundum separated from it by an andalusite shell. Its rare occurrence

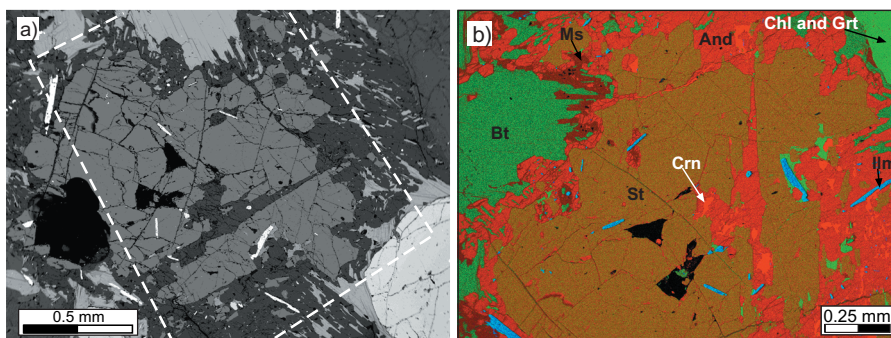


Fig. 2.9a, b: images of staurolite porphyroblast containing corundum (LL57). a) BSE image, white dotted lines delimit area covered by X-ray maps. b) RGB image showing Al (Red), Fe (Green) and Ti (Blue) distributions.

and the unclear crystallisation-deformation relationships make enigmatic the origin of the corundum. As shown in **Figs. 2.9b** and **d** staurolite is always completely or partially replaced by andalusite+biotite aggregates. X-ray element maps of large domains containing staurolite revealed that staurolite is chemically unzoned. Moreover, classified images provided important information about replacement reactions, which will be the argument of a specific section (cf. 4.2). Considering all these features, crystallisation of staurolite probably took place after D_2 deformation, before andalusite crystallisation.

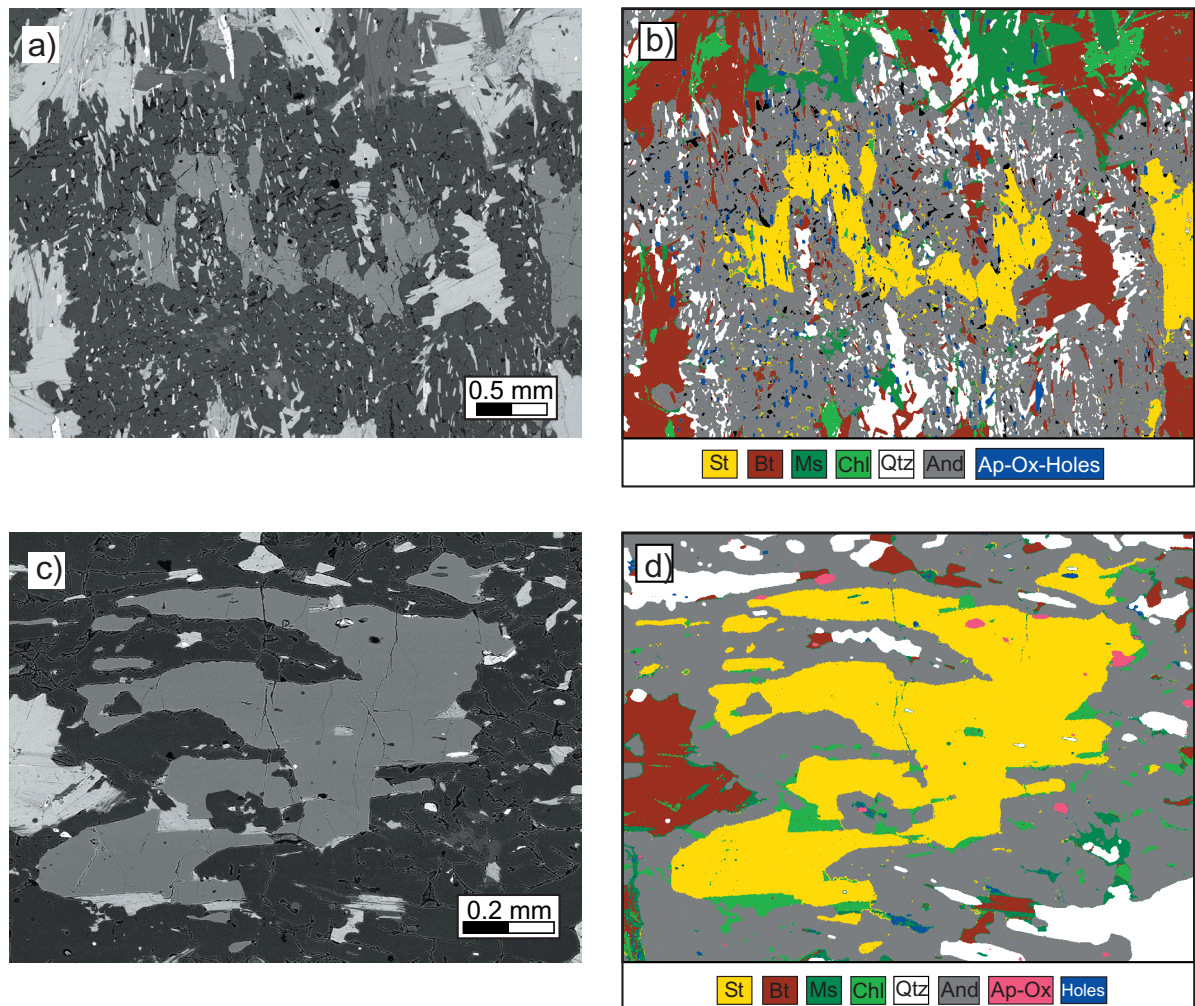


Fig. 2.10a-d: BSE images (a, c) and relative classified images (b, d) of relicts of staurolite porphyroblasts (LL56). See text for explanations.

Andalusite. This aluminosilicate is very abundant and typically it occurs as large poikilitic porphyroblasts (up to 6 cm in length), statically grown on the main S_2 foliation. Alternatively, andalusite grew around others porphyroblasts such as staurolite, garnet, biotite and plagioclase. Often, muscovite-rich layers are mimetically overgrown by poikiloblasts of andalusite. Retrogression caused partial or complete replacement of the aluminosilicate by cryptocrystalline aggregates of white mica.

Feldspars. Textural analyses revealed that plagioclase has a long crystallisation history since it can be pre-, syn- and post-tectonic. Plagioclase is well developed in matrix and it represents an important inclusion in garnet cores. As porphyroblast, it contains curved inclusion trails often continuous with matrix foliation (**Figs. 2.11a, b**). Typically, inclusions of muscovite, quartz, biotite, apatite, tourmaline and Fe-Ti oxides occur. X-ray maps of two syntectonic plagioclase crystals show the presence of albitic-rich core (**Figs. 2.11a, b**). Plagioclase is also visible as static mineral grown on the S_2 foliation (**Fig. 2.11c**). Only in one case, a single crystal of K-feldspar has been observed as inclusion in garnet and it has been interpreted as inherited crystal (of sedimentary origin).

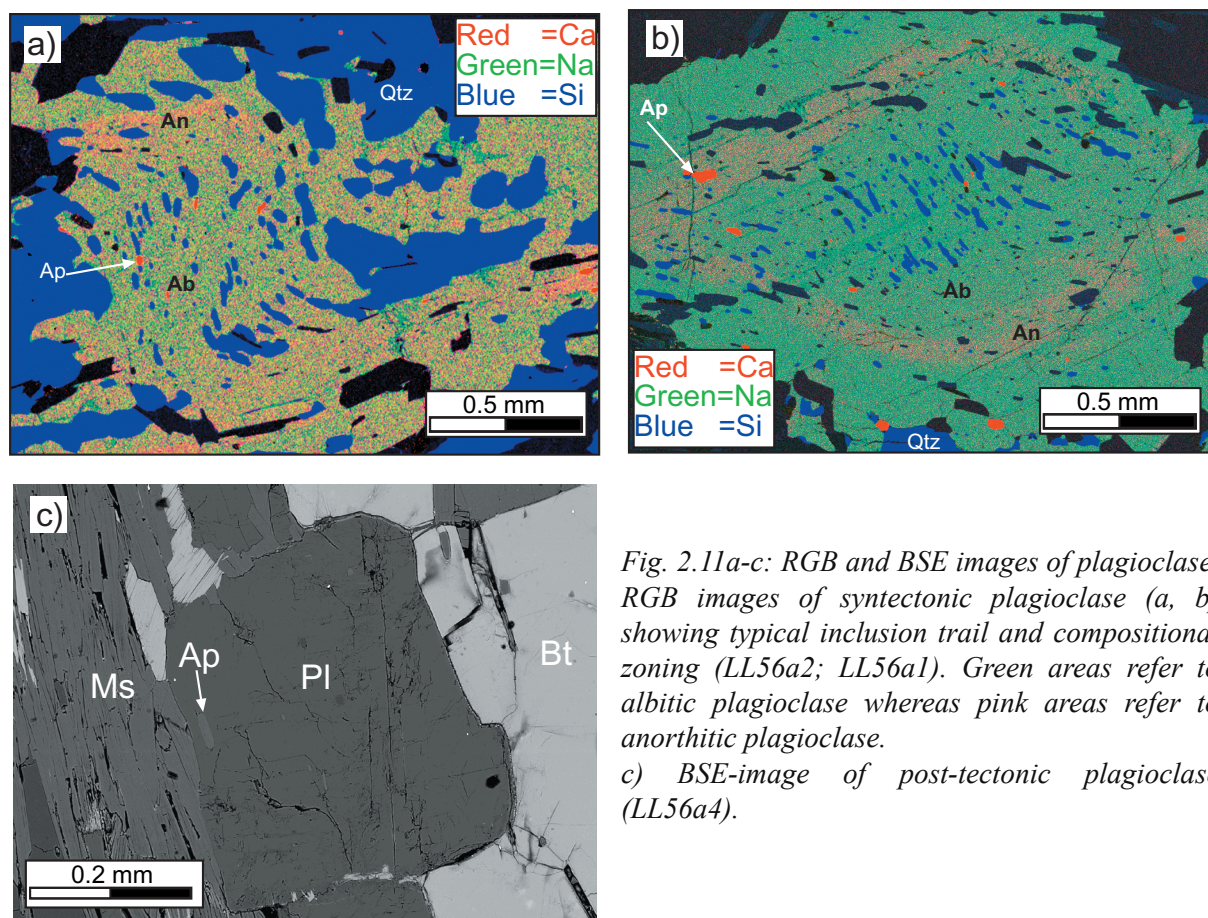


Fig. 2.11a-c: RGB and BSE images of plagioclase. RGB images of syntectonic plagioclase (a, b) showing typical inclusion trail and compositional zoning (LL56a2; LL56a1). Green areas refer to albitic plagioclase whereas pink areas refer to anorthitic plagioclase. c) BSE-image of post-tectonic plagioclase (LL56a4).

White mica. It is the most abundant phase where staurolite and andalusite porphyroblasts are absent. At least three generations of white mica have been recognised. Muscovite crystals included in syntectonic garnet and plagioclase could belong to an older assemblage (Ms I), whereas small elongated plates (Ms II) lying parallel to the regional S_2 foliation grew during D_2 deformation. Muscovite porphyroblasts (Ms III), less commonly than biotite, are oriented perpendicular with respect to S_2 schistosity. These porphyroblasts, sometimes poikilitic, have been considered as post-tectonic. Cryptocrystalline aggregates

of white mica that replace andalusite could be considered the last generation, related to later stages of retrograde metamorphism.

Chlorite. The majority of chlorite crystals constitute the products of retrograde reactions that involved biotite, garnet and, in minor extent, staurolite. Small crystals of chlorite have been recognised as inclusion in garnet and staurolite and have been considered as relict of the prograde metamorphic history.

Oxides. They are very abundant along the foliation planes (S_2) and show spindle shapes. Moreover, the occurrence of oxides as inclusions within main porphyroblasts (**Figs. 2.12a, b**) let to interpret they as pre- to syntectonic. Rarely, at the optical microscope they show anomalous interference colours. BSE images and EDS analyses revealed that spindle are often composed of aggregates of rutile and ilmenite (**Fig. 2.12a**) and in minor extent of quartz. In some cases, ilmenite show Ti-rich exsolution textures (**Fig. 2.12b**). Rarely, ThO_2 occurs as inclusion in biotite.

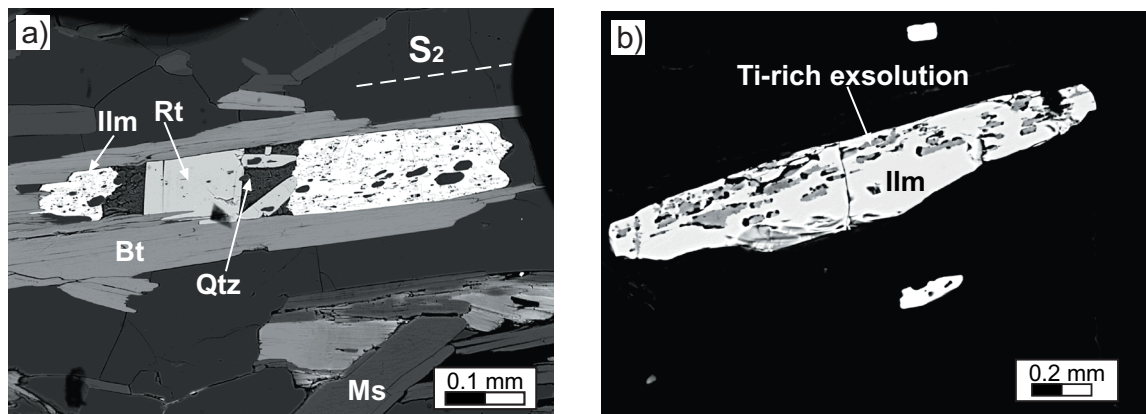


Fig. 2.12a-b: BSE images of pen-like opaques. a) Aggregate of ilmenite, rutile and quartz parallel to the foliation (LL56a2). b) Ilmenite included in staurolite showing Ti-rich exsolution textures (LL56a4). Exsolutions have been emphasized exaggerating contrast.

2.3.1.2 - Paragneisses

These rocks are characterised by two compositional layering. On a macroscopic scale, paragneisses show alternating centimetric thick (up to 8 cm) light (quartz+plagioclase rich) and dark (biotite-rich) layers (**Figs. 2.13a-d**). Each layer is further subdivided in alternating mica-rich and quartz+plagioclase-rich domains (**Figs. 2.13b, d**) that mark the

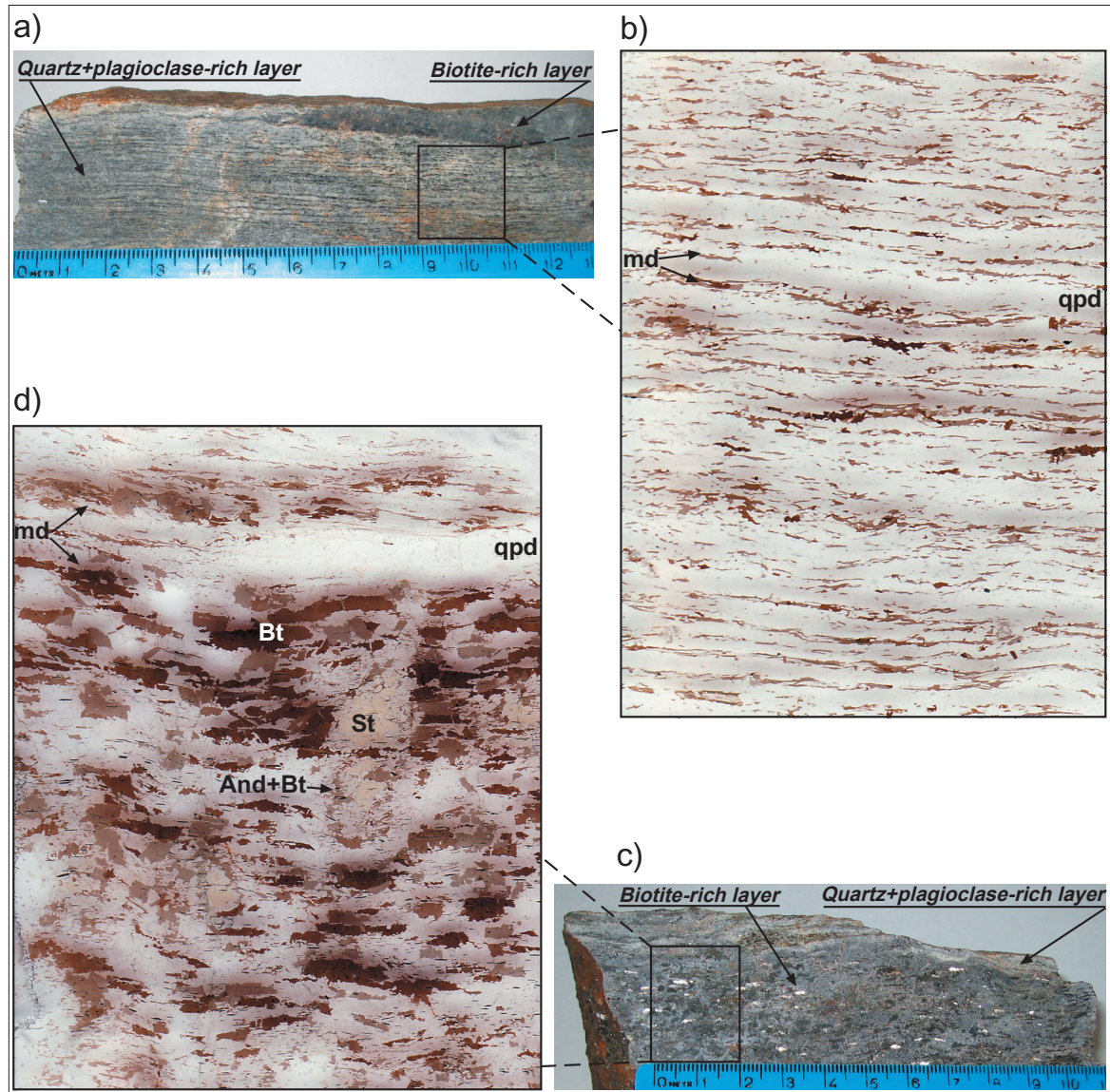


Fig. 2.13a-d: photos (a, c) and scans of thin sections (b, d) relative to LL61a Qtz+Pl-rich layer (a, b) and LL61b Bt-rich layer (c, d). Scans illustrate a further mineralogical alternation of mica-rich domains (md) and Qtz+Pl-rich (qpd) domains within both layers of paragneisses. Layers were in stratigraphic contact.

S_2 foliation. Two representative samples (LL61a2 and LL61b2) of the two layer types have been selected for XRF analyses (**Table 2** in **Appendix 2**). Classification diagram of Herron (1988) shows that these two types occupy different fields (**Fig. 2.3**): litharenite for the quartz+plagioclase-rich layer (LL61a2) and shale for the biotite-rich layer (LL61b2). Triangular diagrams (**Figs. 2.4a-d**) show that micaschists have intermediate chemical

composition between these two representative samples of paragneisses. The analysed biotite-rich layer (LL61b2), that contains altered cordierite porphyroblasts, tends to be closer to the theoretical cordierite composition (**Figs. 2.4a-b**).

Petrographic and microstructural features of biotite-rich and quartz+plagioclase-rich layers of paragneisses are very similar to those of micaschists. For this reason, only distinctive aspects of the paragneisses with respect to the micaschists are described in detail below.

Garnet. It is nearly absent in Bt-rich layers. In Qtz+Pl-rich layers, garnet shows pseudomorphic replacement mainly by biotite, muscovite, quartz and plagioclase (**Figs. 2.14a, b**). This replacement microstructure is generally attributed to retrograde reactions. As observed in micaschists, garnet contains countless fluid inclusions that confer a turbid aspect to the crystal cores (**Figs. 2.14a, b**). At small optical magnifications fluid inclusions

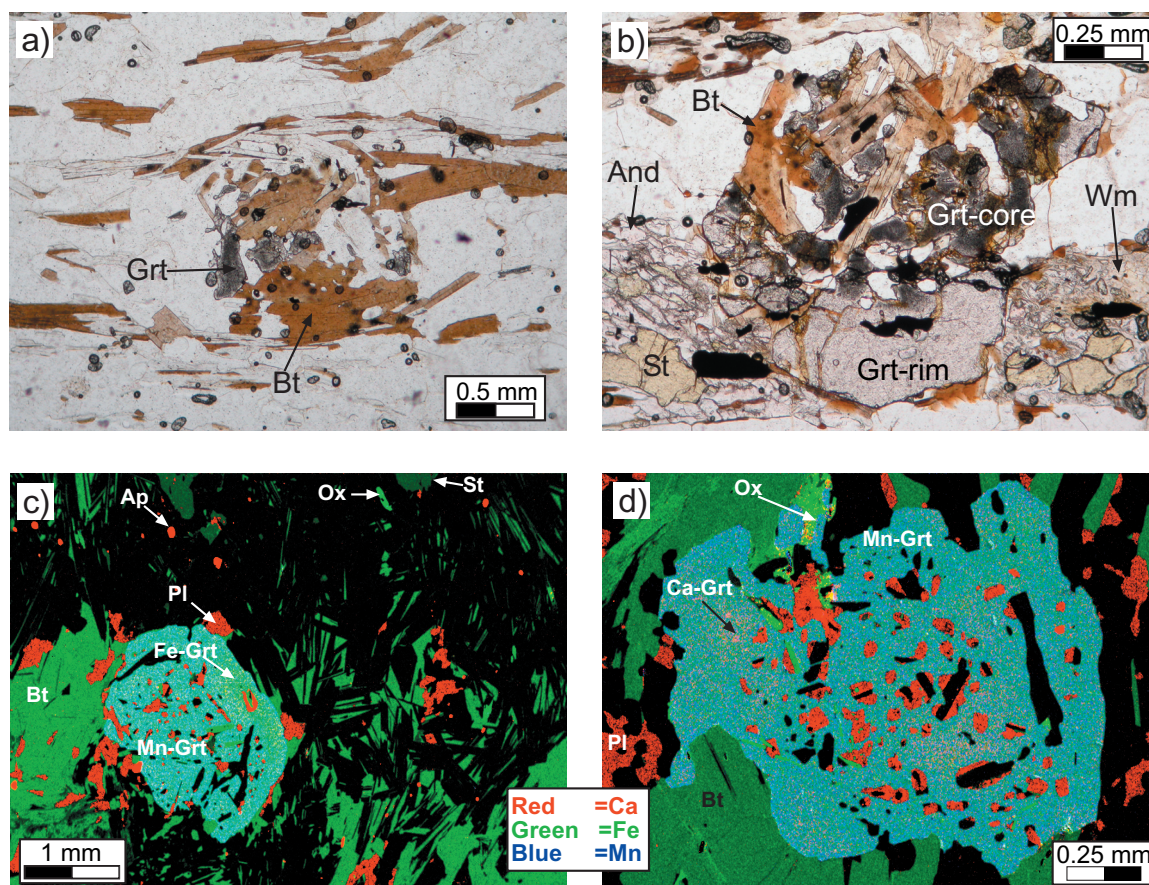


Fig. 2.14a-d: plane-polarized microphotographs (a, b) and RGB images (c, d) of garnet in paragneisses (LL61a1-a2). See text for explanations.

are scattered randomly; a closer examination reveals that they are smaller and very abundant toward the inner core portion. Garnet crystals are also characterised by inclusion-free rims, grown during a post-tectonic crystallisation event (**Fig. 2.14b**). RGB images constructed using Ca, Fe and Mn X-ray element maps show compositional differences between core

and rims of garnet crystals (**Figs. 2.14c, d**). Chemical features are comparable to those observed in micaschists. In fact, Mn zoning shows an initial decrease from core outward and a final increase in the narrow (few microns) rim, where garnet is in contact with matrix. Fe distribution is nearly constant with slight increase towards rims, whereas, Ca locally shows a patchy zoning (**Fig. 2.14d**). Solid inclusions are represented by quartz, biotite, plagioclase, muscovite, ilmenite, and minor, chlorite, tourmaline, zircon, apatite and monazite. Ghanite and xenotime occur only in one case.

Staurolite. It has been mainly observed in mica-rich domains, both as porphyroblasts (**Figs. 2.15a, b, c**) and in small grains (**Fig. 2.14b**). Petrographic and microstructural features of staurolite are comparable to those observed in micaschists. Generally, staurolite shows evidence of replacement by andalusite+biotite aggregates. Furthermore, in staurolite-bearing domains muscovite is rare and it can be found as small plates enclosed in

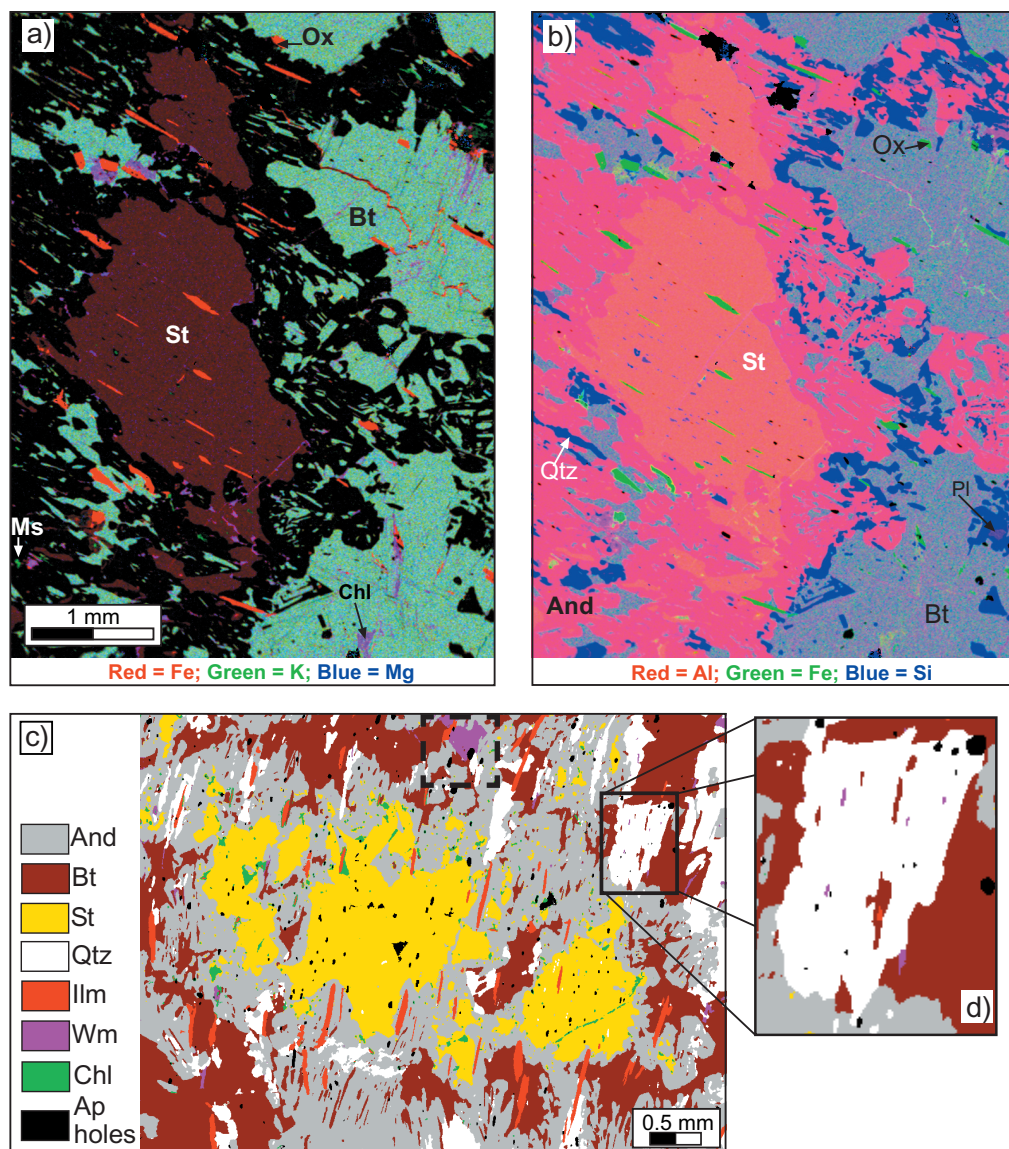


Fig. 2.15a-d: RGB (a, b) and classified (c) images of staurolite porphyroblasts (LL61b1). d) Detail of c) showing small inclusions of white mica within quartz and biotite. See text for explanations.

quartz (**Fig. 2.15d**) or as poikilitic porphyroblasts (**Fig. 2.15c**). In some cases, staurolite is partly replaced by white mica aggregates as consequence of retrograde reactions (Mezger *et al.*, 2004). Reaction domains have been largely studied at the electron microscope. RGB images constructed using X-ray element maps confirmed optical observations and revealed other important features, as for example, the absence of evident chemical zoning of staurolite (**Figs. 2.15a, b**) and the partial chloritisation of biotite (**Fig. 2.15a**).

Aluminosilicate. Fibrolitic sillimanite is well recognisable in all the analysed thin sections and, generally, overgrew large biotite crystals (**Figs. 2.16a**). Fibrolite is rarely in direct contact with andalusite, preferentially nucleates at the rims of biotite and develops toward the matrix (**Figs. 2.16a, b**). CL (cathodoluminescence) images (**Appendix 3**) show a typical reddish tonality for sillimanite overgrown on no-luminescent biotite (**Fig. 2.16b**). Undisturbed aggregates of very fine-grained fibres of sillimanite indicate that their crystallisation took place under post-tectonic conditions (after D₂ deformation). This incipient sillimanite crystallisation is indicative of the sillimanite-in isograd similarly to

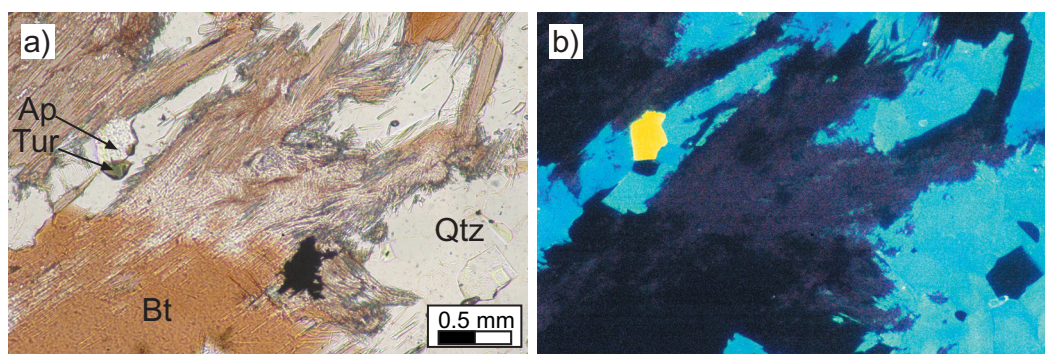


Fig. 2.16a, b: plane-polarized microphotograph (a) and cathodoluminescence image (b) of fibrolitic sillimanite (LL61a2). CL images show the typical reddish tonality for sillimanite overgrew on no-luminescent biotite.

other Calabria areas (*e.g.* Graessner and Schenk, 1999). Coexistence of andalusite and sillimanite could be related to (1) metastable persistence of andalusite in the stability field of sillimanite or (2) metastable persistence of sillimanite in the stability field of andalusite.

During metamorphic retrogression, fine-grained aggregates of white mica partially replaced andalusite.

Cordierite. Cordierite occurs exclusively in Bt-rich layers of paragneisses. In all the analysed samples poikiloblasts of cordierite (up to 5-6 cm) are completely pinitized and contain many inclusions of ilmenite, biotite and muscovite. In plane-polarised light (**Fig. 2.17a**), cryptocrystalline pinite shows light-green to pale-yellow colours that become orange towards rims and in fractures. Under crossed polars (**Fig. 2.17b**), pinite is characterized by low interference colours, typically by shades of grey. Cordierite crystallized post-tectonically, with respect to D₂ deformation, replacing previous And+Bt-

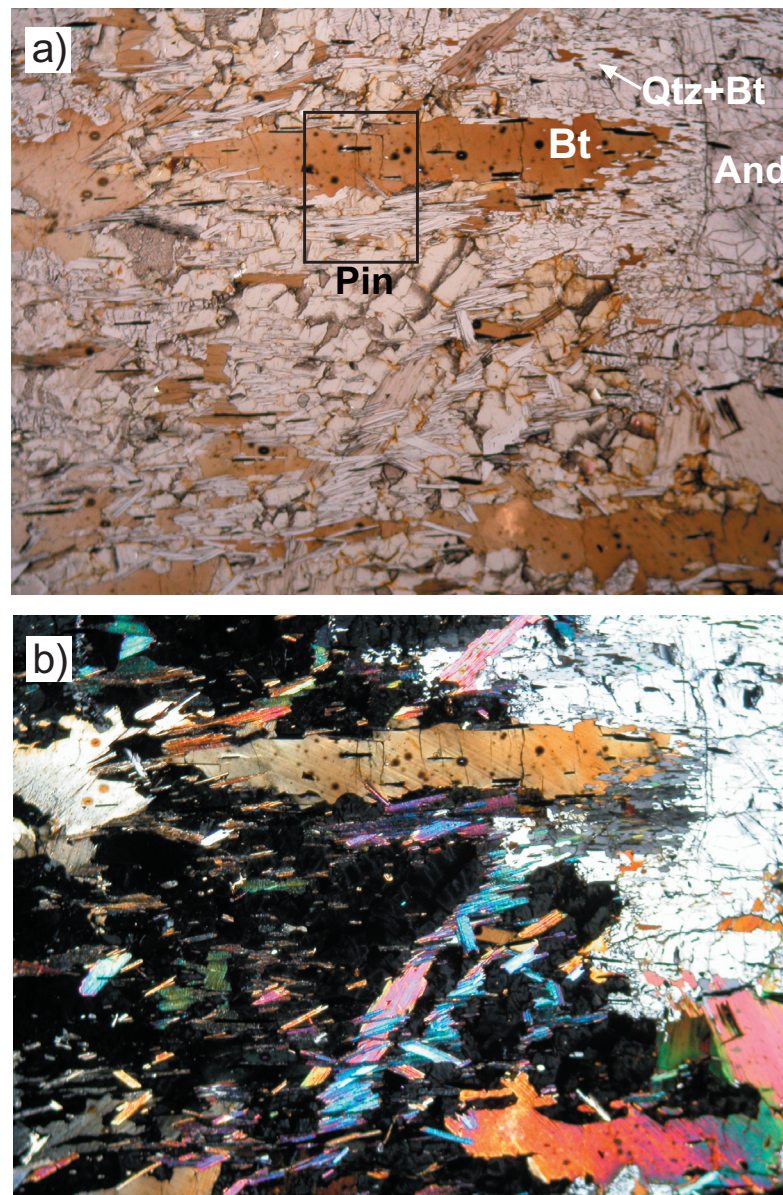


Fig. 2.17a-b: plane-polarized light (a) and crossed-polarised light (b) microphotographs of altered cordierite porphyroblast (LL61b2). Black square indicates location of BSE image of Fig. 3.14.

rich domains. Cordierite-forming reaction effects have been mainly studied collecting X-ray element maps of the inner part of poikilitic porphyroblast (**Figs. 2.18a, b**), of the transition zone between porphyroblast and matrix (**Figs. 2.18c, d**) and of the surrounding matrix, in the neighbourhood of the porphyroblasts (**Figs. 2.18e, f**). With this technique,

it has been possible to unravel the modal abundance of reactants and products of the cordierite-forming reaction. Classified images reveal that muscovite decreases towards the matrix, whereas quartz, andalusite and biotite show an inverse trend.

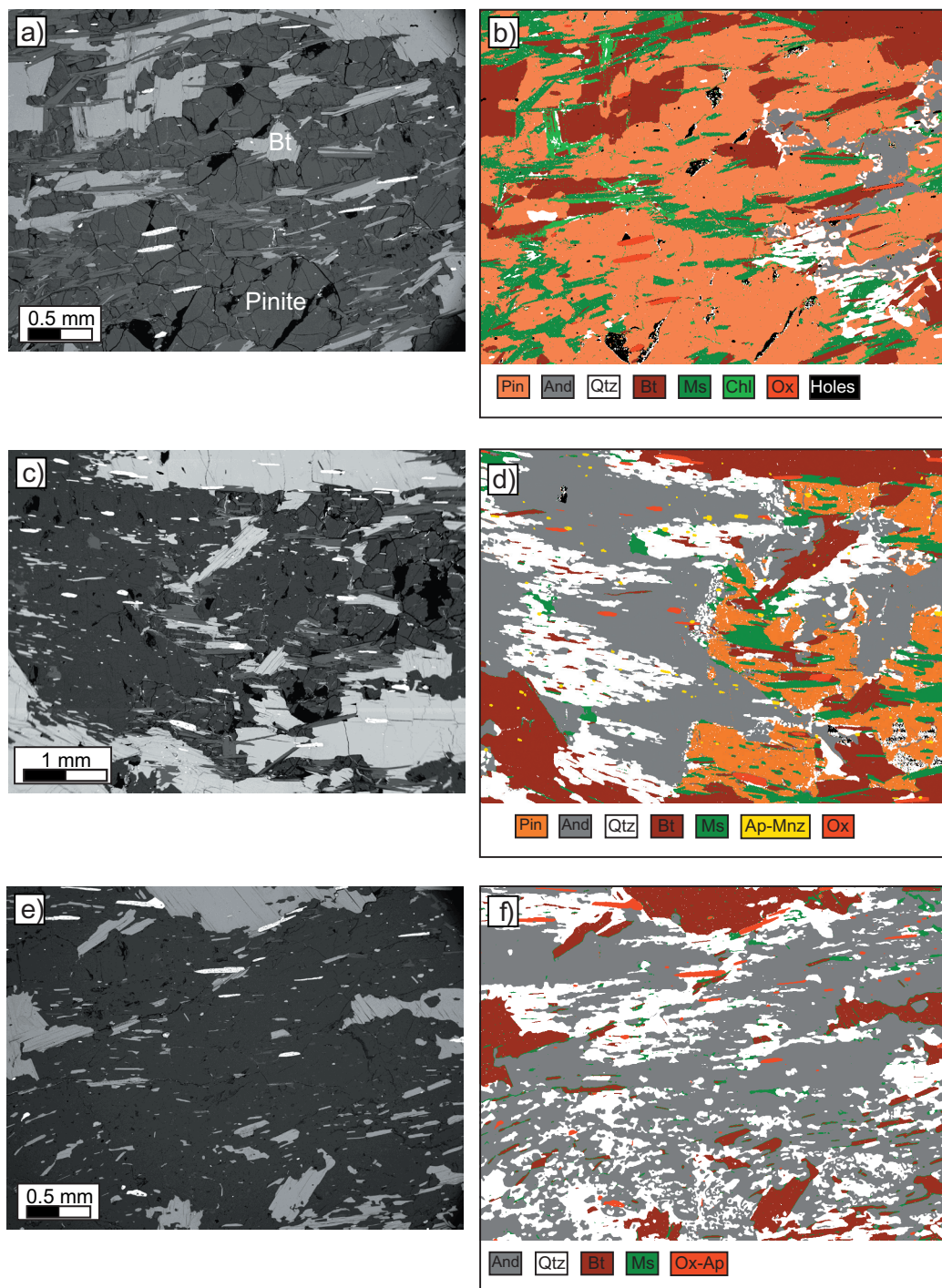


Fig. 2.18a-f: BSE (a, c, e), and classified (b, d, f) images relative to altered cordierite porphyroblast (a, b); transition zone between altered cordierite and matrix (c, d) and matrix, near the altered cordierite porphyroblast (e, f).

Tourmaline. It is present as accessory phase but reaches dimensions comparable with other phases (e.g. muscovite) and shows evidence of static overgrowths.

2.3.2 - Spotted schists with large porphyroblasts

Spotted schists with large porphyroblasts have been observed in several localities of the studied areas (Trionto river, Nica river, Sappo and Acero streams; **Figs. 1.5; 1.14a**). Two main particular features have been observed during fieldwork: a) the systematic occurrence of spotted schists with large porphyroblasts only in correspondence of small granitoid bodies, b) the tectonic juxtaposition of spotted schists with large porphyroblasts with metamorphic rocks unaffected by static growth of minerals.

On macroscopic scale, these rocks are characterised by dark-green to bluish porphyroblasts surrounded by light-grey white-mica rich matrix (**Figs. 2.19a, b**). Moreover, on the foliation planes it is possible to recognise small spots of biotite randomly oriented. Often, porphyroblasts are contoured by reaction halos characterised by the absence or low abundance of biotite spots (Fig. 2.19b).

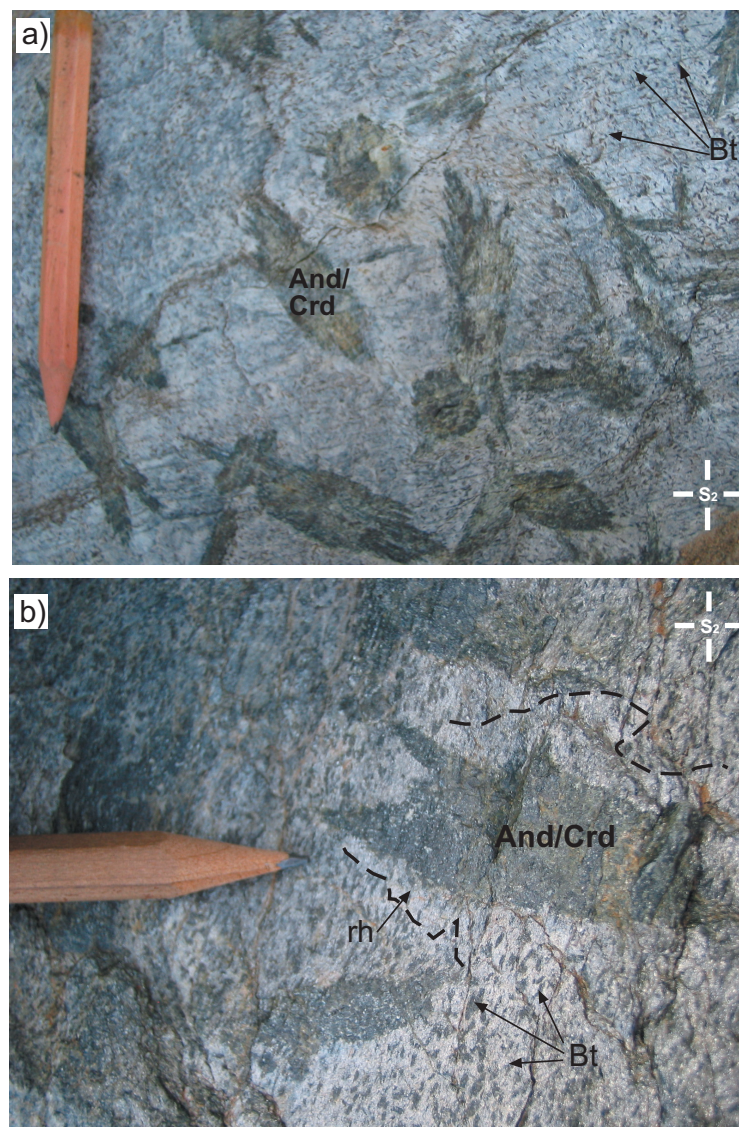


Fig. 2.19a-b: photos of foliation planes of spotted schists with large porphyroblasts. Spots have biotite composition. rh=reaction halo. (a: LL141, Pilla Stream - Mandatoriccio; b: LL161, Trionto River - Cropalati). Entire length of pencil in a) is 8 cm.

Porphyroblasts are easily visible on the S_2 foliation and may reach 30% of the surface. Generally, they lie with their long axis parallel to the regional foliation (S_2) without preferred orientation. Porphyroblasts have pseudo-hexagonal-prismatic shape with cross-section up to 2 cm and greater rectangular longitudinal section, often characterized by cusped terminations (**Figs. 2.19a, b**). Rather frequently, porphyroblasts have sub-rounded shape.

In thin section, these rocks show fine-grained matrix, consisting mainly of quartz, plagioclase, and muscovite, crosscutted by small biotite spots and by large porphyroblasts (**Figs. 2.20a-d**). Matrix-forming minerals are organized in alternating quartz+plagioclase-rich and mica-rich layers, whereas chlorite, apatite, ilmenite, tourmaline and zircon are present as accessory phases. As confirmation of their static growth, porphyroblasts contain numerous inclusions of matrix-forming minerals arranged along planes continuous with external foliation (**Figs. 2.20a-d**).

The rocks investigated are all metamorphosed argillaceous sediments with whole-rock-chemical composition comparable with micaschists and paragneisses (**Figs. 2.3; 2.4b, c, d**).

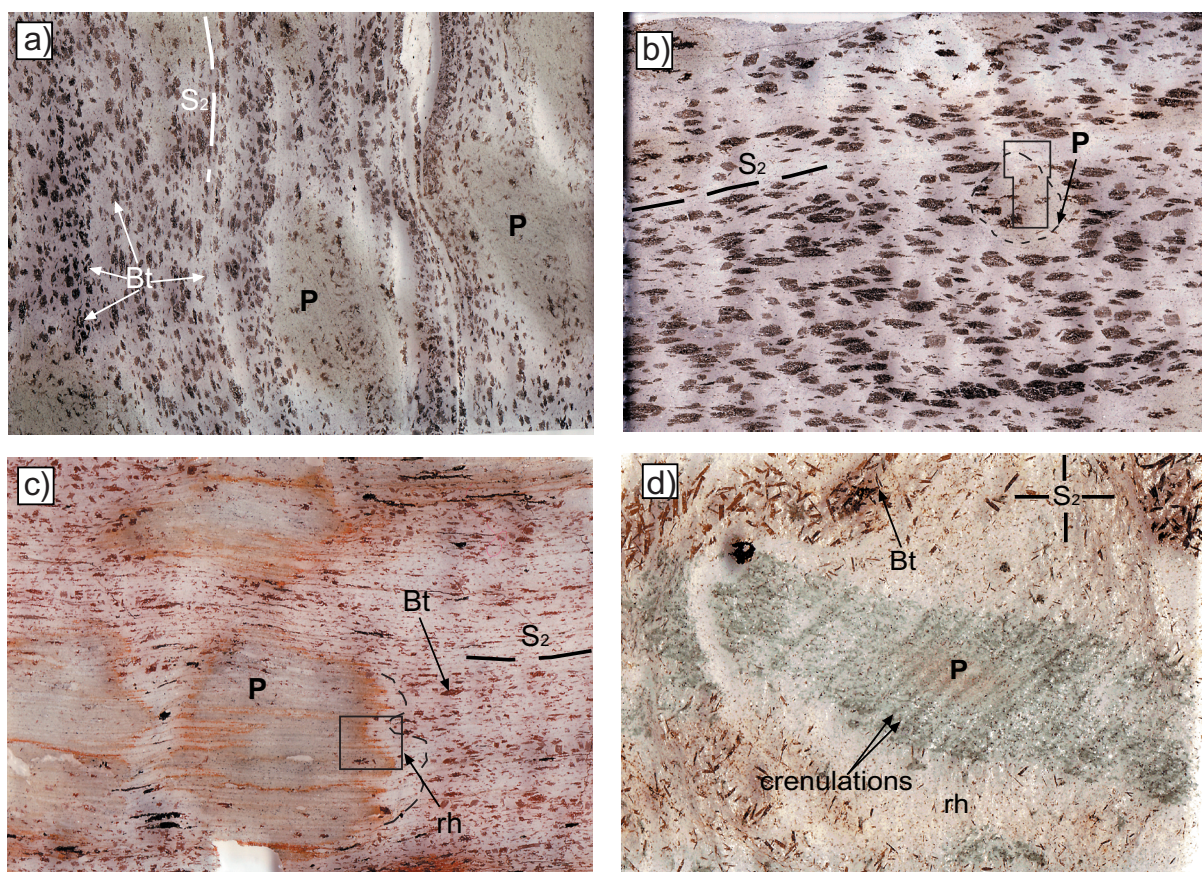


Fig. 2.20a-d: optical scans of some analysed thin sections (3cm x 4.5cm) relative to spotted schists with large porphyroblasts. Porphyroblasts are composed of fine-grained alteration products of andalusite and/or cordierite, in some cases they are surrounded by well-developed reaction halos (rh) and/or show compositional zoning. Black boxes in b) and c) delimit acquired X-ray mosaic showed in Figs. 2.21 and 2.22, respectively. Scan of foliation plane (d) shows later crenulations that overprint static crystallisation of porphyroblasts.

See Figs. 1.5 and 1.14a for location of samples: a) LL161a, Trionto River - Cropalati; b) LL161b, Trionto River - Cropalati; c) LL117, Acero Stream - Mandatoriccio; d) LL141, Sappo Stream - Mandatoriccio.

Andalusite and cordierite porphyroblasts. On macroscopic scale, nature of porphyroblasts can be difficult to establish. Shape, colour and textural characters may be compatible with andalusite and cordierite (**Figs. 2.19; 2.20**).

Difficulties have been founded also at microscopic scale, since original porphyroblasts have been nearly completely replaced by fine-grained alteration products. A useful method to distinguish between the two alternatives has been based on chemical composition of alteration products that, of course, have to be different. In fact, retrograde alteration of andalusite would mainly lead to Al-rich phases such as white mica, whereas the alteration of cordierite would lead to Fe-Mg phyllosilicates together with white mica.

Petrographic analyses allowed to recognize two types of altered porphyroblasts: 1) sub-rounded greenish-light grey porphyroblasts without chemical zoning (**Figs. 2.20a, b**) and 2) dark-grey porphyroblasts, characterised by different optical properties from core toward rims (**Figs. 2.20c, d**).

1) Greenish/light-grey porphyroblasts are composed of K-rich alteration products (**Fig. 2.21a**) suggesting replacement by white mica of an original andalusite. This conclusion is in agreement with the alteration pattern observed around small andalusite

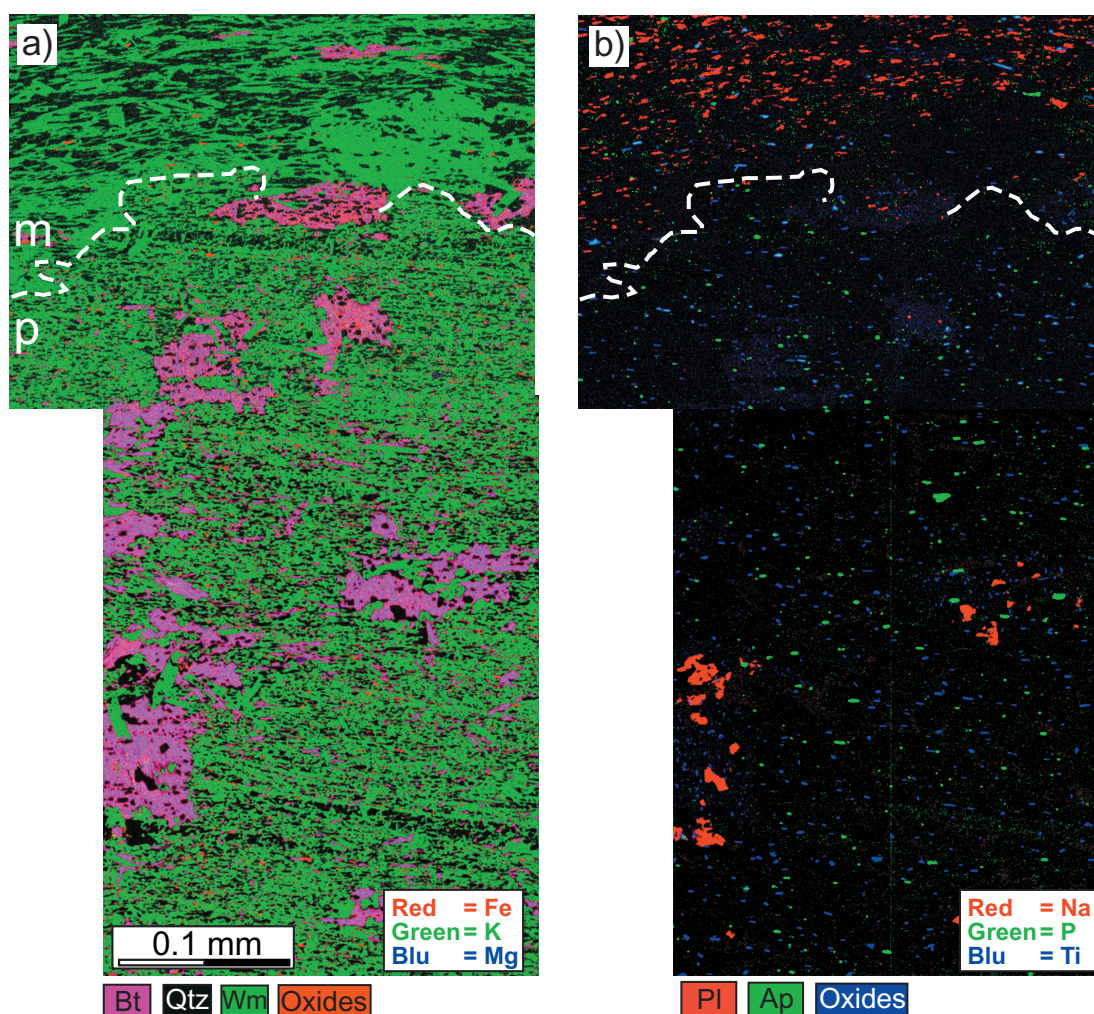


Fig. 2.21 a, b: RGB images of transition zone between altered andalusite porphyroblast and matrix (LL161b). White-dotted line represents porphyroblast (p)-matrix (m) limit.

relicts, surrounded by fine grained but still recognizable aggregates of white mica.

2) Dark-grey porphyroblasts are composed of Fe+Mg+K cryptocrystalline aggregate (**Fig. 2.22a**). This composition could be qualitatively representative of a mixture between white mica and chlorite formed at the expense of an original cordierite. X-ray maps reveal

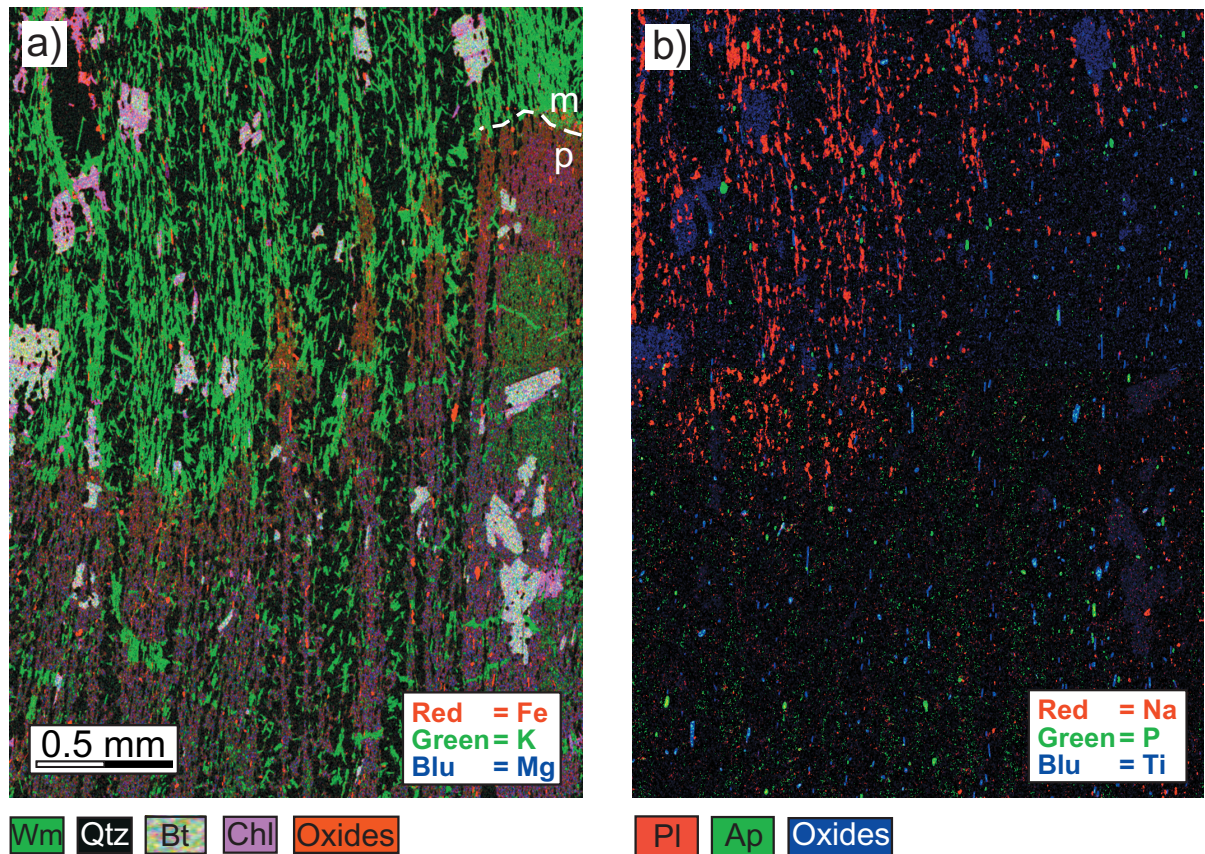


Fig. 2.22a, b: RGB images of transition zone between altered cordierite (pinite) porphyroblast (p) and matrix (m; LL141).

that different optical properties from core outwards (e.g. orange rims; **Fig. 2.20c**) are related to an increase of Fe and Mg contents (**Fig. 2.22a**).

RGB images obtained from X-ray element maps revealed other important porphyroblast-matrix relationships. Generally, both types of porphyroblasts show reaction halos characterized by low abundance of biotite and coarser opaque aggregates. Both in andalusite- and in cordierite-derived porphyroblasts, apatite and Fe-Ti oxides inclusions are more abundant than in the matrix. Instead, albitic plagioclase is rarely observed as inclusion and is more concentrated in the matrix (**Figs. 2.21b, 2.22b**).

Biotite. It is visible as small syntectonic crystals elongated parallel to the S_2 foliation and as poikilitic spots that mimetically overgrew mica-rich layers along the S_2 schistosity.

Generally, these spots have their cleavage perpendicular to the foliation and contain numerous inclusions of quartz, muscovite and small biotite plates. In some cases, spots have a sigmoidal shape and show different optical properties with reddish/brown cores and grey/green rims reflecting partial chloritisation.

White mica. Is the major constituent of the matrix. Syntectonic plates define schistosity, whereas small plates perpendicular to the matrix can be attributed to post-tectonic crystallisation. The white mica forming the alteration product of porphyroblasts defines the last generation of retrograde origin.

CHAPTER 3 - MINERAL CHEMISTRY IN THE MAIN ROCK TYPES OF THE MANDATORICCIO COMPLEX

Mineral analyses have been focused in some porphyroblastic samples of amphibolites, micaschists and paragneisses. Chemical compositions of rock-forming minerals could confirm textural generations defined with petrographic analyses and are necessary for P-T estimates. The quantitative analyses of rock-forming minerals were carried out at the CAMPARIS Service at the University of Paris using two microprobes, the CAMECA SX50 and SX100. Operating conditions, analytical details and chemical microanalyses are reported in **Appendix 3**.

3.1 – AMPHIBOLITES

Electron microprobe data have been obtained for amphibole and plagioclase. Formulae of analysed minerals are listed in **Tables 5** and **6**.

Amphibole.

Analysed amphiboles (**Tables 5**) show a $(\text{Ca}+\text{Na})_{\text{B}}$ cation occupancy greater than 1.5 atoms per formula unit (a.p.f.u.) and very low values (less than 0.5 a.p.f.u.) of $\text{Na}+\text{K}$ in A site. They belong to the calcic group with low Na content and mainly fall in the field of magnesiohornblende (**Fig. 3.1**). The nomenclature of amphibole follows Leake *et al.*, 1997. Classification diagram (**Fig. 3.1**) shows that pre- to syntectonic porphyroblasts and small syntectonic crystals have roughly the same composition, the only difference consists in a minor scattering of Mg value relative to porphyroblasts (**Fig. 3.1**).

Generally, amphibole show compositional variation as a function of pressures and temperatures. Laird & Albee (1981) had summarised the compositional variation of amphiboles with metamorphic grade in a series of diagrams that display the major

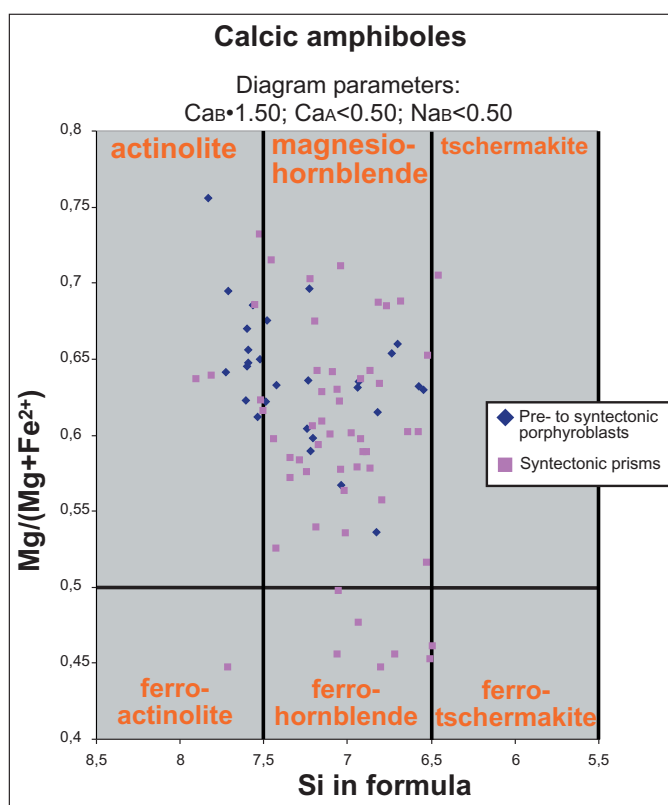


Fig. 3.1: classification diagram used for calcic amphibole, after Leake *et al.* (1997). 84 analyses of 28 amphibole porphyroblasts and 56 syntectonic amphibole prisms.

compositional trends for amphiboles from different metamorphic terranes. Generally, Na(M4) content is very abundant in glaucophane so it can be a measure of the relative pressure of the metamorphism whereas the alkali site occupancy (Na+K)A could reflect the relative temperature of metamorphism (Spear, 1993 and references therein). Plot of Na(M4) against (Na+K)A (**Fig. 3.2**) reflects medium- to low-pressure conditions. For comparison, in the composition plot (**Fig. 3.2**) are also depicted fields of amphiboles from different metamorphic terranes analysed by Laird & Albee (1981). Analysed amphiboles have compositional trends comparable to amphiboles from Haast river medium-pressure terranes and Abukuma low-pressure terranes (**Fig. 3.2**). As for the classification diagram (**Fig. 3.1**), plotted values relative to pre- to syntectonic porphyroblasts and syntectonic prisms do not show systematic differences.

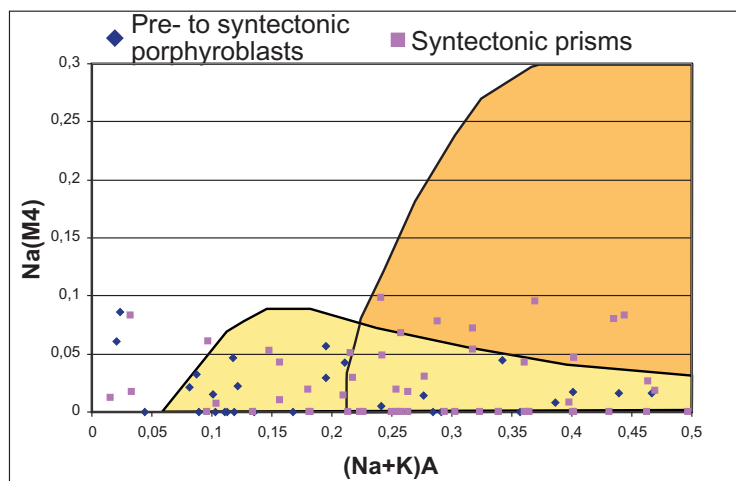


Fig. 3.2: composition plots for amphiboles. Composition fields of low-pressure Abukuma terranes (pale orange) and intermediate-pressure Haast River terrane (pale yellow) from Laird & Albee (1981).

Plagioclase.

In amphibolites with both schistose and gneissic fabric, plagioclase commonly occurs as a fine-grained matrix mineral. Chemical microanalyses (**Table 6**) show that plagioclase have An values varying from $An_{16.6}$ and $An_{80.0}$ (**Fig. 3.3**). Orthoclase mole percentages are very low and reach a maximum value of $Or_{9.0}$.

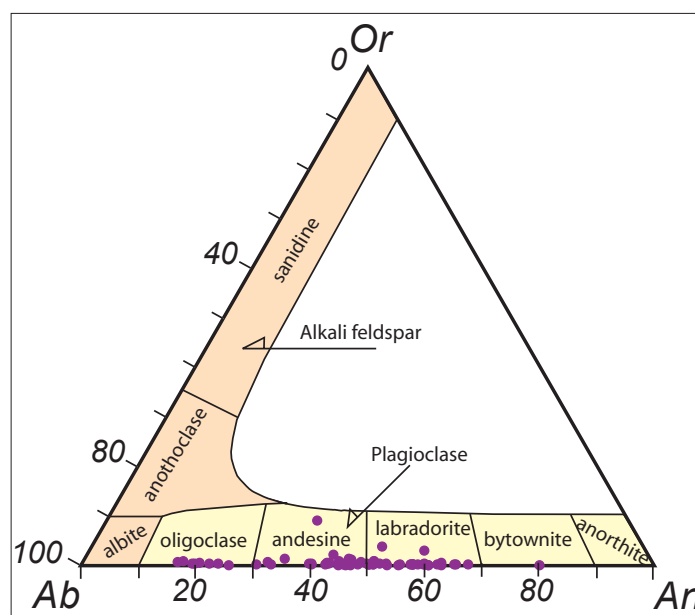


Fig. 3.3: compositions of 65 plagioclase crystals in amphibolites.

3.2 - MICASCHISTS

Garnet.

X-ray maps have been very helpful in order to localise the chemical profiles (**Figs. 3.4a-f**) listed in **Table 7**. Microanalyses confirmed the low Mg content of garnet ($X_{\text{Prp}} < 0.1$) and an high concentration of iron ($0.5 < X_{\text{Alm}} < 0.85$) resulting in high X_{Fe} ($\text{Fe}^{2+}/(\text{Fe}^{2+} + \text{Mg})$)

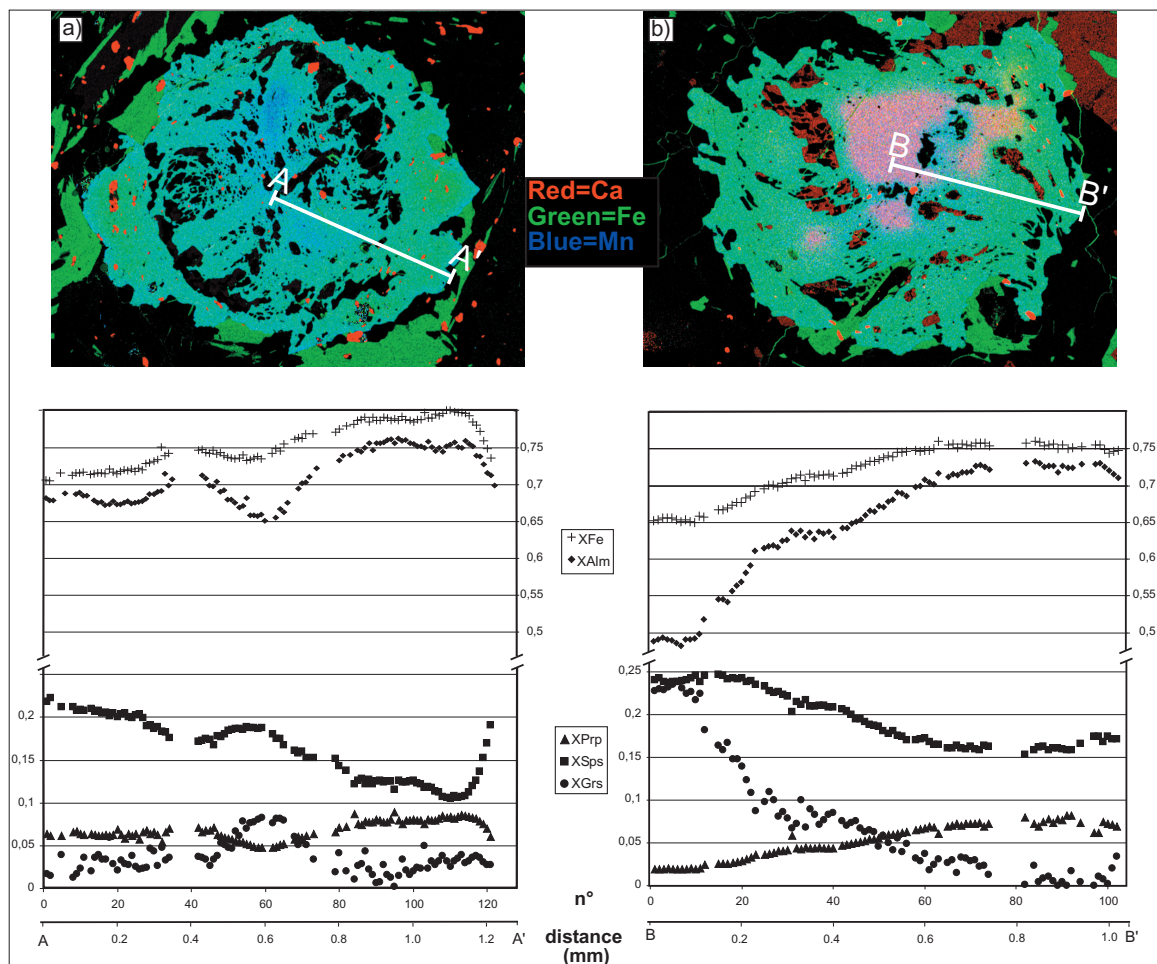


Fig. 3.4a-f: garnet profiles for sample LL56a3 (a, b), LL56a4 (c), LL56b (d) and LL57a (e, f) micaschists. Profiles are depicted on RGB images and refer to typical garnet crystals showing Mn-rich core (a, d) and Ca-rich core (b, c, e, f). Lack or abrupt variations of values are due to the interception of inclusion or chemical halos around inclusion, respectively.

values. Spessartine molecule ($0.1 < X_{\text{Sps}} < 0.25$) shows a typical bell-shaped distributions with inverse features in narrow external rim (**Figs. 3.4a, b, d-f**). Grossular molecule is generally not very abundant ($X_{\text{Grs}} < 0.1$) excepted for Ca-rich cores (**Figs. 3.4b, c, e, f**) where grossular could reach a molar fraction of about 0.25. In some cases, profiles appear humped due to the interception of chemical halos around inclusions.

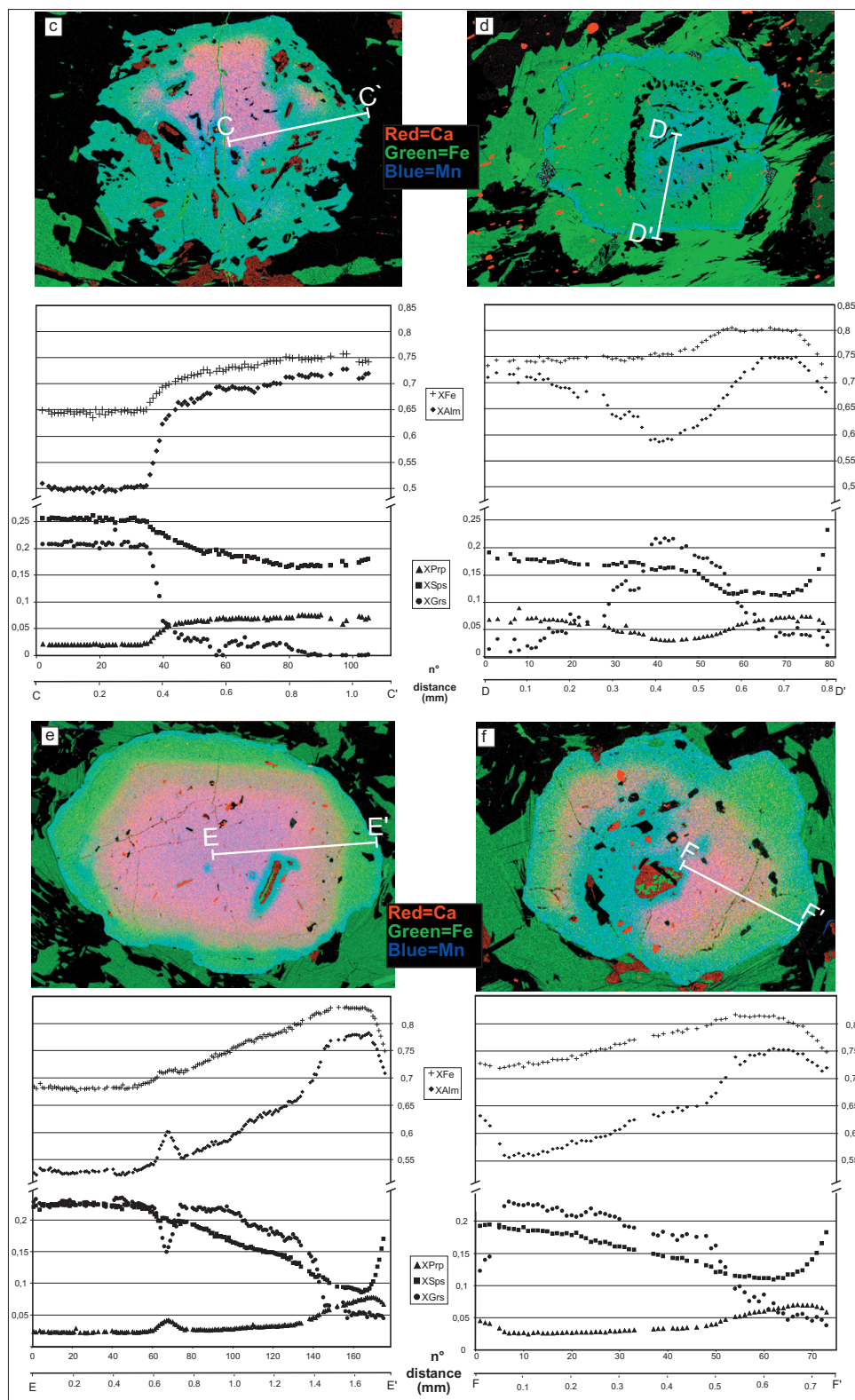


Fig. 3.4a-f: continued

Biotite.

Considering Ti content in biotite as index of metamorphic grade (Cesare *et al.*, 2003 and references therein) a large parte of analysed crystals (**Table 8**) formed under amphibolite facies conditions ($0.19 < \text{Ti} < 0.34$ a.p.f.u.; **Fig. 3.5a, b**). The Al^{VI} content is generally higher

than 0.80 a.p.f.u. (**Fig. 3.5b**). Biotite shows weak Al^{VI} and Ti variations associated to textural site (**Fig. 3.5b**).

Some biotite crystals show low K contents probably resulting from partial chloritisation (cf. 2.3.1.1).

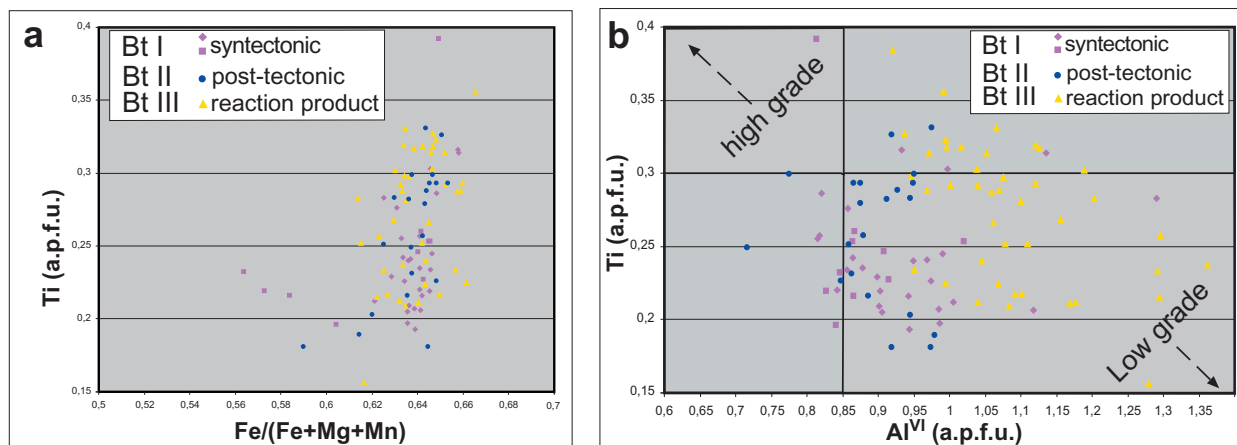


Fig. 3.5a, b: plots of some elements analysed in 99 biotite crystals. (Bt I: 36 analyses; Bt II: 21 analyses; Bt III: 42 analyses). a) Ti vs X_{Fe} ; b) Ti vs Al^{VI} after Schreurs (1985). Square and diamond of syntectonic biotite (Bt I) refer to crystals included in garnet and small plates elongated parallel to the foliation, respectively.

Staurolite.

Staurolite compositions are very similar in all analysed samples (**Table 9**) and X-ray images revealed that is unzoned (**Figs. 2.9b, 2.10b, d**). X_{Mn} ($X_{Mn} = Mn/(Fe+Mg+Mn+Zn)$) and X_{Zn} ($X_{Zn} = Zn/(Fe+Mg+Mn+Zn)$) are very low and varies only slightly ($0.02 < X_{Mn} < 0.04$; $X_{Zn} < 0.07$), whereas X_{Fe} ($X_{Fe} = Fe/(Fe+Mg+Mn+Zn)$) is very significant ($0.77 < X_{Fe} < 0.87$).

Feldspar.

Chemical microanalyses of feldspar are listed in **Table 10**. Matrix-forming plagioclase has mainly oligoclase composition ($Ab_{83.6}-Ab_{69.1}$), similar to plagioclase included in garnet crystals (**Fig. 3.6**). Only in a single case, small K-feldspar crystals ($Or_{98.9}Ab_{0.7}An_{0.3}$) have been identified as inclusions in garnet (**Fig. 3.6**).

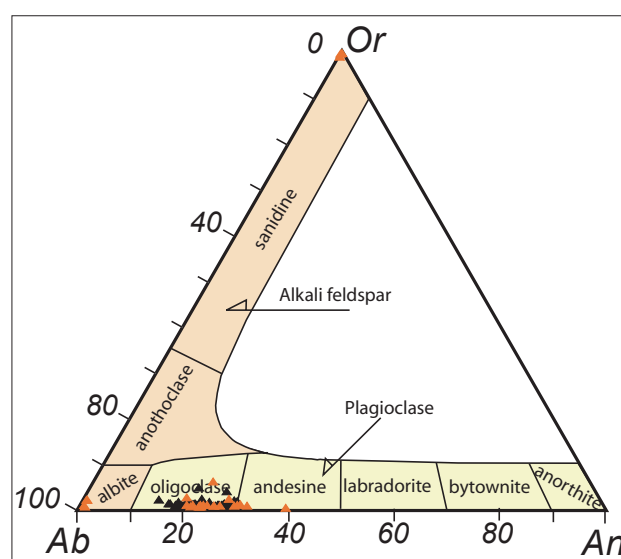


Fig. 3.6: compositions of 103 plagioclase crystals in micaschists. Black and orange triangles refer to syntectonic matrix forming plagioclase (75 analyses) and plagioclase included in garnet (28 analyses), respectively.

White mica.

Different textural generations of white mica have a muscovite composition with low sodium content ($\text{Na} < 0.32$ a.p.f.u., **Table 11**). Muscovite compositions are close to ideal Tschermak's substitution line (**Fig. 3.7**) indicating the lack of ferric muscovite component.

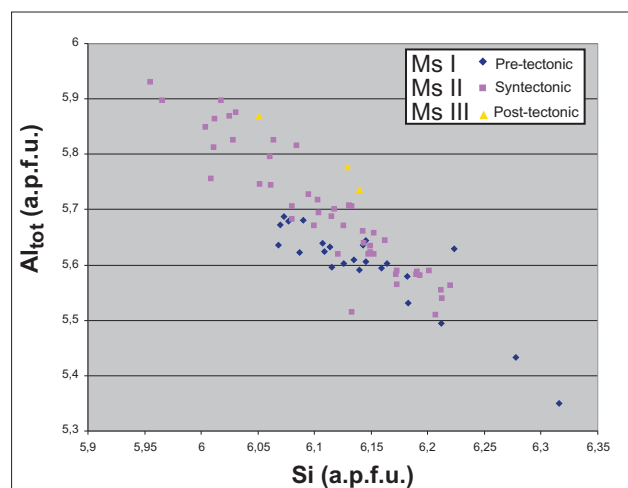


Fig. 3.7: Si vs Al_{tot} of 74 muscovite crystals (Ms I: 24 analyses; Ms II: 47 analyses; Ms III: 3 analyses).

3.3 - PARAGNEISSES

Garnet.

As mentioned in petrographic section (cf. 2.3.1.2) garnet are not very abundant in paragneisses, therefore, only two crystals of garnet have been analysed at the microprobe (Table 12). X-ray maps have been very helpful in order to localise the chemical profiles (Figs. 3.8a, b). Garnet displays a weak Mn zoning characterized by a slightly decrease (≈ 0.1) of X_{Sps} towards outer part of inclusion-rich core and a more pronounced increase of spessartine content in the external part of rims (Figs. 2.14c; 3.8a, b). The Ca content is

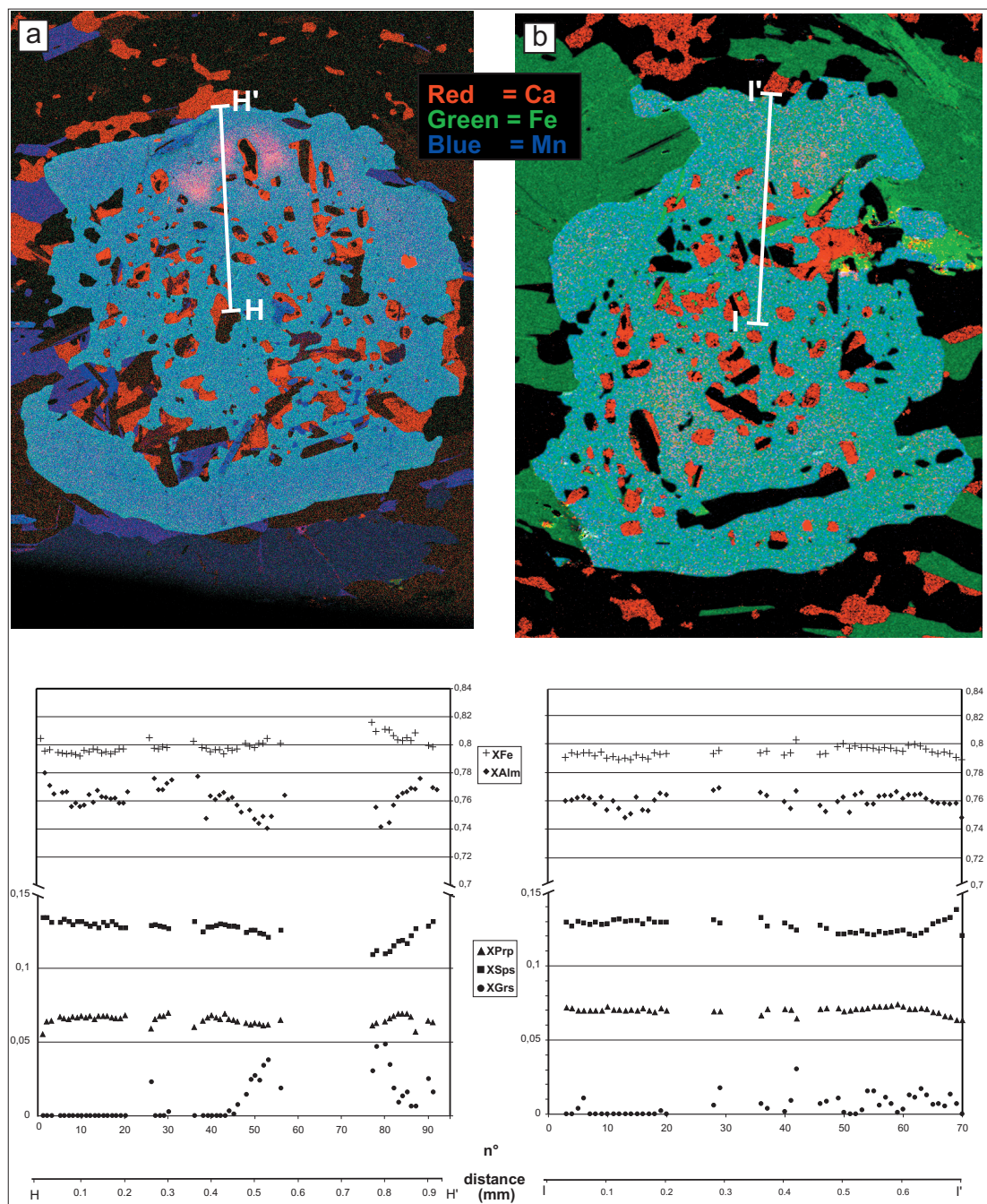


Fig. 3.8a, b: garnet profiles for sample LL61c1. Chemical profiles are depicted on RGB images.

very low ($0 < X_{\text{Grs}} < 0.05$), quasi-homogeneous in the inner core and more irregular towards rims. Pyrope content in garnet shows a very regular trend ($X_{\text{pyr}} \approx 0.07$) interrupted in the outer part of rims where it becomes to decrease. Molecular proportion of almandine in the analysed garnet is very high ($0.75 < X_{\text{Alm}} < 0.77$) and shows a regular trend, except for a slightly decrease in the external part due to retrograde diffusion effects.

Biotite.

Chemical analyses of different textural biotite generations (**Table 13**) do not show significant chemical variations (**Fig. 3.9a**).

Considering Ti and Al^{VI} content in biotite as indicators of temperature (Cesare *et al.*, 2003) of metamorphism, all analysed biotite probably crystallised under low- to intermediate-grade metamorphic conditions (**Fig. 3.9b**).

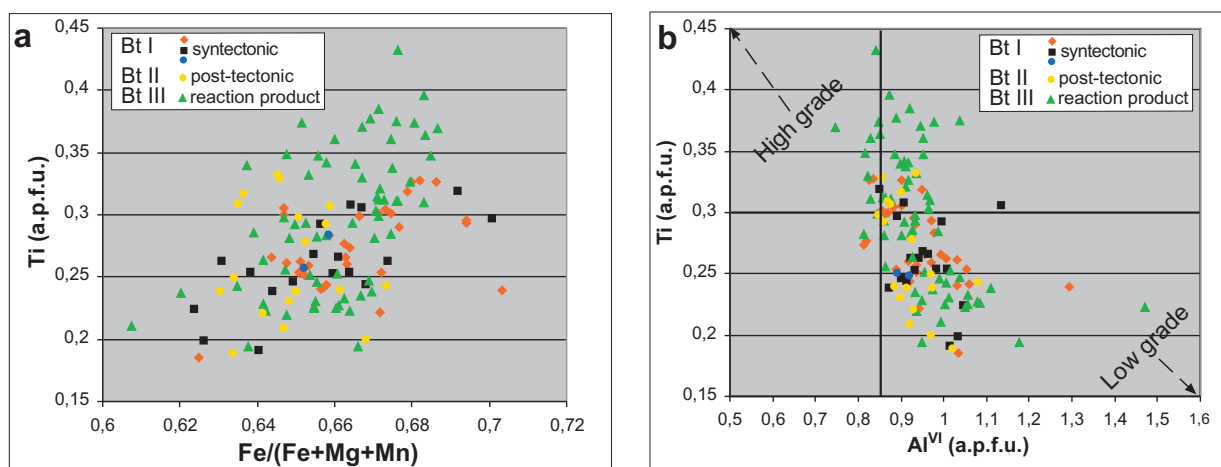


Fig. 3.9a, b: plots of some elements of analysed 134 biotite crystals (Bt I: 52 analyses; Bt II: 18 analyses; Bt III: 64 analyses). a) Ti vs X_{Fe} ; b) Ti vs Al^{VI} after Schreurs (1985). Syntectonic biotite (Bt I): blue circle = Bt included in garnet; black squares = Bt included in quartz; orange diamond = Bt in matrix.

As mentioned in previous sections (cf. 2.3.1.2), biotite has been involved in reactions during the metamorphic history. Microstructural analyses revealed that biotite participates to staurolite-breakdown and cordierite-forming reactions as product and reactant, respectively. In order to quantify possible reaction induced zoning in biotite, fine-spaced chemical profiles have been collected through narrow rims (**Fig. 3.10**; **Table 14**).

Analysed porphyroblasts belong to two different reaction domains: a first one is characterised by partial replacement of staurolite porphyroblast with formation of andalusite and biotite (**Figs. 2.15c**; **3.10**), and a second one consists on cordierite-forming reaction at major expense of biotite and andalusite (**Figs. 2.17**; **2.18a-f**). During staurolite-demise reaction, biotite has been mainly observed as product of reaction (Bt III) even if large porphyroblasts of earlier biotite (Bt II) were present during this reaction. A detailed chemical profile ($\approx 1 \mu\text{m}/\text{analyses}$, **Fig. 3.10**; **Table 14**) through narrow external portion

of one of this large porphyroblast could unravel reaction-induced substitution in biotite crystals.

Biotite porphyroblast in contact with andalusite-biotite aggregate shows (**Fig. 3.10**) a

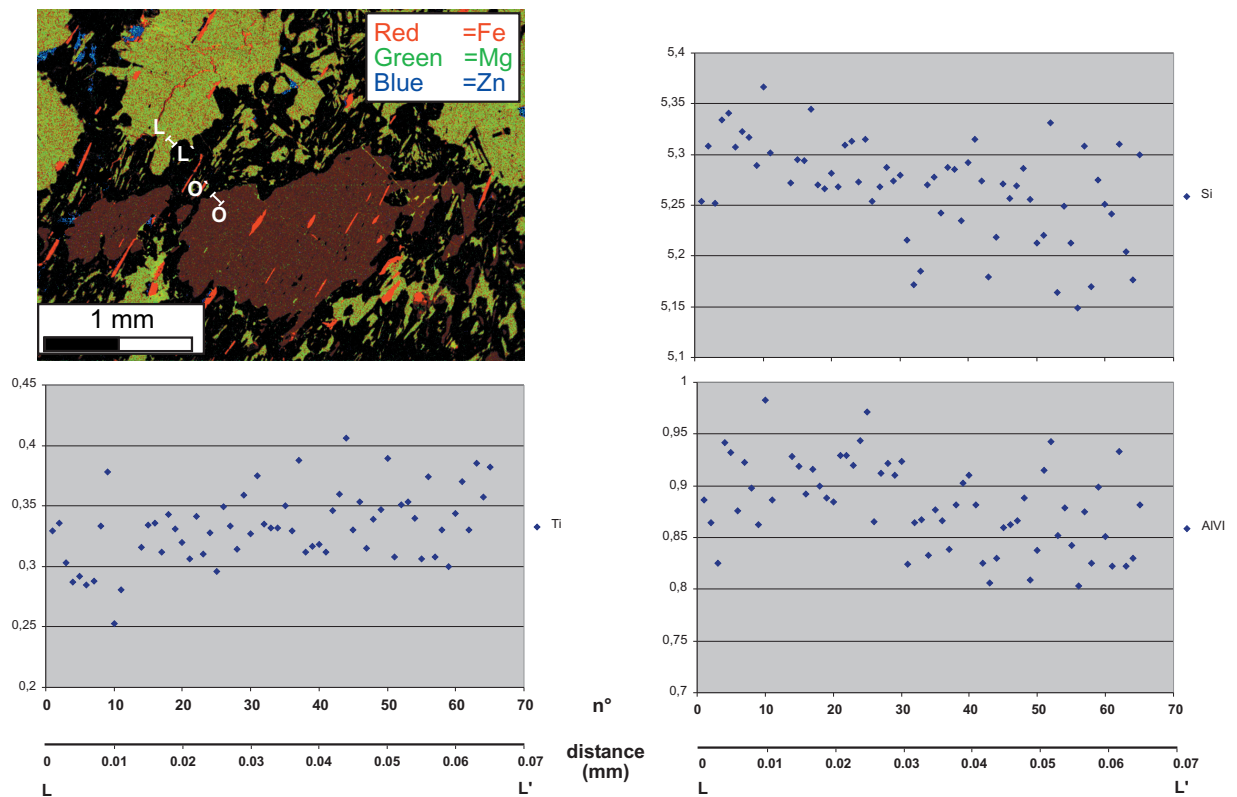


Fig. 3.10: fine-spaced chemical profile through rim of biotite porphyroblast involved in staurolite-demise reaction.

slight increase of Ti and a decrease of Si and Al^{VI} towards the aggregate.

Two parallel chemical profiles through a biotite crystal involved in cordierite-forming reaction have been collected (**Fig. 3.11**; **Table 14**). These profiles are of about 150 μm and 40 μm with a sampling spacing of 5 μm and 1 μm , respectively. Profiles show (**Fig. 3.11**) that Al^{VI} increase whereas Ti, Fe^{2+} and Mg decrease.

The decrease of Mg and Fe^{2+} towards altered cordierite could suggest that, during cordierite formation, these two elements were primarily subtracted from biotite.

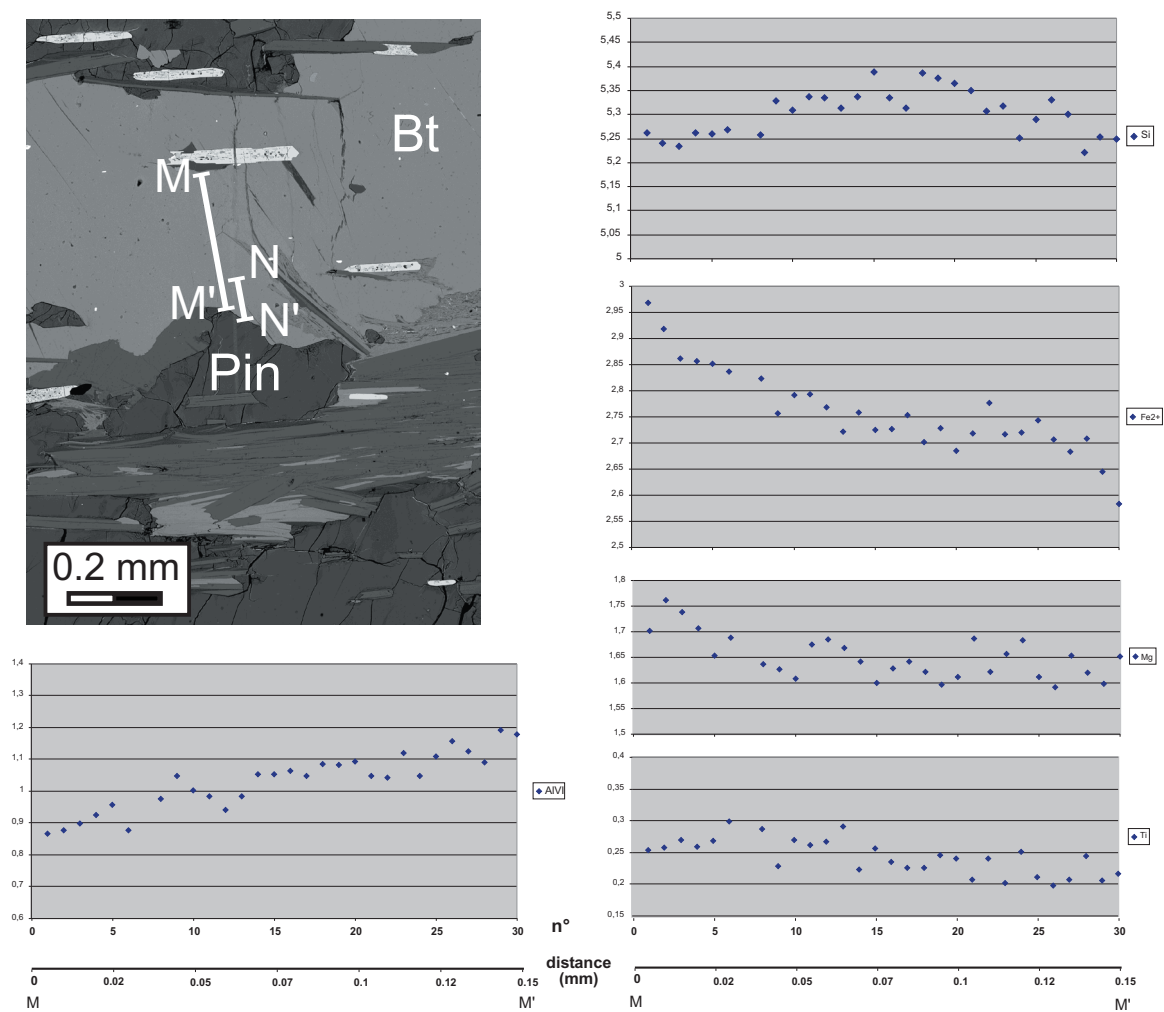


Fig. 3.11: chemical profile through biotite crystal involved in cordierite-forming reaction. BSE image is localised in Fig. 2.17.

Staurolite.

Profiles, random analyses of porphyroblasts and analyses of relict crystals of the single textural generation of staurolite are listed in **Table 15**.

Staurolite can be considered Zn-free ($\text{Zn} < 0.01$ a.p.f.u.). Relict staurolite crystals rimmed by muscovite pseudomorphs show the higher Zn values. This feature could be attributed to the back partitioning of Zn during temperature increase (Mezger *et al.*, 2004).

X-ray elemental maps of two staurolite porphyroblasts revealed that staurolite is unzoned (**Figs. 3.10; 3.12a**). Actually, chemical profiles (**Figs. 3.12a, b**) revealed that major staurolite constituents do not show a clear variation trend except for Mg that moderately decreases towards reaction products (andalusite). The variation of Mg has been attributed to growth effects.

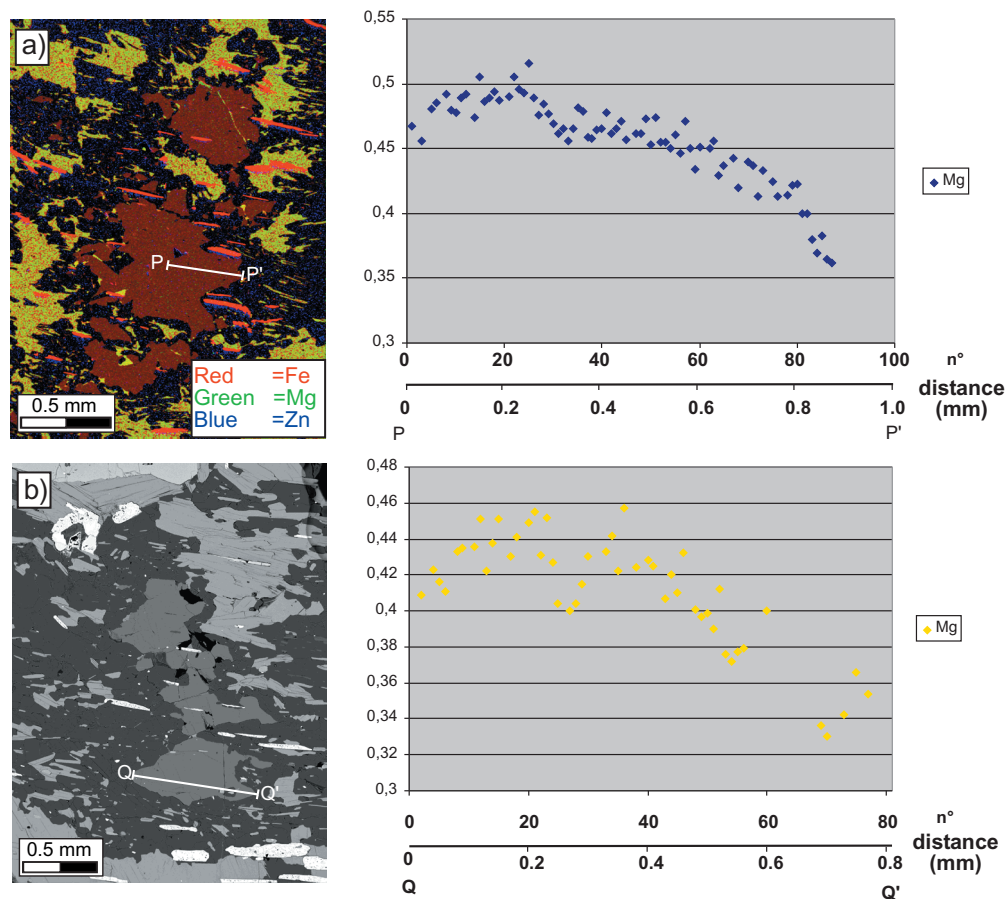


Fig. 3.12a, b: Mg distribution through staurolite porphyroblasts.

Feldspar.

Analyses of feldspar observed in matrix and as inclusion in garnet are shown in **Fig. 3.13** and listed in **Table 16**.

Matrix-forming feldspar have albitic composition ($\text{Or}_{0.1-0.6}\text{Ab}_{77.8-83.1}\text{An}_{16.6-21.9}$) comparable with the composition of plagioclase included in garnet crystals ($\text{Or}_{<5.2}\text{Ab}_{71.5-86.4}\text{An}_{11.9-28.0}$).

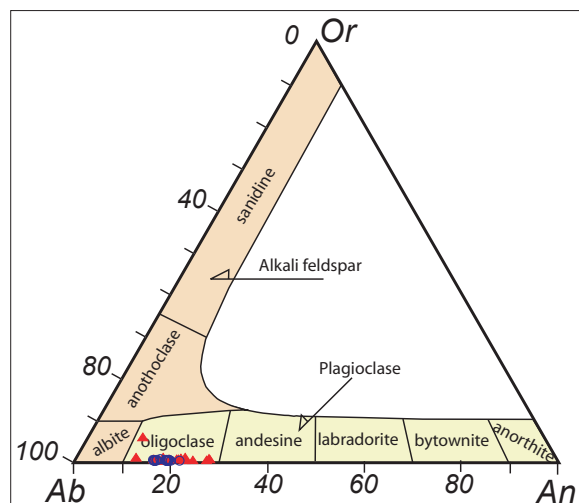


Fig. 3.13: compositions of 16 matrix-forming plagioclases (circles) and 16 plagioclase crystals included in garnet (triangles).

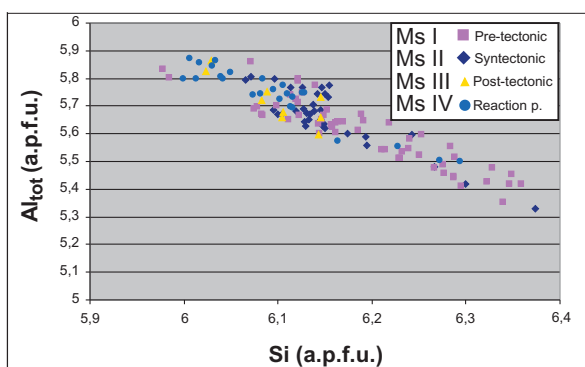


Fig. 3.14: Si vs Al_{tot} of 123 white mica crystals in paragneisses (Ms I: 55 analyses; Ms II: 34 analyses; Ms III: 9 analyses; Ms IV: 25 analyses). Ms IV refers to muscovite formed together with cordierite.

Muscovite compositions are close to ideal Tschermak's substitution line (**Fig. 3.14**) indicating the lack of ferric muscovite component. Muscovite crystals are characterised by low K content ($K < 1.74$ a.p.f.u.) and moderate amounts of paragonite molecule ($0.22 \text{ a.p.f.u.} < Na < 0.41 \text{ a.p.f.u.}$).

Cordierite.

Completely altered cordierite consists of cryptocrystalline intergrowths of white mica and chlorite, known as pinite. Pinite-forming minerals are high hydrous phases resulting very difficult to analyse with microprobe. To reduce destructive effect of X-ray beam, a large parte of analyses listed in **Table 18** have been collected moving X-ray beam. Pinite shows X_{Fe} variable from 0.72 to 0.76.

Fe-Ti oxides.

Opaques, which are commonly aligned along the S_2 schistosity, occur also as prograde inclusions in all the porphyroblasts and have composition of rutile, ilmenite and ilmenorutile (**Table 19**).

White mica.

Different textural generations of white mica have muscovite composition with Si content varying from 5.9 to 6.3 a.p.f.u. (**Table 17**; **Fig. 3.14**). The latest generation of cryptocrystalline white mica formed as alteration product of other phases has not been analysed.

Muscovite compositions are close to ideal Tschermak's substitution line (**Fig. 3.14**) indicating the lack of ferric

CHAPTER 4 - METAMORPHIC EVOLUTION OF THE MANDATORICCIO COMPLEX

The aim of this chapter is the definition of the P-T conditions and the reconstruction of the metamorphic evolution of some samples of the Mandatoriccio complex.

To this end, the first part of this section is dedicated to the reconstruction of the relationships between the deformation and the crystallisation observed mainly in the micaschists (cf. 2.3.1.1), in the paragneisses (cf. 2.3.1.2) and in the spotted schists with large porphyroblasts (cf. 2.3.2). Whereas, the main part is dedicated to the reaction history and to the phase diagram calculations.

4.1 - DEFORMATION-CRYSTALLISATION HISTORY

Microstructural and petrographic studies combined with mineral chemistry have been used to infer relationships between relative chronology of mineral growth and deformation events. If microstructural and petrographic analyses led to recognise relative sequence of mineral growth and different mineral generations, the chemical microanalyses could highlight compositional differences between various generations of minerals.

In the Mandatoriccio complex, a major deformational event (D_2) has been recognised. D_2 deformation event led to the crystallisation of new minerals and the development of main regional schistosity (S_2), affecting a pre-existing S_1 fabric. Porphyroblasts largely developed during a period of deformational quiescence after the D_2 deformation ($D_2 < P$, **Fig. 4.1**). Deformation history ended with later folding (D_3) and retrogression that have caused crenulation of S_2 and replacement of minerals by retrograde products, respectively.

Textural features and deformation-crystallisation relationships observed in porphyroblastic rocks of the Mandatoriccio complex are schematically represented in **Fig. 4.1**.

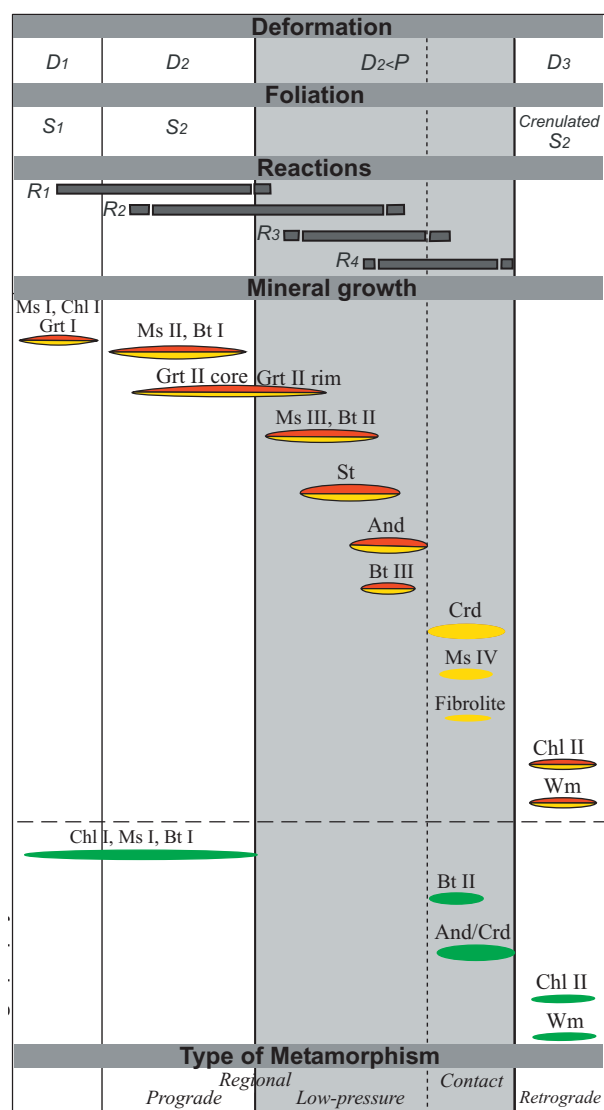
Temporal sequence of porphyroblast growth in micaschists and paragneisses (**Fig. 4.1**) begins with a low-temperature Mn-rich garnet (Grt II core), developed syntectonically with respect to D_2 . This syntectonic phase is documented by: crenulated inclusion trails, deflection of foliation planes and pressure shadows around garnet. Biotite (Bt II) and staurolite porphyroblasts overgrew on the S_2 schistosity during a period of deformational quiescence ($D_2 < P$); simultaneously, garnet develops static overgrowths (Grt II rim). Crystallisation under static conditions continued with andalusite formation at major expense of staurolite and, only in paragneisses, it ended with crystallisation of aggregates of fibrolitic sillimanite and cordierite. Generally, the fibrolite replaces biotite porphyroblasts, whereas cordierite overgrew on And+Bt-rich domains.

Unfortunately, indisputable textural evidence allowing to define the relative timing of crystallisation between fibrolite and cordierite are lacking.

Spotted schists with large porphyroblasts show simpler deformation-crystallisation

history with respect to micaschists and paragneisses (**Fig. 4.1**). Biotite spots (Bt II) and cordierite or andalusite porphyroblasts statically overgrew on a pre-existing mica-rich matrix.

Fig. 4.1: schematic diagram showing relative chronology of mineral growth with respect to deformation (D) and foliation (S) in micaschists (red symbols), paragneisses (yellow symbols) and spotted schists with large porphyroblasts (green symbols). $D_2 < P$ indicates growth interval of mineral "P" post-tectonic with respect to D_2 (terminology after Passchier & Trouw, 1996). Diagram contains also some of the reactions described in the section 4.2.



4.2 - REACTION HISTORY

Reaction history (**Fig. 4.1**) has been reconstructed following qualitative and quantitative approaches. Classical (qualitative) approach is based on observed mineral assemblages, microstructural and petrographic analyses, mineral chemistry and AFM projections (Thompson, 1957, **Figs. 4.2, 4.3**). Mainly, this approach has been helpful for prograde metamorphic reactions that are generally less easy to recognise and quantify due to the lack of some important information, as for example completely consumed reactants.

Quantitative approach has been adopted in favourable cases, when all the reactants and the products were still recognisable. Quantitative treatment consists in attempting to balance reactions by matrix calculations based on the least square method. This approach has been applied to two well-developed reaction domains that mainly involved staurolite porphyroblasts and And+Bt aggregates, respectively. These reaction domains have been observed in micaschists and in paragneisses sampled near the Umbriatico village (**Fig. 1.5**).

Thompson-type projections (AFM diagrams) are widely used for depicting phases compatibilities in metapelitic rocks which contain quartz, muscovite and a H_2O -rich fluid phase in excess. **Figs 4.2 and 4.3** contain AFM diagrams, projected from pure muscovite, quartz and water, relative to representative samples of micaschists (LL56a4) and paragneisses (LL61b2; LL61a2). In these AFM projections, average chemical analyses of minerals and whole-rock compositions are shown. Mineral analyses have been selected from **Tables 7-18 (Appendix 3)** with the only exception for chlorite that represents a possible chlorite composition in natural pelitic schists (Spear, 1993).

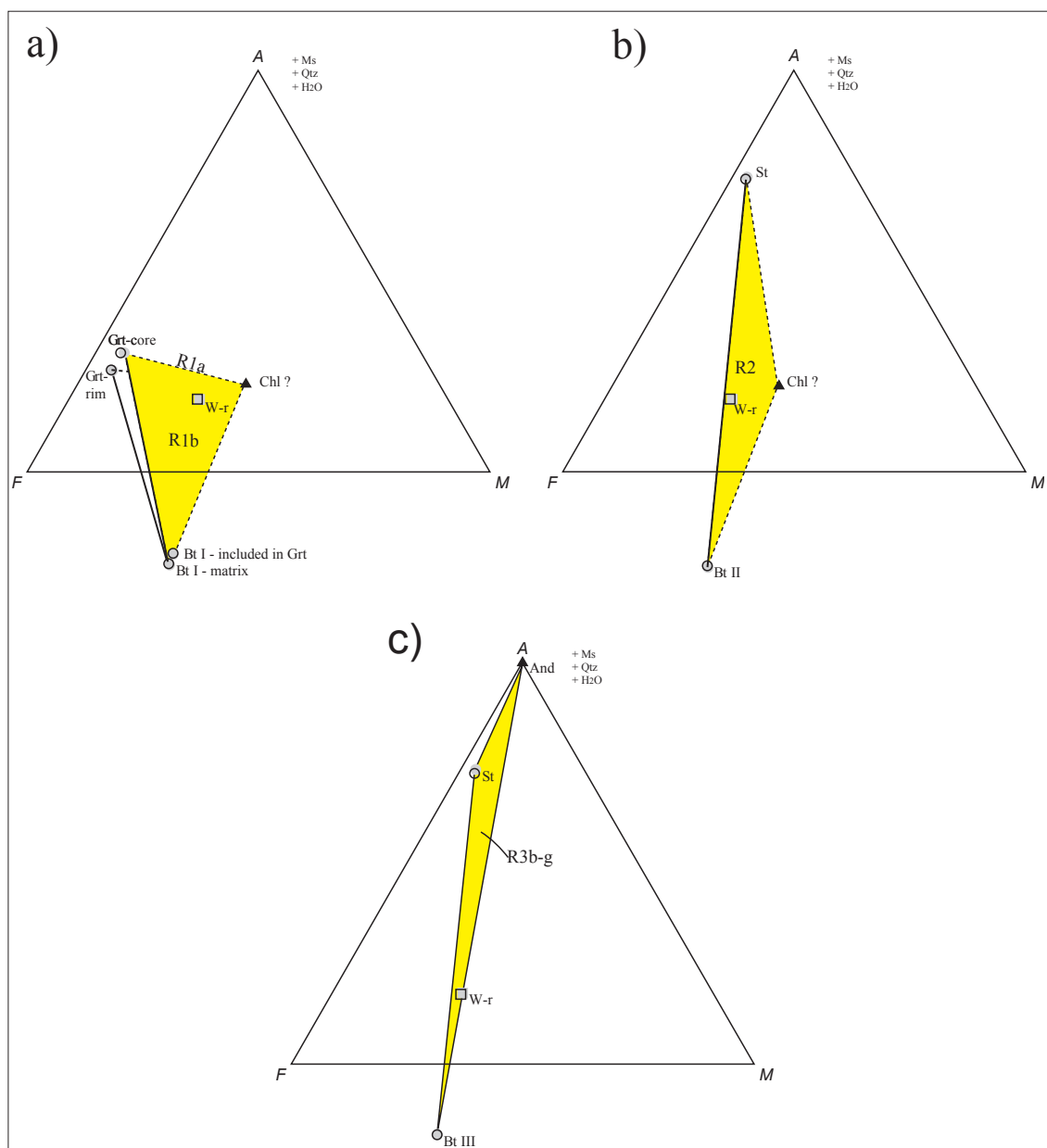


Fig. 4.2: AFM projection from quartz, muscovite and H_2O of coexisting minerals in a micaschist (LL56a4; $W-r$ = XRF-derived-whole-rock composition). Chlorite composition is theoretical. Black circles and squares refer to minerals and whole-rock compositions with $F=FeO+MnO$, respectively. Light-grey symbols refer to minerals and whole-rock compositions with $F=FeO$. Numbered R refers to reactions, see text for explanations.

It is important to consider the imperfection and the not complete thermodynamic validity of the projection scheme. Inaccuracies arise from important assumptions that simplify the effective chemical system, deviating it significantly from the reality.

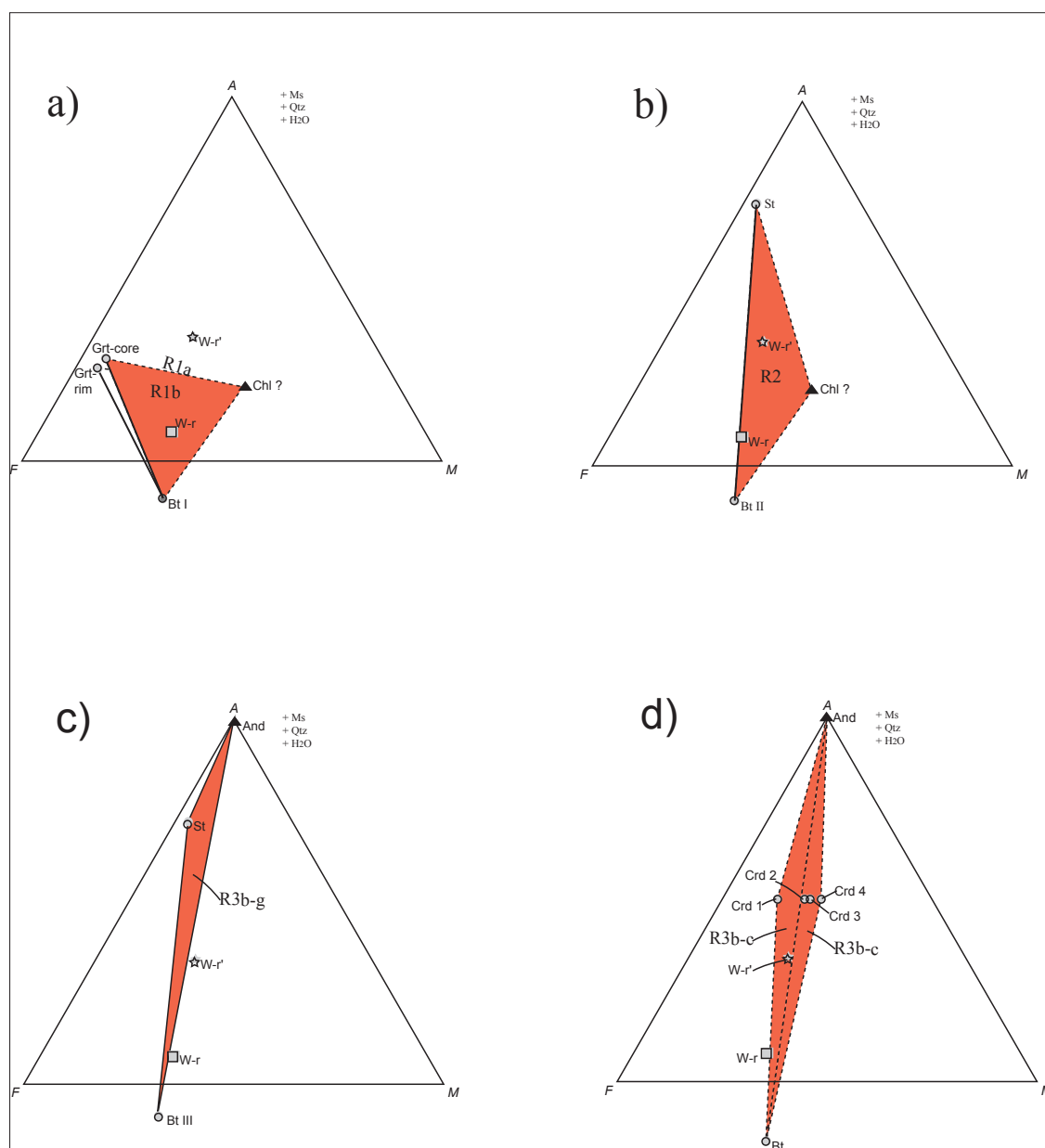


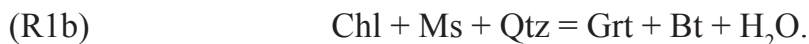
Fig. 4.3: AFM projection from quartz, muscovite and H_2O of coexisting minerals within paragneisses. Garnet has been analysed in the Qtz+Pl-rich layer of paragneiss (LL61a2). Black empty symbols refer to minerals and whole-rock compositions calculated adding MnO to FeO ($F=FeO+MnO$).

W-r and W-r' represent XRF-derived-whole-rock composition of Qtz+Pl-rich (LL61a2) and Bt-rich (LL61b2) layer of paragneiss, respectively. Numbered R refers to reactions, see text for explanations.

Chlorite, andalusite and cordierite compositions are theoretical. In particular, Crd 1 refers to theoretical Crd with an XFe corresponding to that of cores of pinite porphyroblasts (KFMASH system). Crd 2 corresponds to Crd 1 calculated in the complex chemical system NCKFMnMATSH; Crd 3 is the required Crd composition considering real mineral analyses (NCKFMnMATSH system) and opening the system to Na_2O ; Crd 4 corresponds to Crd 2 in a system closed to Na_2O .

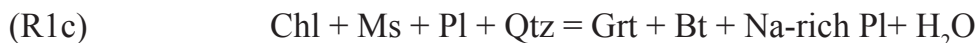
In the AFM diagrams shown in **Figs. 4.2** and **4.3** some essential constituents of minerals, such as Ca, Na, Ti and Zn, are ignored. In the **Figs. 4.2** and **4.3**, the Mn and Fe contents of minerals and rocks have been added and the AF(FeO+MnO)M compositions are depicted with a different colour. Another important approximation in the AFM projections is the use of a Al/K ratio of a pure muscovite (Al/K=3). Nevertheless, the projection scheme is successful showing the projected bulk-rock-compositions close to the pertinent two-phase tie lines and/or within the three-phase regions.

Microstructural evidence suggests that garnet represents the first interesting mineral developed during the prograde metamorphic evolution. The first appearance of garnet could be related to two continuous KFMASH reactions (**Figs. 4.2a, 4.3a**), as indicated by pre-tectonic muscovite (Ms I), chlorite (Chl I) and quartz inclusions:

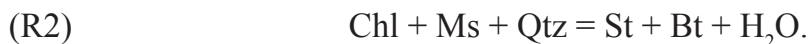


The R1b reaction could explain also the growth of syntectonic biotite (Bt I) crystals. Compatibility diagram relative to paragneisses shows that bulk-rock analysis of Bt-rich layers of paragneisses (LL61b2) is incompatible with garnet-forming reaction (**Fig. 4.3a**). As described in petrographic section (cf. 2.3.1.2), these layers are characterised by low modal abundance of garnet.

Usually, plagioclase represents a garnet inclusion and, probably, it played an important role in garnet-forming reactions. R1c is a possible continuous reaction in the CNKFMASH system:



Crystallisation history continued with the staurolite formation at major expense of muscovite and chlorite.

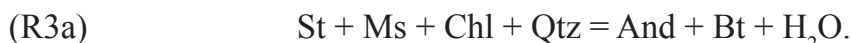


This hypothesis is supported by: i) the occurrence of porphyroblastic staurolite statically overgrown on muscovite-rich layers; ii) the presence of chlorite inclusions in the staurolite porphyroblasts; iii) the lack of evidence for significant participation of garnet in the staurolite-forming reaction.

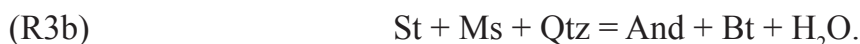
Probably, the continuous KFMASH or KFMASH R2 reaction, that is divariant in the KFMASH system (**Fig. 4.2b; 4.3b**), largely contributed to the growth of biotite porphyroblasts (Bt II). This stage of the reaction history was probably limited by chlorite availability and it contributed reducing muscovite availability from domains and rocks.

As described in previous sections (cf. 2.3.1.1, 2.3.1.2), staurolite shows reaction

coronas mainly composed of andalusite with minor small biotite crystals. Theoretic KFMASH univariant reaction enabling the removal of staurolite and the formation of andalusite is:



This reaction marks andalusite-in isograd in low-Al pelites (Spear, 1993). The studied reaction domains involving staurolite revealed that chlorite was quasi-absent at the beginning of the reaction (R3a), probably because it was entirely consumed by previous reactions (R1a-c; R2). Prograde chlorite has never been found in the matrix around the reaction domains. It constitutes inclusions in staurolite or it represents the result of retrograde reactions. Furthermore, crystallisation of andalusite at the expense of staurolite in the And+St+Bt+Grt assemblage can develop by the KFMASH divariant reaction (**Figs. 4.2c; 4.3c**):



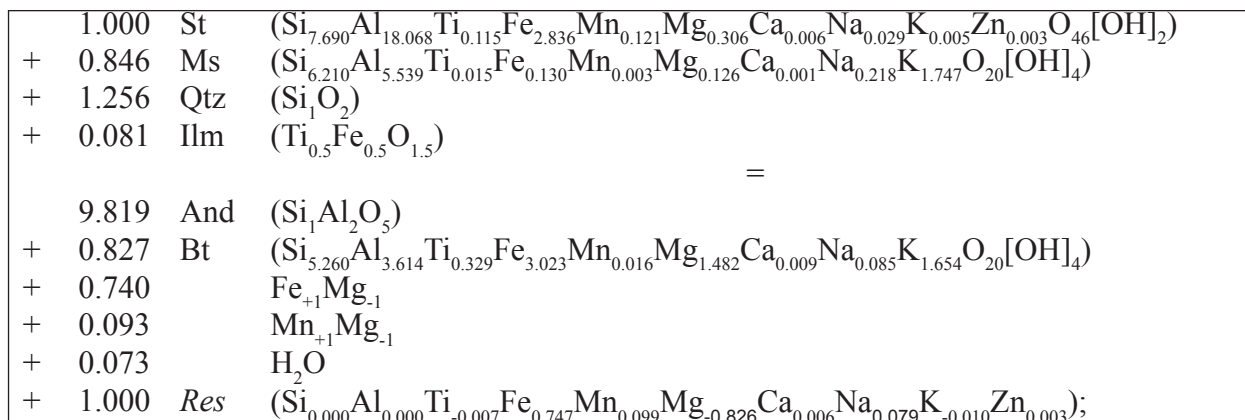
This reaction is predicted by the AFM projections (**Figs. 4.2c; 4.3c**). In the triangular diagram of **Fig. 4.3c** the bulk-rock composition of Bt-rich layer of paragneisses (LL61b2) falls outside the divariant field, probably because the analyses of small biotite (Bt III) used in AFM projections are of bad quality or, alternatively, there was a chlorite participation to the reaction.

Principal component analysis (PCA) applied on X-ray maps played an important role in studying these reaction domains, allowing to detect reactants remnants. Muscovite is quasi-absent in these reaction textures and it is just visible as small inclusions in quartz crystals (**Fig. 2.15d**) or as later poikilitic porphyroblasts (**Fig. 2.15c**). Probably, in some reaction domains, the low availability of muscovite acted as limiting reagent that controlled the quantity of consumed staurolite and formed products. Practically, chlorite has not been considered in modelling staurolite-consuming reaction. Furthermore, other phases (*e.g.* ilmenite) and/or substitution (*e.g.* FeMg_{-1}) have been added to matrix calculations, depending on microstructural evidence, X-ray maps and PCA. Details of mass balance calculations are described in **Appendix 4**.

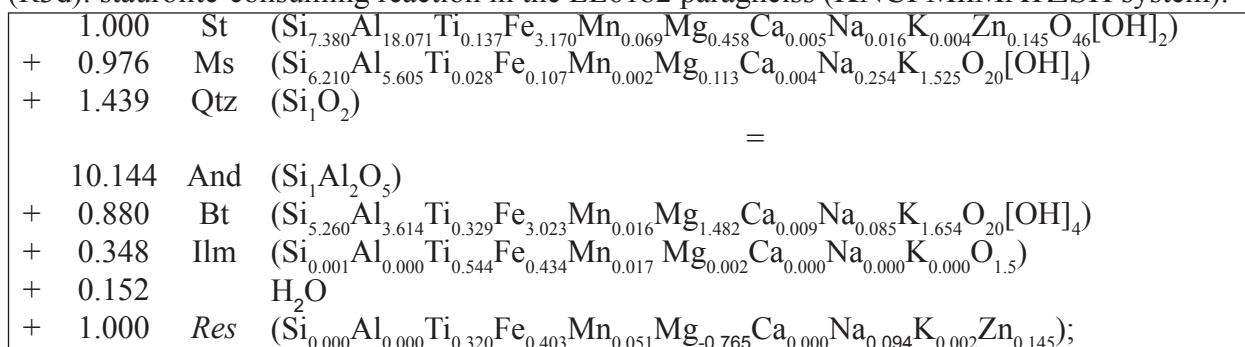
Five andalusite-in reactions have been obtained: one from LL56a4 micaschist (R3c), three from LL61b2 paragneiss (R3d-f) and one from LL61b1 paragneiss (R3g). Reactions R3c-e and R3g have been calculated in the eleven-dimensional composition space K_2O - Na_2O - CaO - FeO - MgO - Al_2O_3 - TiO_2 - ZnO - SiO_2 - H_2O (KNCFMnMATZSH) considering the real compositions of involved minerals. The R3f has been modelled in the KFMASH chemical system, considering simplified chemical compositions of minerals.

The results of the mass balance calculations are reported below.

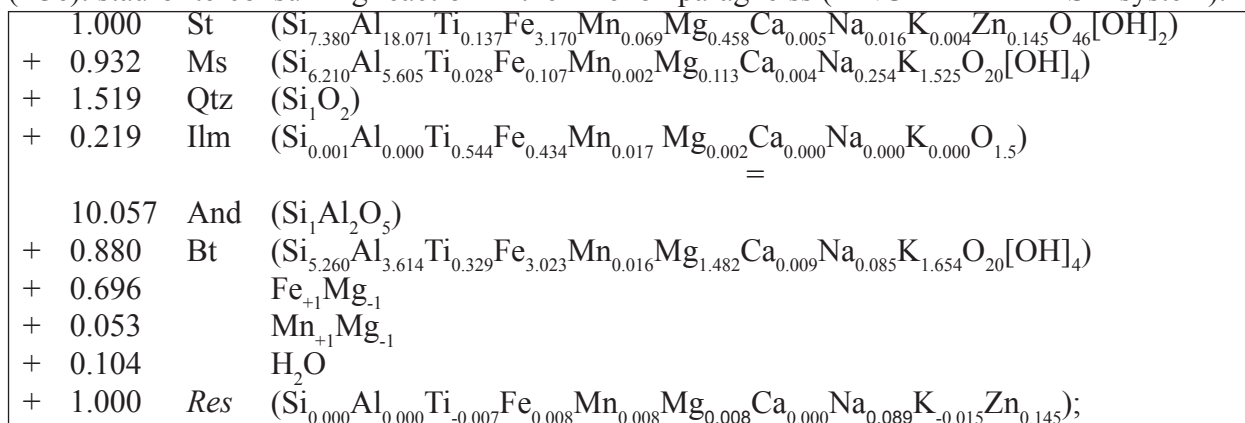
(R3c): staurolite-consuming reaction in the LL56a4 micaschist (KNCFMnMATZSH system).



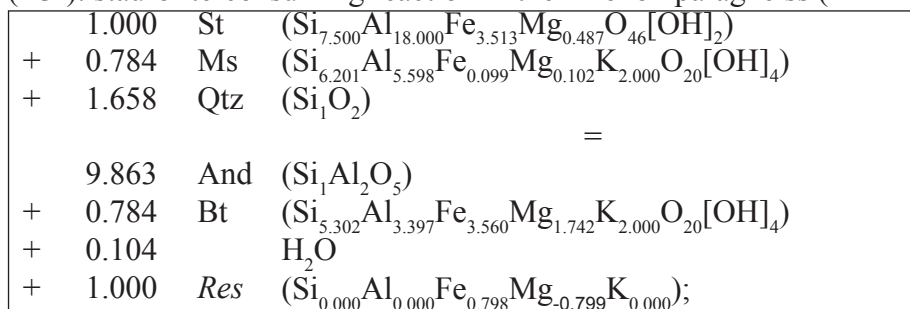
(R3d): staurolite-consuming reaction in the LL61b2 paragneiss (KNCFMnMATZSH system).



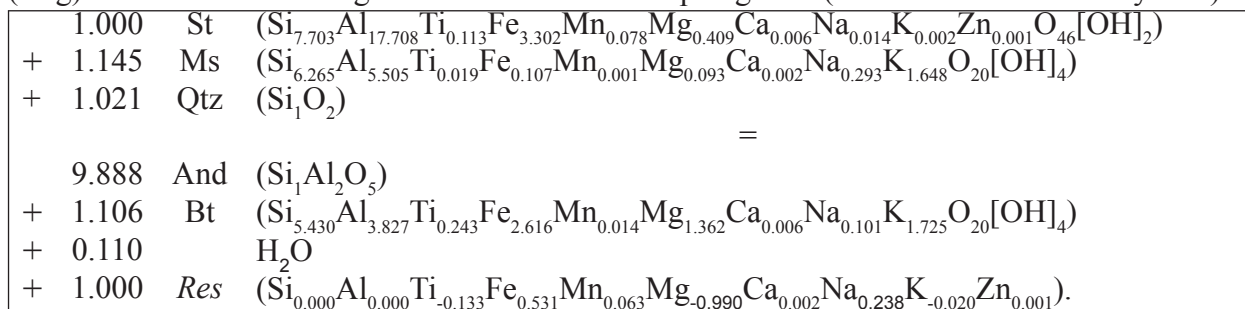
(R3e): staurolite-consuming reaction in the LL61b2 paragneiss (KNCFMnMATZSH system).



(R3f): staurolite-consuming reaction in the LL61b2 paragneiss (KFMASH system).



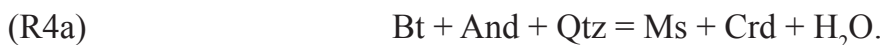
(R3g): staurolite-consuming reaction in the LL61b1 paragneiss (KNCFMnMATZSH system).



Where *Res* represents a residual vector.

Reaction history described until now is plausible for micaschists and paragneisses. Before retrograde evolution, paragneisses experienced other crystallisation events producing fibrolite and cordierite. Unfortunately, there are not undisputable microstructural evidences allowing to place exactly fibrolite crystallisation in the deformation-crystallisation history. For example, evidences of a clear replacement of andalusite by fibrolite are lacking. Probably, fibrolite crystallised as consequence of a heating metamorphic phase occurred just before the retrograde evolution marked by the cordierite crystallisation. Generally, fibrolite resulted from the replacement of the biotite instead of andalusite. According to Kerrick (1987) and Kerrick & Woodsworth (1989), fibrolite should form from the decomposition of biotite, due to the removal of K, Mg and Fe caused by acidic fluids that emanated from adjacent magmatic intrusions. Alternatively, fibrolite development could be related to a series of substitution mechanisms that mainly involve Ti. Ti-Tschermak substitution $[\text{Ti}^{\text{VI}} + 2\text{Al}^{\text{IV}} = (\text{Fe}^{2+}, \text{Mg}) + 2\text{Si}]$ could be the dominant mechanism for incorporation of Ti in the Fe-rich biotite and Mg-rich biotite (Fleet, 2003, and references therein). During fibrolite formation, Ti-Tschermak substitutions could have acted in opposite way, releasing Ti and Al and forming Ti-oxides around biotite and sillimanite fibres over pre-existing biotite, respectively. Rarely, fibrolite shows evidence of a direct replacement of the andalusite (*i.e.* And=Sill).

Generally, the cordierite formation at major expense of andalusite is predicted by the KFMASH divariant reaction (**Fig. 4.3d**):



As mentioned in previous section (cf. 2.3.1.2), cordierite is always altered in pinitite. Due to the lack of microprobe analyses of fresh cordierite, major problems have been tackled. Mathematical modelling of cordierite-forming reaction have been attempted following two approaches:

- a) taking simultaneously the theoretic composition of Fe-cordierite $[\text{Si}_5\text{Al}_4\text{Fe}_2\text{O}_{18}]$ and Mg-cordierite $[\text{Si}_5\text{Al}_4\text{Mg}_2\text{O}_{18}]$;
- b) considering a hypothetical cordierite with a X_{Fe} value corresponding to that of core of

analysed pinites (*i.e.* $X_{\text{Fe}}=0.74$; $\text{Crd}=\text{Si}_{5.315}\text{Al}_{3.742}\text{Ti}_{0.230}\text{Fe}_{2.744}\text{Mn}_{0.015}\text{Mg}_{1.659}\text{Ca}_{0.006}\text{Na}_{0.084}\text{K}_{1.662}\text{O}_{20}[\text{OH}]_4$).

Mass balances involving cordierite have been calculated in the ten-dimensional composition space $\text{K}_2\text{O}-\text{Na}_2\text{O}-\text{CaO}-\text{FeO}-\text{MgO}-\text{Al}_2\text{O}_3-\text{TiO}_2-\text{SiO}_2-\text{H}_2\text{O}$ (KNCFMnMATSH, R4b-d) and in the simplified six-component chemical system KFMASH (R4e). Since muscovite produced contemporary to cordierite contains Na, whereas reactants are almost Na-free, R4c and R4d mass balances have been opened to Na.

Mathematical modelling gives following mass balances:

(R4b):

1.000	Bt	$(\text{Si}_{5.315}\text{Al}_{3.742}\text{Ti}_{0.230}\text{Fe}_{2.744}\text{Mn}_{0.015}\text{Mg}_{1.659}\text{Ca}_{0.006}\text{Na}_{0.084}\text{K}_{1.662}\text{O}_{20}[\text{OH}]_4)$
+	10.545	And $(\text{Si}_1\text{Al}_2\text{O}_5)$
+	10.334	Qtz (Si_1O_2)
+	0.458	H_2O
=		
1.828	Fe-Crd	$(\text{Si}_{5.000}\text{Al}_{4.000}\text{Fe}_{2.000}\text{O}_{18})$
+	1.646	Mg-Crd $(\text{Si}_{5.000}\text{Al}_{4.000}\text{Mg}_{2.000}\text{O}_{18})$
+	1.229	Ms $(\text{Si}_{6.071}\text{Al}_{5.771}\text{Ti}_{0.039}\text{Fe}_{0.095}\text{Mn}_{0.003}\text{Mg}_{0.084}\text{Ca}_{0.003}\text{Na}_{0.280}\text{K}_{1.590}\text{O}_{20}[\text{OH}]_4)$
+	2.129	Ilm $(\text{Si}_{0.008}\text{Al}_{0.004}\text{Ti}_{0.543}\text{Fe}_{0.418}\text{Mn}_{0.022}\text{Mg}_{0.022}\text{Ca}_{0.000}\text{Na}_{0.000}\text{K}_{0.001}\text{O}_{1.5})$
+	2.695	Sub $(\text{Si}_{0.498}\text{Al}_{1.423}\text{Ti}_{-0.362}\text{Fe}_{-0.712}\text{Mn}_{0.006}\text{Mg}_{-0.646}\text{Ca}_{0.000}\text{Na}_{-0.028}\text{K}_{-0.121})$
+	1.000	Res $(\text{Si}_{0.000}\text{Al}_{0.000}\text{Ti}_{-0.002}\text{Fe}_{0.000}\text{Mn}_{-0.054}\text{Mg}_{0.000}\text{Ca}_{0.001}\text{Na}_{-0.092}\text{K}_{0.016})$;

(R4c):

1.000	Bt	$(\text{Si}_{5.315}\text{Al}_{3.742}\text{Ti}_{0.230}\text{Fe}_{2.744}\text{Mn}_{0.015}\text{Mg}_{1.659}\text{Ca}_{0.006}\text{Na}_{0.084}\text{K}_{1.662}\text{O}_{20}[\text{OH}]_4)$
+	5.550	And $(\text{Si}_1\text{Al}_2\text{O}_5)$
+	6.267	Qtz (Si_1O_2)
+	0.116	H_2O
+	0.104	Na_2O
=		
1.286	Fe-Crd	$(\text{Si}_{5.000}\text{Al}_{4.000}\text{Fe}_{2.000}\text{O}_{18})$
+	0.838	Mg-Crd $(\text{Si}_{5.000}\text{Al}_{4.000}\text{Mg}_{2.000}\text{O}_{18})$
+	1.058	Ms $(\text{Si}_{6.071}\text{Al}_{5.771}\text{Ti}_{0.039}\text{Fe}_{0.095}\text{Mn}_{0.003}\text{Mg}_{0.084}\text{Ca}_{0.003}\text{Na}_{0.280}\text{K}_{1.590}\text{O}_{20}[\text{OH}]_4)$
+	0.4588	Ilm $(\text{Si}_{0.008}\text{Al}_{0.004}\text{Ti}_{0.543}\text{Fe}_{0.418}\text{Mn}_{0.022}\text{Mg}_{0.022}\text{Ca}_{0.000}\text{Na}_{0.000}\text{K}_{0.001}\text{O}_{1.5})$
+	0.168	Sub $(\text{Si}_{0.498}\text{Al}_{1.423}\text{Ti}_{-0.362}\text{Fe}_{-0.712}\text{Mn}_{0.006}\text{Mg}_{-0.646}\text{Ca}_{0.000}\text{Na}_{-0.028}\text{K}_{-0.121})$
+	1.000	Res $(\text{Si}_{0.000}\text{Al}_{0.000}\text{Ti}_{0.000}\text{Fe}_{0.000}\text{Mn}_{0.000}\text{Mg}_{0.000}\text{Ca}_{0.003}\text{Na}_{0.000}\text{K}_{0.000})$;

(R4d):

1.000	Bt	$(\text{Si}_{5.315}\text{Al}_{3.742}\text{Ti}_{0.230}\text{Fe}_{2.744}\text{Mn}_{0.015}\text{Mg}_{1.659}\text{Ca}_{0.006}\text{Na}_{0.084}\text{K}_{1.662}\text{O}_{20}[\text{OH}]_4)$
+	2.439	And $(\text{Si}_1\text{Al}_2\text{O}_5)$
+	3.723	Qtz (Si_1O_2)
+	1.389	Sub $(\text{Si}_{0.498}\text{Al}_{1.423}\text{Ti}_{-0.362}\text{Fe}_{-0.712}\text{Mn}_{0.006}\text{Mg}_{-0.646}\text{Ca}_{0.000}\text{Na}_{-0.028}\text{K}_{-0.121})$
+	0.109	Na_2O
+	0.570	Ilm $(\text{Si}_{0.008}\text{Al}_{0.004}\text{Ti}_{0.543}\text{Fe}_{0.418}\text{Mn}_{0.022}\text{Mg}_{0.022}\text{Ca}_{0.000}\text{Na}_{0.000}\text{K}_{0.001}\text{O}_{1.5})$
=		
1.293	Crd	$(\text{Si}_{5.000}\text{Al}_{4.000}\text{Fe}_{1.472}\text{Mg}_{0.527}\text{O}_{18})$
+	0.940	Ms $(\text{Si}_{6.071}\text{Al}_{5.771}\text{Ti}_{0.039}\text{Fe}_{0.095}\text{Mn}_{0.003}\text{Mg}_{0.084}\text{Ca}_{0.003}\text{Na}_{0.280}\text{K}_{1.590}\text{O}_{20}[\text{OH}]_4)$
+	2.000	H_2O
+	1.000	Res $(\text{Si}_{0.000}\text{Al}_{0.000}\text{Ti}_{0.000}\text{Fe}_{0.000}\text{Mn}_{0.033}\text{Mg}_{0.001}\text{Ca}_{0.004}\text{Na}_{0.000}\text{K}_{0.000})$;

(R4e):

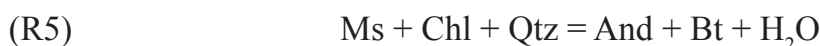
	1.000	Bt	(Si _{5.265} Al _{3.469} Fe _{3.285} Mg _{1.9799} K _{2.000} O ₂₂)
+	6.317	And	(Si ₁ Al ₂ O ₅)
+	7.421	Qtz	(Si ₁ O ₂)
			=
	2.579	Crd	(Si _{5.000} Al _{4.000} Fe _{1.472} Mg _{0.527} O ₁₈)
+	1.000	Ms	(Si _{6.107} Al _{5.786} Fe _{0.057} Mg _{0.049} K _{2.000} O ₂₂)
+	1.000	Res	(Si _{0.000} Al _{0.000} Fe _{-0.571} Mg _{0.571} K _{0.000}).

Where *Sub* is a quantified mineral substitution and *Res* is always a residual vector.

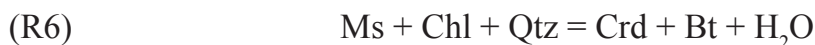
Starting from average chemical analyses of other reaction-involved phases, the first method allowed to obtain different stoichiometric coefficients for Fe-cordierite and Mg-cordierite (R4b, R4c). In this way, the X_{Fe} value of the required cordierite varies from 0.53 in a mass balance closed to Na₂O (R4b) to 0.61 in a mass balance opened to Na₂O (R4c).

AFM diagram (**Fig. 4.3d**) shows that Crd 1 and Crd 2, with an X_{Fe} value corresponding to that of the core of analysed pinite ($X_{\text{Fe}}=0.74$), are more compatible with other minerals and whole-rock compositions. In fact, whole-rock compositions of paragneisses fall outside the hypothetical reaction divariant fields, reconstructed using the cordierite compositions required by the chemical system (Crd 3 and Crd 4 in **Fig. 4.3d**). R4b and R4c reactions predict the formation of ilmenite with cordierite at major expense of andalusite and biotite; ilmenite is necessary to incorporate the Ti released from biotite, which is not accommodated in cordierite.

Some graphical consideration for spotted schists with large porphyroblasts can be argued, too. As described in previous sections, large porphyroblasts are mainly composed of alteration products of cordierite and/or andalusite. In contact metamorphic rocks andalusite and cordierite develop by the hypothetical KFMASH divariant reactions:



and



As described in petrographic section (cf. 2.3.2), spotted schists with large porphyroblasts are characterised by reaction halos well-developed especially around altered cordierite porphyroblasts. Considering that, the R6 reaction predicts the formation of cordierite and biotite, reaction halos could be related to the faster growth of cordierite with respect to biotite. This process lowered Fe and Mg content in the cordierite neighbourhood, obstructing the biotite crystallization.

Schematic P-T diagram in the KFMASH system (**Fig. 4.4**) resumes reconstructed reaction history and shows the location of not-observed reactions, too.

The qualitative topology is redrawn after Pattison & Vogl (2005) and shows only a portion of the full Fe-Mg divariant reaction intervals.

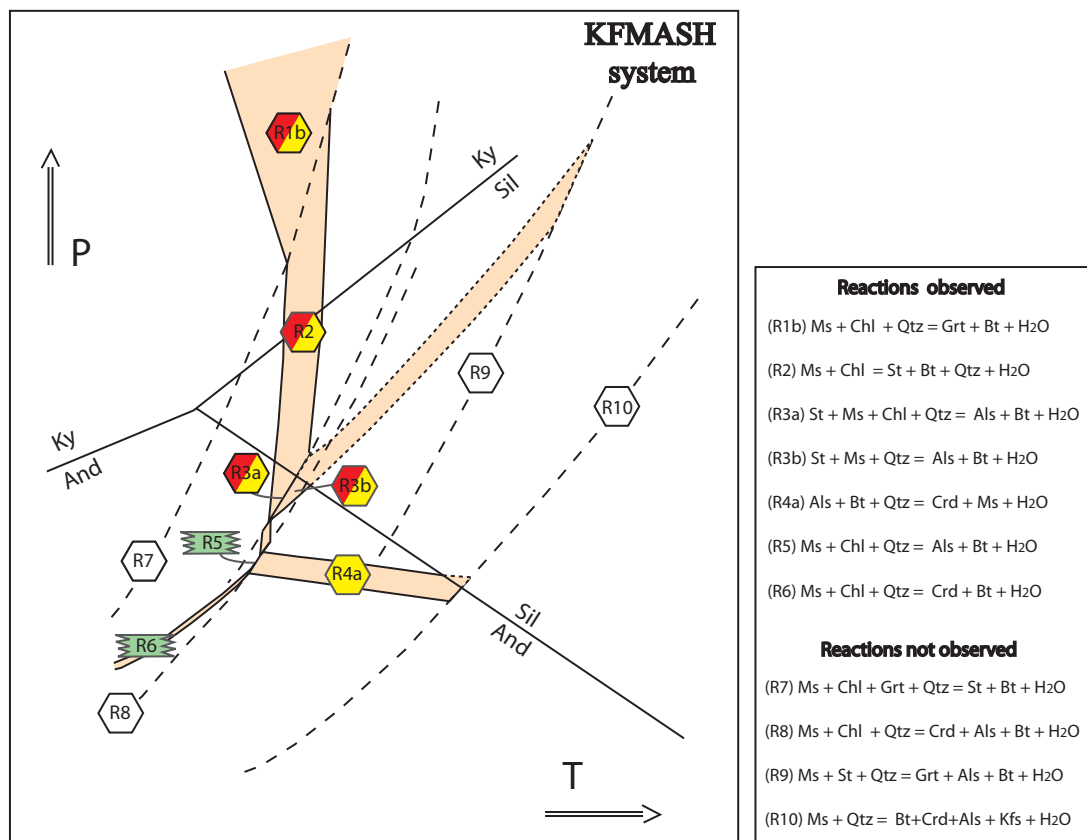


Fig. 4.4: schematic P-T diagram showing observed and not-observed reactions. Observed reactions are discussed in the text. Light-orange fields partially represent divariant reaction intervals. Large dashed lines represent univariant reactions not recognised in analysed rocks, whereas small dashed lines delimit divariant fields not observed. Modified, after Pattison & Vogl (2005). Filled polygons refer to reaction observed respectively in micaschists (red), paragneisses (yellow) and spotted schists (green).

Three main arguments arise from the schematic P-T diagram:

- reactions and mineral-assemblage stabilities involving garnet under-represent its occurrence in metapelitic rocks. Garnet appears and it is stable at intermediate- to high-pressure conditions probably because in the KFMASH system some elements are ignored. For example, Mn and Ca contribute considerably to stabilize garnet at lower pressure (Mahar *et al.*, 1997). According to Spear & Cheney (1989), Symmes & Ferry (1992) and Mahar *et al.* (1997), garnet is not well modelled in KFMASH system, where it occurs as a modally minor phase and a relatively low-reactive one;
- univariant and divariant reactions observed in the micaschists and in the paragneisses are approximately the same, at least until to the andalusite formation at the expense of staurolite (R3b). Cordierite and fibrolitic sillimanite, occurred only

in paragneisses, could be linked to different bulk-rock chemistry, P-T conditions or both;

- c) R5 and R6 reactions observed in spotted schists with large porphyroblasts could reflect effectively different reaction histories with respect to paragneisses. This hypothesis is supported by the fact that spotted schists with large porphyroblasts have chemical composition comparable to cordierite-bearing paragneisses (LL61b2; **Figs. 2.3; 2.4**) and that they did not develop Grt+St assemblages. Reaction sequence observed in spotted schists with large porphyroblasts could be linked to different tectono-metamorphic positions (depth and/or distance from plutons).

AFM projections (**Figs. 4.2, 4.3**) and schematic P-T diagram in the KFMASH system (**Fig. 4.4**) led only to qualitative observations. A more realistic reaction history could arise from phase diagrams constructed for fixed-bulk compositions in chemical systems that also consider “extra” elements, such as Mn, Ca and Na (Hollister, 1966; Symmes & Ferry, 1992; Mahar *et al.*, 1997; Thinkham *et al.*, 2001; Wei *et al.*, 2004). The relative abundance of Mn in selected samples (*i.e.* LL56a4), favoured the nucleation and the development of spessartine-rich garnet during prograde reaction history. Consequently, because of the role of Mn in stabilising garnet, it is more appropriate to consider the KMnFMASH chemical system at least for garnet-formation reactions. The addition of Mn could solve the problem of pressures (a). Phase diagrams constructed for different bulk-rock compositions could led to more correct observations on the tectono-metamorphic evolution of the analysed samples (b, c). In particular, phase diagrams relative to the representative micaschist (LL56a4) and paragneisses (LL61a2; LL61b2) could effectively explain if cordierite and fibrolite formation are related to different metamorphic evolution and/or to different chemical compositions.

Therefore, P-T conditions of modelled reactions will be constrained by phase diagram calculations using bulk-rock and reaction-domain compositions.

4.3 - PRESSURE-TEMPERATURE ESTIMATES

4.3.1 – An overview of available methods

There are several possibilities to decipher the P-T conditions of metamorphic rocks through thermodynamic calculations. Four main methodologies based on mineral and/or whole-rock compositions are commonly used to infer P-T conditions of rocks: 1) conventional geothermobarometers; 2) multi-equilibrium thermobarometry; 3) the Gibbs method and 4) isochemical phase-diagram sections, or simply P-T pseudosections.

1) Conventional geothermometers and geobarometers are mainly based on Fe-Mg ion-exchange reaction between two minerals and on mass-transfer reactions, respectively. Commonly, this method is applied to zoned poikiloblastic garnets, to its inclusions and to matrix minerals (St. On  , 1987). It could provides good estimates of P-T conditions of different garnet-growth stages until to peak metamorphic conditions, pairing matrix minerals with garnet rims. This technique requires good chemical analyses of a rim-core-rim traverse through garnet crystals (at least 50 analysed points), of appropriate mineral inclusions of garnet (*e.g.* plagioclase and biotite), of garnet near solid inclusions to control halo effect and of matrix minerals.

2) Estimates of P-T conditions could also arise from thermodynamic calculations employing internally-consistent data sets (*e.g.* Berman, 1988; Powell & Holland, 1988; Holland & Powell, 1998) using the measured compositions of minerals with a small number of equilibrium conditions. Multi-equilibrium thermobarometry is related to the calculation of multiple reactions based on an internally-consistent dataset. This technique uses particular software, *e.g.* TWQ of Berman (1991) and the “Optimal Thermobarometry” (AverageP-T) option of THERMOCALC (Powell & Holland, 1994).

3) The Gibbs method (Spear & Selverstone, 1983; Spear, 1988) uses chemical compositions of zoned garnet to obtain information about different P-T conditions recorded by garnet during its growth. This method requires knowledge about the evolution of equilibrium assemblage during garnet growth and it is based on five major assumptions: 1) the growth zoning is the only zoning mechanism; 2) the existence of local equilibrium (evidence of local disequilibrium would be the formation of depletion haloes in the matrix around garnet); 3) the low diffusion re-equilibration, that is probably an insignificant problem for sample from the amphibolite facies but becomes increasingly important at higher temperature (granulite facies); 4) the not consideration of minor compounds; 5) the use of a simplified solution model.

All these techniques could be used for metamorphic rocks but there are some limits: i) these methods can give erroneous results because there is no satisfactory method to determine which (if any) matrix mineral compositions were in equilibrium; ii) they are strongly dependent on presence of garnet. In fact, most geothermobarometers are based on reactions between garnet and other phases (Spear, 1993); iii) in presence of garnet

these techniques could not be applied if garnet is inclusion-free or if one of the required inclusions is lacking.

4) A powerful alternative technique for P-T calculations, currently in large expansion, requires the construction of isochemical phase-diagram sections for an appropriate model system. These diagrams, introduced for the first time by Hensen (1971), are very adequate to visualise the dependence of mineral assemblages on bulk-rock composition, since they are drawn for just one particular system composition (*e.g.* Will, 1998).

Pseudosections show the stability of mineral assemblages for a fixed bulk-rock composition and could provide information about the prograde and retrograde evolution of the rocks. In particular, in garnet-bearing metapelites these P-T projections have been largely applied to determine P-T conditions of garnet growth (Vance & Holland, 1993; Vance & Mahar, 1998; Stowell & Tinkham, 2003; Tinkham & Ghent, 2005; Zuluaga *et al.*, 2005). Isopleths of selected garnet composition are plotted in all the mineral assemblages stability fields containing garnet and their intersection could define a point or, more probably, a small field of P-T conditions that could correspond to the P-T conditions of garnet growth. As pointed out by Vance & Holland (1993), P-T trajectories constructed in this way have much smaller uncertainties and are much better constrained than those obtained by thermobarometric methods.

Nonetheless, there are two major limits using P-T pseudosections: a) the choice of the chemical system most appropriate to represent the observed mineral assemblages; b) the effect of fractionation induced by porphyroblasts growth on the equilibrium composition. P-T pseudosections, in fact, could be very helpful to define peak metamorphic conditions and retrograde evolution of the rocks (Tinkham & Ghent, 2005 and references therein) but it is necessary to consider that the equilibrium composition could change during the metamorphic history of rocks (Stuwe, 1997; Marmo *et al.*, 2002; Tinkham & Ghent, 2005; Zuluaga *et al.*, 2005).

4.3.2 - Thermodynamically calculated phase-relations

Selected samples for P-T path reconstructions contain low-modal abundance of garnet (less than 2 %) and they are characterised by several reaction textures involving staurolite, andalusite, biotite and cordierite. Rocks with these petrographic characters are well constrainable by isochemical phase diagram sections (Johnson *et al.*, 2003); therefore, P-T mineral equilibria diagrams have been largely used in this work to reconstruct prograde and retrograde metamorphic evolution of rocks.

P-T phase diagrams have been constructed using THERMOCALC software of Powell & Holland (1988), Powell & Holland (1998), and subsequent upgrades, with fifth upgrade (version 5.5) of the internally consistent thermodynamic dataset (*i.e.* Holland & Powell, 1998) and considering activity-composition relationships for the end members proposed by Holland & Powell (1998) and Wei *et al.* (2004).

The modelling has been performed on a micaschist (LL56a4) and on two representative Qtz+Pl-rich (LL61a2) and Bt-rich (LL61b2) centrimetric thick layers of paragneisses (see **Fig. 1.5** for sample locations). P-T pseudosections of rocks have been calculated using whole-rock compositions, whereas P-T pseudosections of reaction textures have been modelled using reaction domain compositions derived from mass balance calculations. A tentative of reconstruction of prograde garnet growth conditions have been performed only in LL56a4 micaschist that show the relatively higher modal abundance of garnet (*ca.* 1.5 %). Two P-T pseudosections have been constructed for this sample in order to model prograde-garnet growth and post-garnet growth conditions, respectively. Paragneisses have been considered garnet-free and major attention has been focused on modelling observed reaction textures.

P-T modelling required particular attention concerning: a) the choice of the most appropriate chemical system to represent observed mineral assemblages; b) mineral projections to reduce the chemical components of bulk-rock compositions; c) the effect of garnet-growth-induced fractionation on the equilibrium composition.

4.3.2.1 - Chemical system

As a first approximation, the KFMASH chemical system is the more appropriate to represent mineral assemblages in metapelites (Thompson, 1957) and is perhaps the most extensively investigated system in the petrologic literature. On the basis of thermodynamic data, important quantitative predictions are derived from it (*i.e.* invariant points and linked reactions; *e.g.* Thompson, 1976; Spear & Cheney, 1989; Powell & Holland, 1990; Xu *et al.*, 1994). This simple chemical system gives satisfactory representations of the stability fields of mineral assemblages involving ferromagnesian minerals. In fact, chlorite, biotite, staurolite, cordierite and other main metapelitic minerals, such as muscovite, K-feldspar and Al_2SiO_5 -polymorphs, are well-represented. A mineral that is not well-modelled in KFMASH system is the garnet (Hollister, 1966). It occurs as a scarcely represented phase because the thermodynamic stability of mineral assemblages involving garnet are strongly affected by small concentrations of the Ca and Mn minor components (Hollister, 1966; Symmes & Ferry, 1992; Mahar *et al.*, 1997; Tinkham *et al.*, 2001; Wei *et al.*, 2004). Tinkham *et al.* (2001) suggested that the MnNaCaKFMASH system is the minimal one required to adequately model developed mineral assemblages and the composition of garnet in metapelitic rocks. The authors observed that the addition of MnO, CaO and Na_2O in the chemical system was successful in predicting the sequence of assemblages involving garnet and plagioclase, but it failed to predict assemblages involving staurolite, andalusite and cordierite. White *et al.* (2000) considered the effect of TiO_2 and Fe_2O_3 on metapelitic assemblages at greenschist- and amphibolite-facies conditions. They arrived to the conclusion that small and/or moderate amounts of TiO_2 and Fe_2O_3 have little effect on silicate mineral equilibria in metapelites at considered metamorphic facies. In particular, the addition of TiO_2 in the chemical system has little effect on the stability of silicate

assemblages, whereas adding significant amounts of Fe_2O_3 rocks could develop a markedly different metamorphic succession.

Even if $\text{CaO}+\text{Na}_2\text{O}$ and $\text{Fe}_2\text{O}_3+\text{TiO}_2$ are important in understanding mineral equilibrium in metapelites they are not critical for modelling the stability field of ferromagnesian assemblages.

Wei *et al.* (2004) suggest that among the non-KFMASH components, the Mn is the element that should not be neglected in phase equilibrium reconstructions of medium- to low-pressure metapelites. In fact, small amounts of MnO in whole-rock compositions (*ca.* 0.1 wt % of MnO) are particularly important in stabilising garnet (Symmes & Ferry, 1992; Mahar *et al.*, 1997; Wei *et al.*, 2004). The Mn partitioning in garnet during its growth contributes to enlarge garnet-bearing stability fields at the expense of other phases such as chlorite, staurolite and cordierite. Besides garnet, the stability fields of muscovite and Al_2SiO_5 -polymorphs (at intermediate pressure) or K-feldspar (at lower pressure), expand, too.

Following the suggestions of Wei *et al.* (2004), mineral assemblages observed in micaschists and paragneisses of the Mandatoriccio complex have been modelled mainly in the KFAMSH and KMnFMASH systems. In particular, for a relatively garnet-rich micaschist (mode of garnet < 2%) two isochemical phase diagrams have been calculated. The prograde garnet-growth history has been constrained by plotting isopleths in a KMnFMASH P-T pseudosection, whereas the post-garnet growth history has been modeled in the KFMASH system. Due to the scarce abundance of garnet (mode of garnet < 1%) within paragneisses, the KFMASH chemical system has been chosen for modeling mineral assemblages. For a more detailed description of technique followed for XRF data reduction, see **Appendix 5**.

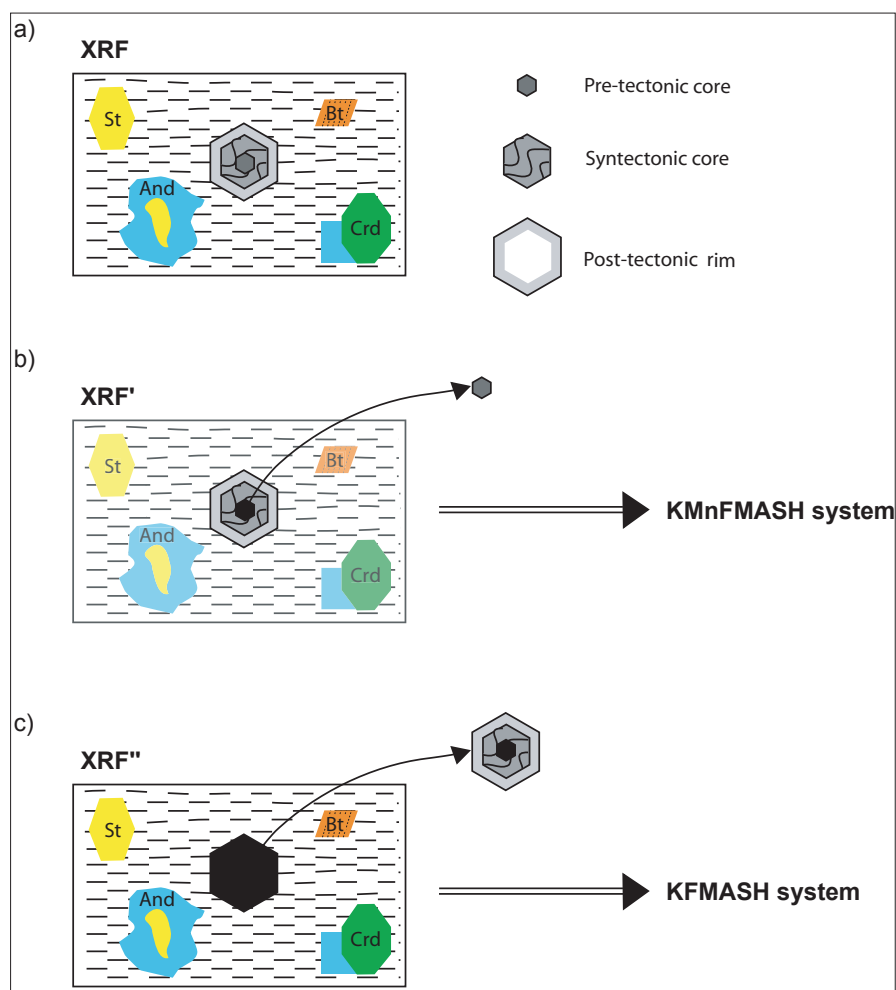
4.3.2.2 – Effective-bulk-rock composition

The effective-bulk-composition is the chemical composition of that part of the system (*i.e.* of the rock) that is really at equilibrium. It could change during the metamorphic history (Stuwe, 1997). In opened systems, major chemical variations could be related to metasomatism and/or to the interaction between fluids and rocks. In closed systems, the growth of zoned minerals represents the most important factor in changing the effective-bulk-rock composition. Pelitic rocks typically contain strongly zoned minerals among which garnet is the most important. Except for high-grade rocks, where diffusion zoning is very important, in low- to medium-grade rocks the chemical variation of garnet is dominated by growth zoning (Spear, 1993). In these cases, elements are trapped in various garnet shells and, therefore, they are subtracted from composition available to the reacting phase assemblages. Garnet rims can be assumed in equilibrium with matrix, while the inner part of garnet crystals is out of equilibrium.

Even if different techniques have been proposed in order to calculate the effective-bulk-rock composition (Marmo *et al.*, 2002; Tinkham & Ghent, 2005; Zuluaga *et al.*,

2005), in this section will be briefly described an alternative procedure. Generally, garnet crystals in micaschists show a syntectonic inclusion-rich core, with moderate values of Mn, surrounded by narrow post-tectonic rim (cf. 2.3.1.1). Only few crystals contain an inner inclusion-free core with high Ca content. P-T conditions of the metamorphic history coeval to garnet growth have been constrained in the KMnFMASH system. In this stage, the bulk rock composition obtained from the X-ray-fluorescence (XRF) analysis has been considered the most appropriate with the only adjustment related to the inner Ca-rich core (XRF'; **Fig. 4.5a, b**). These grossular-rich portions of garnet have been interpreted as inherited or as not in equilibrium during the syntectonic history. Consequently, they have been subtracted from the XRF-derived-bulk-rock composition. In order to model the effect of garnet-growth induced fractionation, pseudosections have been constructed using XRF-bulk-rock composition projected from a theoretical garnet composition (**Fig. 4.5c**). Generally, Mn has a low availability in metapelites and it tends to be incorporated in garnets during growth (Hollister, 1966), so the projection from theoretical composition of garnet implies the subtraction of Mn from the KMnFMASH system (*i.e.* KFMASH system). See **Appendix 5** for a more detailed description of the technique followed for the effective-bulk-rock composition calculations.

Fig. 4.5: graphical representation of the effective-bulk-rock-composition calculation. a) XRF-derived bulk rock composition without chemical adjustments; b) projection of XRF-derived bulk rock composition from Ca-rich pre-tectonic core, this composition (XRF') is more appropriate to model syn- and post-tectonic garnet growth; c) projection of XRF' from remaining garnet composition (XRF''). This composition approximates the equilibrium composition of the system after the garnet growth.



4.3.2.3 - P-T phase diagrams of rocks

Information about the prograde and retrograde evolution of the rocks have been deduced mainly using P-T mineral equilibria diagrams. The modelling has been performed for a micaschist (LL56a4) and for two paragneisses (LL61a2, LL61b2), which bulk-rock analyses are shown in **Table 2 (Appendix 2)**.

MICASCHIST

Micaschist has a MnO content of 0.21 %, twice the amount of MnO in paragneisses (≤ 0.1 %), suggesting the inclusion of MnO as a system component (Spear & Cheney, 1989; Symmes & Ferry, 1992; Mahar *et al.*, 1997; Wei *et al.*, 2004).

The KMnFMASH projection presented here (**Fig. 4.6**) in the P-T range of 0.5-10 kbar and 450-650 °C has been calculated using activity-composition relationships for the end-members proposed by Wei *et al.* (2004). Apart from excess water, seven phases are involved in this pseudosection: chlorite, muscovite, biotite, staurolite, garnet, quartz and one Al_2SiO_5 -polymorphs.

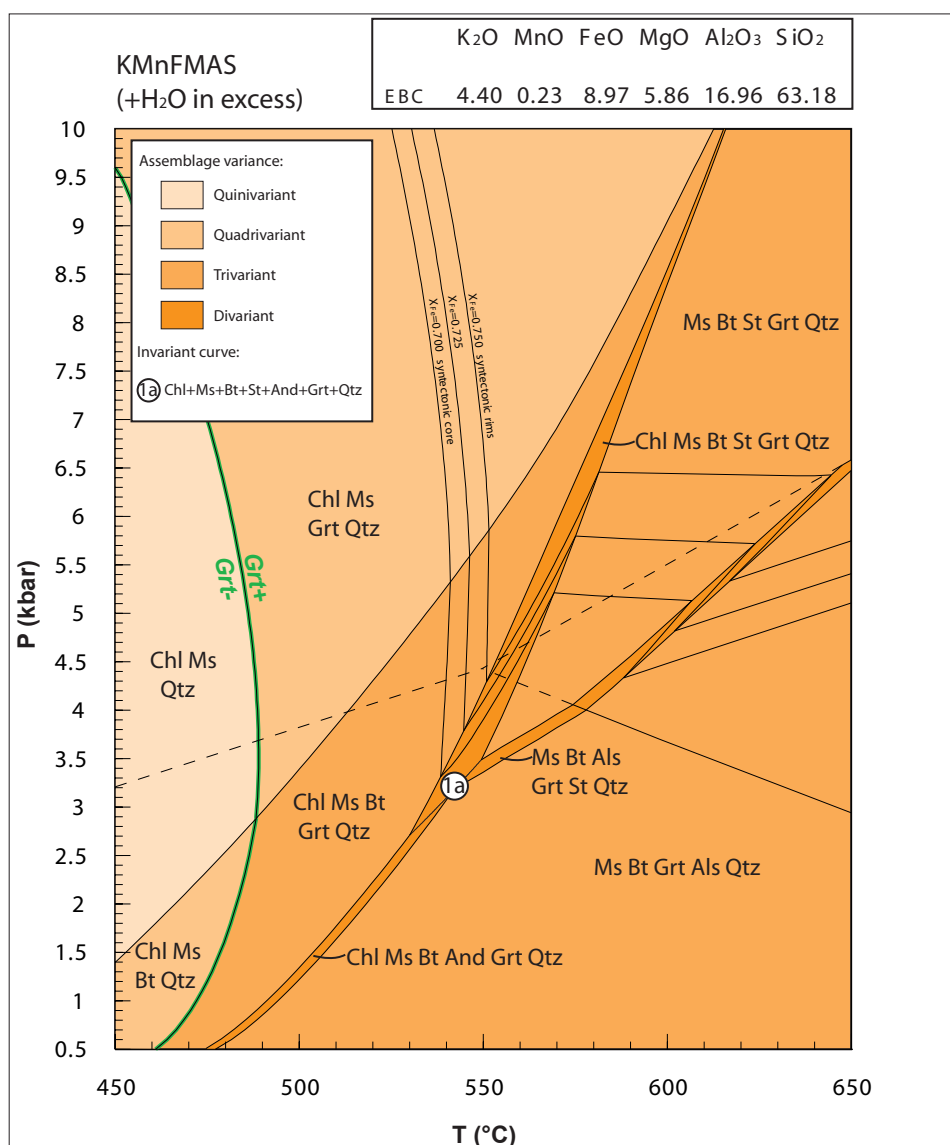


Fig. 4.6: P-T pseudosection calculated for the LL56a4 micaschist with the XRF'-effective-bulk composition (Fig. 4.5b; EBC in mol %). Stable assemblage fields are coloured by assemblage variance. Al_2SiO_5 are absent where dashed. Thick-green curve separates the P-T space in which garnet is not stable from that in which garnet is stable. Measured XFe isopleths of syntectonic garnet are also depicted.

The P-T segment relative to prograde and/or garnet-growth history will be deduced from mineral assemblage stability fields and their relationships with X_{Fe} garnet isopleths. These latter refer to syntectonic garnet composition and do not represent inherited Ca-rich core of garnets. In particular, lower value corresponds to X_{Fe} of inner part of syntectonic core, whereas higher value refers to outer part of syntectonic core.

Petrographic analyses revealed a prograde paragenesis characterized by Chl+Ms+Qtz followed by an enlarged mineral assemblage comprising also garnet and biotite. This latter formed before garnet as documented by Chl+Ms+Bt+Qtz quadrivariant field. Sequence of mineral assemblages combined with the quasi-isothermal isopleths do not give many information about pressure but indicate that the garnet growth took place during increasing temperatures. X_{Fe} isopleth concerning the outer part of syntectonic core comes in contact with staurolite-producing divariant field at P and T of about 4.3 kbar and 550 °C, respectively.

Considering Mn fractionation in garnet during its growth, P-T history reconstructible by KMnKMASH pseudosection end before or at the beginning of the staurolite formation (Chl+Ms+Bt+Grt+St+Qtz divariant field). Therefore, P-T segments relative to the post-garnet-growth-metamorphic conditions are potentially well constrainable in the KFMASH system (**Fig. 4.7**).

As described in previous sections, the projection of the bulk-rock composition from calculated-garnet composition (**Fig. 4.5c**) consisted mainly in the subtraction of MnO from the bulk-rock chemistry, leading to a KFMASH system. KFMASH pseudosection (**Fig. 4.7**) has been calculated in the P-T range of 0.5-10 kbar and 450-700 °C using activity-composition relationships for the end-members proposed by Holland & Powell (1998). Apart from excess water, ten phases are involved in this pseudosection: chlorite, muscovite, biotite, staurolite, garnet, cordierite, quartz, K-feldspar, ortho-pyroxene and one Al_2SiO_5 -polymorphs.

Substantial difference between KMnFMASH and KFMASH pseudosection consist in the stability of garnet-bearing assemblages. In fact, the subtraction of MnO from the chemical system does not lead to a significant change in the phase relationships, except for reducing garnet stability fields to higher P and T conditions. In the KFMASH pseudosection (**Fig. 4.7**) garnet appears at pressures greater than 7 kbar, whereas in the KMnFMASH system garnet is stable for a large portion of the considered P-T space (**Fig. 4.6**).

Consuming-staurolite reaction in the KFMASH system (Ms+Bt+St+And+Qtz divariant field) with andalusite formation occupy a restricted range of P-T conditions (3.3 kbar < P < 4.1 kbar; 545 °C < T < 575 °C). Ms+Bt+And+Qtz assemblage (trivariant field) covers a wide range of P-T conditions and, probably, it represents the peak metamorphic assemblages reached by the micaschist. KFMASH pseudosection predicts also the formation of cordierite at the expense of andalusite and biotite (Ms+Bt+Crd+And+Qtz divariant field) but, in the reality, this reaction has not been observed in micaschist.

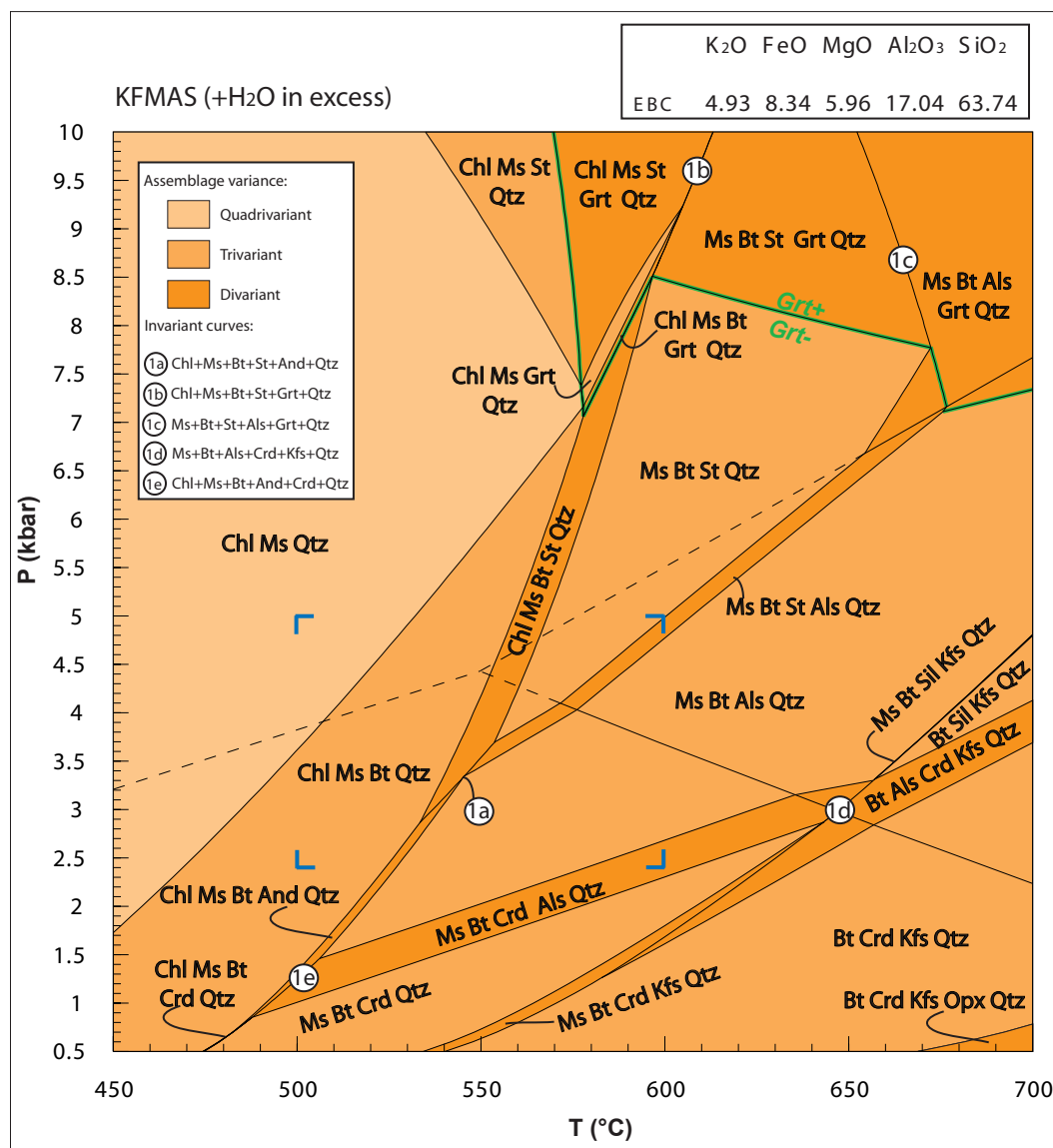


Fig. 4.7: P-T pseudosection calculated for the LL56a4 micaschist with the XRF''-effective-bulk composition (Fig. 4.5c; EBC in mol %). Stable assemblage fields are coloured by assemblage variance. Al_2SiO_5 are absent where dashed. Thick-green lines separate the P-T space in which garnet is not stable from that in which garnet is stable. Blue corners delimit the P-T space considered for the calculation of the P-T pseudosections related to the staurolite reaction domain (Fig. 4.10).

PARAGNEISSES

P-T phase diagrams concerning paragneisses have been calculated in the KFMASH system, focusing the attention on garnet-free assemblages. XRF-bulk-rock composition has been adjusted subtracting P, Ti, Ca and Na by the projection of the XRF-derived-bulk-rock composition from apatite, ilmenite, anorthite and albite, respectively (**Appendix 5**). The KFMASH pseudosection relative to the Qtz+Pl-rich layer of paragneiss (**Fig. 4.8**) has been calculated in the P-T range of 0.5-10 kbar and 450-700 °C using activity-composition relationships for the end-members proposed by Holland & Powell (1998). Apart from excess water, nine phases are involved in this pseudosection: chlorite, muscovite, biotite, staurolite, garnet, cordierite, quartz, K-feldspar and one Al_2SiO_5 -polymorphs. The topologies of the KFMASH pseudosections calculated for the micaschist (**Fig. 4.7**) and for

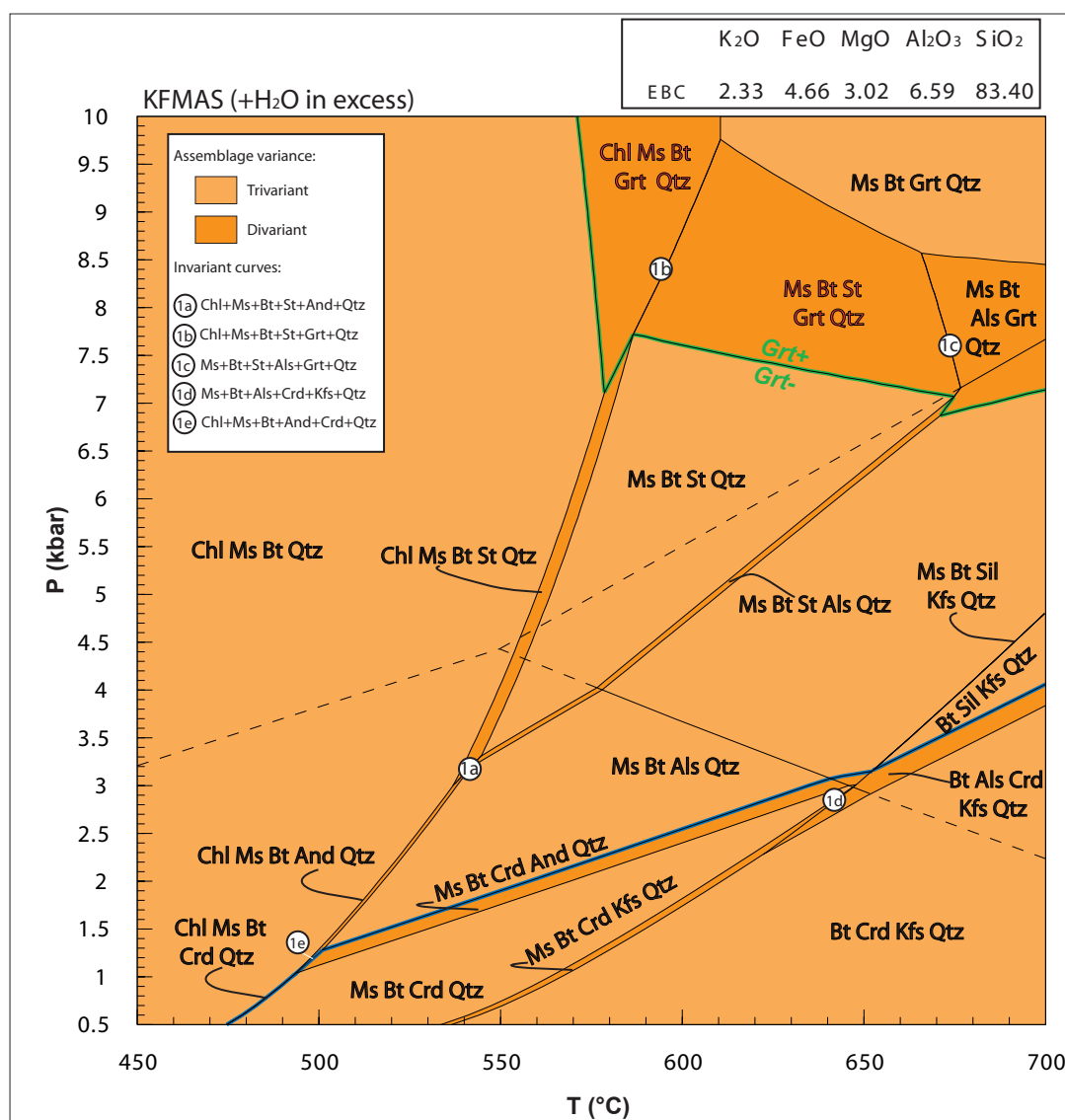
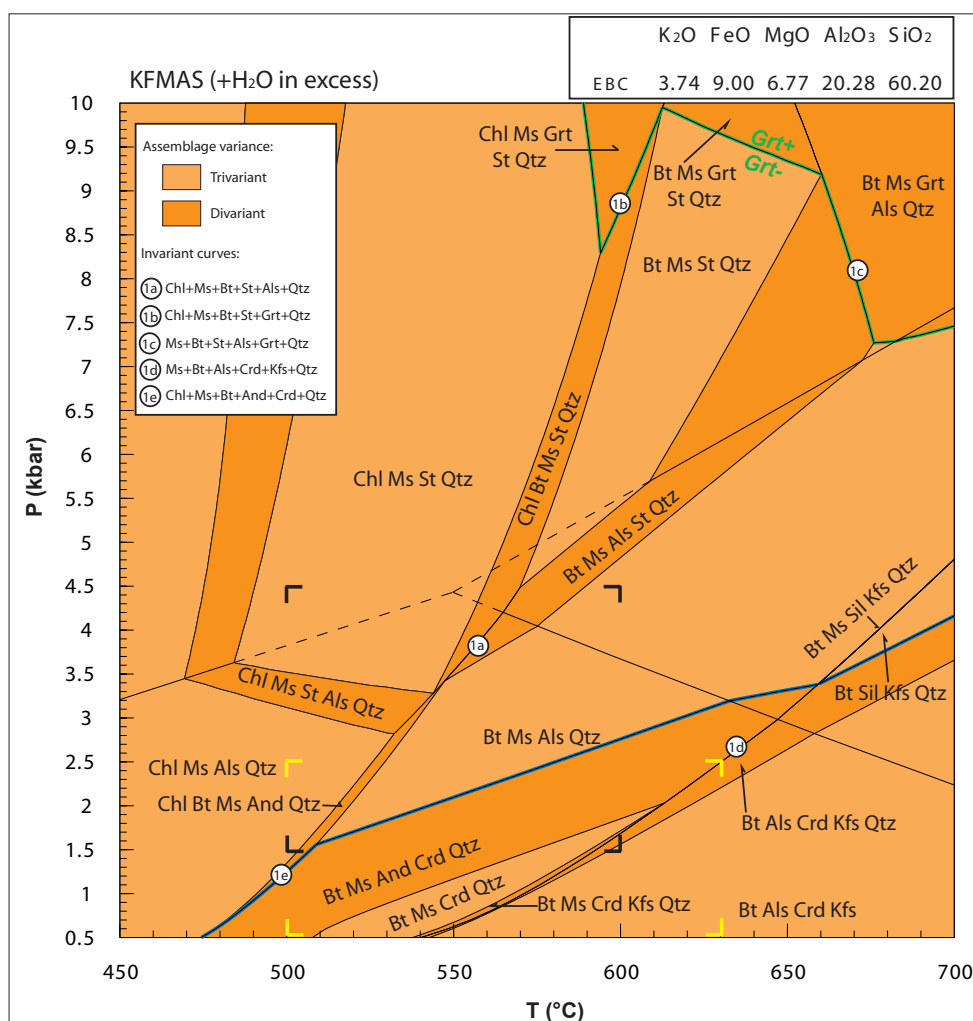


Fig. 4.8: P-T pseudosection calculated for the LL61a2 Qtz+Pl-rich layer of paragneiss with the XRF-derived-effective-bulk composition (EBC in mol %). Stable assemblage fields are coloured by assemblage variance. Al_2SiO_5 are absent where dashed. Thick lines separate P-T spaces in which garnet (green) and cordierite (blue) are stable or not stable.

the Qtz+Pl-rich paragneiss (**Fig. 4.8**) are very similar. Comparing these pseudosections, two major differences have aroused: i) KFMASH phase diagram relative to the LL56a4 micaschist predicts a Chl+Ms+Qtz trivariant fields at low temperatures and high pressures (**Fig. 4.7**), not observed in the LL61a2 paragneiss (**Fig. 4.8**); ii) reaction-divariant fields in paragneiss occupy more restricted P-T conditions with respect to identical divariant fields observed in the micaschist (**Fig. 4.7**). This latter observation reproduces petrographic features observed for micaschists and Qtz+Pl-rich layer of paragneisses at least for the staurolite-bearing assemblages. In fact, micaschists show a more pronounced development of staurolite with respect to Qtz+Pl-rich layers of paragneisses.

As described in petrographic section, the Bt-rich layers of paragneisses are characterised by very low abundance of garnet. In particular, the analysed layer (LL61b2) is garnet-free and, therefore, it has been calculated only a KFMASH pseudosection (**Fig. 4.9**). XRF-derived-bulk-rock composition has been adjusted subtracting P, Ti, Ca and Na by the projection of the XRF-bulk-rock composition from apatite, ilmenite, anorthite and albite, respectively (**Appendix 5**). KFMASH pseudosection (**Fig. 4.9**) has been calculated in the P-T range of 0.5-10 kbar and 450-700 °C using activity-composition relationships for the end-members proposed by Holland & Powell (1998).

Fig. 4.9: P-T pseudosection calculated for the LL61b2 Bt-rich layer of paragneiss with the XRF-derived-effective-bulk composition (EBC in mol %). Stable assemblage fields are coloured by assemblage variance. Al_2SiO_5 are absent where dashed. Thick lines separate P-T spaces in which garnet (green) and cordierite (blue) are stable or not stable. Black and yellow corners delimit P-T space considered for the calculation of the P-T pseudosections related to the staurolite and the cordierite reaction domains, respectively (Figs. 4.12; 4.14).



Apart from excess water, nine phases are involved in this pseudosection: chlorite, muscovite, biotite, staurolite, garnet, cordierite, quartz, K-feldspar and one Al_2SiO_5 -polymorphs.

Comparing the KFMASH pseudosections relative to the LL61a2 and to the LL61b2 paragneiss (**Figs. 4.8** and **4.9**), it is clearly visible that in the latter (**Fig. 4.9**; LL61b2) the staurolite- and the andalusite-bearing assemblages are more widespread, the garnet stability field is slightly reduced and the boundary of the cordierite-bearing assemblages lie at slightly higher pressures and temperatures. Besides these differences in mineral stabilities, it is important to note how Chl+Bt+Ms+St+Qtz , Bt+Ms+Als+St+Qtz and Bt+Ms+Crd+And+Qtz divariant fields vary. These fields delimitate the P-T conditions of observed staurolite-, andalusite- and cordierite-forming reactions, respectively. They are larger in the Bt-rich layer of paragneisses (LL61b2) with respect to the Qtz+Pl-rich layer of paragneisses (LL61a2). Focusing the attention on the cordierite-forming-divariant field (Bt+Ms+Crd+And+Qtz), it is very important to note that also in this case the model quite satisfy reality. In fact, between the two analysed layers of paragneisses, the cordierite has been observed only in the Bt-rich layer (LL61b2).

In summary, P-T phase diagrams revealed a strong dependence between bulk-rock compositions and stability fields of mineral assemblages. In particular, it has been seen that bulk-rock chemistry controls development of mineral assemblages and their P-T conditions of stability. This chemical control on mineral assemblages, coupled with different tectonic positions of investigated samples, could better explain the reconstructed metamorphic history.

4.3.2.4 - P-T phase diagrams of reaction domains

The P-T pseudosections calculated using bulk-rock compositions (**Figs. 4.6-4.9**) show reaction divariant fields with a wide range of possible P-T conditions of stability. Some of these reaction divariant fields quite faithfully reproduce reaction domains observed in analysed samples, but they do not give detailed information about the real evolution of the reactions. A technique that could lead to define a more restricted range of possible P-T conditions recorded by reaction domains consists in plotting the appropriate reactant and product isopleths directly in the reaction divariant fields. In this way, P-T conditions could be defined by the intersections of the isopleths. Unfortunately, isopleths are very unstable in P-T pseudosections calculated using bulk-rock compositions.

In this work it will be proposed an alternative method that allows to constrain better the P-T conditions of reaction domains. This new technique is based on the calculation of P-T pseudosections using the chemical compositions of the reaction domains. In these pseudosections the P-T segment described by the reaction could result from the isopleths and the isomodes relative to the reactants and products. The compositions used for the P-T pseudosection calculations have been obtained by the mass balances (**Appendix 4**). The chemical composition of reaction domains have been calculated before and after the reaction using stoichiometric coefficients and average chemical analyses of reactants and products, respectively. In theory, the compositions before and after the reactions should coincide in a closed chemical system. The compositional differences could be linked to three main factors: a) inaccuracy of microanalyses; b) wrong reactants and/or products; c) inappropriate assumptions and/or simplifications in calculating reaction domain compositions (**Appendix 4**). P-T pseudosections relative to reaction domains could be seen as a detail of bulk rock pseudosections even if mineral stability fields are not always equivalents.

Two main reactions have been modelled by the P-T phase diagrams calculations: the staurolite-consuming reaction and the cordierite-producing reaction. St-consuming reaction with formation of And+Bt aggregates has been observed in micaschists and in paragneisses, whereas the cordierite formation at major expense of andalusite and biotite has been recognised only in the Bt-rich layers of paragneisses. Attempts of reconstruction of the St-consuming reaction have been carried out for the LL56a4 micaschist and for the LL61b2 paragneiss, whereas Crd-forming reaction has been modelled only for the LL61b2 paragneiss. A detailed description of followed procedures and average chemical analyses used for calculations of reaction domain compositions are reported in **Appendix 4**. Considering that the major reactants and products are ferromagnesian silicates, the KFMASH chemical system has been commonly employed to calculate P-T isochemical sections.

4.3.2.4.1 – Staurolite-consuming reaction

Micaschist

Two P-T pseudosections in the KFMASH system have been calculated for R3c staurolite-consuming reaction domain, observed in the LL56a4 micaschist (cf. 4.2). P-T diagram of **Fig. 4.10** contains these two pseudosections calculated using compositions of reactants (composition of the system before the reaction) and products (composition of the system after the reaction).

In the pseudosections (**Fig. 4.10**) are depicted the measured X_{Fe} isopleths ($X_{\text{Fe}} = \text{Fe}^{2+}/(\text{Fe}^{2+} + \text{Mg})$) of the staurolite (reactant) and the biotite (product). A modal profile perpendicular to these isopleths has been calculated through the Bt+Ms+And+St+Qtz reaction divariant

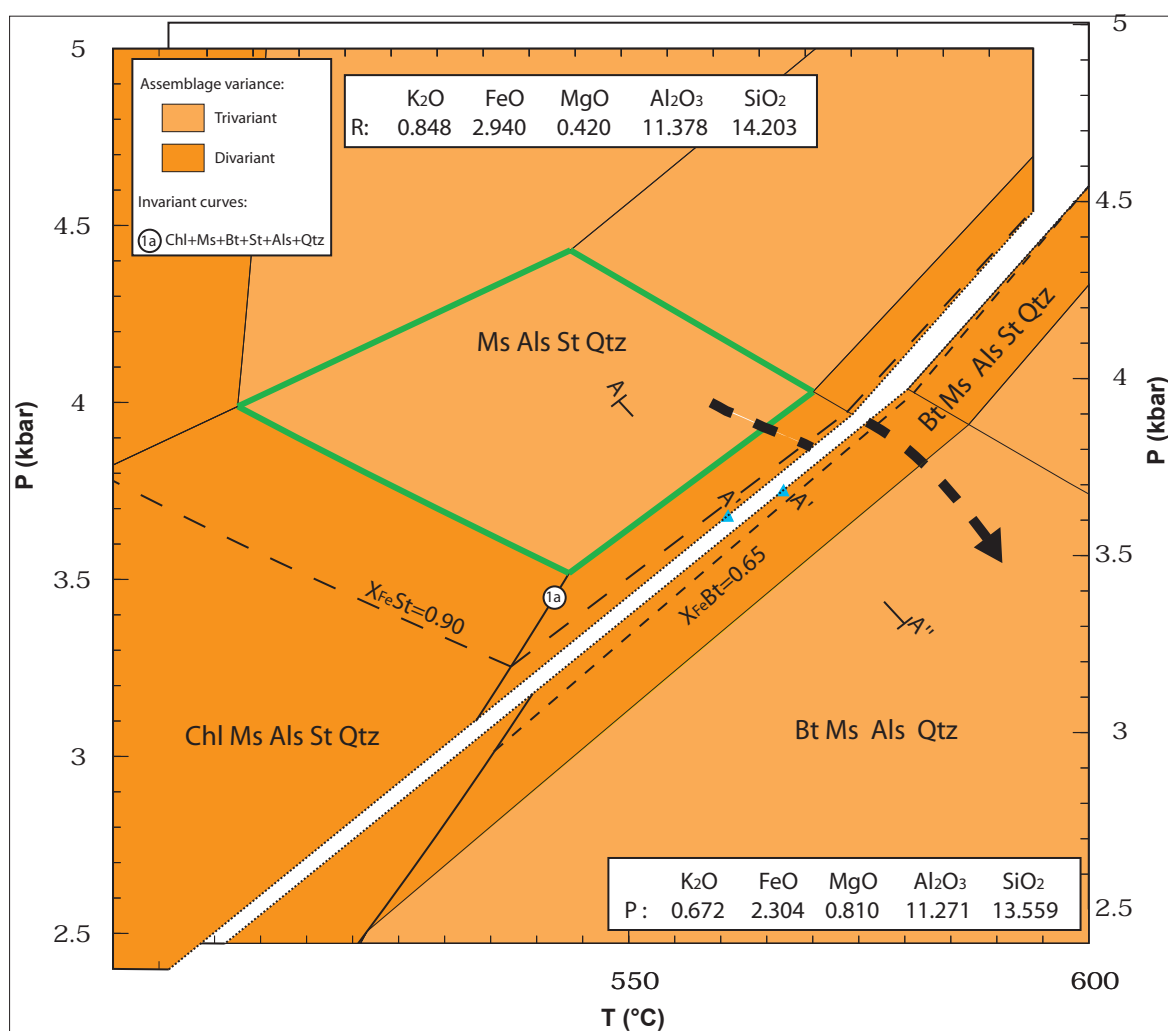


Fig. 4.10: KFMASH P-T pseudosections showing mineral stability fields, coloured by assemblage variance, before and after the staurolite-consuming reaction (LL56a4 micaschist). Dashed lines represent the measured X_{Fe} isopleths of the staurolite and the biotite. Dotted line indicates the boundary between the pseudosections calculated using the reactant (upper part) and product (lower part) composition. A-A'-A'' trace indicates the modal profile (26 points, Fig. 4.11) through the reaction divariant field. Green lines delimit the possible pre-reaction P-T conditions. Black-dashed arrow represents the possible P-T segment. See text for explanations.

field (**Fig. 4.11**), in order to better visualise the modal changes between reactants and products. Major distinctive features between the model (**Figs. 4.10** and **4.11**) and the observed microstructures (cf. 2.3.1.1) consist in: a) absence of biotite and presence of andalusite before reaction; b) persistence of muscovite among products; c) complete demise of staurolite. These discrepancies could be a consequence of analytical errors or inappropriate projections in calculating domain compositions.

Several P-T segments could be traced on the P-T pseudosections for the staurolite-consuming reaction; however, integrating phase diagrams calculations with microstructural observations a segment indicating slightly decompression with increasing temperatures seems to be the most appropriate (**Fig. 4.10**).

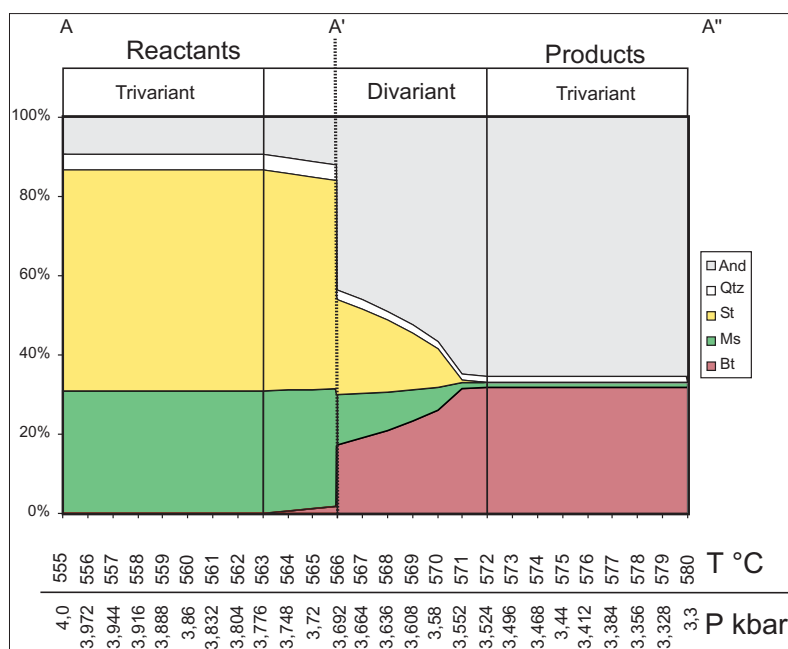


Fig. 4.11: modal changes through the staurolite-consuming reaction along the P-T profile shown in Fig. 4.10. The reaction has been modelled in the LL56a4 micaschist. See text for details.

Bt-rich layer of paragneiss

Staurolite-consuming reaction has been observed in the Bt-rich layers of paragneisses, too. Starting from average mineral analyses and stoichiometric coefficients of reactants and products (cf. balanced reaction R3e in section 4.2) a single pseudosection has been calculated with the average reactant-product composition (**Fig. 4.12**). Isopleths and isomodes relative to the reactants and the products have been depicted in the P-T phase diagram. The consistency between the model and the reality has been emphasized by a modal profile through some fields of the pseudosection (**Fig. 4.13**). In the pseudosection (**Fig. 4.12**) and in the modal profile (**Fig. 4.13**) it is possible to see that the muscovite completely disappears after the reaction, acting as a limiting agent, whereas staurolite persisted to the reaction. The model

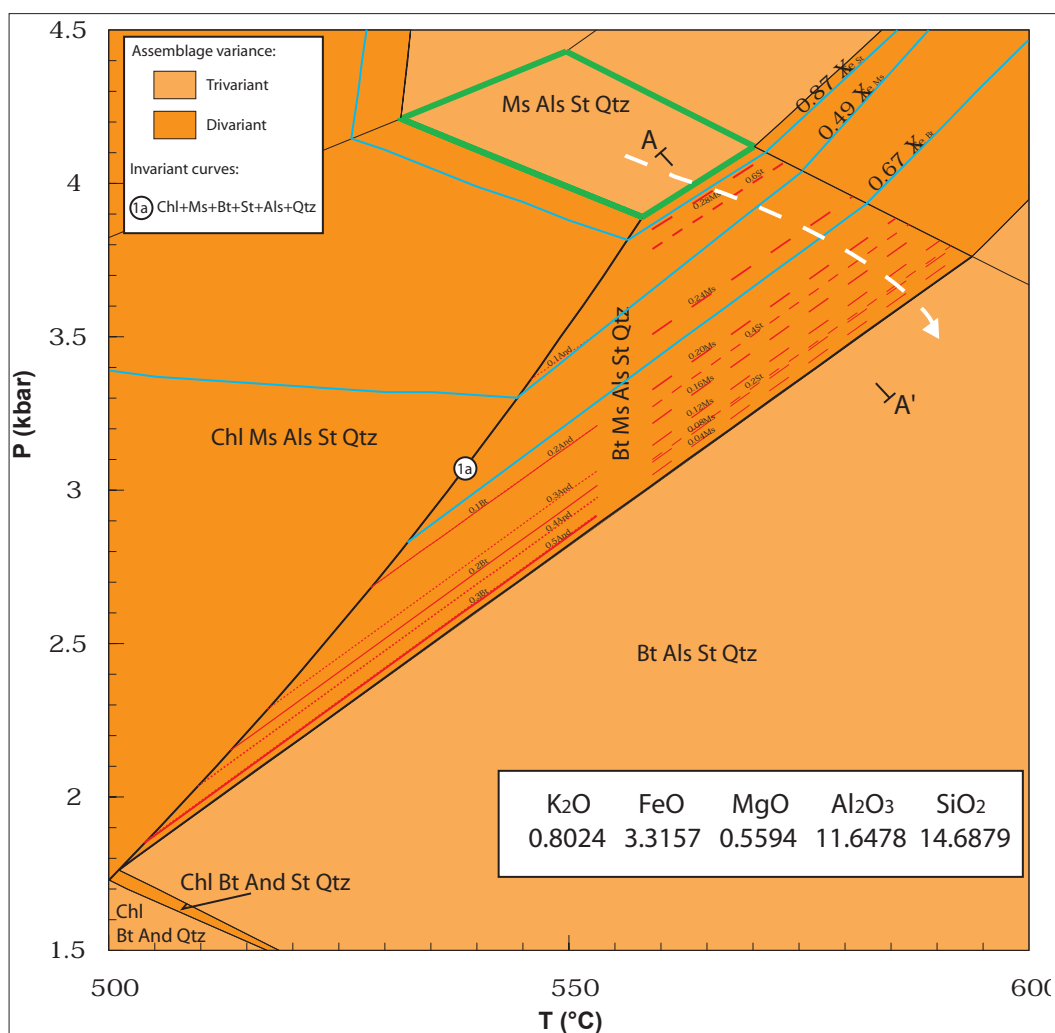


Fig. 4.12: KFMAS P-T pseudosection showing mineral stability fields, coloured by assemblage variance, before and after the staurolite-consuming reaction observed in LL61b2 paragneiss (see text for explanations). Pseudosection has been calculated with the average composition between the reactants and the products compositions. Blue lines represent the measured X_{Fe} isopleths of the staurolite, the biotite and the muscovite. Dashed lines indicate several isomodes of reactants (right side of the divariant domain) and products (left side of the divariant domain). A-A' trace indicates a modal profile (26 points, Fig. 4.13) through reaction divariant field. Green lines delimit the possible pre-reaction P-T conditions. White-dashed arrow represents the possible P-T segment.

predicts the presence of andalusite and the absence of biotite before the reaction. As documented in previous sections, there are not microstructural evidences of growth of andalusite independent to this reaction. Moreover, the petrographic analyses revealed that the biotite was already present before the reaction. Pre-reaction P-T

conditions, delimited by tick-green lines in the pseudosection (**Fig. 4.12**), are very restricted. As observed for the micaschist, the more realistic P-T segment followed by the reaction describes a slight decompression with increasing temperatures (**Fig. 4.12**).

Comparing the P-T pseudosections relative to the staurolite-consuming reaction domains observed in micaschist (**Fig. 4.10**) and in paragneiss (**Fig. 4.12**), it is visible that mineral assemblages and topology are equivalent. The only discrepancy refers to the univariant curve (1a) and the related divariant fields. In LL56a4 micaschist the univariant curve and the divariant fields are stable at lower pressures and temperatures. Consequently, the possible pre-reaction P-T conditions in the micaschist (**Fig. 4.10**), are greater than those in the paragneiss (**Fig. 4.12**).

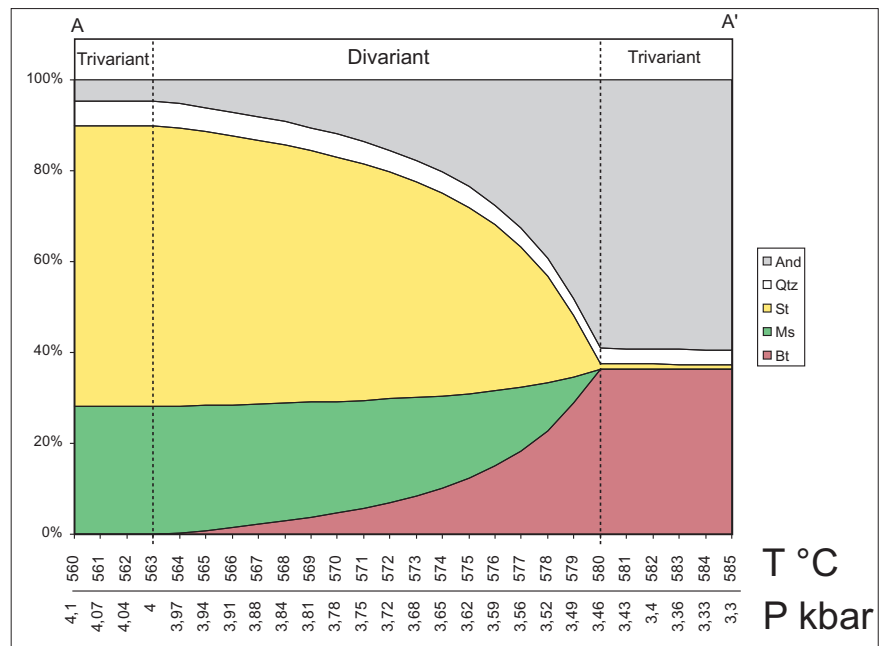


Fig. 4.13: modal changes through the staurolite-consuming reaction along the P-T profile shown in Fig. 4.12. The reaction has been modelled in the LL61b2 paragneiss. See text for details.

4.3.2.4.2 – Cordierite-producing reaction

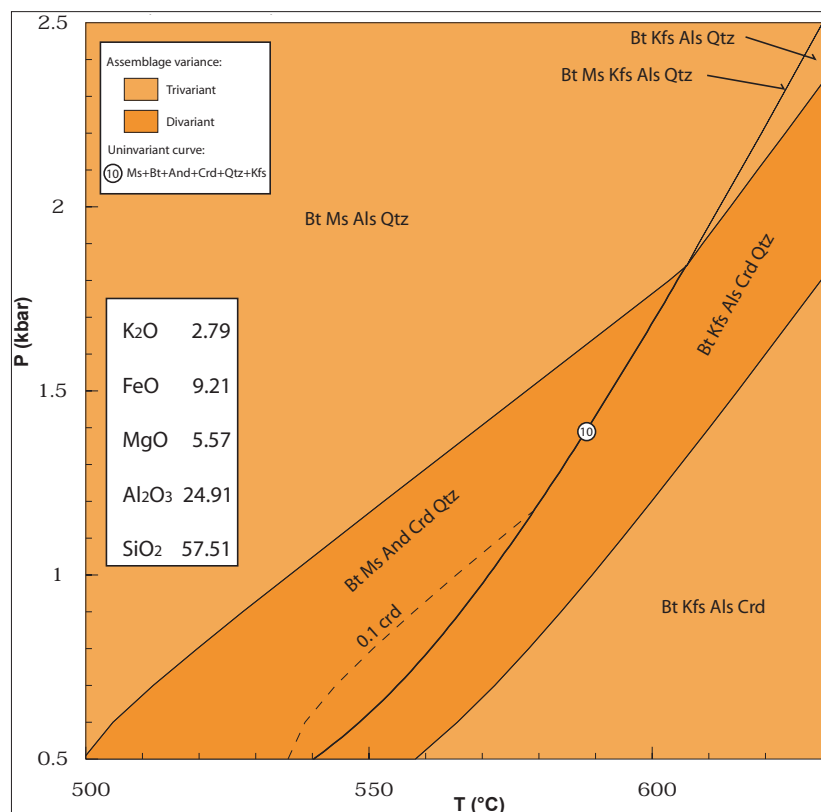
P-T pseudosections have been also calculated for a cordierite-forming reaction domain observed only in the Bt-rich layer of paragneisses. Procedures followed to calculate the domain compositions are described in **Appendix 4** and are similar to those followed for the staurolite-consuming reaction domain. Considering that fresh cordierite has never been found, the P-T pseudosection (**Fig. 4.14**) has been calculated using a composition of the reaction domain that consider a theoretical cordierite composition (cf. R4d balanced reaction in section 4.2).

Also in this case, the pseudosection revealed very helpful in order to reduce the possible P-T space of the cordierite-forming reaction. KFMASH pseudosection (**Fig. 4.14**) has been calculated using the average composition between the reactant and the product composition and it shows that the univariant cordierite-forming reaction is possible only at pressure below 2 kbar and in a narrow T range.

Coherently to the bulk-rock pseudosection (**Fig. 4.9**), the reaction domain pseudosection (**Fig. 4.14**) predicts the cordierite formation in muscovite-bearing assemblages at low pressure, and, precisely, at pressures lower than those of the staurolite-consuming reaction. Temperatures predicted by the P-T pseudosection calculated for this reaction domain (**Fig. 4.14**) seem to be underestimated with respect to those predicted for the crd-bearing assemblages by bulk-rock P-T pseudosection (**Fig. 4.9**).

Combining microstructural evidence with phase diagram calculations, the P-T segment followed by the paragneisses during the cordierite formation could depict a slight decompression with a decrease of temperatures.

Fig. 4.14: P-T pseudosections showing mineral stability fields, coloured by assemblage variance, before and after the cordierite-forming reaction. Reaction has been modelled in the LL61b2 paragneiss with the average composition between the reactants and -products compositions. Dashed line represents 0.1 isomode of cordierite.



4.3.3 – P-T paths

According to the sequence of crystallisation interpreted from petrologic observations, P-T paths relative to the analysed porphyroblastic micaschist and paragneisses have been depicted on the calculated P-T pseudosections.

MICASCHIST

Garnet-bearing micaschist (LL56a4) followed a clockwise P-T path (**Fig. 4.15**). P-T segments have been depicted on two different P-T pseudosections: a KMnFMASH phase diagram, to visualise the prograde-garnet growth, and a KFMASH isochemical section containing information about peak and post-peak metamorphic conditions.

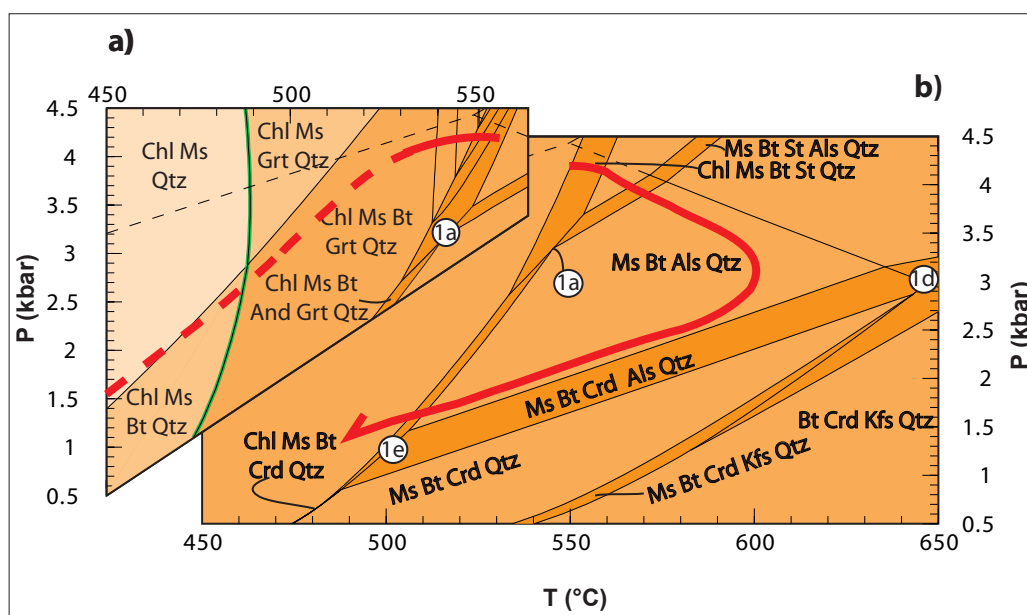


Fig. 4.15a, b: a) particulars of KMnFMASH (Fig. 4.6) and b) KFMASH (Fig. 4.7) P-T pseudosections calculated for the LL56a4 micaschist, illustrating the P-T path (red lines). See Figs. 4.6 and 4.7 for captions and text for explanations.

The initial segment has been inferred mainly from observed mineral assemblages and garnet isopleths. Petrographic analyses revealed a prograde paragenesis characterized by Chl+Ms+Qtz, followed by enlarged mineral assemblages including also garnet and biotite. The beginning of the micaschist metamorphic history was characterised by heating and increasing pressures, until to *c.* 550 °C and *c.* 4.3 kbar. This metamorphic phase is well-documented by the syntectonic features observed within garnets. The relative abundance of Mn in the sample favoured the nucleation and the growth of spessartine-rich garnet prior to the staurolite formation, as supported by the presence of garnet inclusions within staurolite. The heating continued through the Chl+Ms+Bt+St+Qtz KFMASH divariant field, until to *c.* 560 °C, favouring the staurolite formation in response to the chlorite breakdown. Studies (image analysis, mass balance and P-T pseudosections) performed

on the staurolite-consuming reaction domain observed in the LL56a4 micaschist allowed to integrate the reconstructed P-T path with another P-T segment that cross the Ms+Bt+St+And+Qtz divariant field. The appearance of andalusite at major expense of staurolite took place during a slightly decompression in an increasing thermal regime, until to peak metamorphic conditions ($\approx 580^\circ\text{C}$ and ≈ 3.2 kbar). Using the observed retrograde textural relationships and the P-T positions of their associate reaction divariant fields, it has been possible to depict the more appropriate retrograde P-T segment followed by the analysed micaschist. As described above, the peak metamorphic assemblage is constrained to a large trivariant KFMASH field that towards lower pressure and temperature confines with the Chl+Ms+Bt+And+Qtz divariant field. This reaction divariant field contains observed retrograde assemblage characterised by the reappearance of the chlorite at major expense of the biotite. The andalusite alteration in fine-grained white mica aggregates took place in the Chl+Ms+Bt+Qtz trivariant field.

QTZ+PL-RICH LAYER OF PARAGNEISS

The P-T path followed by the Qtz+Pl-rich paragneiss (LL61a2) describes a clockwise trajectory (**Fig. 4.16**) comparable to that of the micaschist. Modal abundance of garnet in this rock is very low; moreover, the few observed garnet crystals show pronounced pseudomorphic replacement textures. Therefore, the Mn fractionation induced by garnet growth has not been considered necessary (cf. 4.3.2.3). As described in previous sections

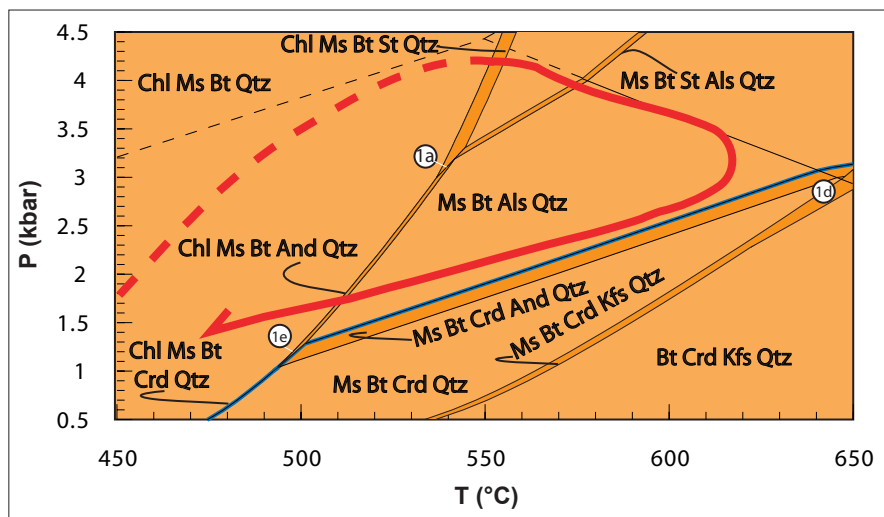


Fig. 4.16: particular of the KFMASH P-T pseudosection calculated for the LL61a2 Qtz+Pl-rich layer of paragneiss (Fig. 4.8), illustrating the P-T path (red lines). See Fig. 4.8 for caption and text for explanations.

(cf. 2.3.1.2), these rocks are characterised by porphyroblastic textures and associate reaction microstructures poorly developed. Consequently, P-T path of LL61a2 has been qualitatively constrained, considering observed mineral assemblages. Reconstructed

P-T path is comparable to that of micaschist from the staurolite formation, through the Chl+Ms+Bt+St+Qtz divariant field, until to the andalusite appearance at major expense of the staurolite (Ms+Bt+St+And+Qtz KFMASH divariant field). At this stage, the P-T path followed by the paragneiss differentiates from the P-T path followed by the analysed micaschist. In fact, the Qtz+Pl-rich layer of paragneisses are characterised by the presence of fibrolitic sillimanite statically overgrown on biotite porphyroblasts. Fibrolite penetrates also in matrix and its relatively late-stage growth is consistent with a prograde P-T segment making a small excursion across the andalusite-sillimanite boundary, before the retrograde metamorphic history. The replacement of the andalusite by cryptocrystalline aggregates of white mica and the chloritisation of biotite represent major observed retrograde textures and they are predicted by the Chl+Ms+Bt+And+Qtz KFMASH reaction divariant field.

BT-RICH LAYER OF PARAGNEISS

Following an identical methodology as above, attempts of P-T path reconstructions have been performed also for the Bt-rich layer of paragneiss (LL61b2). This rock is almost garnet-free and it developed mineral assemblages containing Ms+Bt+And+St+Crd+Qtz, which are some of the most problematic in metamorphic petrology (Pattison *et al.*, 1999). Major problems arise from thermodynamic properties of minerals. In fact, as showed in a typical AFM projection (KFMASH system, **Fig. 4.17**), the staurolite tends to be relatively Fe-rich whereas the cordierite is richer in Mg. These thermodynamic properties result in a potential cordierite+staurolite tie line that cross cut an important observed tie line connecting andalusite and biotite (**Fig. 4.17**). Interpretations about P-T trajectory followed by rocks containing Ms+Bt+Grt+St+And+Crd mineral assemblage have been proposed by several authors (Garcia-Gasco & Torres-Roldán, 1999; Pattison *et al.*, 1999; Mezger *et al.*, 2004; Pattison & Vogl, 2005). This particular mineral assemblage is absent or very rare in contact aureole, whereas it has been reported from regional low-pressure (Andalusite-Sillimanite type) metamorphic terranes (Pattison & Tracy, 1991 and references therein) and it has been interpreted by Holdaway *et al.* (1982; 1988) as an unstable assemblage resulting from polymetamorphism. Recently, this particular mineral assemblage aroused interest of many petrologists concerning its stable or metastable nature (Garcia-Gasco & Torres-Roldán, 1999; Pattison *et al.*, 1999; Mezger *et al.*, 2004; Pattison & Vogl, 2005). Petrologic studies suggest that this assemblage is metastable and is the result of decompression along a clock-wise P-T path. In particular, Pattison *et al.* (1999) explained unstable persistence of staurolite relicts in the stability field of cordierite as the result of decompression with uniform or decreasing temperature

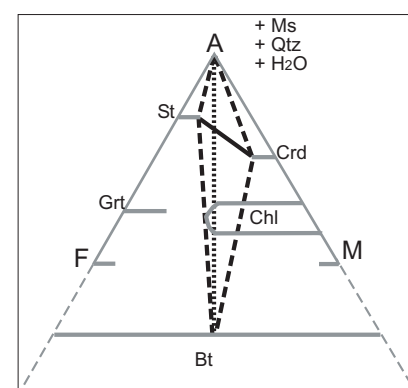


Fig. 4.17: AFM projection showing position of some minerals (after Spear, 1993) and possible tie lines between them.

(Fig. 4.18). The P-T paths proposed by Pattison *et al.* (1999) predict earlier high-pressure-staurolite-bearing assemblages overprinted by low-pressure-cordierite-bearing assemblages, satisfying microtextural relationships observed in LL61b2 paragneiss.

KFMASH pseudosection calculated for the Bt-rich layer of paragneiss (LL61b2;

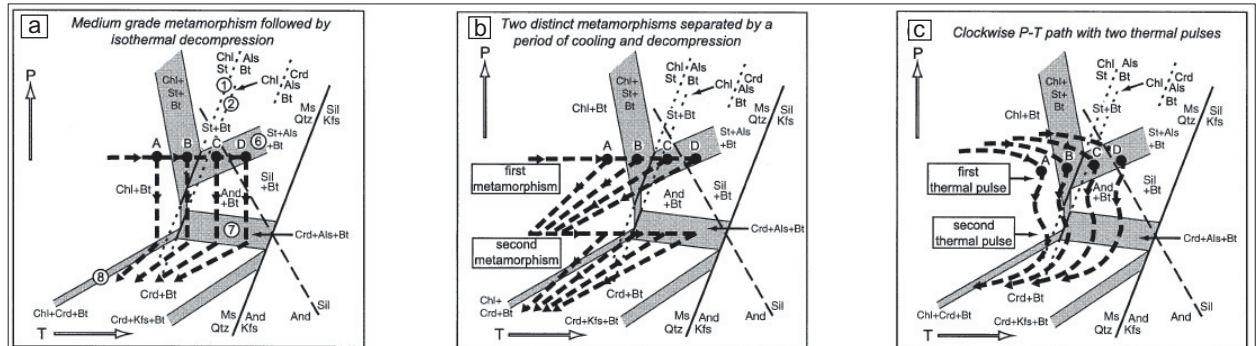


Fig. 4.18: schematic P-T paths proposed by Pattison *et al.* (1999) that could account for the development of Ms+Crd+St+Bt assemblages by polyphase metamorphism. Letters A–D represent assemblages of the Chl (A), St (B), St+And (C) and St+Sil (D) zones of a medium-P metamorphic event. (a) Isobaric heating followed by isothermal decompression, leading to development of a low-P Crd+And overprint on assemblages from the medium-P metamorphism. (b) An early heating results in the development of an St–And sequence. The rocks cool down prior to being affected by a late low-P thermal event. (c) As in (b) with difference that after development of St–And sequence, rocks undergo decompression with minor cooling, and are shortly afterwards affected by another thermal pulse at lower P.

Fig. 4.19) predicts prograde mineral assemblages that do not reproduce faithfully the observed textural relationships. In fact, in the low-pressure (<3 kbar) and low-temperature (<530 °C) side of the KFMASH pseudosection, the andalusite and/or staurolite are unrealistically stable without the biotite, which firstly appears as product of chlorite breakdown (Chl+Ms+Bt+And+Qtz or Chl+Ms+Bt+St+Qtz KFMASH reaction divariant fields). Moreover, the lack of microstructural evidences indicating the existence of an aluminosilicate (Ky or And) before staurolite allow to consider that the pseudosection

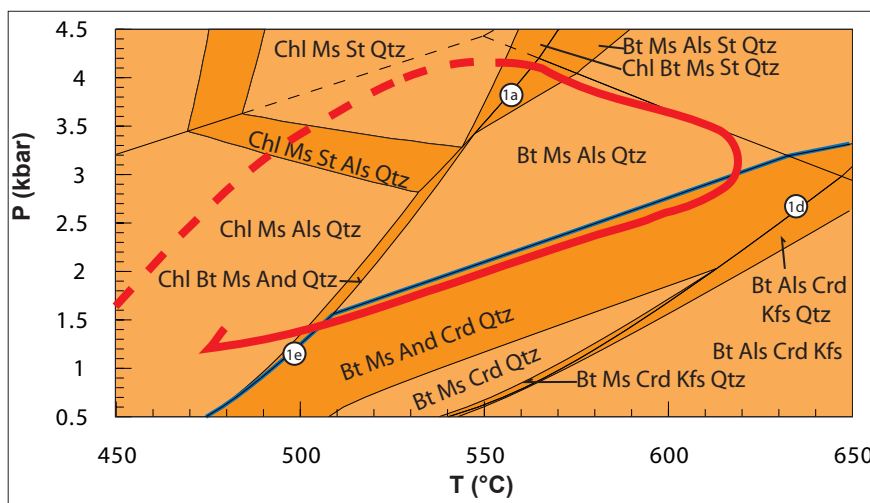


Fig. 4.19: particular of the KFMASH P-T pseudosection calculated for the LL61b2 Bt-rich layer of paragneiss (Fig. 4.9). Phase diagram shows P-T path (red lines) followed by the sample. See Fig. 4.9 for caption and text for explanations.

failed in the prediction of the prograde mineral assemblages. Contrary, observed textural relationships relative to peak and retrograde metamorphic conditions seem to be quite faithfully represented by isochemical P-T diagram. Peak pressure conditions have been reached during chlorite-breakdown reaction in the $\text{Chl}+\text{Ms}+\text{Bt}+\text{St}+\text{Qtz}$ divariant field characterised by the biotite crystallisation and a further development of staurolite. At this stage, the paragneiss experienced a first decompression event that coupled with increasing temperatures led to the andalusite formation at major expense of the staurolite, as documented by microstructural relationships. Observed microtextures indicate that after the andalusite formation, the reaction history continued with the growth of fibrolitic sillimanite and porphyroblastic cordierite.

Concerning the sillimanite crystallisation, the occurrence of fibrolite almost exclusively on biotite crystals, lying away from cordierite and andalusite porphyroblasts, do not provide indisputable textural evidence on the relative growth sequence. Fibrolite appearance could indicate a small excursion of the P-T path across the andalusite-sillimanite boundary, occurred more probably just before retrograde history. In perfect agreement with the models proposed by Pattison *et al.* (1999), after the fibrolite formation the only way to produce cordierite without further significant heating (*e.g.* $T > 670^\circ\text{C}$; **Fig. 4.19**) is by decompression. Unfortunately, the intersection between the P-T segment with the $\text{Ms}+\text{Bt}+\text{And}+\text{Crd}+\text{Qtz}$ KFMASH reaction divariant field is not well constrainable.

An important feature concerning the staurolite-cordierite relationships is that the staurolite is not stable within the cordierite-bearing fields, implying that the staurolite grew and consumed before the cordierite formation, in perfect agreement with the observed microtextures. Consequently, the persistence of staurolite relicts on cordierite stability fields has been considered metastable.

Retrograde metamorphic history of the paragneiss continued with a monotonically decrease of pressure and temperature without significant changes in mineral assemblages until to $\text{Chl}+\text{Ms}+\text{Bt}+\text{And}+\text{Qtz}$ reaction divariant field. It explains the alteration of the cordierite (pinite), the partial chloritisation of the biotite and the replacement of andalusite by fine-grained white mica aggregates. Probably, a single KFMASH P-T pseudosection is not sufficient to model the entire porphyroblastic growth sequence. In fact, it is possible that the static growth of earlier porphyroblasts (*i.e.* staurolite and biotite) prior to later ones (*i.e.* cordierite), caused significant changes of the effective-bulk-rock composition.

4.3.4 - Comparison with conventional thermobarometry

Conventional geothermobarometry has been applied to a garnet-bearing micaschist (LL56a3) sampled at the same outcrop of the LL56a4 sample (at a distance less than 30 cm), largely investigated by phase diagrams. Sample LL56a3 has been selected because it contains an interesting garnet crystal characterised by a large variety of solid inclusions (Figs. 4.20a, b), necessary to apply some conventional geothermobarometers. Plagioclase, biotite and muscovite are abundant among inclusions and they have fairly good chemical analyses. These minerals with quartz, apatite and other accessory phases, define sigmoidal inclusion trails ascribable to the syntectonic history. Garnet is chemically unzoned with a slight enrichment of Mn towards rims (Fig. 4.20a), and it is characterised by a high-Fe content ($0.69 < X_{\text{Alm}} < 0.73$) and a negligible abundance of Ca ($X_{\text{Grs}} < 0.02$).

Temperatures and pressures have been estimated with the garnet-biotite geothermometer

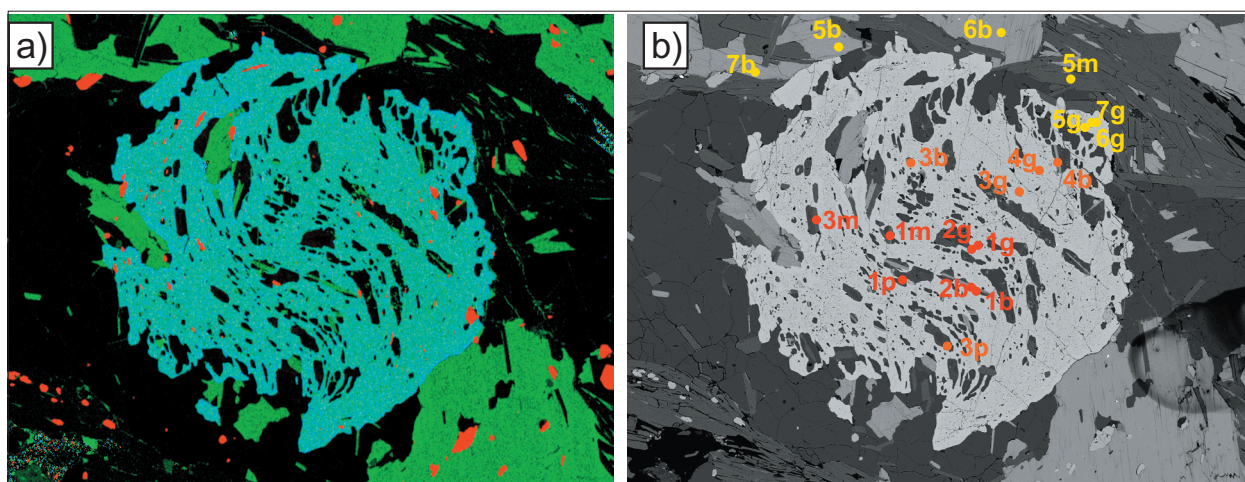


Fig. 4. 20a, b: RGB (a) and BSE (b) images of poikiloblastic garnet in LL56a3 micaschist. g=garnet; b=biotite; p=plagioclase; m=muscovite. Matrix plagioclase is outside the images.

and the garnet-plagioclase-biotite-muscovite geobarometer using GTB Software (Version 2.1; Spear & Kohn, 1999).

Two main criteria have been applied to associate appropriate mineral analyses: a) inclusions have been considered younger towards the end of the sigmoidal trails; b) chemical compositions relative to the core, the intermediate portion and the rims of garnet have been selected from a chemical profile. Chemical analyses are partly localised in Fig. 4.20b. Garnet+biotite pairs have been selected moving from core to rim of garnet following technique proposed by St-Onge (1987).

Compositions immediately inside the retrograde rim (Mn rich narrow rims) have been paired with matrix biotite and have been used in the peak-T calculations. Compositions of matrix biotite have been selected among foliation-parallel crystals not in direct contact with or from the immediate vicinity of garnet grains, to avoid short-range re-equilibration

effects.

Two different garnet-biotite calibrations have been used, because most appropriate for the composition of garnet and biotite. Calibration proposed by Hodges & Spear (1982) represents an empirical modification of the Ferry-Spear calibration (Ferry & Spear, 1978), considering Mn and Ca in garnet. Alternatively, calibration of Kleemann & Reinhardt (1994) considers the same garnet activity model as the Hodges-Spear calibration, whereas it uses a different activity model for the biotite, taking into account the effect of octahedral Al and Ti.

The garnet-plagioclase-biotite-muscovite geobarometer with the calibration of Hodges & Crowley (1985) has been applied to the same garnet+biotite pairs adding appropriate compositions of muscovite and plagioclase.

Using the conventional thermobarometry, two major uncertainties remain: 1) which

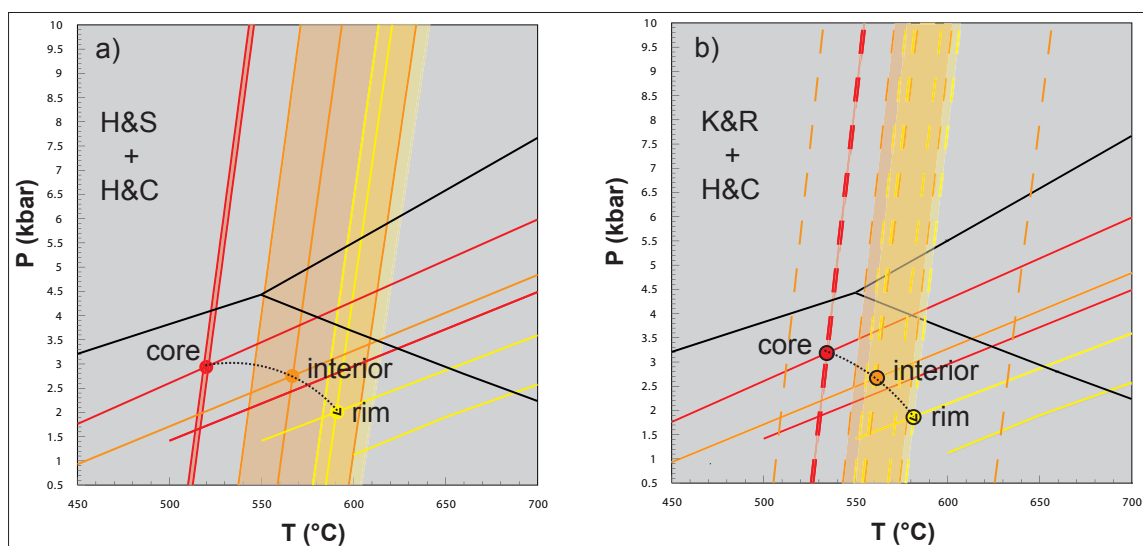


Fig. 4.21: graphical representations of geothermobarometers applied on LL56a3 micaschist. Calibrations used for thermometers are a) Hodges & Spear (1982) and b) Kleeman & Reinhardt (1994). Pressures have been estimated using Garnet-Plagioclase-Biotite-Muscovite barometer with calibration of Hodges & Crowley (1985). Geothermobarometers have been coloured by textural positions moving from core (red lines and fields) to rims (yellow lines and fields) through intermediate microstructural positions (orange lines and fields).

calibration provides the most accurate absolute temperatures, although both calibrations are sensitive to relative temperature differences; 2) the choice and the quality of the appropriate mineral analyses. Moreover, considering that the errors on the P-T estimates are very significant ($\Delta T = \pm 35$ °C; $\Delta P = \pm 1$ kbar), geothermometers and geobarometers should be taken with care.

Comparing the P-T segment attainable by the interpolation of the geothermometer-geobarometer intersections with the P-T paths obtained using phase diagram calculations; it is easily recognisable that conventional geothermobarometers give limited information

about the metamorphic history. P-T conditions determined by the conventional geothermobarometry (**Figs. 4.21a, b**) refer only to the garnet-bearing assemblages. The reconstructed P-T segment indicates a decompression with heating in the andalusite stability field.

CHAPTER 5 - GEOCHRONOLOGY

Geochronologic data relative to some magmatic and metamorphic events recorded by the Hercynian continental crust exposed in Sila are available from literature (Acquafredda *et al.*, 1991; 1992; Ayuso *et al.*, 1994; Thomson, 1994; Caggianelli *et al.*, 2000; Graessner *et al.*, 2000; Festa *et al.*, 2001-02). In this section, existing isotopic ages relative to different crustal levels will be resumed and then new data will be presented.

5.1 - GEOCHRONOLOGIC BACKGROUND

Considering the favourable geological context, allowing observation of a nearly complete section of the Hercynian crust from upper to lower levels, the Sila massif represents an ideal area to reveal the sequence of magmatic, metamorphic and tectonic events during an orogenic cycle. Nonetheless, the number of existing geochronologic data is still inadequate to shed light on some geological critical points.

Graessner *et al.* (2000) obtained U–Pb monazite ages of $304\text{--}300 \pm 0.4$ Ma from migmatitic paragneisses of the lower crust (**Fig. 1.5a**); they suggested that this age reflects the time of growth and recrystallization during peak metamorphism in granulite-facies conditions. Graessner *et al.* (2000) obtained comparable ages ($304\text{--}302 \pm 0.6$ Ma) from two peraluminous granites (**Fig. 1.5a**) that were interpreted as magmatic crystallisation ages of monazite and, thus, emplacement ages of granitoids, synchronous with peak metamorphism in wall rocks.

Magmatic ages obtained by these authors are slightly older (8–15 Ma) than those of Ayuso *et al.* (1994) who reported ages of $293\text{--}289 \pm 1$ Ma ($^{40}\text{Ar}/^{39}\text{Ar}$ of muscovite and hornblende) from various types of calc-alkaline peraluminous and metaluminous granitoids (**Fig. 1.5a**). All these geochronologic data relative to syntectonic granitoids have been considered as emplacement ages. However, the difference of 8–15 Ma between ages of Graessner *et al.* (2000) and Ayuso *et al.* (1994) could be related to the different closure temperatures of the adopted isotopic systems. In light of this consideration, the younger $^{40}\text{Ar}/^{39}\text{Ar}$ ages by Ayuso *et al.* (1994) can be considered cooling ages and can be reconciled with the older dates assuming a reasonable cooling rate for the granitoids.

Ages of post-tectonic intrusions are fewer and have been obtained from leucogranites (Rb/Sr isochron age of 284 ± 14 Ma), exposed near the Cecita Lake, and a pegmatite dyke (Rb/Sr muscovite – whole rock age of 265 ± 3 Ma), from the Mesoraca area, by Caggianelli *et al.* (2000) and Festa *et al.* (2001-02), respectively (**Fig. 1.5a**).

Ages of metamorphic events recorded by upper crustal complexes (Bocchigliero and Mandatoriccio complexes) are poorly determined. In fact, the only geochronologic data available for shallower crustal levels are by Rb/Sr isochron method on whole rock and provided values of 330 ± 4 Ma (Acquafredda *et al.*, 1991) and 326 ± 6 Ma (Acquafredda *et al.*, 1992; **Fig. 5.1a**). These ages refer to low-grade Devonian phyllites and interlayered metavolcanites of the Bocchigliero complex and to amphibolite-facies paragneisses,

porphyritic schists and micaschists of the Mandatoriccio complex, respectively.

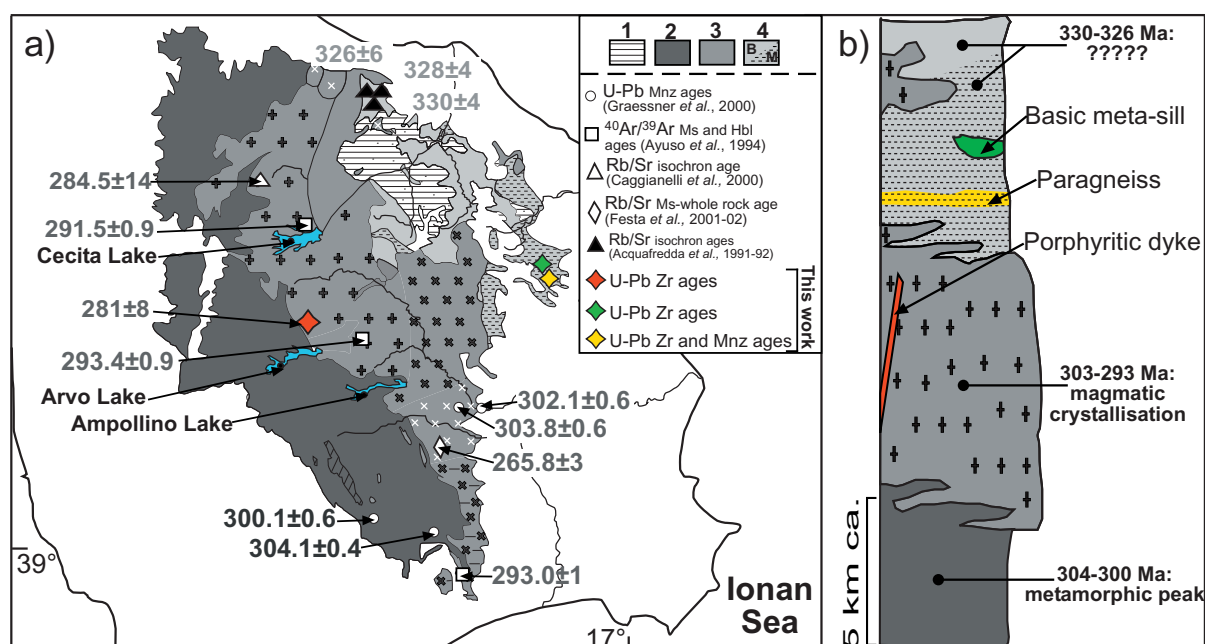


Fig. 5.1a, b: sketch map (a) and schematic reconstruction (b) of the Hercynian continental crust exposed in the Sila massif with location of the main geochronologic data. (1=Mesozoic sedimentary cover; 2=lower crust; 3=granitoids of the intermediate crust; 4=intermediate-upper crust: Bocchigliero complex (B) and Mandatoriccio complex (M)).

Summarising (Fig. 5.1b), geochronologic data relative to the Hercynian evolution of the continental crust exposed in Sila suggest that granulite-facies peak metamorphism in the lower crust took place at 304-300 Ma; coevally, magmatic bodies intruded into the intermediate crust (303-293 Ma). Correspondence between peak-metamorphic age and magmatic emplacement indicates an important link between magmatism and metamorphism. Concerning the Hercynian upper crust exposed in Sila (Bocchigliero and Mandatoriccio complexes), geochronologic data are still inadequate to unravel:

- ages of protoliths and of metamorphism;
- time relationships between metamorphic and magmatic rocks;
- time relationships with lower crustal levels.

In reality, considering the simply metamorphic evolution of the Bocchigliero complex (c.f. 1.3) Rb/Sr age of 330 ± 4 Ma obtained by Acquafredda *et al.* (1991) could date the main metamorphism, whereas, on the basis of existing geochronologic data a tectono-metamorphic reconstruction of the Mandatoriccio complex is still impossible. To this end, new geochronologic analyses have been focused on some rocks in order to obtain ages of protoliths and ages of other metamorphic events. These latter could reflect a time relationships between metamorphic rocks of the upper crust, magmatic rocks of the intermediate crust and metamorphic rocks of the lower crust.

5.2 - NEW GEOCHRONOLOGIC DATA

New geochronologic data have been collected both for magmatic and metamorphic rocks.

Laser-ablation inductively coupled plasma-mass spectrometry (LA-ICP-MS) U-Th-Pb zircon ages have been obtained from a Ms+Bt+Grt+St+And+Crd±Sil paragneiss (LL61b2), a basic meta-sill (LL42c) and a post-tectonic felsic porphyritic dyke (LL134). Basic meta-sill belongs to the Mandatoriccio complex and outcrops near the Umbriatico village (**Figs. 1.5; 5.1**) whereas the porphyritic dyke is exposed close to the Arvo Lake (**Fig. 5.1; Appendix 6**: Liotta *et al.*, submitted). Moreover, LA-ICP-MS U-Th-Pb dating on monazite have been performed on a Ms+Bt+Grt+St+And+Crd±Sil paragneiss (LL61b2) and on a micaschist (LL56a4) of the Mandatoriccio complex.

5.2.1 - Dating methods

U-Th-Pb isotopic data on zircon acquired *in situ* by LA-ICP-MS is a powerful technique because it allows linking isotopic data to a particular zone inside zircon crystals, previously selected and interpreted on Cathodoluminescence (CL) images. In principle, *in situ* LA-ICP-MS U-Th-Pb zircon ages can be linked to different magmatic and/or metamorphic event of zircon growth. Zircon luminescent properties have been interpreted following mainly Hanchar & Miller (1993) and Hoskin & Black (2000). Considering the high closure temperatures of the zircon U-Pb isotopic system (≈ 1000 °C), this technique provides robust temporal constraints for the tectono-metamorphic evolution of the analysed rocks that reached high peak thermal conditions.

In reality, in order to unravel magmatic and metamorphic history of variably overprinted amphibolite-facies-basement units zircon geochronology could results insufficient. In fact, zircon geochronology represents a powerful method for constraining old magmatic events in such settings (Finger *et al.*, 2002 and references therein). However, the dating of metamorphic events remains a difficult task. Zircon may not record metamorphic events if they occurred in a subsolidus P–T range (*e.g.* Rubatto *et al.*, 2000), and the major remnant minerals of an originally medium-grade metamorphic basement such as biotite, muscovite or hornblende, often have disturbed isotope systems. A possible alternative is the dating of monazite, which forms ubiquitously in amphibolite facies (and higher-T) meta-pelitic and meta-greywacke lithologies (Franz *et al.*, 1996). The capability of monazite to retain U-Th-Pb isotopic signatures up to high temperatures and the fact that it yields concordant ages in most cases (*e.g.* Schenk, 1980; Copeland *et al.*, 1988; Parrish, 1990; Mezger, 1990; Lanzirotti & Hanson, 1995) makes it extreme useful to get high-precision ages of geological events. Moreover, monazite has high concentration of U and Th and, typically, it has minimal concentrations of common Pb (Parrish, 1990). These features coupled with a minor risk of isotopic inheritance and a high resistance to Pb loss (Parrish, 1990; Smith & Giletti, 1997) have led to the growing use of monazite as a chronologic tool in metamorphic rocks (Parrish, 1995; Foster *et al.*, 2000). Monazite

internal structures can be observed with a SEM. BSE images of monazite reveal internal compositional variations that are due to contrasts in the average atomic number of elements contained in the mineral and largely reflect differences in the concentrations of light rare earth elements, Th, U and Hf (Hanchar & Miller, 1993; Hawkins & Bowring, 1997, 1999). According to these studies, brighter zones of the crystals reflect higher average atomic number and higher Th/U ratios.

In summary, *in situ* LA-ICP-MS U-Th-Pb zircon dating could represent indisputable dating method at least for the quartz+plagioclase porphyritic dike and for the Amph+Qtz+Pl+Bt meta-sill. Ms+Bt+Grt+St+And+Crd±Sil paragneiss contains well-developed polyphasic garnet that in principle could be well suited for radiometric age dating. In fact, several methods can be applied to this purpose: U-Pb, Sm-Nd and Rb-Sr isotopic system (Spear, 1993 and references therein). Unfortunately, petrographic characteristics of garnet crystals observed in paragneisses (cf. 2.3.1.2), such as small dimensions and high concentration of inclusions, represent an obstacle for the adoption of the above cited geochronologic techniques. Therefore, LA-ICP-MS U-Th-Pb technique have been considered the most appropriate to date the Ms+Bt+Grt+St+And+Crd±Sil paragneiss (LL61b2) and the LL56a4 micaschist.

More details concerning the methodology adopted for *in situ* analyses are described in the **Appendix 7**, whereas, concordia and density diagrams are shown in the following sections and have been constructed using Isoplot program v. 3.0 (Ludwig, 2003).

5.2.2 – *In-situ* U-Th-Pb zircon ages

Analyses have been performed using laser spot sizes of 25 or 10 μm and isotopic compositions have been collected from different portions of selected crystals with contrasting luminescence intensities. Isotopic ratios and concordia ages relative to paragneiss, meta-sill and porphyritic dyke are listed in **Table 20, 21, 22** of **Appendix 7**, respectively.

5.2.2.1 - Paragneiss

Zircons of the LL61b2 paragneiss show a variety of shapes ranging from euhedral–elongated prisms to sub-rounded grains (mean aspect ratio ≈ 3). Internal structures revealed by CL images also vary considerably: oscillatory zoning, convoluted zones, ghost zones and unzoned domains have been recognised. Relic cores with or without oscillatory zoning are often present.

Seventy-three concordant U–Pb ages of forty-eight crystals have been determined (**Table 20**) and range between 2562 ± 44 Ma and 428 ± 10 Ma (**Fig. 5.2a**).

Twenty-five analyses relative to eighteen crystals are older than 700 Ma, whereas, younger ages (<700 Ma) show three major clusters between 428–480 Ma, 520–540 Ma (14 data relative to 12 zircons) and 580–620 Ma (**Figs. 5.2b, c**).

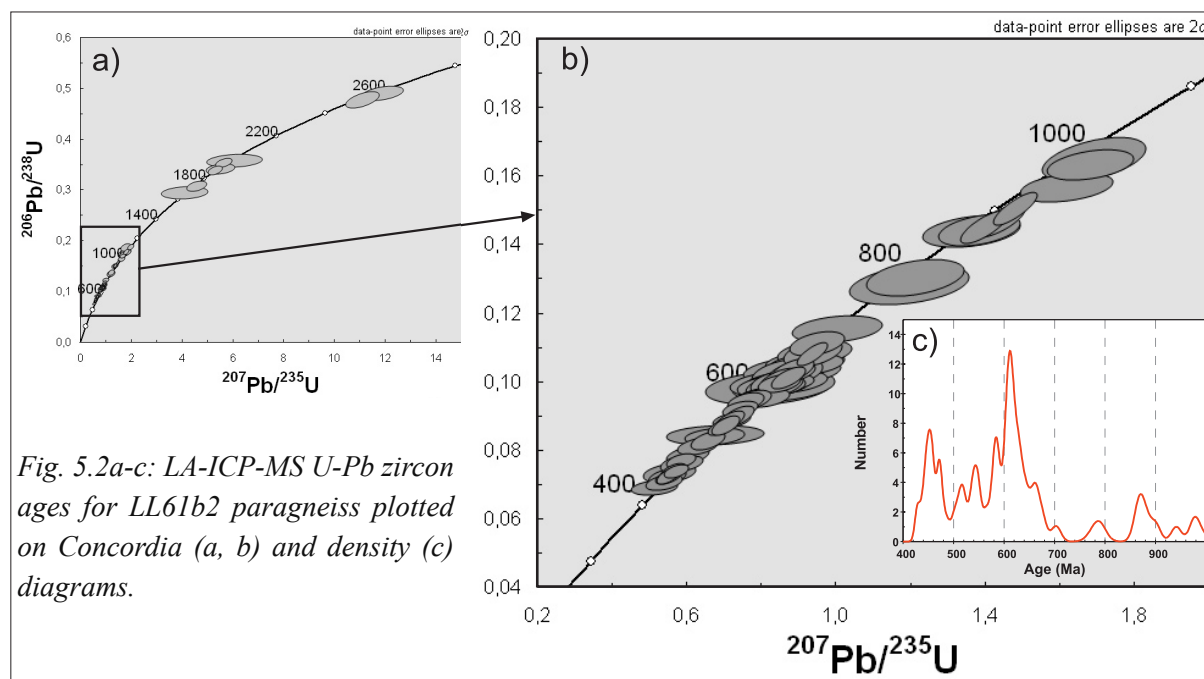


Fig. 5.2a-c: LA-ICP-MS U-Pb zircon ages for LL61b2 paragneiss plotted on Concordia (a, b) and density (c) diagrams.

The Hercynian metamorphic history of the studied paragneisses is unconstrained by zircon geochronology, consequently, all the analysed zircons have been considered as inherited and/or detrital crystals.

U-Pb ages have been interpreted on the basis of CL images (**Figs. 5.3a-f**). Generally, it has been observed that old zircons (>700 Ma) show complex internal structures. The more abundant detrital zircons, pertaining to the first two clusters, are of Silurian-Ordovician and Cambrian ages, respectively. Typically, they are euhedral and show undisturbed oscillatory zoning from core to rim (**Figs. 5.3a-d**); only in few cases narrow rims with irregular luminescent properties have been observed. Zircons showing bright overgrowths of metamorphic origin (Hoskin & Black, 2000) are lacking.

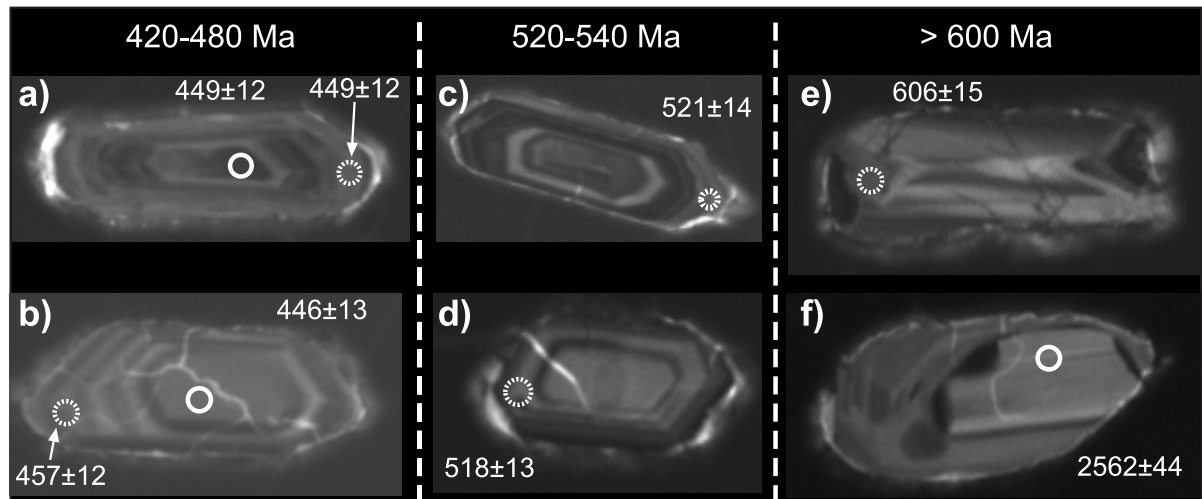


Fig. 5.3a-f: CL images of analysed zircons from LL61b2 paragneiss. Circles have a diameter of $10\ \mu\text{m}$ and represent ablated areas. Dashed circles are relative to rim of crystals.

Zircons with U-Pb ages ranging between ≈ 580 Ma and ≈ 620 Ma show variable shapes and sizes and define the third cluster. Internal structures are very complex (**Fig. 5.3e**) and could vary from oscillatory growth zoning to sector zoning. Several grains contain sub-rounded and partially resorbed cores rimmed by zoned or unzoned shells. Among older zircons (>700 Ma) inherited cores are very common (**Fig. 5.3f**).

5.2.2.2 – Meta-sill

Zircons observed in LL42c basic meta-sill are generally euhedral, very tiny (length $<150\ \mu\text{m}$) and prismatic. Internal zoning is mainly of oscillatory growth zoning (**Fig. 5.4**). Evidence for overgrowths and inherited cores are also presents. Metamorphic rims are poorly developed and, when visible, they are very thin. With the aim of dating the magmatic event related to the emplacement of the protolith, analyses have been concentrated on zircons characterised by well-developed oscillatory zoning, without complex structures. Twenty-two U-Pb concordia ages have been obtained from nineteen zircon crystals (**Table 21**) and range between $1037 \pm 24\ \text{Ma}$ and $248 \pm 8\ \text{Ma}$ (**Fig. 5.5a**). Sixteen U-Pb ages relative to thirteen zircons are younger than 500 Ma (**Figs. 5.5b, c**). The largest zircon population yields weighted average age of $340 \pm 10\ \text{Ma}$ (MSWD=4.1; where the MSWD is the Mean Square Weighted Deviates; **Figs. 5.5b, c**).

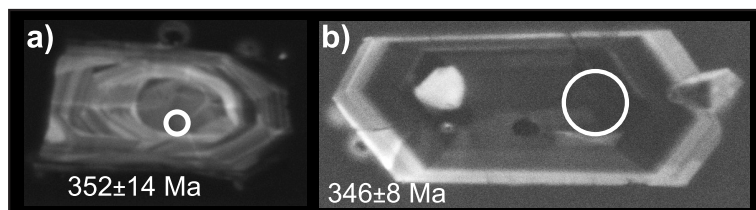


Fig. 5.4a, b: CL images of analysed zircons from LL42c basic meta-sill. Circles represent ablated areas and have a diameter of $10\ \mu\text{m}$ (a) and $25\ \mu\text{m}$ (b).

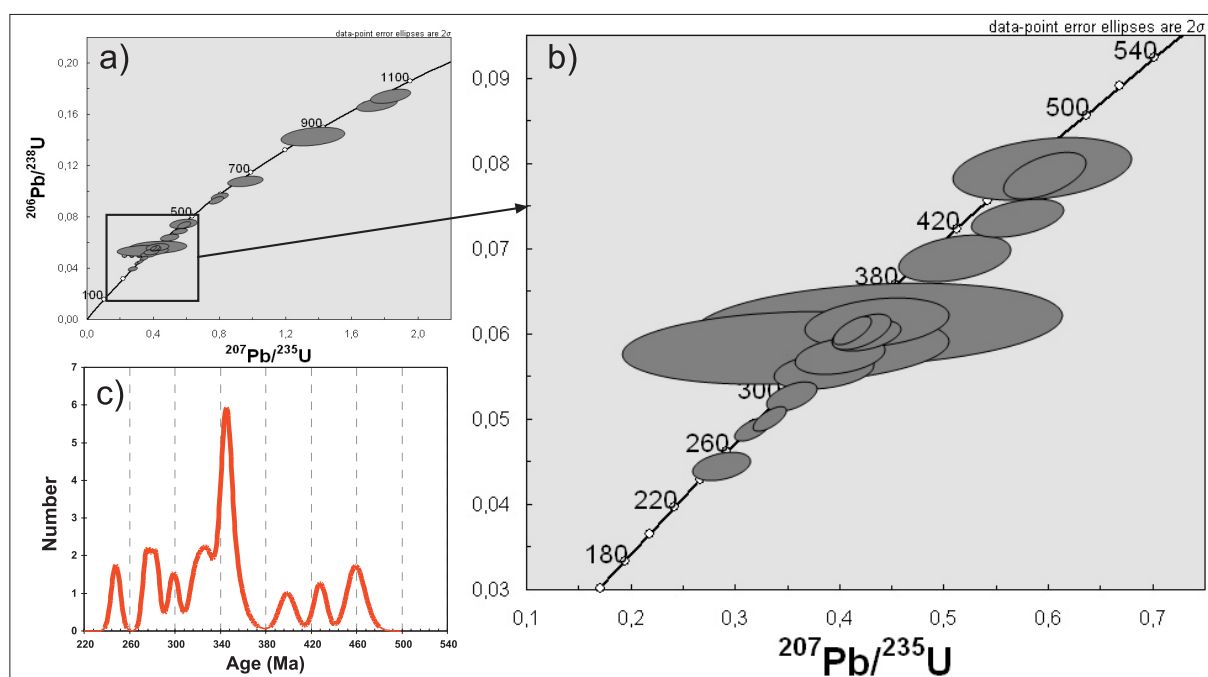


Fig. 5.5a-c: LA-ICP-MS U-Pb zircon ages for LL42c meta-sill plotted on Concordia (a, b) and density (c) diagrams.

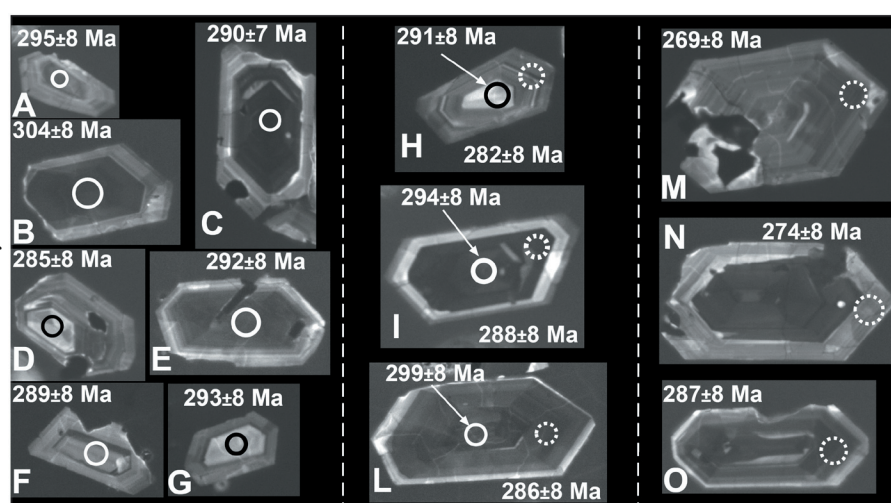
Older ages ($>500\ \text{Ma}$) refer to cores and/or rims of sub-rounded zircons showing complex internal structures, whereas few younger ages ($<300\ \text{Ma}$) are rare (two crystals).

5.2.2.3 – Porphyritic dyke

One porphyritic dyke, in crosscutting relationship with post-tectonic granitoids, represents the product of late magmatic activity. Therefore, the age of this dyke can be useful to constrain the end of the late-Hercynian magmatic activity.

On CL images zircons are euhedral and prismatic in morphology (mean aspect ratio of 2.04) with concentric oscillatory zoning from core to rim (**Fig. 5.6**), indicative of magmatic origin (Hanchar & Miller, 1993). Generally, crystal luminescence is faint in cores and bright in rims (**Fig. 5.6**). Only few crystals show inverse luminescence intensities (D, G, and H in **Fig. 5.6**). In some cases, zircons having a core with an irregular outline (O, **Fig. 5.6**) surrounded by a rim characterized by oscillatory zoning have been observed. These cores probably represent former xenocrystals partially resorbed and then overgrown by shells in equilibrium with the evolving acidic melt.

Fig. 5.6a-o: CL images of analysed zircons from the porphyritic dyke. Circles have a diameter of 25 μm and represent ablated areas. Dashed circles are relative to rim of crystals.



As expected, ages relative to inner portions of crystals are slightly older than those obtained from the outer parts. Ages were interpreted in light of zoning patterns. Undisturbed internal oscillatory zoning of zircons coupled with geochronologic data becoming progressively younger towards the outer crystals parts, is compatible with continuous magmatic growth. Nineteen U-Pb concordia ages (**Fig. 5.7a**) relative to fifteen zircon crystals spread from 308 ± 8 to 265 ± 8 Ma with (**Fig. 5.7b**) with a weighted average age of 287 ± 6 Ma.

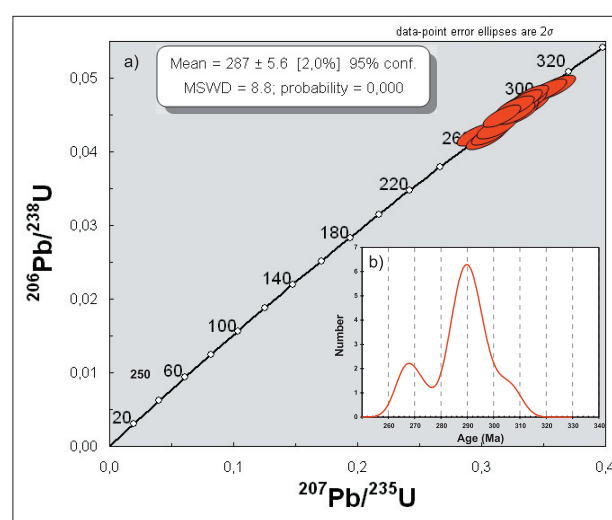


Fig. 5.7a, b: LA-ICP-MS U-Pb zircon ages for the porphyritic dyke plotted on Concordia (a) and density (b) diagrams.

5.2.3 – *In-situ* U-Th-Pb monazite ages

In situ U-Th-Pb analyses of monazite have been carried out directly on two thin sections of LL61b2 paragneiss and on one thin section of LL56a4 micaschist. Before isotopic analyses, the thin sections were analysed by a SEM/BSE to locate and characterize monazite crystals suitable for analyses with LA-ICP-MS. Analyses have been performed using laser spot sizes of 5 μm . Often, isotopic compositions have been collected from different portions of selected crystals with contrasting luminescence intensities.

LA-ICP-MS isotopic ratios and concordia ages relative to paragneiss and micaschist are listed in **Table 23, 24 of Appendix 7**, respectively.

5.2.3.1 – Paragneiss

Each analysed thin sections contains about 30 monazite crystals. They occur mainly along the foliation planes or are included in biotite crystals.

On the basis of BSE images, shapes and internal structures of monazite crystals vary considerably (**Figs. 5.8a-f**). Three major types of monazite crystals occur: elongated grains with maximum dimensions of about 15 x 35 μm (**Fig. 5.8a**); rhomboidal grains with maximum dimensions of about 25 x 35 μm (**Figs. 5.8b-d**) and stubby crystals with maximum dimensions of about 25 x 30 μm (**Figs. 5.8e, f**). All the analysed monazite crystals show sub-rounded contours (**Figs. 5.8a-f**), rarely lobed (**Figs. 5.8e, f**), and in some cases they have small inclusions (**Fig. 5.8f**).

Internal structures revealed by BSE images are very complex. Generally, monazite crystals show internal bands or areas with different luminescent properties (**Figs. 5.8b-f**); rarely, they are nearly homogeneous (**Fig. 5.8a**).

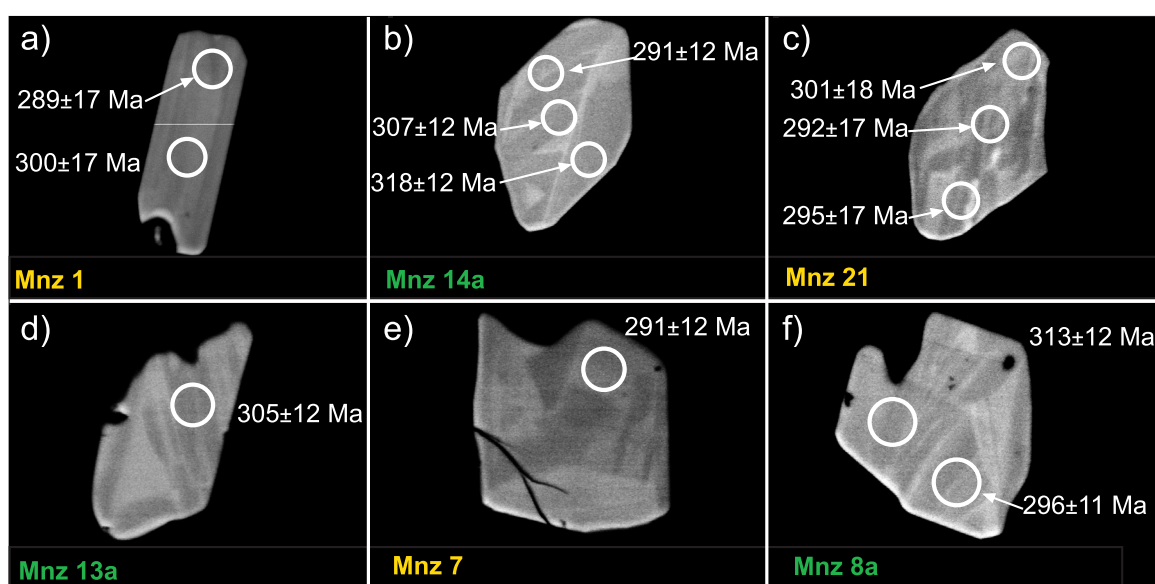


Fig. 5.8a-f: BSE images and U-Pb concordia ages of monazite crystals from LL61b2 paragneiss. Circles represent ablated areas and have a diameter of 5 μm .

Fifty-two *in situ* U-Th-Pb analyses have been carried out on twenty-eight selected monazite crystals (**Table 23**). Thirty-two LA-ICP-MS analyses yielded U-Pb concordia ages close or very close to the concordia curve (**Fig. 5.9a**) with an average age of 298.6 ± 1.2 Ma. However, the most reliable $^{206}\text{Pb}/^{238}\text{U}$ and $^{208}\text{Pb}/^{232}\text{Th}$ ages (**Fig. 5.9b, c**) have been used as a critical test of concordance (e.g. Foster *et al.*, 2000). All the analyses have weighted average $^{206}\text{Pb}/^{238}\text{U}$ and $^{208}\text{Pb}/^{232}\text{Th}$ ages at 292.7 ± 2.8 Ma (MSWD=6.4) and 297.5 ± 2.3 Ma (MSWD=1.3), respectively. These values are comparable within analytical errors. Moreover, the low MSWD values for the weighted mean $^{206}\text{Pb}/^{238}\text{U}$ and $^{208}\text{Pb}/^{232}\text{Th}$

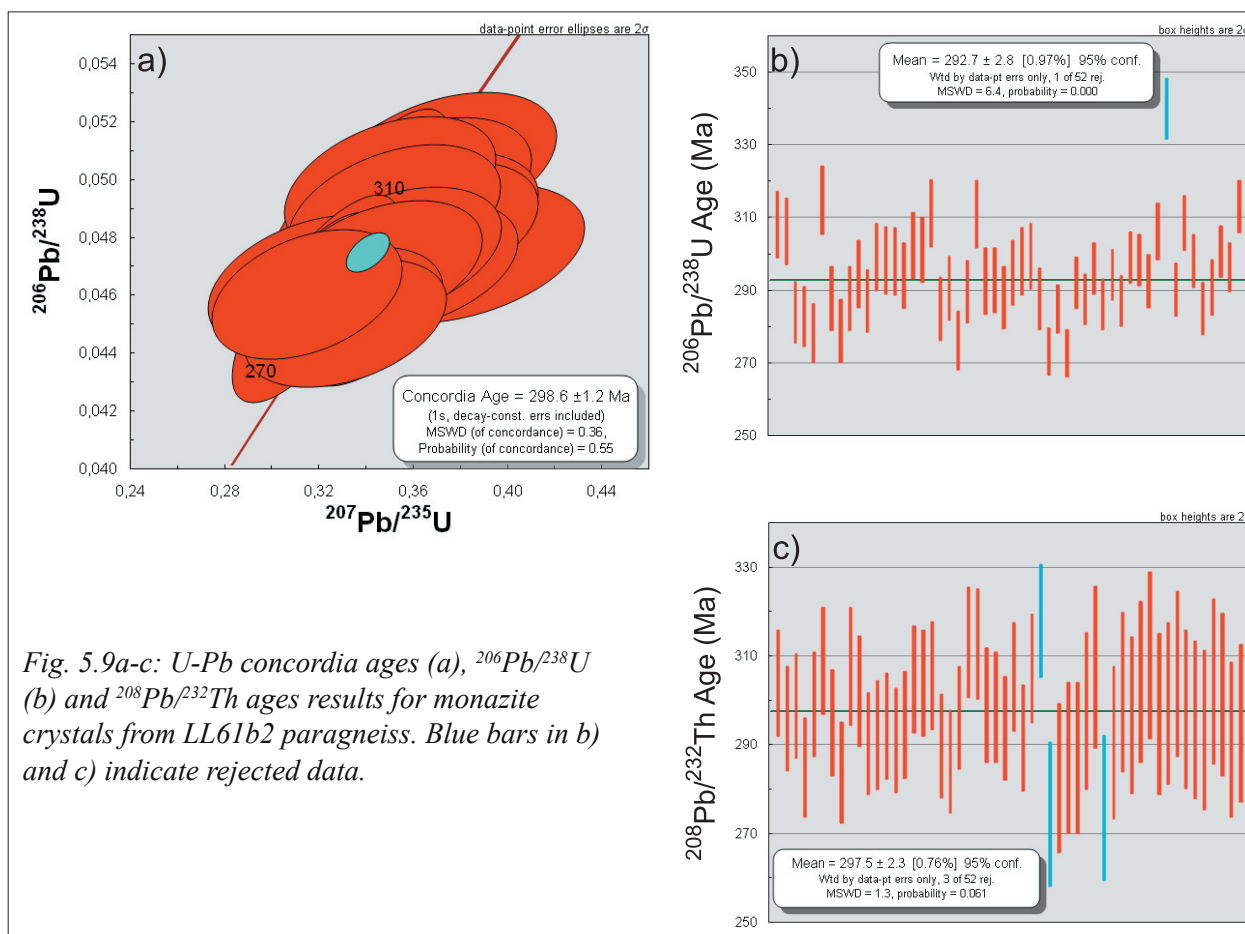


Fig. 5.9a-c: U-Pb concordia ages (a), $^{206}\text{Pb}/^{238}\text{U}$ (b) and $^{208}\text{Pb}/^{232}\text{Th}$ ages results for monazite crystals from LL61b2 paragneiss. Blue bars in b) and c) indicate rejected data.

ages suggest that they could be related to a single metamorphic event. Probably, $^{206}\text{Pb}/^{238}\text{U}$ and $^{208}\text{Pb}/^{232}\text{Th}$ ages above the mean value represent older events or mixed ages due to partial re-homogenisation of the monazite. $^{206}\text{Pb}/^{238}\text{U}$ and $^{208}\text{Pb}/^{232}\text{Th}$ ages below the mean values are probably linked to a slight Pb loss.

5.2.3.2 – Micaschist

Analysed thin section of LL56a4 micaschist contains about 20 monazite crystals. BSE images (Fig. 5.10a-d) revealed that these crystals have an elongated habit with sub-rounded contours. Maximum dimensions observed do not exceed 15 x 25 μm . Internally, monazite crystals are nearly homogeneous (Figs. 5.10b, c) and, in some cases, they show bands with weakly contrasting luminescent properties (Fig. 5.10d). Brighter areas are rarely visible.

Eighteen *in situ* U-Th-Pb analyses have been carried out on nine selected monazite crystals. Seven LA-ICP-MS analyses yielded U-Pb concordia ages close or very close to the concordia curve (Fig. 5.11a) with an average age of 291 ± 7.1 Ma. Considering the $^{206}\text{Pb}/^{238}\text{U}$ and $^{208}\text{Pb}/^{232}\text{Th}$ ages (Fig. 5.11b, c), all the analyses provide weighted mean $^{206}\text{Pb}/^{238}\text{U}$ and $^{208}\text{Pb}/^{232}\text{Th}$ ages at 292.2 ± 4.9 Ma (MSWD=8.0) and 286.6 ± 6.4 Ma (MSWD=3.8), respectively. These values are comparable to the mean concordia age. Also in this case, the low MSWD values for the weighted mean $^{206}\text{Pb}/^{238}\text{U}$ and $^{208}\text{Pb}/^{232}\text{Th}$ ages suggest that they can be related to a single metamorphic event.

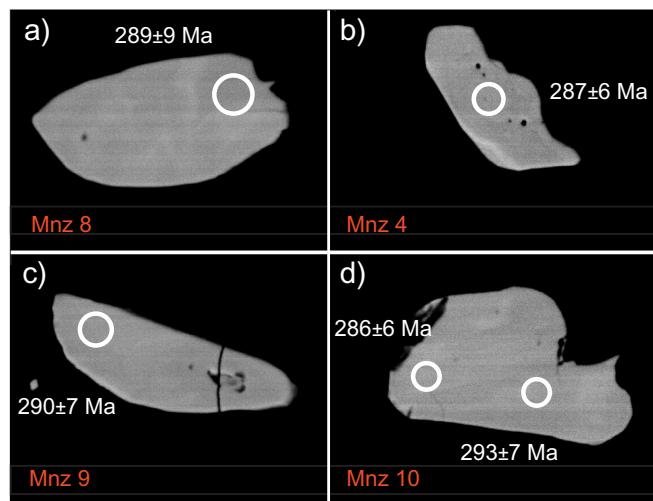


Fig. 5.10a-d: BSE images and U-Pb concordia ages of monazite crystals from LL56a4 micaschist. Circles represent ablated areas and have a diameter of 5 μm .

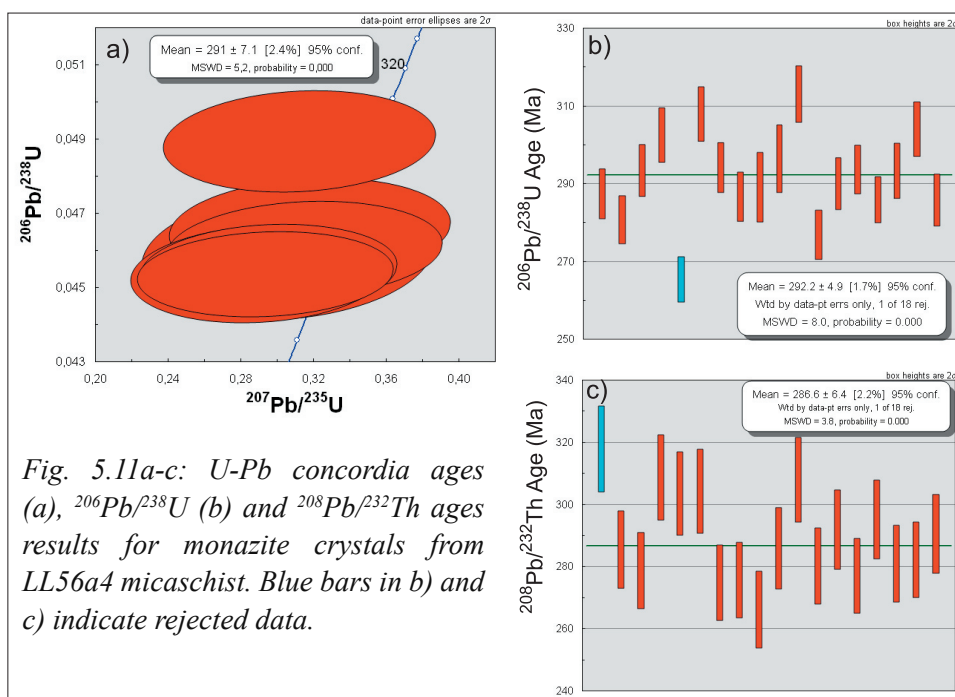


Fig. 5.11a-c: U-Pb concordia ages (a), $^{206}\text{Pb}/^{238}\text{U}$ (b) and $^{208}\text{Pb}/^{232}\text{Th}$ ages results for monazite crystals from LL56a4 micaschist. Blue bars in b) and c) indicate rejected data.

5.2.4 – Interpretation of the U-Th-Pb ages

5.2.4.1 – The Early Palaeozoic sedimentary sequence

Cambrian to Silurian detrital zircons from the paragneiss have typical magmatic features (euhedral shapes with undisturbed oscillatory zoning; Hanchar & Miller, 1993), thus indicating a direct derivation from intrusive–effusive sequences of this time span (≈ 550 Ma – ≈ 430 Ma). The well-preserved shapes of these zircons denote short transport and reworking during sedimentation. Zircon isotope analyses indicate moreover that the metasediments originated from a basement containing significant igneous and metamorphic components related to older orogenic cycle (*e.g.* Cadomian). The few inherited zircons older than 700 Ma are too scanty to define precisely the provenance and affinities. Silurian–Ordovician ages (≈ 430 – 480 Ma) of detrital zircons in the paragneiss represent a maximum depositional stage in the sedimentary sequence. The hypothesis of frequent magmatic activities during the Cambrian–Silurian period is also supported by geological data and other geochronologic data available from the literature. Four main arguments are in favour of this hypothesis:

- a) the protoliths of the studied paragneisses are siliciclastic sediments, with pelitic intercalations, belonging to a volcanoclastic sedimentary sequence as documented by the occurrence of metavolcanites and amphibolites (*cf.* 1.4; 2.1; 2.2);
- b) volcanic rocks of the Palaeozoic sequence of the Bocchigliero complex, tectonically juxtaposed with the studied Mandatoriccio complex (*cf.* 1.3), are mainly Ordovician (Acquafredda *et al.*, 1988; 1994a; 1994b);
- c) *in-situ* U-Pb zircon dating of porphyroids in the Peloritan Mountains from Sicily (Trombetta *et al.*, 2004) and of migmatitic paragneisses of northern Sardinia (Giacomini *et al.*, 2006) suggest the existence of an Ordovician volcanic arc;
- d) on the basis of U-Pb analyses on zircons from augen gneisses exposed in Calabria (Sila, Serre and Aspromonte) Micheletti *et al.* (2007) suggested a Cambrian emplacement age of the magmatic protoliths.

5.2.4.2 – The Hercynian evolution

Geochronologic data relative to the Hercynian evolution have been obtained from U-Pb dating of monazite crystals from the paragneiss and the micaschist and from U-Pb dating of zircon crystals of the basic meta-sill and the felsic porphyritic dyke. Following the subdivision of Faure *et al.*, (1997) the Hercynian geochronologic data fall within the neo-Hercynian (350–320 Ma) and the post-collisional period (320–290 Ma).

The neo-Hercynian period, recognised in the European Hercynian Belt, was characterised by continued convergence controlling the intracontinental tectonic evolution. During Early-Carboniferous time, mafic sills and dykes intruded within the upper crust as documented by U-Pb zircon ages of the basic meta-sill. This hypothesis is in accordance with the occurrence of intercalations of mafic magmatic rocks within the Early

Carboniferous sedimentary sequence of the Calabria-Peloritani terrane (Acquaferdda *et al.*, 1994a). The euhedral shapes and the oscillatory zoning of zircons from the basic meta-sill suggest that the zircon population with an average age of 340 ± 9.6 Ma is of magmatic origin. On the other hand, sub-rounded shapes and complex internal luminescent features of older zircons (>350 Ma) indicate that these are xenocrystals. As found in the paragneiss, the Hercynian metamorphic events did not affect U-Pb isotopic system in zircon. The only three ages younger than 300 Ma are related to two crystals showing magmatic luminescent properties. These ages are difficult to interpret, however they could be the result of the partial inhomogeneous resetting of zircon during the Hercynian metamorphism. Probably, Rb/Sr isochron ages (326 ± 6 Ma) obtained by Acquaferdda *et al.* (1992) on rocks of the Mandatoriccio complex are the only geochronologic data on the neo-Hercynian evolution of the upper crust. These data could be linked to the prograde metamorphic history of the Mandatoriccio complex.

The post-collisional period, characterised by continental collapse and crustal-scale extension (Faure *et al.*, 1997), has been well constrained by U-Pb dating on monazite. U-Pb Hercynian ages have been obtained on monazite from the paragneiss (≈ 298 Ma) and the micaschist (≈ 290 Ma). On the basis of these data, two major considerations can be made on the causes and timing of the late-Hercynian metamorphism in the Sila continental crust.

A first consideration concerns a possible link between the metamorphism and the thermal perturbation related to the ascent and the emplacement of granitoids in the Sila crust. U-Pb monazite ages obtained in this work for upper-crustal-amphibolite-facies paragneisses are comparable with late-Hercynian emplacement ages of mid-crustal granitoids (≈ 290 – 300 Ma; Ayuso *et al.* 1994; Graessner *et al.* 2000). Radiometric ages of the upper crust predate the end of the magmatic activity established by U-Pb zircon dating from a felsic porphyritic dyke (≈ 287 Ma). These geochronologic data suggest a direct link between low-pressure/high-temperature metamorphism and the emplacement of granitoids. An identical connection has been established by Graessner & Schenk (1999) in southern Calabria (Aspromonte massif), where low-pressure/high-temperature metamorphism has been related to the emplacement of granitoids. These authors obtained monazite U-Pb ages from upper-crustal-amphibolite-facies paragneisses ranging from 295 to 293 ± 4 Ma. These values are comparable with monazite and xenotime U-Pb emplacement ages from the peraluminous granites (303 – 302 ± 0.6 Ma) obtained by the same authors and they are compatible with Rb–Sr biotite and muscovite cooling ages (291 – 284 ± 4 Ma) reported by Del Moro *et al.* (1982) for the peraluminous granite of Cittanova (Aspromonte massif).

A second consideration concerns the age of peak metamorphic conditions reached by the lower and the upper Hercynian crust exposed in the Sila massif. U-Pb monazite ages obtained from metamorphic rocks of the upper crust are slightly younger than the U–Pb monazite ages of 304 – 300 ± 0.4 Ma obtained by Graessner *et al.* (2000) from migmatitic paragneisses of the lower crust. This difference suggests a small diachronism of the metamorphic peak in the different crustal levels.

6 - P-T-t PATHS AND TECTONO-METAMORPHIC MODELS

This chapter is dedicated to the presentation and discussion of the P-T-t path followed by the Hercynian upper crustal rocks of the Mandatoriccio complex, integrating P-T estimate (cf. Chapter 4) with geochronologic data (cf. Chapter 5). The tectono-metamorphic model will be compared with those relative to the other Hercynian crustal levels and will be briefly discussed in a possible palaeogeographical scenario.

6.1 – P-T-t PATH AND TECTONO-METAMORPHIC MODEL OF THE HERCYNIAN INTERMEDIATE/UPPER CRUST

On the basis of petrologic and geochronologic data, the P-T-t path followed by the Mandatoriccio complex will be described. Subsequently, the P-T-t path will be discussed in a tectono-metamorphic model accounting for the field data and the deformation-crystallisation history (**Fig. 6.1a-d**).

Considering the P-T paths reconstructed for the analysed samples (**Figs. 4.15, 4.16 and 4.19**), the prograde Hercynian tectono-metamorphic history followed by the Mandatoriccio complex can be schematically subdivided in four main stages: a) thickening; b) peak-pressure condition; c) decompression; d) peak-temperature condition.

a) During the thickening phase, garnet blastesis started up with spessartine-rich syntectonic core developed within micaschists and paragneisses (**Fig. 6.1a**). Coevally, mafic sills and dykes injected the upper crustal volcanoclastic sedimentary sequence (Mandatoriccio complex). This stage can be referred to the neo-Hercynian period (350–320 Ma; Faure *et al.*, 1997), as documented by U-Pb zircon ages of the basic meta-sill (340 ± 9.6 Ma).

b) After reaching the peak-pressure condition (≈ 4 kbar), the upper crust experienced a period of deformation quiescence marked by the static overgrowths of S_2 by Almandine-rich-garnet rims and by porphyroblasts of biotite and staurolite (**Fig. 6.1b**). Probably, this metamorphic phase is related to isotherms relaxation after the thickening episode. Rb/Sr isochron age (326 ± 6 Ma) obtained by Acquafredda *et al.* (1992) on rocks of the Mandatoriccio complex might be indicative of an isotopic re-equilibration of the Rb/Sr isotopic system related to this static phase.

c) The post-collisional period started with the development of andalusite+biotite coronas overgrown on staurolite porphyroblasts (**Fig. 6.1c**). This microtexture, common to micaschists and paragneisses, probably developed as a consequence of incipient extension at growing temperatures. This stage represents a critical point of the metamorphic history, since metamorphic rocks of the intermediate/upper crust started to record a significant thermal perturbation, as evidenced by the curvature change visible in the path (**Fig. 6.1c**).

d) Peak-temperature conditions (≈ 620 °C) were reached at the end of this thermal perturbation. They are well-documented by some reaction textures and mineral assemblages

observed almost exclusively within paragneisses. The later appearance of fibrolitic sillimanite documents a small excursion of the P-T path across the And-Sil boundary due to heating. Stephanian U-Pb ages of monazite crystals from the paragneiss, can be related to this heating phase. Similar monazite U-Pb ages from the micaschist combined with the lack of fibrolitic sillimanite suggest that, during the same thermal pulse, micaschists recorded temperatures slightly lower than those reached by paragneisses. Geologic, geochronologic and petrographic data suggest that the thermal peak recorded by the intermediate/upper crust could be strictly connected with the emplacement of huge masses of granitoids in the middle crust (**Fig. 6.1d**).

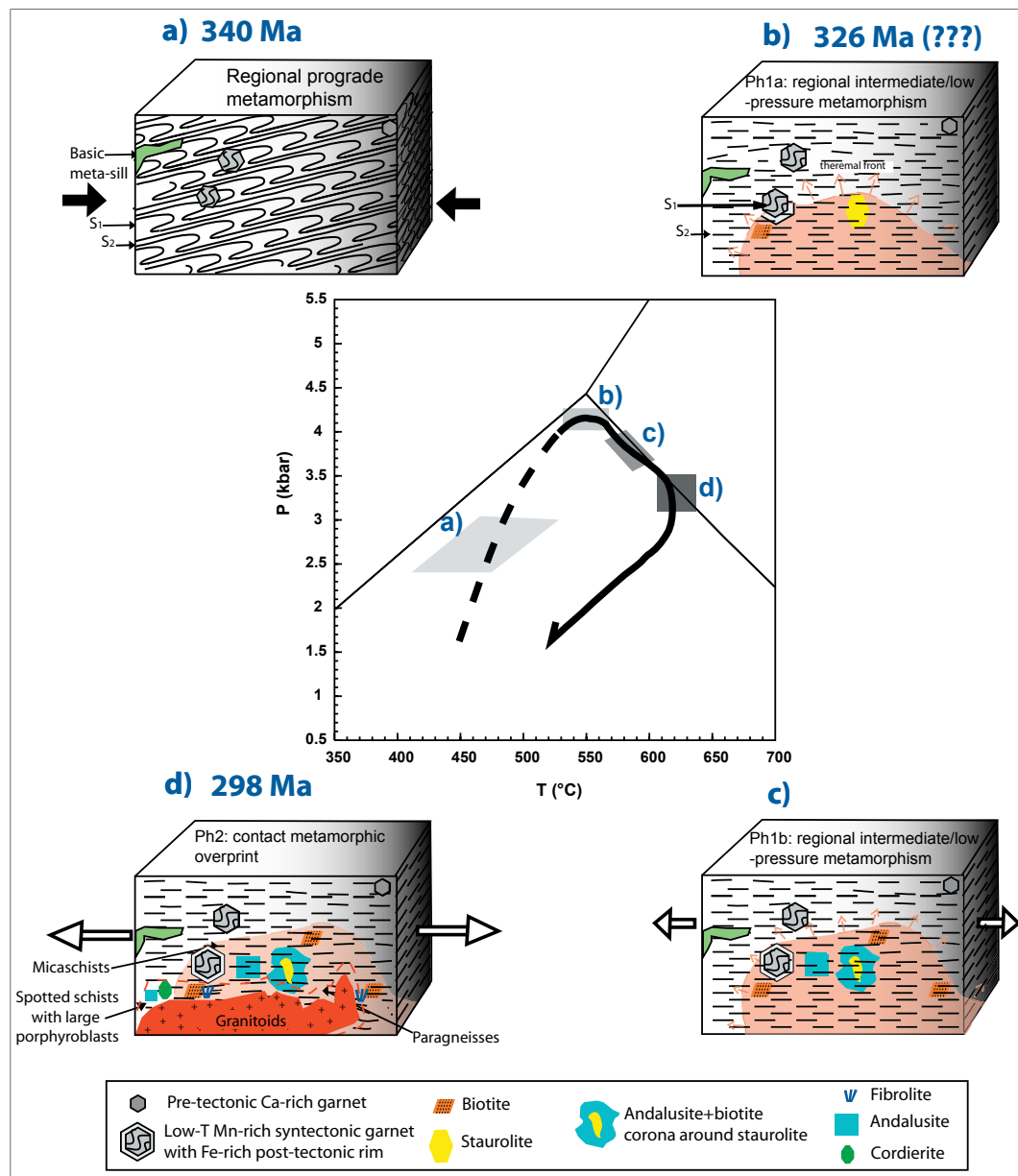


Fig. 6.1: P-T path and schematic tectono-metamorphic model of the prograde metamorphic evolution. a) Thickening; b) peak-pressure conditions; c) decompression; d) peak-temperature conditions. In d) are represented possible tectono-metamorphic positions of different lithologies. Pink areas represent crustal volumes affected by regional HT metamorphism; red-dashed line delimits the crustal volumes overprinted by the contact metamorphism. See text for explanations.

Probably, the lithospheric extension favoured the ascent and the emplacement of granitoids in the relatively heated crust, with further exhumation of the metamorphic rocks.

Local heating linked to plutonic bodies has been also recorded by rocks not affected by the intermediate- to low-pressure/high-temperature regional metamorphism described above. Spotted schists with large porphyroblasts recorded the local thermal perturbation linked to the granitoids (**Fig. 6.1d**). Geologic and chemical features suggest that the reaction history of the spotted schists with large porphyroblasts was not strongly controlled by the bulk chemistry and it took place outside of the crustal volumes affected by the intermediate- to low-pressure/high-temperature regional metamorphism (**Fig. 6.1d**). Probably, the well-developed porphyroblastic texture was favoured by the relative high fluid content of these rocks not affected by previous dehydration reactions, such as those recorded in micaschists and paragneisses (*e.g.* chlorite breakdown with garnet or staurolite formation).

Retrograde evolution was mainly characterised by hydration reactions causing the total or partial replacement of existing minerals. During the retrograde evolution, cordierite porphyroblasts developed on Bt-rich layers of paragneisses.

6.1.1 - Comparison with P-T-t paths followed by other crustal levels

The reconstructed P-T-t path (**Fig. 6.1**) refers to rocks ascribed to the intermediate/upper portion of the Hercynian continental crust exposed in the Sila Massif. These rocks belong to a near continuous and complete cross-section through the Hercynian continental crust (Dubois, 1976; Schenk, 1980); therefore, the P-T-t estimates relative to lower, intermediate and upper crust should be consistent with a unique geological scenario.

Graessner & Schenk (2001) proposed a clockwise P-T path for the Hercynian lower crustal section exposed in Sila. The P-T path is composed by a poorly documented prograde segment, characterised by heating and loading in the stability field of sillimanite (**Fig. 6.2**). Peak metamorphic conditions estimated by these authors are ≈ 740 °C and ≈ 4 kbar for the upper part of the lower crust, and ≈ 770 °C and ≈ 6 kbar for the basal part of the lower crust. These authors dated the peak metamorphic event at about 300 Ma. Comparable peak metamorphic estimates relative to the Sila lower crust have been obtained by Le Breton (1983; $T > 650$ °C, $P > 4.5$ -5 kbar), Althaus & Istrate (1990; $T = 690$ -740 °C and $P < 6$ -8 kbar) and by Caggianelli & Prosser (2001; $T = 740$ °C and $P = 4.2$ kbar). In the reconstruction proposed by Graessner & Schenk (2001), after the peak metamorphism, the lower crustal rocks experienced a nearly isothermal decompression, of about 1 kbar, followed by a stage of near isobaric cooling.

Intermediate crust is mainly composed by granitoid rocks. Estimates of emplacement pressures for granodiorites and tonalites of Savelli, Rovale and Belcastro have been determined by Caggianelli *et al.* (1997). Magmatic crystallisation took place at different crustal levels (**Fig. 6.2**) varying from about 3 kbar and 731 °C (Savelli and Rovale areas) to about 5 kbar and 700 °C (Belcastro area), resulting in inferred emplacement depth comprised

between 8 and 15-17 km. The P-T conditions of emplacement have been determined by Caggianelli & Prosser (2001) also in a hornfels of the Bocchigliero complex containing the Ms+Qtz+Bt+And+Crd±Fib mineral assemblage. Thermobarometry indicates equilibrium at $P = 2.2$ kbar and $T = 560$ °C (**Fig. 6.2**). According to geochronologic determinations, the emplacement of granitoids in the middle crust took place in tight time interval between 300 and 290 Ma *ca.* (Ayuso *et al.*, 1994; Graessner *et al.*, 2000).

Concerning the intermediate/upper crust, the P-T path of the Mandatoriccio complex reconstructed in the present work is significantly different and more detailed with respect to the P-T path reconstructed by Borghi *et al.* (1992). In fact, in the P-T path proposed by Borghi *et al.* (1992) the peak-temperature condition is nearly coincident with the peak-pressure condition. In addition, the path of Borghi *et al.* (1992) appears unaffected by the thermal perturbation linked to the intrusion of the granitoids, being devoid of the previously described curvature change and presenting a nearly isothermal decompression without any evidence of further heating.

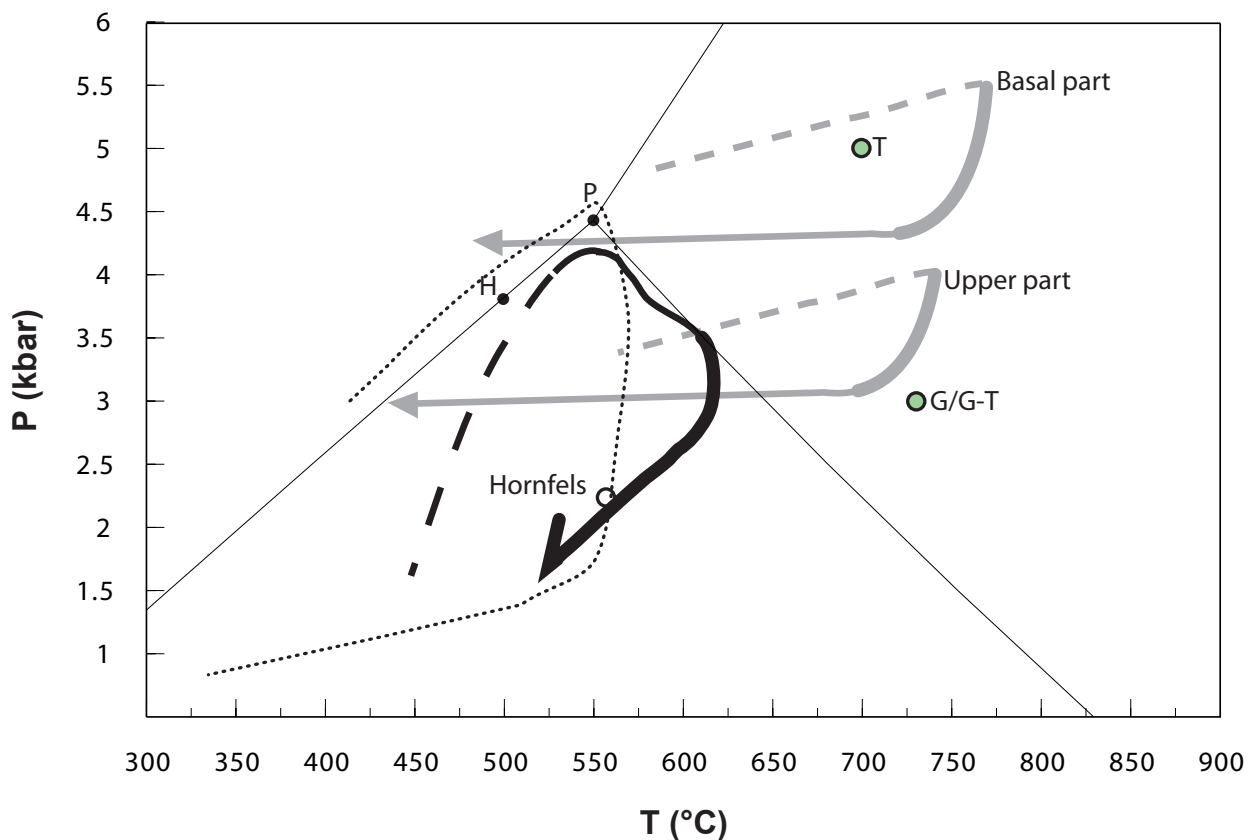


Fig. 6.2: P-T paths of the Hercynian continental crust exposed in Sila massif. Lower crust (Graessner & Schenk, 2001): thick-grey lines. Intermediate crust (Caggianelli *et al.*, 1997): green-filled circles (T=tonalite; G/G-T=granodiorite/granodiorite-tonalite). Upper crust: thick-black line (this work), dotted line (Borghi *et al.*, 1992); white filled circle (Caggianelli & Prosser, 2001). Thick segments of the P-T paths refer to the decompression P-T history directly comparable. See text for explanations. H and P represent triple point positions after Holdaway (1971) and Pattison (1992), respectively.

Focusing the attention on the P-T paths followed by the intermediate/upper crust (this work) and the lower crust (Graessner & Schenk, 2001) several interesting points emerge:

- the upper part of the lower crust and the intermediate/upper crust experienced similar peak pressure conditions, indicating similar crustal depth soon after the thickening episode;
- in the lower crust, peak-pressure and peak-temperature conditions were reached in the same time;
- after peak-temperature conditions the two crustal levels recorded a decompression event of about 1 kbar but with different cooling paths.

These points raise some problems that are briefly commented below.

The major inconsistency between the P-T paths relative to upper- and lower-crustal levels concerns the peak-pressure conditions. The results of the present work indicate that, probably, the peak-pressure conditions estimated by Graessner & Schenk (2001) are underestimated. This is a typical problem when investigating high-grade metamorphic rocks, since the record of the P-T history before the temperature peak is hardly preserved. Consequently, in light of the results obtained in this thesis and considering the evidence emerging from new paths determined for the Hercynian lower crust exposed in other areas of the Calabria (*e.g.* Acquafredda *et al.*, 2006), the P-T paths proposed by Graessner & Schenk (2001) could be devoid of a decompression segment preceding the peak-temperature condition.

A further comment deserves a comparison of the cooling histories during decompression, after the thermal peak. The temperature decrease in the lower crust is moderate, since the decompression path is nearly vertical. On the other hand, the cooling path determined for the upper crust is characterized by a pronounced temperature decrease. The different cooling rates in the lower and upper crustal levels, after the peak-temperature conditions, could be explained in terms of different heat transfer rates after the thermal perturbation. In fact, heat loss to the surface is faster in the upper/intermediate crust.

The final comment concerns the P-T history following the decompression event. The metamorphic history of the lower crust is characterized by isobaric cooling ending with the Tertiary exhumation. For the upper/intermediate crust petrologic methods adopted in this thesis were unable to reveal this part of the story. However, fission track dating by Thompson (1994) seems to indicate that the Mandatoriccio complex rocks resided at moderate depth in the upper crust at least up to the Jurassic time.

In conclusion,

- 1) the prograde metamorphic evolution is more constrained in the intermediate/upper crust than in the lower crust;
- 2) the P-T paths followed by the upper/intermediate and the lower crust are only apparently different, in reality, after a deeper analysis, they can be well consistent with the same geologic scenario.

6.1.2 – Implications for the crustal scale tectono-metamorphic model

Two major models have been proposed in order to explain the evolution of the Sila massif. These crustal-scale models have been reconstructed chiefly on the basis of petrologic studies of the lower crust.

Schenk (1984; 1989; 1990) and Graessner & Schenk (2001) proposed that a crustal thickening event was responsible for metamorphic heating, subsequent crustal uplift and the isobaric cooling. In this model crustal thickening occurred at about 300 Ma, 30–40 Ma later than the collisional stage of the western European Hercynian belt (Arthaud & Matte, 1977; Burg *et al.*, 1987; Ledru *et al.*, 1989), giving no explanation to the metamorphic stage recorded at 330–326 Ma (Acquafredda *et al.*, 1991; 1992) in the Hercynian upper crust exposed in Sila.

Alternatively, Caggianelli *et al.* (2000), Del Moro *et al.* (2000), Caggianelli & Prosser (2002) and Caggianelli *et al.* (2007) proposed that exhumation and granitoids emplacement took place in a framework of post-collisional lithospheric extension, similarly to the tectonic evolution of the French Massif Central (Faure, 1995; Ledru *et al.*, 2001), the Sardinia Massif (Carmignani *et al.*, 1992; 1994; Di Vincenzo *et al.*, 2004) and the Ivrea zone (Brodie & Rutter, 1987; Handy & Zingg, 1991).

New petrologic and geochronologic data obtained for the intermediate/upper crust provide important contributions in order to suggest the more appropriate crustal-scale tectono-metamorphic model. The P-T path reconstructed for the intermediate/upper crust is compatible with a post-collisional extensional framework.

In conclusion, the extensional tectonics after collision is the possible tectono-metamorphic setting able to explain LP/HT metamorphism in the upper crust, ascent and emplacement of granitoids in the intermediate crust (Ayuso *et al.*, 1994; Caggianelli *et al.* 2000; Caggianelli & Prosser, 2002) and high-temperature metamorphism in the lower crust (Schenk 1980; 1990; Graessner & Schenk, 2001), simultaneously.

6.1.3 - Palaeogeographical implications

In the previous palaeogeographical reconstructions, the Mandatoriccio complex is considered as a Cadomian (Bouillin *et al.*, 1984; 1987) or as an Ordovician basement (Acquafredda *et al.*, 1988) partly overprinted during the Hercynian orogeny. These reconstructions are mainly based on the different metamorphic features of the adjacent Mandatoriccio and Bocchigliero complexes. The palaeogeographical reconstruction proposed by Acquafredda *et al.* (1988; 1994a), is based on the consideration that the thermal regional metamorphism, observed in the Mandatoriccio complex, is anorogenic and is related to tensional processes which led to the formation of Palaeozoic basins. In this reconstruction the Mandatoriccio complex formed a part of the basement on which the Bocchigliero basin developed (**Fig. 6.3a**). The lack of clasts derived from the Mandatoriccio complex led these authors to suggest that the Mandatoriccio complex did not constitute the direct siliciclastic source of the Bocchigliero Palaeozoic sequence, because it was lying at greater depths.

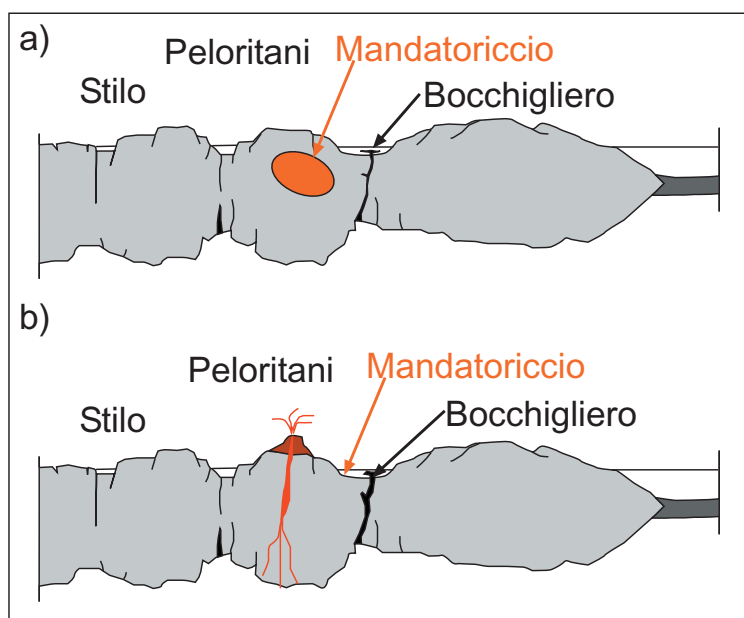


Fig. 6.3a, b: Cambro-Ordovician reconstructions of the Calabria-Peloritani terrane inspired to Acquafredda *et al.* (1994). The reconstructions show the palaeopositions of the Mandatoriccio and the Bocchigliero complexes according to Acquafredda *et al.* (1994; a) and this work (b).

New geologic and geochronologic data suggest an alternative palaeogeographical scenario. Cambrian to Silurian detrital zircons from the paragneiss of the Mandatoriccio complex show typical magmatic features, thus indicating a direct derivation from intrusive–effusive sequences of this time span (≈ 550 Ma – ≈ 430 Ma). Moreover, zircon isotope analyses indicate that the metasediments of the Mandatoriccio complex originated from a basement containing significant igneous and metamorphic components related to older orogenic cycle (*e.g.* Cadomian). These data suggest that the volcanoclastic sequence of the Mandatoriccio complex originated in a sedimentary basin, before the Silurian time. Therefore, the Mandatoriccio and the Bocchigliero sequences were coeval and, probably, they were deposited in the same sedimentary basin during the Cambro-Ordovician time (**Fig. 6.3b**), as suggested by similar geologic and geochronologic features (Acquafredda

et al., 1988; 1994a; 1994b). This palaeogeographical scenario is coherent with large-scale reconstructions proposed for other Hercynian terranes on the basis of new geologic and geochronologic data (Trombetta *et al.*, 2004; Giacomini *et al.*, 2006; Micheletti *et al.*, 2007). In particular, based on new geological and geochronologic data from the Hercynian rocks exposed in Sardinia, Giacomini *et al.* (2006) proposed a new geodynamic scenario, largely inspired from the palaeogeographical reconstructions of Stampfli *et al.* (2002) and von Raumer *et al.* (2003). According to Giacomini *et al.*, (2006), Calabria-Peloritani terranes belonged to the European Hunic terranes located between the Prototethys and the Palaeotethys (**Fig. 6.4a**). This latter oceanic domain represents a back-arc basin system developed in the north Gondwana margin during the Early Palaeozoic (Giacomini *et al.*, 2006). Subsequently, the northern passive margin of the Palaeotethys evolved in an active margin in the Devonian time (**Fig. 6.4b**; Giacomini *et al.*, 2006). The volcanoclastic sedimentary protoliths of the Mandatoriccio complex formed in the back arc basin with the protoliths of the Bocchigliero complex (**Fig. 6.4a**). Probably, during the continental collision the Bocchigliero complex overthrust the Mandatoriccio complex and it was not affected by later metamorphic events due to its higher crustal position. This pre-Hercynian detachment could explain the different metamorphic features developed in the two intermediate/upper crustal metamorphic complexes.

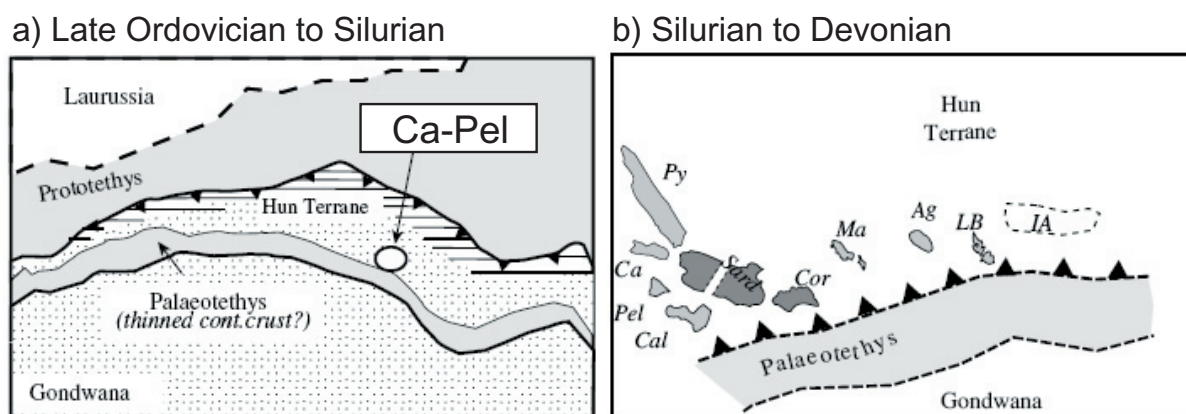


Fig. 6.4a, b: possible palaeogeographical reconstruction of the pre-Hercynian plate arrangement at the northern Gondwana margin, modified after Giacomini *et al.* (2006). Sard: Sardinia; Cor: Corsica; Py: Pyrenees; Ca: Catalan coastal range; Ma: Maures; Pel: Peloritani (Sicily); Cal: Calabria; Ag: Argentera; LB: Ligurian Briançonnais; IA: other intra-alpine massifs.

CHAPTER 7 – SUMMARY AND CONCLUSIONS

The most important results of the present work are listed below.

1) Petrographic, microstructural and field observations revealed that the Mandatoriccio complex shows two major heterogeneities. The first one refers to the distribution of the observed lithologies, whereas the second one refers to the distribution of small late-Hercynian intrusive bodies. Based on these heterogeneities, the studied area has been subdivided into two major sub-areas: the Umbriatico village sub-area, with prevailing acid metavolcanites and amphibolites and few intercalations of micaschists and paragneisses, and the Sappo stream sub-area, with dominant siliciclastic metasediments and rare intercalations of acid metavolcanites and amphibolites. These lithologic variations reflect the primary distribution of siliciclastic and volcanic rocks in the sedimentary basin. These two sub-areas are characterised by a second relevant heterogeneity concerning the distribution of aplite and pegmatite veins and other late-Hercynian granitic bodies. In the Umbriatico village sub-area, the basement rocks are intensely crosscut by aplite and pegmatite veins, whereas granitoid bodies are lacking. On the other hand, in the Sappo stream sub-area pegmatite and aplite veins are uncommon, whereas small granitic bodies aligned along cataclastic shear zones have been observed. The spatial distribution of the minor intrusive bodies have been attributed to a different distance from the main granodiorite body (Sila batolith). In fact, in the Sappo stream area the granitoids and the related contact metamorphic rocks (spotted schists with large porphyroblasts) are tectonically juxtaposed with metamorphic rocks without a contact metamorphic overprint. These observations suggest that small granitic bodies have been emplaced during the later (middle-Miocene to recent) tectonic evolution. Differences in the distribution of the intrusive rocks and the different distances from the main granodiorite intrusion justify the observed textural heterogeneity. In fact, the metamorphic rocks around the Umbriatico village show well-developed porphyroblastic textures resulting particularly interesting for petrologic investigations.

2) New geologic, petrographic and geochronologic data led to formulate a new hypothesis on the genesis of protoliths of the Mandatoriccio complex. Until now, the origin of this complex was unclear. In many reconstructions, the Mandatoriccio complex was considered as a pre-Hercynian basement weakly affected by the Hercynian metamorphic events.

U-Pb ages and internal features of zircons suggest that the protoliths of the Mandatoriccio complex formed in a sedimentary basin filled by Cambrian to Silurian magmatic products as well as by siliciclastic sediments derived from older igneous and metamorphic rocks. A similar sedimentary sequence with volcanoclastic intercalations has been reconstructed by other authors for the low-grade Bocchigliero complex. Actually, these complexes are tectonically juxtaposed and show a different Hercynian metamorphic

overprint. The analogous sedimentary features and the different metamorphic characters suggest that these complexes derive from the same sedimentary basin and that they were separated before the Hercynian evolution, following different metamorphic histories. The tectonic contact between the two complexes has not been detected because of the later Alpine-Apennine overprint.

3) Phase diagram calculations permitted to obtain a detailed reconstruction of the P-T evolution of the Mandatoriccio complex. Micaschists and paragneisses of the Mandatoriccio complex followed a clockwise P-T path characterised by four main prograde phases that include thickening, peak-pressure condition, decompression and peak-temperature condition. During the thickening phase, garnet blastesis started up with spessartine-rich syntectonic core developed within micaschists and paragneisses. During this phase, mafic sills and dykes injected (340 ± 9.6 Ma) the upper crustal volcanoclastic sedimentary sequence of the Mandatoriccio complex. After reaching the peak-pressure condition (≈ 4 kbar), the upper crust experienced a period of deformation quiescence marked by the static overgrowths of S_2 by Almandine-rich-garnet rims and by porphyroblasts of biotite and staurolite. Probably, this metamorphic phase is related to isotherms relaxation after the thickening episode recorded by the Rb/Sr isotopic system (326 ± 6 Ma isochron age; Acquafredda *et al.*, 1992). The post-collisional period was mainly characterised by decompression with increasing temperature. This stage is documented by the andalusite+biotite coronas overgrown on staurolite porphyroblasts and represents a critical point of the metamorphic history, since metamorphic rocks begin to record a significant thermal perturbation. Peak-temperature conditions (≈ 620 °C) were reached at the end of this stage. They are well constrained by reaction textures and mineral assemblages observed almost exclusively within paragneisses. The later appearance of fibrolitic sillimanite documents a small excursion of the P-T path across the And-Sil boundary due to the heating pulse. Stephanian U-Pb ages of monazite crystals from the studied paragneisses, can be related to this heating phase. Similar monazite U-Pb ages from the analysed micaschists combined with the lack of fibrolitic sillimanite suggest that, during the same thermal perturbation, micaschists recorded temperatures slightly lower than those reached by paragneisses. Geologic, geochronologic and petrographic data suggest that the thermal peak recorded by the intermediate/upper crust could be strictly connected with the emplacement of huge masses of granitoids in the middle crust. Probably, the lithospheric extension favoured ascent and emplacement of granitoids in the relatively heated crust which further exhumation of the metamorphic rocks. The metamorphic history ended with the crystallisation of cordierite at major expenses of andalusite. Summarising, the Ms+Bt+St+And+Sill+Crd mineral assemblage observed in the paragneisses is the result of a polyphase evolution and is characterised by the unstable persistence of the staurolite in the stability fields of the cordierite. The reconstructed metamorphic history suggests that after peak pressure conditions the Hercynian intermediate/upper crust experienced a large-scale extensional tectonics. Probably, crustal extensional shear zones promoted

decompression, heating and exhumation in the upper crust and favoured the emplacement of large masses of granitoids in the intermediate crust.

4) Finally, comparing the tectono-metamorphic evolutions of different crustal levels of a LP/HT metamorphic belt, three major observations can be done:

- i) the petrologic path of the intermediate/upper crustal level is more reliable to shed light on the prograde metamorphic evolution;
- ii) the thermal peak of the LP/HT metamorphism in the upper/intermediate crust is strictly related to the ascent and emplacement of granitoids;
- iii) the reconstruction of the tectono-metamorphic evolution in all the crustal levels is needed to obtain a correct tectono-metamorphic model.

REFERENCES

- Acquafredda, P., Lorenzoni, S., Zanettin-Lorenzoni, E., 1988. La sequenza Paleozoica dell'Unità di Bocchigliero (Sila, Calabria). *Rend. Soc. Geol. It.*, 11, 5-22.
- Acquafredda, P., Lorenzoni, S., Zanettin-Lorenzoni, E., 1994a. Palaeozoic sequences and evolution of the Calabrian-Peloritan Arc (Southern Italy). *Terra Nova*, 6, 582-594.
- Acquafredda, P., Lorenzoni, S., Zanettin-Lorenzoni, E., 1994b. The Bocchigliero Palaeozoic sequence in the context of the Calabrian-Peloritan Hercynian Range (Italy). *Geological Journal*, 29, 45-58.
- Acquafredda, P., Barbieri, M., Lorenzoni, S., Zanettin-Lorenzoni, E., 1991. The age of volcanism and metamorphism of the Bocchigliero Paleozoic sequence (Sila – southern Italy). *Rend. Fis. Acc. Lincei*, 9, 145-156.
- Acquafredda, P., Barbieri, M., Lorenzoni, S., Trudu, C., Zanettin-Lorenzoni, E., 1992. Metamorphism of the Mandatoriccio Unit in the context of the Hercynian and pre-Hercynian evolution of the Calabrian-Peloritan Arc (Southern Italy). *Rend. Acc. Lincei*, 3, 151-161.
- Acquafredda, P., Fornelli, A., Paglionico A., Piccarreta, G., 2006. Petrological evidence for crustal thickening and extension in the Serre granulite terrane (Calabria, southern Italy). *Geological Magazine*, 143, 145–163.
- Amodio-Morelli, L., Bonardi, G., Colonna, V., Dietrich, D., Giunta, G., Ippolito, F., Liguori, V., Lorenzoni, S., Paglionico, A., Perrone, V., Piccarreta, G., Russo, M., Scandone, P., Zanettin-Lorenzoni, E., Zuppetta, A., 1976. L'arco calabro-peloritano nell'orogene appenninico-maghrebide. *Memorie della Società Geologica Italiana* 17, 1-60.
- Althaus, E., Istrate, G., 1990. Granulite facies conditions derived from fluid inclusions: Sila massif, Calabria, Italy. *Neues Jahrbuch für Mineralogie, Monatshefte*, 2, 65-75.
- Alvarez, W., Coccozza, T., Wezel, F.C., 1974. Fragmentation of the Alpine orogenic belt by microplate dispersal. *Nature*, 248, 309–314.
- Arthaud, F., Matte, P., 1977. Late Paleozoic strike slip faulting in southern Europe and northern Africa: result of right lateral shear zone between the Appalachians and Oural. *Geol. Soc. Am. Bull.*, 88, 1305–1320.
- Ayuso, R.A., Messina, A., De Vivo, B., Russo, S., Woodruff, L.G., Sutter, J.F., Belkin H.E., 1994. Geochemistry and argon thermochronology of the Variscan Sila batholith, southern Italy: source rocks and magmas evolution. *Contributions to Mineralogy and Petrology*, 117, 87-109.
- Barker, A. J., 1990. Introduction to metamorphic textures and microstructures. Chapman & Hall, London, 264 pp.
- Barton, M. D., Hanson, R. B., 1989. Magmatism and the development of low-pressure metamorphic

- belts: implications from the western United States and thermal modelling. *Geological Society of America Bulletin*, 101, 1051-1065.
- Bell, T. H., Rubenach, M. J., 1983. Sequential porphyroblast growth and crenulation cleavage development during progressive deformation. *Tectonophysics*, 92, 171–194.
- Berman, R. G., 1988. Internally-consistent thermodynamic data for minerals in the system $\text{Na}_2\text{O}-\text{K}_2\text{O}-\text{CaO}-\text{MgO}-\text{FeO}-\text{Fe}_2\text{O}_3-\text{Al}_2\text{O}_3-\text{SiO}_2-\text{TiO}_2-\text{H}_2\text{O}-\text{CO}_2$. *Journal of Petrology*, 29, 445-522.
- Berman, R. G., 1991. Thermobarometry using multi-equilibrium calculations: a new technique, with petrological applications. *Canadian Mineralogist*, 29, 833-855.
- Bodorkos, S., Sandiford, M., Oliver, N. H. S., Cawood, P. A., 2002. High-T, low-P metamorphism in the Palaeoproterozoic Halls Creek Orogen, northern Australia: the middle crustal response to a mantle-related transient thermal pulse. *Journal of Metamorphic Geology*, 20, 217-237.
- Bonardi, G., Cavazza, W., Perrone, V., Rossi, S., 2001. Calabria-Peloritani terrane and northern Ionian sea. In: Vai, G.B., Martini, I.P. (Eds), *Anatomy of an Orogen: The Apennines and Adjacent Mediterranean Basins*. Kluwer Academic Publishers, Dordrecht, Boston, London, pp. 287-306.
- Bonardi, G., de Capoa, P., Di Staso, A., Perrone, V., Sonnino, M., Tramontana, M., 2005. The age of the Paludi Formation: a major constraint to the beginning of the Apulia-verging orogenic transport in the northern sector of the Calabria–Peloritani Arc. *Terra Nova*, 00, 1-7.
- Borghi, A., Colonna, V., Compagnoni, R., 1992. Structural and metamorphic evolution of the Bocchigliero and the Mandatoriccio Complexes in the Sila Nappe (Calabrian-Peloritan Arc, Southern Italy). In: *Contributions to the Geology of Italy with special regard to the Paleozoic basements*. (L. Carmignani & F.P. Sassi eds.) IGCP newsletter, Siena, 276 (5), 321-334.
- Borsi, S., Dubois, R., 1968. Données géochronologiques sur l'histoire hercynienne et alpine de la Calabre centrale. *Rend. Acad. Sci. Paris*, 266 -D, 71-75.
- Bouillin, J.P., Baudelot, S., Majestè-Menjoulas, C., 1984. Mise en évidence du Cambro-Ordovicien en Calabre centrale (Italie). Affinités paléogéographiques et conséquences structurales. *C.r. Acad., Sci., Paris*, 298, 89-92.
- Bouillin, J.P., Majestè-Menjoulas, C., Baudelot, S., Cygan, C., Fournier-Vinas, C.H., 1987. Les formations paleozoiques de l'arc calabro-peloritan dans leur cadre structural. *Bull., Soc., Geol., It.*, 106, 683-698.
- Brodie, K.H., Rutter, E.H., 1987. Deep crustal extensional faulting in the Ivrea zone of Northern Italy. *Tectonophysics*, 140, 193-212.
- Burg, J.P., Bale, P., Brun, J.P., Girardeau, J., 1987. Stretching lineation and transport direction in the Ibero-Armorican arc during the Siluro-Devonian collision. *Geodin. Acta*, 1, 71–87.
- Burton, A. M., 1971. Relazione generale, carta geologica della Calabria. Cassa per il Mezzogiorno, Roma, 120 pp.

- Caggianelli, A., Prosser, G., 2001. An exposed cross-section of the late Hercynian and intermediate continental crust in the Sila nappe (Calabria, southern Italy). *Periodico di Mineralogia*, 70, 277–301.
- Caggianelli, A., Prosser, G., 2002. Thermal perturbation of the continental crust after intraplate of thick granitoid sheets: a comparison with the crustal sections in Calabria (Italy). *Geological Magazine*, 139, 699–706.
- Caggianelli, A., Prosser, G., Del Moro, A., 2000. Cooling and exhumation history of deep seated and shallow level, late Hercynian granitoids from Calabria. *Geological Journal*, 35, 33–42.
- Caggianelli, A., Prosser, G., Di Battista, P., 1997. Textural feature and fabric analysis of granitoids emplaced at different depths: the example of the Hercynian tonalites and granodiorites from Calabria. *Miner. Petrogr. Acta*, 15, 11–26.
- Caggianelli, A., Liotta, D., Prosser, G., Ranalli, G., 2007. Pressure-temperature evolution of the late Hercynian Calabria continental crust: compatibility with post-collisional extensional tectonics. *Terra Nova*, 19, 502–514.
- Carmichael, D. M., 1978. Metamorphic bathozones and bathogrades: a measure of the depth of post-metamorphic uplift and erosion on the regional scale. *American Journal of Science*, 278, 769–797.
- Carmignani, L., Barca, S., Cappelli, B., Di Pisa, A., Gattiglio, M., Oggiano, G., Pertusati, P. C., 1992. A tentative geodynamic model for the Hercynian basement of Sardinia. In: Carmignani, L., and Sassi, F. P. (eds), *Contributions to the Geology of Italy with special regard to the Paleozoic basements*. IGCP, 267-Newsletter, 5, Siena, 61–88.
- Carmignani, L., Carosi, R., Di Pisa, A., Gattiglio, M., Musumeci, G., Oggiano, G., Pertusati, P.C., 1994. The Hercynian chain in Sardinia (Italy). *Geodin. Acta*, 7, 31–47.
- Carrigan, C. W., Mukasa, S. B., Haydoutov, I., Kolcheva, Kristina, 2005. Age of Variscan magmatism from the Balkan sector of the orogen, central Bulgaria. *Lithos*, 82, 125–147.
- Cesare, B., Cruciani, G., Russo, U., 2003. Hydrogen deficiency in Ti-rich biotite from anatectic metapelites (El Joyazo - SE Spain): crystal-chemical aspects and implications for high-temperature petrogenesis. *American Mineralogist*, 88, 583–595.
- Colonna, V., Lorenzoni, S., Zanettin-Lorenzoni, E., 1973. Sull'esistenza di due complessi metamorfici lungo il bordo sub-orientale del massiccio "granitico" delle Serre (Calabria). Estratto dal Bol. Della Soc. Geol. It., 92, 801–830.
- Copeland, P., Parrish, R. R., Harrison, T. M., 1988. Identification of inherited radiogenic Pb in monazite and its implications for U-Pb systematics. *Nature*, 333, 760–763.
- De Yoreo, J. J., Lux, D. R., Guidotti, C. V., 1990. The role of crustal anatexis and magma migration in the thermal evolution of regions of thickened continental crust. In: Daly, J.S., Cliff, R.A. and Yardley, B.W.D., (eds.), *Evolution of metamorphic belts*. Geological Society of London, Spec Publ 43, pp 187–202.

- De Yoreo, J. J., Lux, D. R., Guidotti, C. V., 1991. Thermal modelling in low-pressure/high temperature metamorphic belts. *Tectonophysics*, 188, 209-238.
- De Vivo, B., Lorenzoni, S., Orsi, G., Zanettin-Lorenzoni, E., 1978. Inquadramento delle mineralizzazioni metallifere ed a grafite nelle unità tettoniche della Calabria. Primo contributo: la Sila e le Serre. *Ind. Mineraria*, 29, 108-120.
- Del Moro, A., Pardini, G., Maccarrone, E., Rottura, A., 1982. Studio radiometrico Rb–Sr di granitoidi peraluminosi dell’Arco Calabro-Peloritano. *Rendiconti Società Italiana di Mineralogia e Petrologia*, 38, 1015–1026.
- Del Moro, A., Fornelli, A., Piccarreta, G., 2000. Tectonothermal history of the Hercynian continental crust of the Serre (southern Calabria, Italy) monitored by Rb–Sr biotite resetting. *Terra Nova*, 12, 239–243.
- Di Vincenzo, G., Carosi, R., Palmeri, R., 2004. The relationship between tectono-metamorphic evolution and argon isotope records in white mica: constraints from in situ $^{40}\text{Ar}/^{39}\text{Ar}$ laser analysis of the Variscan basement of Sardinia. *J. Petrol.*, 45, 1013–1043.
- Dubois, R., 1971. Définition d’un socle antéhercynien en Calabre. *C. R. Acad. Sci. Paris*, 272, 2052–2055.
- Dubois, R., 1976. La suture calabro-apenninique Crétacée-Eocène et l’ouverture Tyrrhenienne neogene: étude pétrographique et structurale de la Calabre centrale. PhD Thesis, Univ. P. et M. Curie, Paris.
- England, P. C., Thompson, A. B., 1984. Pressure-Temperature-Time paths of regional metamorphism I. Heat transfer during the evolution of regions of thickened continental crust. *Journal of Petrology*, 25, 4, 894-928.
- Eskola, P., 1915. On the relations between the chemical and mineralogical composition in the metamorphic rocks of the Orijärvi region. *Bull. Comm. Geol. Finlande*, 44.
- Faure, M., 1995. Late orogenic carboniferous extensions in the Variscan French Massif Central. *Tectonics*, 14, 132–153.
- Faure, M., Leloix, C., Roig, J.Y., 1997. L’évolution polycyclique de la chaîne hercynienne. *Bulletin de la Société Géologique de France*, 168, 695– 705.
- Ferry, J. M., Spear, F. S., 1978. Experimental calibration of the partitioning of Fe and Mg between biotite and garnet. *Contributions to Mineralogy and Petrology*, 66, 113-117.
- Festa, V., Caggianelli, A., Liotta, D., Prosser, G., Del Moro, A., 2001-02. Structural features of a ductile shear zone in late-Hercynian granitoids (Sila Massif, Calabria). *GeoActa*, 1, 165-176.
- Festa, V., Di Battista, P., Caggianelli, A., Liotta D., 2003. Exhumation and tilting of the late Hercynian continental crust in the Serre Massif (southern Calabria, Italy). *Bollettino della Società Geologica Italiana*, 2, 79–88.
- Finger, F., Krenn, E., Riegler, G., Romano, S. & Zulauf, G., 2002. Resolving Cambrian,

- Carboniferous, Permian and Alpine monazite generations in the polymetamorphic basement of eastern Crete, Greece by means of the electron microprobe. *Terra Nova*, 14, 233–240.
- Fleet, M. E., 2003. Rock-forming minerals. Volume 3A: Micas. University of Western Ontario, Canada, 758 pp.
- Foster, G., Kinny, P., Vance, D., Prince, C., Harris, N., 2000. The significance of monazite U–Th–Pb age data in metamorphic assemblages; a combined study of monazite and garnet chronometry. *Earth Planet. Sci. Lett.*, 181, 327–340.
- Franz, G., Andrehs, G. and Rhede, D., 1996. Crystal chemistry of monazite and xenotime from Saxothuringian-Moldanubian metapelites, NE Bavaria, Germany. *Eur. J. Mineral.*, 8, 1097–1118.
- Franzini, M., Leoni, L., 1972. A full matrix correction in X-ray fluorescence analysis. *Atti Soc. tosc. Sci. nat., Mem., A*, 79, 7-22.
- Franzini, M., Leoni, L., Saitta, M., 1975. Revisione di una metodologia analitica per fluorescenza-X, basata sulla correzione completa degli effetti di matrice. *Rend. Soc. Ital. Mineral. e Petrol.*, 31, 2, 36-378.
- García-Casco, A., Torres-Roldán, R. L., 1999. Natural metastable reactions involving garnet, staurolite and cordierite: implications for petrogenetic grids and the extensional collapse of the Betic-Rif Belt. *Contributions of Mineralogy and Petrology*, 136, 131-153.
- Giacomini, F., Bomparola, R. M., Ghezzo, C., Guldbransen, H., 2006. The geodynamic evolution of the Southern European Variscides: constraints from the U/Pb geochronology and geochemistry of the lower Paleozoic magmatic-sedimentary sequences of Sardinia (Italy). *Contributions of Mineralogy and Petrology*, 152, 19–42.
- Godard, G., Chat, C., 1994. PETROCALC; a petrological software to manage relational databases of chemical analyses. Abstracts of the General Meeting of the International Mineralogical Association. 16; Pages 147. 1994.
- Graessner, T., Schenk, V., 1999. Low-pressure metamorphism of Palaeozoic pelites in the Aspromonte, southern Calabria: constraints for the thermal evolution in the Calabrian crustal cross-section during the Hercynian orogeny. *Journal of Metamorphic Geology*, 17, 157-172.
- Graessner, T., Schenk, V., 2001. An exposed Hercynian deep crustal section in the Sila Massif of northern Calabria: mineral chemistry, petrology and a P–T path of granulite-facies metapelitic migmatites and metabasites. *Journal of Petrology*, 42, 931–961.
- Graessner, T., Schenk, V., Brocker, M., Mezger, K., 2000. Geochronological constraints on the timing of granitoid magmatism, metamorphism and post-metamorphic cooling in the Hercynian crustal cross-section of Calabria. *Journal of Metamorphic Geology*, 18, 409–421.
- Gurrieri, S., Lorenzoni, S., Zannetin-Lorenzoni, E., 1978. L'unità pre-alpina di Bocchigliero (Sila-Calabria). *Boll. Soc. Geol. It.*, 97, 711-716.
- Hanchar, J.M., Miller, C.F., 1993. Zircon zonation patterns as revealed by cathodoluminescence

- and back-scattered electron images: implications for interpretation of complex crustal histories. *Chem. Geol.*, 110, 1–13.
- Handy, M. R., Zingg, A., 1991. The tectonic and rheological evolution of an attenuated cross section of the continental crust – Ivrea crustal section, Southern Alps, Northwestern Italy and Southern Switzerland. *Geological Society of America Bulletin*, 103, 236-253.
- Hawkins, D. P., Bowring, S. A., 1997. U-Pb systematics of monazite and xenotime: case studies from the Paleoproterozoic of the Grand Canyon, Arizona. *Contributions to Mineralogy and Petrology*, 127, 87-103.
- Hawkins, D. P., Bowring, S. A., 1999. U-Pb monazite, xenotime and titanite geochronological constraints on the prograde to post-peak metamorphic thermal history of Paleoproterozoic migmatites from the Grand Canyon, Arizona. *Contributions to Mineralogy and Petrology*, 134, 150-169.
- Hensen, B. J., 1971. Theoretical phase relations involving cordierite and garnet in the system $\text{MgO-FeO-Al}_2\text{O}_3\text{-SiO}_2$. *Contributions to Mineralogy and Petrology*, 31, 191-214.
- Herron, M. M., 1988. Geochemical classification of terrigenous sands and shales from core or log data. *Journal of Sedimentary Petrology*, 58, 820-829.
- Hietanen, A., 1967. On the facies series in various types of metamorphism. *Journal of Geology*, 75, 187-214.
- Hodges, K. V., Crowley, P. D., 1985. Error estimation and empirical geothermobarometry for pelitic system. *American Mineralogist*, 70, 702-709.
- Hodges, K. V., Spear, F. S., 1982. Geothermometry, geobarometry and the Al_2SiO_5 triple point at Mt. Moosilauke, New Hampshire. *American Mineralogist*, 67, 1118-1134.
- Holdaway, M. J., 1971. Stability of andalusite and the aluminium silicate phase diagram. *American Journal of Science*, 271, 97-131.
- Holdaway, M. J., Dutrow, B. L., Hinton, R. W., 1988. Devonian and carboniferous metamorphism in west-central Maine: The muscovite-almandine geobarometer and the staurolite problem revisited. *American Mineralogist*, 73, 20-47.
- Holdaway, M. J., Guidotti, C. V., Novak, J. M., Henry, W. E., 1982. Polymetamorphism in medium to high grade pelitic metamorphic rocks, west-central Maine. *Geological Society of America Bulletin*, 93, 572-584.
- Holland, T. J. B., Powell, R., 1990. An enlarged and updated internally consistent thermodynamic dataset with uncertainties and correlations: the system $\text{K}_2\text{O-Na}_2\text{O-CaO-MgO-FeO-Fe}_2\text{O}_3\text{-Al}_2\text{O}_3\text{-TiO}_2\text{-SiO}_2\text{-C-H}_2\text{-O}_2$. *Journal of Metamorphic Geology*, 8, 89-124.
- Holland, T. J. B., Powell, R., 1998. An internally consistent thermodynamic data set for phases of petrological interest. *Journal of Metamorphic Geology*, 16, 309-343.
- Hollister, L. S., 1966. Garnet zoning: an interpretation based on Rayleigh fractionation model.

- Science, 154, 1647-1651.
- Hoskin, P.W.O., Black, L.P., 2000. Metamorphic zircon formation by solid-state recrystallization of protolith igneous zircon. *Journal of Metamorphic Geology*, 18, 4, 423–439.
- Johnson, T. E., Brown, M., Solar, G. S., 2003. Low-pressure subsolidus and suprasolidus phase equilibria in the MnNCKFMASH system: Constraints on conditions of regional metamorphism in western Maine, northern Appalachians. *American Mineralogist*, 88, 624-638.
- Kerrick, D. M., 1987. Fibrolite in contact aureoles of Donegal, Ireland. *American Mineralogist* 72, 240–54.
- Kerrick, D. M. & Woodsworth, G. J., 1989. Aluminum silicates in the Mount Raleigh pendant, British Columbia. *Journal of Metamorphic Geology*, 7, 547–63.
- Kleemann, U., Reinhardt, J., 1994. Garnet-biotite thermometry revisited: the effect of Al^{VI} and Ti in biotite. *European Journal of Mineralogy*, 6, 925-941.
- Kretz, R., 1983. Symbols for rock-forming minerals. *American Mineralogist*, 68, 277-279.
- Laird, J., Albee, A. L., 1981. Pressure-temperature and time indicators in mafic schists: their application to reconstructing the polymetamorphic history of Vermont. *American Journal of Science*, 281, 127-175.
- Lang, H.M., Dunn, G.R., 1990. Sequential porphyroblasts growth during deformation in a low-pressure metamorphism terrain, Orrs Island-Harpswell Neck, Maine. *Journal of Metamorphic Geology*, 8, 199-216.
- Langone, A., Gueguen, E., Prosser, G., Caggianelli, A., Rottura, A., 2006. The Curinga-Girifalco fault zone (northern Serre, Calabria) and its significance within the Alpine tectonic evolution of the western Mediterranean. *Journal of Geodynamics*, 42, 140-158.
- Lanzirotti, A., Hanson, G. N., 1995. U-Pb dating of major and accessory minerals formed during metamorphism and deformation of metapelites. *Geochimica et Cosmochimica Acta*, 59, 2513-2526.
- Le Breton, N., 1983. Réflexion a propos de quelques géothermomètres et géobaromètres des roches métapélitiques. Application aux gneiss pélitiques de Grande Sila (Calabre Centrale, Italie). Thèse de Doctorat, Université d'Orleans, 223 pp.
- Leake, B. E., *et al.*, 1997. Nomenclature of amphiboles: report of the subcommittee on amphiboles of the international mineralogical association commission on new mineral names. *Mineralogical Magazine*, 61, 295-321.
- Ledru, P., Courrioux, G., Dallain, C., Lardeaux, J.M., Montel, J.M., Vanderhaeghe, O., Vitel, G., 2001. The Velay dome (French Massif Central): melt generation and granite emplacement during orogenic evolution. *Tectonophysics*, 342, 207–237.
- Ledru, P., Lardeaux, J.M., Santallier, D., Autran, A., Quenardel, J.M., Floc'h, J.P., Lerouge, G., Maillet, N., Marchand, J., Ploquin, A., 1989. Où sont les nappes dans le Massif Central

- française. *Bull. Soc. Géol. France*, 5, 605–618.
- Leoni, L., Saitta, M., 1976. X-ray fluorescence analysis of 29 trace elements in rock and mineral standards. *Rend. Soc. It. Miner. Petrol.*, 32, 497-510.
- Leoni, L., Menichini, M., Saitta, M., 1982. Determination of S, Cl and F in silicate rocks by X-ray fluorescence analyses. In: Heyden and Son., (Eds), *X-Ray Spectrometry*. London, United Kingdom.
- Liotta, D., Caggianelli, A., Kruhl, J. H., Festa, V., Prosser, G., Langone, A. Multiple injections of magmas along a Hercynian mid-crustal shear zone (Sila Massif, Calabria, Italy). Submitted to the *Journal of Structural Geology*.
- Lorenzoni, S., Zanettin-Lorenzoni, E., 1979. Problemi di correlazione tettonica Sila-Aspromonte. Il significato dell'Unità ercinica di Mandatoriccio e dei graniti ad Al_2SiO_5 . *Boll. Soc. Geol. It.*, 98, 227-238.
- Lorenzoni, S., Zanettin-Lorenzoni, E., 1983. Note illustrative alla carta geologica della Sila alla scala 1:200000. *Mem. Soc. Geol. It.*, 36, 317-342.
- Lorenzoni, S., Messina, A., Russo, S., Stagno, F., Zanettin-Lorenzoni, E., 1978. Le magmatiti dell'Unità di Longobucco (Sila-Calabria). *Boll. Soc. Geol. It.*, 97, 727-738.
- Ludwig, K.R., 2003. User's Manual for A Geochronological Toolkit for Microsoft Excel. Berkeley Geochronology Center, Spec Publ, vol. 4.
- Lux D. R., De Yoreo, J. J., Guidotti, C. V., Decker, E. R., 1986. Role of plutonism in low-pressure metamorphic belt formation. *Nature*, 323, 794-797.
- Magri, G., Sidoti, G., Spada, A., 1965. Rilevamento geologico sul versante settentrionale della Sila (Calabria). *Mem. E Note Ist. Geol. Appl.*, Napoli, 9, 1-59.
- Mahar, E. M., Baker, J. M., Powell, R., Holland, T. J. B., Howell, N., 1997. The effect of Mn on stability in metapelites. *Journal of Metamorphic Geology*, 15, 223-238.
- Marmo, B. A., Clarke, G. K., Powell, R., 2002. Fractionation of bulk rock composition due to porphyroblasts growth: effects on eclogite facies mineral equilibria, Pam Peninsula, New Caledonia. *Journal of Metamorphic Geology*, 20, 151-165.
- Matte, P., 2002. Variscides between the Appalachians and the Urals: similarities and differences between Paleozoic subduction and collision belts. In: Martinez Catalan, J. R., Hatcher, R. D., Arenas, R., and Díaz García, F., [eds.], *Variscan-Appalachian dynamics: the building of the late Paleozoic basement*: Bulder, Colorado, Geological Society of America, Special Paper, 364, 239-251.
- Messina, A., Barbieri, M., Compagnoni, R., De Vivo, B., Perrone, V., Russo, S. and Scott, B. A., 1991. Geological and petrochemical study of the Sila nappe granitoids. *Boll. Soc. Geol. Ital.*, 110, 165–206.
- Mezger, K., 1990. Geochronology in granulites. In: Vielzeuf, D., Vidal, P.H. (eds.), *Granulites and*

- crustal evolution. Kluwer Academic Publishers, Dordrecht, pp. 451-470.
- Mezger, J. E., Passchier, C. W., Régnier, J.L., 2004. Metastable staurolite-cordierite assemblage of the Bossòst dome: Late Variscan decompression and polyphase metamorphism in the Axial Zone of Central Pyrenees. *Comptes Rendus Geoscience*, 336, 827-837.
- Micheletti, F., Barbey, P., Fornelli, A., Piccarreta, G., Deloule, E., 2007. Latest Precambrian to Early Cambrian U–Pb zircon ages of augen gneisses from Calabria (Italy), with inference to the Alboran microplate in the evolution of the peri-Gondwana terranes. *Int. J. Earth Sci.*, 96, 5, 843–860.
- Miyashiro, A., 1961. Evolution of metamorphic belts. *Journal of Petrology*, 2, 3, 277-311.
- Miyazaki, K., Okumura, K., 2002. Thermal modelling in shallow subduction: an application to low P/T metamorphism of the Cretaceous Shimanto Accretionary Complex, Japan. *Journal of Metamorphic Geology*, 20, 441-452.
- Ogniben, L., 1962. Le Argille scagliose e i sedimenti messiniani a sinistra del Trionto (Rossano, Cosenza). *Geologica Romana*, I, 255-282.
- Okudaira, T., 1996. Temperature-time path for the low-pressure Ryoke metamorphism, Japan, based on chemical zoning garnet. *Journal of Metamorphic Geology*, 14, 427-440.
- Oxburg, E. R., Turcotte, D. L., 1971. Origin of paired metamorphic belts and crustal dilatation in island arc regions. *Journal of Geophysical Research*, 76, 1315-1327.
- Palumbo, N., 1995. L'unità metamorfica di Mandatoriccio nella zona di Umbriatico (Sila Grande) – sequenza vulcano-sedimentaria, evoluzione metamorfica, implicazioni geodinamiche. Tesi di Laurea, Università di Bari.
- Parrish, R. R., 1990. U-Pb dating of monazite and its application to geological problems. *Canadian Journal of Earth Sciences*, 27, 1431-1450.
- Parrish, R. R., 1995. Thermal evolution of the southeastern Canadian Cordillera, *Can. J. Earth Sci.*, 32, 1618-1642.
- Passchier, C.W., Trouw, R.A.J., 1996. *Microtectonics*. Springer-Verlag, Berlin.
- Pattison, D. R. M., 1992. Stability of andalusite and sillimanite and Al_2SiO_5 triple point: constraints from the Ballachulish aureole, Scotland. *Journal of Geology*, 100, 423-446.
- Pattison, D. R. M., Tracy, R. J., 1991. Phase equilibria and thermobarometry of metapelites. In: *Contact Metamorphism*, Kerrick, D. M., (Ed.), Mineralogical Society of America Reviews, 26, 105-206.
- Pattison, D. R. M., Vogl, J. J., 2005. Contrasting sequences of metapelitic mineral-assemblages in the aureole of the tilted Nelson Batholith, British Columbia: Implications for phase equilibria and pressure determination in Andalusite-Sillimanite-Type settings. *The Canadian Mineralogists*, 43, 51-88.

- Pattison, D. R. M., Spear, F. S., Cheney, J. T., 1999. Polymetamorphic origin of muscovite+cordierite+staurolite+biotite assemblages: implications for the metapelitic petrogenetic grid and for P-T paths. *Journal of Metamorphic Geology*, 17, 685-703.
- Pearce, J. A., 1996. A user's guide to basalt discrimination diagrams. In : Bailes (Ed.), *Trace element geochemistry of volcanic rocks; applications for massive sulphide exploration*, Short Course Notes - Geological Association of Canada, 12, p. 79-113.
- Pin, C., Vielzeuf, D., 1983. Granulites and related rocks in Variscan median Europe: a dualistic interpretation. *Tectonophysics*, 93, 47-74.
- Powell, R., Holland, T. J. B., 1988. An internally consistent thermodynamic dataset with uncertainties and correlations. III. Application methods, worked examples and computer program. *Journal of Metamorphic Geology*, 6, 173-204.
- Powell, R., Holland, T. J. B., 1990. Calculated mineral equilibria in the pelite system, KFMASH (K_2O -FeO-MgO- Al_2O_3 - SiO_2 - H_2O). *American Mineralogist*, 75, 367-380.
- Powell, R., Holland, T. J. B., 1994. Optimal geothermometry and geobarometry. *American Mineralogist*, 79, 120-133.
- Rossetti, F., Faccenna, C., Goffé, B., Patrick, M., Argentieri, A., Funiciello, R., Mattei, M., 2001. Alpine structural and metamorphic signature of the Sila Piccola Massif nappe stack (Calabria, Italy): Insights for the tectonic evolution of the Calabrian Arc. *Tectonics*, 20, 112-133.
- Rottura, A., Bargossi, G. M., Caironi, V. *et al.*, 1990. Petrogenesis of contrasting Hercynian granitoids from the Calabrian Arc, southern Italy. *Lithos*, 24, 97-119.
- Rubatto, D., Williams, I.S., Buick, I.S., 2000. Zircon and monazite response to prograde metamorphism in the Reynolds Range, central Australia. *Contributions to Mineralogy and Petrology*, 140, 458-468.
- Santantonio, M., Teale, T., 1987. An example of the use of detrital episodes in elucidating complex basin histories: the Caloveto and Longobucco Groups of NE Calabria, Southern Italy. In: J.K. Legget and G.G. Zuffa (eds); *Marine Clastic Sedimentology*, Graham and Trotman, London, pp. 62-74.
- Sandiford, M., Hand, M., McLaren, S., 1998. High geothermal gradient metamorphism during thermal subsidence. *Earth and Planetary Science Letters*, 163, 149-165.
- Schenk, V., 1980 - U-Pb and Rb-Sr radiometric dates and their correlation with metamorphic events in the granulite-facies basement of the Serre, southern Calabria (Italy). *Contributions to Mineralogy and Petrology*, 73, 23-38.
- Schenk, V., 1984. Petrology of felsic granulites, metapelites metabasics, ultramafics, and metacarbonates from southern Calabria (Italy): prograde metamorphism, uplift and cooling of a former lower crust. *Journal of Petrology*, 25, 255-298.
- Schenk, V., 1989. P-T-t paths of the lower crust in the Hercynian fold belt of southern Calabria. In: Daly J.S., Cliff R.A., Yardley B.W.D. (eds): *Evolution of metamorphic belts*. Geological

- Society of London, Spec Publ 43, pp 337–342
- Schenk, V., 1990. The exposed crustal cross section of southern Calabria, Italy: structure and evolution of a segment of Hercynian crust. In: Salisbury MH, Fountain DM (eds) Exposed cross-sections of the continental crust. Kluwer, Dordrecht, pp 21–42
- Schreurs, J., 1985. Prograde metamorphism of metapelites, garnet-biotite thermometry and prograde changes of biotite chemistry in high-grade rocks of West Uusimaa, southwest Finland. *Lithos*, 18, 69-80.
- Selli, R., 1957. Sulla trasgressione del Miocene nell'Italia meridionale. *Geologica Romana*, I, 255-282.
- Smith, H. A., Giletti, B.J., 1997. Pb diffusion in monazite, *Geochim. Cosmochim. Acta*, 51, 1047-1055.
- Spear, F. S., 1988. The Gibbs method and Duhem's theorem: the quantitative relationships among P, T, chemical potential, phase composition and reaction progress in igneous and metamorphic systems. *Contributions to Mineralogy and Petrology*, 99, 249-256.
- Spear, F. S., 1993. Metamorphic phase equilibria and Pressure-Temperature-Time Paths. Mineralogical Society of America, Washington.
- Spear, F. S., Cheney, J. T., 1989. A petrogenetic grid for pelitic schists in the system $\text{SiO}_2\text{-Al}_2\text{O}_3\text{-FeO-MgO-K}_2\text{O-H}_2\text{O}$. *Contributions to Mineralogy and Petrology*, 101, 149-164.
- Spear, F. S., Selverstone, J., 1983. Quantitative P–T path from zoned minerals; theory and tectonic applications. *Contributions to Mineralogy and Petrology*, 83, 348-357.
- Spear, F.S., Kohn, M.J., 1999. Program thermobarometry, Version 2.1. Manual to computer program, 42pp.
- St. On  , M.R., 1987. Zoned poikiloblastic garnets: P–T paths and syn-metamorphic uplift through 30 km of structural depth, Wopmay Orogen, Canada. *Journal of Petrology*, 28, 1-22.
- Stampfli, G. M., von Raumer, J. F., Borel, G. D., 2002. Paleozoic evolution of pre-Variscan terranes: from Gondwana to variscan collision. In: Martinez Catalan, J. R., Hatcher, R. D., Arenas, R., and D  az Garc  a, F., [eds.], Variscan-Appalachian dynamics: the building of the late Paleozoic basement: Bulder, Colorado, Geological Society of America, Special Paper, 364, 263-280.
- Stowell, H.H., Tinkham, D.K., 2003. Integration of phase equilibria modelling and garnet Sm–Nd chronology for construction of P–T–t paths: examples from the Cordilleran Coast Plutonic Complex, USA. In *Geochronology: Linking the Isotopic Record with Petrology and Textures* (D. Vance, W. Muller & I. Villa, eds.). *Geol. Soc., Spec. Publ.* 220, 119-145.
- St  we, K., 1997. Effective bulk composition changes due to cooling: a model of predicting complexities in retrograde reaction textures. *Contributions to Mineralogy and Petrology*, 129, 43-52.
- Symmes, G. H., Ferry, J. M., 1992. The effect of whole-rock Mn-content on the stability of garnet

- in pelite schists during metamorphism. *Journal of Metamorphic Geology*, 10, 221-237.
- Thompson, J. B., 1957. The graphical analyses of mineral assemblages in pelitic schists. *American Journal of Sciences*, 42, 842-858.
- Thompson, A. B., 1976. Mineral reactions in pelitic rocks. II. Calculation of some P-T-X (Fe-Mg) phase relations. *American Journal of Sciences*, 276, 425-454.
- Thompson, A. B., 1981. The pressure-temperature (P,T) plane viewed by geophysicists and petrologists. *Terra Cognita*, Spec Issue, 11-20.
- Thompson, A. B., England, P. C., 1984. Pressure-Temperature-time paths of regional metamorphism II. Their inference and interpretation using mineral assemblages in metamorphic rocks. *Journal of Petrology*, 25, 929-955.
- Thomson, S. N., 1994. Fission track analysis of the crystalline basement rocks of the Calabrian Arc, southern Italy: evidence of Oligo-Miocene late-orogenic extension and erosion. *Tectonophysics*, 238, 331-352.
- Tiepolo, M., Bottazzi, P., Palenzona, M., Vannucci, R., 2003. A laser probe coupled with ICP – Double –Focusing Sector-Field mass spectrometer from in situ analysis of geological samples and U-Pb dating of zircon. *The Canadian Mineralogist*, 41, 259-272.
- Tinkham, D. K., Ghent, E. D., 2005. Estimating p-t conditions of garnet growth with isochemical phase-diagram sections and the problem of effective bulk-composition. *The Canadian Mineralogist*, 43, 35-50.
- Tinkham, D. K., Zuluaga, C. A., Stowell, H. H., 2001. Metapelite phase equilibria modelling in MnNCKFMASH: the effect of variable Al_2O_3 and $\text{MgO}/(\text{MgO}+\text{FeO})$ on mineral stability. *Geological Materials Research*, 3, 1-42.
- Trombetta, A., Cirrincione, R., Corfu, F., Mazzoleni, P., Pezzino, A., 2004. Mid-Ordovician U–Pb ages of porphyroids in the Peloritan Mountains (NE Sicily): paleogeographical implications for the evolution of the Alboran microplate. *J. Geol. Soc. London*, 161, 265–276.
- Van Dijk, J.P., Bello, M., Brancaloni, G.P., Cantarella, G., Costa, V., Frixia, A., Golfetto, F., Merlini, S., Riva, M., Torricelli, S., Toscano, C., Zerilli, A., 2000. A regional structural model for the northern sector of the Calabrian Arc (southern Italy). *Tectonophysics*, 324, 267-320.
- Vance, D., Holland, T., 1993. A detailed isotopic and petrological study of a single garnet from the Gassetts Schist, Vermont. *Contributions to Mineralogy and Petrology*, 114, 101-118.
- Vance, D., Mahar, E., 1998. Pressure–temperature paths from P–T pseudosections and zoned garnets: potential, limitations and examples from the Zaskar Himalaya, NW India. *Contributions to Mineralogy and Petrology*, 132, 225-245.
- Vielzeuf, D., Pin, C., 1989. Geodynamic implications of Hercynian granulitic rocks. In: Daly, J.S., Cliff, R.A. and Yardley, B.W.D. (eds.): *Evolution of metamorphic belts*. *Geol. Soc. Spec. Publ.* 43, 343–348.

- Vilà, M., Pin. C., Liesa, M., Enrique, P., 2007. LPHT metamorphism in a late orogenic transpressional setting, Albera Massif, NE Iberia: implications for the geodynamic evolution of the Variscan Pyrenees. *Journal of Metamorphic Geology*, 25, 321-347.
- von Raumer, J. F., Stampfli, G. M., Bussy, F., 2003. Gondwana-derived microcontinents: the constituents of the Variscan and Alpine collisional orogens. *Tectonophysics*, 365, 7-22.
- Wei, C. J., Powell, R., Clarke, G. L., 2004. Calculated phase equilibria for low-and medium-pressure metapelites in the KFMASH and KMnFMASH systems. *Journal of Metamorphic Geology*, 22, 495-508.
- White, R. W., Powell, T. J., Holland, T. J. B., Worley, B. A., 2000. The effect of TiO₂ and Fe₂O₃ on metapelitic assemblages at greenschist and amphibolite facies conditions: mineral equilibria calculations in the system K₂O-FeO-MgO-Al₂O₃-SiO₂-TiO₂-Fe₂O₃. *Journal of Metamorphic Geology*, 18, 497-511.
- Will, T. M., 1998. Phase diagrams and their application to determine Pressure-Temperature Paths of metamorphic rocks. *N. Jb. Miner. Abh.*, 174, 103-130.
- Winchester, J. A., Floyd, P. A., 1977. Geochemical discrimination of different magma series and their differentiation products using immobile elements. *Chemical Geology*, 20, 4, 325-343.
- Xu, G., Will, T., Powell, R., (1994). A calculated petrogenetic grid for the system K₂O-FeO-MgO-Al₂O₃-SiO₂-H₂O with particular reference to contact metamorphosed pelites. *Journal of Metamorphic Geology*, 12, 99-119.
- Young, J., Teale, C.T., Bown, P.R., 1986. Revision of the stratigraphy of the Longobucco Group (Liassic, southern Italy); based on new data from nannofossils and ammonites. *Eclogae geol. Helv*, 79, 117-135.
- Zuffa, G.G., De Rosa, R., 1978. Petrologia delle successioni torbiditiche eoceniche della Sila nord-orientale (Calabria). *Mem. Soc. Geol. It.*, 18, 31-55.
- Zuluaga, C. A., Stowell, H. H., Tinkham, D. K., 2005. The effect of zoned garnet on metapelite pseudosections topology and calculated metamorphic P-T paths. *American Mineralogist*, 90, 1619-1628.
- Zwart, H. J., 1962. On the determination of polymetamorphic mineral associations and its application to the Bosost area (Central Pyrenees). *Geologische Rundschau*, 52, 38-65.

LIST OF TABLES

Table	Description	Appendix
1	XRF-whole rock analyses of amphibolites	2
2	XRF-whole rock analyses of silico-clastic metasediments	2
3	Mineral abbreviation	3
4	Standards used for mineral analyses	3
5	Amphibole analyses in amphibolites	3
6	Plagioclase analyses in amphibolites	3
7	Garnet analyses in micaschists	3
8	Biotite analyses in micaschists	3
9	Staurolite analyses in micaschists	3
10	Feldspar analyses in micaschists	3
11	White mica analyses in micaschists	3
12	Garnet analyses in paragneisses	3
13	Biotite analyses in paragneisses	3
14	Biotite profiles analyses in paragneisses	3
15	Staurolite analyses in paragneisses	3
16	Feldspar analyses in paragneisses	3
17	White mica analyses in paragneisses	3
18	Altered-cordierite analyses in paragneisses	3
19	Fe-Ti oxide analyses in paragneisses	3
20	Isotopic ratios and concordia ages of zircons from the paragneiss	7
21	Isotopic ratios and concordia ages of zircons from the meta-sill	7
22	Isotopic ratios and concordia ages of zircons from the porphyritic dike	7
23	Isotopic ratios and concordia ages of monazites from the paragneiss	7
24	Isotopic ratios and concordia ages of monazites from the micaschist	7



ALMA MATER STUDIORUM-UNIVERSITÀ DI BOLOGNA

DOTTORATO IN SCIENZE DELLA TERRA
XX° CICLO

SETTORE SCIENTIFICO DISCIPLINARE GEO/07

Titolo della Tesi

***Metamorfismo Ercinico di Bassa-Pressione: Evoluzione Tettonico-
Metamorfica del Complesso di Mandatoriccio
(Massiccio della Sila - Calabria)***

APPENDIXES

Presentata dal Dott. Antonio Langone

Coordinatore del dottorato:

Prof. William Cavazza

Relatori

Prof. Rottura A.

Prof. Caggianelli A.

Prof. Godard G.

Prof. Prosser G.

Esame finale anno 2008

The Curinga-Girifalco fault zone (northern Serre, Calabria) and its significance within the Alpine tectonic evolution of the western Mediterranean

A. Langone ^a, , E. Gueguen ^b, G. Prosser ^c, A. Caggianelli ^d, A. Rottura ^a

^a Dipartimento di Scienze della Terra e Geologico-Ambientali, Piazza di Porta San Donato 1, 40126 Bologna, Italy

^b Istituto di Metodologie per l'Analisi Ambientale, C.N.R., C.da S. Loja, 85050 Tito Scalo (PZ), Italy

^c Dipartimento di Scienze Geologiche, Macchia Romana, 85100 Potenza, Italy

^d Dipartimento Geomineralogico, Via Orabona 4, 70125 Bari, Italy

Received 25 January 2006; received in revised form 26 June 2006; accepted 27 June 2006

Journal of Geodynamics 42 (2006) 140–158

The Curinga-Girifalco fault zone (northern Serre, Calabria) and its significance within the Alpine tectonic evolution of the western Mediterranean

A. Langone^{a,*}, E. Gueguen^b, G. Prosser^c, A. Caggianelli^d, A. Rottura^a

^a *Dipartimento di Scienze della Terra e Geologico-Ambientali, Piazza di Porta San Donato 1, 40126 Bologna, Italy*

^b *Istituto di Metodologie per l'Analisi Ambientale, C.N.R., C.da S. Loja, 85050 Tito Scalco (PZ), Italy*

^c *Dipartimento di Scienze Geologiche, Macchia Romana, 85100 Potenza, Italy*

^d *Dipartimento Geomineralogico, Via Orabona 4, 70125 Bari, Italy*

Received 25 January 2006; received in revised form 26 June 2006; accepted 27 June 2006

Abstract

Hercynian basement rocks and Mesozoic ophiolites of the Calabria-Peloritani terrane drifted in the present position during the opening of western Mediterranean basins (namely Liguro-Provençal and Tyrrhenian basins) since the Oligocene. Basement rocks were partly involved by Alpine (late Cretaceous–Eocene) deformation and metamorphism before the onset of the drifting process. Even though the kinematics of the Alpine deformation in Calabria has been already defined, restoration of structural and kinematic data to the original position and orientation before the opening of the western Mediterranean has never been performed. In this work we present new structural and petrological data on a major tectonic contact of Alpine age exposed in central Calabria (Serre Massif). Structural and kinematic data are then restored at the original orientation in the early Oligocene time, to allow a correct tectonic interpretation.

In the Serre Massif the Hercynian basement is sliced into three nappes emplaced during the Alpine orogeny. The upper nappe is formed by a nearly continuous section of the Hercynian crust, consisting of medium- to high-grade metamorphic rocks in the lower portion. The intermediate nappe mainly consists of orthogneisses, whereas the lower nappe is chiefly composed of phyllites. The contacts between the Alpine nappes are outlined by well developed mylonitic and cataclastic rocks. The Curinga-Girifalco Line is a well exposed shear zone that overprints mainly metapelitic rocks of the upper nappe and granitoid orthogneisses of the intermediate nappe. Mylonites of the intermediate nappe typically show overgrowths on garnet and hornblende with grossular-rich and tschermakitic composition, respectively. The Alpine mineral assemblage indicates that deformation took place in epidote-amphibolite facies at pressures ranging from 0.75 to 0.9 GPa.

In the investigated area mylonites strike roughly WNW–ESE, with shallow dips towards SSW. Kinematic indicators in mylonites are mostly consistent with a top-to-the-SE shear sense in the present geographic coordinates. The mylonitic belt is affected by later extensional faults outlined by South-dipping cataclastic horizons. Published geochronological data indicate that mylonites and cataclastics developed in Eocene and early Miocene times, respectively.

Considering rotational parameters coming from paleomagnetic studies and large-scale palinspastic reconstructions, the shear sense of the Curinga-Girifalco Line has been restored to the early Oligocene position and orientation. Through restoration a top-to-the-S shear sense is obtained. This result is in striking agreement with the convergence direction between Africa and W-Europe/Iberia during Eocene, computed from the North Atlantic magnetic anomalies. Our geodynamic reconstruction, combined with structural

DOI of the original article: [10.1016/j.jog.2006.06.003](https://doi.org/10.1016/j.jog.2006.06.003)

* Corresponding author. Tel.: +39 051 2094930; fax: +39 051 2094904.

E-mail address: langone@geomin.unibo.it (A. Langone).

and petrological evidence, allows to relate the Curinga–Girifalco mylonites to a thrust related to the southeastern front of the double-verging Alpine chain. The adopted method could be used also for other exotic terranes, such as the Kabylie or the Corsica–Sardinia, to better constrain geometry and evolution of the southern Alpine belt.

© 2006 Elsevier Ltd. All rights reserved.

Keywords: Western Mediterranean evolution; Calabria–Peloritani terrane; Alpine metamorphic overprint; Shear zone; Palinspastic reconstruction

1. Introduction

The Calabria–Peloritani terrane is an exotic fragment, mainly consisting of Hercynian basement rocks, located between the Sicilian Maghrebides and the Southern Apennines (Fig. 1a). According to classical interpretations (e.g., Alvarez et al., 1974), the Hercynian basement, together with ophiolite-bearing nappes, underwent deformation and metamorphism during Paleogene (Borsi and Dubois, 1968; Rossetti et al., 2001) within the southern branch of the Alpine chain (Southern Alpine belt in Fig. 1b). Southeastward drifting of the Calabria–Peloritani terrane to the present position took place during the opening of western Mediterranean basins (or Liguro–Provençal and Tyrrhenian basins), since the Oligocene. Plate kinematics reconstructions in the Mediterranean area have always been very controversial due to the lack of well-defined oceanic magnetic anomalies and to complex tectonic history. Large scale Africa–Europe plate kinematics is usually reconstructed by using North Atlantic magnetic anomalies providing a regional framework in which more local marine and land geological information need to be placed. The interferences between orogenic and extensional processes leading to tectonic inversion make difficult to correlate land geology information and fairly complicates our understanding of the western Mediterranean evolution. Consequently, most of the reconstructions are based on marine geophysics and geology data. However, these models have to be confirmed by the structural and stratigraphical evidences derived from land survey. This is usually done by placing stratigraphic and sedimentary information on a paleogeographic sketch, structural data being used only for shortening or extension directions (D’Argenio et al., 1973; Mostardini and Merlini, 1986; Dercourt et al., 1986).

This paper aims to discuss new structural, kinematic and petrological data recently collected in central Calabria (northern Serre area) along a major Alpine shear zone (Schenk, 1980). This shear zone is located at the base of the main crystalline nappe of Calabria making this a key area to reconstruct the kinematics of the Alpine deformation. Structural and microstructural analyses are used to constrain kinematics, whereas petrology indicates depth and thermal conditions during shear zone development. Structural and kinematic data are then restored to the original position

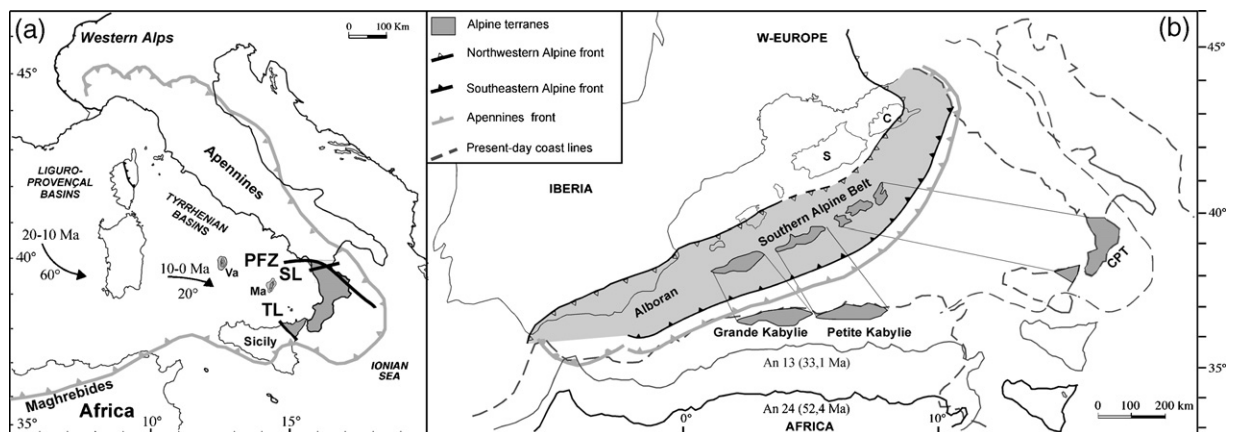


Fig. 1. (a) Tectonic sketch map of the Apennines and the Tyrrhenian Sea (modified after Gueguen et al., 2001). The major strike-slip faults that bound the Calabria–Peloritani terrane and the main rotational phases experienced by this area during the opening of Liguro–Provençal Basin (60° counterclockwise) and Tyrrhenian sea (20° clockwise) are also represented. The counterclockwise rotation is the same for the entire Calabria–Peloritani terrane; the clockwise rotation is referred only to the central–southern Calabria. Abbreviations: SL, Sangineto Line; PFZ, Pollino Fault Zone; TL, Taormina Line; Va, Vavilon basin; Ma, Marsili basin. (b) Pre-rift framework of the western Mediterranean showing the final position of the Calabria–Peloritani and Kabylie terranes after post-Oligocene migration, according to Alvarez et al. (1974) and Gueguen et al. (1998). In the reconstruction are also reported paleoposition of Africa at An 24 and An 13. Abbreviations: CPT, Calabria–Peloritani terrane; S, Sardinia; C, Corsica; An, Magnetic anomaly.

and orientation; distances and angles are derived from regional palinspastic reconstructions computed following a quantitative approach (Gueguen et al., 1998). This reconstruction, mainly based on structural and kinematic data, is then used to verify consistency of plate tectonics models of the Mediterranean area, with particular emphasis on the convergence direction between Africa and W-Europe/Iberia during Eocene.

2. Geological setting

Due to its long and complex geological history, the western Mediterranean area has always been an intricate puzzle in geodynamic reconstructions. In fact, this area has been involved in all the major geodynamic and tectonic events since the Hercynian times. As a consequence, the origin and position of the Calabria crystalline terrains has been thoroughly discussed in the literature (Argand, 1916; Ogniben, 1969; Dubois, 1970; Alvarez et al., 1974; Amodio-Morelli et al., 1976; Vai, 1992; Cello et al., 1996; Bonardi et al., 2001; Rossetti et al., 2001). Hereafter, we will briefly review the geodynamics of the Liguro-Provençal and Tyrrhenian basins that is closely connected to the evolution of the Calabria-Peloritani terrane.

2.1. Regional outline of the central–western Mediterranean

The evolution of the southern Alpine belt, now dismembered around the western Mediterranean basins (Fig. 1b), is still very controversial. The most debated topic is the dip of the subduction during the late Cretaceous–Paleogene in the double-verging Alpine chain. Some authors (Alvarez, 1976; Réhault et al., 1984; Doglioni, 1991; Doglioni et al., 1999; Guerrera et al., 2005) argue in favour of a SE-dipping Alpine type subduction and main northwestward vergence of the chain (Haccard et al., 1972; Amodio-Morelli et al., 1976; Bonardi et al., 1994; Cello et al., 1996). Other authors (Dercourt et al., 1986; Séranne, 1999) think that the subduction already started in the southern Alpine belt with a NW-dipping Apennine polarity, with a main vergence towards the southeast (Rossetti et al., 2001; Faccenna et al., 2001).

However, starting from late Eocene the geodynamical framework of the western Mediterranean area underwent dramatic changes when the European continental lithosphere began to be involved in the subduction in the western Alps (Stampfli et al., 2002 and references therein). As a consequence, the northwestern front of the Alpine system reached the stage of continental collision (Fig. 1b). In this stage the subduction rate of European lithosphere decreased while the Africa–Europe plate convergence rate, linked to the opening of the Atlantic ocean, remained almost steady. This led to a progressive increase of deformation along the southeastern front of the southern Alpine belt, giving rise to the Apennines front during the Oligocene (Fig. 1b). Therefore, the Neogene and Quaternary geodynamics of the western Mediterranean was dominated by the roughly eastward migration of the Apennines–Maghrebides arc in the general frame of slow convergence between Africa and Europe. Coevally, extension propagated towards the southeast in the hangingwall of the retreating west-dipping subduction zone (Réhault et al., 1984; Malinverno and Ryan, 1986; Doglioni, 1991; Gueguen et al., 1997, 1998). The evidences for the subduction of the Adriatic plate underneath Italy have been deeply reinforced through time by geophysical and geochemical data (Mongelli et al., 1975; Peccerillo, 1985; Finetti and Del Ben, 1986; Beccaluva et al., 1989; Spakman, 1989; Amato et al., 1993; Serri et al., 1993; Selvaggi and Chiarabba, 1995). More recently, Lucente et al. (1999) clearly imaged a high-velocity anomaly that flattens at the lower-upper mantle discontinuity beneath the Tyrrhenian sea, consistently with the presence of a long subducted slab. The presence of a still active subduction under the Apennine chain is questioned by some authors (i.e., Carminati et al., 1998; Wortel and Spakman, 2000) that envisage slab breakoff episodes during the late Miocene–Pliocene.

Starting from 118 Ma the relative motion of Africa with respect to Europe followed a counterclockwise path with orientations varying from SW–NE to S–N. However, the convergence direction for the last 10 Ma is still controversial: northwestwards (Dewey et al., 1989; Mazzoli and Helman, 1994; Rosenbaum et al., 2002); northwards (Srivastava et al., 1990); northeastwards (Albarelo et al., 1995). The amount of shortening during the whole Tertiary is estimated to about 150 km in the western Alboran area (Fig. 1b) and increases significantly further East (Tunisia), up to 250 km (Campan, 1995) or 300 km (Dewey et al., 1989).

The West-directed subduction retreated eastward up the present position underneath the Apennines and Maghrebides (Fig. 1b). In the hangingwall of the subduction back-arc extension opened irregular troughs as the Liguro-Provençal and Tyrrhenian basins (Réhault et al., 1984; Malinverno and Ryan, 1986; Royden et al., 1987; Doglioni, 1991). Lithospheric swells, sort of boudins, were isolated between those basins, such as the Corsica-Sardinia microplate

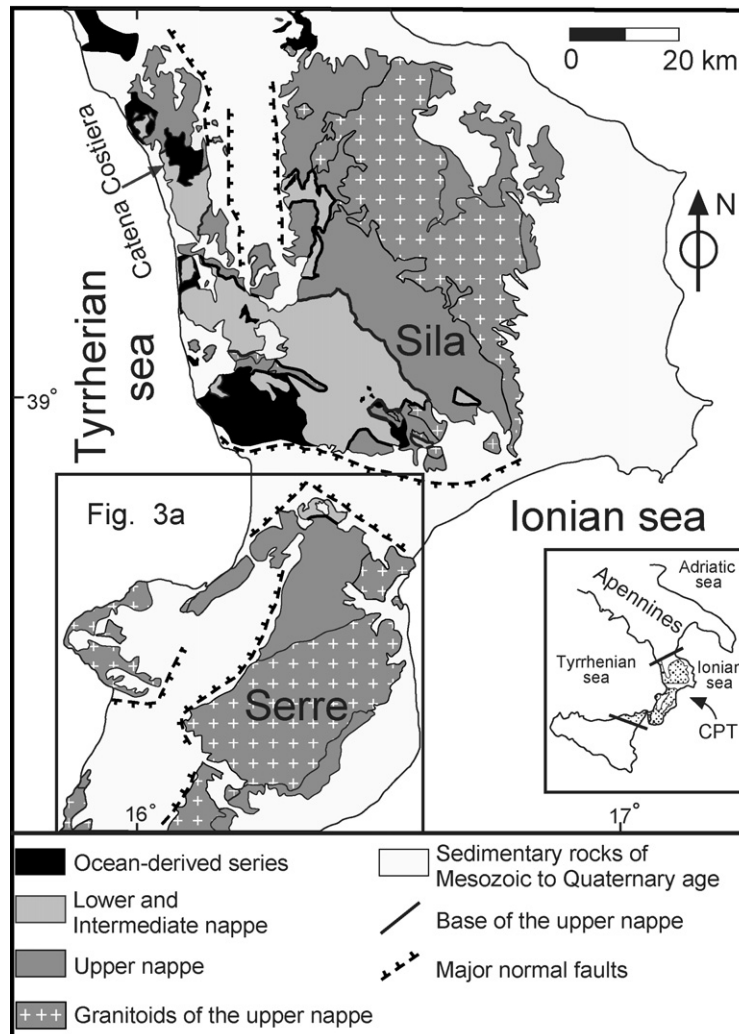


Fig. 2. Geological sketch map of the northern–central Calabria, inspired to Amodio-Morelli et al. (1976), Schenk (1990) and Bonardi et al. (2001).

and the Balearic promontory (Gueguen et al., 1997). Coevally, the Alpine-Betic orogen was dismembered in several fragments, like the Kabylean and Calabria-Peloritani terranes, that migrated southeastward and overthrust the Apennine–Maghrebide chain (Alvarez et al., 1974; Réhault et al., 1984; Gueguen et al., 1997). These fragments are well recognisable since consist mostly of metamorphic and igneous rocks, that differ from the sedimentary rocks typical of the Apennine–Maghrebide orogeny. The Calabria-Peloritani crystalline fragment represents an exotic terrane located between the Sicilian Maghrebides and the southern Apennines. This block is bounded by important strike-slip faults of regional importance (Fig. 1a), namely the Sangineto Line (Amodio-Morelli et al., 1976) or Pollino Fault Zone (Van Dijk and Scheepers, 1995; Perrone, 1996) to the North and the Taormina Line to the South (Ghissetti and Vezzani, 1981). In the following section, we will describe the regional geology of northern–central Calabria, addressing in particular the Alpine deformation in the northern Serre area (Figs. 2 and 3a).

2.2. Geology of northern Serre

The northern Serre area (central Calabria, Figs. 2 and 3a) is mainly characterized by outcrops of the Hercynian continental crust, locally overprinted by Alpine deformation and retrograde metamorphism (Paglionico and Piccarreta, 1976). In northern Calabria (Sila and Catena Costiera; Fig. 2) tectonic units derived from the Hercynian continental crust overlie oceanic-derived series related to the Jurassic rifting (Dietrich, 1976), whereas these series are not observed

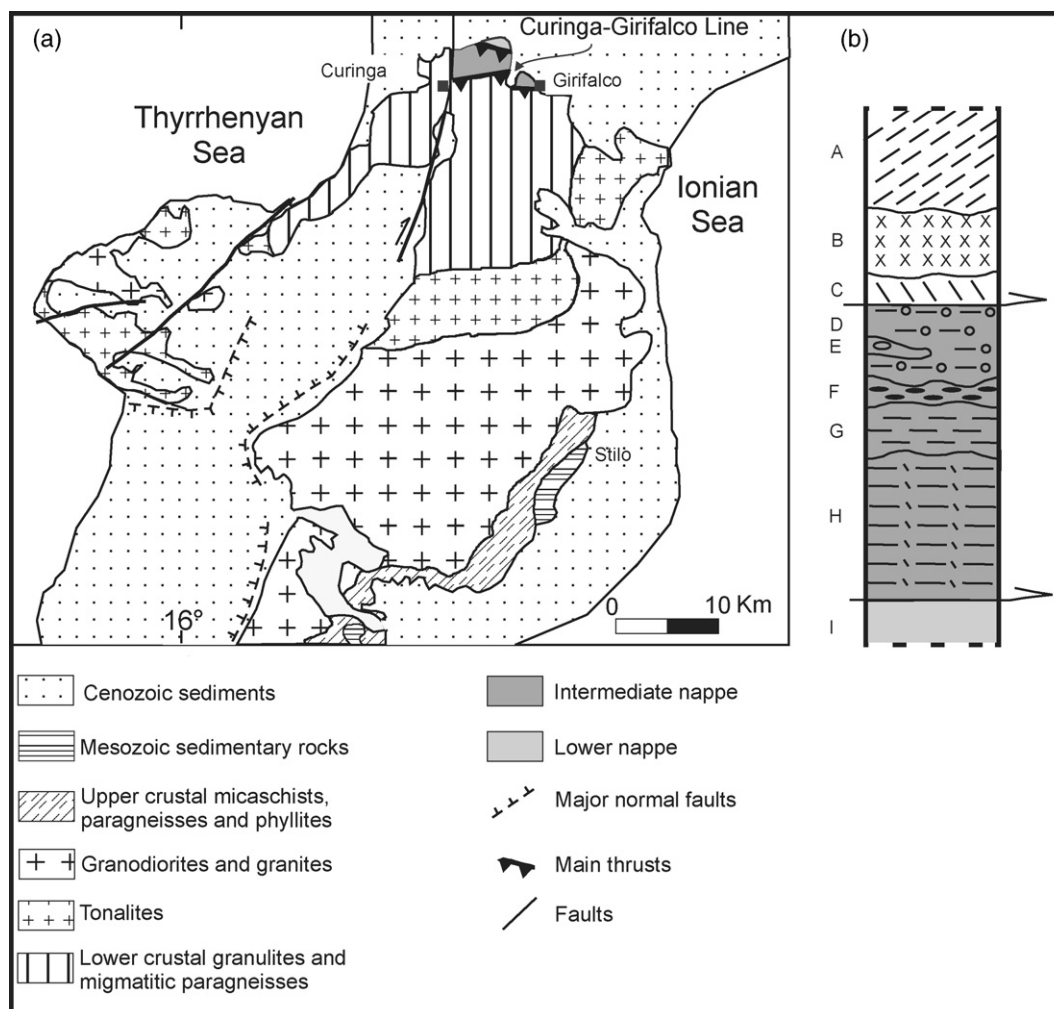


Fig. 3. (a) Schematic geology of the Serre Massif (modified after Schenk, 1990; Rottura et al., 1991; Bonardi et al., 2001); (b) lithological and tectonic sketch across the nappe pile, inspired to Amodio-Morelli et al. (1976) and Paglionico and Piccarreta (1976): (A) fine-grained to coarse-grained fels; (B) metabasic rocks; (C) migmatitic paragneisses; (D) granitoid orthogneisses; (E) amphibolite lenses; (F) augen gneisses; (G) leucocratic orthogneisses; (H) paragneisses and micaschists; (I) phyllites.

in central and southern Calabria (Amodio-Morelli et al., 1976; Bonardi et al., 2001). The continental crust mainly consists of three nappes (Dubois, 1970) that can be distinguished on the basis of the different Hercynian and Alpine overprints.

The upper nappe has a considerable thickness and represents a nearly continuous section of the Hercynian crust (Schenk, 1980) well recognizable both in northern and in central Calabria (Serre; Fig. 3a). It is composed of granulite facies metamorphic rocks, overlain by thick granitoid sheets in the intermediate level, followed upwards by medium- to low-grade metamorphic rocks. The main metamorphism, responsible also for partial melting in the lower crust, was synchronous to intrusion of granitoids and took place during the late stages of the Hercynian orogeny (Graessner et al., 2000).

The intermediate and lower nappes have a minor thicknesses and are composed of Hercynian medium to low-grade metamorphic rocks. The Alpine metamorphic overprint locally affected both nappes along some shear zones. In the northern Serre area the intermediate nappe mainly consists of orthogneisses with some paragneisses and micaschists (Paglionico and Piccarreta, 1976), whereas the lower nappe is chiefly composed of phyllites (Fig. 3b), locally overlain by Mesozoic sediments in the Catena Costiera area (Dietrich, 1976; Fig. 2). A Rb–Sr age on white mica of 268 ± 4 Ma has been obtained by Schenk (1980) on a mylonitic orthogneiss of the intermediate nappe. This age resulted from a

sample containing both tiny Alpine white mica and larger Hercynian mica fishes. For this reason it was considered by Schenk (1980) as a mixed age.

The nappe pile has been built up during the Alpine orogeny and all tectonic contacts are outlined by well-developed mylonites and cataclastic rocks. The contact between the upper and intermediate nappes (Fig. 2) separates the base of the thick crustal section from amphibolite-facies gneisses and shows the best developed Alpine overprint. In the northern Serre area this contact is known as the Curinga-Girifalco Line (Fig. 3a). Schenk (1981) compared this structure to a segment of the Insubric Line that in the western Alps separates the crustal section of the Ivrea zone to the South, unaffected by the Alpine event, from the Sesia zone to the North, overprinted by intense Alpine metamorphism. Rb–Sr method on biotite yielded an Eocene age (43 ± 1 Ma) on a mylonitic orthogneiss from the intermediate nappe (Schenk, 1980). Using the fission track method on zircon and apatite Thomson (1994, 1998) proposed that the low temperature history of the Curinga-Girifalco Line developed during crustal extensional movements between 18 and 15 Ma.

3. The Curinga-Girifalco Line

The Curinga-Girifalco Line is characterized by cataclastic and mylonitic rocks arranged in a 400 m thick belt (Fig. 4a and b). The deformation zone mainly consists of mylonites that generally overprint migmatitic paragneisses of the upper nappe and granitoid orthogneisses of the intermediate nappe (Fig. 4b). Mylonites derived from the migmatitic paragneisses have been identified as the mylonites of the Curinga-Girifalco Line by Spiegel (2003). Thin bands of incohesive grey cataclasites, produced at lower T conditions, are found chiefly near the contact between the upper and the intermediate nappe with a thickness of some meters.

3.1. Field and structural data

In the analysed area the Curinga-Girifalco Line is roughly oriented WNW–ESE and the main contact dips of 37° to the SSW (197°N ; Fig. 4a). The shear zone is offset by younger faults showing strike-slip or extensional kinematics. Migmatitic paragneisses of the upper nappe are present in the hangingwall, whereas orthogneisses and paragneisses of the intermediate nappe are mostly located in the footwall. A minor sheet of migmatitic paragneisses is enclosed within the lithologies of the intermediate nappe along the Pilla stream and South of the Iacurso village (Fig. 4a).

The aim of the field work was to reconstruct the deformation history and sense of shear of the Curinga-Girifalco Line. A detailed mapping of the tectonites and of their relationships with the less deformed host rocks has been performed. Furthermore, in order to better constrain the geometry of the shear zone, particular attention has been dedicated to measurements of lineation and foliation both in the migmatitic paragneisses and in the granitoid orthogneisses. Even if outcropping conditions are quite good over the entire area, two localities, close to the Girifalco psychiatric hospital and the hydroelectric central (Fig. 4a), resulted of particular interest showing the entire deformed belt. In fact, weakly deformed rocks of both footwall and hangingwall as well as highly deformed rocks of the shear zone can be observed there.

In the studied area foliation presents a variable attitude due to late folding events. The main foliation in the migmatitic paragneisses is mostly defined by a compositional layering inherited from the Hercynian fabric. The Alpine event reworked this original fabric that now appears strongly flattened and sheared. A prevailing South-dipping attitude of the foliation was widely recognized (Fig. 5a). Lineations on foliation planes plunge at low angle towards 104°N and 150°N (Fig. 5a). These are outlined by both stretched quartz crystals and aligned biotite flakes. The main foliation of granitoid orthogneisses gently dips towards East and South (Fig. 5b). The lineations are defined by elongated quartz grains, aligned biotite flakes and feldspar porphyroclasts. Their orientation is broadly northwest–southeast, but a wide scatter in the southeast quadrant is observed (Fig. 5b). Close to the Addolorata church in Girifalco village (Fig. 4a), granitoid orthogneiss display two distinct lineations, plunging to 140°N and 280°N on the same mylonitic foliation. This suggests a polyphase deformation history of the intermediate nappe. Summing up, lineations with slightly different orientations (about 140 – 150°N and 105 – 110°N) are observed in both hangingwall and footwall rocks of the Curinga-Girifalco Line. As shown above, all lineations display similar features and thus can be referred to the Alpine deformation. The Hercynian fabric is well preserved in the upper nappe South of the Curinga-Girifalco Line where foliations and variably oriented stretching lineations are related to granulite facies metamorphism (Kruhl and Huntemann, 1991).

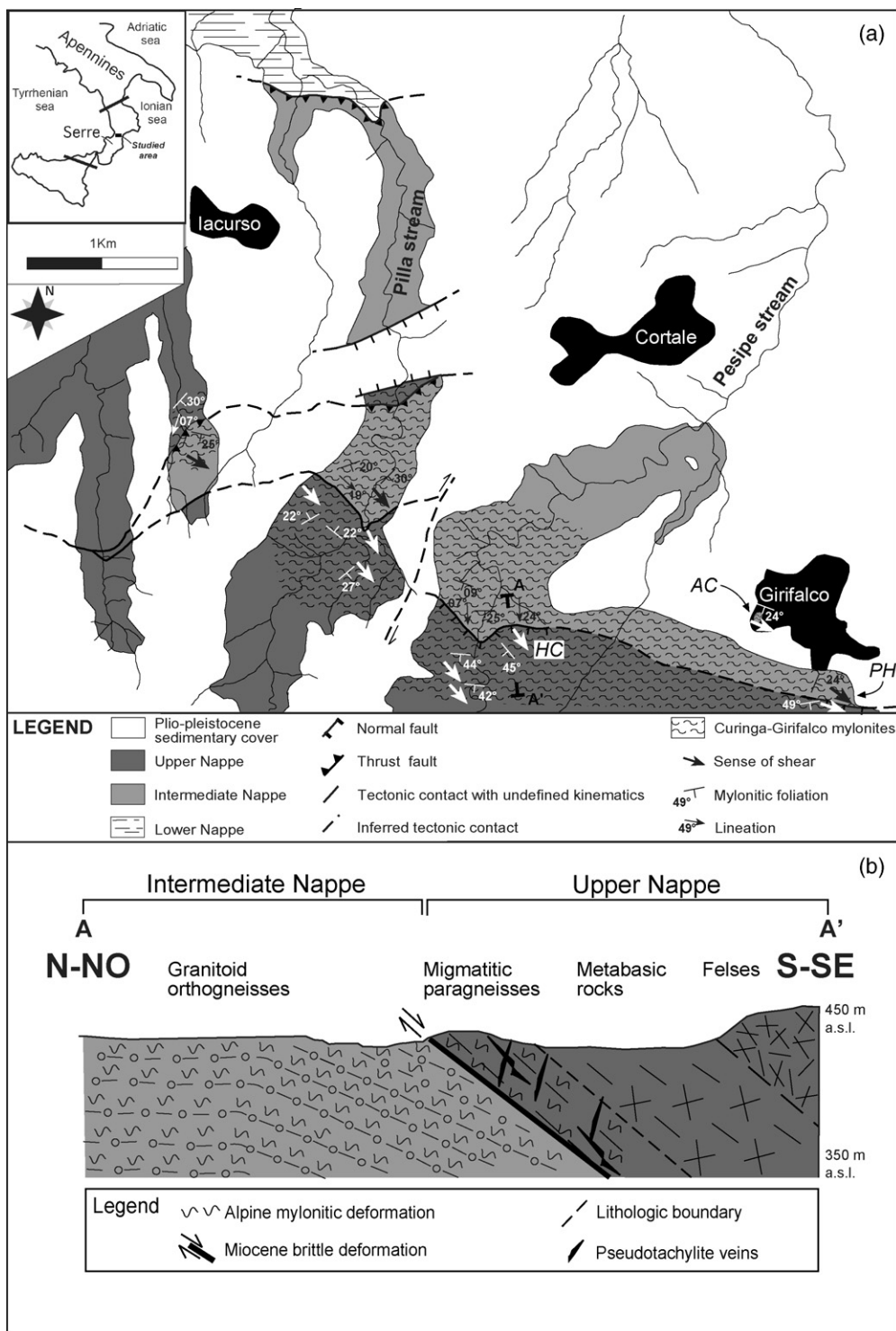


Fig. 4. (a) Geological map of the studied area (northern Serre), based on original 1:5000 mapping, showing the Curinga-Girifalco mylonites and the distribution of the kinematics and structural data. *Abbreviations:* HC, hydroelectric central; AC, Addolorata church; PH, psychiatric hospital; (b) cross-section showing the main features of the Curinga-Girifalco Line at the hydroelectric central (A–A' in the geological map).

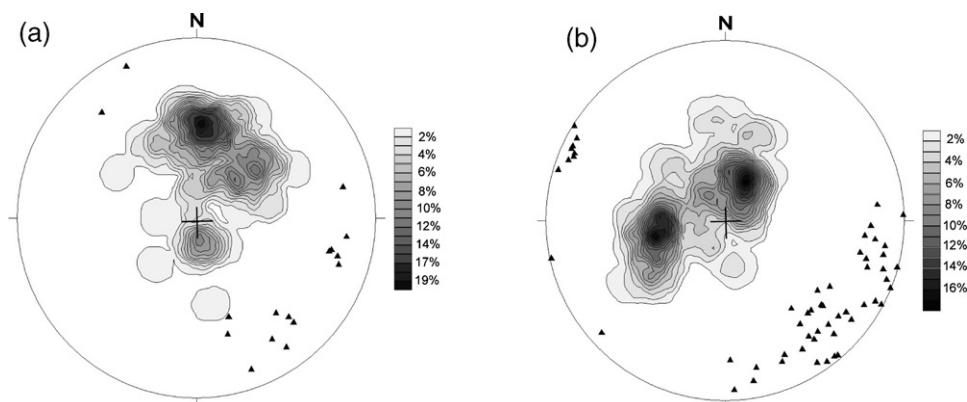


Fig. 5. Structural data from the Curinga-Girifalco mylonites. Stereoplots show contour line of the poles to the mylonitic foliation of migmatitic paragneisses (a: 90 data) and granitoid orthogneisses (b: 134 data). Equal-area projection, lower hemisphere, search area 1.0%; peak 20% in paragneisses, 18.66% in orthogneisses. Small triangles represent stretching and mineral lineation of migmatitic paragneisses (a, 17 data) and granitoid orthogneisses (b, 55 data).

3.2. Petrography and microstructures of the Curinga-Girifalco mylonites

The Hercynian mineral paragenesis of migmatitic paragneisses mainly consists of quartz + garnet + sillimanite + biotite \pm K-feldspar and \pm plagioclase defining amphibolite/granulite facies conditions. Cordierite has been locally recognized by Spiegel (2003). During the late-Hercynian evolution (300–290 Ma) high grade metapelites experienced peak metamorphic conditions in a T range of 680–800 °C and P range of 0.55–0.75 GPa (Schenk, 1984, 1990). In the migmatitic paragneisses two main fabrics related to the Hercynian and Alpine deformations, respectively, can be recognized. The Hercynian fabric is characterized by alternating leucocratic and melanocratic layers, e.g., quartz- and feldspar-rich leucosome and biotite- and sillimanite-rich melanosome, respectively, that define a migmatitic layering of stromatic type (Ashworth, 1985). Generally, the foliation wraps around different porphyroblasts (garnet, K-feldspar, sillimanite aggregates) of variable size (0.5–4.5 mm), following an anastomosing pattern.

During the Alpine orogenesis, migmatitic paragneisses experienced a metamorphic overprint and deformation at lower temperature conditions (Fig. 6a). The Alpine metamorphic event caused a partial mineral reequilibration. Chloritization of biotite and garnet, formation of white mica and quartz at the expense of K-feldspar and sillimanite are locally observed. Sillimanite breakdown is very incomplete, as documented by well recognisable prismatic crystals that are commonly boudinaged with precipitation of white mica, biotite and oxides in necks and extensional fractures.

Widespread pseudotachylite veins, with thickness ranging from few cm to 1 m, are generally parallel or at low angles to the mylonitic foliation and often display an ultramylonitic fabric (Fig. 6b). Matrix mainly contains biotite, whereas clasts are represented by sillimanite, quartz and feldspar, both in single crystals and in aggregates. The presence of ductilely deformed pseudotachylites in the mylonites is indicative of T conditions typical of the brittle–ductile transition, where pseudotachylite-forming events are intermittent in an overall ductile regime (Passchier, 1982, 1985; Swanson, 1992). Incomplete retrograde reactions and abundance of pseudotachylite veins indicate that deformation took place in water-deficient conditions (Passchier, 1985). As pointed out by Spiegel (2003), this is a consequence of the low water content in the fluid phase of the metapelitic protolith.

Orthogneisses of the intermediate nappe are the main lithology affected by shearing in the footwall of the Curinga-Girifalco Line. These are metagranitoid rocks mostly composed of quartz + K-feldspar + muscovite + biotite \pm garnet \pm epidote and \pm plagioclase. Amphibolite lenses, consisting of hornblende + plagioclase + quartz + epidote + phengite \pm biotite, chlorite and sphene, are closely associated with the orthogneisses. The Hercynian fabric, locally observed in migmatitic paragneisses, is here not recognizable and the main fabric is related to the Alpine metamorphic event. In the orthogneisses K-feldspar porphyroclasts are generally wrapped by thin layers of mica and quartz grains defining an anastomosing foliation (Fig. 6c). The ductile Alpine event determined the formation of a mylonitic foliation, reduction of porphyroclast size and development of rare pseudotachylite veins. Mylonitization is accompanied by crystallization of small grains of biotite, white mica and epidote along the foliation planes. Retrograde reactions, such as chloritization of biotite and sericitization of K-feldspar, are locally observed.

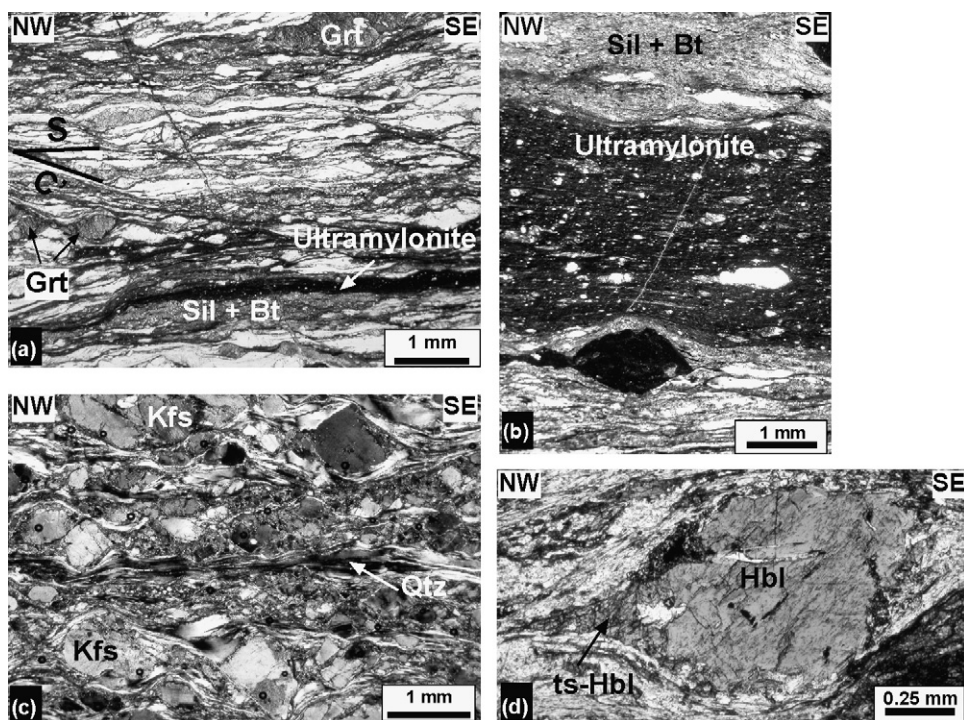


Fig. 6. Micrographs of the Curinga-Girifalco mylonites. (a) Typical fabric characters of a mylonite derived from migmatitic paragneisses (plane polarized light); (b) pseudotachylites showing an ultramylonitic fabric in the migmatitic paragneisses (crossed polars); (c) mylonites derived from granitoid orthogneisses (crossed polars); (d) sigmoidal hornblende porphyroclasts with tails of bluish tschermakitic hornblende. Mineral symbols according to Kretz (1983).

The presence of stable biotite on the foliation planes in almost all the examined mylonites indicates temperatures higher than 400 °C. Both in the migmatitic paragneisses and in the granitoid orthogneisses mylonitization promoted different intracrystalline deformation mechanisms. Effects of these mechanisms are mostly visible in quartz that is generally present as stretched crystals. This phase shows deformation bands and subgrain boundaries as a consequence of recovery, combined with dynamic recrystallization by bulge nucleation and subgrain rotation (White, 1977; Urai et al., 1986). The latter recrystallization mechanism is outlined by the gradual transition of aggregates of subgrains to aggregates of new grains. The widespread evidence of dynamic recrystallization by subgrain rotation in quartz is consistent with deformation taking place at intermediate temperatures (about 400–500 °C) according to Stipp et al. (2002). Other mineral phases such as feldspar, mica, garnet and sillimanite show mainly microfaulting, kinking and boudinage. Incipient intracrystalline deformation is locally observed in K-feldspars. In amphibolite lenses hornblende makes up porphyroclasts with a sigmoidal shape (Fig. 6d), wrapped by mica flakes and epidote grains.

3.3. *P–T conditions of deformation*

P–T conditions during mylonitization favoured formation of rare overgrowths around some minerals. These are observed in the lithologies of the intermediate nappe. We recognized overgrowths of garnet in granitoid orthogneisses and overgrowths of bluish tschermakitic hornblende around green hornblende porphyroclasts in metabasic rocks. The orthogneisses (Qtz + Kfs + Pl + Phe ± Grt) show a mylonitic fabric characterized by the presence of K-feldspar porphyroclasts surrounded by a quartz–mica-rich fine-grained matrix. Here are dispersed small subhedral garnets (<1 mm) fractured and surrounded by tiny grains frequently concentrated along tails (Fig. 7a). By using a scanning electron microscope and back scattered electron (BSE) images (Fig. 7b) we have seen that the tails consist of very small garnet clasts partially welded by overgrowths. The latter show strong compositional contrast with respect to the former grains, appearing darker in BSE images. SEM/EDS analyses (Table 1) reveal that the main compositional difference resides in the proportion of the grossular molecule. In particular, average grossular content in garnet overgrowths is

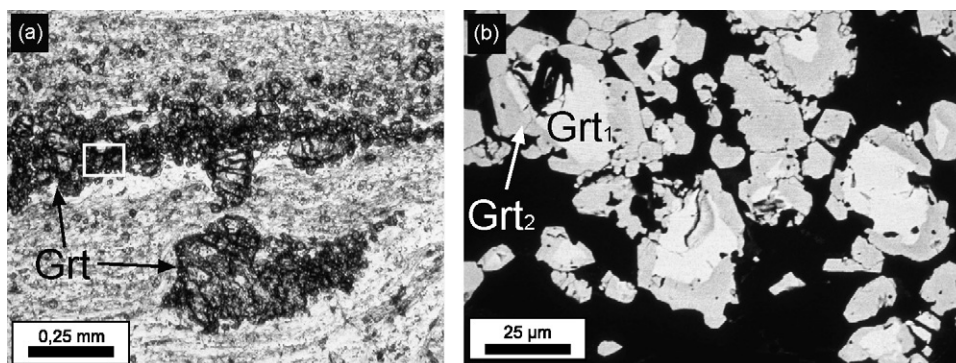


Fig. 7. (a) Small garnets with tail composed of tiny garnet grains in a mylonitic orthogneiss; (b) SEM–BSE image showing a detail (white box in (a)) of the tiny garnet grains: grossular-rich overgrowths developed during the Alpine event appear in a darker grey tone.

Table 1

Selected mineral compositions by SEM–EDS analyses in orthogneiss and amphibolite from the intermediate nappe

	Orthogneiss					Amphibolite			
	Grt core	Grt overgrowth	Phe	Phe	P1	Hb1 core	Hb1 overgrowth	Phe	P1
SiO ₂	36.10	37.13	50.80	48.18	64.19	44.43	42.45	48.63	67.52
TiO ₂						0.78	0.30	0.47	
Al ₂ O ₃	20.96	21.11	30.22	28.16	21.82	10.86	15.23	30.31	19.91
FeO	30.01	19.81	3.18	6.74		17.09	18.01	3.05	0.18
MnO	9.70	7.07		0.44		0.20	0.25	0.13	
MgO	0.96	0.38	1.17	1.65		9.90	7.74	2.19	
CaO	1.44	14.06			2.39	11.11	10.15		0.55
Na ₂ O			0.60	0.27	10.35	2.13	2.62	0.24	11.54
K ₂ O			10.66	10.67	0.14	0.42	0.61	10.54	0.04
tot.	99.17	99.57	96.63	96.11	98.89	96.93	97.36	95.56	99.74
ΣO	12	12	22	22	8	23	23	22	8
Si	2.98	2.97	6.70	6.55	2.86	6.69	6.39	6.50	2.96
Ti						0.09	0.03	0.05	
Al	2.04	2.00	4.70	4.52	1.15	1.93	2.70	4.78	1.03
Fe	2.07	1.33	0.35	0.77		2.15	2.26	0.34	0.01
Mn	0.68	0.48		0.05		0.03	0.03	0.01	
Mg	0.12	0.05	0.23	0.33		2.22	1.74	0.44	
Ca	0.13	1.21			0.11	1.79	1.63		0.03
Na			0.15	0.07	0.89	0.62	0.76	0.06	0.98
K			1.79	1.85	0.01	0.08	0.12	1.80	
Σcat	8.01	8.03	13.93	14.15	5.02	15.61	15.67	13.99	5.01
Alm%	69	41							
Pyr%	4	2							
Sps%	23	16							
Grs%	4	41							
Ab%					88				97
An%					11				3
Or%					1				

Mineral symbols according to Kretz (1983), analyses were performed at Dipartimento Geomineralogico (University of Bari) by a Cambridge S360 SEM equipped with a LINK AN 10,000 ED detector. Operating conditions were: 15 kV accelerating potential, 1 nA probe current, 25 mm working distance, standards by Microanalysis Consultants Ltd.

around 44% whereas it amounts to about 3% in the original fragments. Notable differences exist also for proportions in almandine (39% versus 70%), pyrope (1% versus 6%) and spessartine (16% versus 23%). To estimate P – T conditions of deformation we assumed that garnet overgrowths were in equilibrium with phases present in the fine-grained matrix. Garnet–phengite thermometer (calibration of Green and Hellman, 1982) and garnet–plagioclase–white mica–quartz barometer (calibration of Hodges and Crowley, 1985) have been adopted. Results indicate a temperature of $525 \pm 50^\circ\text{C}$ and a pressure of 0.9 ± 0.1 GPa during deformation.

Amphibolite lenses (Hbl + Pl + Qtz + Ep + Phe \pm Bt \pm Chl \pm Spn) show overgrowth textures such as rims and tails of bluish-tschermakitic hornblende around porphyroclasts of green-hornblende. Other small crystals of bluish-amphibole are recognizable throughout foliation planes. Composition of main phases in amphibolite lenses by SEM/EDS analyses is given in Table 1. In comparing cores and overgrowths of amphiboles, wide compositional differences can be observed. The overgrowths are decidedly richer in Al (average values of 2.64 versus 1.98, atoms p.f.u.) and poorer in Si with respect to cores of porphyroclasts. In addition, overgrowths are characterized by a higher Fe/(Fe + Mg) ratio (0.570 versus 0.493). Negligible or minor differences can be observed for the other elements. The Al content in amphibole is influenced both by tschermak ($[\text{Mg,Fe}]\text{Si}^{\text{IV}} = \text{Al}^{\text{VI}}\text{Al}^{\text{IV}}$) and edenite ($\text{Si} = \text{NaAl}^{\text{IV}}$) exchange, sensible to P and T , respectively. Therefore, the observed notable contrast in Al content, together with the negligible difference in Na content between core and overgrowths, point to a major role of the tschermak exchange.

In order to obtain additional information we have also tried to determine P – T conditions of deformation by applying amphibole–plagioclase thermometry (calibration of Holland and Blundy, 1994) and phengite barometry (calibration of Massone and Schreyer, 1987). Owing to the low anorthite content detected in plagioclase, only the thermometer A by Holland and Blundy (1994) was used. Results indicate P – T conditions for deformation of $570 \pm 40^\circ\text{C}$ and 0.75 ± 0.1 GPa.

In synthesis, thermobarometrical estimates on orthogneisses and amphibolites of the intermediate nappe suggest that deformation took place in the epidote–amphibolite facies at P ranging between 0.75 and 0.9 GPa.

3.4. Shear sense indicators

Radiometric ages indicate that the tectonic evolution of the Curinga-Girifalco Line includes two main deformation events. An early Eocene mylonitic event is indicated by Rb/Sr ages on biotite (Schenk, 1980), whereas a subsequent early Miocene cataclastic event is suggested by contrasting thermal histories in the footwall and hangingwall of the Curinga-Girifalco Line obtained by zircon and apatite fission track analyses (Thomson, 1994). Various shear sense indicators, observed mainly in thin section, have been used to determine the kinematics of the Curinga-Girifalco mylonites. In mylonites derived from migmatitic paragneisses kinematic indicators are mostly C' -type shear bands (Berthé et al., 1979; Fig. 6a). Winged porphyroclasts, of δ - and σ -type (Passchier and Simpson, 1986), are present only in ultramylonitic bands (Fig. 8a). In the granitoid orthogneisses the best developed kinematic indicators are represented by synthetic and antithetic microfaults crosscutting K-feldspar porphyroclasts and, in minor extent, C' -type shear bands and δ/σ -type winged porphyroclasts (Fig. 8b and c). Ribbons formed by quartz aggregates are characterized by both lattice and shape preferred orientations in migmatitic paragneisses and in granitoid orthogneisses (Fig. 8c). The results of the kinematic analysis indicate mainly SE-directed shearing for the examined mylonites (Figs. 4a and 9). In particular, this shear sense is observed in granitoid orthogneisses at the Addolorata church (Girifalco village), along the 285°N plunging stretching lineation. Grey inchoesive fine-grained cataclasites with thickness of about some meters are localized mainly between migmatitic paragneisses and granitoid orthogneisses. Kinematics of the later cataclastic deformation is top-to-the-SW, as documented by C -type shear bands (Fig. 10). In the present-day coordinates this is consistent with extensional movements along the Curinga-Girifalco Line, with synchronous tectonic exhumation of the footwall block. This extensional brittle deformation is coherent with the contrasting footwall and hangingwall thermal histories reconstructed by Thomson (1994, 1998) using fission track thermochronology.

4. Discussion

The structural data related to ductile deformation along the Curinga-Girifalco Line can be referred to Alpine deformation, since Eocene ages (43 ± 1 Ma) have been obtained (Schenk, 1980). Therefore, the present-day orientation of the lineation data doesn't describe anymore the original deformation field and has to be restored to the initial position to be interpreted in terms of Alpine deformation.

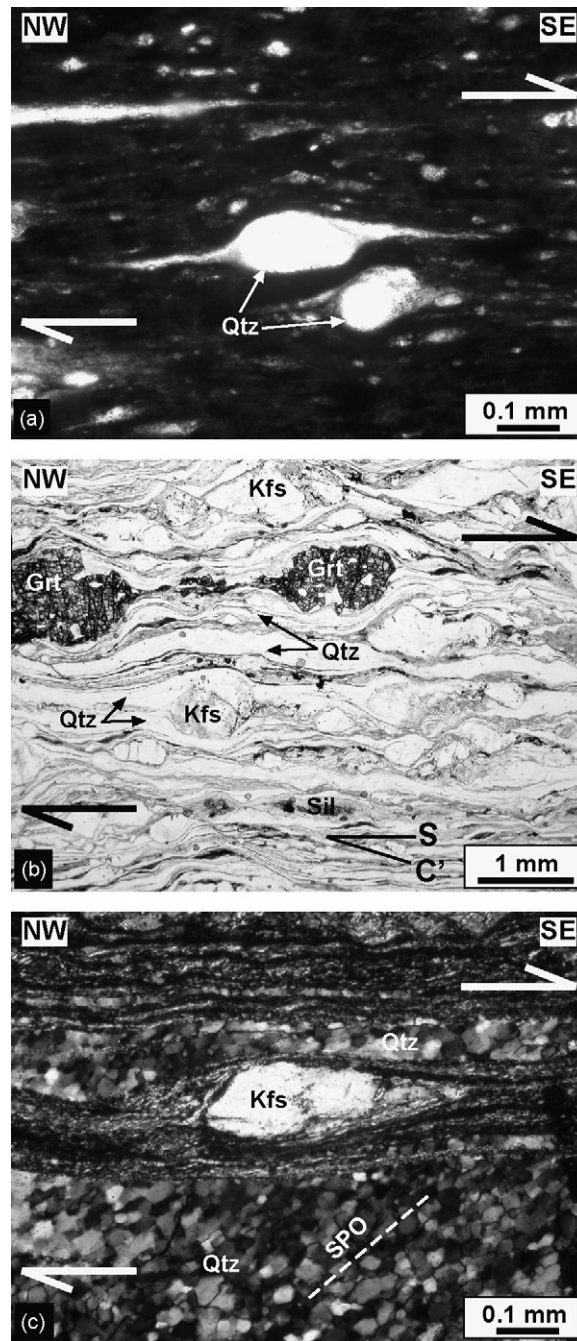


Fig. 8. Micrographs showing shear sense indicators in the Curinga-Girifalco mylonites; (a) σ -type winged porphyroblast of quartz in ultramylonitic layer of a migmatitic paragneiss (plane polarized light); (b) S–C' type shear bands in mylonitic granitoid orthogneiss (plane polarized light); (c) σ -type winged porphyroblast and SPO (shape preferred orientations) of quartz crystals in fine-grained layers in a granitoid orthogneiss (crossed polars). All kinematic indicators show a dextral shear sense.

During the Oligo-Miocene evolution of the western Mediterranean, the Calabria-Peloritani terrane experienced two main rotational phases (Fig. 1a and b).

The first phase is related to the opening of the Liguro-Provençal basin that led to a counterclockwise rotation of the Corsica-Sardinia microplate of about 60° around a pole located at 42.7°N and 9.6°E (Gueguen, 1995; Gueguen et al., 1997). This is in good agreement with geophysical modeling (Chamot-Rooke et al., 1999) and with paleomagnetic

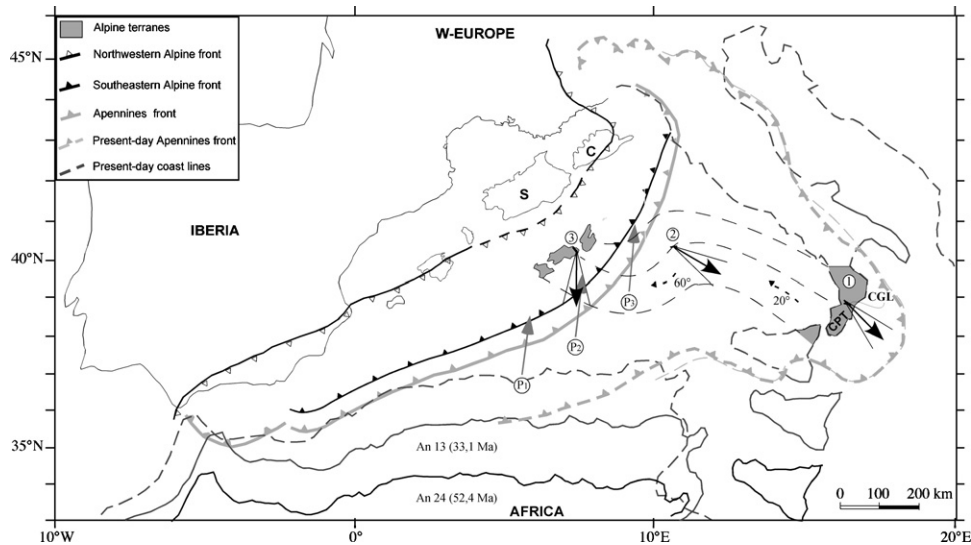


Fig. 11. Palinspastic reconstruction of the Calabria-Peloritani terrane at the Oligo-Miocene time (modified after Gueguen et al., 1998) with paleoposition of Africa at An 24 and An 13. Black arrows represent the shear transport direction with 95% confidence values of the Curinga-Girifalco Line. These lineations ($135 \pm 14^\circ\text{N}$) have been carried back in the original position and orientation: 1 = present-day; 2 = after the opening of the Liguro-Provençal basin; 3 = initial position. After restoration shear sense becomes top-to-the-S. Black dashed flow lines depict the post-Eocene migration of the Calabria-Peloritani terrane and black dashed arrows show rotations applied to lineations. Grey arrows represent the convergence direction between Africa and W-Europe/Iberia computed at three points (P_1 , P_2 , P_3) located in the vicinity of the paleoposition of the Calabria-Peloritani terrane (see text for explanations). Direction of convergence is in good agreement with restored kinematics.

To draw a palinspastic reconstruction of the Alpine fabric elements, the western Mediterranean basins have been restored to the pre-rift situation reversing the rotation path. After restoration, the linear fabric elements of the Curinga-Girifalco mylonites assume a nearly North–South direction (Fig. 11) with a South-directed tectonic transport. This orientation corresponds to the original deformation field in this segment of the Alpine chain during the Eocene.

To understand the significance of the restored kinematic data and to give a better interpretation of the palinspastic reconstruction, the orientation of linear fabric elements has been compared with regional tectonic regimes active during the Eocene–Oligocene times (Fig. 11).

Unfortunately, due to the lack of oceanic-type magnetic anomalies between Africa and Europe, it is not possible to reconstruct directly the relative motion of the two plates. Thus the kinematics of the Africa versus W-Europe/Iberia system has to be determined indirectly through a more complex circuit that considers the motion of both W-Europe/Iberia and Africa plates referred to North America.

Since ductile deformation has been dated at 43 ± 1 Ma (Schenk, 1980) we need to compare the restored direction of tectonic transport obtained along the Curinga-Girifalco Line with the coeval relative motion between Africa and W-Europe/Iberia. This can be obtained by computing the relative intermediate Euler pole for the period between magnetic anomalies An 24 and An 13, dated at 52.4 and 33.1 Ma using the magnetostratigraphic time scale by Cande and Kent (1995) and Huestis and Acton (1997), respectively. In the present study, we used the parameters of Müller et al. (1990) for relative motion of Africa versus North America and Srivastava et al. (1990) for relative motion of W-Europe/Iberia versus North America (Table 2). The results are shown in Table 3. Using these finite Euler poles we computed the following intermediate rotation parameters: pole located at 36.68°N and 26.19°W with counterclockwise rotation of 3.69° .

Table 2

Euler poles for relative motion of Africa vs. North America and of W-Europe/Iberia vs. North America

Finite poles	Lat.	Lon.	Rot.	References
AFR/NAM _{0–24}	78.33	–2.64	–16.91	Müller et al. (1990)
AFR/NAM _{0–13}	75.37	1.12	–10.04	Müller et al. (1990)
IBE/NAM _{0–24}	72.98	133.28	–12.94	Srivastava et al. (1990)
IBE/NAM _{0–13}	76.34	117.33	–7.98	Srivastava et al. (1990)

Table 3

Finite Euler poles obtained from rotational parameters in Table 2

Finite poles	Lat.	Lon.	Rot.	References
AFR/IBE _{0–24}	31.45	–18.58	–7.87	Müller et al. (1990), Srivastava et al. (1990)
AFR/IBE _{0–13}	26.94	–12.27	–4.24	Müller et al. (1990), Srivastava et al. (1990)

Table 4

Coordinates of three points (P₁, P₂, P₃) located in the vicinity of the paleoposition of the Calabria-Peloritani terrane (see Fig. 11)

Points	Lat.	Lon.
P ₁	37.00	5.50
P ₂	37.50	7.30
P ₃	39.20	9.10

These parameters have been applied to three points (Table 4) located close to the restored position of the Calabria-Peloritani terrane (Fig. 11) in order to compute their motion during the An 24–An 13 period. Following this approach the local convergence direction between Africa and W-Europe/Iberia has been computed.

As shown on the palinspastic map (Fig. 11), the mean orientation of the restored lineations is in very good agreement with the regional tectonic regime. In particular lineations are sub-parallel to the convergence direction between Africa and the W-Europe/Iberia system. The reconstructed convergence direction together with the pressure increase recorded in the footwall of the Curinga-Girifalco Line indicate that the tectonic transport direction is connected to thrusting in an overall ductile deformation regime. Instead, the development of brittle extensional faults is related to the opening of the western Mediterranean basins and exhumation of the Calabria-Peloritani terrane, as confirmed by the zircon fission track ages (Thomson, 1994, 1998).

Summarizing, the post-Paleocene tectonic evolution of the northern Serre includes two main tectonic events. During the Eocene part of the basement of Calabria was affected by Alpine deformation. In this scenario several shear zones, such as the Curinga-Girifalco Line, were activated. In particular, the South-directed tectonic transport of the Curinga-Girifalco mylonites could be related to thrusting at the southeastern front of the Alpine chain (Fig. 11). After continental collision the Alpine chain experienced a post-collisional extension recorded by brittle fault-rocks of the Curinga-Girifalco Line.

5. Conclusions

Field and microscopic observations of the fault rocks from the Curinga-Girifalco Line provide new information on the tectono-metamorphic evolution of the Calabria-Peloritani terrane after the Paleocene. Two main events characterized the long-lived deformation history of the examined shear zone. An early ductile event of Eocene age was followed during Miocene by a localized brittle deformation along the previous shear zone. Structural and microstructural analysis of the fault rocks revealed a top-to-the-SE shear sense for mylonitic deformation and top-to-the-SW movement during the brittle event. Petrological investigations of different overgrowth textures in mylonitic granitoid orthogneisses and amphibolites indicate that deformation took place in the epidote-amphibolite facies at pressure ranging from 0.75 to 0.9 GPa. This is in agreement with the high-pressure overprint documented in continent-derived units and with the blueschist facies metamorphism experienced by ocean-derived rocks in various areas of the Calabria-Peloritani terrane (De Roeve et al., 1974; Amodio-Morelli et al., 1976; Piccarreta, 1981; Platt and Compagnoni, 1990; Rossetti et al., 2001). Deformation and metamorphic events can be linked to a significant Eocene tectonic episode highlighted by geochronological methods (Borsi and Dubois, 1968; Schenk, 1980; Beccaluva et al., 1981; Prosser et al., 2003).

Interpretation of earlier fabric elements in the Calabria-Peloritani terrane and in other exotic terranes, based on present-day coordinates, is however misleading. Therefore, structural, petrological and metamorphic data have to be restored in the original coordinates. This kind of paleotectonic reconstruction allows a correct interpretation of the mylonitic and cataclastic fabrics associated to the Curinga-Girifalco Line. For the paleotectonic reconstruction we considered that during the evolution of the central–western Mediterranean basins the Calabria-Peloritani terrane and

thus the Curinga-Girifalco Line migrated towards SE–SSE and experienced simultaneously rotation and tilting. In our restored paleotectonic scenario kinematics of deformation is top-to-the-S. This direction is in good agreement with regional plate tectonic regime during Eocene time. In the original setting barometrical estimates and structural data of mylonites indicate thickening above the Curinga-Girifalco Line, coherently with a contractional tectonic regime. Therefore, we interpret this important shear zone as a thrust of the southeastern front of the Alpine chain acting during Eocene time. The method adopted in this paper can be applied to the other Alpine fragments dispersed in peri-Mediterranean area (e.g., Corsica, Kabylie) in order to improve our understanding of the southern Alpine belt.

Acknowledgments

This paper benefited from careful review by K. Ben, L. Jolivet and an anonymous referee. Financial support from PRIN 2004 project (D. Liotta) and from Ateneo funding from Bari and Potenza Universities are acknowledged. Special thanks to Ascone family for their hospitality during field work.

References

- Albarelo, D., Mantovani, E., Babbucci, D., Tamburelli, C., 1995. Africa-Eurasia kinematics: main constraints and uncertainties. *Tectonophysics* 243, 25–36.
- Alvarez, W., 1976. The former continuation of the Alps. *Geol. Soc. Am. Bull.* 87, 891–896.
- Alvarez, W., Coccozza, T., Wezel, F.C., 1974. Fragmentation of the Alpine orogenic belt by microplate dispersal. *Nature* 248, 309–313.
- Amato, A., Alessandrini, B., Cimmini, G., Frepoli, A., Selvaggi, G., 1993. Active and remnant subducted slabs beneath Italy: evidence from seismic tomography and seismicity. *Anal. Geofisica* 36, 201–214.
- Amodio-Morelli, L., Bonardi, G., Colonna, V., Dietrich, D., Giunta, G., Ippolito, F., Liguori, V., Lorenzoni, S., Paglionico, A., Perrone, V., Piccarreta, G., Russo, M., Scandone, P., Zanettin-Lorenzoni, E., Zuppetta, A., 1976. L'arco calabro-peloritano nell'orogene appenninico-maghrebide. *Memorie della Società Geologica Italiana* 17, 1–60.
- Argand, E., 1916. Sur l'arc des Alpes Occidentales. *Eclogae Geologicae Helveticae* 14, 145–191.
- Ashworth, J.R., 1985. Introduction. In: Ashworth, J.R. (Ed.), *Migmatites*. Blackie, Glasgow and London.
- Auzende, J.M., Bonnin, J., Olivet, J.L., 1973. The origin of the Western Mediterranean basin. *J. Geol. Soc. Lond.* 19, 607–620.
- Beccaluva, L., Chiesa, S., Delaloye, M., 1981. K/Ar age determinations on some Tethyan ophiolites. *Rendiconti della Società Italiana di Mineralogia e Petrologia* 37, 869–880.
- Beccaluva, L., Brotzu, P., Macciotta, G., Morbidelli, L., Serri, G., Traversa, G., 1989. Cainozoic Tectono-Magmatic evolution and inferred mantle sources in the Sardo-Tyrrhenian Area. In: *The Lithosphere in Italy*. Accademia Nazionale dei Lincei, pp. 229–248.
- Berthé, D., Choukroune, P., Jegouzo, P., 1979. Orthogneiss, mylonite and non coaxial deformation of granites: the example of the South Armorican shear zone. *J. Struct. Geol.* 1, 31–42.
- Bonardi, G., De Capoa, P., Fioretti, B., Perrone, V., 1994. Some remarks on the Calabria-Peloritani Arc and its relationship with the southern Apennines. *Bollettino di Geofisica Teorica ed Applicata* 36, 483–492.
- Bonardi, G., Cavazza, W., Perrone, V., Rossi, S., 2001. Calabria-Peloritani terrane and northern Ionian sea. In: Vai, G.B., Martini, I.P. (Eds.), *Anatomy of an Orogen: The Apennines and Adjacent Mediterranean Basins*. Kluwer Academic Publishers, Dordrecht, Boston, London, pp. 287–306.
- Borsi, S., Dubois, R., 1968. Données géochronologiques sur l'histoire hercynienne et alpine de la Calabre centrale. *Comptes Rendus de l'Académie des Sciences Paris* 266 (D), 71–75.
- Campan, A., 1995. Analyse cinématique de l'Atlantique équatorial: implications sur l'évolution de l'Atlantique Sud et sur la frontière de plaques Amérique du Nord/Amérique du Sud. Thesis, Univ. P. & M. Curie Paris VI.
- Cande, S.C., Kent, D.V., 1995. Revised calibration of the geomagnetic polarity timescale for the Late Cretaceous and Cainozoic. *J. Geophys. Res.* 100, 6093–6095.
- Carminati, E., Wortel, M.J.R., Spakman, W., Sabadini, R., 1998. The role of slab detachment in the opening of the western-central Mediterranean basins. Some geological and geophysical evidence. *Earth Planet. Sci. Lett.* 160, 651–665.
- Cello, G., Invernizzi, C., Mazzoli, S., 1996. Structural signature of tectonic processes in the Calabrian Arc, southern Italy: evidence from the oceanic-derived Diamante-Terranova unit. *Tectonics* 15, 187–200.
- Chamot-Rooke, N., Gaulier, J.M., Jestin, F., 1999. Constraints on Moho depth and crustal thickness in the Liguro-Provençal basin from a 3D gravity inversion: geodynamic implications. In: Durand, B., Jolivet, L., Horvath, F., Séranne, M. (Eds.), *The Mediterranean Basins: Tertiary Extension within the Alpine Orogen*. Geological Society, London, pp. 37–61 (Special Publications 156).
- D'Argenio, B., Pescatore, T., Scandone, P., 1973. Schema geologico dell'Appennino Meridionale (Campania e Lucania). *Atti del Convegno: "Moderne vedute sulla geologia dell'Appennino"* (Roma 16–18 febr. 1972). Accademia Nazionale dei Lincei 183, 49–72.
- De Roever, E.W.F., Piccarreta, G., Beunk, F.F., Kieft, C., 1974. Blue amphiboles from north-western and central Calabria (Italy). *Periodico di Mineralogia* 43, 1–37.
- Dercourt, J., Zonenshain, L.P., Ricou, L.E., Kazmin, V.G., Le Pichon, X., Knipper, A.L., Grandjacquet, C., Sbertshikov, I.M., Geysant, J., Lepvrier, C., Pechersky, D.H., Boulain, J., Sibuet, J.C., Savostin, L.A., Sorokhtin, O., Westphal, M., Bazhenov, M.L., Lauer, J.P., Bijou-Duval, B., 1986.

- Geological evolution of the Tethys belt from the Atlantic to the Pamirs since the Lias. In: Aubouin, J., Le Pichon, X., Monin, A.S. (Eds.), *Evolution of the Tethys. Tectonophysics*, vol. 123, pp. 241–315.
- Dewey, J.F., Helman, M.L., Turco, E., Hutton, D.H.V., Knott, S.D., 1989. Kinematics of the western Mediterranean. In: Coward, M.P., Dietrich, D., Park, R.G. (Eds.), *Alpine Tectonics*. Geological Society, London, pp. 265–283 (Special Publications 45).
- Dietrich, D., 1976. La geologia della Catena Costiera calabra tra Cetraro e Guardia Piemontese. *Memorie della Società Geologica Italiana* 17, 61–121.
- Dogliioni, C., 1991. A proposal of kinematic modelling for W-dipping subductions - Possible applications to the Tyrrhenian–Apennines system. *Terra Nova* 3, 423–434.
- Dogliioni, C., Gueguen, E., Harabaglia, P., 1999. On the origin of west-directed subduction zones and applications to the western Mediterranean. In: Durand, B., Jolivet, L., Horvath, F., Séranne, M. (Eds.), *The Mediterranean Basins: Tertiary Extension within the Alpine Orogen*. Geological Society, London, pp. 541–561 (Special Publications 156).
- Dubois, R., 1970. Phase de serrage, nappes de socle et métamorphisme alpin à la jonction Calabre-Apennin: la suture calabro-apenninique. *Revue de Géographie Physique et de Géologie Dynamique* 12 (3), 221–254.
- Edel, J.B., 1979. Paleomagnetic study of the Tertiary volcanics of Sardinia. *J. Geophys.* 45, 259–280.
- Faccenna, C., Funicello, F., Giardini, D., Lucente, P., 2001. Episodic back-arc extension during restricted mantle convection in the Central Mediterranean. *Earth Planet. Sci. Lett.* 187, 105–116.
- Finetti, I., Del Ben, A., 1986. Geophysical study of the Tyrrhenian opening. *Bolletino di Geofisica Teorica ed Applicata* 28 (110), 75–155.
- Ghisetti, F., Vezzani, L., 1981. Contribution of structural analysis to understanding the geodynamic evolution of the Calabrian Arc (Southern Italy). *J. Struct. Geol.* 3, 371–381.
- Graessner, T., Schenk, V., Bröcker, M., Mezger, K., 2000. Geochronological constraints on the timing of granitoid magmatism, metamorphism and post-metamorphic cooling in the Hercynian crustal cross-section of Calabria. *J. Metamorphic Geol.* 18, 409–421.
- Green, T.H., Hellman, P.L., 1982. Fe-Mg partitioning between coexisting garnet and phengite at high pressure, and comments on a garnet-phengite geothermometer. *Lithos* 15, 253–266.
- Gueguen, E., 1995. Le Bassin Liguro-Provençal: un véritable océan. Exemple de segmentation des marges et de hiatus cinématiques. Implications sur les processus d'amincissement crustal. PhD thesyes, Univ. Brest, 315 pp.
- Gueguen, E., Doglioni, C., Fernandez, M., 1997. Lithospheric boudinage in the western Mediterranean back-arc basins. *Terra Nova* 9, 184–187.
- Gueguen, E., Doglioni, C., Fernandez, M., 1998. On the post-25 Ma geodynamic evolution of the western Mediterranean. *Tectonophysics* 298, 259–269.
- Gueguen, E., Tomasi, P., Scherneck, H.G., Haas, R., Campbell, J., 2001. Recent crustal movements: geological meaning of European geodetic VLBI network observation. In: Behrend, D., Rius, A. (Eds.), *Proceedings of the 15th Working Meeting on European VLBI for Geodesy and Astrometry*. Institut d'Estudis Espacials de Catalunya, Consejo Superior de Investigaciones Científicas, Barcelona, Spain.
- Guerrera, F., Martín-Martín, M., Perrone, V., Tramontana, M., 2005. Tectono-sedimentary evolution of the southern branch of the Western Tethys (Maghrebian Flysch Basin and Lucanian Ocean): consequences for Western Mediterranean geodynamics. *Terra Nova* 17, 358–367.
- Haccard, D., Lorenz, C., Grandjacquet, C., 1972. Essai sur l'évolution tectogénétique de la liaison Alpes-Apennins (de la Ligurie à la Calabre). *Memorie della Società Geologica Italiana* 11, 309–341.
- Hodges, K.V., Crowley, P.D., 1985. Error estimation and empirical geothermobarometry for pelitic systems. *Am. Mineral.* 70, 702–709.
- Holland, T., Blundy, J., 1994. Non-ideal interactions in calcic amphiboles and their bearing on amphibole-plagioclase thermometry. *Contrib. Mineral. Petrol.* 116, 433–447.
- Huestis, S.P., Acton, G.D., 1997. On the construction of geomagnetic timescale from non-prejudicial treatment of magnetic anomaly data from multiply ridges. *Geophys. J. Int.* 129, 176–182.
- Kretz, R., 1983. Symbols for rock-forming minerals. *Am. Mineral.* 68, 277–279.
- Kruhl, J.H., Huntemann, T., 1991. The structural state of the former lower continental crust in Calabria (S. Italy). *Geologische Rundschau* 80, 289–302.
- Lucente, F.P., Chiarabba, C., Cimini, G., Giardini, D., 1999. Tomographic constraints on the geodynamic of the Italian region. *J. Geophys. Res.* 104, 20307–20327.
- Malinverno, A., Ryan, W.B.F., 1986. Extension in the Tyrrhenian Sea and shortening in the Apennines as a result of arc migration driven by sinking of the lithosphere. *Tectonics* 5, 227–245.
- Massone, H., Schreyer, W., 1987. Phengite geobarometry based on the limiting assemblage with K-feldspar, phlogopite and quartz. *Contrib. Mineral. Petrol.* 77, 38–46.
- Mazzoli, S., Helman, M., 1994. Neogene patterns of relative plate motion for Africa–Europe: some implications for recent central Mediterranean tectonics. *Geologische Rundschau* 83, 464–468.
- Mongelli, F., Loddo, M., Calcagnile, G., 1975. Some observations on the Apennines gravity field. *Earth Planet. Sci. Lett.* 24, 385–393.
- Montigny, R., Edel, J.B., Thuizat, R., 1981. Oligo-Miocene rotation of Sardinia: K–Ar ages and paleomagnetism data of tertiary volcanics. *Earth Planet. Sci. Lett.* 54, 261–271.
- Mostardini, F., Merlini, S., 1986. Appennino centro-meridionale: sezioni geologiche e proposta di modello strutturale. *Memorie della Società Geologica Italiana* 35, 177–202.
- Müller, R.D., Sandwell, D.T., Tucholke, B.E., Sclater, J.G., Shaw, P.R., 1990. Depth to basement and geoid expression in the Kane Fracture Zone: a comparison. *Mar. Geophys. Res.* 13, 105–129.
- Ogniben, L., 1969. Schema introduttivo alla geologia del confine calabro-lucano. *Memorie della Società Geologica Italiana* 8, 453–763.
- Paglianico, A., Piccarreta, G., 1976. Le Unità del Fiume Pomo e di Castagna nelle Serre Settentrionali (Calabria). *Bollettino della Società Geologica Italiana* 95, 27–37.

- Passchier, C.W., 1982. Pseudotachylite and the development of ultramylonite bands in the Saint-Barthélemy Massif, French Pyrenees. *J. Struct. Geol.* 4, 69–79.
- Passchier, C.W., 1985. Water-deficient mylonite zone—an example from the Pyrenees. *Lithos* 18, 115–127.
- Passchier, C.W., Simpson, C., 1986. Porphyroclast systems as kinematic indicators. *J. Struct. Geol.* 8, 831–843.
- Peccerillo, A., 1985. Roman comagmatic province (central Italy): evidence for subduction-related magma genesis. *Geology* 13, 103–106.
- Perrone, V., 1996. Une nouvelle hypothèse sur la position paléogéographique et l'évolution tectonique des Unités de Verbicaro et de San Donato (région Calabro-Lucanienne; Italie): implications sur la limite Alpes-Appennin en Calabre. *Comptes Rendus de l'Académie des Sciences Paris* 322 (IIa), 877–884.
- Piccarreta, G., 1981. Deep rooted overthrusting und blueschistic metamorphism in compressive continental margins. An example from Calabria (southern Italy). *Geol. Mag.* 118 (5), 539–544.
- Platt, J.P., Compagnoni, R., 1990. Alpine ductile deformation and metamorphism in a Calabrian basement nappe (Aspromonte, south Italy). *Eclogae Geologicae Helveticae* 83, 41–58.
- Prosser, G., Caggianelli, A., Rottura, A., Del Moro, A., 2003. Strain localisation driven by marble layers: the Palmi shear zone (Calabria-Peloritani terrane, southern Italy). *GeoActa* 2, 155–166.
- Réhault, J.P., Mascle, J., Boillot, G., 1984. Evolution géodynamique de la Méditerranée depuis l'Oligocène. *Memorie della Società Geologica Italiana* 27, 85–96.
- Rossetti, F., Faccenna, C., Goffé, B., Patrick, M., Argentieri, A., Funicello, R., Mattei, M., 2001. Alpine structural and metamorphic signature of the Sila Piccola Massif nappe stack (Calabria, Italy): insights for the tectonic evolution of the Calabrian Arc. *Tectonics* 20, 112–133.
- Rosenbaum, G., Lister, G.S., Duboz, C., 2002. Reconstruction of the tectonic evolution of the western Mediterranean since the Oligocene. In: Rosenbaum, G., Lister, G.S. (Eds.), *Reconstruction of the Evolution of the Alpine-Himalayan Orogen*. *J. Virtual Explorer* 8, 107–130.
- Rottura, A., Del Moro, A., Pinarelli, L., Petrini, R., Peccerillo, A., Caggianelli, A., Bargossi, G., Piccarreta, G., 1991. Relationships between intermediate and acidic rocks in orogenic granitoid suites: petrological, geochemical, and isotopic (Sr, Nd, Pb) data from Capo Vaticano (Southern Calabria, Italy). *Chem. Geol.* 92, 153–176.
- Royden, L., Patacca, E., Scandone, P., 1987. Segmentation and configuration of subducted lithosphere in Italy: an important control on thrust-belt and foredeep-basin evolution. *Geology* 15, 714–717.
- Savelli, C., 2005. Post-Eocene calcalkaline activity and basin opening in the western and central Mediterranean region: implications for magma source metasomatism linked to Hercynian orogeny. *Bollettino della Società Geologica Italiana* 4, 119–125.
- Scheepers, P.J.J., Langereis, C.G., Zijderveld, J.D.A., Hilgen, F.J., 1994. Paleomagnetic evidence for a Pleistocene clockwise rotation of the Calabro-Peloritan block (southern Italy). *Tectonophysics* 230, 19–48.
- Schenk, V., 1980. U-Pb and Radiometric Dates and their Correlation with Metamorphic Events in the Granulite-Facies Basement of the Serre, southern Calabria (Italy). *Contrib. Mineral. Petrol.* 73, 23–38.
- Schenk, V., 1981. Synchronous uplift of the lower crust of the Ivrea Zone and of southern Calabria and its possible consequences for the Hercynian orogeny in southern Europe. *Earth Planet. Sci. Lett.* 56, 305–320.
- Schenk, V., 1984. Petrology of Felsic Granulites, Metapelites, Metabasics, Ultramafics, and Metacarbonates from southern Calabria (Italy): prograde metamorphism, uplift and cooling of a former lower crust. *J. Petrol.* 25, 255–298.
- Schenk, V., 1990. The exposed crustal cross section of southern Calabria, Italy: structure and evolution of a segment of Hercynian crust. In: Salinsbury, M.H., Fountain, D.M. (Eds.), *Exposed Cross-Sections of Continental Crust*. Kluwer Academic Publishers, Dordrecht, pp. 21–42.
- Selvaggi, G., Chiarabba, C., 1995. Seismicity and P-wave velocity image of the southern Tyrrhenian subduction zone. *Geophys. J. Int.* 121, 818–826.
- Séranne, M., 1999. The Gulf of Lion continental margin (NW Mediterranean) revisited by IBS: an overview. In: Durand, B., Jolivet, L., Horvath, F., Séranne, M. (Eds.), *The Mediterranean Basins: Tertiary Extension within the Alpine Orogen*. Geological Society, London, pp. 15–36 (Special Publications 156).
- Serri, G., Innocenti, F., Manetti, P., 1993. Geochemical and petrological evidence of the subduction of delaminated Adriatic continental lithosphere in the genesis of the Neogene-Quaternary magmatism of central Italy. *Tectonophysics* 223, 117–147.
- Spakman, W., 1989. Tomographic images of the upper mantle below central Europe and the Mediterranean. *Terra Nova* 2, 542–553.
- Spiegel, C., 2003. Mylonitization, dry shearing and exhumation of the lower crust: the Curinga-Girifalco Line (Calabria, South Italy). In: Meschede, M., Kulemann, J. (Eds.), *Plate Margins and Orogeny. Comparative Studies*. *Neues Jahrbuch für Geologie und Paläontologie*, vol. 250 (2–5), pp. 359–390.
- Srivastava, S.P., Roest, W.R., Kovacs, L.C., Oakey, G., Lévesque, S., Verhoef, J., Macnab, R., 1990. Motion of Iberia since the Late Jurassic: results from detailed aeromagnetic measurements in the Newfoundland Basin. *Tectonophysics* 184, 229–260.
- Stampfli, G.M., Borel, G.D., Marchant, R., Mosar, J., 2002. Western Alps geological constraints on western Tethyan reconstructions. In: Rosenbaum, G., Lister, G.S. (Eds.), *Reconstruction of the Evolution of the Alpine-Himalayan Orogen*. *Journal of the Virtual Explorer* 8, pp. 77–106.
- Stipp, M., Stünitz, H., Heilbronner, R., Schmid, S.M., 2002. Dynamic recrystallization of quartz: correlation between natural and experimental conditions. In: De Meer, S., Drury, M.R., De Bresser, J.H.P., Pennock, G.M. (Eds.), *Deformation Mechanisms, Rheology and Tectonics: Current Status and Future Perspectives*. Geological Society, London, pp. 171–190 (Special Publications 200).
- Swanson, M.T., 1992. Fault structure, wear mechanisms and rupture processes in pseudotachylite generation. *Tectonophysics* 204, 223–242.
- Thomson, S.T., 1994. Fission track analysis of the crystalline basement rocks of the Calabrian Arc, southern Italy: evidence of Oligo-Miocene late-orogenic extension and erosion. *Tectonophysics* 238, 331–352.
- Thomson, S.T., 1998. Assessing the nature of tectonic contacts using fission track thermochronology: an example from the Calabrian Arc, southern Italy. *Terra Nova* 10, 32–36.
- Urai, J.L., Means, W.D., Lister, G.S., 1986. Dynamic recrystallization of minerals. *Am. Geophys. Union Monogr.* 36, 161–199.

- Vai, G.B., 1992. Il segmento Calabro-Peloritano dell'orogene ercinico. Disaggregazione palinspastica. *Bollettino della Società Geologica Italiana* 111, 109–129.
- Van Dijk, J.P., Scheepers, P.J.J., 1995. Neotectonic rotation in the Calabrian Arc; implications for a Pliocene-Recent geodynamic scenario for the Central Mediterranean. *Earth Sci. Rev.* 39, 207–246.
- Vigliotti, L., Kent, D.V., 1990. Paleomagnetic results of Tertiary sediments from Corsica: evidence of post-Eocene rotation. *Phys. Earth Planet. Interiors* 62, 97–108.
- White, S.H., 1977. Geological significance of recovery and recrystallization processes in quartz. *Tectonophysics* 39, 143–170.
- Wortel, M.J.R., Spakman, W., 2000. Subduction and slab detachment in the Mediterranean-Carpathian region. *Science* 290, 1910–1917.

APPENDIX 2: X-RAY FLUORESCENCE (XRF) ANALYSES OF ROCKS.

Major and trace elements have been analysed from twenty-one metasedimentary rocks of terrigenous origin and sixteen amphibolites from the Mandatoriccio complex. Analyses have been performed at the Dipartimento di Scienze della Terra e Geologico-Ambientali (University of Bologna) using a Philips PW 1480 XRF spectrometer, equipped with an Rh target tube. The concentration of major elements has been obtained following the method proposed by Franzini *et al.* (1975). The concentration of the trace elements has been determined using the coefficients proposed by Franzini & Leoni (1972), Leoni & Saitta (1976) and Leoni *et al.* (1982). Contents of H₂O and other volatile phases have been determined by loss on ignition (LOI).

The analyses relative to amphibolites and metasedimentary rocks of terrigenous origin are listed in **Tables 1** and **2**, respectively.

Bulk-rock compositions and some theoretical mineral compositions have been represented in conventional ACF e l'A'KF (Eskola, 1915) and AFM (Thompson, 1957) triangular diagrams. Molar proportions are used in all these diagrams, therefore, XRF-derived bulk chemistries, expressed in % of oxides, have been converted. Usually, F apex of triangular diagrams corresponds to the molar proportion of iron. Due to the important substitution between manganese and ferrous iron, molar proportion of MnO are added to FeO, in some specified diagrams.

Sample	LL 42c	LL 44	LL 45	LL 46	LL 48	LL 50	LL 51	LL 53b	LL 58a	LL 60	LL 62b	LL 63	LL 79	LL 81	LL 82b	LL 123
SiO ₂	50,95	46,19	47,46	46,08	49,90	54,30	53,61	47,28	50,18	50,53	47,52	48,95	51,43	44,77	42,66	49,98
TiO ₂	1,36	1,91	1,33	1,05	1,45	1,81	1,81	1,93	1,13	1,29	1,51	1,52	1,28	1,41	1,55	1,44
Al ₂ O ₃	15,86	14,85	16,55	14,56	13,57	14,00	14,18	14,35	15,46	16,12	16,30	15,15	15,33	14,56	15,45	15,93
Fe ₂ O ₃	12,06	13,60	11,30	12,21	11,24	12,64	13,03	13,66	10,14	10,61	11,65	11,06	10,95	13,67	14,58	11,38
MnO	0,23	0,23	0,18	0,19	0,20	0,21	0,20	0,22	0,18	0,20	0,20	0,20	0,20	0,20	0,20	0,23
MgO	8,01	8,27	8,71	12,02	8,31	5,02	4,87	8,31	8,12	6,78	7,94	7,38	6,89	11,32	10,93	8,13
CaO	8,63	11,52	10,81	9,50	10,82	5,72	6,76	10,96	10,02	9,87	11,37	12,34	10,02	7,88	7,87	10,47
Na ₂ O	0,70	1,96	2,39	1,35	2,46	5,35	4,81	2,12	3,11	3,37	2,31	2,31	2,89	2,06	2,23	0,64
K ₂ O	0,79	0,56	0,24	1,23	0,53	0,06	0,08	0,30	0,24	0,14	0,21	0,18	0,08	0,86	0,88	0,64
P ₂ O ₅	0,15	0,25	0,21	0,14	0,27	0,26	0,29	0,24	0,13	0,23	0,22	0,24	0,30	0,16	0,19	0,16
LOI	1,27	0,67	0,80	1,66	1,25	0,63	0,37	0,63	1,28	0,87	0,76	0,66	0,62	3,11	3,46	1,01
Tot.	100,01	100,01	99,98	99,99	100,00	100,00	100,01	100,00	99,99	100,01	99,99	99,99	99,99	100,00	100,00	100,01
Sc	53	40	31	24	43	40	41	43	33	30	32	44	34	29	29	49
V	302	284	209	169	259	279	282	301	216	218	219	261	214	214	229	304
Cr	409	333	351	408	200	56	53	313	320	275	334	871	264	122	204	413
Co	53	52	45	61	43	41	42	53	41	38	45	39	40	65	67	48
Ni	70	83	94	152	23	9	9	73	80	55	98	48	72	157	139	76
Cu	19	36	61	54	56	5	10	68	28	6	69	44	58	429	109	27
Zn	117	108	87	98	87	104	104	112	71	87	281	86	91	100	99	97
Rb	17	24	14	56	22	5	n.d.	13	13	8	10	n.d.	5	46	35	27
Sr	57	187	208	130	185	107	130	169	245	121	241	183	410	251	256	70
Y	22	31	25	24	35	43	42	33	24	37	27	29	45	28	27	34
Zr	31	137	112	77	178	231	234	137	106	193	112	128	271	112	143	73
Nb	10	10	8	5	12	13	13	10	6	11	8	11	12	11	14	7
Ba	246	176	107	217	175	6	15	130	118	16	118	129	17	187	197	145
La	49	17	7	n.d.	12	15	27	7	9	13	7	11	26	n.d.	11	8
Ce	76	24	18	19	19	48	41	23	22	31	28	35	69	23	31	2
Pb	12	6	5	8	10	9	10	104	6	11	11	9	9	6	11	14
Th	5	n.d.	n.d.	n.d.	n.d.	11	8	8	8	5	5	n.d.	6	6	n.d.	n.d.

Table 1: whole-rock geochemical data for analysed amphibolites from studied area. Oxides (wt.%); trace elements (ppm)

Sample	LL 42b	LL 56a	LL56a4	LL 56b	LL 56c	LL 57a	LL 61a	LL61b2	LL 80	LL 122	LL 124	LL141	LL 142	LL 154	LL 161a	LL 161b	LL 161c
	Parag.	Micasc.	Micasc.	Micasc.	Micasc.	Micasc.	Parag.	Parag.	Parag.	Parag.	Micasc.	Spot. Sc.	Parag.	Spot. Sc.	Spot. Sc.	Spot. Sc.	Spot. Sc.
SiO ₂	68,46	53,15	52,92	50,25	42,44	39,21	75,21	48,39	47,20	56,65	54,14	57,56	64,03	63,06	59,50	63,01	56,98
TiO ₂	0,68	1,09	1,07	1,23	1,58	1,82	0,60	1,87	2,08	1,07	1,05	0,73	0,76	0,75	0,89	0,78	0,94
Al ₂ O ₃	13,49	22,52	23,18	24,27	28,06	29,12	11,09	27,07	20,11	18,51	22,81	21,88	17,58	18,95	20,78	18,34	22,43
Fe ₂ O ₃	5,19	9,54	9,64	10,37	13,14	14,65	5,74	10,90	12,62	8,06	9,09	6,63	4,71	6,77	7,53	7,13	7,82
MnO	0,10	0,17	0,21	0,21	0,30	0,30	0,08	0,10	0,23	0,27	0,27	0,09	0,10	0,08	0,09	0,08	0,09
MgO	2,92	2,52	2,82	3,01	3,83	4,07	1,71	3,47	3,57	4,49	2,81	3,06	1,83	2,11	2,41	2,34	2,35
CaO	4,63	0,52	0,65	0,60	1,08	0,53	0,37	0,51	4,37	5,69	0,68	0,80	2,36	0,43	0,39	0,34	0,37
Na ₂ O	1,81	1,13	1,20	1,15	1,51	0,85	0,69	0,38	4,13	2,23	1,24	1,24	2,51	1,06	1,34	1,13	1,29
K ₂ O	1,47	6,26	5,38	6,10	5,71	6,37	3,09	4,49	3,82	2,01	5,03	3,01	3,51	3,51	3,45	3,03	3,91
P ₂ O ₅	0,13	0,20	0,21	0,13	0,08	0,02	0,08	0,33	0,78	0,16	0,16	0,10	0,25	0,14	0,17	0,14	0,15
LOI	1,12	2,90	2,73	2,68	2,26	3,06	1,34	2,49	1,09	0,85	2,72	4,90	2,35	3,14	3,44	3,68	3,68
Tot.	100,00	100,00	100,01	100,00	99,99	100,00	100,00	100,00	100,00	99,99	100,00	100,00	99,99	100,00	99,99	100,00	100,01
Sc	11	28	28	28	38	48	13	42	37	48	28	19	16	17	25	17	29
V	85	156	158	167	217	270	53	218	175	212	160	125	64	110	136	105	141
Cr	76	120	132	146	184	213	41	231	18	168	130	106	43	89	108	93	116
Co	13	25	28	35	45	51	12	37	29	39	28	17	7	21	23	23	26
Ni	28	39	42	59	78	83	21	64	7	54	52	49	16	44	45	36	44
Cu	225	50	37	25	13	13	10	38	7	30	47	43	18	20	26	38	34
Zn	47	111	129	117	204	268	53	332	117	130	124	112	69	129	119	113	123
Rb	83	201	200	212	218	244	97	190	304	133	231	105	125	179	156	128	207
Sr	185	69	22	105	156	59	21	0	136	184	17	89	77	11	39	19	29
Y	24	33	35	37	37	40	25	39	69	35	31	30	56	37	29	30	38
Zr	124	147	158	159	217	222	226	310	524	219	162	146	367	181	181	147	194
Nb	7	20	17	24	28	26	9	35	24	18	25	9	20	27	22	18	24
Ba	129	729	635	754	607	1247	266	687	324	1119	718	633	365	461	460	435	535
La	23	41	41	42	53	55	25	16	46	37	44	23	48	29	36	40	48
Ce	52	84	84	90	102	110	54	25	84	89	85	56	105	75	97	65	95
Pb	21	25	28	30	46	16	20	29	21	32	29	18	23	14	29	19	30
Th	12	15	16	17	25	23	9	25	13	15	16	10	23	16	15	20	16

Table 2: whole-rock geochemical data for analysed metapelites and meta-arenites from studied area. Oxides (wt.%); trace elements (ppm)

APPENDIX 3: ANALYTICAL AND IMAGING TECHNIQUES

Optical cathodoluminescences

Thin sections of selected paragneisses have been analysed by Nikon optical microscope equipped with a Cathodyne (cool cathode) at the Biomineralisation and Palaeoenvironment Department of Pierre and Marie Curie University of Paris.

X-ray mapping

Selected samples of the studied rocks were examined using a JEOL JSM 840A and a Gemini Zeiss scanning electron microscopes (SEM) using a back-scattered electron detector (BSE). Selected porphyroblasts of garnet, plagioclase and staurolite and reaction domains were mapped for the major elements (Al, Ca, Fe, K, Mg, Mn, Na, P, Si, Ti,) using a powerful software (SPIRIT-PGT).

X-ray maps have a 1024 x 768 pixel resolution and have been acquired using 25-30 frames (2-3 hours). The images have a linear scale but all the maps have been corrected and calibrated using the software SPIRIT. X-ray mapping has been performed at the Camparis Service of the Paris 6/7 University.

Principal component analysis (PCA), image analysis and image classification

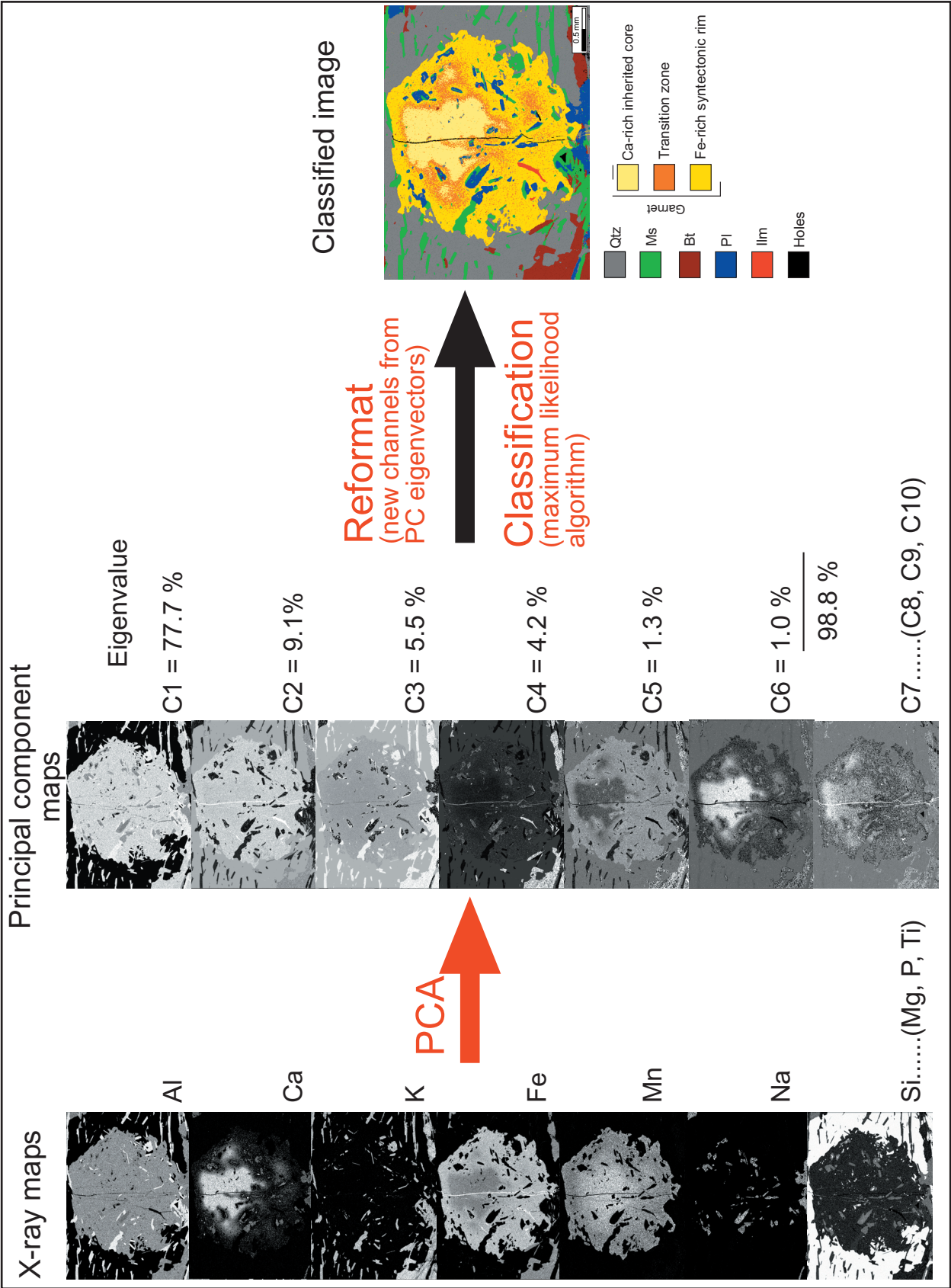
Principal component analysis (PCA) involves a mathematical procedure that transforms a number of possibly correlated variables into the same number of uncorrelated variables (eigenvectors), characterised by different importance (eigenvalues) and called principal components. The first principal component accounts for as much of the variability in the data as possible, and each succeeding component accounts for as much of the remaining variability as possible.

Traditionally, principal component analysis is performed on a square symmetric matrix of type SSCP (pure sums of squares and cross products), Covariance (scaled sums of squares and cross products) and Correlations (sums of squares and cross products from standardized data). Concerning the treatment of chemical data it has been used the Covariance matrix.

Principal component analysis has been performed also on X-ray element maps.

Several thin sections have been analysed to reconstruct the petrological evolution of the Mandatoriccio complex. First, the samples were observed under a light microscope to recognise reaction microstructures which have been analysed in detail under a scanning electron microscope. Some EDS (Energy Dispersive Spectrometer) X-ray maps have been made on the most interesting microstructures. The image analysis has been performed with EDS X-ray maps using the software Multispec (<http://dynamo.ecn.purdue.edu/~biehl/MultiSpec/>). For this purpose a multichannel TIFF image has been created, in which each channel represents an elemental map. This multichannel image has been firstly treated by PCA, then the remaining image has been analysed again by using the “maximum likelihood” classification algorithm (phase analysis). Classification permits to correlate

each pixel to a particular phase (in this case mineral). In practice, Multispec permits to clusterize and classify in different colours the phases contained in the image. Methodology is schematically shown below.



Mineral abbreviations

Mineral abbreviations are after Kretz (1983) except for italic ones.

Symbol	Mineral
Ab	albite
Alm	almandine
And	andalusite
Adr	andradite
An	anorthite
Ap	apatite
Bt	biotite
Chl	chlorite
Crd	cordierite
Crn	corundum
<i>Fib</i>	<i>fibrolite</i>
Grt	garnet
Grs	grossularite
Ilm	ilmenite
Kfs	K feldspar
Ky	kyanite
Ms	muscovite
Or	orthoclase
Opx	orthopyroxene
<i>Pin</i>	<i>pinite</i>
Pl	plagioclase
Prp	pyrope
Qtz	quartz
Rt	rutile
Sil	sillimanite
Sps	spessartine
St	staurolite
Tur	tourmaline
Zrn	zircon
<i>Wm</i>	<i>white mica</i>

Table 3: list of used mineral symbols.

Mineral chemical analyses

Mineral analyses have been performed with a Cameca SX50 and SX100 wavelength-dispersive electron microprobes at the CAMPARIS Service of the Paris 6/7 University. Operating conditions for electron microprobe analyses were a ≈ 1 micron beam diameter, a 15kV accelerating voltage and a beam currents varying from 5 to 40 nA. In particular, a beam current of 5 nA has been used for pinite whereas a beam current of 10 nA has been adopted for micas, staurolite, amphibole and plagioclase. A higher beam current (40 nA) has been used to analyse garnet, K-feldspar and ilmenite. The signal used for all elements is the $K\alpha$. Standard used are listed in **Table 4**.

Element	Standard used
Al	Orthoclase
Ca	Diopside
Cl	Scapolite
F	CaF ₂
K	Orthoclase
Fe	Fe ₂ O ₃
Mg	Diopside
Mn	MnTiO ₃
Na	Albite
Si	Diopside
Ti	MnTiO ₃
Zn	ZnS ₂

Table 4: list of standards used for mineral chemical analyses.

Chemical analyses of amphibole and plagioclase relative to amphibolites are listed in Tables 5 and 6 whereas chemical analyses of interesting minerals contained in micaschists and paragneisses are listed in Tables 7 to 11 and 12 to 19, respectively. H₂O for amphibole, biotite, muscovite and pinite is recalculated from stoichiometry.

Sample Descrip.	LL47		LL44		LL44		LL44		LL48		LL 63		LL 63		LL 63b		LL 62b		LL 62b		LL 62b		LL 46		LL 46		LL 46		LL 46	
	Porph.	LL47	Porph.	LL44	Porph.	LL44	Porph.	LL44	Porph.	LL48	Porph.	LL 63	Porph.	LL 63	Porph.	LL 63b	Porph.	LL 62b	Porph.	LL 62b	Porph.	LL 62b	Porph.	LL 46	Porph.	LL 46	Porph.	LL 46	Porph.	
SiO2	53.27	54.40	53.25	50.42	49.79	50.42	50.28	51.74	50.93	51.44	51.77	52.13	52.34	45.91	51.06	46.90	47.80	46.31	55.24	45.25	44.85	46.31	55.24	45.25	44.85	46.31	55.24	45.25	44.85	
TiO2	0.32	0.21	0.28	0.58	0.67	0.58	0.45	0.74	0.44	0.23	0.19	0.27	0.19	0.29	0.38	0.48	0.40	0.40	0.00	0.51	0.40	0.43	0.00	0.51	0.40	0.43	0.00	0.51	0.40	
Al2O3	4.40	3.51	3.87	7.49	7.66	7.49	6.93	4.50	4.99	4.14	3.51	3.58	3.29	10.26	8.78	9.14	12.06	12.06	1.76	13.33	13.95	12.41	1.76	13.33	13.95	12.41	1.76	13.33	13.95	
Fe2O3	0.00	0.00	0.00	0.00	0.00	0.00	0.00	0.00	0.60	0.63	0.51	0.34	0.92	1.35	1.43	1.78	1.85	0.00	0.01	0.00	0.00	0.00	0.01	0.00	0.00	0.00	0.01	0.00	0.00	
FeO	12.83	12.71	14.34	14.99	15.77	15.77	15.32	15.06	13.85	13.31	13.58	13.37	13.39	13.14	12.59	12.88	12.83	12.13	10.56	12.70	12.41	11.85	10.56	12.70	12.41	11.85	10.56	12.70	12.41	
MnO	0.21	0.20	0.21	0.19	0.23	0.19	0.31	0.32	0.28	0.28	0.32	0.29	0.25	0.18	0.21	0.24	0.28	0.26	0.25	0.22	0.12	0.19	0.25	0.22	0.12	0.19	0.25	0.22	0.12	
MgO	15.66	16.24	14.66	12.51	12.51	12.70	13.15	13.35	13.41	13.87	14.01	14.32	15.25	11.78	14.71	12.36	12.52	12.87	18.32	12.22	11.86	12.90	18.32	12.22	11.86	12.90	18.32	12.22	11.86	
CaO	11.55	10.69	12.06	11.74	11.63	11.77	11.78	11.78	12.62	12.64	12.45	12.95	11.27	12.23	11.76	12.20	12.65	11.89	11.35	11.87	12.07	12.07	11.35	11.87	12.07	12.07	11.35	11.87	12.07	
Na2O	0.59	0.37	0.36	0.71	0.76	0.76	0.73	0.35	0.42	0.37	0.35	0.35	0.31	1.08	0.34	0.89	0.92	1.31	0.16	1.58	1.44	1.36	0.16	1.58	1.44	1.36	0.16	1.58	1.44	
K2O	0.01	0.04	0.09	0.28	0.23	0.23	0.23	0.10	0.09	0.08	0.06	0.07	0.01	0.25	0.04	0.20	0.13	0.13	0.00	0.20	0.26	0.19	0.00	0.20	0.26	0.19	0.00	0.20	0.26	
H2O	2.11	2.11	2.10	2.07	2.09	2.08	2.08	2.06	2.01	2.05	2.02	2.01	1.96	2.02	2.05	1.99	2.03	2.06	2.11	2.02	2.05	2.04	2.11	2.02	2.05	2.04	2.11	2.02	2.05	
F	0.00	0.00	0.00	0.00	0.00	0.00	0.00	0.00	0.09	0.00	0.05	0.10	0.22	0.00	0.00	0.07	0.07	0.00	0.00	0.10	0.01	0.07	0.00	0.10	0.01	0.07	0.00	0.10	0.01	
Cl	0.00	0.00	0.00	0.00	0.00	0.00	0.00	0.00	0.00	0.00	0.00	0.00	0.01	0.01	0.00	0.00	0.01	0.00	0.00	0.01	0.01	0.01	0.00	0.01	0.01	0.01	0.00	0.01	0.01	

Table 5: microprobe analyses of 28 amphibole porphyroblasts and 56 syntectonic amphibole prisms from amphibolite schists and gneisses. Analyses are shown in Fig. 3.1.

[illegible]

Table 5: continued

[illegible]

Table 5: continued

Sample Descrip.	LL 46 Prism.	LL 53b Prism.	LL 53b Prism.	LL 53b Prism.	LL 53b Prism.	LL 50 Prism.	LL 50 Prism.	LL 50 Prism.	LL 50 Prism.	LL 79 Prism.	LL 79 Prism.	LL 79 Prism.	LL 82b Prism.	LL 82b Prism.	LL 82b Prism.	LL 58a Prism.	LL 58a Prism.	LL 51 Prism.	LL 51 Prism.
SiO ₂	47.04	45.37	49.03	48.43	48.07	45.31	44.98	45.66	42.48	49.59	49.02	48.46	53.95	52.44	52.44	51.93	48.11	47.03	45.16
TiO ₂	0.32	0.49	0.52	0.48	0.58	0.90	0.78	0.75	0.62	0.30	0.63	0.53	0.56	0.23	0.23	0.36	0.60	0.31	0.52
Al ₂ O ₃	11.07	12.65	7.42	9.10	8.98	8.74	9.33	9.72	10.50	6.55	6.98	7.63	7.95	3.79	3.79	7.85	4.11	7.92	8.06
Fe ₂ O ₃	0.41	0.37	0.33	0.00	0.34	0.00	1.04	0.67	3.25	0.00	0.00	0.00	0.00	1.00	1.00	0.75	1.46	0.51	2.17
FeO	11.41	16.40	15.20	15.50	15.16	19.44	19.26	19.92	17.94	15.33	15.09	15.63	15.55	12.89	12.67	11.76	12.74	20.46	17.95
MnO	0.25	0.24	0.27	0.31	0.21	0.18	0.32	0.23	0.30	0.37	0.25	0.25	0.23	0.15	0.15	0.45	0.37	0.28	0.23
MgO	13.30	10.20	12.81	11.85	12.00	9.12	9.26	9.05	8.32	12.75	12.58	12.26	11.97	15.89	15.45	13.36	13.43	9.61	9.44
CaO	12.43	11.68	11.29	11.69	11.83	11.12	11.04	11.25	11.42	10.64	11.29	11.00	11.26	12.24	12.41	11.65	11.65	10.60	11.15
Na ₂ O	1.17	1.19	0.71	0.84	0.75	1.21	1.36	1.28	1.56	0.64	0.66	0.71	0.76	0.09	0.14	0.87	0.82	1.12	0.91
K ₂ O	0.20	0.34	0.13	0.19	0.23	0.24	0.34	0.32	0.33	0.09	0.05	0.10	0.15	0.01	0.07	0.17	0.11	0.19	0.34
H ₂ O	2.07	2.03	2.02	2.04	2.04	1.90	1.99	1.92	1.76	1.96	1.92	1.92	1.92	2.02	2.07	2.03	2.04	2.00	1.94
F	0.00	0.03	0.07	0.03	0.03	0.14	0.00	0.17	0.41	0.15	0.00	0.22	0.22	0.11	0.00	0.07	0.10	0.00	0.03
Cl	0.00	0.00	0.01	0.02	0.00	0.00	0.00	0.03	0.00	0.00	0.00	0.00	0.00	0.00	0.00	0.01	0.00	0.00	0.00
F-12O	0.00	0.02	0.04	0.02	0.02	0.08	0.00	0.10	0.24	0.08	0.00	0.13	0.13	0.07	0.00	0.04	0.06	0.00	0.02
Cl-12O	0.00	0.00	0.01	0.01	0.00	0.00	0.00	0.02	0.00	0.00	0.00	0.00	0.00	0.00	0.00	0.01	0.00	0.00	0.00
Total	99.67	100.98	99.77	100.47	100.20	98.24	99.70	100.89	98.71	98.30	98.57	98.62	98.85	99.26	98.99	99.36	99.28	99.96	97.89
Si	6.82	6.64	7.17	7.05	7.02	6.92	6.79	6.81	6.53	7.34	7.24	7.18	7.15	7.90	7.81	7.50	7.04	7.06	6.92
Al IV	1.19	1.37	0.83	0.95	0.98	1.08	1.21	1.19	1.47	0.66	0.76	0.82	0.85	0.10	0.19	0.50	0.96	0.94	1.08
Tot IV	8.00	8.00	8.00	8.00	8.00	8.00	8.00	8.00	8.00	8.00	8.00	8.00	8.00	8.00	8.00	8.00	8.00	8.00	8.00
Ti	0.04	0.05	0.06	0.05	0.06	0.10	0.09	0.08	0.07	0.43	0.07	0.06	0.06	0.00	0.00	0.04	0.07	0.04	0.06
Al VI	0.71	0.82	0.45	0.61	0.56	0.49	0.45	0.52	0.43	0.08	0.46	0.51	0.54	0.09	0.16	0.20	0.41	0.45	0.38
Fe ₃ +	0.05	0.04	0.04	0.00	0.04	0.00	0.12	0.08	0.38	0.00	0.00	0.00	0.00	0.00	0.00	0.08	0.16	0.06	0.25
Fe ₂ M1	1.36	1.93	1.77	1.82	1.79	2.39	2.32	2.37	2.24	1.79	1.79	1.84	1.84	1.53	1.52	1.34	1.58	2.41	2.21
MnM1	0.03	0.03	0.03	0.04	0.03	0.02	0.04	0.03	0.04	0.04	0.03	0.03	0.03	0.02	0.02	0.03	0.05	0.04	0.03
MgM1	2.83	2.14	2.66	2.48	2.52	2.00	1.99	1.92	1.85	2.65	2.66	2.57	2.53	3.36	3.30	3.26	2.82	2.02	2.08
CaM1	0.00	0.00	0.00	0.00	0.00	0.00	0.00	0.00	0.00	0.00	0.00	0.00	0.00	0.00	0.00	0.00	0.00	0.00	0.00
Tot M1	5.00	5.00	5.00	5.00	5.00	5.00	5.00	5.00	5.00	5.00	5.00	5.00	5.00	5.00	5.00	5.00	5.00	5.00	5.00
Fe M2	0.02	0.08	0.09	0.07	0.06	0.09	0.12	0.11	0.07	0.11	0.08	0.10	0.08	0.03	0.02	0.06	0.06	0.16	0.09
Mn M2	0.00	0.00	0.00	0.00	0.00	0.00	0.00	0.00	0.00	0.00	0.00	0.00	0.00	0.00	0.00	0.00	0.00	0.00	0.00
Mg M2	0.05	0.09	0.14	0.09	0.09	0.08	0.10	0.09	0.05	0.16	0.12	0.14	0.11	0.07	0.04	0.14	0.11	0.13	0.08
Ca M2	1.93	1.83	1.77	1.82	1.85	1.82	1.79	1.80	1.88	1.69	1.79	1.75	1.78	1.89	1.93	1.81	1.83	1.71	1.83
Na M2	0.00	0.00	0.00	0.02	0.00	0.01	0.00	0.00	0.00	0.04	0.02	0.01	0.03	0.01	0.02	0.00	0.00	0.00	0.00
Tot M2	2.00	2.00	2.00	2.00	2.00	2.00	2.00	2.00	2.00	2.00	2.00	2.00	2.00	2.00	2.00	2.00	2.00	2.00	2.00
Na A	0.33	0.34	0.20	0.22	0.21	0.35	0.40	0.37	0.46	0.14	0.17	0.19	0.19	0.01	0.02	0.13	0.23	0.33	0.27
K A	0.04	0.06	0.02	0.04	0.04	0.05	0.07	0.06	0.07	0.02	0.01	0.02	0.03	0.00	0.01	0.00	0.02	0.04	0.07
Tot A	0.37	0.40	0.23	0.25	0.26	0.40	0.46	0.43	0.53	0.16	0.18	0.21	0.22	0.02	0.03	0.13	0.25	0.36	0.34
Tot Cat	15.37	15.40	15.23	15.25	15.26	15.40	15.46	15.43	15.53	15.16	15.18	15.21	15.22	15.02	15.03	15.13	15.25	15.36	15.34
F	0.00	0.02	0.03	0.02	0.02	0.07	0.00	0.08	0.20	0.07	0.00	0.10	0.10	0.05	0.00	0.03	0.05	0.00	0.02
Cl	0.00	0.00	0.00	0.00	0.00	0.00	0.00	0.01	0.00	0.00	0.00	0.00	0.00	0.00	0.00	0.00	0.00	0.00	0.00
OH	2.00	1.98	1.97	1.98	1.98	1.93	2.00	1.91	1.80	1.93	2.00	1.90	1.90	1.95	2.00	1.96	1.95	2.00	1.98
ΣO	22	22	22	22	22	22	22	22	22	22	22	22	22	22	22	22	22	22	22

Table 5: continued

Sample	LL47	LL47	LL47	LL47	LL47	LL47	LL47	LL47	LL47	LL47	LL47	LL47	LL47	LL47	LL47	LL47	LL47	LL47	LL47	LL47	LL47	LL47	LL47	LL47	LL47	LL47	LL47	LL47	LL47	LL47	LL47	LL47	LL47	LL47	LL47	LL47	LL47	LL47	LL47	LL47	LL47	LL47	LL47	LL47	LL47	LL47	LL47	LL47	LL47	LL47	LL47	LL47	LL47	LL47	LL47	LL47	LL47	LL47	LL47	LL47	LL47	LL47	LL47	LL47	LL47	LL47	LL47	LL47	LL47	LL47	LL47	LL47	LL47	LL47	LL47	LL47	LL47	LL47	LL47	LL47	LL47	LL47	LL47	LL47	LL47	LL47	LL47	LL47	LL47	LL47	LL47	LL47	LL47	LL47	LL47	LL47	LL47	LL47	LL47	LL47	LL47	LL47	LL47	LL47	LL47	LL47	LL47	LL47	LL47	LL47	LL47	LL47	LL47	LL47	LL47	LL47	LL47	LL47	LL47	LL47	LL47	LL47	LL47	LL47	LL47	LL47	LL47	LL47	LL47	LL47	LL47	LL47	LL47	LL47	LL47	LL47	LL47	LL47	LL47	LL47	LL47	LL47	LL47	LL47	LL47	LL47	LL47	LL47	LL47	LL47	LL47	LL47	LL47	LL47	LL47	LL47	LL47	LL47	LL47	LL47	LL47	LL47	LL47	LL47	LL47	LL47	LL47	LL47	LL47	LL47	LL47	LL47	LL47	LL47	LL47	LL47	LL47	LL47	LL47	LL47	LL47	LL47	LL47	LL47	LL47	LL47	LL47	LL47	LL47	LL47	LL47	LL47	LL47	LL47	LL47	LL47	LL47	LL47	LL47	LL47	LL47	LL47	LL47	LL47	LL47	LL47	LL47	LL47	LL47	LL47	LL47	LL47	LL47	LL47	LL47	LL47	LL47	LL47	LL47	LL47	LL47	LL47	LL47	LL47	LL47	LL47	LL47	LL47	LL47	LL47	LL47	LL47	LL47	LL47	LL47	LL47	LL47	LL47	LL47	LL47	LL47	LL47	LL47	LL47	LL47	LL47	LL47	LL47	LL47	LL47	LL47	LL47	LL47	LL47	LL47	LL47	LL47	LL47	LL47	LL47	LL47	LL47	LL47	LL47	LL47	LL47	LL47	LL47	LL47	LL47	LL47	LL47	LL47	LL47	LL47	LL47	LL47	LL47	LL47	LL47	LL47	LL47	LL47	LL47	LL47	LL47	LL47	LL47	LL47	LL47	LL47	LL47	LL47	LL47	LL47	LL47	LL47	LL47	LL47	LL47	LL47	LL47	LL47	LL47	LL47	LL47	LL47	LL47	LL47	LL47	LL47	LL47	LL47	LL47	LL47	LL47	LL47	LL47	LL47	LL47	LL47	LL47	LL47	LL47	LL47	LL47	LL47	LL47	LL47	LL47	LL47	LL47	LL47	LL47	LL47	LL47	LL47	LL47	LL47	LL47	LL47	LL47	LL47	LL47	LL47	LL47	LL47	LL47	LL47	LL47	LL47	LL47	LL47	LL47	LL47	LL47	LL47	LL47	LL47	LL47	LL47	LL47	LL47	LL47	LL47	LL47	LL47	LL47	LL47	LL47	LL47	LL47	LL47	LL47	LL47	LL47	LL47	LL47	LL47	LL47	LL47	LL47	LL47	LL47	LL47	LL47	LL47	LL47	LL47	LL47	LL47	LL47	LL47	LL47	LL47	LL47	LL47	LL47	LL47	LL47	LL47	LL47	LL47	LL47	LL47	LL47	LL47	LL47	LL47	LL47	LL47	LL47	LL47	LL47	LL47	LL47	LL47	LL47	LL47	LL47	LL47	LL47	LL47	LL47	LL47	LL47	LL47	LL47	LL47	LL47	LL47	LL47	LL47	LL47	LL47	LL47	LL47	LL47	LL47	LL47	LL47	LL47	LL47	LL47	LL47	LL47	LL47	LL47	LL47	LL47	LL47	LL47	LL47	LL47	LL47	LL47	LL47	LL47	LL47	LL47	LL47	LL47	LL47	LL47	LL47	LL47	LL47	LL47	LL47	LL47	LL47	LL47	LL47	LL47	LL47	LL47	LL47	LL47	LL47	LL47	LL47	LL47	LL47	LL47	LL47	LL47	LL47	LL47	LL47	LL47	LL47	LL47	LL47	LL47	LL47	LL47	LL47	LL47	LL47	LL47	LL47	LL47	LL47	LL47	LL47	LL47	LL47	LL47	LL47	LL47	LL47	LL47	LL47	LL47	LL47	LL47	LL47	LL47	LL47	LL47	LL47	LL47	LL47	LL47	LL47	LL47	LL47	LL47	LL47	LL47	LL47	LL47	LL47	LL47	LL47	LL47	LL47	LL47	LL47	LL47	LL47	LL47	LL47	LL47	LL47	LL47	LL47	LL47	LL47	LL47	LL47	LL47	LL47	LL47	LL47	LL47	LL47	LL47	LL47	LL47	LL47	LL47	LL47	LL47	LL47	LL47	LL47	LL47	LL47	LL47	LL47	LL47	LL47	LL47	LL47	LL47	LL47	LL47	LL47	LL47	LL47	LL47	LL47	LL47	LL47	LL47	LL47	LL47	LL47	LL47	LL47	LL47	LL47	LL47	LL47	LL47	LL47	LL47	LL47	LL47	LL47	LL47	LL47	LL47	LL47	LL47	LL47	LL47	LL47	LL47	LL47	LL47	LL47	LL47	LL47	LL47	LL47	LL47	LL47	LL47	LL47	LL47	LL47	LL47	LL47	LL47	LL47	LL47	LL47	LL47	LL47	LL47	LL47	LL47	LL47	LL47	LL47	LL47	LL47	LL47	LL47	LL47	LL47	LL47	LL47	LL47	LL47	LL47	LL47	LL47	LL47	LL47	LL47	LL47	LL47	LL47	LL47	LL47	LL47	LL47	LL47	LL47	LL47	LL47	LL47	LL47	LL47	LL47	LL47	LL47	LL47	LL47	LL47	LL47	LL47	LL47	LL47	LL47	LL47	LL47	LL47	LL47	LL47	LL47	LL47	LL47	LL47	LL47	LL47	LL47	LL47	LL47	LL47	LL47	LL47	LL47	LL47	LL47	LL47	LL47	LL47	LL47	LL47	LL47	LL47	LL47	LL47	LL47	LL47	LL47	LL47	LL47	LL47	LL47	LL47	LL47	LL47	LL47	LL47	LL47	LL47	LL47	LL47	LL47	LL47	LL47	LL47	LL47	LL47	LL47	LL47	LL47	LL47	LL47	LL47	LL47	LL47	LL47	LL47	LL47	LL47	LL47	LL47	LL47	LL47	LL47	LL47	LL47	LL47	LL47	LL47	LL47	LL47	LL47	LL47	LL47	LL47	LL47	LL47	LL47	LL47	LL47	LL47	LL47	LL47	LL47	LL47	LL47	LL47	LL47	LL47	LL47	LL47	LL47	LL47	LL47	LL47	LL47	LL47	LL47	LL47	LL47	LL47	LL47	LL47	LL47	LL47	LL47	LL47	LL47	LL47	LL47	LL47	LL47	LL47	LL47	LL47	LL47	LL47	LL47	LL47	LL47	LL47	LL47	LL47	LL47	LL47	LL47	LL47	LL47	LL47	LL47	LL47	LL47	LL47	LL47	LL47	LL47	LL47	LL47	LL47	LL47	LL47	LL47	LL47	LL47	LL47	LL47	LL47	LL47	LL47	LL47	LL47	LL47	LL47	LL47	LL47	LL47	LL47	LL47	LL47	LL47	LL47	LL47	LL47	LL47	LL47	LL47	LL47	LL47	LL47	LL47	LL47	LL47	LL47	LL47	LL47	LL47	LL47	LL47	LL47	LL47	LL47	LL47	LL47	LL47	LL47	LL47	LL47	LL47	LL47	LL47	LL47	LL47	LL47	LL47	LL47	LL47	LL47	LL47	LL47	LL47	LL47	LL47	LL47	LL47	LL47	LL47	LL47	LL47	LL47	LL47	LL47	LL47	LL47	LL47	LL47	LL47	LL47	LL47	LL47	LL47	LL47	LL47	LL47	LL47	LL47	LL47	LL47	LL47	LL47	LL47	LL47	LL47	LL47	LL47	LL47	LL47	LL47	LL47	LL47	LL47	LL47	LL47	LL47	LL47	LL47	LL47	LL47	LL47	LL47	LL47	LL47	LL47	LL47	LL47	LL47	LL47	LL47	LL47	LL47	LL47	LL47	LL47	LL47	LL47	LL47	LL47	LL47	LL47	LL47	LL47	LL47	LL47	LL47	LL47	LL47	LL
--------	------	------	------	------	------	------	------	------	------	------	------	------	------	------	------	------	------	------	------	------	------	------	------	------	------	------	------	------	------	------	------	------	------	------	------	------	------	------	------	------	------	------	------	------	------	------	------	------	------	------	------	------	------	------	------	------	------	------	------	------	------	------	------	------	------	------	------	------	------	------	------	------	------	------	------	------	------	------	------	------	------	------	------	------	------	------	------	------	------	------	------	------	------	------	------	------	------	------	------	------	------	------	------	------	------	------	------	------	------	------	------	------	------	------	------	------	------	------	------	------	------	------	------	------	------	------	------	------	------	------	------	------	------	------	------	------	------	------	------	------	------	------	------	------	------	------	------	------	------	------	------	------	------	------	------	------	------	------	------	------	------	------	------	------	------	------	------	------	------	------	------	------	------	------	------	------	------	------	------	------	------	------	------	------	------	------	------	------	------	------	------	------	------	------	------	------	------	------	------	------	------	------	------	------	------	------	------	------	------	------	------	------	------	------	------	------	------	------	------	------	------	------	------	------	------	------	------	------	------	------	------	------	------	------	------	------	------	------	------	------	------	------	------	------	------	------	------	------	------	------	------	------	------	------	------	------	------	------	------	------	------	------	------	------	------	------	------	------	------	------	------	------	------	------	------	------	------	------	------	------	------	------	------	------	------	------	------	------	------	------	------	------	------	------	------	------	------	------	------	------	------	------	------	------	------	------	------	------	------	------	------	------	------	------	------	------	------	------	------	------	------	------	------	------	------	------	------	------	------	------	------	------	------	------	------	------	------	------	------	------	------	------	------	------	------	------	------	------	------	------	------	------	------	------	------	------	------	------	------	------	------	------	------	------	------	------	------	------	------	------	------	------	------	------	------	------	------	------	------	------	------	------	------	------	------	------	------	------	------	------	------	------	------	------	------	------	------	------	------	------	------	------	------	------	------	------	------	------	------	------	------	------	------	------	------	------	------	------	------	------	------	------	------	------	------	------	------	------	------	------	------	------	------	------	------	------	------	------	------	------	------	------	------	------	------	------	------	------	------	------	------	------	------	------	------	------	------	------	------	------	------	------	------	------	------	------	------	------	------	------	------	------	------	------	------	------	------	------	------	------	------	------	------	------	------	------	------	------	------	------	------	------	------	------	------	------	------	------	------	------	------	------	------	------	------	------	------	------	------	------	------	------	------	------	------	------	------	------	------	------	------	------	------	------	------	------	------	------	------	------	------	------	------	------	------	------	------	------	------	------	------	------	------	------	------	------	------	------	------	------	------	------	------	------	------	------	------	------	------	------	------	------	------	------	------	------	------	------	------	------	------	------	------	------	------	------	------	------	------	------	------	------	------	------	------	------	------	------	------	------	------	------	------	------	------	------	------	------	------	------	------	------	------	------	------	------	------	------	------	------	------	------	------	------	------	------	------	------	------	------	------	------	------	------	------	------	------	------	------	------	------	------	------	------	------	------	------	------	------	------	------	------	------	------	------	------	------	------	------	------	------	------	------	------	------	------	------	------	------	------	------	------	------	------	------	------	------	------	------	------	------	------	------	------	------	------	------	------	------	------	------	------	------	------	------	------	------	------	------	------	------	------	------	------	------	------	------	------	------	------	------	------	------	------	------	------	------	------	------	------	------	------	------	------	------	------	------	------	------	------	------	------	------	------	------	------	------	------	------	------	------	------	------	------	------	------	------	------	------	------	------	------	------	------	------	------	------	------	------	------	------	------	------	------	------	------	------	------	------	------	------	------	------	------	------	------	------	------	------	------	------	------	------	------	------	------	------	------	------	------	------	------	------	------	------	------	------	------	------	------	------	------	------	------	------	------	------	------	------	------	------	------	------	------	------	------	------	------	------	------	------	------	------	------	------	------	------	------	------	------	------	------	------	------	------	------	------	------	------	------	------	------	------	------	------	------	------	------	------	------	------	------	------	------	------	------	------	------	------	------	------	------	------	------	------	------	------	------	------	------	------	------	------	------	------	------	------	------	------	------	------	------	------	------	------	------	------	------	------	------	------	------	------	------	------	------	------	------	------	------	------	------	------	------	------	------	------	------	------	------	------	------	------	------	------	------	------	------	------	------	------	------	------	------	------	------	------	------	------	------	------	------	------	------	------	------	------	------	------	------	------	------	------	------	------	------	------	------	------	------	------	------	------	------	------	------	------	------	------	------	------	------	------	------	------	------	------	----

Table 6: microprobe analyses of 65 syntectonic plagioclase from amphibolite schists and gneisses. Analyses are shown in Fig. 3.3.

Table 6: continued

Table 6: continued

Sample	LL 79	LL 82b	LL 82b	LL 82b	LL 82b	LL 82b	LL 82b	LL 82b	LL 58a	LL 58a	LL 58a	LL 58a	LL 58a	LL 51	LL 51	LL 51
SiO2	57,22	59,69	52,48	56,19	49,00	56,14	56,49	58,91	58,90	54,63	54,78	61,56	61,62	63,81		
TiO2	0,00	0,00	3,02	0,00	0,00	0,00	0,03	0,07	0,13	0,02	0,16	0,00	0,00	0,00		
Al2O3	28,38	25,87	26,71	28,60	27,60	28,10	27,87	25,16	26,05	27,52	27,97	24,33	24,76	22,99		
Fe2O3	0,11	0,02	0,10	0,26	6,58	0,01	0,30	0,10	0,00	0,11	0,07	0,13	0,11	0,15		
FeO	0,00	0,00	0,00	0,00	0,00	0,00	0,00	0,00	0,00	0,00	0,00	0,00	0,00	0,00		
MnO	0,00	0,00	0,00	0,00	0,13	0,01	0,00	0,00	0,00	0,00	0,00	0,00	0,00	0,05		
MgO	0,00	0,01	0,02	0,02	4,00	0,02	0,02	0,01	0,00	0,03	0,01	0,00	0,02	0,00		
CaO	9,67	6,94	12,41	9,40	7,42	9,60	9,18	6,75	6,98	9,86	9,97	5,03	5,57	3,65		
Na2O	6,22	7,96	4,98	6,34	4,59	6,50	6,45	8,45	7,78	6,12	6,37	8,81	8,84	10,05		
K2O	0,00	0,11	0,03	0,15	0,14	0,00	0,38	0,04	0,04	0,00	0,08	0,05	0,01	0,13		
Total	101,59	100,59	99,74	100,96	99,46	100,37	100,72	99,49	99,88	98,29	99,42	99,91	100,92	100,83		
Si	2,53	2,65	2,40	2,50	2,27	2,52	2,53	2,65	2,63	2,50	2,49	2,73	2,71	2,80		
Al	1,48	1,35	1,44	1,50	1,51	1,48	1,47	1,33	1,37	1,49	1,50	1,27	1,29	1,19		
Ti	0,00	0,00	0,10	0,00	0,00	0,00	0,00	0,00	0,00	0,00	0,01	0,00	0,00	0,00		
Fe3+	0,00	0,00	0,00	0,01	0,23	0,00	0,01	0,00	0,00	0,00	0,00	0,00	0,00	0,01		
Mn	0,00	0,00	0,00	0,00	0,01	0,00	0,00	0,00	0,00	0,00	0,00	0,00	0,00	0,00		
Mg	0,00	0,00	0,00	0,00	0,28	0,00	0,00	0,00	0,00	0,00	0,00	0,00	0,00	0,00		
Ca	0,46	0,33	0,61	0,45	0,37	0,46	0,44	0,33	0,33	0,48	0,49	0,24	0,26	0,17		
Na	0,53	0,68	0,44	0,55	0,41	0,57	0,56	0,74	0,67	0,54	0,56	0,76	0,75	0,86		
K	0,00	0,01	0,00	0,01	0,01	0,00	0,02	0,00	0,00	0,00	0,00	0,00	0,00	0,01		
Tot Cat	5,00	5,02	5,00	5,02	5,07	5,03	5,03	5,05	5,02	5,02	5,04	5,01	5,02	5,03		
ΣO	8	8	8	8	8	8	8	8	8	8	8	8	8	8		
Or	0,00	0,59	0,18	0,87	1,07	0,00	2,11	0,22	0,20	0,03	0,42	0,26	0,05	0,69		
Ab	53,80	67,09	42,00	54,51	52,24	55,07	54,79	69,24	66,72	52,88	53,40	75,82	74,13	82,70		
An	46,20	32,32	57,82	44,63	46,68	44,93	43,10	30,54	33,08	47,09	46,18	23,92	25,82	16,61		

Table 6: continued

[illegible]

Table 7: A-A' chemical profile of garnet crystal from LL56a3 micaschist. Analyses are shown in Fig. 3.4a.

[illegible]

Table 7: A-A' chemical profile continued.

[illegible]

Table 7: A-A' chemical profile continued.

Table 7: A-A' chemical profile continued.

Sample Descript.	LL 56a3		LL 56a3		LL 56a3		LL 56a3		LL 56a3		LL 56a3		LL 56a3		LL 56a3		LL 56a3	
	Grt A-A'	Grt A-A'	Grt A-A'	Grt A-A'	Grt A-A'	Grt A-A'	Grt A-A'	Grt A-A'	Grt A-A'	Grt A-A'	Grt A-A'	Grt A-A'	Grt A-A'	Grt A-A'	Grt A-A'	Grt A-A'	Grt A-A'	
SiO2	35.90	36.58	35.00	36.52	35.92	36.57	36.55	36.47	36.34	36.45	35.80	36.24	36.61	36.61	36.61	36.65	36.43	
TiO2	0.47	0.03	0.27	0.00	0.00	0.01	0.00	0.02	0.00	0.00	0.00	0.01	0.04	0.01	0.02	0.18	0.18	
Al2O3	20.70	20.88	20.42	20.98	20.94	20.98	20.93	20.93	20.91	20.87	21.86	20.84	20.83	20.87	20.76	20.74	20.74	
Fe2O3	0.38	0.68	1.02	0.70	0.22	0.60	0.81	0.73	0.69	0.83	0.00	0.86	0.83	0.97	1.00	0.62	0.62	
FeO	34.10	33.93	33.60	33.62	33.85	33.71	33.69	33.51	33.40	33.39	33.39	33.39	33.29	33.56	33.28	33.58	33.58	
MnO	5.48	5.52	5.47	5.02	5.55	5.48	5.53	5.57	5.41	5.38	5.12	5.22	5.21	5.00	4.96	4.73	4.73	
MgO	1.95	1.93	2.01	2.20	1.99	1.99	2.00	2.02	1.99	2.00	1.86	2.01	2.00	2.01	2.05	2.13	2.13	
CaO	1.36	1.27	1.38	1.13	1.25	1.37	1.40	1.46	1.56	1.69	1.70	1.71	1.97	2.00	2.15	1.96	1.96	
Na2O	0.03	0.02	0.03	0.02	0.03	0.02	0.02	0.01	0.02	0.00	0.04	0.00	0.02	0.02	0.01	0.00	0.00	
K2O	0.01	0.00	0.06	0.00	0.01	0.00	0.01	0.00	0.00	0.01	0.02	0.00	0.00	0.00	0.00	0.00	0.00	
Total	100.38	100.84	100.63	98.77	100.86	99.08	100.73	100.92	100.71	100.33	100.63	99.79	100.29	100.79	101.04	100.88	100.38	
Si	2.93	2.96	2.96	2.91	2.96	2.96	2.96	2.96	2.95	2.96	2.92	2.95	2.96	2.96	2.96	2.96	2.96	
Al IV	0.07	0.04	0.04	0.10	0.04	0.04	0.04	0.04	0.05	0.05	0.08	0.05	0.04	0.05	0.05	0.04	0.04	
Tot IV	3.00	3.00	3.00	3.00	3.00	3.00	3.00	3.00	3.00	3.00	3.00	3.00	3.00	3.00	3.00	3.00	3.00	
Al VI	1.92	1.96	1.94	1.90	1.99	1.96	1.95	1.95	1.96	1.95	2.02	1.95	1.95	1.94	1.94	1.94	1.94	
Ti	0.03	0.00	0.00	0.02	0.00	0.00	0.00	0.00	0.00	0.00	0.00	0.00	0.00	0.00	0.00	0.01	0.01	
Fe3+	0.02	0.04	0.06	0.06	0.04	0.01	0.04	0.05	0.04	0.05	0.00	0.05	0.05	0.06	0.06	0.04	0.04	
Tot S1	1.97	2.00	2.00	1.98	2.00	2.00	2.00	2.00	2.00	2.00	2.02	2.00	2.00	2.00	2.00	2.00	1.99	
Fe2+	2.33	2.30	2.28	2.33	2.29	2.28	2.28	2.27	2.27	2.26	2.28	2.27	2.25	2.27	2.25	2.28	2.28	
Mn	0.38	0.38	0.38	0.35	0.38	0.38	0.38	0.38	0.37	0.37	0.35	0.36	0.36	0.34	0.34	0.33	0.33	
Mg	0.24	0.23	0.24	0.27	0.24	0.24	0.24	0.24	0.24	0.24	0.23	0.24	0.24	0.24	0.25	0.26	0.26	
Ca	0.12	0.11	0.12	0.10	0.11	0.12	0.12	0.13	0.14	0.15	0.15	0.15	0.17	0.17	0.19	0.17	0.17	
Na	0.01	0.00	0.00	0.00	0.00	0.00	0.00	0.00	0.00	0.00	0.01	0.00	0.00	0.00	0.00	0.00	0.00	
K	0.00	0.00	0.00	0.01	0.00	0.00	0.00	0.00	0.00	0.00	0.00	0.00	0.00	0.00	0.00	0.00	0.00	
Tot S2	3.07	3.02	3.02	3.07	3.03	3.02	3.02	3.02	3.03	3.02	3.01	3.03	3.02	3.02	3.02	3.03	3.03	
Tot Cat	8.04	8.02	8.02	8.05	8.02	8.02	8.02	8.02	8.03	8.02	8.03	8.03	8.02	8.02	8.02	8.02	8.02	
ΣO	12	12	12	12	12	12	12	12	12	12	12	12	12	12	12	12	12	
Prp																		
Alm	7.75	7.71	8.04	8.91	7.95	7.96	7.99	8.05	7.99	7.99	7.53	8.07	7.99	7.99	8.18	8.48	8.48	
Grs	76.00	76.11	75.53	76.27	75.85	75.64	75.46	75.11	75.18	74.92	75.78	75.10	74.54	74.96	74.43	75.17	75.17	
Sps	2.74	1.58	1.26	0.17	1.48	2.14	1.57	2.00	2.39	2.34	4.93	2.33	3.15	2.81	3.15	3.78	3.78	
Adr	12.36	12.53	12.46	11.53	12.61	12.45	12.54	12.65	12.34	12.23	11.76	11.90	11.81	11.31	11.24	10.71	10.71	
XMg	1.14	2.07	2.71	3.13	2.11	1.81	2.44	2.19	2.10	2.52	0.00	2.61	2.50	2.93	3.01	1.86	1.86	
XMg	0.08	0.08	0.08	0.09	0.08	0.08	0.08	0.08	0.08	0.08	0.08	0.08	0.08	0.08	0.09	0.09	0.09	
XPpr																		
XAlm	0.08	0.08	0.08	0.09	0.08	0.08	0.08	0.08	0.08	0.08	0.08	0.08	0.08	0.08	0.08	0.08	0.08	
XGrs	0.76	0.76	0.76	0.76	0.76	0.76	0.75	0.75	0.75	0.75	0.76	0.75	0.75	0.75	0.74	0.75	0.75	
XSps	0.03	0.02	0.01	0.00	0.03	0.02	0.02	0.02	0.02	0.02	0.05	0.02	0.03	0.03	0.03	0.04	0.04	
XSps	0.12	0.13	0.12	0.12	0.13	0.12	0.13	0.13	0.12	0.12	0.12	0.12	0.12	0.11	0.11	0.11	0.11	
XAdr	0.01	0.02	0.03	0.03	0.02	0.02	0.02	0.02	0.02	0.03	0.00	0.03	0.03	0.03	0.03	0.02	0.02	

Table 7: A-A' chemical profile continued.

Sample Descrip.	LL 56a3			LL 56a3			LL 56a3			LL 56a3			LL 56a3			LL 56a3			LL 56a3		
	Grt A-A'	Grt A-A'	Grt A-A'	Grt A-A'	Grt A-A'	Grt A-A'	Grt A-A'	Grt A-A'	Grt A-A'	Grt A-A'	Grt A-A'	Grt A-A'	Grt A-A'	Grt A-A'	Grt A-A'	Grt A-A'	Grt A-A'	Grt A-A'	Grt A-A'	Grt A-A'	
SiO2	36,81	36,59	36,53	36,17	35,85	36,71	36,60	36,75	36,72	36,83	36,56	36,58	37,36	36,81	36,59	36,53	36,17	35,85	36,71	36,60	
TiO2	0,01	0,00	0,01	0,03	0,41	0,00	0,03	0,00	0,02	0,05	0,02	0,01	0,00	0,01	0,00	0,01	0,03	0,41	0,00	0,03	
Al2O3	20,82	20,88	20,68	20,74	20,87	20,80	20,90	20,90	20,99	20,77	20,77	20,77	20,47	20,82	20,88	20,68	20,74	20,87	20,80	20,90	
Fe2O3	0,86	0,96	0,93	0,83	0,31	0,75	0,66	0,73	0,56	0,69	0,85	0,69	0,71	0,86	0,96	0,93	0,83	0,31	0,75	0,66	
FeO	33,72	33,83	33,55	33,17	33,92	33,68	33,43	33,02	32,94	32,46	31,89	31,65	30,28	33,72	33,83	33,55	33,17	33,92	33,68	33,43	
MnO	4,67	4,65	4,77	4,65	4,73	4,77	4,94	5,30	5,55	6,02	6,72	7,44	8,16	4,67	4,65	4,77	4,65	4,73	4,77	4,94	
MgO	2,08	2,10	2,05	2,08	2,16	2,13	2,10	2,07	2,04	1,97	1,87	1,74	1,47	2,08	2,10	2,05	2,08	2,16	2,13	2,10	
CaO	2,02	1,90	2,09	2,07	1,68	1,80	1,81	2,05	1,93	2,00	1,97	1,67	1,68	2,02	1,90	2,09	2,07	1,68	1,80	1,81	
Na2O	0,01	0,03	0,01	0,02	0,00	0,01	0,02	0,00	0,00	0,00	0,02	0,00	0,01	0,01	0,03	0,01	0,02	0,00	0,01	0,02	
K2O	0,00	0,00	0,01	0,01	0,01	0,01	0,00	0,00	0,01	0,01	0,00	0,00	0,00	0,00	0,00	0,01	0,01	0,01	0,00	0,00	
Total	100,99	100,94	100,83	99,71	99,82	100,72	100,39	100,81	100,77	100,81	100,67	100,55	100,14	100,99	100,94	100,83	99,71	99,82	100,72	100,39	
Si	2,97	2,96	2,95	2,95	2,93	2,97	2,97	2,97	2,97	2,98	2,96	2,97	3,03	2,97	2,96	2,95	2,95	2,93	2,97	2,97	
AlIV	0,03	0,05	0,05	0,05	0,07	0,03	0,03	0,03	0,03	0,03	0,04	0,03	0,00	0,03	0,05	0,05	0,05	0,07	0,03	0,03	
Tot IV	3,00	3,00	3,00	3,00	3,00	3,00	3,00	3,00	3,00	3,00	3,00	3,00	3,03	3,00	3,00	3,00	3,00	3,00	3,00	3,00	
Al VI	1,95	1,94	1,94	1,95	1,93	1,96	1,96	1,96	1,96	1,95	1,95	1,96	1,96	1,95	1,94	1,94	1,95	1,93	1,96	1,96	
Ti	0,00	0,00	0,00	0,00	0,03	0,00	0,00	0,00	0,00	0,00	0,00	0,00	0,00	0,00	0,00	0,00	0,00	0,03	0,00	0,00	
Fe3+	0,05	0,06	0,06	0,05	0,02	0,05	0,04	0,05	0,03	0,04	0,05	0,04	0,04	0,05	0,06	0,06	0,05	0,02	0,05	0,04	
Tot S1	2,00	2,00	2,00	2,00	1,98	2,00	2,00	2,00	2,00	2,00	2,00	2,00	2,00	2,00	2,00	2,00	2,00	1,98	2,00	2,00	
Fe2+	2,27	2,29	2,27	2,27	2,32	2,28	2,27	2,23	2,23	2,19	2,16	2,15	2,05	2,27	2,29	2,27	2,27	2,32	2,28	2,27	
Mn	0,32	0,32	0,33	0,32	0,33	0,33	0,34	0,36	0,38	0,41	0,46	0,51	0,56	0,32	0,32	0,33	0,32	0,33	0,33	0,34	
Mg	0,25	0,25	0,25	0,25	0,26	0,26	0,25	0,25	0,25	0,24	0,23	0,21	0,18	0,25	0,25	0,25	0,25	0,26	0,26	0,25	
Ca	0,17	0,17	0,18	0,18	0,16	0,16	0,16	0,18	0,17	0,17	0,17	0,15	0,15	0,17	0,17	0,18	0,18	0,16	0,16	0,16	
Na	0,00	0,00	0,00	0,00	0,00	0,00	0,00	0,00	0,00	0,00	0,00	0,00	0,00	0,00	0,00	0,00	0,00	0,00	0,00	0,00	
K	0,00	0,00	0,00	0,00	0,00	0,00	0,00	0,00	0,00	0,00	0,00	0,00	0,00	0,00	0,00	0,00	0,00	0,00	0,00	0,00	
Tot S2	3,02	3,03	3,03	3,03	3,06	3,02	3,02	3,02	3,02	3,02	3,02	3,02	2,94	3,02	3,03	3,03	3,03	3,06	3,02	3,02	
Tot Cat	8,02	8,03	8,02	8,03	8,04	8,02	8,02	8,02	8,02	8,01	8,02	8,02	7,97	8,02	8,03	8,02	8,03	8,04	8,02	8,02	
ΣO	12	12	12	12	12	12	12	12	12	12	12	12	12	12	12	12	12	12	12	12	
Prp	8,30	8,38	8,18	8,39	8,60	8,50	8,40	8,26	8,15	7,87	7,48	6,97	6,03	8,30	8,38	8,18	8,39	8,60	8,50	8,40	
Alm	75,36	75,64	75,03	74,96	75,85	75,49	75,14	73,86	73,73	72,73	71,58	71,25	69,91	75,36	75,64	75,03	74,96	75,85	75,49	75,14	
Grs	3,19	2,56	3,20	3,48	3,89	2,92	3,21	3,65	3,83	3,64	3,10	2,73	2,77	3,19	2,56	3,20	3,48	3,89	2,92	3,21	
Sps	10,56	10,52	10,80	10,65	10,72	10,83	11,25	12,02	12,59	13,67	15,28	16,97	19,08	10,56	10,52	10,80	10,65	10,72	10,83	11,25	
Adr	2,60	2,89	2,79	2,52	0,94	2,25	2,00	2,21	1,70	2,10	2,56	2,09	2,21	2,60	2,89	2,79	2,52	0,94	2,25	2,00	
XMg	0,09	0,09	0,09	0,09	0,09	0,09	0,09	0,09	0,09	0,08	0,08	0,07	0,06	0,09	0,09	0,09	0,09	0,09	0,09	0,09	
XPrp	0,08	0,08	0,08	0,08	0,09	0,09	0,08	0,08	0,08	0,08	0,07	0,07	0,06	0,08	0,08	0,08	0,08	0,09	0,09	0,08	
XAlm	0,75	0,76	0,75	0,75	0,76	0,75	0,75	0,74	0,74	0,73	0,72	0,71	0,70	0,75	0,76	0,75	0,75	0,76	0,75	0,75	
XGrs	0,03	0,03	0,03	0,03	0,04	0,04	0,03	0,04	0,04	0,04	0,03	0,03	0,03	0,03	0,03	0,03	0,03	0,04	0,04	0,03	
XSps	0,11	0,11	0,11	0,11	0,11	0,11	0,11	0,12	0,13	0,14	0,15	0,17	0,19	0,11	0,11	0,11	0,11	0,11	0,11	0,11	
XAdr	0,03	0,03	0,03	0,03	0,01	0,02	0,02	0,02	0,02	0,02	0,03	0,02	0,02	0,03	0,03	0,03	0,03	0,01	0,02	0,02	

Table 7: A-A' chemical profile continued.

Sample Descrip.	LL 56a3 Grt B-B'	LL 56a3 Grt B-B'	LL 56a3 Grt B-B'	LL 56a3 Grt B-B'	LL 56a3 Grt B-B'	LL 56a3 Grt B-B'	LL 56a3 Grt B-B'	LL 56a3 Grt B-B'	LL 56a3 Grt B-B'	LL 56a3 Grt B-B'	LL 56a3 Grt B-B'	LL 56a3 Grt B-B'	LL 56a3 Grt B-B'	LL 56a3 Grt B-B'	LL 56a3 Grt B-B'	LL 56a3 Grt B-B'	LL 56a3 Grt B-B'	LL 56a3 Grt B-B'	LL 56a3 Grt B-B'	LL 56a3 Grt B-B'
SiO2	37,31	37,12	36,94	37,09	37,15	37,24	37,08	37,13	37,01	37,01	37,11	36,91	36,93	36,84	37,08	36,94	36,91	36,91	36,61	36,61
TiO2	0,18	0,10	0,19	0,12	0,17	0,16	0,12	0,16	0,14	0,08	0,12	0,15	0,11	0,08	0,11	0,09	0,14	0,16	0,16	0,16
Al2O3	20,30	20,63	20,47	20,46	20,60	20,50	20,44	20,41	20,41	20,55	20,51	20,36	20,48	20,47	20,38	20,43	20,47	20,37	20,37	20,37
Fe2O3	0,76	0,56	0,69	0,67	0,60	0,60	0,91	0,85	0,65	0,84	0,62	0,98	0,61	0,77	0,77	0,85	0,62	0,65	0,65	0,65
MnO	21,60	21,93	22,00	21,85	21,92	21,74	21,57	21,94	21,83	21,97	22,20	23,14	24,23	24,24	24,12	24,75	25,08	25,19	25,19	25,19
MgO	0,49	0,48	0,49	0,49	0,47	0,48	0,49	0,49	0,50	0,49	0,51	0,60	0,64	0,64	0,64	0,68	0,70	0,71	0,71	0,71
CaO	8,64	8,61	8,69	8,77	8,85	8,93	8,99	8,71	8,54	8,44	8,45	7,36	6,32	6,32	6,60	6,04	5,78	5,52	5,52	5,52
Na2O	0,01	0,01	0,03	0,00	0,02	0,01	0,03	0,02	0,00	0,03	0,00	0,01	0,01	0,01	0,01	0,01	0,01	0,01	0,01	0,01
K2O	0,00	0,00	0,00	0,00	0,01	0,00	0,01	0,01	0,01	0,00	0,00	0,00	0,00	0,00	0,00	0,00	0,01	0,01	0,01	0,01
Total	99,80	100,11	99,98	99,90	100,34	100,19	100,21	100,31	99,73	100,23	100,02	100,37	100,12	100,17	100,33	100,42	100,29	99,83	99,83	99,83
Si	3,01	2,99	2,99	3,00	2,99	3,00	2,99	2,99	3,00	2,99	3,00	2,98	2,99	2,99	3,00	2,99	2,99	2,98	2,98	2,98
Al IV	0,00	0,01	0,02	0,00	0,01	0,00	0,01	0,01	0,00	0,01	0,00	0,02	1,95	1,94	0,00	0,01	1,95	1,94	1,94	1,94
Tot IV	3,01	3,00	3,00	3,00	3,00	3,00	3,00	3,00	3,00	3,00	3,00	3,00	3,00	3,00	3,00	3,00	3,00	3,00	3,00	3,00
AL VI	1,93	1,95	1,94	1,94	1,94	1,94	1,93	1,93	1,94	1,94	1,95	1,92	1,95	1,94	1,94	1,94	1,95	1,94	1,94	1,94
Ti	0,01	0,01	0,01	0,01	0,01	0,01	0,01	0,01	0,01	0,01	0,01	0,01	0,01	0,01	0,01	0,01	0,01	0,01	0,01	0,01
Fe3+	0,05	0,03	0,04	0,04	0,04	0,04	0,06	0,05	0,04	0,05	0,04	0,06	0,04	0,05	0,05	0,05	0,04	0,04	0,04	0,04
Tot S1	1,99	1,99	1,99	1,99	1,99	1,99	1,99	1,99	1,99	2,00	1,99	1,99	1,99	2,00	1,99	2,00	1,99	1,99	1,99	1,99
Fe2+	1,46	1,48	1,49	1,48	1,48	1,46	1,45	1,48	1,48	1,48	1,50	1,56	1,64	1,64	1,63	1,68	1,70	1,72	1,72	1,72
Mn	0,72	0,73	0,72	0,71	0,72	0,72	0,72	0,72	0,73	0,74	0,72	0,74	0,74	0,74	0,73	0,73	0,73	0,73	0,73	0,73
Mg	0,06	0,06	0,06	0,06	0,06	0,06	0,06	0,06	0,06	0,06	0,06	0,07	0,08	0,08	0,08	0,08	0,08	0,09	0,09	0,09
Ca	0,75	0,74	0,75	0,76	0,76	0,77	0,78	0,75	0,74	0,73	0,73	0,64	0,55	0,55	0,57	0,52	0,50	0,48	0,48	0,48
Na	0,00	0,00	0,00	0,00	0,00	0,00	0,00	0,00	0,00	0,00	0,00	0,00	0,00	0,00	0,00	0,00	0,00	0,00	0,00	0,00
K	0,00	0,00	0,00	0,00	0,00	0,00	0,00	0,00	0,00	0,00	0,00	0,00	0,00	0,00	0,00	0,00	0,00	0,00	0,00	0,00
Tot S2	2,99	3,01	3,02	3,01	3,02	3,01	3,02	3,02	3,01	3,01	3,01	3,02	3,01	3,01	3,01	3,01	3,01	3,02	3,02	3,02
Tot Cat	7,99	8,00	8,01	8,00	8,01	8,00	8,01	8,01	8,00	8,01	8,00	8,01	8,00	8,01	8,00	8,01	8,01	8,01	8,01	8,01
ΣO	12	12	12	12	12	12	12	12	12	12	12	12	12	12	12	12	12	12	12	12
Prp	1,97	1,93	1,96	1,98	1,88	1,92	1,95	1,95	2,01	1,94	2,02	2,40	2,55	2,55	2,57	2,71	2,81	2,85	2,85	2,85
Alm	48,90	49,14	49,29	49,07	48,96	48,63	48,29	49,08	49,12	49,24	49,82	51,85	54,57	54,60	54,23	55,65	56,42	56,91	56,91	56,91
Grs	22,74	23,02	22,85	23,20	23,50	23,78	23,03	22,41	22,63	21,70	22,42	18,16	16,38	15,90	16,69	14,82	14,80	13,99	13,99	13,99
Sps	24,20	24,20	23,82	23,71	23,85	23,86	23,99	24,00	24,26	24,59	23,86	24,63	24,64	24,60	24,17	24,26	24,10	24,26	24,26	24,26
Adr	2,32	1,70	2,09	2,04	1,82	1,81	2,74	2,55	1,99	2,54	1,88	2,97	1,86	2,34	2,34	2,57	1,87	2,00	2,00	2,00
XMg	0,03	0,03	0,03	0,03	0,03	0,03	0,03	0,03	0,03	0,03	0,03	0,03	0,03	0,03	0,03	0,03	0,03	0,03	0,03	0,03
XPrp	0,02	0,02	0,02	0,02	0,02	0,02	0,02	0,02	0,02	0,02	0,02	0,02	0,03	0,03	0,03	0,03	0,03	0,03	0,03	0,03
XAlm	0,49	0,49	0,49	0,49	0,49	0,49	0,48	0,49	0,49	0,49	0,50	0,52	0,55	0,55	0,54	0,56	0,56	0,57	0,57	0,57
XGrs	0,23	0,23	0,23	0,23	0,23	0,24	0,23	0,22	0,22	0,22	0,18	0,16	0,16	0,16	0,17	0,15	0,15	0,15	0,15	0,15
XSps	0,24	0,24	0,24	0,24	0,24	0,24	0,24	0,24	0,24	0,25	0,24	0,25	0,25	0,25	0,24	0,24	0,24	0,24	0,24	0,24
XAdr	0,02	0,02	0,02	0,02	0,02	0,02	0,03	0,03	0,02	0,03	0,02	0,03	0,02	0,02	0,02	0,03	0,02	0,02	0,02	0,02

Table 7: B-B' chemical profile of garnet crystal from LL56a3 micascist. Analyses are shown in Fig. 3.4b.

Sample Descrip.	LL 56a3		LL 56a3		LL 56a3		LL 56a3		LL 56a3		LL 56a3		LL 56a3		LL 56a3		LL 56a3		LL 56a3	
	Grt	B'-B'	Grt	B'-B'	Grt	B'-B'	Grt	B'-B'	Grt	B'-B'	Grt	B'-B'	Grt	B'-B'	Grt	B'-B'	Grt	B'-B'	Grt	B'-B'
SiO2	36.54	36.74	36.66	36.24	36.01	36.06	36.06	36.62	36.51	36.75	36.17	36.62	36.35	36.56	36.15	36.62	36.54	36.72	36.73	36.68
TiO2	0.06	0.05	0.04	0.07	0.22	0.06	0.06	0.07	0.30	0.06	0.09	0.05	0.09	0.05	0.04	0.05	0.03	0.05	0.10	0.07
Al2O3	20.41	20.32	20.42	20.79	20.69	21.04	21.04	20.41	20.44	20.32	20.29	20.40	21.12	20.31	21.14	20.38	20.36	20.51	20.41	20.54
Fe2O3	0.84	0.91	1.01	0.55	0.30	0.58	1.24	0.58	0.83	1.08	1.00	0.23	1.32	0.73	1.22	1.18	1.15	0.88	1.04	
FeO	25.67	26.15	27.07	27.29	27.34	27.50	27.44	28.00	27.75	28.06	28.06	28.19	28.47	27.99	28.49	27.89	28.26	28.32	28.29	
MnO	10.41	10.44	10.29	10.20	9.92	9.91	9.95	9.95	9.88	9.67	8.83	9.42	9.33	9.50	9.26	9.22	9.21	9.26	9.19	
MgO	0.77	0.81	0.90	0.91	0.91	0.97	1.00	1.00	1.01	1.03	1.45	1.08	1.06	1.12	1.09	1.08	1.11	1.10	1.10	
CaO	5.15	4.71	4.07	3.97	4.08	4.08	4.10	4.10	3.88	3.87	3.37	3.76	3.71	3.76	3.89	4.16	3.72	3.87	4.08	
Na2O	0.00	0.01	0.04	0.00	0.02	0.05	0.02	0.02	0.02	0.02	0.05	0.01	0.02	0.01	0.01	0.01	-0.01	0.02	0.01	
K2O	0.01	0.00	0.00	0.00	0.00	0.03	0.00	0.00	0.00	0.00	0.12	0.00	0.01	0.00	0.00	0.00	-0.01	0.00	0.00	
Total	99.87	100.14	100.49	100.02	99.49	100.27	100.85	100.85	100.87	100.55	99.43	100.73	100.38	100.61	100.79	100.64	100.39	101.01	100.48	100.83
Si	2.98	2.99	2.98	2.96	2.95	2.94	2.97	2.97	2.96	2.98	2.97	2.97	2.95	2.97	2.93	2.97	2.97	2.98	2.97	
Al IV	1.94	1.94	1.93	1.96	1.95	1.96	0.03	0.03	1.91	1.93	1.93	1.92	1.98	1.91	0.07	0.03	1.92	0.03	1.93	
Tot IV	3.00	3.00	3.00	3.00	3.00	3.00	3.00	3.00	3.00	3.00	3.00	3.00	3.00	3.00	3.00	3.00	3.00	3.00	3.00	
Al VI	1.94	1.94	1.93	1.96	1.95	1.96	1.92	1.92	1.91	1.93	1.93	1.92	1.98	1.91	1.95	1.92	1.92	1.94	1.93	
Ti	0.00	0.00	0.00	0.00	0.01	0.00	0.00	0.00	0.02	0.00	0.01	0.00	0.01	0.00	0.00	0.00	0.00	0.01	0.00	
Fe3+	0.05	0.06	0.06	0.03	0.02	0.04	0.08	0.08	0.05	0.07	0.06	0.07	0.01	0.08	0.05	0.08	0.07	0.05	0.06	
Tot S1	2.00	2.00	2.00	2.00	1.99	2.00	2.00	2.00	1.98	2.00	2.00	2.00	2.00							

Table 7: B-B' chemical profile continued.

Sample Descrip.	LL 56a3 Grt B-B'	LL 56a3 Grt B-B'	LL 56a3 Grt B-B'	LL 56a3 Grt B-B'	LL 56a3 Grt B-B'	LL 56a3 Grt B-B'	LL 56a3 Grt B-B'	LL 56a3 Grt B-B'	LL 56a3 Grt B-B'	LL 56a3 Grt B-B'	LL 56a3 Grt B-B'	LL 56a3 Grt B-B'	LL 56a3 Grt B-B'	LL 56a3 Grt B-B'	LL 56a3 Grt B-B'	LL 56a3 Grt B-B'	LL 56a3 Grt B-B'	LL 56a3 Grt B-B'	LL 56a3 Grt B-B'
SiO2	36.71	36.60	36.80	36.62	36.88	36.76	36.68	35.98	36.53	36.41	36.71	36.59	36.52	35.90	36.45	36.87	36.50	36.59	36.20
TiO2	0.04	0.03	0.06	0.06	0.05	0.04	0.03	0.20	0.03	0.04	0.05	0.05	0.07	0.04	0.07	0.09	0.06	0.04	0.07
Al2O3	21.03	20.73	20.40	20.49	20.46	20.46	20.47	20.48	20.48	20.31	20.54	20.48	20.41	20.96	20.53	20.51	20.45	20.38	20.86
Fe2O3	0.00	0.90	1.17	0.95	0.94	1.08	1.11	0.85	1.00	1.31	1.03	1.13	1.26	0.59	1.14	1.04	1.15	1.15	0.52
FeO	28.03	28.68	28.64	28.79	28.91	29.10	29.33	29.56	29.44	29.81	29.93	30.18	30.29	30.63	30.73	30.68	31.06	31.04	31.38
MnO	8.42	9.10	9.00	8.75	8.55	8.58	8.42	8.26	8.20	8.14	7.94	7.81	7.97	7.66	7.65	7.53	7.46	7.51	7.53
MgO	1.15	1.18	1.20	1.23	1.25	1.27	1.31	1.34	1.36	1.39	1.45	1.49	1.48	1.52	1.55	1.56	1.63	1.63	1.66
CaO	3.87	3.60	3.67	3.54	3.62	3.48	3.35	3.16	3.23	2.97	3.13	2.94	2.76	2.52	2.57	2.81	2.31	2.20	1.85
Na2O	0.02	0.01	0.00	0.02	0.01	0.00	0.01	0.00	0.01	0.01	0.01	0.02	0.02	0.00	0.02	0.01	0.00	0.00	0.02
K2O	0.15	0.00	0.00	0.02	0.01	0.00	0.00	0.00	0.01	0.00	0.00	0.00	0.00	0.02	0.01	0.01	0.00	0.00	0.01
Total	99.42	100.83	100.94	100.47	100.68	100.79	100.70	99.84	100.30	100.40	100.80	100.68	100.77	99.82	100.72	101.12	100.63	100.55	100.10
Si	2.99	2.96	2.98	2.97	2.99	2.98	2.97	2.95	2.97	2.97	2.97	2.97	2.96	2.94	2.96	2.98	2.97	2.97	2.95
Al IV	2.01	1.94	0.02	1.93	1.94	0.02	1.93	1.92	1.94	1.91	1.93	1.93	1.91	1.96	1.92	1.93	1.92	0.03	1.96
Tot IV	3.00	3.00	3.00	3.00	3.00	3.00	3.00	3.00	3.00	3.00	3.00	3.00	3.00	3.00	3.00	3.00	3.00	3.00	3.00
Al VI	2.01	1.94	1.92	1.93	1.94	1.93	1.93	1.92	1.94	1.91	1.93	1.93	1.91	1.96	1.92	1.93	1.92	1.93	1.96
Ti	0.00	0.00	0.00	0.00	0.00	0.00	0.00	0.01	0.00	0.00	0.00	0.00	0.01	0.00	0.00	0.01	0.00	0.00	0.00
Fe3+	0.00	0.06	0.07	0.06	0.06	0.07	0.07	0.05	0.06	0.08	0.06	0.07	0.08	0.04	0.07	0.06	0.07	0.07	0.03
Tot S1	2.02	2.00	2.00	2.00	2.00	2.00	2.00	1.99	2.00	2.00	2.00	2.00	2.00	2.00	2.00	1.99	2.00	2.00	2.00
Fe2+	1.91	1.94	1.94	1.96	1.96	1.97	1.99	2.02	2.00	2.03	2.03	2.05	2.06	2.10	2.09	2.07	2.11	2.11	2.14
Mn	0.58	0.62	0.62	0.60	0.59	0.59	0.58	0.57	0.57	0.56	0.54	0.54	0.55	0.53	0.53	0.52	0.51	0.52	0.52
Mg	0.14	0.14	0.14	0.15	0.15	0.15	0.16	0.16	0.17	0.17	0.18	0.18	0.18	0.19	0.19	0.19	0.20	0.20	0.20
Ca	0.34	0.31	0.32	0.31	0.31	0.30	0.29	0.28	0.28	0.26	0.27	0.26	0.24	0.22	0.22	0.24	0.20	0.19	0.16
Na	0.00	0.00	0.00	0.00	0.00	0.00	0.00	0.00	0.00	0.00	0.00	0.00	0.00	0.00	0.00	0.00	0.00	0.00	0.00
K	0.02	0.00	0.00	0.00	0.00	0.00	0.00	0.00	0.00	0.00	0.00	0.00	0.00	0.00	0.00	0.00	0.00	0.00	0.00
Tot S2	2.99	3.02	3.02	3.02	3.01	3.01	3.02	3.04	3.02	3.02	3.02	3.02	3.02	3.03	3.03	3.02	3.02	3.02	3.03
Tot Cat	8.00	8.02	8.01	8.02	8.01	8.01	8.01	8.03	8.02	8.02	8.02	8.02	8.02	8.03	8.02	8.01	8.02	8.01	8.03
ΣO	12	12	12	12	12	12	12	12	12	12	12	12	12	12	12	12	12	12	12
Prp	4.69	4.70	4.78	4.95	5.00	5.10	5.24	5.39	5.48	5.58	5.82	5.95	5.91	6.10	6.20	6.24	6.53	6.56	6.68
Alm	64.34	64.30	64.23	64.87	65.07	65.37	65.93	66.63	66.44	67.24	67.15	67.83	68.03	69.11	69.01	68.64	69.83	69.93	70.78
Grs	11.39	7.60	7.00	7.34	7.60	6.73	6.28	6.54	6.29	4.58	5.89	5.01	4.13	5.48	3.94	4.94	3.17	2.86	3.75
Sps	19.58	20.67	20.45	19.97	19.48	19.51	19.17	18.86	18.75	18.60	18.03	17.77	18.12	17.52	17.40	17.06	17.00	17.15	17.20
Adr	0.00	2.73	3.54	2.88	2.85	3.29	3.37	2.59	3.04	4.00	3.12	3.44	3.81	1.79	3.45	3.13	3.48	3.50	1.59
XMg	0.05	0.05	0.05	0.06	0.06	0.06	0.06	0.06	0.06	0.06	0.06	0.06	0.06	0.07	0.07	0.07	0.07	0.07	0.07
XPrp	0.05	0.05	0.05	0.05	0.05	0.05	0.05	0.05	0.05	0.06	0.06	0.06	0.06	0.06	0.06	0.06	0.07	0.07	0.07
XAlm	0.64	0.64	0.64	0.65	0.65	0.65	0.66	0.67	0.66	0.67	0.67	0.68	0.68	0.69	0.69	0.69	0.70	0.70	0.71
XGrs	0.11	0.08	0.07	0.07	0.08	0.07	0.06	0.07	0.06	0.05	0.06	0.05	0.04	0.05	0.04	0.05	0.03	0.03	0.04
XSps	0.20	0.21	0.20	0.20	0.19	0.20	0.19	0.19	0.19	0.19	0.18	0.18	0.18	0.18	0.17	0.17	0.17	0.17	0.17
XAdr	0.00	0.03	0.04	0.03	0.03	0.03	0.03	0.03	0.03	0.04	0.03	0.03	0.04	0.02	0.03	0.03	0.03	0.04	0.02

Table 7: B-B' chemical profile continued.

Sample Descrip.	LL 56a3		LL 56a3		LL 56a3		LL 56a3		LL 56a3		LL 56a3		LL 56a3		LL 56a3		LL 56a3		LL 56a3	
	Grt B-B'	Grt B-B'	Grt B-B'	Grt B-B'	Grt B-B'	Grt B-B'	Grt B-B'	Grt B-B'	Grt B-B'	Grt B-B'	Grt B-B'	Grt B-B'	Grt B-B'	Grt B-B'	Grt B-B'	Grt B-B'	Grt B-B'	Grt B-B'	Grt B-B'	Grt B-B'
SiO2	36.70	36.69	36.53	36.74	36.53	36.72	35.98	36.29	36.56	36.30	35.58	36.21	36.54	35.77	36.07	36.55	36.58	36.22	36.88	
TiO2	0.00	0.05	0.21	0.01	0.02	0.05	0.03	0.05	0.06	0.57	0.03	0.04	0.04	0.04	0.00	0.00	0.00	0.05	0.00	
Al2O3	20.48	20.41	20.49	20.49	20.80	20.44	21.04	21.01	20.91	20.36	20.84	21.03	20.47	20.27	21.38	20.46	20.60	20.56	20.53	
Fe2O3	1.31	1.33	0.83	1.00	0.79	1.14	0.57	0.60	0.58	0.41	0.59	0.62	1.01	1.15	0.41	1.13	0.97	0.85	1.10	
Fo	31.44	31.30	32.04	31.61	31.86	31.82	31.89	32.01	32.07	32.64	32.01	32.33	32.01	31.99	32.74	32.39	32.20	32.13	32.41	
MnO	7.41	7.29	7.29	7.04	7.06	7.19	7.06	7.02	7.15	7.07	6.90	7.20	7.11	6.64	6.99	7.10	7.13	6.92	7.05	
MgO	1.73	1.72	1.53	1.74	1.75	1.80	1.76	1.82	1.82	1.82	1.80	1.73	1.81	1.95	1.82	1.72	1.86	1.93	1.85	
CaO	2.01	2.25	1.97	1.99	1.87	1.72	1.75	1.75	1.61	1.47	1.40	1.45	1.49	1.24	1.25	1.33	1.31	1.26	1.37	
Na2O	0.00	0.00	0.00	0.00	0.03	0.02	0.01	0.00	0.01	0.03	0.01	0.02	0.01	0.02	0.02	0.01	0.00	0.01	0.00	
K2O	0.00	0.00	0.00	0.01	0.00	0.00	0.00	0.01	0.00	0.00	0.01	0.01	0.00	0.05	0.00	0.01	0.00	0.00	0.01	
Total	101.09	101.04	100.89	100.64	100.72	100.89	100.08	100.54	100.75	100.67	99.17	100.64	100.49	99.12	100.68	100.69	100.65	99.93	101.18	
Si	2.97	2.97	2.96	2.98	2.96	2.97	2.94	2.95	2.96	2.95	2.93	2.94	2.97	2.95	2.93	2.97	2.97	2.96	2.98	
Al IV	0.03	0.03	0.04	1.94	1.95	1.93	1.96	0.05	1.96	0.05	1.96	1.96	1.93	1.92	1.98	0.03	0.03	1.94	0.02	
Tot IV	3.00	3.00	3.00	3.00	3.00	3.00	3.00	3.00	3.00	3.00	3.00	3.00	3.00	3.00	3.00	3.00	3.00	3.00	3.00	
Al VI	1.92	1.91	1.92	1.94	1.95	1.93	1.96	1.96	1.96	1.91	1.96	1.96	1.93	1.92	1.98	1.93	1.94	1.94	1.93	
Ti	0.00	0.00	0.01	0.00	0.00	0.00	0.00	0.00	0.00	0.04	0.00	0.00	0.00	0.00	0.00	0.00	0.00	0.00	0.00	
Fe3+	0.08	0.08	0.05	0.06	0.05	0.07	0.04	0.04	0.04	0.03	0.04	0.04	0.06	0.07	0.03	0.07	0.06	0.05	0.07	
Tot S1	2.00	2.00	1.99	2.00	2.00	2.00	2.00	2.00	2.00	1.97	2.00	2.00	2.00	2.00	2.00	2.00	2.00	2.00	2.00	
Fe2+	2.13	2.12	2.17	2.14	2.16	2.16	2.18	2.17	2.17	2.22	2.21	2.20	2.18	2.21	2.22	2.20	2.19	2.20	2.19	
Mn	0.51	0.50	0.50	0.48	0.49	0.49	0.49	0.48	0.49	0.49	0.48	0.50	0.49	0.46	0.48	0.49	0.48	0.48	0.48	
Mg	0.21	0.21	0.19	0.21	0.21	0.22	0.21	0.22	0.22	0.22	0.22	0.21	0.22	0.24	0.22	0.21	0.23	0.24	0.22	
Ca	0.17	0.20	0.17	0.17	0.16	0.15	0.15	0.15	0.14	0.13	0.12	0.13	0.13	0.11	0.11	0.12	0.11	0.11	0.12	
Na	0.00	0.00	0.00	0.00	0.00	0.00	0.00	0.00	0.00	0.00	0.00	0.00	0.00	0.00	0.00	0.00	0.00	0.00	0.00	
K	0.00	0.00	0.00	0.00	0.00	0.00	0.00	0.00	0.00	0.00	0.00	0.00	0.00	0.01	0.00	0.00	0.00	0.00	0.00	
Tot S2	3.02	3.02	3.03	3.01	3.02	3.02	3.03	3.03	3.02	3.06	3.04	3.03	3.02	3.03	3.04	3.02	3.02	3.02	3.01	
Tot Cat	8.02	8.02	8.02	8.01	8.02	8.01	8.03	8.03	8.02	8.03	8.03	8.03	8.02	8.03	8.04	8.02	8.02	8.02	8.01	
ΣO	12	12	12	12	12	12	12	12	12	12	12	12	12	12	12	12	12	12	12	
Prp	6.90	6.86	6.11	6.97	7.02	7.20	7.05	7.26	7.25	7.22	7.30	6.91	7.29	7.95	7.27	6.91	7.45	7.79	7.39	
Alm	70.50	70.14	71.72	71.21	71.55	71.49	71.81	71.77	71.89	72.66	72.75	72.55	72.18	73.05	73.29	73.05	72.51	72.70	72.68	
Grs	1.80	2.43	3.13	2.70	2.96	1.49	3.32	3.21	2.87	2.26	2.26	2.30	1.25	0.08	2.34	0.39	0.83	1.07	0.59	
Sps	16.83	16.54	16.52	16.07	16.04	16.36	16.10	15.95	16.24	15.93	15.88	16.36	16.23	15.36	15.85	16.21	16.26	15.86	16.01	
Adr	3.98	4.03	2.52	3.05	2.41	3.45	1.73	1.82	1.75	1.25	1.82	1.88	3.06	3.56	1.25	3.45	2.95	2.59	3.34	
XMg	0.07	0.07	0.06	0.07	0.07	0.08	0.07	0.08	0.08	0.08	0.08	0.07	0.08	0.08	0.08	0.07	0.08	0.08	0.08	
XPrp	0.07	0.07	0.06	0.07	0.07	0.07	0.07	0.07	0.07	0.07	0.07	0.07	0.07	0.08	0.07	0.07	0.07	0.08	0.07	
XAlm	0.71	0.70	0.72	0.71	0.72	0.71	0.72	0.72	0.72	0.73	0.73	0.73	0.72	0.73	0.73	0.73	0.73	0.73	0.73	
XGrs	0.02	0.02	0.03	0.03	0.03	0.01	0.03	0.03	0.03	0.02	0.02	0.02	0.01	0.02	0.02	0.00	0.01	0.01	0.01	
XSps	0.17	0.17	0.17	0.16	0.16	0.16	0.16	0.16	0.16	0.16	0.16	0.16	0.16	0.15	0.16	0.16	0.16	0.16	0.16	
XAdr	0.04	0.04	0.03	0.03	0.02	0.03	0.02	0.02	0.02	0.01	0.02	0.02	0.03	0.04	0.01	0.03	0.03	0.03	0.03	

Table 7: B-B' chemical profile continued.

Sample Descrip.	LL 56a3 Grt B-B'	LL 56a3 Grt B-B'	LL 56a3 Grt B-B'	LL 56a3 Grt B-B'	LL 56a3 Grt B-B'	LL 56a3 Grt B-B'	LL 56a3 Grt B-B'	LL 56a3 Grt B-B'	LL 56a3 Grt B-B'	LL 56a3 Grt B-B'	LL 56a3 Grt B-B'	LL 56a3 Grt B-B'
SiO2	36.37	36.79	36.26	35.54	36.63	35.53	36.42	36.86	36.70	36.59	36.64	36.72
TiO2	0.00	0.00	0.01	0.00	0.00	0.01	0.00	0.01	0.01	0.02	0.00	0.03
Al2O3	20.31	20.55	20.55	20.91	20.65	20.97	20.24	20.76	20.59	20.68	20.67	20.61
Fe2O3	1.45	1.09	1.15	0.60	0.90	0.80	1.14	0.74	0.78	0.98	0.70	0.49
FeO	32.09	32.36	32.12	31.82	32.39	31.90	32.07	32.57	32.14	32.13	31.70	31.38
MnO	7.09	7.01	6.96	6.86	7.27	6.56	7.60	7.68	7.37	7.68	7.48	7.46
MgO	1.94	1.92	2.05	2.01	1.84	2.49	1.51	1.54	1.85	1.82	1.77	1.71
CaO	1.25	1.29	1.21	1.23	1.10	0.97	1.19	1.17	1.10	1.12	1.44	1.70
Na2O	0.00	0.01	0.00	0.02	0.01	0.04	0.01	0.00	0.01	0.01	0.01	0.01
K2O	0.02	0.00	0.01	0.06	0.01	0.01	0.02	0.00	0.01	0.00	0.00	0.00
Total	100.52	101.01	100.34	99.06	100.79	99.28	100.20	101.32	100.56	101.03	100.39	100.10
Si	2.96	2.98	2.95	2.93	2.97	2.92	2.98	2.98	2.98	2.96	2.98	2.99
Al IV	0.04	1.93	1.93	0.07	0.03	1.95	0.02	0.02	1.95	1.94	1.96	1.97
Tot IV	3.00	3.00	3.00	3.00	3.00	3.00	3.00	3.00	3.00	3.00	3.00	3.00
Al VI	1.91	1.93	1.93	1.96	1.95	1.95	1.93	1.95	1.95	1.94	1.96	1.97
Ti	0.00	0.00	0.00	0.00	0.00	0.00	0.00	0.00	0.00	0.00	0.00	0.00
Fe3+	0.09	0.07	0.07	0.04	0.06	0.05	0.07	0.05	0.05	0.06	0.04	0.03
Tot S1	2.00	2.00	2.00	2.00	2.00	2.00	2.00	2.00	2.00	2.00	2.00	2.00
Fe2+	2.19	2.19	2.19	2.19	2.20	2.19	2.19	2.20	2.18	2.18	2.16	2.14
Mn	0.49	0.48	0.48	0.48	0.50	0.46	0.53	0.53	0.51	0.53	0.52	0.52
Mg	0.24	0.23	0.25	0.25	0.22	0.31	0.19	0.19	0.22	0.22	0.21	0.21
Ca	0.11	0.11	0.11	0.11	0.10	0.09	0.10	0.10	0.10	0.10	0.13	0.15
Na	0.00	0.00	0.00	0.00	0.00	0.01	0.00	0.00	0.00	0.00	0.00	0.00
K	0.00	0.00	0.00	0.01	0.00	0.00	0.00	0.00	0.00	0.00	0.00	0.00
Tot S2	3.02	3.01	3.03	3.04	3.02	3.05	3.01	3.01	3.01	3.02	3.01	3.01
Tot Cat	8.02	8.01	8.02	8.04	8.02	8.04	8.01	8.01	8.01	8.02	8.01	8.01
ΣO	12	12	12	12	12	12	12	12	12	12	12	12
Prp	7.74	7.68	8.23	8.17	7.37	10.03	6.13	6.14	7.45	7.26	7.11	6.90
Alm	71.80	72.67	72.37	72.43	72.91	72.12	72.88	73.05	72.54	72.08	71.59	71.06
Grs	0.00	0.40	0.00	1.75	0.42	0.38	0.00	1.11	0.78	0.25	2.04	3.44
Sps	16.07	15.95	15.89	15.81	16.57	15.03	17.49	17.45	16.84	17.44	17.12	17.12
Adr	4.39	3.30	3.51	1.85	2.74	2.44	3.50	2.25	2.39	2.97	2.14	1.49
XMg	0.08	0.08	0.09	0.08	0.08	0.10	0.06	0.06	0.08	0.07	0.07	0.07
XPrp	0.08	0.08	0.08	0.08	0.07	0.10	0.06	0.06	0.07	0.07	0.07	0.07
XAlm	0.72	0.73	0.72	0.72	0.73	0.72	0.73	0.73	0.73	0.72	0.72	0.71
XGrs	0.00	0.00	0.00	0.02	0.00	0.00	0.00	0.01	0.01	0.00	0.02	0.03
XSps	0.16	0.16	0.16	0.16	0.17	0.15	0.17	0.17	0.17	0.17	0.17	0.17
XAdr	0.04	0.03	0.04	0.02	0.03	0.02	0.04	0.02	0.02	0.03	0.02	0.01

Table 7: B-B' chemical profile continued.

Sample Descrip.	LL 56a4 Grt C-C'	LL 56a4 Grt C-C'	LL 56a4 Grt C-C'	LL 56a4 Grt C-C'	LL 56a4 Grt C-C'	LL 56a4 Grt C-C'	LL 56a4 Grt C-C'	LL 56a4 Grt C-C'	LL 56a4 Grt C-C'	LL 56a4 Grt C-C'	LL 56a4 Grt C-C'	LL 56a4 Grt C-C'	LL 56a4 Grt C-C'	LL 56a4 Grt C-C'	LL 56a4 Grt C-C'	LL 56a4 Grt C-C'	LL 56a4 Grt C-C'	LL 56a4 Grt C-C'	LL 56a4 Grt C-C'
SiO2	36,67	36,60	36,63	36,59	36,64	36,72	36,84	36,58	36,70	36,75	36,81	36,71	36,70	36,65	36,63	36,74	36,50	36,42	36,60
TiO2	0,21	0,12	0,12	0,16	0,15	0,09	0,10	0,12	0,14	0,10	0,14	0,10	0,13	0,10	0,11	0,15	0,14	0,12	0,16
Al2O3	20,24	20,17	20,15	20,19	20,11	20,15	20,21	20,16	20,19	20,09	20,19	20,21	20,13	20,10	20,14	20,02	20,10	19,95	20,18
Fe2O3	0,26	0,44	0,51	0,47	0,66	0,66	0,60	0,52	0,46	0,72	0,54	0,57	0,61	0,67	0,65	0,71	0,57	0,78	0,48
FeO	22,16	21,80	21,62	21,99	21,88	21,65	21,52	21,76	21,71	21,55	21,78	21,73	21,81	21,55	21,80	21,28	21,96	21,74	22,10
MnO	10,95	10,87	10,99	11,06	11,07	10,93	10,89	10,85	10,89	11,00	10,90	10,98	10,86	11,01	10,95	11,14	10,77	11,09	10,91
MgO	0,51	0,49	0,49	0,49	0,49	0,48	0,49	0,48	0,48	0,49	0,48	0,49	0,49	0,48	0,49	0,51	0,51	0,50	0,47
CaO	7,30	7,48	7,57	7,60	7,75	7,71	7,79	7,76	7,69	7,66	7,60	7,65	7,70	7,71	7,73	7,70	7,79	7,63	7,69
Na2O	0,04	0,01	0,00	0,01	0,02	0,03	0,02	0,02	0,02	0,01	0,02	0,02	0,01	0,00	0,00	0,01	0,00	0,00	0,02
K2O	0,00	0,00	0,00	0,00	0,00	0,00	0,00	0,00	0,00	0,01	0,00	0,00	0,00	0,00	0,00	0,00	0,00	0,00	0,00
Total	98,33	97,98	98,08	98,55	98,77	98,41	98,47	98,24	98,29	98,39	98,46	98,45	98,44	98,26	98,49	98,27	98,35	98,22	98,62
Si	3,01	3,01	3,01	3,00	3,00	3,01	3,02	3,01	3,01	3,02	3,02	3,01	3,01	3,01	3,01	3,02	3,00	3,00	3,00
Al IV	0,00	0,00	0,00	0,00	0,00	0,00	0,00	0,00	0,00	0,00	0,00	0,00	0,00	0,00	0,00	0,00	0,00	0,00	0,00
Tot IV	3,01	3,01	3,01	3,00	3,00	3,01	3,02	3,01	3,01	3,02	3,02	3,01	3,01	3,01	3,01	3,02	3,00	3,00	3,00
Al VI	1,96	1,96	1,95	1,95	1,94	1,95	1,95	1,95	1,95	1,94	1,95	1,95	1,95	1,95	1,95	1,94	1,95	1,94	1,95
Ti	0,01	0,01	0,01	0,01	0,01	0,01	0,01	0,01	0,01	0,01	0,01	0,01	0,01	0,01	0,01	0,01	0,01	0,01	0,01
Fe3+	0,02	0,03	0,03	0,03	0,04	0,04	0,04	0,03	0,03	0,05	0,03	0,04	0,04	0,04	0,04	0,04	0,04	0,05	0,03
Tot S1	1,99	1,99	1,99	1,99	1,99	1,99	1,99	1,99	1,99	1,99	1,99	1,99	1,99	1,99	1,99	1,99	1,99	1,99	1,99
Fe2+	1,52	1,50	1,49	1,51	1,50	1,49	1,47	1,50	1,49	1,48	1,49	1,49	1,50	1,48	1,50	1,46	1,51	1,50	1,52
Mn	0,76	0,76	0,77	0,77	0,77	0,76	0,76	0,76	0,76	0,76	0,76	0,76	0,75	0,77	0,76	0,78	0,75	0,77	0,76
Mg	0,06	0,06	0,06	0,06	0,06	0,06	0,06	0,06	0,06	0,06	0,06	0,06	0,06	0,06	0,06	0,06	0,06	0,06	0,06
Ca	0,64	0,66	0,67	0,67	0,68	0,68	0,68	0,68	0,68	0,67	0,67	0,67	0,68	0,68	0,68	0,68	0,69	0,67	0,68
Na	0,01	0,00	0,00	0,00	0,00	0,01	0,00	0,00	0,00	0,00	0,00	0,00	0,00	0,00	0,00	0,00	0,00	0,00	0,00
K	0,00	0,00	0,00	0,00	0,00	0,00	0,00	0,00	0,00	0,00	0,00	0,00	0,00	0,00	0,00	0,00	0,00	0,00	0,00
Tot S2	2,99	2,98	2,98	3,01	3,01	2,99	2,98	3,00	2,99	2,98	2,98	2,99	2,99	2,98	3,00	2,98	3,01	3,01	3,01
Tot Cat	7,99	7,99	7,99	8,00	8,00	7,99	7,99	8,00	7,99	7,99	7,99	7,99	7,99	7,99	8,00	7,99	8,00	8,00	8,00
ΣO	12	12	12	12	12	12	12	12	12	12	12	12	12	12	12	12	12	12	12
Prp	2,09	2,02	2,03	1,98	1,99	1,98	2,02	1,97	1,96	2,01	1,99	2,02	2,01	1,97	1,99	2,10	2,09	2,03	1,91
Alm	50,93	50,38	49,89	50,22	49,85	49,82	49,58	49,96	49,98	49,69	50,17	49,92	50,08	49,62	49,93	49,11	50,18	49,83	50,40
Grs	20,70	20,76	20,82	20,77	20,58	20,67	21,11	21,21	21,24	20,37	20,74	20,75	20,77	20,66	20,69	20,56	21,04	20,00	21,00
Sps	25,49	25,46	25,68	25,58	25,55	25,48	25,42	25,23	25,39	25,68	25,43	25,54	25,26	25,67	25,40	26,04	24,91	25,74	25,21
Adr	0,80	1,38	1,58	1,45	2,03	2,05	1,88	1,62	1,44	2,25	1,68	1,77	1,89	2,09	1,99	2,20	1,77	2,41	1,48
XMg	0,03	0,03	0,03	0,03	0,03	0,03	0,03	0,03	0,03	0,03	0,03	0,03	0,03	0,03	0,03	0,03	0,03	0,03	0,02
XPrp	0,02	0,02	0,02	0,02	0,02	0,02	0,02	0,02	0,02	0,02	0,02	0,02	0,02	0,02	0,02	0,02	0,02	0,02	0,02
XAlm	0,51	0,50	0,50	0,50	0,50	0,50	0,50	0,50	0,50	0,50	0,50	0,50	0,50	0,50	0,50	0,49	0,50	0,50	0,50
XGrs	0,21	0,21	0,21	0,21	0,21	0,21	0,21	0,21	0,21	0,20	0,21	0,21	0,21	0,21	0,21	0,21	0,21	0,20	0,21
XSps	0,25	0,25	0,26	0,26	0,26	0,25	0,25	0,25	0,25	0,26	0,25	0,26	0,25	0,26	0,25	0,26	0,25	0,26	0,25
XAdr	0,01	0,01	0,02	0,01	0,02	0,02	0,02	0,02	0,01	0,02	0,02	0,02	0,02	0,02	0,02	0,02	0,02	0,02	0,01

Table 7: C-C' chemical profile of garnet crystal from LL56a4 micascist. Analyses are shown in Fig. 3.4c.

Sample Descrip.	LL 56a4						LL 56a4						LL 56a4						LL 56a4					
	Grt C-C'	Grt C-C'	Grt C-C'	Grt C-C'	Grt C-C'	Grt C-C'	Grt C-C'	Grt C-C'	Grt C-C'	Grt C-C'	Grt C-C'	Grt C-C'	Grt C-C'	Grt C-C'	Grt C-C'	Grt C-C'	Grt C-C'	Grt C-C'						
SiO2	36.54	36.62	36.67	37.77	36.91	36.71	36.74	36.88	36.74	36.71	36.90	36.72	36.82	36.87	36.65	36.55	36.53	36.63						
TiO2	0.09	0.14	0.19	0.11	0.09	0.15	0.14	0.14	0.14	0.16	0.18	0.13	0.18	0.18	0.15	0.13	0.14	0.15						
Al2O3	20.11	20.10	20.01	20.67	20.12	20.15	20.09	20.19	20.09	20.07	20.04	20.10	20.07	20.03	20.15	20.10	19.89	19.81						
Fe2O3	0.71	0.59	0.69	0.17	0.75	0.49	0.65	0.43	0.65	0.61	0.67	0.58	0.58	0.68	0.54	0.59	0.82	0.78						
FeO	21.65	21.70	21.72	20.95	21.50	21.77	21.78	21.73	21.78	21.77	21.74	21.78	21.70	21.85	22.98	23.89	24.78	25.81						
MnO	11.08	10.86	10.95	10.35	10.75	10.74	10.97	10.81	10.97	10.98	10.73	10.68	10.70	10.60	10.30	10.06	9.80	9.86						
MgO	0.50	0.50	0.48	0.46	0.50	0.49	0.48	0.49	0.48	0.50	0.48	0.50	0.53	0.55	0.66	0.80	0.96	1.09						
CaO	7.81	7.80	7.80	7.93	7.72	7.65	7.52	7.59	7.52	7.51	7.53	7.55	7.54	7.53	7.06	6.30	5.43	4.61						
Na2O	0.02	0.02	0.02	0.01	0.02	0.01	0.01	0.01	0.01	0.01	0.01	0.00	0.01	0.01	0.02	0.02	0.01	0.02						
K2O	0.00	0.00	0.01	0.00	0.00	0.00	0.00	0.00	0.00	0.00	0.00	0.00	0.00	0.00	0.00	0.00	0.00	0.00						
Total	98.50	98.33	98.52	98.42	98.35	98.16	98.37	98.09	98.37	98.32	98.29	98.03	98.11	98.30	98.51	98.44	98.36	98.91						
Si	3.00	3.01	3.01	3.06	3.02	3.02	3.02	3.02	3.02	3.01	3.03	3.02	3.02	3.02	3.01	3.01	3.01	3.01						
AlIV	0.00	0.00	0.00	0.00	0.00	0.00	0.00	0.00	0.00	0.00	0.00	0.00	0.00	0.00	0.00	0.00	0.00	0.00						
Tot IV	3.00	3.01	3.01	3.06	3.02	3.02	3.02	3.02	3.02	3.01	3.03	3.02	3.02	3.02	3.01	3.01	3.01	3.01						
AL VI	1.95	1.95	1.93	1.98	1.94	1.95	1.94	1.96	1.94	1.94	1.94	1.95	1.94	1.94	1.95	1.95	1.93	1.93						
Ti	0.01	0.01	0.01	0.01	0.01	0.01	0.01	0.01	0.01	0.01	0.01	0.01	0.01	0.01	0.01	0.01	0.01	0.01						
Fe3+	0.04	0.04	0.04	0.01	0.05	0.03	0.04	0.03	0.04	0.04	0.04	0.04	0.04	0.04	0.03	0.04	0.05	0.05						
Tot S1	1.99	1.99	1.99	1.99	1.99	1.99	1.99	1.99	1.99	1.99	1.99	1.99	1.99	1.99	1.99	1.99	1.99	1.99						
Fe2+	1.49	1.49	1.49	1.42	1.47	1.50	1.50	1.49	1.50	1.50	1.49	1.50	1.49	1.50	1.58	1.64	1.71	1.77						
Mn	0.77	0.76	0.76	0.71	0.75	0.75	0.76	0.75	0.76	0.76	0.75	0.74	0.74	0.74	0.72	0.70	0.68	0.69						
Mg	0.06	0.06	0.06	0.06	0.06	0.06	0.06	0.06	0.06	0.06	0.06	0.06	0.07	0.07	0.08	0.10	0.12	0.13						
Ca	0.69	0.69	0.69	0.69	0.68	0.67	0.66	0.67	0.66	0.66	0.66	0.67	0.66	0.66	0.62	0.56								

Table 7: C-C' chemical profile continued.

Sample Descrip.	LL 56a4 Grt C-C'	LL 56a4 Grt C-C'	LL 56a4 Grt C-C'	LL 56a4 Grt C-C'	LL 56a4 Grt C-C'	LL 56a4 Grt C-C'	LL 56a4 Grt C-C'	LL 56a4 Grt C-C'	LL 56a4 Grt C-C'	LL 56a4 Grt C-C'	LL 56a4 Grt C-C'	LL 56a4 Grt C-C'	LL 56a4 Grt C-C'	LL 56a4 Grt C-C'	LL 56a4 Grt C-C'	LL 56a4 Grt C-C'	LL 56a4 Grt C-C'	LL 56a4 Grt C-C'	LL 56a4 Grt C-C'
SiO2	36.35	36.34	36.13	36.04	36.22	36.15	36.41	36.36	36.34	36.36	36.25	36.42	36.41	36.06	36.23	36.05	36.31	36.26	36.06
TiO2	0.06	0.05	0.02	0.07	0.06	0.02	0.09	0.05	0.06	0.03	0.09	0.29	0.07	0.05	0.04	0.00	0.04	0.05	0.21
Al2O3	20.11	19.90	19.89	19.85	19.94	19.88	19.67	19.97	19.99	19.87	19.84	19.70	19.93	19.76	19.90	19.77	19.98	20.16	19.90
Fe2O3	0.93	1.11	1.03	0.98	1.19	1.28	1.22	1.26	1.23	1.28	1.18	1.02	1.35	1.38	1.24	1.49	1.18	1.05	0.88
FeO	28.01	28.38	28.82	28.65	29.14	28.79	29.14	29.17	29.43	29.42	29.64	29.99	29.90	30.20	30.36	30.11	30.10	30.31	30.34
MnO	9.49	9.24	9.02	9.02	8.90	8.81	8.65	8.65	8.54	8.45	8.23	8.40	8.45	8.45	8.17	8.34	8.23	8.11	7.92
MgO	1.36	1.44	1.48	1.47	1.53	1.54	1.53	1.58	1.60	1.61	1.56	1.57	1.66	1.64	1.68	1.71	1.66	1.66	1.71
CaO	2.93	2.61	2.18	2.33	2.22	2.43	2.21	2.43	2.29	2.22	2.28	2.09	1.97	1.46	1.58	1.49	1.84	1.87	1.78
Na2O	0.00	0.00	0.01	0.00	0.00	0.01	0.01	0.01	0.02	0.01	0.01	0.00	0.01	0.00	0.00	0.00	0.00	0.01	0.03
K2O	-0.01	0.00	0.00	0.00	0.00	0.00	0.00	0.00	0.00	0.00	0.01	0.00	0.02	0.00	0.00	0.00	0.01	0.00	0.01
Total	99.23	99.09	98.58	98.41	99.21	98.91	98.93	99.49	99.50	99.24	99.08	99.47	99.77	99.01	99.21	98.97	99.35	99.48	98.83
Si	2.99	2.99	2.99	2.99	2.98	2.98	3.00	2.98	2.98	2.99	2.99	2.99	2.98	2.98	2.99	2.98	2.99	2.98	2.98
AlIV	0.01	0.01	0.01	0.01	0.02	0.02	0.00	0.02	0.02	0.01	0.01	0.01	0.02	0.02	0.01	0.02	0.01	0.02	0.02
Tot IV	3.00	3.00	3.00	3.00	3.00	3.00	3.00	3.00	3.00	3.00	3.00	3.00	3.00	3.00	3.00	3.00	3.00	3.00	3.00
AL VI	1.94	1.92	1.93	1.93	1.92	1.92	1.91	1.92	1.92	1.92	1.92	1.90	1.91	1.91	1.92	1.91	1.92	1.93	1.92
Ti	0.00	0.00	0.00	0.00	0.00	0.00	0.01	0.00	0.00	0.00	0.01	0.02	0.00	0.00	0.00	0.00	0.00	0.00	0.01
Fe3+	0.06	0.07	0.06	0.06	0.07	0.08	0.08	0.08	0.08	0.08	0.07	0.06	0.08	0.09	0.08	0.09	0.07	0.07	0.06
Tot S1	2.00	2.00	2.00	2.00	2.00	2.00	1.99	2.00	2.00	2.00	1.99	1.98	2.00	2.00	2.00	2.00	2.00	2.00	1.99
Fe2+	1.93	1.96	2.00	1.99	2.01	1.99	2.01	2.00	2.02	2.02	2.04	2.06	2.05	2.09	2.09	2.08	2.07	2.08	2.10
Mn	0.66	0.64	0.63	0.63	0.62	0.62	0.60	0.60	0.59	0.59	0.58	0.58	0.59	0.59	0.57	0.58	0.57	0.56	0.56
Mg	0.17	0.18	0.18	0.18	0.19	0.19	0.19	0.19	0.20	0.20	0.19	0.19	0.20	0.20	0.21	0.20	0.20	0.20	0.21
Ca	0.26	0.23	0.19	0.21	0.20	0.22	0.20	0.21	0.20	0.20	0.20	0.18	0.17	0.13	0.14	0.13	0.16	0.17	0.16
Na	0.00	0.00	0.00	0.00	0.00	0.00	0.00	0.00	0.00	0.00	0.00	0.00	0.00	0.00	0.00	0.00	0.00	0.00	0.00
K	0.00	0.00	0.00	0.00	0.00	0.00	0.00	0.00	0.00	0.00	0.00	0.00	0.00	0.00	0.00	0.00	0.00	0.00	0.00
Tot S2	3.01	3.01	3.01	3.01	3.01	3.01	3.00	3.01	3.01	3.01	3.01	3.02	3.01	3.01	3.01	3.01	3.01	3.02	3.03
Tot Cat	8.01	8.00	8.01	8.01	8.01	8.01	8.00	8.01	8.01	8.01	8.01	8.00	8.01	8.01	8.01	8.01	8.01	8.01	8.01
ΣO	12	12	12	12	12	12	12	12	12	12	12	12	12	12	12	12	12	12	12
Prp	5.54	5.89	6.08	6.02	6.23	6.31	6.27	6.43	6.51	6.56	6.36	6.35	6.74	6.73	6.88	7.00	6.77	6.74	6.97
Alm	63.95	65.01	66.43	66.04	66.64	66.07	67.07	66.50	67.09	67.33	67.87	68.22	68.04	69.33	69.54	69.01	68.79	69.08	69.46
Grs	5.69	4.23	3.24	3.84	2.84	3.17	2.70	3.20	2.92	2.58	3.03	2.97	1.59	0.01	0.81	0.00	1.74	2.23	2.50
Sps	21.95	21.43	21.06	21.05	20.61	20.48	20.16	19.98	19.72	19.59	19.09	19.34	19.49	19.65	18.96	19.37	19.05	18.72	18.36
Adr	2.87	3.44	3.20	3.04	3.68	3.98	3.81	3.89	3.77	3.95	3.66	3.12	4.14	4.28	3.82	4.62	3.65	3.24	2.72
XMg	0.06	0.06	0.07	0.06	0.07	0.07	0.07	0.07	0.07	0.07	0.07	0.07	0.07	0.07	0.07	0.07	0.07	0.07	0.07
XPrp	0.06	0.06	0.06	0.06	0.06	0.06	0.06	0.06	0.07	0.07	0.06	0.06	0.07	0.07	0.07	0.07	0.07	0.07	0.07
XAlm	0.64	0.65	0.66	0.66	0.67	0.66	0.67	0.67	0.67	0.67	0.68	0.68	0.68	0.69	0.70	0.69	0.69	0.69	0.69
XGrs	0.06	0.04	0.03	0.04	0.03	0.03	0.03	0.03	0.03	0.03	0.03	0.03	0.02	0.00	0.01	0.00	0.02	0.02	0.02
XSps	0.22	0.21	0.21	0.21	0.21	0.20	0.20	0.20	0.20	0.20	0.19	0.19	0.19	0.20	0.19	0.19	0.19	0.19	0.18
XAdr	0.03	0.03	0.03	0.03	0.04	0.04	0.04	0.04	0.04	0.04	0.04	0.03	0.04	0.04	0.04	0.05	0.04	0.03	0.03

Table 7: C-C' chemical profile continued.

Sample Descrip.	LL 56a4 Grt C-C'	LL 56a4 Grt C-C'	LL 56a4 Grt C-C'	LL 56a4 Grt C-C'	LL 56a4 Grt C-C'	LL 56a4 Grt C-C'	LL 56a4 Grt C-C'	LL 56a4 Grt C-C'	LL 56a4 Grt C-C'	LL 56a4 Grt C-C'	LL 56a4 Grt C-C'	LL 56a4 Grt C-C'	LL 56a4 Grt C-C'	LL 56a4 Grt C-C'	LL 56a4 Grt C-C'	LL 56a4 Grt C-C'	LL 56a4 Grt C-C'	LL 56a4 Grt C-C'	LL 56a4 Grt C-C'
SiO2	36,10	36,34	36,33	36,11	36,34	36,04	36,10	36,31	36,25	36,26	36,31	36,48	36,21	36,43	36,30	36,40	36,41	36,10	36,12
TiO2	0,31	0,08	0,03	0,04	0,05	0,02	0,02	0,02	0,00	0,05	0,08	0,05	0,05	0,05	0,01	0,02	0,08	0,03	0,03
Al2O3	19,98	20,08	19,87	19,57	19,77	19,69	19,90	19,80	19,80	19,89	19,88	20,06	19,88	19,91	20,00	20,06	19,91	19,97	19,88
Fe2O3	0,90	1,14	1,11	0,89	1,30	1,44	1,41	1,17	1,32	1,38	1,32	1,15	1,23	1,20	1,04	1,14	1,29	1,18	1,15
FeO	30,52	30,36	30,05	28,82	30,15	29,88	29,88	30,27	30,34	30,50	30,57	30,86	30,60	30,66	31,05	31,24	31,22	31,29	31,11
MnO	8,04	8,03	7,94	7,23	7,95	7,84	7,91	7,76	7,56	7,64	7,49	7,37	7,39	7,30	7,11	7,20	7,31	7,08	7,15
MgO	1,70	1,75	1,69	1,63	1,68	1,66	1,69	1,69	1,71	1,62	1,69	1,73	1,74	1,75	1,74	1,75	1,74	1,83	1,86
CaO	1,89	1,84	1,90	2,03	1,91	2,08	2,18	2,00	1,93	2,09	2,09	1,98	1,92	2,04	1,75	1,71	1,71	1,49	1,42
Na2O	0,00	0,01	0,01	0,01	0,00	0,01	0,00	0,02	0,00	0,00	0,00	0,00	0,02	0,00	0,00	0,00	0,00	0,00	0,02
K2O	0,00	0,01	0,00	0,11	0,00	0,00	0,00	0,00	0,00	0,00	0,00	0,00	0,01	0,00	0,00	0,00	0,00	0,00	0,00
Total	99,45	99,63	98,91	96,44	99,15	98,65	99,07	99,23	98,90	99,43	99,43	99,67	99,07	99,32	98,98	99,52	99,68	98,97	98,73
Si	2,97	2,98	3,00	3,03	2,99	2,99	2,98	2,99	2,99	2,98	2,98	2,99	2,99	2,99	2,99	2,99	2,99	2,98	2,99
AlIV	0,03	0,02	0,00	0,00	0,01	0,02	0,02	0,01	0,01	0,02	0,02	0,01	0,02	0,01	0,01	0,01	0,01	0,02	0,01
TotIV	3,00	3,00	3,00	3,03	3,00	3,00	3,00	3,00	3,00	3,00	3,00	3,00	3,00	3,00	3,00	3,00	3,00	3,00	3,00
Al VI	1,91	1,92	1,93	1,94	1,91	1,91	1,91	1,93	1,92	1,91	1,91	1,92	1,92	1,92	1,94	1,93	1,91	1,92	1,93
Ti	0,02	0,01	0,00	0,00	0,00	0,00	0,00	0,00	0,00	0,00	0,01	0,00	0,00	0,00	0,00	0,00	0,01	0,00	0,00
Fe3+	0,06	0,07	0,07	0,06	0,08	0,09	0,09	0,07	0,08	0,09	0,08	0,07	0,08	0,07	0,06	0,07	0,08	0,07	0,07
Tot S1	1,98	2,00	2,00	2,00	2,00	2,00	2,00	2,00	2,00	2,00	2,00	2,00	2,00	2,00	2,00	2,00	2,00	2,00	2,00
Fe2+	2,10	2,08	2,07	2,03	2,08	2,07	2,06	2,08	2,09	2,10	2,10	2,11	2,11	2,11	2,14	2,14	2,14	2,16	2,15
Mn	0,56	0,56	0,56	0,51	0,55	0,55	0,55	0,54	0,53	0,53	0,52	0,51	0,52	0,51	0,50	0,50	0,51	0,50	0,50
Mg	0,21	0,21	0,21	0,20	0,21	0,21	0,21	0,21	0,21	0,20	0,21	0,21	0,21	0,21	0,21	0,21	0,21	0,23	0,23
Ca	0,17	0,16	0,17	0,18	0,17	0,18	0,19	0,18	0,17	0,18	0,18	0,17	0,17	0,18	0,16	0,15	0,15	0,13	0,13
Na	0,00	0,00	0,00	0,00	0,00	0,00	0,00	0,00	0,00	0,00	0,00	0,00	0,00	0,00	0,00	0,00	0,00	0,00	0,00
K	0,00	0,00	0,00	0,01	0,00	0,00	0,00	0,00	0,00	0,00	0,00	0,00	0,00	0,00	0,00	0,00	0,00	0,00	0,00
Tot S2	3,04	3,02	3,00	2,94	3,01	3,01	3,01	3,01	3,00	3,01	3,01	3,01	3,01	3,01	3,01	3,01	3,01	3,01	3,01
Tot Cat	8,02	8,01	8,00	7,97	8,00	8,01	8,01	8,01	8,00	8,01	8,01	8,01	8,01	8,00	8,00	8,01	8,01	8,01	8,01
ΣO	12	12	12	12	12	12	12	12	12	12	12	12	12	12	12	12	12	12	12
Prp	6,88	7,09	6,91	6,99	6,87	6,81	6,89	6,90	7,01	6,61	6,87	7,00	7,10	7,11	7,10	7,10	7,04	7,48	7,63
Alm	69,18	69,06	69,04	69,19	69,09	68,79	68,38	69,26	69,72	69,62	69,72	70,23	70,11	70,04	71,23	71,26	71,09	71,71	71,54
Grs	2,73	1,85	2,14	3,39	1,57	1,65	2,05	2,25	1,58	1,87	2,06	2,25	1,83	2,27	1,94	1,50	1,02	0,74	0,60
Sps	18,45	18,50	18,47	17,57	18,44	18,28	18,34	17,98	17,59	17,67	17,30	16,99	17,15	16,89	16,52	16,64	16,87	16,43	16,66
Adr	2,77	3,50	3,44	2,87	4,03	4,48	4,34	3,61	4,10	4,24	4,05	3,53	3,82	3,70	3,21	3,50	3,98	3,65	3,57
XMg	0,07	0,07	0,07	0,07	0,07	0,07	0,07	0,07	0,07	0,07	0,07	0,07	0,08	0,08	0,07	0,07	0,07	0,08	0,08
XPrp	0,07	0,07	0,07	0,07	0,07	0,07	0,07	0,07	0,07	0,07	0,07	0,07	0,07	0,07	0,07	0,07	0,07	0,07	0,08
XAlm	0,69	0,69	0,69	0,69	0,69	0,69	0,68	0,69	0,70	0,70	0,70	0,70	0,70	0,70	0,71	0,71	0,71	0,72	0,72
XGrs	0,03	0,02	0,02	0,03	0,02	0,02	0,02	0,02	0,02	0,02	0,02	0,02	0,02	0,02	0,02	0,01	0,01	0,01	0,01
XSps	0,18	0,19	0,18	0,18	0,18	0,18	0,18	0,18	0,18	0,18	0,17	0,17	0,17	0,17	0,17	0,17	0,17	0,16	0,17
XAdr	0,03	0,03	0,03	0,03	0,04	0,04	0,04	0,04	0,04	0,04	0,04	0,04	0,04	0,04	0,03	0,04	0,04	0,04	0,04

Table 7: C-C' chemical profile continued.

Sample Descrip.	LL 56a4 Grt C-C'	LL 56a4 Grt C-C'	LL 56a4 Grt C-C'	LL 56a4 Grt C-C'	LL 56a4 Grt C-C'	LL 56a4 Grt C-C'	LL 56a4 Grt C-C'	LL 56a4 Grt C-C'	LL 56a4 Grt C-C'	LL 56a4 Grt C-C'	LL 56a4 Grt C-C'
SiO2	35,86	36,11	36,10	36,21	36,23	35,94	35,90	36,08	35,89	36,01	36,19
TiO2	0,04	0,03	0,02	0,04	0,03	0,01	0,00	0,01	0,02	0,00	0,00
Al2O3	19,87	19,76	19,81	19,92	19,82	19,63	19,82	19,79	19,75	19,73	19,83
Fe2O3	1,27	1,48	1,17	1,25	1,37	1,44	1,48	1,19	1,28	1,39	1,27
FeO	31,01	31,27	31,19	31,33	31,48	31,19	31,60	31,83	31,86	31,14	31,25
MnO	7,21	7,21	7,24	7,16	7,26	7,15	7,28	7,58	7,24	7,50	7,68
MgO	1,80	1,83	1,82	1,84	1,79	1,85	1,69	1,44	1,60	1,81	1,77
CaO	1,52	1,37	1,26	1,41	1,28	1,19	1,17	0,99	0,98	1,09	1,02
Na2O	0,01	0,02	0,00	0,02	0,00	0,00	0,01	0,00	0,00	0,00	0,00
K2O	0,00	0,00	0,01	0,00	0,00	0,00	0,00	0,00	0,00	0,00	0,00
Total	98,60	99,09	98,63	99,18	99,25	98,41	98,96	98,91	98,64	98,68	99,01
Si	2,97	2,98	2,99	2,98	2,99	2,99	2,97	2,99	2,98	2,99	2,99
Al IV	0,03	0,02	0,01	0,02	0,01	0,01	0,03	0,01	0,02	0,02	0,01
Tot IV	3,00	3,00	3,00	3,00	3,00	3,00	3,00	3,00	3,00	3,00	3,00
AL VI	1,92	1,90	1,92	1,92	1,91	1,91	1,91	1,93	1,92	1,91	1,92
Ti	0,00	0,00	0,00	0,00	0,00	0,00	0,00	0,00	0,00	0,00	0,00
Fe3+	0,08	0,09	0,07	0,08	0,09	0,09	0,09	0,07	0,08	0,09	0,08
Tot S1	2,00	2,00	2,00	2,00	2,00	2,00	2,00	2,00	2,00	2,00	2,00
Fe2+	2,15	2,16	2,16	2,16	2,17	2,17	2,19	2,21	2,21	2,16	2,16
Mn	0,51	0,50	0,51	0,50	0,51	0,50	0,51	0,53	0,51	0,53	0,54
Mg	0,22	0,23	0,23	0,23	0,22	0,23	0,21	0,18	0,20	0,22	0,22
Ca	0,14	0,12	0,11	0,12	0,11	0,11	0,10	0,09	0,09	0,10	0,09
Na	0,00	0,00	0,00	0,00	0,00	0,00	0,00	0,00	0,00	0,00	0,00
K	0,00	0,00	0,00	0,00	0,00	0,00	0,00	0,00	0,00	0,00	0,00
Tot S2	3,02	3,01	3,01	3,01	3,01	3,01	3,01	3,01	3,01	3,01	3,01
Tot Cat	8,02	8,01	8,01	8,01	8,01	8,01	8,01	8,00	8,01	8,01	8,01
ΣO	12	12	12	12	12	12	12	12	12	12	12
Prp	7,39	7,44	7,49	7,52	7,28	7,57	6,86	5,89	6,50	7,37	7,17
Alm	71,34	71,33	71,90	71,75	71,76	71,40	71,83	72,87	72,80	71,01	71,21
Grs	0,52	0,00	0,08	0,27	0,00	0,00	0,00	0,00	0,00	0,00	0,00
Sps	16,79	16,67	16,91	16,61	16,76	16,58	16,77	17,57	16,76	17,33	17,71
Adr	3,95	4,57	3,63	3,86	4,20	4,45	4,54	3,68	3,95	4,29	3,90
XMg	0,08	0,08	0,08	0,08	0,08	0,08	0,07	0,06	0,07	0,08	0,07
XPrp	0,07	0,07	0,07	0,08	0,07	0,08	0,07	0,06	0,06	0,07	0,07
XAlm	0,71	0,71	0,72	0,72	0,72	0,71	0,72	0,73	0,71	0,71	0,71
XGrs	0,01	0,00	0,00	0,00	0,00	0,00	0,00	0,00	0,00	0,00	0,00
XSps	0,17	0,17	0,17	0,17	0,17	0,17	0,17	0,18	0,17	0,17	0,18
XAdr	0,04	0,05	0,04	0,04	0,04	0,04	0,05	0,04	0,04	0,04	0,04

Table 7: C-C' chemical profile continued.

Sample Descrip.	LL 56b Grt D-D'	LL 56b Grt D-D'	LL 56b Grt D-D'	LL 56b Grt D-D'	LL 56b Grt D-D'	LL 56b Grt D-D'	LL 56b Grt D-D'	LL 56b Grt D-D'	LL 56b Grt D-D'	LL 56b Grt D-D'	LL 56b Grt D-D'	LL 56b Grt D-D'	LL 56b Grt D-D'	LL 56b Grt D-D'	LL 56b Grt D-D'	LL 56b Grt D-D'
SiO2	35.98	35.53	35.83	35.75	35.51	36.04	35.86	36.04	35.34	35.58	35.62	36.16	36.07	36.52	35.91	35.89
TiO2	0.01	0.01	0.02	0.00	0.00	0.02	0.05	0.00	0.64	0.20	0.04	0.03	0.06	0.05	0.04	0.14
Al2O3	20.88	21.70	20.76	21.48	20.92	20.72	20.65	20.72	20.29	20.71	22.20	20.94	20.75	21.01	20.64	22.05
Fe2O3	0.59	0.02	0.82	0.14	0.85	0.70	0.88	0.96	0.47	0.44	0.00	0.63	0.64	0.64	0.88	0.71
FeO	31.36	32.01	31.60	31.82	30.90	31.35	31.33	31.25	31.98	31.13	31.48	30.90	30.65	30.88	30.46	29.97
MnO	8.34	7.90	8.21	7.85	7.61	7.77	7.77	7.78	7.71	7.79	7.60	7.59	7.64	7.84	7.62	7.45
MgO	1.68	1.72	1.56	1.72	2.20	1.73	1.75	1.77	1.62	1.70	1.69	1.70	1.66	1.68	1.61	1.53
CaO	1.08	1.12	1.16	1.24	1.28	1.40	1.43	1.57	1.51	1.62	1.82	2.19	2.26	2.29	2.41	2.68
Na2O	0.01	0.01	0.01	0.02	0.01	0.01	0.03	0.00	0.02	0.01	0.01	0.03	0.00	0.01	0.02	0.02
K2O	0.01	0.00	0.00	0.01	0.01	0.00	0.00	0.00	0.00	0.00	0.01	0.00	0.00	0.00	0.00	0.00
Total	99.94	100.03	99.97	100.04	99.29	99.77	99.75	100.09	99.58	99.19	100.46	100.16	99.73	100.90	99.61	100.17
Si	2.95	2.91	2.94	2.92	2.92	2.95	2.94	2.95	2.92	2.93	2.89	2.95	2.95	2.95	2.95	2.91
Al IV	0.05	0.09	0.06	0.08	0.08	0.06	0.06	0.06	0.08	0.07	0.11	0.05	0.05	0.05	0.06	0.09
Tot IV	3.00	3.00	3.00	3.00	3.00	3.00	3.00	3.00	3.00	3.00	3.00	3.00	3.00	3.00	3.00	3.00
AL VI	1.96	2.00	1.95	1.99	1.95	1.94	1.94	1.94	1.89	1.95	2.02	1.96	1.95	1.96	1.94	2.02
Ti	0.00	0.00	0.00	0.00	0.00	0.00	0.00	0.00	0.04	0.01	0.00	0.00	0.00	0.00	0.00	0.00
Fe3+	0.04	0.00	0.05	0.01	0.05	0.06	0.05	0.06	0.03	0.03	0.00	0.04	0.04	0.04	0.05	0.00
Tot S1	2.00	2.00	2.00	2.00	2.00	2.00	2.00	2.00	1.96	1.99	2.02	2.00	2.00	2.00	2.00	2.03
Fe2+	2.15	2.19	2.17	2.18	2.13	2.15	2.15	2.14	2.21	2.15	2.14	2.11	2.10	2.09	2.09	2.07
Mn	0.58	0.55	0.57	0.54	0.53	0.54	0.54	0.54	0.54	0.54	0.52	0.53	0.53	0.54	0.53	0.52
Mg	0.21	0.21	0.19	0.21	0.27	0.21	0.21	0.22	0.20	0.21	0.21	0.21	0.20	0.20	0.20	0.19
Ca	0.10	0.10	0.10	0.11	0.11	0.12	0.13	0.14	0.13	0.14	0.16	0.19	0.20	0.20	0.21	0.23
Na	0.00	0.00	0.00	0.00	0.00	0.01	0.01	0.00	0.00	0.00	0.00	0.00	0.00	0.00	0.00	0.00
K	0.00	0.00	0.00	0.00	0.00	0.00	0.00	0.00	0.00	0.00	0.00	0.00	0.00	0.00	0.00	0.00
Tot S2	3.03	3.05	3.03	3.04	3.04	3.03	3.03	3.03	3.08	3.05	3.03	3.03	3.03	3.03	3.03	3.01
Tot Cat	8.03	8.05	8.03	8.04	8.04	8.03	8.03	8.03	8.04	8.03	8.04	8.03	8.02	8.02	8.03	8.03
ΣO	12	12	12	12	12	12	12	12	12	12	12	12	12	12	12	12
Prp	6.78	6.90	6.28	6.92	8.89	6.98	7.05	7.12	6.49	6.87	6.78	6.81	6.68	6.69	6.49	6.16
Alm	70.97	71.89	71.54	71.60	69.94	71.04	70.98	70.55	71.68	70.54	70.71	69.57	69.29	69.02	69.03	68.85
Grs	1.32	3.18	0.86	3.15	1.13	1.92	1.48	1.62	2.91	3.38	5.22	4.39	4.57	4.62	4.31	7.77
Sps	19.13	17.97	18.82	17.90	17.44	17.92	17.82	17.80	17.50	17.88	17.29	17.31	17.42	17.74	17.49	17.22
Adr	1.81	0.05	2.50	0.43	2.60	2.15	2.68	2.91	1.42	1.33	0.00	1.93	1.96	1.93	2.69	0.00
XMg	0.07	0.07	0.07	0.07	0.09	0.07	0.07	0.07	0.07	0.07	0.07	0.07	0.07	0.07	0.07	0.07
XPrp	0.07	0.07	0.06	0.07	0.09	0.07	0.07	0.07	0.06	0.07	0.07	0.07	0.07	0.07	0.06	0.06
XAlm	0.71	0.72	0.72	0.72	0.70	0.71	0.71	0.71	0.72	0.71	0.71	0.70	0.69	0.69	0.69	0.68
XGrs	0.01	0.03	0.01	0.03	0.01	0.02	0.01	0.02	0.03	0.03	0.05	0.04	0.05	0.05	0.04	0.08
XSps	0.19	0.18	0.19	0.18	0.17	0.18	0.18	0.18	0.18	0.18	0.17	0.17	0.17	0.17	0.17	0.17
XAdr	0.02	0.00	0.02	0.00	0.03	0.02	0.03	0.03	0.01	0.01	0.00	0.02	0.02	0.02	0.03	0.03

Table 7: D-D' chemical profile of garnet crystal from LL56b micaschist. Analyses are shown in Fig. 3.4d.

Table 7: D-D' chemical profile continued.

Sample Descrip.	LL 56b Grt D-D'	LL 56b Grt D-D'	LL 56b Grt D-D'	LL 56b Grt D-D'	LL 56b Grt D-D'	LL 56b Grt D-D'	LL 56b Grt D-D'	LL 56b Grt D-D'	LL 56b Grt D-D'	LL 56b Grt D-D'	LL 56b Grt D-D'	LL 56b Grt D-D'	LL 56b Grt D-D'	LL 56b Grt D-D'	LL 56b Grt D-D'	LL 56b Grt D-D'	LL 56b Grt D-D'	LL 56b Grt D-D'	LL 56b Grt D-D'
SiO ₂	36.62	36.52	36.35	36.58	36.72	36.70	36.86	36.34	36.43	35.79	36.51	36.27	36.74	36.27	36.39	36.25	36.40	36.19	36.41
TiO ₂	0.08	0.08	0.06	0.05	0.09	0.01	0.02	0.05	0.00	0.07	0.02	0.02	0.00	0.00	0.02	0.02	0.03	0.02	0.02
Al ₂ O ₃	21.02	20.94	21.06	20.88	20.93	20.97	21.13	21.09	20.93	20.71	20.90	21.00	20.98	21.15	20.97	21.09	21.66	20.76	21.01
Fe ₂ O ₃	0.31	0.46	0.33	0.34	0.60	0.44	0.40	0.34	0.86	0.86	0.85	0.68	0.55	0.92	0.92	0.53	0.17	1.02	0.84
FeO	27.36	27.52	27.99	27.99	28.58	28.86	29.37	29.84	30.18	30.60	31.37	31.57	32.11	32.35	33.02	33.27	33.68	33.30	33.40
MnO	6.94	6.89	6.34	6.12	5.88	5.72	5.53	5.23	5.10	5.07	5.08	5.24	5.30	5.10	5.23	5.16	5.05	4.99	4.96
MgO	0.84	0.86	0.90	0.94	0.98	1.04	1.10	1.19	1.26	1.29	1.47	1.50	1.57	1.62	1.68	1.70	1.72	1.78	1.81
CaO	6.82	6.84	6.62	6.62	6.68	6.25	6.16	5.66	5.50	4.83	4.35	3.91	3.38	3.25	2.71	2.38	2.51	2.33	2.42
Na ₂ O	0.01	0.01	0.00	0.03	0.00	0.01	0.00	0.01	0.03	0.01	0.00	0.01	0.02	0.02	0.00	0.01	0.01	0.02	0.02
K ₂ O	0.01	0.01	0.00	0.00	0.00	0.00	0.00	0.00	0.00	0.01	0.01	0.00	0.00	0.00	0.01	0.00	0.00	0.00	0.00
Total	100.00	99.93	99.65	99.56	100.47	100.00	100.56	99.75	100.30	99.23	100.58	100.20	100.64	100.29	100.96	100.42	101.23	100.40	100.89
Si	2.97	2.96	2.96	2.97	2.96	2.97	2.97	2.95	2.95	2.94	2.95	2.95	2.97	2.94	2.94	2.95	2.93	2.94	2.95
Al IV	0.04	0.04	0.05	0.03	0.04	0.03	0.03	0.05	0.05	0.06	0.05	0.05	0.03	0.06	0.06	0.06	0.07	0.06	0.06
Tot IV	3.00	3.00	3.00	3.00	3.00	3.00	3.00	3.00	3.00	3.00	3.00	3.00	3.00	3.00	3.00	3.00	3.00	3.00	3.00
AL VI	1.97	1.96	1.97	1.97	1.95	1.97	1.97	1.97	1.95	1.94	1.95	1.96	1.97	1.97	1.94	1.96	1.99	1.94	1.95
Ti	0.01	0.01	0.00	0.00	0.01	0.00	0.00	0.00	0.00	0.00	0.00	0.00	0.00	0.00	0.00	0.00	0.00	0.00	0.00
Fe ³⁺	0.02	0.03	0.02	0.02	0.04	0.03	0.02	0.02	0.05	0.05	0.05	0.04	0.03	0.03	0.06	0.03	0.01	0.06	0.05
Tot S1	2.00	2.00	2.00	2.00	1.99	2.00	2.00	2.00	2.00	2.00	2.00	2.00	2.00	2.00	2.00	2.00	2.00	2.00	2.00
Fe ²⁺	1.85	1.87	1.90	1.90	1.93	1.95	1.98	2.03	2.04	2.10	2.12	2.15	2.17	2.20	2.23	2.26	2.27	2.27	2.26
Mn	0.48	0.46	0.44	0.42	0.40	0.39	0.38	0.36	0.35	0.35	0.35	0.36	0.36	0.35	0.36	0.36	0.35	0.34	0.34
Mg	0.10	0.10	0.11	0.11	0.12	0.13	0.13	0.14	0.15	0.16	0.18	0.18	0.19	0.20	0.20	0.21	0.21	0.22	0.22
Ca	0.59	0.59	0.58	0.58	0.58	0.54	0.53	0.49	0.48	0.43	0.38	0.34	0.29	0.28	0.24	0.21	0.22	0.20	0.21
Na	0.00	0.00	0.00	0.01	0.00	0.00	0.00	0.00	0.00	0.00	0.00	0.00	0.00	0.00	0.00	0.00	0.00	0.00	0.00
K	0.00	0.00	0.00	0.00	0.00	0.00	0.00	0.00	0.00	0.00	0.00	0.00	0.00	0.00	0.00	0.00	0.00	0.00	0.00
Tot S2	3.02	3.03	3.03	3.02	3.03	3.02	3.02	3.03	3.03	3.04	3.03	3.03	3.02	3.03	3.03	3.03	3.04	3.03	3.03
Tot Cat	8.02	8.02	8.02	8.02	8.02	8.02	8.02	8.02	8.03	8.03	8.02	8.03	8.02	8.03	8.03	8.03	8.04	8.03	8.03
ΣO	12	12	12	12	12	12	12	12	12	12	12	12	12	12	12	12	12	12	12
Prp	3.34	3.43	3.60	3.78	3.88	4.16	4.37	4.75	5.03	5.19	5.85	6.01	6.28	6.48	6.69	6.80	6.79	7.12	7.22
Alm	61.32	61.71	62.91	63.12	63.74	64.83	65.54	67.04	67.60	69.20	70.15	70.84	71.99	72.58	73.73	74.64	74.72	74.83	74.62
Grs	18.63	18.26	18.06	18.12	17.28	16.66	16.41	15.28	13.18	11.40	9.92	9.19	8.04	7.76	4.98	5.22	6.64	3.61	4.42
Sps	15.75	15.20	14.42	13.97	13.29	13.02	12.49	11.91	11.57	11.61	11.52	11.90	12.03	11.60	11.82	11.72	11.35	11.35	11.22
Adr	0.95	1.39	1.01	1.02	1.82	1.33	1.19	1.02	2.61	2.61	2.56	2.06	1.67	1.58	2.78	1.62	0.50	3.09	2.52
X _{Mg}	0.04	0.04	0.04	0.05	0.05	0.05	0.05	0.06	0.06	0.06	0.07	0.07	0.07	0.07	0.07	0.07	0.07	0.08	0.08
X _{Prp}	0.03	0.03	0.04	0.04	0.04	0.04	0.04	0.05	0.05	0.05	0.06	0.06	0.06	0.06	0.07	0.07	0.07	0.07	0.07
X _{Alm}	0.61	0.62	0.63	0.63	0.64	0.65	0.66	0.67	0.68	0.69	0.70	0.71	0.72	0.73	0.74	0.75	0.75	0.75	0.75
X _{Grs}	0.19	0.18	0.18	0.18	0.17	0.17	0.16	0.15	0.13	0.11	0.10	0.09	0.08	0.08	0.05	0.05	0.07	0.04	0.04
X _{Sps}	0.16	0.15	0.14	0.14	0.13	0.13	0.12	0.12	0.12	0.12	0.12	0.12	0.12	0.12	0.12	0.12	0.11	0.11	0.11
X _{Adr}	0.01	0.01	0.01	0.01	0.02	0.01	0.01	0.01	0.03	0.03	0.03	0.02	0.02	0.02	0.03	0.02	0.00	0.03	0.03

Table 7: D-D' chemical profile continued.

Sample Descrip.	LL 56b Grt D-D'	LL 56b Grt D-D'	LL 56b Grt D-D'	LL 56b Grt D-D'	LL 56b Grt D-D'	LL 56b Grt D-D'	LL 56b Grt D-D'	LL 56b Grt D-D'	LL 56b Grt D-D'	LL 56b Grt D-D'	LL 56b Grt D-D'
SiO ₂	36.58	36.49	36.30	36.40	36.37	36.40	36.60	36.86	36.62	36.12	
TiO ₂	0.03	0.04	0.00	0.03	0.00	0.02	0.03	0.04	0.01	0.04	
Al ₂ O ₃	21.01	21.02	20.99	21.24	20.90	21.02	20.94	20.94	20.69	20.41	
Fe ₂ O ₃	0.88	0.87	0.75	0.38	0.86	0.81	0.91	0.68	0.86	0.58	
FeO	33.51	33.60	33.24	33.43	32.94	32.71	32.42	31.50	30.69	29.82	
MnO	5.16	5.03	5.18	5.40	5.35	5.81	6.16	7.14	8.20	10.05	
MgO	1.79	1.85	1.80	1.62	1.85	1.85	1.84	1.70	1.55	1.15	
CaO	2.34	2.30	2.25	2.23	2.29	2.24	2.27	2.40	2.12	1.31	
Na ₂ O	0.01	0.00	0.00	0.01	0.01	0.02	0.01	0.01	0.02	0.00	
K ₂ O	0.00	0.00	0.00	0.10	0.00	0.00	0.00	0.00	0.00	0.00	
Total	101.31	101.19	100.53	100.84	100.57	100.88	101.17	101.27	100.75	99.48	
Si	2.95	2.94	2.95	2.95	2.95	2.94	2.95	2.97	2.97	2.98	
Al IV	0.05	0.06	0.05	0.05	0.05	0.06	0.05	0.03	0.03	0.02	
Tot IV	3.00	3.00	3.00	3.00	3.00	3.00	3.00	3.00	3.00	3.00	
Al VI	1.94	1.94	1.95	1.97	1.95	1.95	1.94	1.95	1.95	1.96	
Ti	0.00	0.00	0.00	0.00	0.00	0.00	0.00	0.00	0.00	0.00	
Fe ³⁺	0.05	0.05	0.05	0.02	0.05	0.05	0.06	0.04	0.05	0.04	
Tot S1	2.00	2.00	2.00	2.00	2.00	2.00	2.00	2.00	2.00	2.00	
Fe ²⁺	2.26	2.27	2.26	2.26	2.23	2.21	2.19	2.12	2.08	2.06	
Mn	0.35	0.34	0.36	0.37	0.37	0.40	0.42	0.49	0.56	0.70	
Mg	0.22	0.22	0.22	0.20	0.22	0.22	0.22	0.20	0.19	0.14	
Ca	0.20	0.20	0.20	0.19	0.20	0.19	0.20	0.21	0.18	0.12	
Na	0.00	0.00	0.00	0.00	0.00	0.00	0.00	0.00	0.00	0.00	
K	0.00	0.00	0.00	0.01	0.00	0.00	0.00	0.00	0.00	0.00	
Tot S2	3.03	3.03	3.03	3.03	3.03	3.03	3.03	3.02	3.02	3.01	
Tot Cat	8.03	8.03	8.03	8.03	8.03	8.03	8.03	8.02	8.02	8.01	
ΣO	12	12	12	12	12	12	12	12	12	12	
Prp	7.09	7.32	7.21	6.46	7.41	7.36	7.32	6.74	6.21	4.69	
Alm	74.61	74.78	74.55	74.89	73.86	73.09	72.29	70.27	69.02	68.20	
Grs	4.01	3.94	4.22	5.25	3.98	3.97	3.75	4.80	3.49	2.05	
Sps	11.64	11.34	11.77	12.25	12.14	13.14	13.91	16.14	18.67	23.27	
Adr	2.65	2.62	2.26	1.16	2.61	2.43	2.73	2.05	2.61	1.78	
X _{Mg}	0.08	0.08	0.08	0.07	0.08	0.08	0.08	0.07	0.07	0.05	
X _{Prp}	0.07	0.07	0.07	0.06	0.07	0.07	0.07	0.07	0.06	0.05	
X _{Alm}	0.75	0.75	0.75	0.75	0.74	0.73	0.72	0.70	0.69	0.68	
X _{Grs}	0.04	0.04	0.04	0.05	0.04	0.04	0.04	0.05	0.03	0.02	
X _{Sps}	0.12	0.11	0.12	0.12	0.12	0.13	0.14	0.16	0.19	0.23	
X _{Adr}	0.03	0.03	0.02	0.01	0.03	0.02	0.03	0.02	0.03	0.02	

Table 7: D-D' chemical profile continued.

Table 7: E-E' chemical profile of garnet crystal from LL57a micaschist. Analyses are shown in Fig. 3.4e.

Sample Descrip.	LL 57a	LL 57a	LL 57a	LL 57a	LL 57a	LL 57a	LL 57a	LL 57a	LL 57a	LL 57a	LL 57a	LL 57a	LL 57a	LL 57a	LL 57a	LL 57a	LL 57a
	Grt E-E'	Grt E-E'	Grt E-E'	Grt E-E'	Grt E-E'	Grt E-E'	Grt E-E'	Grt E-E'	Grt E-E'	Grt E-E'	Grt E-E'	Grt E-E'	Grt E-E'	Grt E-E'	Grt E-E'	Grt E-E'	Grt E-E'
SiO2	36.18	36.22	36.32	36.32	36.55	36.32	36.26	36.19	36.02	35.96	36.47	36.06	36.35	35.95	36.27	36.36	36.20
TiO2	0.13	0.10	0.13	0.09	0.08	0.15	0.14	0.10	0.15	0.12	0.16	0.15	0.12	0.18	0.16	0.12	0.13
Al2O3	20.79	20.58	20.54	20.54	20.60	20.62	20.76	20.43	20.61	20.83	20.59	20.43	20.52	20.43	20.52	20.49	20.47
Fe2O3	0.00	0.00	0.00	0.00	0.00	0.00	0.00	0.00	0.00	0.00	0.00	0.00	0.00	0.00	0.00	0.00	0.00
FeO	22.46	22.88	22.75	22.82	22.88	22.79	22.74	22.72	22.87	22.89	22.79	22.68	22.72	22.63	22.85	22.74	22.64
MnO	9.43	9.65	9.64	9.69	9.65	9.54	9.65	9.55	9.50	9.45	9.53	9.40	9.52	9.44	9.28	9.63	9.53
MgO	0.68	0.54	0.53	0.52	0.54	0.53	0.54	0.57	0.56	0.60	0.55	0.55	0.54	0.56	0.55	0.54	0.55
CaO	7.45	7.56	7.51	7.47	7.71	7.52	7.49	7.42	7.38	7.38	7.83	7.96	7.91	7.93	7.97	7.88	7.73
Na2O	0.09	0.02	0.02	0.02	0.03	0.01	0.04	0.02	0.04	0.03	0.01	0.02	0.04	0.06	0.03	0.01	0.01
K2O	0.01	0.00	0.00	0.00	0.00	0.00	0.00	0.00	0.02	0.03	0.00	0.00	0.00	0.01	0.00	0.00	0.00
Total	97.23	97.56	97.46	98.06	97.51	97.62	97.66	97.00	97.16	97.29	97.94	97.28	97.73	97.19	97.64	97.83	97.27
Si	2.99	2.99	3.00	3.00	3.00	2.99	2.99	3.00	2.99	2.98	3.00	2.99	3.00	2.98	2.99	3.00	3.00
Al IV	0.01	0.01	0.00	0.00	0.00	0.01	0.01	0.00	0.01	0.02	0.00	0.01	0.00	0.02	0.01	0.00	0.00
Tot IV	3.00	3.00	3.00	3.00	3.00	3.00	3.00	3.00	3.00	3.00	3.00	3.00	3.00	3.00	3.00	3.00	3.00
Al VI	2.02	2.00	2.00	2.00	2.00	2.01	2.01	2.00	2.00	2.01	1.99	1.98	1.99	1.98	1.99	2.00	1.98
Ti	0.01	0.01	0.01	0.01	0.01	0.01	0.01	0.01	0.01	0.01	0.01	0.01	0.01	0.01	0.01	0.01	0.01
Fe3+	0.00	0.00	0.00	0.00	0.00	0.00	0.00	0.00	0.00	0.00	0.00	0.00	0.00	0.00	0.00	0.00	0.00
Tot S1	2.02	2.00	2.01	2.00	2.02	2.02	2.02	2.01	2.01	2.02	2.00	1.99	2.00	1.99	2.00	2.00	2.00
Fe2+	1.55	1.58	1.57	1.58	1.57	1.57	1.57	1.58	1.59	1.59	1.57	1.57	1.57	1.57	1.58	1.57	1.58
Mn	0.66	0.68	0.67	0.68	0.67	0.67	0.67	0.67	0.67	0.66	0.66	0.66	0.67	0.66	0.65	0.67	0.67
Mg	0.08	0.07	0.07	0.06	0.07	0.07	0.07	0.07	0.07	0.07	0.07	0.07	0.07	0.07	0.07	0.07	0.07
Ca	0.66	0.67	0.67	0.66	0.68	0.67	0.66	0.66	0.66	0.66	0.69	0.71	0.70	0.71	0.71	0.70	0.69
Na	0.01	0.00	0.00	0.00	0.01	0.00	0.01	0.00	0.01	0.01	0.00	0.00	0.01	0.01	0.01	0.00	0.00
K	0.00	0.00	0.00	0.00	0.00	0.00	0.00	0.00	0.00	0.00	0.00	0.00	0.00	0.00	0.00	0.00	0.00
Tot S2	2.97	3.00	2.98	2.99	2.97	2.98	2.98	2.98	2.99	2.99	2.99	3.01	3.00	3.02	3.00	2.99	3.01
Tot Cat	8.00	8.00	7.99	8.00	7.99	8.00	8.00	7.99	8.00	8.00	8.00	8.01	8.00	8.01	8.00	8.00	8.00
ΣO	12	12	12	12	12	12	12	12	12	12	12	12	12	12	12	12	12
Prp	2.83	2.23	2.21	2.15	2.22	2.20	2.25	2.37	2.32	2.47	2.25	2.36	2.22	2.30	2.24	2.23	2.28
Alm	52.51	52.84	52.81	52.91	52.60	52.97	52.79	52.94	53.25	53.25	52.45	52.22	52.27	52.20	52.61	52.21	52.44
Grs	22.31	22.37	22.33	22.20	22.71	22.38	22.26	22.16	22.02	22.01	23.09	23.50	23.33	23.44	23.51	23.17	22.60
Sps	22.34	22.57	22.66	22.74	22.47	22.45	22.69	22.53	22.41	22.27	22.22	21.93	22.18	22.06	21.64	22.35	22.38
Adr	0.00	0.00	0.00	0.00	0.00	0.00	0.00	0.00	0.00	0.00	0.00	0.00	0.00	0.00	0.00	0.00	0.00
XMg	0.04	0.03	0.03	0.03	0.03	0.03	0.03	0.03	0.03	0.03	0.03	0.03	0.03	0.03	0.03	0.03	0.03
XPrp	0.03	0.02	0.02	0.02	0.02	0.02	0.02	0.02	0.02	0.02	0.02	0.02	0.02	0.02	0.02	0.02	0.02
XAlm	0.53	0.53	0.53	0.53	0.53	0.53	0.53	0.53	0.53	0.53	0.52	0.52	0.52	0.52	0.53	0.52	0.53
XGrs	0.22	0.22	0.22	0.22	0.23	0.22	0.22	0.22	0.22	0.23	0.23	0.23	0.23	0.23	0.24	0.23	0.23
XSps	0.22	0.23	0.23	0.23	0.22	0.22	0.23	0.23	0.22	0.22	0.22	0.22	0.22	0.22	0.22	0.22	0.22
XAdr	0.00	0.00	0.00	0.00	0.00	0.00	0.00	0.00	0.00	0.00	0.00	0.00	0.00	0.00	0.00	0.00	0.00

Table 7: E-E' chemical profile continued.

[illegible]

Table 7: E-E' chemical profile continued.

Table 7: E-E' chemical profile continued.

Sample Descrip.	LL 57a Grt E-E'	LL 57a Grt E-E'	LL 57a Grt E-E'	LL 57a Grt E-E'	LL 57a Grt E-E'	LL 57a Grt E-E'	LL 57a Grt E-E'	LL 57a Grt E-E'	LL 57a Grt E-E'	LL 57a Grt E-E'	LL 57a Grt E-E'	LL 57a Grt E-E'	LL 57a Grt E-E'	LL 57a Grt E-E'	LL 57a Grt E-E'	LL 57a Grt E-E'	LL 57a Grt E-E'	LL 57a Grt E-E'	
SiO2	36.43	36.27	36.39	36.26	36.34	36.13	36.26	36.32	36.54	36.25	36.37	36.33	36.18	36.21	36.32	36.31	36.41	35.81	36.18
TiO2	0.07	0.13	0.11	0.08	0.08	0.09	0.10	0.09	0.12	0.12	0.05	0.10	0.10	0.11	0.06	0.09	0.09	0.05	0.07
Al2O3	20.76	20.67	20.72	20.65	20.65	20.73	20.64	20.72	20.83	20.57	20.68	20.60	20.63	20.62	20.68	20.62	20.67	20.65	20.76
Fe2O3	0.00	0.00	0.00	0.00	0.00	0.00	0.06	0.00	0.00	0.00	0.00	0.00	0.00	0.00	0.00	0.00	0.00	0.00	0.00
FeO	25.27	25.31	25.19	25.34	25.34	25.48	25.54	25.36	25.69	25.88	25.94	26.00	26.06	25.99	26.21	26.54	26.70	26.85	27.12
MnO	7.75	7.42	7.65	7.42	7.50	7.42	7.48	7.19	7.42	7.14	7.05	7.06	6.94	6.87	6.83	6.85	6.71	6.64	6.71
MgO	0.65	0.66	0.64	0.66	0.65	0.68	0.68	0.67	0.67	0.69	0.67	0.70	0.69	0.69	0.72	0.72	0.72	0.74	0.74
CaO	7.38	7.32	7.39	7.45	7.45	7.34	7.39	7.49	7.33	7.26	7.18	7.12	7.08	7.12	6.93	6.70	6.76	6.56	6.47
Na2O	0.01	0.03	0.01	0.02	0.01	0.01	0.02	0.02	0.02	0.02	0.02	0.01	0.02	0.04	0.00	0.03	0.02	0.03	0.01
K2O	0.00	0.00	0.00	0.00	0.00	0.00	0.02	0.00	0.01	0.00	0.00	0.01	0.00	0.00	0.00	0.00	0.00	0.01	0.00
Total	98.32	97.81	98.10	98.02	98.02	97.87	98.17	97.87	98.63	97.93	97.95	97.94	97.71	97.68	97.75	97.87	98.08	97.33	98.06
Si	2.99	2.99	2.99	2.98	2.99	2.98	2.98	2.99	2.99	2.99	3.00	2.99	2.99	2.99	3.00	2.99	3.00	2.98	2.98
Al IV	0.01	0.01	0.01	0.02	0.01	0.02	0.02	0.01	0.01	0.01	0.01	0.01	0.01	0.01	0.00	0.01	0.00	0.03	0.02
Tot IV	3.00	3.00	3.00	3.00	3.00	3.00	3.00	3.00	3.00	3.00	3.00	3.00	3.00	3.00	3.00	3.00	3.00	3.00	3.00
Al VI	2.00	2.00	2.00	1.99	1.99	1.99	1.98	2.00	2.00	1.99	2.00	1.99	2.00	2.00	2.01	2.00	2.00	2.00	2.00
Ti	0.00	0.01	0.01	0.01	0.01	0.01	0.01	0.01	0.01	0.01	0.00	0.01	0.01	0.01	0.00	0.01	0.01	0.00	0.01
Fe3+	0.00	0.00	0.00	0.00	0.00	0.00	0.00	0.00	0.00	0.00	0.00	0.00	0.00	0.00	0.00	0.00	0.00	0.00	0.00
Tot S1	2.00	2.01	2.01	2.00	2.00	2.00	1.99	2.01	2.00	2.00	2.00	2.00	2.00	2.01	2.01	2.00	2.01	2.00	2.00

Table 7: E-E' chemical profile continued.

Table 7: E-E' chemical profile continued.

Sample Descrip.	LL 57a		LL 57a		LL 57a		LL 57a		LL 57a		LL 57a		LL 57a		LL 57a		LL 57a		LL 57a	
	Grt	E-E'	Grt	E-E'	Grt	E-E'	Grt	E-E'	Grt	E-E'	Grt	E-E'	Grt	E-E'	Grt	E-E'	Grt	E-E'	Grt	E-E'
SiO2	36.13	35.94	36.12	36.07	36.23	36.41	36.42	35.39	35.89	35.77	36.14	35.94	35.92	35.88	36.08	35.94	36.24	35.67	35.79	
TiO2	0.05	0.04	0.04	0.01	0.00	0.08	0.01	0.00	0.03	0.00	0.03	0.01	0.03	0.00	0.01	0.01	0.01	0.03	0.04	
Al2O3	20.65	20.64	20.78	20.89	20.76	20.79	20.63	20.87	20.70	20.61	20.78	21.08	20.66	20.61	20.67	20.52	20.76	20.63	20.87	
Fe2O3	0.00	0.00	0.00	0.05	0.00	0.00	0.09	0.00	0.16	0.00	0.06	0.00	0.24	0.13	0.48	0.47	0.30	0.34	0.05	
FeO	28.50	28.32	28.61	28.84	28.88	28.93	29.48	29.65	30.29	4.83	4.75	4.63	4.81	4.68	33.26	33.06	4.35	33.55	33.67	
MnO	5.90	5.99	5.65	5.73	5.62	5.64	5.41	5.01	4.92	4.83	4.75	4.63	4.81	4.68	4.59	4.49	4.35	4.06	4.04	
MgO	0.82	0.83	0.82	0.86	0.89	0.90	0.91	1.05	1.06	1.12	1.12	1.18	1.24	1.34	1.39	1.41	1.43	1.55	1.60	
CaO	5.83	5.76	6.02	5.95	5.81	5.61	5.54	4.91	5.01	4.51	4.73	4.05	3.70	2.77	2.69	2.72	2.52	2.44	2.42	
Na2O	0.01	0.03	0.02	0.03	0.01	0.02	0.01	0.02	0.02	0.01	0.02	0.08	0.04	0.01	0.03	0.02	0.03	0.02	0.01	
K2O	0.00	0.00	0.00	0.01	0.00	0.00	0.01	0.01	0.01	0.00	0.00	0.08	0.00	0.01	0.00	0.00	0.02	0.00	0.00	
Total	97.89	97.54	98.06	98.44	98.20	98.38	98.51	97.37	98.09	97.41	98.53	97.81	98.44	98.14	99.20	98.64	99.36	98.30	98.48	
Si	2.99	2.98	2.98	2.97	2.99	2.99	2.99	2.94	2.97	2.98	2.98	2.97	2.97	2.98	2.97	2.97	2.97	2.96	2.96	
Al IV	0.01	0.02	0.02	0.03	0.02	0.01	0.01	0.06	0.03	0.02	0.02	0.03	0.03	0.02	0.03	0.03	0.03	0.04	0.04	
Tot IV	3.00	3.00	3.00	3.00	3.00	3.00	3.00	3.00	3.00	3.00	3.00	3.00	3.00	3.00	3.00	3.00	3.00	3.00	3.00	
Al VI	2.00	2.00	2.00	2.00	2.00	2.01	1.99	1.99	1.99	2.00	1.99	2.03	1.98	1.99	1.97	1.97	1.98	1.98	1.99	
Ti	0.00	0.00	0.00	0.00	0.00	0.01	0.00	0.03	0.00	0.00	0.00	0.00	0.00	0.00	0.00	0.00	0.00	0.00	0.00	
Fe3+	0.00	0.00	0.00	0.00	0.00	0.00	0.01	0.00	0.01	0.00	0.00	0.00	0.02	0.01	0.03	0.03	0.02	0.02	0.00	
Tot S1	2.00	2.00	2.00	2.00	2.00	2.01	2.00	2.02	2.00	2.00	2.00	2.03	2.00	2.00	2.00	2.00	2.00	2.00	2.00	
Fe2+	1.97	1.97	1.97	1.99	1.99	1.99	2.03	2.06	2.10	2.13	2.13	2.13	2.20	2.27	2.29	2.29	2.31	2.33	2.33	
Mn	0.41	0.42	0.40	0.39	0.39	0.39	0.38	0.35	0.35	0.34	0.33	0.33	0.34	0.33	0.32	0.32	0.30	0.29	0.28	
Mg	0.10	0.10	0.10	0.11	0.11	0.11	0.11	0.13	0.13	0.14	0.14	0.15	0.15	0.17	0.17	0.17	0.18	0.19	0.20	
Ca	0.52	0.51	0.53	0.52	0.51	0.49	0.49	0.44	0.44	0.40	0.42	0.36	0.33	0.25	0.24	0.24	0.22	0.22	0.21	
Na	0.00	0.01	0.00	0.00	0.00	0.00	0.00	0.00	0.00	0.00	0.00	0.01	0.01	0.00	0.01	0.00	0.00	0.00	0.00	
K	0.00	0.00	0.00	0.00	0.00	0.00	0.00	0.00	0.00	0.00	0.00	0.01	0.00	0.00	0.00	0.00	0.00	0.00	0.00	
Tot S2	3.00	3.01	3.01	3.02	3.01	2.99	3.01	2.99	3.02	3.01	3.02	2.98	3.02	3.01	3.02	3.02	3.02	3.03	3.02	
Tot Cat	8.01	8.01	8.01	8.02	8.01	8.00	8.00	8.01	8.02	8.01	8.01	8.01	8.02	8.01	8.02	8.02	8.02	8.02	8.02	
ΣO	12	12	12	12	12	12	12	12	12	12	12	12	12	12	12	12	12	12	12	
Prp	3.36	3.42	3.38	3.50	3.65	3.71	3.69	4.36	4.35	4.63	4.56	4.92	5.06	5.51	5.67	5.75	5.81	6.36	6.53	
Alm	65.66	65.48	65.76	65.85	66.24	66.59	67.50	69.15	69.50	70.70	70.61	71.95	72.89	75.39	75.86	75.81	76.79	77.03	77.02	
Grs	17.21	17.06	17.72	17.22	17.06	16.54	15.98	14.66	14.22	13.36	13.66	12.15	10.15	7.78	6.41	6.54	6.46	6.12	6.94	
Sps	13.77	14.04	13.15	13.26	13.05	13.16	12.55	11.82	11.44	11.31	10.98	10.98	11.18	10.92	10.60	10.44	10.03	9.45	9.36	
Adr	0.00	0.00	0.00	0.17	0.00	0.00	0.28	0.00	0.49	0.00	0.19	0.00	0.73	0.41	1.46	1.47	0.91	1.05	1.16	
XMg	0.04	0.04	0.04	0.04	0.04	0.04	0.04	0.05	0.05	0.05	0.05	0.06	0.06	0.06	0.06	0.06	0.06	0.07	0.07	
XPrp	0.03	0.03	0.03	0.03	0.04	0.04	0.04	0.04	0.04	0.05	0.05	0.05	0.05	0.06	0.06	0.06	0.06	0.06	0.07	
XAlm	0.66	0.65	0.66	0.66	0.66	0.67	0.68	0.69	0.69	0.71	0.71	0.72	0.73	0.75	0.76	0.76	0.77	0.77	0.77	
XGrs	0.17	0.17	0.18	0.17	0.17	0.17	0.16	0.15	0.14	0.13	0.14	0.12	0.10	0.08	0.06	0.07	0.06	0.06	0.07	
XSps	0.14	0.14	0.13	0.13	0.13	0.13	0.13	0.12	0.11	0.11	0.11	0.11	0.11	0.11	0.11	0.10	0.10	0.09	0.09	
XAdr	0.00	0.00	0.00	0.00	0.00	0.00	0.00	0.00	0.00	0.00	0.00	0.00	0.01	0.00	0.01	0.01	0.01	0.01	0.00	

Table 7: E-E' chemical profile continued.

Table 7: E-E' chemical profile continued.

[illegible]

Table 7: F-F' chemical profile continued.

[illegible]

Table 7: F-F' chemical profile continued.

Sample Descrip.	LL 57a Grt F-F'	LL 57a Grt F-F'	LL 57a Grt F-F'	LL 57a Grt F-F'	LL 57a Grt F-F'	LL 57a Grt F-F'	LL 57a Grt F-F'
SiO2	35,95	36,04	36,25	36,16	35,87	36,38	36,00
TiO2	0,00	0,02	0,02	0,02	0,02	0,00	0,00
Al2O3	20,65	20,64	20,76	20,42	20,53	20,75	20,55
Fe2O3	0,42	0,32	0,21	0,49	0,53	0,28	0,32
FeO	32,77	32,56	32,70	32,02	31,84	31,77	31,07
MnO	5,05	5,23	5,33	5,72	6,03	6,53	7,10
MgO	1,70	1,71	1,70	1,70	1,66	1,59	1,42
CaO	2,18	2,17	2,14	2,18	2,08	2,02	1,90
Na2O	0,02	0,02	0,02	0,01	0,02	0,02	0,03
K2O	0,00	0,00	0,00	0,01	0,00	0,00	0,00
Total	98,73	98,71	99,15	98,74	98,62	99,40	98,54
Si	2,97	2,97	2,98	2,98	2,97	2,98	2,98
Al IV	0,03	0,03	0,02	0,02	0,04	0,02	0,02
Tot IV	3,00	3,00	3,00	3,00	3,00	3,00	3,00
AL VI	1,97	1,98	1,98	1,97	1,97	1,98	1,98
Ti	0,00	0,00	0,00	0,00	0,00	0,00	0,00
Fe3+	0,03	0,02	0,01	0,03	0,03	0,02	0,02
Tot S1	2,00	2,00	2,00	2,00	2,00	2,00	2,00
Fe2+	2,26	2,25	2,24	2,21	2,20	2,18	2,15
Mn	0,35	0,37	0,37	0,40	0,42	0,45	0,50
Mg	0,21	0,21	0,21	0,21	0,21	0,20	0,20
Ca	0,19	0,19	0,19	0,19	0,18	0,18	0,17
Na	0,00	0,00	0,00	0,00	0,00	0,00	0,00
K	0,00	0,00	0,00	0,00	0,00	0,00	0,00
Tot S2	3,02	3,02	3,02	3,01	3,02	3,01	3,01
Tot Cat	8,02	8,02	8,01	8,01	8,02	8,01	8,01
ΣO	12	12	12	12	12	12	12
Prp	6,92	6,98	6,94	6,93	6,93	6,72	6,51
Alm	74,99	74,52	74,52	73,38	72,97	72,33	71,35
Grs	5,10	5,39	5,59	4,89	4,46	5,04	4,60
Sps	11,70	12,13	12,29	13,28	14,01	15,06	16,54
Adr	1,30	0,99	0,66	1,51	1,64	0,85	1,01
XMg	0,07	0,07	0,07	0,07	0,07	0,07	0,07
XPrp	0,07	0,07	0,07	0,07	0,07	0,07	0,07
XAlm	0,75	0,75	0,75	0,73	0,73	0,72	0,71
XGrs	0,05	0,05	0,06	0,05	0,04	0,05	0,05
XSps	0,12	0,12	0,12	0,13	0,14	0,15	0,17
XAdr	0,01	0,01	0,01	0,02	0,02	0,01	0,01

Table 7: F-F' chemical profile continued.

[illegible]

Table 8: microprobe analyses of 36 syntectonic biotite (Bt I; * indicates biotite included in garnet), 21 porphyroblastic biotite (Bt II) and 42 biotite produced by staurolite demise reaction (Bt III). Analyses are shown in Fig. 3.5.

Table 8: continued

Table 8: continued

Table 8: continued

Sample	LL 57a	LL 57a	LL 56b	LL 56b	LL 56b	LL 56b	LL 56b	LL 56b	LL 56b	LL 56a2	LL 56a2	LL 56a2	LL 56a2	LL 56a2	LL 57b	LL 57b	LL 57b	LL 56d
Descrip.	Bt III - r.p.	Bt III - r.p.	Bt III - r.p.	Bt III - r.p.	Bt III - r.p.	Bt III - r.p.	Bt III - r.p.	Bt III - r.p.	Bt III - r.p.	Bt III - r.p.	Bt III - r.p.	Bt III - r.p.	Bt III - r.p.	Bt III - r.p.	Bt III - r.p.	Bt III - r.p.	Bt III - r.p.	Bt III - r.p.
SiO2	33.66	33.82	33.97	33.71	34.03	35.05	34.41	34.51	34.41	34.62	35.64	34.73	34.62	35.02	34.46	34.50	34.31	34.27
TiO2	3.00	2.49	2.21	2.26	1.83	2.46	2.68	2.00	2.52	2.46	2.08	2.18	1.87	2.65	2.79	1.80	1.81	2.57
Al2O3	19.76	20.73	22.07	20.57	20.12	21.17	19.68	21.47	20.66	20.05	22.16	20.96	22.29	20.81	20.39	20.64	20.31	20.02
FeO	21.82	21.56	20.11	20.44	21.23	21.80	22.13	19.89	21.90	21.19	19.99	20.65	19.99	21.79	21.68	21.75	21.77	21.68
MnO	0.14	0.19	0.16	0.22	0.15	0.23	0.18	0.13	0.27	0.19	0.03	0.19	0.08	0.23	0.25	0.18	0.14	0.12
MgO	6.07	6.13	6.73	6.63	7.00	6.90	6.71	6.62	6.98	6.78	6.47	7.15	6.77	6.55	6.46	6.92	7.04	6.94
CaO	0.00	0.01	0.11	0.03	0.01	0.02	0.02	0.05	0.04	0.02	0.03	0.02	0.01	0.06	0.08	0.00	0.01	0.03
Na2O	0.16	0.16	0.17	0.22	0.18	0.22	0.19	0.21	0.20	0.16	0.24	0.21	0.22	0.32	0.26	0.20	0.18	0.22
K2O	7.82	7.84	6.92	7.34	7.58	7.67	7.45	7.50	7.32	7.44	7.67	8.48	8.72	8.72	8.76	8.48	8.63	8.99
F	0.00	0.03	0.10	0.20	0.00	0.12	0.21	0.28	0.14	0.37	0.00	0.00	0.00	0.00	0.07	0.07	0.00	0.31
(Cl)	0.00	0.04	0.02	0.02	0.03	0.00	0.00	0.00	0.00	0.01	0.00	0.01	0.00	0.00	0.00	0.02	0.00	0.02
F-12O	0.00	0.02	0.06	0.12	0.00	0.07	0.12	0.16	0.08	0.21	0.00	0.00	0.00	0.00	0.04	0.04	0.00	0.18
Cl-12O	0.00	0.03	0.02	0.01	0.02	0.00	0.00	0.00	0.00	0.01	0.00	0.01	0.00	0.00	0.00	0.02	0.00	0.02
H2O	3.80	3.81	3.81	3.70	3.80	3.90	3.75	3.73	3.83	3.68	3.96	3.91	3.93	3.95	3.87	3.85	3.86	3.73
Total	96.23	96.76	96.34	95.25	95.97	99.50	97.32	96.26	98.20	96.80	98.28	98.48	98.53	100.10	99.03	98.38	98.07	98.71
Si	5.32	5.30	5.27	5.33	5.36	5.32	5.36	5.36	5.29	5.39	5.40	5.32	5.28	5.32	5.30	5.33	5.32	5.33
Al IV	2.69	2.71	2.74	2.68	2.64	2.68	2.64	2.64	2.71	2.61	2.60	2.68	2.72	2.68	2.70	2.67	2.68	2.70
Tot IV	8.00	8.00	8.00	8.00	8.00	8.00	8.00	8.00	8.00	8.00	8.00	8.00	8.00	8.00	8.00	8.00	8.00	8.00
AL VI	0.99	1.12	1.30	1.16	1.09	1.10	0.97	1.29	1.04	1.07	1.36	1.11	1.29	1.04	0.99	1.08	1.04	0.95
Ti	0.36	0.29	0.26	0.27	0.22	0.28	0.31	0.23	0.29	0.29	0.24	0.25	0.22	0.30	0.32	0.21	0.21	0.30
Fe2+	2.88	2.82	2.61	2.70	2.80	2.76	2.88	2.58	2.82	2.76	2.53	2.65	2.55	2.77	2.79	2.81	2.83	2.80
Mn	0.02	0.03	0.02	0.03	0.02	0.03	0.02	0.02	0.04	0.02	0.00	0.02	0.01	0.03	0.03	0.02	0.02	0.01
Mg	1.43	1.43	1.56	1.56	1.64	1.56	1.56	1.53	1.60	1.57	1.46	1.63	1.54	1.48	1.48	1.59	1.63	1.60
Tot S1	5.68	5.69	5.74	5.71	5.77	5.73	5.75	5.66	5.79	5.72	5.60	5.67	5.61	5.62	5.62	5.72	5.72	5.66
Ca	0.00	0.00	0.02	0.01	0.00	0.00	0.00	0.01	0.01	0.00	0.01	0.00	0.00	0.01	0.01	0.00	0.00	0.01
Na	0.05	0.05	0.05	0.07	0.06	0.06	0.06	0.06	0.06	0.05	0.07	0.06	0.07	0.09	0.08	0.06	0.05	0.09
K	1.58	1.57	1.37	1.48	1.52	1.48	1.48	1.49	1.44	1.48	1.48	1.66	1.70	1.69	1.72	1.67	1.71	1.71
Tot S2	1.63	1.61	1.44	1.55	1.58	1.55	1.54	1.56	1.50	1.53	1.56	1.72	1.77	1.79	1.81	1.73	1.76	1.83
Tot Cat	15.30	15.31	15.17	15.26	15.35	15.29	15.29	15.22	15.29	15.25	15.16	15.39	15.38	15.41	15.43	15.45	15.49	15.39
F	0.00	0.01	0.05	0.10	0.00	0.06	0.11	0.14	0.07	0.18	0.00	0.00	0.00	0.00	0.03	0.03	0.00	0.15
Cl	0.00	0.01	0.01	0.01	0.01	0.00	0.00	0.00	0.00	0.00	0.00	0.00	0.00	0.00	0.00	0.01	0.00	0.01
OH	4.00	3.98	3.94	3.89	3.99	3.94	3.90	3.86	3.93	3.82	4.00	4.00	4.00	4.00	3.97	3.96	4.00	3.85
ΣO	22	22	22	22	22	22	22	22	22	22	22	22	22	22	22	22	22	22

Table 8: continued

Campione	LL 56b	LL 56b	LL 56b	LL 57a	LL 57a	LL 57a	LL 57a	LL 57a	LL 57a	LL 57a	LL 57a	LL 57a	LL 57a	LL 57a	LL 57a	LL 57a	LL 57a
SiO ₂	27,28	27,36	27,13	26,54	27,29	27,02	27,06	26,89	27,09	26,79	27,07	27,21	26,82	27,57			
TiO ₂	0,34	0,66	0,69	0,72	0,39	0,43	0,67	0,59	0,41	0,46	0,40	0,53	0,52	0,48			
Al ₂ O ₃	55,07	55,54	55,47	53,42	53,39	54,19	53,69	54,37	54,03	53,64	55,15	54,12	54,35	53,82			
FeO	12,48	12,75	12,52	12,94	12,82	13,00	12,59	12,88	12,86	12,93	13,52	13,53	13,06	13,53			
MnO	0,54	0,54	0,51	0,57	0,54	0,39	0,49	0,48	0,45	0,46	0,51	0,49	0,42	0,54			
MgO	1,00	0,94	0,73	0,73	0,90	1,19	0,74	0,68	1,03	1,13	1,32	1,33	0,70	0,73			
ZnO	0,34	0,65	0,69	0,57	0,80	0,34	1,26	0,57	0,00	0,32	0,69	0,54	0,46	0,11			
CaO	0,00	0,04	0,00	0,01	0,00	0,00	0,03	0,00	0,04	0,04	0,04	0,00	0,00	0,00			
Na ₂ O	0,04	0,03	0,03	0,01	0,03	0,05	0,01	0,00	0,03	0,04	0,00	0,01	0,04	0,01			
K ₂ O	0,03	0,01	0,00	0,01	0,00	0,00	0,00	0,00	0,00	0,00	0,01	0,01	0,01	0,00			
Total	97,13	98,50	97,77	95,53	96,16	96,62	96,53	96,46	95,93	95,80	98,71	97,77	96,38	96,80			
Si	7,60	7,54	7,52	7,56	7,72	7,59	7,63	7,57	7,64	7,59	7,48	7,59	7,56	7,73			
Al IV	0,40	0,46	0,48	0,44	0,28	0,41	0,37	0,43	0,36	0,41	0,52	0,42	0,44	0,27			
Tot IV	8	8	8	8	8	8	8	8	8	8	8	8	8	8			
Al VI	17,68	17,57	17,65	17,50	17,51	17,53	17,49	17,61	17,61	17,51	17,44	17,37	17,61	17,53			
Ti	0,07	0,14	0,14	0,16	0,08	0,09	0,14	0,12	0,09	0,10	0,08	0,11	0,11	0,10			
Tot S1	17,75	17,71	17,80	17,66	17,59	17,62	17,63	17,73	17,69	17,61	17,52	17,48	17,72	17,63			
Fe ²⁺	2,91	2,94	2,90	3,08	3,03	3,06	2,97	3,03	3,04	3,06	3,12	3,16	3,08	3,18			
Mn	0,13	0,13	0,12	0,14	0,13	0,09	0,12	0,11	0,11	0,11	0,12	0,12	0,10	0,13			
Mg	0,42	0,38	0,30	0,31	0,38	0,50	0,31	0,29	0,43	0,48	0,54	0,55	0,29	0,31			
Zn	0,07	0,13	0,14	0,12	0,17	0,07	0,26	0,12	0,00	0,07	0,14	0,11	0,10	0,02			
Ca	0,00	0,01	0,00	0,00	0,00	0,00	0,01	0,00	0,01	0,01	0,01	0,00	0,00	0,00			
Na	0,02	0,01	0,02	0,01	0,02	0,03	0,01	0,00	0,02	0,02	0,00	0,01	0,02	0,00			
K	0,01	0,00	0,00	0,00	0,00	0,00	0,00	0,00	0,00	0,00	0,00	0,01	0,00	0,00			
Tot S2	3,55	3,61	3,48	3,66	3,73	3,75	3,68	3,55	3,60	3,75	3,94	3,94	3,59	3,64			
Tot Cat	29,31	29,32	29,28	29,32	29,32	29,37	29,30	29,29	29,30	29,36	29,46	29,42	29,32	29,27			
ΣO	46	46	46	46	46	46	46	46	46	46	46	46	46	46			
XMg	0,12	0,11	0,09	0,08	0,10	0,13	0,09	0,08	0,12	0,13	0,14	0,14	0,08	0,08			

Table 9: 28 microprobe analyses of staurolite porphyroblasts from micaschists

Campione	LL 56b	LL 56b	LL 56b	LL 56a2	LL 56a2	LL 56a2	LL 56a2	LL 56a2	LL 57b	LL 57b	LL 57b	LL 57b	LL 57b	LL 56d	LL 56d	LL 56d
SiO2	27,22	27,53	27,49	27,22	27,77	27,82	28,39	27,33	27,49	26,72	26,96	26,80	26,77	27,11	26,77	27,11
TiO2	0,39	0,40	0,33	0,76	0,76	0,78	0,66	0,46	0,43	0,46	0,58	0,62	0,30	0,43	0,62	0,43
Al2O3	54,57	54,52	53,79	56,16	55,74	56,43	55,67	55,73	56,20	56,24	56,47	56,43	56,97	56,43	56,97	56,43
FeO	12,21	12,38	12,29	12,46	12,41	12,37	12,80	12,84	12,56	12,32	12,23	13,07	13,20	13,09	13,20	13,09
MnO	0,53	0,50	0,55	0,51	0,48	0,49	0,56	0,34	0,41	0,47	0,31	0,57	0,63	0,61	0,57	0,61
MgO	0,98	1,04	1,10	0,95	1,08	0,96	0,97	1,20	0,89	0,91	0,72	1,12	1,09	0,77	1,12	0,77
ZnO	0,80	1,28	1,14	1,01	0,45	0,21	0,55	0,74	0,72	1,03	0,76	0,75	0,94	0,89	0,75	0,89
CaO	0,00	0,00	0,03	0,00	0,07	0,00	0,00	0,00	0,00	0,04	0,02	0,04	0,05	0,00	0,04	0,00
Na2O	0,06	0,03	0,00	0,03	0,00	0,00	0,01	0,06	0,00	0,02	0,03	0,05	0,00	0,00	0,05	0,00
K2O	0,00	0,00	0,00	0,00	0,00	0,03	0,00	0,07	0,01	0,00	0,00	0,00	0,00	0,00	0,00	0,00
Total	96,76	97,68	96,72	99,09	98,76	99,09	99,60	98,79	98,72	98,20	98,10	99,46	99,94	99,34	99,94	99,34
Si	7,62	7,66	7,72	7,46	7,60	7,58	7,72	7,51	7,54	7,39	7,44	7,34	7,30	7,43	7,30	7,43
Al IV	0,38	0,34	0,28	0,54	0,40	0,42	0,28	0,49	0,46	0,61	0,57	0,66	0,70	0,57	0,66	0,57
Tot IV	8	8	8	8	8	8	8	8	8	8	8	8	8	8	8	8
Al VI	17,63	17,54	17,52	17,59	17,59	17,69	17,55	17,57	17,71	17,71	17,79	17,55	17,62	17,65	17,62	17,65
Ti	0,08	0,08	0,07	0,16	0,16	0,16	0,13	0,10	0,09	0,10	0,12	0,13	0,06	0,09	0,13	0,09
TotS1	17,72	17,62	17,59	17,75	17,75	17,84	17,69	17,66	17,80	17,80	17,91	17,67	17,68	17,74	17,68	17,74
Fe2+	2,86	2,88	2,89	2,86	2,84	2,82	2,91	2,95	2,88	2,85	2,82	2,99	3,01	3,00	3,01	3,00
Mn	0,13	0,12	0,13	0,12	0,11	0,11	0,13	0,08	0,10	0,11	0,07	0,13	0,15	0,14	0,15	0,14
Mg	0,41	0,43	0,46	0,39	0,44	0,39	0,39	0,49	0,36	0,38	0,30	0,46	0,44	0,31	0,46	0,31
Zn	0,17	0,26	0,24	0,21	0,09	0,04	0,11	0,15	0,15	0,21	0,16	0,15	0,19	0,18	0,15	0,18
Ca	0,00	0,00	0,01	0,00	0,02	0,00	0,00	0,00	0,00	0,01	0,01	0,01	0,01	0,00	0,01	0,00
Na	0,03	0,02	0,00	0,01	0,00	0,00	0,01	0,03	0,00	0,01	0,02	0,03	0,00	0,00	0,03	0,00
K	0,00	0,00	0,00	0,00	0,00	0,01	0,00	0,03	0,00	0,00	0,00	0,00	0,00	0,00	0,00	0,00
Tot S2	3,59	3,71	3,72	3,58	3,50	3,37	3,55	3,73	3,49	3,56	3,37	3,77	3,80	3,64	3,77	3,64
Tot Cat	29,31	29,33	29,31	29,33	29,25	29,22	29,24	29,40	29,29	29,36	29,28	29,45	29,48	29,37	29,48	29,37
ΣO	46	46	46	46	46	46	46	46	46	46	46	46	46	46	46	46
XMg	0,12	0,12	0,12	0,11	0,13	0,12	0,11	0,13	0,10	0,11	0,09	0,12	0,12	0,09	0,12	0,09

Table 9: continued

Sample	LL56a1	LL56a1	LL56a1	LL56a1	LL56a1	LL56a1	LL56a1	LL56a1	LL56a1	LL56a1	LL56a1	LL56a3	LL56a3	LL56a3	LL56a3	LL56a3	LL56a4	LL56a4	LL56a4	LL56a4	LL56a4	LL56a4	LL56a4	LL56a4	LL56a4
Descript.	Pl synt.	Pl synt.	Pl synt.	Pl synt.	Pl synt.	Pl synt.	Pl synt.	Pl synt.	Pl synt.	Pl synt.	Pl synt.	Pl synt.	Pl synt.	Pl synt.	Pl synt.	Pl synt.	Pl synt.	Pl synt.	Pl synt.	Pl synt.	Pl synt.	Pl synt.	Pl synt.	Pl synt.	Pl synt.
SiO2	63,29	64,27	64,16	63,89	62,88	64,30	60,69	63,00	62,18	61,02	61,53	63,62	63,35	63,04	63,84	62,94	62,66	62,21	62,72	63,44	61,61				
TiO2	0,00	0,00	0,00	0,01	0,03	0,00	0,02	0,01	0,04	0,06	0,00	0,00	0,00	0,02	0,00	0,01	0,04	0,00	0,00	0,00	0,01				
Al2O3	23,07	22,29	23,17	23,46	23,42	22,94	24,76	23,39	23,95	24,48	24,52	23,12	23,17	23,19	22,95	23,15	23,27	22,97	22,13	22,46	23,55				
Fe2O3	0,02	0,02	0,07	0,00	0,07	0,01	0,00	0,00	0,00	0,07	0,02	0,08	0,12	0,01	0,08	0,10	0,00	0,09	0,07	0,05	0,11				
MnO	0,01	0,00	0,00	0,00	0,00	0,00	0,02	0,05	0,00	0,00	0,00	0,00	0,08	0,02	0,00	0,00	0,00	0,00	0,03	0,00	0,02				
MgO	0,00	0,02	0,02	0,00	0,00	0,00	0,00	0,01	0,02	0,01	0,01	0,00	0,01	0,00	0,00	0,00	0,00	0,00	0,01	0,00	0,00				
CaO	4,72	3,21	4,07	4,56	4,72	4,48	6,85	4,97	4,63	6,05	6,08	4,45	4,54	4,70	4,50	4,53	4,81	4,49	4,15	4,32	5,54				
Na2O	9,64	10,12	9,76	9,71	9,61	9,75	8,72	9,52	9,18	8,96	8,58	9,40	9,76	9,45	9,74	9,47	9,25	9,25	9,44	9,42	8,89				
K2O	0,13	0,31	0,23	0,10	0,10	0,12	0,07	0,10	0,80	0,06	0,04	0,10	0,05	0,10	0,15	0,12	0,07	0,14	0,09	0,09	0,02				
Total	100,88	100,24	101,49	101,74	100,83	101,57	101,13	101,04	100,79	100,70	100,78	100,77	101,09	100,54	101,24	100,32	100,10	99,15	98,64	99,79	99,76				
Si	2,78	2,83	2,80	2,78	2,77	2,80	2,68	2,77	2,75	2,70	2,72	2,79	2,78	2,78	2,80	2,78	2,77	2,78	2,81	2,81	2,74				
Al	1,20	1,16	1,19	1,21	1,22	1,18	1,29	1,21	1,25	1,28	1,28	1,20	1,20	1,21	1,18	1,21	1,21	1,21	1,17	1,17	1,24				
Ti	0,00	0,00	0,00	0,00	0,00	0,00	0,00	0,00	0,00	0,00	0,00	0,00	0,00	0,00	0,00	0,00	0,00	0,00	0,00	0,00	0,00				
Fe3+	0,00	0,00	0,00	0,00	0,00	0,00	0,00	0,00	0,00	0,00	0,00	0,00	0,00	0,00	0,00	0,00	0,00	0,00	0,00	0,00	0,00				
Mn	0,00	0,00	0,00	0,00	0,00	0,00	0,00	0,00	0,00	0,00	0,00	0,00	0,00	0,00	0,00	0,00	0,00	0,00	0,00	0,00	0,00				
Mg	0,00	0,00	0,00	0,00	0,00	0,00	0,00	0,00	0,00	0,00	0,00	0,00	0,00	0,00	0,00	0,00	0,00	0,00	0,00	0,00	0,00				
Ca	0,22	0,15	0,19	0,21	0,22	0,21	0,32	0,23	0,22	0,29	0,29	0,21	0,21	0,22	0,21	0,21	0,23	0,22	0,20	0,21	0,27				
Na	0,82	0,87	0,83	0,82	0,82	0,83	0,75	0,81	0,79	0,77	0,73	0,80	0,83	0,81	0,83	0,81	0,79	0,80	0,82	0,81	0,77				
K	0,01	0,02	0,01	0,01	0,01	0,01	0,00	0,01	0,05	0,00	0,00	0,01	0,00	0,01	0,01	0,01	0,00	0,01	0,01	0,01	0,00				
Tot Cat	5,03	5,03	5,02	5,03	5,04	5,02	5,05	5,03	5,05	5,04	5,02	5,01	5,03	5,02	5,03	5,02	5,02	5,02	5,01	5,01	5,02				
ΣO	8	8	8	8	8	8	8	8	8	8	8	8	8	8	8	8	8	8	8	8	8				
Or	0,71	1,69	1,22	0,56	0,56	0,66	0,36	0,56	4,28	0,30	0,22	0,58	0,29	0,57	0,81	0,64	0,41	0,78	0,52	0,51	0,14				
Ab	78,14	83,65	80,29	78,96	78,24	79,23	69,47	77,18	74,85	72,61	71,69	78,82	79,31	78,01	79,01	78,60	77,38	78,23	80,03	79,37	74,28				
An	21,15	14,67	18,49	20,48	21,21	20,11	30,17	22,27	20,87	27,09	28,10	20,60	20,40	21,43	20,18	20,76	22,22	20,99	19,45	20,12	25,59				

Table 10: microprobe analyses of syntectonic plagioclase (Pl synt. 75) and of plagioclase included in garnet (Pl* 28) from micaschists. Analyses are shown in Fig. 3.6.

[illegible]

Table 10: continued

Sample	LL 56d	LL 56d	LL 56d	LL 56d	LL 56d	LL 56d	LL 56d	LL 56d	LL 56d	LL 56d	LL 56d	LL 56d	LL 56d	LL 56d	LL 56d	LL 56d	LL 56d	LL 56d
Descript.	Pl synt.	Pl synt.	Pl synt.	Pl synt.	Pl synt.	Pl synt.	Pl synt.	Pl synt.	Pl synt.	Pl synt.	Pl synt.	Pl synt.	Pl synt.	Pl synt.	Pl synt.	Pl synt.	Pl synt.	Pl synt.
SiO2	62,58	59,81	61,36	61,81	60,99	60,39	61,12	60,39	61,57	62,04	62,94	62,63	61,34	60,03	61,14	61,92	61,16	61,07
TiO2	0,00	0,00	0,06	0,19	0,00	0,09	0,00	0,16	0,00	0,00	0,00	0,05	0,03	0,14	0,00	0,08	0,16	0,16
Al2O3	24,80	25,04	24,27	24,82	25,77	25,35	24,26	25,09	24,40	24,66	23,96	24,24	25,34	25,18	24,97	24,96	24,94	25,02
Fe2O3	0,00	0,12	0,03	0,09	0,13	0,08	0,12	0,07	0,13	0,03	0,00	0,00	0,07	0,10	0,08	0,03	0,00	0,00
MnO	0,00	0,00	0,03	0,00	0,02	0,01	0,00	0,03	0,00	0,00	0,00	0,00	0,00	0,02	0,02	0,00	0,00	0,01
MgO	0,00	0,07	0,00	0,02	0,01	0,00	0,00	0,00	0,00	0,00	0,01	0,01	0,00	0,04	0,00	0,03	0,00	0,01
CaO	4,97	5,68	5,11	6,08	6,32	6,49	4,72	6,14	5,61	5,36	4,55	5,00	6,05	6,22	6,02	6,15	6,14	5,88
K2O	8,92	8,33	8,64	8,47	8,41	8,56	8,72	7,96	8,66	8,88	9,19	9,14	8,51	8,04	8,36	8,35	8,25	8,52
Total	101,45	99,15	99,70	101,52	101,72	101,02	99,25	99,97	100,46	101,03	100,72	101,17	101,37	100,01	100,69	101,60	100,74	100,79
Si	2,73	2,68	2,73	2,71	2,67	2,67	2,73	2,69	2,72	2,73	2,77	2,75	2,69	2,67	2,70	2,71	2,70	2,70
Al	1,28	1,32	1,27	1,28	1,33	1,32	1,28	1,32	1,27	1,28	1,24	1,25	1,31	1,32	1,30	1,29	1,30	1,30
Ti	0,00	0,00	0,00	0,01	0,00	0,00	0,00	0,01	0,00	0,00	0,00	0,00	0,00	0,01	0,00	0,00	0,01	0,00
Fe3+	0,00	0,00	0,00	0,00	0,00	0,00	0,00	0,00	0,00	0,00	0,00	0,00	0,00	0,00	0,00	0,00	0,00	0,00
Mn	0,00	0,00	0,00	0,00	0,00	0,00	0,00	0,00	0,00	0,00	0,00	0,00	0,00	0,00	0,00	0,00	0,00	0,00
Mg	0,00	0,01	0,00	0,00	0,00	0,00	0,00	0,00	0,00	0,00	0,00	0,00	0,00	0,00	0,00	0,00	0,00	0,00
Ca	0,23	0,27	0,24	0,29	0,30	0,31	0,23	0,29	0,27	0,25	0,21	0,24	0,28	0,30	0,29	0,29	0,29	0,28
Na	0,76	0,73	0,75	0,72	0,71	0,73	0,76	0,69	0,74	0,76	0,78	0,78	0,72	0,70	0,72	0,71	0,73	0,73
K	0,01	0,01	0,01	0,00	0,00	0,00	0,02	0,01	0,01	0,00	0,01	0,01	0,00	0,01	0,01	0,01	0,01	0,00
Tot Cat	5,01	5,02	5,01	5,01	5,02	5,04	5,01	5,00	5,01	5,02	5,01	5,02	5,01	5,01	5,01	5,00	5,00	5,02
ΣO	8	8	8	8	8	8	8	8	8	8	8	8	8	8	8	8	8	8
Or	1,00	0,50	1,09	0,27	0,42	0,26	1,73	0,78	0,48	0,29	0,46	0,58	0,19	1,31	0,62	0,48	0,54	0,62
Ab	75,70	72,28	74,54	71,41	70,36	70,31	75,66	69,57	73,28	74,76	78,17	76,34	71,65	69,15	71,10	70,73	70,49	71,82
An	23,31	27,23	24,37	28,32	29,21	29,43	22,61	29,65	26,24	24,94	21,37	23,08	28,17	29,54	28,28	28,79	28,97	27,36

Table 10: continued

Sample	LL 56d	LL 56d	LL 56d	LL 56d	LL 56d	LL 56d	LL 56d	LL 56d	LL 56d	LL 56d	LL 56d	LL 56a3	LL 56a3	LL 56a3	LL 56a3	LL 56a3	LL 56a3	LL 56a3	LL 56a3
Descript.	Pl synt.	Pl synt.	Pl synt.	Pl synt.	Pl synt.	Pl synt.	Pl synt.	Pl synt.	Pl synt.	Pl synt.	Pl synt.	Pl synt.	Pl *	Pl *	Pl *	Pl *	Pl *	Pl *	Pl *
SiO2	61,59	61,28	61,30	60,63	60,95	58,47	58,74	60,31	59,89	60,39	60,48	61,81	68,16	62,07	60,54	62,17	70,28	61,82	62,62
TiO2	0,00	0,02	0,00	0,00	0,06	0,05	0,00	0,05	0,08	0,00	0,09	0,00	0,00	0,01	0,00	0,05	0,00	0,00	0,03
Al2O3	24,96	25,23	25,10	25,11	25,31	26,67	25,05	26,03	25,19	25,15	25,11	24,56	20,01	24,44	24,78	24,09	18,24	23,97	23,73
Fe2O3	0,01	0,16	0,02	0,05	0,00	0,17	0,06	0,00	0,14	0,02	0,06	0,00	0,63	0,24	0,47	0,41	0,51	0,22	0,51
MnO	0,00	0,00	0,00	0,02	0,00	0,00	0,00	0,07	0,07	0,05	0,09	0,00	0,11	0,01	0,12	0,00	0,02	0,11	0,05
MgO	0,02	0,00	0,00	0,00	0,00	0,05	0,07	0,02	0,00	0,00	0,01	0,00	0,03	0,00	0,01	0,00	0,02	0,00	0,01
CaO	6,04	5,96	6,18	5,99	6,20	5,94	5,94	5,76	6,15	6,08	6,05	5,54	0,19	5,90	6,04	5,50	0,16	5,81	5,05
Na2O	8,52	8,35	8,48	8,34	8,23	7,73	7,93	8,44	8,65	8,69	8,71	8,71	11,74	8,87	8,49	8,81	10,81	9,23	9,32
K2O	0,11	0,18	0,09	0,08	0,07	0,17	0,25	0,62	0,10	0,05	0,03	0,07	0,43	0,06	0,33	0,05	0,40	0,05	0,09
Total	101,25	101,18	101,17	100,22	100,81	99,25	98,03	101,31	100,26	100,43	100,63	100,69	101,30	101,59	100,77	101,08	100,42	101,12	101,43
Si	2,71	2,69	2,70	2,69	2,69	2,62	2,67	2,66	2,67	2,68	2,68	2,73	2,96	2,72	2,68	2,73	3,05	2,73	2,75
Al	1,29	1,31	1,30	1,31	1,32	1,41	1,34	1,35	1,32	1,32	1,31	1,28	1,02	1,26	1,30	1,25	0,93	1,25	1,23
Ti	0,00	0,00	0,00	0,00	0,00	0,00	0,00	0,00	0,00	0,00	0,00	0,00	0,00	0,00	0,00	0,00	0,00	0,00	0,00
Fe3+	0,00	0,01	0,00	0,00	0,00	0,01	0,00	0,00	0,01	0,00	0,00	0,00	0,02	0,01	0,02	0,01	0,02	0,01	0,03
Mn	0,00	0,00	0,00	0,00	0,00	0,00	0,00	0,00	0,00	0,00	0,00	0,00	0,00	0,00	0,00	0,00	0,00	0,00	0,00
Mg	0,00	0,00	0,00	0,00	0,00	0,00	0,00	0,00	0,00	0,00	0,00	0,00	0,00	0,00	0,00	0,00	0,00	0,00	0,00
Ca	0,28	0,28	0,29	0,29	0,29	0,29	0,29	0,27	0,29	0,29	0,29	0,26	0,01	0,28	0,29	0,26	0,01	0,27	0,24
Na	0,73	0,71	0,72	0,72	0,70	0,67	0,70	0,72	0,75	0,75	0,75	0,75	0,99	0,75	0,73	0,75	0,91	0,79	0,80
K	0,01	0,01	0,01	0,00	0,00	0,01	0,01	0,04	0,01	0,00	0,00	0,00	0,02	0,00	0,02	0,00	0,02	0,00	0,01
Tot Cat	5,02	5,01	5,02	5,01	5,01	5,01	5,02	5,04	5,04	5,04	5,04	5,01	5,03	5,02	5,04	5,01	4,94	5,05	5,03
ΣO	8	8	8	8	8	8	8	8	8	8	8	8	8	8	8	8	8	8	8
Or	0,59	1,02	0,48	0,43	0,38	1,00	1,42	3,37	0,55	0,29	0,16	0,40	2,32	0,30	1,80	0,27	2,33	0,27	0,46
Ab	71,43	70,99	70,94	71,27	70,33	69,50	69,73	70,16	71,41	71,92	72,13	73,72	96,83	72,92	70,49	74,13	96,89	74,01	76,58
An	27,99	27,99	28,58	28,30	29,29	29,50	28,85	26,47	28,04	27,80	27,71	25,88	0,85	26,78	27,71	25,60	0,78	25,73	22,96

Table 10: continued

Table 11: chemical analyses of 3 textural generation of white mica (24 Ms I; 47 Ms II; 3 Ms III) from micaschists. Analyses are shown in Fig. 3.7.

Table 11: continued

Table 11: continued

Sample Descrip.	LL 56a2		LL 56a2		LL 57b		LL 57b		LL 57b		LL 57b		LL 56d		LL 56d		LL 56d		LL 56b		LL 56b		LL 56b	
	Ms II	Ms II	Ms II	Ms II	Ms II	Ms II	Ms II	Ms II	Ms II	Ms II	Ms II	Ms II	Ms II	Ms II	Ms II	Ms II	Ms II	Ms II	Ms II	Ms II	Ms II	Ms II	Ms II	
SiO2	45,99	44,45	44,84	45,77	45,17	45,43	45,52	44,74	46,22	45,40	44,96	44,51	43,59	45,13	45,40	44,93								
TiO2	0,32	0,29	0,22	0,63	0,14	0,52	0,23	0,25	0,35	1,01	0,68	0,26	0,40	0,20	0,41	0,35								
Al2O3	35,18	36,74	37,07	36,38	37,55	36,85	37,10	36,69	36,85	36,90	36,89	37,61	36,56	36,10	35,98	36,98								
FeO	1,07	0,94	0,81	1,17	0,88	0,76	0,85	1,00	0,92	0,91	0,79	0,94	0,79	0,85	0,85	0,87								
MnO	0,03	0,00	0,04	0,02	0,05	0,03	0,06	0,01	0,02	0,10	0,00	0,05	0,00	0,00	0,00	0,01								
MgO	0,82	0,47	0,40	0,35	0,30	0,39	0,36	0,36	0,34	0,49	0,44	0,37	0,48	0,38	0,41	0,32								
CaO	0,01	0,00	0,00	0,02	0,00	0,00	0,02	0,00	0,00	0,01	0,00	0,01	0,04	0,04	0,07	0,01								
Na2O	0,85	1,00	1,05	0,96	0,98	1,04	1,06	1,23	1,13	1,00	0,99	1,02	0,93	1,05	0,95	1,11								
K2O	9,09	9,60	9,23	8,97	9,45	9,17	9,14	9,41	9,91	9,57	9,57	9,67	9,41	8,29	8,36	8,34								
(F)	0,00	0,00	0,04	0,00	0,12	0,04	0,16	0,08	0,04	0,08	0,04	0,00	0,08	0,27	0,11	0,00								
(Cl)	0,02	0,03	0,01	0,00	0,02	0,04	0,00	0,00	0,00	0,04	0,02	0,00	0,01	0,01	0,01	0,01								
F-12O	0,00	0,00	0,02	0,00	0,07	0,02	0,09	0,05	0,02	0,05	0,02	0,00	0,05	0,16	0,07	0,00								
Cl-12O	0,01	0,03	0,01	0,00	0,01	0,03	0,00	0,00	0,00	0,03	0,01	0,00	0,01	0,01	0,01	0,01								
H2O	4,45	4,43	4,44	4,50	4,44	4,46	4,43	4,41	4,53	4,48	4,46	4,48	4,34	4,29	4,38	4,45								
Total	97,83	97,95	98,12	98,77	99,03	98,70	98,86	98,13	100,31	99,95	98,84	98,92	96,61	96,50	96,86	97,35								
Si	6,19	6,00	6,03	6,10	6,02	6,06	6,06	6,03	6,10	6,01	6,01	5,96	5,97	6,13	6,14	6,05								
Al IV	1,81	2,00	1,98	1,90	1,98	1,94	1,94	1,97	1,91	1,99	1,99	2,05	2,03	1,87	1,86	1,95								
Tot IV	8	8	8	8	8	8	8	8	8	8	8	8	8	8	8	8								
Al VI	3,77	3,85	3,89	3,82	3,92	3,86	3,89	3,85	3,82	3,77	3,82	3,89	3,86	3,91	3,88	3,92								
Ti	0,03	0,03	0,02	0,06	0,01	0,05	0,02	0,03	0,04	0,10	0,07	0,03	0,04	0,02	0,04	0,04								
Fe2+	0,12	0,11	0,09	0,13	0,10	0,09	0,09	0,11	0,10	0,10	0,09	0,11	0,09	0,10	0,10	0,10								
Mn	0,00	0,00	0,00	0,00	0,01	0,00	0,01	0,00	0,00	0,01	0,00	0,01	0,00	0,00	0,00	0,00								
Mg	0,16	0,09	0,08	0,07	0,06	0,08	0,07	0,07	0,07	0,10	0,09	0,07	0,10	0,08	0,08	0,06								
Tot S1	4,09	4,08	4,09	4,09	4,09	4,08	4,08	4,07	4,03	4,08	4,07	4,10	4,09	4,10	4,10	4,12								
Ca	0,00	0,00	0,00	0,00	0,00	0,00	0,00	0,00	0,00	0,00	0,00	0,00	0,01	0,01	0,01	0,00								
Na	0,22	0,26	0,27	0,25	0,25	0,27	0,28	0,32	0,29	0,26	0,26	0,26	0,25	0,28	0,25	0,29								
K	1,56	1,65	1,58	1,53	1,61	1,56	1,55	1,62	1,67	1,62	1,63	1,65	1,64	1,44	1,44	1,43								
Tot S2	1,79	1,92	1,85	1,78	1,86	1,83	1,83	1,94	1,96	1,87	1,89	1,91	1,90	1,72	1,70	1,72								
Tot Cat	13,88	14,00	13,95	13,86	13,95	13,90	13,91	14,00	13,99	13,95	13,96	14,01	13,99	13,82	13,80	13,84								
F	0,00	0,00	0,02	0,00	0,05	0,02	0,07	0,03	0,02	0,03	0,02	0,00	0,04	0,12	0,05	0,00								
Cl	0,00	0,01	0,00	0,00	0,00	0,01	0,00	0,00	0,00	0,01	0,00	0,00	0,00	0,00	0,00	0,00								
OH	4,00	3,99	3,98	4,00	3,95	3,97	3,93	3,97	3,98	3,96	3,98	4,00	3,96	3,88	3,95	4,00								
ΣO	22	22	22	22	22	22	22	22	22	22	22	22	22	22	22	22								

Table 11: continued

Sample Descrip.	LL 61c1 Grt H-H'	LL 61c1 Grt H-H'	LL 61c1 Grt H-H'	LL 61c1 Grt H-H'	LL 61c1 Grt H-H'	LL 61c1 Grt H-H'	LL 61c1 Grt H-H'	LL 61c1 Grt H-H'	LL 61c1 Grt H-H'	LL 61c1 Grt H-H'	LL 61c1 Grt H-H'	LL 61c1 Grt H-H'	LL 61c1 Grt H-H'	LL 61c1 Grt H-H'	LL 61c1 Grt H-H'	LL 61c1 Grt H-H'	LL 61c1 Grt H-H'	LL 61c1 Grt H-H'	LL 61c1 Grt H-H'
SiO2	35.91	35.85	35.88	35.82	35.98	35.68	35.77	35.91	35.61	35.77	35.60	35.56	35.29	35.69	35.39	35.76	35.71	35.78	35.64
TiO2	0.05	0.02	0.02	0.04	0.02	0.00	0.00	0.00	0.00	0.05	0.02	0.05	0.00	0.04	0.10	0.03	0.01	0.05	0.05
Al2O3	20.07	20.10	20.07	20.22	20.09	19.98	20.08	20.06	19.96	20.05	19.98	19.80	19.85	19.97	19.88	20.10	19.91	19.76	19.86
Fe2O3	0.99	1.01	1.30	1.19	1.13	1.55	1.50	1.54	1.44	1.28	1.50	1.21	1.37	1.27	1.38	1.30	1.51	1.59	1.24
FeO	34.25	33.87	34.05	34.07	33.87	33.80	33.95	33.85	33.58	33.85	33.77	33.58	33.55	33.67	33.72	33.82	33.80	33.88	33.70
MnO	5.81	5.81	5.75	5.75	5.79	5.80	5.73	5.80	5.75	5.67	5.63	5.61	5.53	5.70	5.62	5.77	5.70	5.62	5.52
MgO	1.36	1.58	1.61	1.67	1.64	1.65	1.69	1.67	1.69	1.66	1.69	1.60	1.67	1.68	1.68	1.66	1.65	1.65	1.69
CaO	0.75	0.72	0.74	0.74	0.78	0.81	0.81	0.84	0.85	0.88	0.90	0.85	0.80	0.86	0.86	0.86	0.83	0.83	0.82
Na2O	0.00	0.00	0.02	0.02	0.01	0.01	0.00	0.00	0.01	0.02	0.00	0.01	0.02	0.01	0.00	0.01	0.01	0.01	0.01
K2O	0.02	0.01	0.01	0.00	0.00	0.01	0.00	0.00	0.00	0.00	0.01	0.00	0.00	0.00	0.00	0.00	0.00	0.00	0.00
Total	99.23	98.96	99.45	99.54	99.31	99.28	99.53	99.65	98.89	99.24	99.11	98.28	98.09	98.89	98.62	99.30	99.13	99.17	98.53
Si	2.97	2.97	2.96	2.96	2.97	2.95	2.95	2.96	2.96	2.96	2.95	2.97	2.96	2.96	2.95	2.96	2.96	2.97	2.97
Al IV	0.03	0.03	0.04	0.05	0.03	0.05	0.05	0.04	0.04	0.04	0.05	0.03	0.05	0.04	0.05	0.04	0.04	0.04	0.03
Tot IV	3.00	3.00	3.00	3.00	3.00	3.00	3.00	3.00	3.00	3.00	3.00	3.00	3.00	3.00	3.00	3.00	3.00	3.00	3.00
Al VI	1.93	1.94	1.92	1.92	1.93	1.90	1.91	1.91	1.91	1.91	1.90	1.92	1.91	1.92	1.90	1.92	1.90	1.89	1.92
Ti	0.00	0.00	0.00	0.00	0.00	0.00	0.00	0.00	0.00	0.00	0.00	0.00	0.00	0.00	0.01	0.00	0.00	0.00	0.00
Fe3+	0.06	0.06	0.08	0.07	0.07	0.10	0.09	0.10	0.09	0.08	0.09	0.08	0.09	0.08	0.09	0.08	0.09	0.10	0.08
Tot S1	2.00	2.00	2.00	2.00	2.00	2.00	2.00	2.00	2.00	2.00	2.00	2.00	2.00	2.00	1.99	2.00	2.00	2.00	2.00
Fe2+	2.37	2.35	2.35	2.35	2.34	2.34	2.34	2.33	2.33	2.34	2.34	2.35	2.35	2.34	2.35	2.34	2.34	2.35	2.35
Mn	0.41	0.41	0.40	0.40	0.41	0.41	0.40	0.41	0.40	0.40	0.40	0.40	0.39	0.40	0.40	0.40	0.40	0.39	0.39
Mg	0.17	0.20	0.20	0.21	0.20	0.20	0.21	0.21	0.21	0.20	0.21	0.20	0.21	0.21	0.21	0.21	0.20	0.20	0.21
Ca	0.07	0.06	0.07	0.07	0.07	0.07	0.07	0.07	0.08	0.08	0.08	0.08	0.07	0.08	0.08	0.08	0.07	0.07	0.07
Na	0.00	0.00	0.00	0.00	0.00	0.00	0.00	0.00	0.00	0.00	0.00	0.00	0.00	0.00	0.00	0.00	0.00	0.00	0.00
K	0.00	0.00	0.00	0.00	0.00	0.00	0.00	0.00	0.00	0.00	0.00	0.00	0.00	0.00	0.00	0.00	0.00	0.00	0.00
Tot S2	3.02	3.02	3.02	3.03	3.02	3.02	3.02	3.02	3.02	3.03	3.03	3.02	3.02	3.02	3.03	3.02	3.02	3.02	3.02
Tot Cat	8.02	8.02	8.02	8.02	8.02	8.02	8.02	8.02	8.02	8.02	8.03	8.02	8.02	8.02	8.03	8.02	8.02	8.02	8.02
ΣO	12	12	12	12	12	12	12	12	12	12	12	12	12	12	12	12	12	12	12
Prp	5.52	6.40	6.44	6.71	6.60	6.57	6.72	6.65	6.78	6.67	6.77	6.54	6.76	6.77	6.76	6.67	6.60	6.60	6.83
Alm	78.01	77.10	76.52	76.59	76.67	75.62	75.83	75.59	75.69	76.46	75.88	76.74	76.29	76.27	76.17	76.22	75.87	75.86	76.64
Grs	0.00	0.00	0.00	0.00	0.00	0.00	0.00	0.00	0.00	0.00	0.00	0.00	0.00	0.00	0.00	0.00	0.00	0.00	0.00
Sps	13.41	13.41	13.09	13.09	13.28	13.13	12.95	13.12	13.13	12.97	12.81	12.99	12.74	13.07	12.87	13.16	12.95	12.73	12.71
Adr	3.06	3.09	3.95	3.61	3.45	4.68	4.51	4.65	4.40	3.91	4.55	3.73	4.22	3.89	4.20	3.95	4.58	4.81	3.82
XMg	0.06	0.07	0.07	0.07	0.07	0.07	0.07	0.07	0.07	0.07	0.07	0.07	0.07	0.07	0.07	0.07	0.07	0.07	0.07
XFe	0.80	0.80	0.80	0.79	0.79	0.79	0.79	0.79	0.79	0.80	0.79	0.80	0.80	0.79	0.79	0.79	0.80	0.80	0.80
XPrp	0.06	0.06	0.06	0.07	0.07	0.07	0.07	0.07	0.07	0.07	0.07	0.07	0.07	0.07	0.07	0.07	0.07	0.07	0.07
XAlm	0.78	0.77	0.77	0.77	0.77	0.76	0.76	0.76	0.76	0.76	0.76	0.77	0.76	0.76	0.76	0.76	0.76	0.76	0.77
XGrs	0.00	0.00	0.00	0.00	0.00	0.00	0.00	0.00	0.00	0.00	0.00	0.00	0.00	0.00	0.00	0.00	0.00	0.00	0.00
XSps	0.13	0.13	0.13	0.13	0.13	0.13	0.13	0.13	0.13	0.13	0.13	0.13	0.13	0.13	0.13	0.13	0.13	0.13	0.13
XAdr	0.03	0.03	0.04	0.04	0.03	0.05	0.05	0.05	0.04	0.04	0.05	0.04	0.04	0.04	0.04	0.04	0.05	0.05	0.04

Table 12: H-H' chemical profile of garnet crystal from LL61c1 Qtz+Pl-rich layer of paragneiss. Analyses are shown in Fig. 3.8a.

Table 12: H-H' chemical profile continued.

[illegible]

Table 12: H-H' chemical profile continued.

Sample Descrip.	LL 61c1		LL 61c1		LL 61c1		LL 61c1		LL 61c1		LL 61c1		LL 61c1		LL 61c1		LL 61c1		LL 61c1		LL 61c1	
	Grt-I'	Grt-I'	Grt-I'	Grt-I'	Grt-I'	Grt-I'	Grt-I'	Grt-I'	Grt-I'	Grt-I'	Grt-I'	Grt-I'	Grt-I'	Grt-I'	Grt-I'	Grt-I'	Grt-I'	Grt-I'	Grt-I'	Grt-I'	Grt-I'	
SiO2	35.81	35.44	35.69	35.38	35.81	35.82	35.59	35.59	35.59	35.61	35.24	35.62	35.43	35.69	35.59	35.48	35.97	35.52	35.87			
TiO2	0.00	0.02	0.06	0.54	0.03	0.03	0.19	0.02	0.01	0.00	0.04	0.02	0.03	0.03	0.00	0.03	0.02	0.05	0.25			
Al2O3	20.18	20.02	20.04	19.82	20.04	20.15	19.85	20.10	20.03	20.16	19.74	19.96	19.92	20.09	19.90	19.85	20.21	19.93	20.12			
Fe2O3	1.27	1.34	1.12	0.91	1.33	1.39	1.31	1.50	1.25	1.43	1.70	1.59	1.18	1.55	1.49	1.35	1.04	1.20	0.87			
FeO	33.57	33.30	33.18	33.69	33.38	33.31	33.43	33.30	33.29	33.28	32.92	33.33	32.98	33.36	33.02	33.19	33.45	33.33	33.76			
MnO	5.65	5.48	5.58	5.61	5.53	5.61	5.53	5.58	5.67	5.73	5.63	5.72	5.57	5.60	5.69	5.56	5.57	5.56	5.68			
MgO	1.78	1.75	1.71	1.73	1.72	1.72	1.71	1.79	1.73	1.74	1.72	1.75	1.69	1.77	1.72	1.68	1.75	1.70	1.71			
CaO	1.00	1.16	1.30	1.33	1.29	1.42	1.26	1.27	1.11	1.19	1.31	1.12	1.25	1.32	1.25	1.15	1.16	1.04	1.11			
Na2O	0.01	0.01	0.01	0.01	0.01	0.00	0.03	0.01	0.00	0.02	0.02	0.00	0.00	0.00	0.01	0.01	0.00	0.02	0.00			
K2O	0.00	0.01	0.00	0.00	0.00	0.00	0.00	0.00	0.00	0.01	0.00	0.00	0.00	0.01	0.01	0.00	0.01	0.00	0.01			
Total	99.27	98.52	98.68	99.03	99.13	99.45	98.89	99.18	98.78	99.17	98.31	99.11	98.05	99.41	98.67	98.30	99.17	98.35	99.39			
Si	2.96	2.95	2.96	2.94	2.96	2.95	2.95	2.94	2.96	2.95	2.94	2.95	2.96	2.95	2.96	2.96	2.97	2.96	2.96			
Al IV	0.04	0.05	0.04	0.06	0.04	0.05	0.05	0.06	0.04	0.05	0.06	0.05	0.04	0.05	0.04	0.04	0.03	0.04	0.04			
Tot IV	3.00	3.00	3.00	3.00	3.00	3.00	3.00	3.00	3.00	3.00	3.00	3.00	3.00	3.00	3.00	3.00	3.00	3.00	3.00			
AL VI	1.92	1.91	1.92	1.88	1.91	1.91	1.90	1.90	1.92	1.91	1.89	1.90	1.92	1.90	1.91	1.91	1.93	1.92	1.92			
Ti	0.00	0.00	0.00	0.03	0.00	0.00	0.01	0.00	0.00	0.00	0.00	0.00	0.00	0.00	0.00	0.00	0.00	0.00	0.02			
Fe3+	0.08	0.08	0.07	0.06	0.08	0.09	0.08	0.09	0.08	0.09	0.11	0.10	0.07	0.10	0.09	0.09	0.06	0.08	0.05			
Tot S1	2.00	2.00	2.00	1.97	2.00	2.00	1.99	2.00	2.00	2.00	2.00	2.00	2.00	2.00	2.00	2.00	2.00	2.00	1.99			
Fe2+	2.32	2.32	2.30	2.34	2.31	2.30	2.32	2.30	2.31	2.30	2.30	2.31	2.31	2.30	2.30	2.32	2.31	2.32	2.33			
Mn	0.40	0.39	0.39	0.39	0.39	0.39	0.39	0.39	0.40	0.40	0.40	0.40	0.39	0.39	0.40	0.39	0.39	0.39	0.40			
Mg	0.22	0.22	0.21	0.21	0.21	0.21	0.21	0.22	0.21	0.22	0.21	0.22	0.21	0.22	0.21	0.21	0.22	0.21	0.21			
Ca	0.09	0.10	0.12	0.12	0.11	0.13	0.11	0.11	0.10	0.11	0.12	0.10	0.11	0.12	0.11	0.10	0.10	0.09	0.10			
Na	0.00	0.00	0.00	0.00	0.00	0.00	0.01	0.00	0.00	0.00	0.00	0.00	0.00	0.00	0.00	0.00	0.00	0.00	0.00			
K	0.00	0.00	0.00	0.00	0.00	0.00	0.00	0.00	0.00	0.00	0.00	0.00	0.00	0.00	0.00	0.00	0.00	0.00	0.00			
Tot S2	3.02	3.03	3.02	3.07	3.02	3.03	3.04	3.03	3.02	3.03	3.03	3.03	3.02	3.03	3.02	3.02	3.02	3.02	3.04			
Tot Cat	8.02	8.03	8.02	8.03	8.02	8.03	8.03	8.03	8.02	8.03	8.03	8.03	8.02	8.03	8.02	8.02	8.02	8.02	8.02			
ΣO	12	12	12	12	12	12	12	12	12	12	12	12	12	12	12	12	12	12	12			
Prp	7.19	7.13	6.98	6.98	6.98	6.99	6.95	7.23	7.02	7.05	6.97	7.04	6.96	7.13	6.98	6.87	7.14	6.96	6.94			
Alm	75.99	76.07	76.21	76.30	76.15	75.81	76.26	75.37	76.02	75.44	74.84	75.08	76.29	75.35	75.31	76.06	76.55	76.41	76.75			
Grs	0.00	0.00	0.36	1.08	0.00	0.00	0.00	0.00	0.00	0.00	0.00	0.00	0.02	0.00	0.00	0.00	0.21	0.00	0.56			
Sps	12.95	12.67	12.99	12.86	12.79	12.93	12.77	12.80	13.11	13.15	12.97	13.04	13.05	12.81	13.13	12.91	12.90	12.92	13.09			
Adr	3.87	4.12	3.46	2.78	4.09	4.27	4.02	4.59	3.85	4.37	5.23	4.84	3.68	4.72	4.57	4.17	3.21	3.71	2.67			
XMg	0.07	0.07	0.07	0.07	0.07	0.07	0.07	0.08	0.07	0.07	0.07	0.07	0.07	0.07	0.07	0.07	0.07	0.07	0.07			
XFe	0.79	0.79	0.79	0.79	0.79	0.79	0.79	0.79	0.79	0.79	0.79	0.79	0.79	0.79	0.79	0.79	0.79	0.79	0.79			
XPrp	0.07	0.07	0.07	0.07	0.07	0.07	0.07	0.07	0.07	0.07	0.07	0.07	0.07	0.07	0.07	0.07	0.07	0.07	0.07			
XAlm	0.76	0.76	0.76	0.76	0.76	0.76	0.76	0.75	0.76	0.75	0.75	0.75	0.76	0.75	0.75	0.76	0.77	0.76	0.77			
XGrs	0.00	0.00	0.00	0.01	0.00	0.00	0.00	0.00	0.00	0.00	0.00	0.00	0.00	0.00	0.00	0.00	0.00	0.00	0.01			
XSps	0.13	0.13	0.13	0.13	0.13	0.13	0.13	0.13	0.13	0.13	0.13	0.13	0.13	0.13	0.13	0.13	0.13	0.13	0.13			
XAdr	0.04	0.04	0.03	0.03	0.04	0.04	0.04	0.05	0.04	0.04	0.05	0.05	0.04	0.05	0.05	0.04	0.03	0.04	0.03			

Table 12: |-" chemical profile of garnet crystal from LL61c1 Qtz+Pl-rich layer of paragneiss. Analyses are shown in Fig. 3.8b.

Sample Descrip.	LL 61c1 Grt I-I'	LL 61c1 Grt I-I'	LL 61c1 Grt I-I'	LL 61c1 Grt I-I'	LL 61c1 Grt I-I'	LL 61c1 Grt I-I'	LL 61c1 Grt I-I'	LL 61c1 Grt I-I'	LL 61c1 Grt I-I'	LL 61c1 Grt I-I'	LL 61c1 Grt I-I'	LL 61c1 Grt I-I'	LL 61c1 Grt I-I'	LL 61c1 Grt I-I'	LL 61c1 Grt I-I'
SiO ₂	35.87	35.78	36.02	35.86	35.68	35.61	35.74	35.92	36.07	35.83	34.54	35.97	35.96	36.16	36.24
TiO ₂	0.51	0.08	0.04	0.03	0.02	0.59	0.04	0.02	0.00	0.00	0.01	0.00	0.01	0.02	-0.03
Al ₂ O ₃	20.09	19.99	20.04	19.81	19.83	19.76	20.02	19.89	19.96	19.97	18.66	19.98	20.07	20.18	20.21
Fe ₂ O ₃	0.50	0.90	1.14	1.25	1.30	0.47	1.25	1.36	1.19	1.49	1.74	1.41	1.19	1.11	1.09
FeO	34.07	33.25	33.37	32.92	32.67	33.72	32.97	32.78	33.05	33.30	31.67	33.68	33.42	33.20	33.17
MnO	5.63	5.68	5.45	5.52	5.38	5.37	5.46	5.38	5.22	5.23	5.09	5.28	5.32	5.24	5.23
MgO	1.71	1.63	1.73	1.72	1.71	1.59	1.73	1.74	1.73	1.70	1.64	1.75	1.74	1.75	1.77
CaO	1.14	1.18	1.33	1.38	1.67	1.55	1.55	1.73	1.63	1.60	1.46	1.29	1.34	1.70	1.67
Na ₂ O	0.03	0.00	0.00	0.02	0.01	0.00	0.02	0.01	0.02	0.00	0.01	0.00	0.02	0.04	0.02
K ₂ O	0.02	0.00	0.01	0.00	0.01	0.01	0.00	0.00	0.00	0.00	0.00	0.00	0.00	0.01	0.00
Total	99.58	98.48	99.14	98.49	98.28	98.66	98.78	98.83	98.88	99.12	94.81	99.26	99.06	99.41	99.37
Si	2.96	2.98	2.97	2.98	2.97	2.96	2.96	2.97	2.98	2.96	2.99	2.97	2.97	2.97	2.98
Al IV	0.05	0.03	0.03	0.02	0.03	0.04	0.04	0.03	0.02	0.04	0.02	0.03	0.03	0.03	0.02
Tot IV	3.00	3.00	3.00	3.00	3.00	3.00	3.00	3.00	3.00	3.00	3.00	3.00	3.00	3.00	3.00
AL VI	1.91	1.93	1.92	1.92	1.92	1.90	1.92	1.91	1.93	1.91	1.89	1.91	1.93	1.93	1.94
Ti	0.03	0.01	0.00	0.00	0.00	0.04	0.00	0.00	0.00	0.00	0.00	0.00	0.00	0.00	0.00
Fe ₃ +	0.03	0.06	0.07	0.08	0.08	0.03	0.08	0.09	0.07	0.09	0.11	0.09	0.07	0.07	0.07
Tot S1	1.97	2.00	2.00	2.00	2.00	1.96	2.00	2.00	2.00	2.00	2.00	2.00	2.00	2.00	2.00
Fe ₂ +	2.35	2.31	2.30	2.29	2.28	2.34	2.29	2.27	2.29	2.30	2.29	2.32	2.31	2.28	2.28
Mn	0.39	0.40	0.38	0.39	0.38	0.38	0.38	0.38	0.37	0.37	0.37	0.37	0.37	0.37	0.36
Mg	0.21	0.20	0.21	0.21	0.21	0.20	0.21	0.22	0.21	0.21	0.21	0.22	0.21	0.22	0.22
Ca	0.10	0.11	0.12	0.12	0.15	0.14	0.14	0.15	0.14	0.14	0.14	0.11	0.12	0.15	0.15
Na	0.00	0.00	0.00	0.00	0.00	0.00	0.00	0.00	0.00	0.00	0.00	0.00	0.00	0.01	0.00
K	0.00	0.00	0.00	0.00	0.00	0.00	0.00	0.00	0.00	0.00	0.00	0.00	0.00	0.00	0.00
Tot S2	3.06	3.02	3.02	3.01	3.02	3.06	3.02	3.02	3.01	3.02	3.01	3.02	3.02	3.02	3.01
Tot Cat	8.03	8.01	8.01	8.01	8.02	8.02	8.02	8.01	8.01	8.02	8.01	8.02	8.02	8.02	8.01
ΣO	12	12	12	12	12	12	12	12	12	12	12	12	12	12	12
Prp	6.89	6.67	7.06	7.07	7.03	6.44	7.08	7.13	7.11	6.93	6.96	7.09	7.10	7.13	7.21
Alm	76.94	76.60	76.39	75.97	75.45	76.69	75.66	75.27	75.96	76.25	75.22	76.41	76.61	75.79	75.80
Grs	1.77	0.67	0.37	0.18	0.90	3.05	0.70	0.87	1.09	0.10	0.00	0.00	0.28	1.54	1.52
Sps	12.87	13.26	12.65	12.89	12.58	12.37	12.69	12.51	12.15	12.13	12.24	12.16	12.35	12.12	12.10
Adr	1.54	2.81	3.53	3.90	4.05	1.45	3.87	4.21	3.71	4.60	5.59	4.34	3.67	3.42	3.37
XlMg	0.07	0.07	0.07	0.07	0.07	0.07	0.07	0.08	0.07	0.07	0.07	0.07	0.07	0.08	0.08
XFe	0.80	0.79	0.79	0.79	0.79	0.80	0.79	0.79	0.80	0.80	0.80	0.80	0.80	0.80	0.80
XPrp	0.07	0.07	0.07	0.07	0.07	0.06	0.07	0.07	0.07	0.07	0.07	0.07	0.07	0.07	0.07
XAlm	0.77	0.77	0.76	0.76	0.75	0.77	0.76	0.75	0.76	0.76	0.75	0.76	0.77	0.76	0.76
XGrs	0.02	0.01	0.00	0.00	0.01	0.03	0.01	0.01	0.01	0.00	0.00	0.00	0.00	0.02	0.01
XSps	0.13	0.13	0.13	0.13	0.13	0.12	0.13	0.13	0.12	0.12	0.12	0.12	0.12	0.12	0.12
XAdr	0.02	0.03	0.04	0.04	0.04	0.01	0.04	0.04	0.04	0.05	0.06	0.04	0.04	0.03	0.03

Table 12: I-I' chemical profile continued.

Sample Descrip.	LL 61c1 Grt I-I'	LL 61c1 Grt I-I'	LL 61c1 Grt I-I'	LL 61c1 Grt I-I'	LL 61c1 Grt I-I'	LL 61c1 Grt I-I'	LL 61c1 Grt I-I'	LL 61c1 Grt I-I'	LL 61c1 Grt I-I'	LL 61c1 Grt I-I'
SiO ₂	35.98	35.96	36.04	36.08	35.89	35.84	36.11	35.75	36.18	36.04
TiO ₂	0.07	0.03	0.00	0.02	0.01	0.00	0.00	0.04	0.04	0.01
Al ₂ O ₃	20.04	20.15	20.17	19.93	19.93	20.13	20.17	19.93	20.15	20.20
Fe ₂ O ₃	1.26	1.00	1.08	0.80	0.98	1.20	1.22	1.28	1.02	1.11
FeO	33.36	33.35	33.38	33.28	32.93	33.14	33.24	33.00	33.19	33.19
MnO	5.35	5.21	5.20	5.23	5.30	5.52	5.61	5.61	5.72	5.95
MgO	1.78	1.73	1.74	1.75	1.75	1.68	1.67	1.61	1.60	1.55
CaO	1.44	1.50	1.52	1.43	1.46	1.48	1.52	1.54	1.52	1.41
Na ₂ O	0.02	0.01	0.00	0.01	0.02	0.02	0.01	0.00	0.00	0.00
K ₂ O	0.00	0.00	0.00	0.00	0.00	0.00	0.00	0.00	0.00	0.00
Total	99.30	98.94	99.12	98.77	98.23	99.01	99.55	98.76	99.43	99.45
Si	2.97	2.97	2.97	2.98	2.99	2.96	2.97	2.97	2.98	2.97
Al IV	0.03	0.03	0.03	0.02	0.02	0.04	0.03	0.03	0.02	0.03
Tot IV	3.00	3.00	3.00	3.00	3.00	3.00	3.00	3.00	3.00	3.00
Al VI	1.91	1.93	1.93	1.95	1.94	1.93	1.92	1.92	1.93	1.93
Ti	0.00	0.00	0.00	0.00	0.00	0.00	0.00	0.00	0.00	0.00
Fe ³⁺	0.08	0.06	0.07	0.05	0.06	0.07	0.08	0.08	0.06	0.07
Tot S1	2.00	2.00	2.00	2.00	2.00	2.00	2.00	2.00	2.00	2.00
Fe ²⁺	2.30	2.30	2.30	2.30	2.29	2.29	2.29	2.29	2.28	2.29
Mn	0.37	0.37	0.36	0.37	0.37	0.39	0.39	0.39	0.40	0.42
Mg	0.22	0.21	0.21	0.22	0.21	0.21	0.21	0.20	0.20	0.19
Ca	0.13	0.13	0.13	0.13	0.13	0.13	0.13	0.14	0.13	0.12
Na	0.00	0.00	0.00	0.00	0.00	0.00	0.00	0.00	0.00	0.00
K	0.00	0.00	0.00	0.00	0.00	0.00	0.00	0.00	0.00	0.00
Tot S2	3.02	3.02	3.01	3.01	3.01	3.02	3.02	3.02	3.01	3.02
Tot Cat	8.02	8.02	8.01	8.01	8.01	8.02	8.02	8.02	8.01	8.02
ΣO	12	12	12	12	12	12	12	12	12	12
Prp	7.26	7.08	7.10	7.15	7.09	6.87	6.79	6.59	6.52	6.31
Alm	76.16	76.42	76.41	76.46	76.17	75.95	75.82	75.82	75.78	75.82
Grs	0.32	1.30	1.12	1.72	1.26	0.65	0.69	0.55	1.31	0.68
Sps	12.37	12.10	12.05	12.18	12.42	12.82	12.95	13.06	13.23	13.76
Adr	3.88	3.09	3.32	2.49	3.06	3.70	3.75	3.98	3.15	3.44
XlMg	0.08	0.07	0.07	0.07	0.07	0.07	0.07	0.07	0.07	0.07
XFe	0.80	0.80	0.80	0.80	0.80	0.79	0.79	0.79	0.79	0.79
XPrp	0.07	0.07	0.07	0.07	0.07	0.07	0.07	0.07	0.07	0.06
XAlm	0.76	0.76	0.76	0.76	0.76	0.76	0.76	0.76	0.76	0.76
XGrs	0.00	0.01	0.01	0.02	0.01	0.01	0.01	0.01	0.01	0.01
XSps	0.12	0.12	0.12	0.12	0.12	0.13	0.13	0.13	0.13	0.14
XAdr	0.04	0.03	0.03	0.02	0.03	0.04	0.04	0.04	0.03	0.03

Table 12: I-I' chemical profile continued.

Sample Descrip.	LL 61c1 Bt I	LL 61c1 Bt I	LL 61c1 Bt I	LL 61c1 Bt I	LL 61c1 Bt I	LL 61c1 Bt I	LL 61c1 Bt I	LL 61c1 Bt I	LL 61c1 Bt I	LL 61a2 Bt I	LL 61a2 Bt I	LL 61a2 Bt I	LL 61a2 Bt I	LL 61a2 Bt I	LL 61a2 Bt I	LL 61a2 Bt I	LL 61b2 Bt I				
SiO ₂	34.17	34.12	33.95	34.07	33.79	33.79	33.79	34.07	33.95	34.46	33.75	34.26	34.38	34.16	33.97	34.21	33.91	33.58	33.34	34.33	34.60
TiO ₂	2.81	2.58	2.56	2.17	2.35	2.35	2.35	2.17	2.22	1.57	1.89	2.57	2.75	2.60	2.79	2.05	2.50	2.48	2.56	2.55	2.05
Al ₂ O ₃	19.21	19.54	19.61	19.52	19.14	19.07	19.92	19.92	19.83	19.71	19.94	19.54	20.03	19.55	19.23	21.84	19.95	20.23	19.73	19.91	19.83
FeO	23.77	23.56	23.29	23.90	23.86	23.57	22.62	22.62	23.10	21.32	23.64	22.53	23.49	23.74	24.02	22.40	23.48	23.53	24.16	23.98	22.41
MnO	0.15	0.21	0.20	0.18	0.05	0.07	0.11	0.11	0.15	0.07	0.05	0.10	0.22	0.15	0.11	0.18	0.09	0.12	0.20	0.13	0.14
MgO	6.13	6.35	6.43	6.45	6.75	6.70	6.39	6.71	6.50	7.13	6.46	6.84	6.11	6.38	6.10	6.26	5.76	6.24	6.43	5.85	6.47
CaO	0.03	0.01	0.05	0.07	0.00	0.04	0.02	0.04	0.00	0.08	0.04	0.01	0.01	0.00	0.00	0.00	0.00	0.00	0.01	0.03	0.06
Na ₂ O	0.27	0.25	0.24	0.28	0.22	0.21	0.29	0.29	0.24	0.22	0.24	0.23	0.24	0.29	0.27	0.29	0.24	0.27	0.22	0.24	0.24
K ₂ O	8.62	8.94	8.88	8.26	8.72	8.68	8.87	8.80	9.01	8.66	8.73	9.11	7.95	8.09	8.20	8.10	8.54	8.53	7.88	8.72	7.24
(F)	0.22	0.28	0.20	0.23	0.15	0.23	0.23	0.21	0.10	0.31	0.27	0.15	0.13	0.34	0.27	0.29	0.03	0.21	0.05	0.15	0.41
(Cl)	0.01	0.00	0.01	0.00	0.01	0.02	0.00	0.00	0.00	0.00	0.00	0.00	0.01	0.02	0.00	0.01	0.00	0.02	0.03	0.00	0.01
F-12O	0.13	0.16	0.11	0.13	0.09	0.13	0.13	0.12	0.06	0.18	0.16	0.09	0.07	0.20	0.16	0.08	0.02	0.12	0.03	0.09	0.24
Cl-12O	0.01	0.00	0.01	0.00	0.01	0.02	0.00	0.00	0.00	0.00	0.00	0.00	0.01	0.02	0.00	0.01	0.00	0.02	0.00	0.01	0.01
H ₂ O	3.75	3.73	3.76	3.74	3.77	3.71	3.73	3.75	3.81	3.68	3.71	3.80	3.82	3.70	3.76	3.71	3.83	3.75	3.80	3.81	3.64
Total	99.04	99.45	99.09	98.76	98.90	98.34	98.13	98.45	98.86	97.11	98.61	99.08	99.08	98.87	99.61	98.75	98.30	98.85	98.37	99.65	96.94
Si	5.31	5.29	5.28	5.31	5.30	5.30	5.28	5.31	5.28	5.40	5.27	5.30	5.31	5.30	5.27	5.29	5.30	5.22	5.22	5.30	5.41
Al IV	2.69	2.71	2.73	2.70	2.70	2.70	2.72	2.70	2.72	2.60	2.73	2.70	2.69	2.70	2.73	2.71	2.70	2.78	2.78	2.70	2.59
Tot IV	8	8	8	8	8	8	8	8	8	8	8	8	8	8	8	8	8	8	8	8	8
AL VI	0.84	0.86	0.87	0.89	0.81	0.82	0.96	0.94	0.92	1.03	0.94	0.87	0.95	0.88	0.90	0.83	1.29	0.93	0.85	0.93	1.06
Ti	0.33	0.30	0.30	0.25	0.27	0.28	0.27	0.25	0.26	0.19	0.22	0.30	0.32	0.30	0.33	0.33	0.24	0.29	0.30	0.30	0.24
Fe ₂ +	3.09	3.05	3.03	3.11	3.11	3.09	2.96	2.95	3.01	2.79	3.09	2.92	3.03	3.08	3.10	3.14	2.90	3.07	3.16	3.10	2.93
Mn	0.02	0.03	0.03	0.02	0.01	0.01	0.02	0.02	0.02	0.01	0.01	0.01	0.03	0.02	0.02	0.02	0.02	0.01	0.03	0.02	0.02
Mg	1.42	1.47	1.49	1.50	1.57	1.57	1.49	1.56	1.51	1.67	1.50	1.58	1.41	1.48	1.40	1.45	1.21	1.34	1.50	1.35	1.51
Tot S1	5.70	5.71	5.71	5.78	5.77	5.76	5.68	5.70	5.71	5.69	5.76	5.68	5.73	5.76	5.74	5.77	5.66	5.69	5.84	5.69	5.76
Ca	0.00	0.00	0.01	0.01	0.00	0.01	0.00	0.01	0.00	0.01	0.01	0.00	0.00	0.00	0.00	0.00	0.01	0.00	0.00	0.01	0.01
Na	0.08	0.07	0.07	0.08	0.07	0.06	0.09	0.09	0.07	0.07	0.07	0.07	0.07	0.09	0.08	0.09	0.07	0.08	0.07	0.07	0.07
K	1.71	1.77	1.76	1.64	1.73	1.74	1.77	1.75	1.79	1.73	1.74	1.80	1.57	1.60	1.61	1.61	1.52	1.70	1.69	1.72	1.44
Tot S2	1.80	1.84	1.84	1.74	1.80	1.81	1.86	1.84	1.86	1.81	1.82	1.87	1.64	1.69	1.69	1.70	1.60	1.78	1.77	1.64	1.53
Tot Cat	15.49	15.55	15.55	15.51	15.57	15.57	15.54	15.55	15.57	15.50	15.58	15.55	15.37	15.45	15.43	15.46	15.26	15.46	15.52	15.48	15.28
F	0.11	0.14	0.10	0.11	0.07	0.12	0.11	0.10	0.05	0.15	0.13	0.07	0.06	0.17	0.13	0.14	0.07	0.01	0.03	0.07	0.20
Cl	0.00	0.00	0.00	0.00	0.00	0.01	0.00	0.00	0.00	0.00	0.00	0.00	0.00	0.01	0.00	0.00	0.00	0.00	0.01	0.00	0.00
OH	3.89	3.86	3.90	3.89	3.93	3.88	3.89	3.90	3.95	3.85	3.87	3.93	3.94	3.83	3.87	3.86	3.93	3.99	3.97	3.93	3.79
ΣO	22	22	22	22	22	22	22	22	22	22	22	22	22	22	22	22	22	22	22	22	22
XFe	0.68	0.67	0.67	0.67	0.66	0.66	0.66	0.65	0.66	0.63	0.67	0.65	0.68	0.67	0.69	0.68	0.70	0.69	0.67	0.69	0.66

Table 13: microprobe analyses of different textural generations of biotite. 52 Bt I (Bt * = biotite included in quartz, plagioclase and garnet); 18 Bt II; 64 Bt III (product of staurolite demise reaction). Analyses are shown in Fig. 3.9.

[illegible]

Table 13: continued

Sample Descrip.	LL 61b2		LL 61b2		LL 61b2		LL 61c2		LL 61c2		LL 61b1		LL 61b1		LL 61b1		LL 61b1		LL 61b1		LL 61b1		LL 61b2		LL 61b2		LL 61b2	
	Bt I*	Bt I*	Bt I*	Bt I*	Bt I*	Bt I*	Bt I*	Bt I*	Bt I*	Bt I*	Bt II	Bt II	Bt II	Bt II	Bt II	Bt II	Bt II	Bt II	Bt II	Bt II	Bt II	Bt II	Bt II	Bt II	Bt II	Bt II	Bt II	Bt II
SiO2	34.19	34.31	34.06	33.82	34.39	33.97	33.65	33.65	34.41	33.45	34.43	34.56	34.84	33.91	34.61	34.24	34.23	34.57	34.54	34.23	34.07	33.98						
TiO2	2.25	2.29	2.59	2.27	1.91	1.68	2.15	2.13	1.99	1.75	1.61	2.05	1.90	2.03	2.52	1.71	2.64	2.57	2.39	2.09	2.82	2.68						
Al2O3	19.83	19.73	20.65	20.02	19.99	20.15	20.27	20.35	19.65	19.68	19.98	19.67	19.61	19.35	19.47	19.90	19.58	19.33	19.65	20.63	19.43	19.34						
FeO	22.30	23.02	21.73	23.19	21.38	22.00	22.37	22.42	23.08	22.91	21.96	23.01	22.76	23.16	23.11	23.37	22.87	23.03	22.53	23.29	21.94	22.18						
MnO	0.06	0.14	0.17	0.19	0.13	0.12	0.11	0.15	0.12	0.13	0.05	0.13	0.11	0.11	0.10	0.12	0.21	0.10	0.05	0.14	0.14	0.07						
MgO	7.29	6.73	5.98	6.56	7.17	7.30	7.66	7.49	6.96	6.94	7.10	6.88	7.08	6.59	6.68	6.45	6.52	6.87	6.70	6.25	6.68	7.06						
CaO	0.04	0.00	0.01	0.00	0.01	0.04	0.00	0.00	0.01	0.10	0.00	0.06	0.01	0.01	0.03	0.00	0.00	0.01	0.02	0.03	0.00	0.00						
Na2O	0.22	0.26	0.19	0.17	0.27	0.23	0.25	0.20	0.28	0.21	0.26	0.28	0.28	0.26	0.36	0.23	0.28	0.25	0.28	0.18	0.29	0.32						
K2O	7.79	7.59	7.34	7.81	7.79	7.55	8.66	8.54	9.02	8.48	8.78	8.84	8.78	9.08	9.01	9.03	8.96	8.76	8.78	7.24	7.57	7.40						
(F)	0.14	0.14	0.15	0.29	0.11	0.28	0.57	0.27	0.19	0.26	0.10	0.23	0.16	0.14	0.25	0.22	0.09	0.22	0.14	0.29	0.16	0.15						
Cl	0.00	0.01	0.02	0.01	0.02	0.00	0.00	0.03	0.02	0.02	0.00	0.03	0.01	0.02	0.00	0.01	0.01	0.01	0.00	0.00	0.02	0.02						
F-12O	0.08	0.08	0.09	0.17	0.07	0.16	0.33	0.16	0.11	0.15	0.06	0.14	0.09	0.08	0.15	0.13	0.05	0.13	0.08	0.17	0.10	0.09						
Cl-12O	0.00	0.01	0.02	0.01	0.01	0.00	0.00	0.02	0.01	0.02	0.00	0.02	0.01	0.01	0.00	0.01	0.01	0.01	0.00	0.00	0.00	0.01						
H2O	3.79	3.79	3.76	3.70	3.78	3.70	3.61	3.74	3.79	3.68	3.81	3.77	3.81	3.76	3.78	3.75	3.83	3.78	3.81	3.73	3.75	3.75						
Total	97.84	97.95	96.57	97.90	96.90	96.89	99.05	98.84	99.42	97.55	97.98	99.38	99.29	98.35	99.83	98.92	99.17	99.40	98.84	97.96	96.77	96.87						
Si	5.31	5.34	5.33	5.28	5.37	5.32	5.20	5.21	5.32	5.27	5.36	5.34	5.37	5.31	5.33	5.33	5.30	5.33	5.34	5.31	5.34	5.33						
Al-IV	2.69	2.66	2.67	2.72	2.63	2.68	2.80	2.79	2.68	2.73	2.64	2.67	2.63	2.69	2.67	2.68	2.70	2.67	2.66	2.69	2.66	2.67						
Tot-IV	8	8	8	8	8	8	8	8	8	8	8	8	8	8	8	8	8	8	8	8	8	8						
Al-VI	0.94	0.95	1.13	0.96	1.05	1.04	0.89	0.92	0.90	0.92	1.02	0.91	0.93	0.89	0.86	0.97	0.88	0.85	0.93	1.08	0.94	0.90						
Ti	0.26	0.27	0.31	0.27	0.22	0.20	0.25	0.25	0.23	0.21	0.19	0.24	0.22	0.24	0.29	0.20	0.31	0.30	0.28	0.24	0.33	0.32						
Fe2+	2.90	2.99	2.84	3.03	2.79	2.88	2.89	2.90	2.98	3.02	2.86	2.97	2.93	3.04	2.97	3.04	2.96	2.97	2.92	3.02	2.88	2.91						
Mn	0.01	0.02	0.02	0.03	0.02	0.02	0.01	0.02	0.02	0.02	0.01	0.02	0.02	0.02	0.01	0.02	0.03	0.01	0.01	0.02	0.02	0.01						
Mg	1.69	1.56	1.40	1.53	1.67	1.70	1.77	1.73	1.60	1.63	1.65	1.58	1.63	1.54	1.53	1.50	1.51	1.58	1.55	1.45	1.56	1.65						
Tot-S1	5.80	5.79	5.70	5.81	5.75	5.83	5.81	5.82	5.73	5.79	5.72	5.72	5.72	5.71	5.67	5.72	5.68	5.71	5.67	5.81	5.73	5.78						
Ca	0.01	0.00	0.00	0.00	0.00	0.01	0.00	0.00	0.00	0.02	0.00	0.01	0.00	0.00	0.01	0.00	0.00	0.00	0.00	0.01	0.00	0.00						
Na	0.07	0.08	0.06	0.05	0.08	0.07	0.07	0.06	0.08	0.08	0.06	0.08	0.08	0.08	0.11	0.07	0.08	0.07	0.09	0.06	0.09	0.10						
K	1.54	1.51	1.46	1.56	1.55	1.51	1.71	1.69	1.78	1.70	1.74	1.74	1.73	1.82	1.77	1.79	1.77	1.73	1.73	1.43	1.51	1.48						
Tot-S2	1.62	1.59	1.53	1.61	1.64	1.58	1.78	1.74	1.86	1.81	1.81	1.83	1.81	1.89	1.88	1.86	1.85	1.80	1.82	1.49	1.60	1.58						
Tot-Cat	15.42	15.38	15.23	15.42	15.39	15.42	15.59	15.56	15.59	15.59	15.53	15.55	15.54	15.61	15.55	15.58	15.53	15.51	15.50	15.30	15.33	15.36						
F	0.07	0.07	0.08	0.14	0.06	0.14	0.28	0.13	0.09	0.13	0.05	0.11	0.08	0.07	0.12	0.11	0.04	0.11	0.07	0.14	0.08	0.08						
Cl	0.00	0.00	0.01	0.00	0.00	0.00	0.00	0.01	0.00	0.01	0.00	0.01	0.00	0.01	0.00	0.00	0.00	0.00	0.00	0.00	0.00	0.00						
OH	3.93	3.93	3.92	3.86	3.94	3.86	3.72	3.86	3.90	3.87	3.95	3.88	3.92	3.93	3.88	3.89	3.96	3.89	3.93	3.86	3.92	3.92						
ΣO	22	22	22	22	22	22	22	22	22	22	22	22	22	22	22	22	22	22	22	22	22	22						
XFe	0.63	0.65	0.67	0.66	0.62	0.63	0.62	0.62	0.65	0.65	0.63	0.65	0.64	0.66	0.66	0.67	0.66	0.65	0.65	0.67	0.65	0.64						

Table 13: continued

Sample Descrip.	LL 61b2		LL 61b2		LL 61b1		LL 61b1		LL 61b1		LL 61b1		LL 61b1		LL 61b1		LL 61b1	
	Bt II	Bt III	Bt II	Bt III	Bt II	Bt III	Bt II	Bt III	Bt II	Bt III	Bt II	Bt III	Bt II	Bt III	Bt II	Bt III	Bt II	Bt III
SiO2	33.59	33.94	34.26	34.05	34.51	34.41	34.67	34.48	33.99	34.78	34.53	34.41	34.07	34.31	34.60	34.05	34.30	33.88
TiO2	2.79	2.61	2.03	2.12	1.67	2.01	1.93	2.56	3.20	2.09	1.96	2.25	3.21	2.67	1.90	2.51	2.64	1.88
Al2O3	19.42	19.02	19.66	19.71	19.67	19.35	20.07	19.73	19.35	20.02	19.76	19.16	20.04	19.41	19.94	19.50	19.67	19.24
FeO	22.93	22.22	22.22	22.13	22.53	23.06	22.25	22.07	23.14	21.65	22.49	21.90	21.65	23.34	21.50	22.39	22.93	22.64
MnO	0.12	0.13	0.09	0.08	0.14	0.10	0.11	0.13	0.12	0.14	0.10	0.13	0.06	0.14	0.15	0.10	0.07	0.13
MgO	6.99	7.09	7.25	7.12	7.11	6.41	6.37	6.69	6.03	6.91	6.99	6.79	5.79	6.33	6.63	6.71	6.66	5.92
CaO	0.00	0.01	0.02	0.02	0.00	0.03	0.02	0.01	0.00	0.05	0.01	0.02	0.09	0.01	0.04	0.02	0.00	0.04
Na2O	0.34	0.31	0.34	0.34	0.30	0.25	0.21	0.25	0.20	0.27	0.23	0.26	0.21	0.23	0.24	0.23	0.21	0.23
K2O	7.16	7.46	7.30	7.51	8.89	8.85	8.72	8.96	8.78	8.84	8.83	8.88	8.02	8.95	8.74	8.92	9.06	8.41
(F)	0.18	0.18	0.32	0.28	0.19	0.16	0.23	0.17	0.21	0.34	0.32	0.20	0.25	0.11	0.16	0.12	0.07	0.17
(Cl)	0.01	0.00	0.01	0.03	0.01	0.03	0.02	0.00	0.02	0.01	0.00	0.02	0.01	0.04	0.01	0.01	0.00	0.02
F-12O	0.10	0.10	0.19	0.16	0.11	0.09	0.14	0.10	0.12	0.20	0.19	0.12	0.15	0.06	0.10	0.07	0.04	0.10
Cl-12O	0.01	0.00	0.01	0.02	0.01	0.02	0.02	0.00	0.01	0.01	0.00	0.01	0.01	0.03	0.00	0.01	0.01	0.00
H2O	3.74	3.73	3.68	3.69	3.77	3.76	3.75	3.79	3.75	3.72	3.72	3.74	3.73	3.79	3.75	3.82	3.80	3.77
Total	97.19	96.61	97.06	96.94	98.72	98.35	98.25	98.77	98.69	98.69	98.82	97.85	97.36	99.04	97.29	98.86	98.60	98.03
Si	5.27	5.34	5.35	5.33	5.35	5.37	5.38	5.34	5.30	5.37	5.35	5.40	5.36	5.30	5.37	5.35	5.30	5.35
Al IV	2.73	2.66	2.65	2.67	2.65	2.63	2.62	2.67	2.71	2.63	2.66	2.60	2.64	2.70	2.63	2.65	2.70	2.65
Tot IV	8	8	8	8	8	8	8	8	8	8	8	8	8	8	8	8	8	8
AL VI	0.86	0.87	0.97	0.97	0.95	0.93	1.06	0.93	0.85	1.01	0.95	0.93	1.04	0.86	1.05	0.91	0.96	0.97
Ti	0.33	0.31	0.24	0.25	0.19	0.24	0.23	0.30	0.37	0.24	0.23	0.26	0.38	0.31	0.22	0.29	0.25	0.31
Fe2+	3.01	2.93	2.90	2.90	2.92	3.01	2.89	2.86	3.01	2.79	2.91	2.86	2.82	3.04	2.81	2.90	2.93	2.99
Mn	0.02	0.02	0.01	0.01	0.02	0.01	0.01	0.02	0.02	0.02	0.01	0.02	0.01	0.02	0.01	0.01	0.01	0.01

Table 13: continued

Table 13: continued

Sample Descrip.	LL 61b2 Bt III	LL 61b2 Bt III	LL 61b2 Bt III	LL 61b2 Bt III	LL 61b2 Bt III	LL 61b2 Bt III	LL 61b2 Bt III	LL 61b2 Bt III	LL 61b2 Bt III	LL 61b2 Bt III	LL 61b2 Bt III	LL 61b2 Bt III	LL 61b2 Bt III	LL 61c2 Bt III	LL 61c2 Bt III
SiO ₂	34,15	34,17	34,37	34,31	33,74	34,05	34,21	34,26	33,90	34,04	33,81	34,07	33,92	33,92	34,06
TiO ₂	2,91	3,21	1,93	2,11	2,92	2,81	2,42	2,92	2,13	2,41	1,65	2,09	3,69	2,48	2,97
Al ₂ O ₃	19,75	20,12	20,47	20,09	19,51	19,45	19,25	19,63	19,74	19,60	21,01	19,99	19,32	19,45	20,43
FeO	22,35	21,97	22,60	23,23	22,08	22,40	22,33	23,17	22,77	23,25	22,54	22,96	23,11	23,13	22,03
MnO	0,13	0,11	0,13	0,12	0,15	0,14	0,14	0,12	0,04	0,08	0,11	0,15	0,15	0,09	0,04
MgO	7,07	6,53	6,61	6,79	6,41	6,59	7,00	6,47	6,54	6,74	6,27	6,29	6,12	6,50	6,12
CaO	0,00	0,00	0,00	0,03	0,07	0,03	0,05	0,00	0,02	0,00	0,01	0,02	0,00	0,00	0,00
Na ₂ O	0,28	0,24	0,28	0,26	0,25	0,24	0,24	0,31	0,26	0,29	0,19	0,29	0,26	0,33	0,25
K ₂ O	7,52	7,34	7,33	7,32	7,16	7,20	7,20	7,16	7,08	7,29	7,33	7,35	7,37	7,24	7,32
(F)	0,23	0,27	0,09	0,12	0,05	0,29	0,14	0,12	0,00	0,15	0,32	0,20	0,13	0,09	0,18
(Cl)	0,01	0,02	0,01	0,00	0,00	0,01	0,01	0,02	0,01	0,03	0,00	0,01	0,00	0,03	0,00
F-1120	0,13	0,16	0,05	0,07	0,03	0,17	0,08	0,07	0,00	0,09	0,19	0,12	0,08	0,05	0,10
Cl-1120	0,01	0,01	0,01	0,00	0,00	0,01	0,01	0,01	0,01	0,02	0,00	0,01	0,00	0,02	0,00
H ₂ O	3,76	3,73	3,81	3,81	3,78	3,68	3,75	3,80	3,80	3,76	3,67	3,73	3,78	3,77	3,75
Total	98,06	97,58	97,61	98,15	96,08	96,76	96,68	97,93	96,31	97,57	96,77	97,06	97,81	96,99	97,94
Si	5,29	5,30	5,34	5,32	5,33	5,34	5,37	5,32	5,35	5,32	5,30	5,34	5,29	5,33	5,32
Al IV	2,71	2,70	2,66	2,68	2,68	2,66	2,63	2,68	2,66	2,68	2,70	2,66	2,71	2,67	2,63
Tot IV	8	8	8	8	8	8	8	8	8	8	8	8	8	8	8
AL VI	0,90	0,98	1,08	0,99	0,95	0,94	0,93	0,92	1,01	0,93	1,18	1,04	0,84	0,93	0,98
Ti	0,34	0,37	0,23	0,25	0,35	0,33	0,29	0,34	0,25	0,28	0,19	0,25	0,43	0,29	0,24
Fe ²⁺	2,90	2,85	2,94	3,01	2,91	2,94	2,93	3,01	3,00	3,04	2,95	3,01	3,01	3,04	2,98
Mn	0,02	0,02	0,02	0,02	0,02	0,02	0,02	0,02	0,01	0,01	0,02	0,02	0,02	0,01	0,01
Mg	1,63	1,51	1,53	1,57	1,51	1,54	1,64	1,50	1,54	1,57	1,47	1,47	1,42	1,52	1,44
Tot S1	5,78	5,73	5,79	5,83	5,74	5,77	5,80	5,78	5,81	5,83	5,81	5,78	5,73	5,80	5,72
Ca	0,00	0,00	0,00	0,01	0,01	0,00	0,01	0,00	0,00	0,00	0,00	0,00	0,00	0,00	0,00
Na	0,09	0,07	0,09	0,08	0,08	0,07	0,07	0,09	0,08	0,09	0,06	0,09	0,08	0,10	0,10
K	1,49	1,45	1,45	1,45	1,44	1,44	1,44	1,42	1,42	1,45	1,46	1,47	1,47	1,45	1,48
Tot S2	1,57	1,52	1,54	1,53	1,53	1,52	1,52	1,51	1,51	1,54	1,52	1,56	1,55	1,55	1,57
Tot Cat	15,35	15,25	15,33	15,36	15,27	15,29	15,32	15,30	15,32	15,37	15,33	15,34	15,28	15,35	15,29
F	0,11	0,13	0,05	0,06	0,02	0,14	0,07	0,06	0,00	0,08	0,16	0,10	0,06	0,04	0,08
Cl	0,00	0,01	0,00	0,00	0,00	0,00	0,00	0,01	0,00	0,01	0,00	0,00	0,00	0,01	0,00
OH	3,89	3,86	3,95	3,94	3,98	3,85	3,93	3,94	4,00	3,92	3,84	3,90	3,94	3,95	3,89
ΣO	22	22	22	22	22	22	22	22	22	22	22	22	22	22	22
XFe	0,64	0,65	0,65	0,66	0,66	0,65	0,64	0,67	0,66	0,66	0,67	0,67	0,68	0,66	0,67

Table 13: continued

[illegible]

Table 14: chemical profiles of biotite crystals. Analyses are shown in Fig. 3.10 and 3.11.

Sample Descrip.	LL61b2 Prof. D-D'	LL61b2 Prof. D-D'	LL61b2 Prof. D-D'	LL61b2 Prof. D-D'	LL61b2 Prof. D-D'	LL61b2 Prof. D-D'	LL61b2 Prof. D-D'	LL61b2 Prof. D-D'	LL61b2 Prof. D-D'	LL61b2 Prof. D-D'	LL61b2 Prof. D-D'	LL61b2 Prof. D-D'	LL61b2 Prof. D-D'	LL61b2 Prof. D-D'	LL61b2 Prof. D-D'	LL61b2 Prof. D-D'	LL61b2 Prof. D-D'
SiO ₂	33,61	33,85	33,46	33,85	33,94	33,91	34,13	33,96	33,68	34,03	34,07	33,80	33,19	32,62	32,62	32,62	33,18
TiO ₂	2,81	2,72	2,58	2,89	2,63	2,81	2,53	3,00	2,83	2,68	3,08	2,78	3,18	2,81	2,78	2,78	2,78
Al ₂ O ₃	19,61	19,58	19,73	19,58	19,55	20,03	19,92	19,81	19,77	19,85	19,93	19,79	19,48	19,76	19,65	19,65	19,03
FeO	22,55	23,30	22,95	22,42	23,08	23,02	22,58	23,62	23,08	23,42	22,95	22,79	22,90	23,13	23,14	23,28	23,28
MnO	0,17	0,12	0,00	0,14	0,21	0,00	0,05	0,04	0,09	0,08	0,17	0,03	0,11	0,10	0,01	0,01	0,08
MgO	6,44	6,26	6,18	6,15	6,15	6,11	6,21	6,23	6,01	6,10	6,15	6,30	6,33	6,23	6,21	6,21	6,16
CaO	0,07	0,00	0,01	0,00	0,00	0,05	0,04	0,07	0,05	0,02	0,01	0,01	0,04	0,05	0,00	0,00	0,02
Na ₂ O	0,28	0,29	0,23	0,23	0,20	0,22	0,23	0,29	0,25	0,25	0,20	0,26	0,32	0,30	0,25	0,25	0,25
K ₂ O	8,38	8,41	8,48	8,36	8,30	8,45	8,68	8,37	8,58	8,50	8,47	8,35	8,42	8,32	8,45	8,45	8,41
(F)	0,00	0,00	0,00	0,00	0,00	0,00	0,00	0,00	0,00	0,00	0,00	0,00	0,00	0,00	0,00	0,00	0,00
(Cl)	0,00	0,00	0,00	0,00	0,00	0,00	0,00	0,00	0,00	0,00	0,00	0,00	0,00	0,00	0,00	0,00	0,00
F-1120	0,00	0,00	0,00	0,00	0,00	0,00	0,00	0,00	0,00	0,00	0,00	0,00	0,00	0,00	0,00	0,00	0,00
Cl-1120	0,00	0,00	0,00	0,00	0,00	0,00	0,00	0,00	0,00	0,00	0,00	0,00	0,00	0,00	0,00	0,00	0,00
H ₂ O	3,83	3,84	3,81	3,82	3,83	3,86	3,85	3,88	3,83	3,86	3,87	3,84	3,82	3,78	3,77	3,77	3,78
Total	97,74	98,38	97,45	97,44	97,90	98,47	98,21	99,27	98,17	98,79	98,91	97,95	97,79	97,09	96,88	96,88	96,95
Si	5,27	5,28	5,27	5,31	5,31	5,27	5,32	5,25	5,27	5,29	5,27	5,28	5,22	5,17	5,19	5,27	5,27
Al IV	2,73	2,72	2,73	2,69	2,69	2,73	2,69	2,75	2,73	2,71	2,73	2,72	2,78	2,83	2,82	2,73	2,73
Tot IV	8	8	8	8	8	8	8	8	8	8	8	8	8	8	8	8	8
AL VI	0,89	0,88	0,93	0,93	0,92	0,94	0,97	0,87	0,91	0,92	0,91	0,92	0,82	0,86	0,87	0,83	0,83
Ti	0,33	0,32	0,31	0,34	0,31	0,33	0,30	0,35	0,33	0,31	0,36	0,33	0,38	0,34	0,33	0,33	0,33
Fe ²⁺	2,96	3,04	3,02	2,94	3,02	2,99	2,94	3,06	3,02	3,04	2,97	2,98	3,01	3,07	3,08	3,09	3,09
Mn	0,02	0,02	0,00	0,02	0,03	0,00	0,01	0,01	0,01	0,01	0,02	0,00	0,02	0,01	0,00	0,01	0,01
Mg	1,50	1,46	1,45	1,44	1,44	1,42	1,44	1,44	1,40	1,41	1,42	1,47	1,48	1,47	1,47	1,46	1,46
Tot S1	5,70	5,72	5,71	5,67	5,72	5,68	5,66	5,71	5,68	5,70	5,68	5,70	5,71	5,75	5,75	5,72	5,72
Ca	0,01	0,00	0,00	0,00	0,00	0,01	0,01	0,01	0,01	0,00	0,00	0,00	0,01	0,01	0,00	0,00	0,00
Na	0,08	0,09	0,07	0,07	0,06	0,07	0,07	0,09	0,08	0,08	0,06	0,08	0,10	0,09	0,08	0,08	0,08
K	1,68	1,67	1,70	1,67	1,66	1,68	1,72	1,65	1,71	1,68	1,67	1,66	1,69	1,68	1,71	1,70	1,70
Tot S2	1,77	1,76	1,77	1,75	1,72	1,75	1,80	1,75	1,80	1,76	1,74	1,74	1,79	1,78	1,79	1,78	1,78
Tot Cat	15,47	15,48	15,48	15,41	15,43	15,43	15,46	15,46	15,47	15,46	15,42	15,44	15,50	15,54	15,54	15,51	15,51
F	0,00	0,00	0,00	0,00	0,00	0,00	0,00	0,00	0,00	0,00	0,00	0,00	0,00	0,00	0,00	0,00	0,00
Cl	0,00	0,00	0,00	0,00	0,00	0,00	0,00	0,00	0,00	0,00	0,00	0,00	0,00	0,00	0,00	0,00	0,00
OH	4,00	4,00	4,00	4,00	4,00	4,00	4,00	4,00	4,00	4,00	4,00	4,00	4,00	4,00	4,00	4,00	4,00
ΣO	22	22	22	22	22	22	22	22	22	22	22	22	22	22	22	22	22
XFe	0,66	0,68	0,68	0,67	0,68	0,68	0,67	0,68	0,68	0,68	0,68	0,67	0,67	0,68	0,68	0,68	0,68

Table 14: continued.

Sample Descrip.	LL61b2 Prof. D-D'	LL61b2 Prof. D-D'	LL61b2 Prof. D-D'	LL61b2 Prof. D-D'	LL61b2 Prof. D-D'	LL61b2 Prof. D-D'	LL61b2 Prof. D-D'	LL61b2 Prof. D-D'	LL61b2 Prof. D-D'	LL61b2 Prof. D-D'	LL61b2 Prof. D-D'	LL61b2 Prof. D-D'	LL61b2 Prof. D-D'	LL61b2 Prof. D-D'	LL61b2 Prof. D-D'	LL61b2 Prof. D-D'	LL61b2 Prof. D-D'
SiO ₂	33,21	33,26	33,56	33,97	32,94	33,36	33,59	33,47	32,70	33,13	33,29	33,17	33,88	33,63	33,42	33,31	32,91
TiO ₂	2,93	2,78	3,27	2,67	2,65	2,67	2,82	2,92	3,02	3,42	2,77	2,96	2,70	2,87	2,93	3,30	2,58
Al ₂ O ₃	19,21	19,51	19,13	19,62	19,58	19,35	19,13	19,12	19,44	19,46	19,23	19,30	19,62	19,45	19,16	19,66	19,77
FeO	22,53	23,18	22,73	23,40	22,84	22,86	22,93	23,07	23,47	22,62	22,76	22,95	23,38	23,01	23,62	22,71	23,02
MnO	0,00	0,13	0,21	0,19	0,22	0,15	0,18	0,10	0,07	0,22	0,08	0,14	0,22	0,01	0,01	0,07	0,15
MgO	6,02	6,08	6,02	6,37	6,08	6,07	6,09	6,46	6,20	6,11	6,46	6,10	6,32	6,19	6,28	6,44	6,09
CaO	0,00	0,03	0,04	0,03	0,06	0,01	0,06	0,00	0,05	0,03	0,04	0,00	0,01	0,05	0,02	0,00	0,03
Na ₂ O	0,22	0,21	0,23	0,21	0,25	0,27	0,34	0,24	0,25	0,24	0,24	0,20	0,28	0,12	0,26	0,24	0,23
K ₂ O	8,79	8,79	8,43	8,35	8,31	8,14	8,32	8,20	8,45	8,47	8,10	8,31	8,65	8,42	8,36	8,41	8,38
(F)	0,00	0,00	0,00	0,00	0,00	0,00	0,00	0,00	0,00	0,00	0,00	0,00	0,00	0,00	0,00	0,00	0,00
(Cl)	0,00	0,00	0,00	0,00	0,00	0,00	0,00	0,00	0,00	0,00	0,00	0,00	0,00	0,00	0,00	0,00	0,00
F-1/2O	0,00	0,00	0,00	0,00	0,00	0,00	0,00	0,00	0,00	0,00	0,00	0,00	0,00	0,00	0,00	0,00	0,00
Cl-1/2O	0,00	0,00	0,00	0,00	0,00	0,00	0,00	0,00	0,00	0,00	0,00	0,00	0,00	0,00	0,00	0,00	0,00
H ₂ O	3,77	3,80	3,81	3,85	3,77	3,78	3,79	3,81	3,79	3,81	3,79	3,78	3,86	3,82	3,81	3,83	3,78
Total	96,68	97,77	97,41	98,65	96,71	96,66	97,05	97,39	97,43	97,51	96,78	96,93	98,89	97,57	97,89	97,97	96,94
Si	5,28	5,24	5,29	5,29	5,24	5,29	5,32	5,27	5,18	5,22	5,27	5,26	5,27	5,29	5,26	5,21	5,22
Al IV	2,72	2,76	2,71	2,72	2,77	2,71	2,69	2,73	2,82	2,78	2,73	2,74	2,73	2,71	2,74	2,79	2,78
Tot IV	8	8	8	8	8	8	8	8	8	8	8	8	8	8	8	8	8
AL VI	0,88	0,87	0,84	0,88	0,90	0,91	0,88	0,83	0,81	0,83	0,86	0,86	0,87	0,89	0,81	0,84	0,92
Ti	0,35	0,33	0,39	0,31	0,32	0,32	0,31	0,35	0,36	0,41	0,33	0,35	0,32	0,34	0,35	0,39	0,31
Fe ²⁺	3,00	3,06	2,99	3,05	3,04	3,03	3,03	3,04	3,11	2,98	3,01	3,04	3,04	3,03	3,11	2,97	3,05
Mn	0,00	0,02	0,03	0,03	0,03	0,02	0,03	0,01	0,01	0,03	0,01	0,02	0,03	0,00	0,00	0,01	0,02
Mg	1,43	1,43	1,41	1,48	1,44	1,43	1,44	1,52	1,46	1,43	1,53	1,44	1,47	1,45	1,47	1,50	1,44
Tot S1	5,65	5,70	5,66	5,74	5,72	5,72	5,69	5,74	5,75	5,68	5,74	5,72	5,72	5,70	5,74	5,71	5,74
Ca	0,00	0,01	0,01	0,00	0,01	0,00	0,01	0,00	0,01	0,01	0,01	0,00	0,00	0,01	0,00	0,00	0,01
Na	0,07	0,06	0,07	0,06	0,08	0,08	0,11	0,08	0,08	0,07	0,07	0,06	0,08	0,04	0,08	0,07	0,07
K	1,78	1,77	1,70	1,66	1,69	1,65	1,68	1,65	1,71	1,70	1,64	1,68	1,72	1,69	1,68	1,68	1,70
Tot S2	1,85	1,84	1,77	1,72	1,77	1,73	1,79	1,72	1,79	1,78	1,72	1,74	1,80	1,73	1,76	1,75	1,77
Tot Cat	15,50	15,53	15,43	15,46	15,50	15,45	15,48	15,47	15,54	15,46	15,46	15,46	15,52	15,44	15,50	15,46	15,51
F	0,00	0,00	0,00	0,00	0,00	0,00	0,00	0,00	0,00	0,00	0,00	0,00	0,00	0,00	0,00	0,00	0,00
Cl	0,00	0,00	0,00	0,00	0,00	0,00	0,00	0,00	0,00	0,00	0,00	0,00	0,00	0,00	0,00	0,00	0,00
OH	4,00	4,00	4,00	4,00	4,00	4,00	4,00	4,00	4,00	4,00	4,00	4,00	4,00	4,00	4,00	4,00	4,00
ΣO	22	22	22	22	22	22	22	22	22	22	22	22	22	22	22	22	22
XFe	0,68	0,68	0,68	0,67	0,68	0,68	0,68	0,67	0,68	0,68	0,66	0,68	0,67	0,68	0,68	0,66	0,68

Table 14: continued.

[illegible]

Table 14: continued.

Sample Descrip.	LL61b2 Prof. E-E'	LL61b2 Prof. E-E'	LL61b2 Prof. E-E'	LL61b2 Prof. E-E'	LL61b2 Prof. E-E'	LL61b2 Prof. E-E'	LL61b2 Prof. E-E'	LL61b2 Prof. E-E'	LL61b2 Prof. E-E'	LL61b2 Prof. E-E'	LL61b2 Prof. E-E'	LL61b2 Prof. E-E'	LL61b2 Prof. E-E'	LL61b2 Prof. E-E'	LL61b2 Prof. E-E'	LL61b2 Prof. E-E'	LL61b2 Prof. E-E'	LL61b2 Prof. E-E'	LL61b2 Prof. E-E'
SiO ₂	33,10	33,29	33,54	33,76	34,71	34,56	34,20	33,99	33,90	34,16	34,62	34,10	34,11	34,83	35,02				
TiO ₂	2,27	2,18	2,27	2,54	2,11	2,34	2,23	2,26	2,47	1,90	2,19	1,99	1,93	1,93	2,12				
Al ₂ O ₃	19,66	19,67	20,01	19,62	20,04	20,56	19,82	19,49	19,87	20,19	19,99	20,22	20,34	20,30	20,48				
FeO	21,65	21,62	21,74	21,73	22,35	21,47	21,73	21,09	20,77	21,11	20,94	20,84	21,14	20,89	21,24				
MnO	0,10	0,11	0,09	0,23	0,04	0,12	0,16	0,25	0,08	0,20	0,13	0,07	0,08	0,09	0,09				
MgO	7,38	7,24	7,07	7,26	7,40	7,09	7,03	7,20	7,14	7,05	6,90	6,98	7,07	7,04	6,97				
CaO	0,03	0,00	0,00	0,02	0,01	0,04	0,01	0,00	0,00	0,01	0,01	0,01	0,04	0,00	0,04				
Na ₂ O	0,27	0,27	0,25	0,39	0,26	0,20	0,30	0,24	0,36	0,27	0,23	0,24	0,31	0,29	0,32				
K ₂ O	8,28	8,38	8,46	8,41	7,78	8,35	8,47	8,09	8,30	8,41	8,40	8,66	8,65	8,61	8,29				
(F)	0,00	0,00	0,00	0,00	0,00	0,00	0,00	0,00	0,00	0,00	0,00	0,00	0,00	0,00	0,00				
(Cl)	0,00	0,00	0,00	0,00	0,00	0,00	0,00	0,00	0,00	0,00	0,00	0,00	0,00	0,00	0,00				
F-1/2O	0,00	0,00	0,00	0,00	0,00	0,00	0,00	0,00	0,00	0,00	0,00	0,00	0,00	0,00	0,00				
Cl-1/2O	0,00	0,00	0,00	0,00	0,00	0,00	0,00	0,00	0,00	0,00	0,00	0,00	0,00	0,00	0,00				
H ₂ O	3,79	3,79	3,82	3,84	3,90	3,91	3,84	3,82	3,83	3,84	3,85	3,83	3,85	3,88	3,91				
Total	96,52	96,55	97,25	97,79	98,59	98,33	97,18	96,96	96,73	97,14	97,26	96,94	97,53	97,85	98,46				
Si	5,23	5,26	5,26	5,27	5,34	5,26	5,34	5,34	5,31	5,34	5,39	5,34	5,31	5,39	5,38				
Al IV	2,77	2,74	2,74	2,73	2,66	2,74	2,66	2,67	2,69	2,66	2,61	2,67	2,69	2,61	2,62				
Tot IV	8	8	8	8	8	8	8	8	8	8	8	8	8	8	8				
AL VI	0,90	0,93	0,96	0,88	0,97	0,98	0,97	0,94	0,98	1,05	1,05	1,06	1,05	1,09	1,08				
Ti	0,27	0,26	0,27	0,30	0,24	0,29	0,26	0,27	0,29	0,22	0,26	0,24	0,23	0,23	0,25				
Fe ²⁺	2,86	2,86	2,85	2,84	2,88	2,82	2,79	2,77	2,72	2,76	2,73	2,73	2,75	2,70	2,73				
Mn	0,01	0,02	0,01	0,03	0,01	0,01	0,01	0,03	0,01	0,03	0,02	0,01	0,01	0,01	0,01				
Mg	1,74	1,71	1,65	1,69	1,70	1,64	1,68	1,69	1,67	1,64	1,60	1,63	1,64	1,62	1,60				
Tot S1	5,78	5,76	5,74	5,73	5,80	5,74	5,72	5,69	5,68	5,70	5,65	5,66	5,68	5,65	5,66				
Ca	0,00	0,00	0,00	0,00	0,00	0,01	0,01	0,00	0,00	0,00	0,00	0,00	0,01	0,00	0,01				
Na	0,08	0,08	0,08	0,12	0,08	0,06	0,07	0,09	0,11	0,08	0,07	0,07	0,09	0,09	0,09				
K	1,67	1,69	1,69	1,67	1,53	1,65	1,61	1,71	1,66	1,68	1,67	1,73	1,72	1,70	1,62				
Tot S2	1,76	1,77	1,77	1,79	1,61	1,72	1,70	1,81	1,77	1,76	1,74	1,80	1,82	1,78	1,72				
Tot Cat	15,54	15,53	15,51	15,52	15,40	15,45	15,42	15,50	15,45	15,46	15,39	15,47	15,50	15,43	15,39				
F	0,00	0,00	0,00	0,00	0,00	0,00	0,00	0,00	0,00	0,00	0,00	0,00	0,00	0,00	0,00				
Cl	0,00	0,00	0,00	0,00	0,00	0,00	0,00	0,00	0,00	0,00	0,00	0,00	0,00	0,00	0,00				
OH	4,00	4,00	4,00	4,00	4,00	4,00	4,00	4,00	4,00	4,00	4,00	4,00	4,00	4,00	4,00				
ΣO	22	22	22	22	22	22	22	22	22	22	22	22	22	22	22				
XFe	0,62	0,63	0,63	0,63	0,63	0,63	0,63	0,62	0,62	0,63	0,63	0,63	0,63	0,62	0,63				

Table 14: continued.

Sample Descrip.	LL61b2 Prof. E-E'	LL61b2 Prof. E-E'	LL61b2 Prof. E-E'	LL61b2 Prof. E-E'	LL61b2 Prof. E-E'	LL61b2 Prof. E-E'	LL61b2 Prof. E-E'	LL61b2 Prof. E-E'	LL61b2 Prof. E-E'	LL61b2 Prof. E-E': E'	LL61b2 Prof. F-F': F	LL61b2 Prof. F-F'	LL61b2 Prof. F-F'	LL61b2 Prof. F-F'	LL61b2 Prof. F-F'	LL61b2 Prof. F-F'
SiO ₂	34,88	34,10	33,95	33,83	33,96	33,90	33,76	33,37	33,50	33,67	34,36	34,12	34,15	34,48	34,56	33,68
TiO ₂	2,07	1,75	2,04	1,71	2,12	1,80	1,68	2,08	1,74	1,84	1,90	1,88	1,71	2,00	1,98	1,93
Al ₂ O ₃	20,57	20,00	20,28	20,52	20,49	20,80	20,65	20,67	21,31	21,40	21,07	20,26	20,51	20,56	20,69	20,67
FeO	20,88	20,72	21,23	20,67	20,69	21,06	20,59	20,70	20,16	19,82	20,57	20,45	20,13	20,05	20,20	20,68
MnO	0,18	0,06	0,11	0,00	0,10	0,07	0,08	0,14	0,16	0,10	0,10	0,08	0,11	0,13	0,16	0,06
MgO	7,03	7,21	6,96	7,07	7,18	6,94	6,79	6,94	6,84	7,11	7,32	7,14	6,92	7,14	6,78	7,00
CaO	0,04	0,01	0,00	0,00	0,02	0,07	0,00	0,00	0,04	0,10	0,04	0,22	0,23	0,09	0,04	0,00
Na ₂ O	0,19	0,28	0,35	0,24	0,24	0,29	0,26	0,30	0,23	0,35	0,32	0,43	0,35	0,26	0,28	0,35
K ₂ O	8,59	8,83	8,40	8,42	8,41	8,56	8,52	8,75	8,66	8,63	8,66	8,50	8,39	8,69	8,39	8,59
(F)	0,00	0,00	0,00	0,00	0,00	0,00	0,00	0,00	0,00	0,00	0,00	0,00	0,00	0,00	0,00	0,00
(Cl)	0,00	0,00	0,00	0,00	0,00	0,00	0,00	0,00	0,00	0,00	0,00	0,00	0,00	0,00	0,00	0,00
F-1/2O	0,00	0,00	0,00	0,00	0,00	0,00	0,00	0,00	0,00	0,00	0,00	0,00	0,00	0,00	0,00	0,00
Cl-1/2O	0,00	0,00	0,00	0,00	0,00	0,00	0,00	0,00	0,00	0,00	0,00	0,00	0,00	0,00	0,00	0,00
H ₂ O	3,90	3,82	3,84	3,81	3,81	3,85	3,81	3,83	3,82	3,85	3,90	3,84	3,82	3,86	3,86	3,83
Total	98,32	96,78	97,15	96,28	96,49	97,39	96,28	97,09	96,45	96,86	98,25	96,92	96,33	97,26	96,94	96,77
Si	5,37	5,35	5,31	5,32	5,25	5,29	5,33	5,22	5,25	5,25	5,29	5,33	5,36	5,35	5,37	5,28
Al IV	2,64	2,65	2,69	2,68	2,75	2,71	2,67	2,78	2,75	2,75	2,71	2,67	2,65	2,65	2,63	2,72
Tot IV	8	8	8	8	8	8	8	8	8	8	8	8	8	8	8	8
AL VI	1,09	1,05	1,04	1,12	1,05	1,11	1,16	1,09	1,19	1,18	1,11	1,06	1,15	1,11	1,17	1,10
Ti	0,24	0,21	0,24	0,20	0,25	0,21	0,20	0,24	0,21	0,22	0,22	0,22	0,20	0,23	0,23	0,23
Fe ²⁺	2,69	2,72	2,78	2,72	2,72	2,74	2,71	2,71	2,65	2,58	2,65	2,67	2,64	2,60	2,63	2,71
Mn	0,02	0,01	0,02	0,00	0,01	0,01	0,01	0,02	0,02	0,01	0,01	0,01	0,02	0,02	0,02	0,01
Mg	1,61	1,69	1,62	1,66	1,68	1,61	1,59	1,62	1,60	1,65	1,68	1,66	1,62	1,65	1,57	1,63
Tot S1	5,65	5,67	5,69	5,70	5,72	5,68	5,67	5,68	5,66	5,64	5,67	5,63	5,62	5,62	5,62	5,68
Ca	0,01	0,00	0,00	0,00	0,00	0,01	0,00	0,00	0,01	0,02	0,01	0,04	0,04	0,02	0,01	0,00
Na	0,06	0,09	0,11	0,07	0,07	0,09	0,08	0,09	0,07	0,11	0,10	0,13	0,11	0,08	0,09	0,11
K	1,69	1,77	1,68	1,69	1,69	1,70	1,71	1,75	1,73	1,72	1,70	1,70	1,68	1,72	1,66	1,72
Tot S2	1,75	1,86	1,78	1,76	1,76	1,80	1,79	1,84	1,81	1,84	1,80	1,86	1,82	1,82	1,76	1,82
Tot Cat	15,40	15,52	15,48	15,46	15,48	15,48	15,45	15,52	15,47	15,48	15,48	15,49	15,44	15,43	15,37	15,50
F	0,00	0,00	0,00	0,00	0,00	0,00	0,00	0,00	0,00	0,00	0,00	0,00	0,00	0,00	0,00	0,00
Cl	0,00	0,00	0,00	0,00	0,00	0,00	0,00	0,00	0,00	0,00	0,00	0,00	0,00	0,00	0,00	0,00
OH	4,00	4,00	4,00	4,00	4,00	4,00	4,00	4,00	4,00	4,00	4,00	4,00	4,00	4,00	4,00	4,00
ΣO	22	22	22	22	22	22	22	22	22	22	22	22	22	22	22	22
XFe	0,62	0,62	0,63	0,62	0,62	0,63	0,63	0,63	0,62	0,61	0,61	0,62	0,62	0,61	0,63	0,62

Table 14: continued.

Sample Descrip.	LL61b2 Prof. F-F'	LL61b2 Prof. F-F'	LL61b2 Prof. F-F'	LL61b2 Prof. F-F'	LL61b2 Prof. F-F'	LL61b2 Prof. F-F'	LL61b2 Prof. F-F'	LL61b2 Prof. F-F'	LL61b2 Prof. F-F'	LL61b2 Prof. F-F'	LL61b2 Prof. F-F'	LL61b2 Prof. F-F'	LL61b2 Prof. F-F'	LL61b2 Prof. F-F'	LL61b2 Prof. F-F'	LL61b2 Prof. F-F'	LL61b2 Prof. F-F'	LL61b2 Prof. F-F'
SiO2	34,40	34,15	34,98	34,92	34,86	34,56	34,91	35,41	34,27	34,35	34,36	34,32	34,32	34,32	34,32	34,32	35,02	34,63
TiO2	1,69	1,83	1,63	1,85	1,69	1,71	1,99	1,82	1,78	1,95	1,79	1,95	1,82	2,12	1,37	1,82	1,23	1,61
Al2O3	21,24	20,79	20,59	21,01	20,84	20,27	21,05	20,90	21,20	21,19	21,33	20,84	20,84	21,27	20,80	21,25	20,85	21,30
FeO	20,97	20,42	20,46	21,01	20,00	20,48	20,86	20,48	20,70	20,19	20,14	20,14	20,31	19,97	20,22	19,73	20,35	21,06
MnO	0,13	0,14	0,11	0,03	0,14	0,22	0,11	0,19	0,11	0,10	0,21	0,21	0,14	0,02	0,00	0,13	0,13	0,13
MgO	7,23	7,18	7,21	7,14	7,08	7,14	7,23	6,88	6,95	7,29	7,03	7,03	6,75	7,06	6,79	6,79	7,05	7,00
CaO	0,00	0,00	0,00	0,07	0,00	0,02	0,01	0,01	0,01	0,00	0,11	0,11	0,12	0,23	0,16	0,22	0,10	0,03
Na2O	0,18	0,27	0,28	0,25	0,30	0,34	0,36	0,29	0,41	0,33	0,32	0,32	0,28	0,25	0,24	0,30	0,19	0,25
K2O	8,88	8,68	8,87	8,72	8,55	8,64	8,85	8,58	8,58	8,93	8,39	8,39	8,96	8,50	8,24	8,51	8,85	8,40
(F)	0,00	0,00	0,00	0,00	0,00	0,00	0,00	0,00	0,00	0,00	0,00	0,00	0,00	0,00	0,00	0,00	0,00	0,00
(Cl)	0,00	0,00	0,00	0,00	0,00	0,00	0,00	0,00	0,00	0,00	0,00	0,00	0,00	0,00	0,00	0,00	0,00	0,00
F-1/2O	0,00	0,00	0,00	0,00	0,00	0,00	0,00	0,00	0,00	0,00	0,00	0,00	0,00	0,00	0,00	0,00	0,00	0,00
Cl-1/2O	0,00	0,00	0,00	0,00	0,00	0,00	0,00	0,00	0,00	0,00	0,00	0,00	0,00	0,00	0,00	0,00	0,00	0,00
H2O	3,90	3,86	3,89	3,92	3,88	3,85	3,93	3,92	3,88	3,90	3,92	3,92	3,88	3,89	3,82	3,89	3,88	3,90
Total	98,63	97,32	98,01	98,91	97,35	97,23	99,30	98,49	97,89	98,23	98,22	98,22	97,86	97,68	95,97	97,56	97,64	98,31
Si	5,29	5,31	5,39	5,34	5,39	5,38	5,32	5,42	5,30	5,29	5,36	5,36	5,37	5,30	5,39	5,38	5,41	5,32
Al IV	2,71	2,69	2,61	2,66	2,61	2,62	2,68	2,58	2,70	2,71	2,64	2,64	2,63	2,70	2,61	2,62	2,59	2,68
Tot IV	8	8	8	8	8	8	8	8	8	8	8	8	8	8	8	8	8	8
AL VI	1,13	1,12	1,13	1,13	1,19	1,10	1,10	1,19	1,16	1,13	1,21	1,21	1,17	1,16	1,23	1,24	1,21	1,18
Ti	0,20	0,21	0,19	0,21	0,20	0,20	0,23	0,21	0,21	0,23	0,21	0,21	0,21	0,25	0,16	0,21	0,14	0,19
Fe2+	2,70	2,66	2,64	2,69	2,59	2,67	2,66	2,62	2,68	2,60	2,58	2,58	2,63	2,58	2,65	2,54	2,63	2,71
Mn	0,02	0,02	0,01	0,00	0,02	0,03	0,01	0,02	0,01	0,01	0,03	0,03	0,02	0,00	0,00	0,02	0,02	0,02
Mg	1,66	1,66	1,66	1,63	1,63	1,66	1,64	1,57	1,60	1,67	1,60	1,60	1,55	1,62	1,59	1,56	1,63	1,60
Tot S1	5,70	5,67	5,63	5,66	5,62	5,65	5,65	5,61	5,66	5,64	5,63	5,63	5,58	5,61	5,64	5,57	5,63	5,70
Ca	0,00	0,00	0,00	0,01	0,00	0,00	0,00	0,00	0,00	0,00	0,02	0,02	0,02	0,04	0,03	0,04	0,02	0,00
Na	0,05	0,08	0,09	0,08	0,09	0,10	0,11	0,09	0,12	0,10	0,09	0,09	0,08	0,08	0,07	0,09	0,06	0,08
K	1,74	1,72	1,75	1,70	1,69	1,72	1,72	1,68	1,69	1,75	1,64	1,64	1,77	1,67	1,65	1,67	1,74	1,65
Tot S2	1,79	1,80	1,83	1,79	1,78	1,82	1,83	1,76	1,82	1,85	1,75	1,75	1,87	1,79	1,75	1,80	1,82	1,73
Tot Cat	15,49	15,47	15,46	15,44	15,40	15,47	15,47	15,37	15,47	15,49	15,38	15,38	15,44	15,40	15,39	15,36	15,45	15,42
F	0,00	0,00	0,00	0,00	0,00	0,00	0,00	0,00	0,00	0,00	0,00	0,00	0,00	0,00	0,00	0,00	0,00	0,00
Cl	0,00	0,00	0,00	0,00	0,00	0,00	0,00	0,00	0,00	0,00	0,00	0,00	0,00	0,00	0,00	0,00	0,00	0,00
OH	4,00	4,00	4,00	4,00	4,00	4,00	4,00	4,00	4,00	4,00	4,00	4,00	4,00	4,00	4,00	4,00	4,00	4,00
ΣO	22	22	22	22	22	22	22	22	22	22	22	22	22	22	22	22	22	22
XFe	0,62	0,61	0,61	0,62	0,61	0,62	0,62	0,63	0,63	0,61	0,62	0,62	0,63	0,61	0,63	0,62	0,62	0,63

Table 14: continued.

Sample Descrip.	LL6'lb2		LL6'lb2		LL6'lb2		LL6'lb2		LL6'lb2		LL6'lb2		LL6'lb2		LL6'lb2		LL6'lb2		LL6'lb2		LL6'lb2	
	Prof. F-F'	Prof. F-F'	Prof. F-F'	Prof. F-F'	Prof. F-F'	Prof. F-F'	Prof. F-F'	Prof. F-F'	Prof. F-F'	Prof. F-F'	Prof. F-F'	Prof. F-F'	Prof. F-F'	Prof. F-F'	Prof. F-F'	Prof. F-F'	Prof. F-F'	Prof. F-F'	Prof. F-F'	Prof. F-F'	Prof. F-F'	
SiO2	34.12	34.63	34.35	34.55	34.77	34.71	34.93	34.97	34.43	34.56	34.78	34.95	34.79	35.16	34.86							
TiO2	1.61	1.98	1.63	1.59	1.87	1.69	1.90	1.65	1.71	1.79	1.65	1.45	1.80	1.71	1.47							
Al2O3	21.16	21.54	20.90	20.93	21.17	21.11	21.14	21.38	21.45	21.53	21.66	21.58	21.42	21.53	21.60							
FeO	20.73	19.92	20.49	20.62	20.24	20.06	20.06	19.60	19.85	20.36	19.93	20.20	19.80	19.70	19.10							
MnO	0.24	0.00	0.02	0.19	0.08	0.15	0.16	0.03	0.03	0.18	0.12	0.17	0.09	0.15	0.19							
MgO	7.14	7.05	6.68	6.85	6.78	6.92	6.76	6.69	6.94	6.95	6.75	6.81	6.99	6.77	6.67							
CaO	0.06	0.00	0.04	0.03	0.01	0.05	0.04	0.00	0.00	0.05	0.00	0.07	0.04	0.02	0.06							
Na2O	0.30	0.29	0.28	0.21	0.33	0.37	0.30	0.26	0.24	0.29	0.35	0.35	0.31	0.27	0.29							
K2O	8.76	8.43	8.79	8.52	8.39	8.56	8.44	8.52	8.67	8.70	8.83	8.62	8.47	8.39	8.39							
(F)	0.00	0.00	0.00	0.00	0.00	0.00	0.00	0.00	0.00	0.00	0.00	0.00	0.00	0.00	0.00							
(Cl)	0.00	0.00	0.00	0.00	0.00	0.00	0.00	0.00	0.00	0.00	0.00	0.00	0.00	0.00	0.00							
F-1/2O	0.00	0.00	0.00	0.00	0.00	0.00	0.00	0.00	0.00	0.00	0.00	0.00	0.00	0.00	0.00							
Cl-1/2O	0.00	0.00	0.00	0.00	0.00	0.00	0.00	0.00	0.00	0.00	0.00	0.00	0.00	0.00	0.00							
H2O	3.88	3.90	3.85	3.86	3.89	3.88	3.89	3.88	3.87	3.91	3.90	3.91	3.90	3.91	3.87							
Total	98.00	97.75	97.02	97.35	97.52	97.49	97.64	96.97	97.19	98.31	97.96	98.11	97.60	97.62	96.49							
Si	5.28	5.32	5.35	5.36	5.37	5.36	5.38	5.41	5.33	5.31	5.35	5.36	5.35	5.40	5.41							
Al IV	2.72	2.68	2.65	2.64	2.63	2.64	2.62	2.59	2.67	2.69	2.65	2.64	2.65	2.60	2.60							
Tot IV	8	8	8	8	8	8	8	8	8	8	8	8	8	8	8							
AL VI	1.14	1.22	1.20	1.19	1.22	1.21	1.22	1.30	1.25	1.20	1.27	1.27	1.24	1.30	1.35							
Ti	0.19	0.23	0.19	0.19	0.22	0.20	0.22	0.19	0.20	0.21	0.19	0.17	0.21	0.20	0.17							
Fe2+	2.68	2.56	2.67	2.68	2.61	2.59	2.59	2.53	2.57	2.61	2.56	2.59	2.55	2.53	2.48							
Mn	0.03	0.00	0.00	0.03	0.01	0.02	0.02	0.00	0.00	0.02	0.02	0.02	0.01	0.02	0.03							
Mg	1.65	1.62	1.55	1.58	1.56	1.59	1.55	1.54	1.60	1.59	1.55	1.56	1.60	1.55	1.54							
Tot S1	5.69	5.63	5.61	5.66	5.62	5.61	5.60	5.57	5.62	5.64	5.58	5.61	5.61	5.59	5.57							
Ca	0.01	0.00	0.01	0.00	0.00	0.01	0.01	0.00	0.00	0.01	0.00	0.01	0.01	0.00	0.01							
Na	0.09	0.09	0.08	0.06	0.10	0.11	0.09	0.08	0.07	0.09	0.10	0.10	0.09	0.08	0.09							
K	1.73	1.65	1.75	1.69	1.65	1.69	1.66	1.68	1.71	1.71	1.73	1.69	1.66	1.64	1.66							
Tot S2	1.83	1.74	1.84	1.76	1.75	1.81	1.76	1.76	1.79	1.80	1.83	1.80	1.76	1.73	1.76							
Tot Cat	15.51	15.37	15.45	15.41	15.37	15.42	15.35	15.33	15.41	15.44	15.42	15.41	15.37	15.32	15.32							
F	0.00	0.00	0.00	0.00	0.00	0.00	0.00	0.00	0.00	0.00	0.00	0.00	0.00	0.00	0.00							
Cl	0.00	0.00	0.00	0.00	0.00	0.00	0.00	0.00	0.00	0.00	0.00	0.00	0.00	0.00	0.00							
OH	4.00	4.00	4.00	4.00	4.00	4.00	4.00	4.00	4.00	4.00	4.00	4.00	4.00	4.00	4.00							
ΣO	22	22	22	22	22	22	22	22	22	22	22	22	22	22	22							
ΣFe	0.62	0.61	0.63	0.63	0.63	0.62	0.62	0.62	0.62	0.62	0.62	0.62	0.61	0.62	0.62							
ΣF																						

Table 14: continued.

Sample	LL61b1	LL61b1	LL61b1	LL61b1	LL61b1	LL61b1	LL61b1	LL61b1	LL61b1	LL61b1	LL61b1	LL61b1	LL61b1	LL61b1	LL61b1	LL61b1	LL61b1	LL61b1
Descrip. Prof. A-A':A	Prof. A-A'	Prof. A-A'	Prof. A-A'	Prof. A-A'	Prof. A-A'	Prof. A-A'	Prof. A-A'	Prof. A-A'	Prof. A-A'	Prof. A-A'	Prof. A-A'	Prof. A-A'	Prof. A-A'	Prof. A-A'	Prof. A-A'	Prof. A-A'	Prof. A-A'	Prof. A-A'
SiO2	26,99	27,38	27,18	27,88	27,53	27,33	27,13	27,14	27,47	27,03	27,23	27,12	27,04	27,41	27,48	27,41	27,41	27,48
TiO2	0,56	0,47	0,55	0,49	0,56	0,49	0,38	0,41	0,55	0,46	0,48	0,39	0,40	0,44	0,48	0,44	0,44	0,48
Al2O3	52,97	52,47	52,85	52,60	52,63	52,87	53,08	52,60	52,94	53,09	53,02	52,87	52,73	52,88	52,67	52,88	52,88	52,67
FeO	13,88	13,97	13,88	13,58	13,86	13,71	13,78	14,09	13,96	13,82	13,80	13,72	14,03	13,79	13,64	13,79	13,79	13,64
MnO	0,32	0,30	0,32	0,29	0,25	0,31	0,29	0,35	0,37	0,25	0,29	0,33	0,34	0,30	0,37	0,30	0,30	0,37
MgO	0,97	1,00	0,98	0,98	1,03	1,03	1,03	1,06	1,00	1,03	1,07	1,01	1,04	1,06	1,08	1,06	1,06	1,08
ZnO	0,01	0,00	0,01	0,00	0,00	0,00	0,02	0,00	0,00	0,01	0,01	0,00	0,01	0,01	0,00	0,01	0,01	0,00
CaO	0,00	0,02	0,06	0,01	0,03	0,02	0,00	0,00	0,00	0,03	0,00	0,00	0,00	0,00	0,02	0,00	0,00	0,02
Na2O	0,00	0,03	0,00	0,01	0,03	0,04	0,03	0,04	0,03	0,00	0,05	0,00	0,01	0,06	0,05	0,06	0,06	0,05
K2O	0,00	0,00	0,02	0,02	0,02	0,00	0,01	0,00	0,00	0,02	0,01	0,01	0,00	0,00	0,00	0,00	0,00	0,00
Total	95,68	95,63	95,86	95,85	95,93	95,80	95,76	95,69	96,32	95,73	95,95	95,46	95,61	95,94	95,79	95,94	95,94	95,79
Si	7,68	7,79	7,72	7,89	7,80	7,75	7,70	7,73	7,76	7,68	7,72	7,72	7,70	7,76	7,79	7,76	7,76	7,79
Al IV	0,33	0,21	0,29	0,11	0,20	0,25	0,30	0,27	0,24	0,32	0,29	0,28	0,30	0,24	0,21	0,24	0,24	0,21
Tot IV	8	8	8	8	8	8	8	8	8	8	8	8	8	8	8	8	8	8
Al VI	17,43	17,38	17,40	17,43	17,38	17,42	17,46	17,37	17,38	17,45	17,42	17,46	17,41	17,42	17,40	17,42	17,42	17,40
Ti	0,12	0,10	0,12	0,10	0,12	0,11	0,08	0,09	0,12	0,10	0,10	0,08	0,09	0,09	0,10	0,09	0,09	0,10
TotS1	17,54	17,48	17,51	17,53	17,50	17,53	17,54	17,46	17,50	17,55	17,52	17,55	17,49	17,51	17,50	17,51	17,51	17,50
Fe2+	3,30	3,32	3,30	3,21	3,29	3,25	3,27	3,36	3,30	3,28	3,27	3,27	3,34	3,27	3,24	3,27	3,27	3,24
Mn	0,08	0,07	0,08	0,07	0,06	0,08	0,07	0,09	0,09	0,06	0,07	0,08	0,08	0,07	0,09	0,07	0,07	0,09
Mg	0,41	0,42	0,42	0,41	0,43	0,44	0,44	0,45	0,42	0,44	0,45	0,43	0,44	0,45	0,46	0,45	0,45	0,46
Zn	0,00	0,00	0,00	0,00	0,00	0,00	0,00	0,00	0,00	0,00	0,00	0,00	0,00	0,00	0,00	0,00	0,00	0,00
Ca	0,00	0,01	0,02	0,00	0,01	0,01	0,00	0,00	0,00	0,01	0,00	0,00	0,00	0,00	0,01	0,00	0,00	0,01
Na	0,00	0,02	0,00	0,00	0,02	0,02	0,02	0,02	0,02	0,00	0,03	0,00	0,01	0,03	0,03	0,03	0,03	0,03
K	0,00	0,00	0,01	0,01	0,01	0,00	0,00	0,00	0,00	0,01	0,00	0,01	0,00	0,00	0,00	0,00	0,00	0,00
Tot S2	3,79	3,84	3,82	3,71	3,81	3,79	3,80	3,91	3,83	3,80	3,82	3,78	3,87	3,82	3,82	3,82	3,82	3,82
Tot Cat	29,33	29,32	29,33	29,24	29,30	29,32	29,35	29,37	29,32	29,34	29,34	29,33	29,37	29,33	29,32	29,33	29,33	29,32
ΣO	46	46	46	46	46	46	46	46	46	46	46	46	46	46	46	46	46	46
XMg	0,11	0,11	0,11	0,11	0,11	0,12	0,12	0,12	0,11	0,12	0,12	0,11	0,11	0,12	0,12	0,12	0,12	0,12

Table 15: chemical profiles (A-A'; B-B'; C-C') through staurolite porphyroblasts and analyses of staurolite relicts. Analyses are shown in Fig. 3.12.

Sample	LL61b1	LL61b1	LL61b1	LL61b1	LL61b1	LL61b1	LL61b1	LL61b1	LL61b1	LL61b1	LL61b1	LL61b1	LL61b1	LL61b1	LL61b1	LL61b1	LL61b1
Descrip.	Prof. A-A'	Prof. A-A'	Prof. A-A'	Prof. A-A'	Prof. A-A'	Prof. A-A'	Prof. A-A'	Prof. A-A'	Prof. A-A'	Prof. A-A'	Prof. A-A'	Prof. A-A'	Prof. A-A'	Prof. A-A'	Prof. A-A'	Prof. A-A'	Prof. A-A'
SiO ₂	27,61	27,37	27,29	27,34	26,82	27,04	27,35	27,35	27,09	27,08	26,88	27,01	27,18	26,75	26,92	26,92	26,92
TiO ₂	0,39	0,36	0,38	0,40	0,52	0,38	0,43	0,50	0,47	0,50	0,45	0,56	0,56	0,54	0,81	0,81	0,81
Al ₂ O ₃	53,12	53,11	53,04	53,32	53,22	52,95	53,04	52,86	53,06	52,94	52,67	52,62	52,55	53,11	52,66	52,66	52,66
FeO	14,01	14,12	14,01	13,77	14,07	13,93	14,06	14,07	13,82	14,26	13,76	14,16	13,89	14,14	13,84	13,84	13,84
MnO	0,30	0,33	0,41	0,26	0,35	0,32	0,11	0,33	0,33	0,32	0,26	0,27	0,39	0,32	0,36	0,36	0,36
MgO	1,03	1,07	1,01	0,96	0,95	0,95	0,98	1,02	1,02	1,05	0,99	1,08	1,00	1,01	1,00	1,00	1,00
ZnO	0,00	0,00	0,02	0,01	0,01	0,00	0,01	0,00	0,00	0,01	0,00	0,00	0,01	0,00	0,02	0,02	0,02
CaO	0,03	0,00	0,01	0,04	0,03	0,01	0,02	0,03	0,00	0,00	0,00	0,00	0,02	0,02	0,00	0,00	0,00
Na ₂ O	0,01	0,07	0,00	0,01	0,00	0,01	0,04	0,03	0,03	0,02	0,05	0,03	0,02	0,02	0,00	0,00	0,00
K ₂ O	0,00	0,01	0,00	0,00	0,00	0,00	0,00	0,02	0,00	0,00	0,02	0,00	0,01	0,02	0,00	0,00	0,00
Total	96,50	96,45	96,16	96,11	95,97	95,59	96,04	96,21	95,83	96,18	95,07	95,73	95,63	95,94	95,61	95,61	95,61
Si	7,78	7,73	7,72	7,73	7,62	7,70	7,74	7,74	7,69	7,68	7,69	7,69	7,74	7,60	7,67	7,67	7,67
Al IV	0,22	0,27	0,28	0,27	0,39	0,30	0,26	0,26	0,31	0,32	0,31	0,31	0,26	0,40	0,33	0,33	0,33
Tot IV	8	8	8	8	8	8	8	8	8	8	8	8	8	8	8	8	8
Al VI	17,42	17,40	17,42	17,49	17,42	17,46	17,44	17,37	17,44	17,36	17,45	17,34	17,37	17,39	17,34	17,34	17,34
Ti	0,08	0,08	0,08	0,08	0,11	0,08	0,09	0,11	0,10	0,11	0,10	0,12	0,12	0,12	0,17	0,17	0,17
Tot S1	17,50	17,48	17,50	17,57	17,53	17,54	17,53	17,48	17,54	17,47	17,54	17,46	17,49	17,51	17,51	17,51	17,51
Fe ²⁺	3,30	3,33	3,32	3,26	3,34	3,32	3,33	3,33	3,28	3,38	3,29	3,37	3,31	3,36	3,30	3,30	3,30
Mn	0,07	0,08	0,10	0,06	0,08	0,08	0,03	0,08	0,08	0,08	0,06	0,07	0,09	0,08	0,09	0,09	0,09
Mg	0,43	0,45	0,43	0,40	0,40	0,40	0,42	0,43	0,43	0,44	0,42	0,46	0,42	0,43	0,43	0,43	0,43
Zn	0,00	0,00	0,00	0,00	0,00	0,00	0,00	0,00	0,00	0,00	0,00	0,00	0,00	0,00	0,01	0,01	0,01
Ca	0,01	0,00	0,00	0,01	0,01	0,00	0,01	0,01	0,00	0,00	0,00	0,00	0,01	0,01	0,00	0,00	0,00
Na	0,01	0,04	0,00	0,01	0,00	0,01	0,02	0,02	0,02	0,01	0,03	0,02	0,01	0,01	0,00	0,00	0,00
K	0,00	0,01	0,00	0,00	0,00	0,00	0,00	0,01	0,00	0,00	0,01	0,00	0,00	0,01	0,00	0,00	0,00
Tot S2	3,82	3,91	3,85	3,74	3,84	3,81	3,80	3,87	3,81	3,91	3,81	3,91	3,85	3,89	3,82	3,82	3,82
Tot Cat	29,32	29,38	29,35	29,31	29,37	29,34	29,33	29,35	29,35	29,38	29,35	29,37	29,34	29,40	29,33	29,33	29,33
ΣO	46	46	46	46	46	46	46	46	46	46	46	46	46	46	46	46	46
XMg	0,11	0,12	0,11	0,11	0,10	0,11	0,11	0,11	0,11	0,11	0,11	0,12	0,11	0,11	0,11	0,11	0,11

Table 15: continued

Sample	LL61b1	LL61b1	LL61b1	LL61b1	LL61b1	LL61b1	LL61b1	LL61b1	LL61b1	LL61b1	LL61b1	LL61b1	LL61b1	LL61b1	LL61b1	LL61b1	LL61b1
Descrip.	Prof. A-A'	Prof. A-A'	Prof. A-A'	Prof. A-A'	Prof. A-A'	Prof. A-A'	Prof. A-A'	Prof. A-A'	Prof. A-A'	Prof. A-A'	Prof. A-A'	Prof. A-A'	Prof. A-A'	Prof. A-A'	Prof. A-A'	Prof. A-A'	Prof. A-A'
SiO ₂	26,75	27,00	27,08	27,28	26,98	26,81	26,88	27,31	27,31	27,22	27,09	26,74	27,18	26,76	28,16	26,88	26,88
TiO ₂	0,61	0,61	0,73	0,64	0,76	0,64	0,65	0,73	0,73	0,54	0,75	0,57	0,62	0,59	0,54	0,55	0,55
Al ₂ O ₃	53,26	52,92	52,75	52,47	52,88	52,73	53,35	52,51	52,51	52,95	52,65	53,20	52,89	52,68	52,53	53,07	53,07
FeO	14,25	13,88	14,24	13,82	14,04	14,06	13,87	13,67	13,67	13,92	13,88	14,07	13,86	14,14	13,86	13,93	13,93
MnO	0,32	0,27	0,41	0,41	0,33	0,30	0,29	0,34	0,34	0,41	0,33	0,24	0,38	0,40	0,40	0,32	0,32
MgO	0,96	0,99	0,97	1,02	0,95	0,93	0,94	0,92	0,92	0,97	0,89	0,88	0,89	0,89	0,95	0,79	0,79
ZnO	0,01	0,00	0,00	0,00	0,02	0,00	0,00	0,00	0,00	0,00	0,00	0,01	0,00	0,02	0,01	0,02	0,02
CaO	0,03	0,03	0,00	0,02	0,01	0,00	0,01	0,00	0,00	0,01	0,00	0,02	0,02	0,04	0,07	0,02	0,02
Na ₂ O	0,01	0,03	0,01	0,00	0,04	0,02	0,01	0,02	0,02	0,03	0,04	0,04	0,05	0,02	0,00	0,00	0,00
K ₂ O	0,00	0,00	0,00	0,02	0,00	0,02	0,00	0,03	0,03	0,00	0,02	0,02	0,02	0,00	0,04	0,00	0,00
Total	96,21	95,71	96,20	95,68	96,00	95,51	96,00	95,53	95,53	96,04	95,64	95,78	95,91	95,53	96,57	95,58	95,58
Si	7,59	7,67	7,68	7,76	7,66	7,65	7,62	7,77	7,77	7,71	7,71	7,61	7,71	7,64	7,92	7,65	7,65
Al IV	0,42	0,33	0,32	0,24	0,34	0,35	0,38	0,23	0,23	0,29	0,29	0,40	0,29	0,36	0,08	0,35	0,35
Tot IV	8	8	8	8	8	8	8	8	8	8	8	8	8	8	8	8	8
AL VI	17,38	17,40	17,31	17,35	17,35	17,38	17,43	17,38	17,38	17,40	17,37	17,44	17,40	17,37	17,35	17,46	17,46
Ti	0,13	0,13	0,16	0,14	0,16	0,14	0,14	0,16	0,16	0,11	0,16	0,12	0,13	0,13	0,11	0,12	0,12
Tot S1	17,51	17,53	17,46	17,48	17,51	17,52	17,57	17,53	17,53	17,51	17,53	17,56	17,53	17,50	17,46	17,58	17,58
Fe ²⁺	3,38	3,30	3,38	3,29	3,33	3,35	3,29	3,25	3,25	3,30	3,30	3,35	3,29	3,38	3,26	3,32	3,32
Mn	0,08	0,06	0,10	0,10	0,08	0,07	0,07	0,08	0,08	0,10	0,08	0,06	0,09	0,10	0,10	0,08	0,08
Mg	0,41	0,42	0,41	0,43	0,40	0,40	0,40	0,39	0,39	0,41	0,38	0,37	0,38	0,38	0,40	0,34	0,34
Zn	0,00	0,00	0,00	0,00	0,00	0,00	0,00	0,00	0,00	0,00	0,00	0,00	0,00	0,00	0,00	0,00	0,00
Ca	0,01	0,01	0,00	0,01	0,00	0,00	0,00	0,00	0,00	0,00	0,00	0,01	0,01	0,01	0,02	0,01	0,01
Na	0,00	0,02	0,01	0,00	0,02	0,01	0,00	0,01	0,01	0,02	0,02	0,02	0,03	0,01	0,00	0,00	0,00
K	0,00	0,00	0,00	0,01	0,00	0,01	0,00	0,01	0,01	0,00	0,01	0,01	0,01	0,00	0,02	0,00	0,00
Tot S2	3,88	3,81	3,89	3,83	3,84	3,84	3,76	3,75	3,75	3,83	3,79	3,81	3,80	3,88	3,80	3,74	3,74
Tot Cat	29,39	29,34	29,36	29,32	29,35	29,36	29,34	29,28	29,28	29,34	29,32	29,37	29,33	29,38	29,26	29,32	29,32
ΣO	46	46	46	46	46	46	46	46	46	46	46	46	46	46	46	46	46
XMg	0,11	0,11	0,11	0,11	0,11	0,10	0,11	0,10	0,10	0,11	0,10	0,10	0,10	0,10	0,11	0,09	0,09

Table 15: continued

Sample	LL61b1	LL61b1	LL61b1	LL61b1	LL61b1	LL61b1	LL61b1	LL61b1	LL61b1	LL61b1	LL61b1	LL61b1	LL61b1	LL61b1	LL61b1	LL61b1
Descrip.	Prof. A-A'	Prof. A-A'	Prof. A-A'	Prof. A-A'	Prof. B-B'	Prof. B-B'	Prof. B-B'	Prof. B-B'	Prof. B-B'	Prof. B-B'	Prof. B-B'	Prof. B-B'	Prof. B-B'	Prof. B-B'	Prof. B-B'	Prof. B-B'
SiO2	27,28	27,02	27,15	26,88	26,36	26,96	27,07	26,48	26,53	26,47	26,41	26,56	26,52	26,91	26,90	26,90
TiO2	0,64	0,69	0,65	0,52	0,46	0,36	0,31	0,39	0,48	0,34	0,30	0,50	0,41	0,37	0,43	0,43
Al2O3	53,22	52,70	52,97	53,07	54,39	53,77	53,63	53,84	53,77	53,63	53,83	53,83	53,66	53,44	53,66	53,66
FeO	14,05	14,35	13,86	13,86	13,50	13,39	13,53	13,65	13,93	13,78	13,58	13,50	13,80	13,73	13,49	13,49
MnO	0,39	0,27	0,40	0,37	0,28	0,33	0,32	0,32	0,35	0,28	0,33	0,35	0,32	0,35	0,26	0,26
MgO	0,78	0,81	0,87	0,84	1,11	1,08	1,14	1,15	1,17	1,13	1,13	1,16	1,16	1,12	1,20	1,20
ZnO	0,01	0,00	0,00	0,00	0,01	0,01	0,00	0,01	0,02	0,02	0,01	0,00	0,00	0,00	0,01	0,01
CaO	0,00	0,00	0,02	0,03	0,00	0,04	0,02	0,00	0,01	0,01	0,00	0,00	0,03	0,00	0,01	0,01
Na2O	0,01	0,01	0,03	0,02	0,00	0,01	0,03	0,03	0,00	0,02	0,03	0,02	0,04	0,00	0,04	0,04
K2O	0,00	0,00	0,00	0,00	0,03	0,02	0,00	0,02	0,00	0,00	0,00	0,01	0,01	0,01	0,01	0,01
Total	96,39	95,86	95,94	95,58	96,13	95,99	96,05	95,89	96,25	95,69	95,61	95,93	95,97	95,94	96,01	96,01
Si	7,71	7,69	7,70	7,65	7,45	7,62	7,65	7,51	7,51	7,53	7,51	7,52	7,52	7,63	7,61	7,61
Al IV	0,30	0,31	0,30	0,35	0,55	0,38	0,35	0,49	0,49	0,47	0,49	0,48	0,48	0,37	0,39	0,39
Tot IV	8	8	8	8	8	8	8	8	8	8	8	8	8	8	8	8
Al VI	17,42	17,36	17,41	17,46	17,57	17,54	17,51	17,51	17,44	17,50	17,55	17,50	17,46	17,48	17,49	17,49
Ti	0,14	0,15	0,14	0,11	0,10	0,08	0,07	0,08	0,10	0,07	0,06	0,11	0,09	0,08	0,09	0,09
TotS1	17,56	17,51	17,54	17,57	17,66	17,62	17,58	17,59	17,54	17,58	17,61	17,60	17,55	17,56	17,58	17,58
Fe2+	3,32	3,42	3,29	3,30	3,19	3,17	3,20	3,24	3,30	3,28	3,23	3,20	3,27	3,25	3,19	3,19
Mn	0,09	0,07	0,10	0,09	0,07	0,08	0,08	0,08	0,08	0,07	0,08	0,08	0,08	0,09	0,06	0,06
Mg	0,33	0,34	0,37	0,35	0,47	0,46	0,48	0,49	0,49	0,48	0,48	0,49	0,49	0,47	0,51	0,51
Zn	0,00	0,00	0,00	0,01	0,00	0,00	0,00	0,00	0,00	0,00	0,00	0,00	0,00	0,00	0,00	0,00
Ca	0,00	0,00	0,01	0,01	0,00	0,01	0,01	0,00	0,00	0,00	0,00	0,00	0,01	0,00	0,00	0,00
Na	0,01	0,01	0,02	0,01	0,00	0,00	0,01	0,02	0,00	0,01	0,02	0,01	0,02	0,00	0,02	0,02
K	0,00	0,00	0,00	0,00	0,01	0,01	0,00	0,01	0,00	0,00	0,00	0,00	0,01	0,00	0,00	0,00
Tot S2	3,75	3,83	3,77	3,76	3,74	3,73	3,78	3,83	3,88	3,84	3,80	3,79	3,88	3,82	3,79	3,79
Tot Cat	29,30	29,33	29,32	29,34	29,40	29,35	29,36	29,42	29,42	29,42	29,41	29,39	29,43	29,37	29,37	29,37
ΣO	46	46	46	46	46	46	46	46	46	46	46	46	46	46	46	46
ΣMg	0,09	0,09	0,10	0,09	0,13	0,12	0,13	0,13	0,13	0,13	0,13	0,13	0,13	0,12	0,13	0,13

Table 15: continued

Sample	LL 61b1	LL 61b1	LL 61b1	LL 61b1	LL 61b1	LL 61b1	LL 61b1	LL 61b1	LL 61b1	LL 61b1	LL 61b1	LL 61b1	LL 61b1	LL 61b1	LL 61b1	LL 61b1	LL 61b1
Descrip. Prof. B-B'	Prof. B-B'	Prof. B-B'	Prof. B-B'	Prof. B-B'	Prof. B-B'	Prof. B-B'	Prof. B-B'	Prof. B-B'	Prof. B-B'	Prof. B-B'	Prof. B-B'	Prof. B-B'	Prof. B-B'	Prof. B-B'	Prof. B-B'	Prof. B-B'	Prof. B-B'
SiO2	26,90	27,38	26,57	26,51	26,56	26,54	26,90	26,83	27,07	26,36	26,47	26,21	26,39	26,72	26,77	26,77	26,77
TiO2	0,42	0,31	0,37	0,30	0,37	0,38	0,45	0,40	0,43	0,33	0,44	0,44	0,35	0,29	0,26	0,26	0,26
Al2O3	53,27	53,57	53,63	53,77	53,79	53,60	53,72	53,20	53,23	53,93	54,29	53,83	54,26	54,03	53,98	53,98	53,98
FeO	13,80	13,77	13,73	13,77	13,75	13,78	13,71	13,40	13,46	13,72	13,53	13,47	14,17	13,46	13,50	13,50	13,50
MnO	0,29	0,34	0,32	0,18	0,36	0,38	0,36	0,35	0,34	0,38	0,29	0,31	0,22	0,35	0,35	0,35	0,35
MgO	1,15	1,17	1,17	1,15	1,16	1,19	1,18	1,16	1,22	1,16	1,13	1,14	1,13	1,11	1,10	1,10	1,10
ZnO	0,01	0,01	0,03	0,00	0,00	0,02	0,00	0,00	0,01	0,01	0,00	0,00	0,00	0,00	0,00	0,00	0,00
CaO	0,00	0,01	0,00	0,00	0,00	0,01	0,01	0,01	0,00	0,02	0,04	0,00	0,00	0,00	0,01	0,01	0,01
Na2O	0,04	0,00	0,02	0,02	0,03	0,00	0,01	0,03	0,00	0,02	0,02	0,00	0,02	0,03	0,04	0,04	0,04
K2O	0,00	0,02	0,00	0,00	0,03	0,00	0,00	0,02	0,00	0,00	0,00	0,02	0,00	0,02	0,00	0,00	0,00
Total	95,88	96,58	95,83	95,69	96,05	95,90	96,35	95,41	95,76	95,92	96,21	95,43	96,54	96,02	96,01	96,01	96,01
Si	7,63	7,70	7,54	7,53	7,53	7,53	7,59	7,64	7,67	7,48	7,48	7,47	7,45	7,56	7,57	7,57	7,57
Al IV	0,37	0,30	0,46	0,47	0,47	0,47	0,41	0,36	0,33	0,52	0,53	0,53	0,55	0,44	0,43	0,43	0,43
Tot IV	8	8	8	8	8	8	8	8	8	8	8	8	8	8	8	8	8
Al VI	17,44	17,47	17,49	17,54	17,49	17,46	17,46	17,48	17,46	17,51	17,55	17,54	17,50	17,57	17,57	17,57	17,57
Ti	0,09	0,07	0,08	0,06	0,08	0,08	0,10	0,09	0,09	0,07	0,09	0,09	0,07	0,06	0,06	0,06	0,06
TotS1	17,53	17,53	17,57	17,60	17,57	17,55	17,55	17,57	17,55	17,58	17,64	17,63	17,57	17,63	17,62	17,62	17,62
Fe2+	3,27	3,24	3,26	3,27	3,26	3,27	3,24	3,19	3,19	3,26	3,20	3,21	3,35	3,18	3,19	3,19	3,19
Mn	0,07	0,08	0,08	0,04	0,09	0,09	0,09	0,09	0,08	0,09	0,07	0,08	0,05	0,08	0,08	0,08	0,08
Mg	0,49	0,49	0,49	0,49	0,49	0,51	0,50	0,49	0,52	0,49	0,48	0,48	0,48	0,47	0,46	0,46	0,46
Zn	0,00	0,00	0,01	0,00	0,00	0,01	0,00	0,00	0,00	0,00	0,00	0,00	0,00	0,00	0,00	0,00	0,00
Ca	0,00	0,00	0,00	0,00	0,00	0,00	0,00	0,00	0,00	0,01	0,01	0,00	0,00	0,00	0,00	0,00	0,00
Na	0,02	0,00	0,01	0,01	0,01	0,00	0,00	0,02	0,00	0,01	0,01	0,00	0,01	0,02	0,02	0,02	0,02
K	0,00	0,01	0,00	0,00	0,01	0,00	0,00	0,01	0,00	0,00	0,00	0,01	0,00	0,01	0,00	0,00	0,00
Tot S2	3,86	3,83	3,85	3,81	3,86	3,87	3,83	3,80	3,79	3,85	3,76	3,78	3,88	3,76	3,76	3,76	3,76
Tot Cat	29,39	29,36	29,41	29,41	29,43	29,42	29,38	29,37	29,34	29,44	29,40	29,41	29,46	29,39	29,39	29,39	29,39
ΣO	46	46	46	46	46	46	46	46	46	46	46	46	46	46	46	46	46
XMg	0,13	0,13	0,13	0,13	0,13	0,13	0,13	0,13	0,14	0,13	0,13	0,13	0,12	0,13	0,12	0,12	0,12

Table 15: continued

Sample	LL 61b1	LL 61b1	LL 61b1	LL 61b1	LL 61b1	LL 61b1	LL 61b1	LL 61b1	LL 61b1	LL 61b1	LL 61b1	LL 61b1	LL 61b1	LL 61b1	LL 61b1	LL 61b1	LL 61b1
Descript. Prof. B-B'	Prof. B-B'	Prof. B-B'	Prof. B-B'	Prof. B-B'	Prof. B-B'	Prof. B-B'	Prof. B-B'	Prof. B-B'	Prof. B-B'	Prof. B-B'	Prof. B-B'	Prof. B-B'	Prof. B-B'	Prof. B-B'	Prof. B-B'	Prof. B-B'	Prof. B-B'
SiO2	26,72	26,35	26,48	26,33	26,18	26,67	26,67	26,58	26,36	26,41	26,70	26,75	26,77	26,24	26,62	26,42	26,42
TiO2	0,31	0,38	0,41	0,45	0,46	0,27	0,27	0,37	0,31	0,32	0,37	0,35	0,40	0,38	0,37	0,40	0,40
Al2O3	54,22	54,21	53,81	54,15	54,28	53,87	53,87	54,32	53,89	53,58	53,78	53,65	53,58	54,02	54,09	53,87	53,87
FeO	13,70	13,79	13,29	13,80	13,56	13,56	13,56	13,90	13,74	13,45	13,49	13,41	13,53	13,41	13,67	13,50	13,50
MnO	0,29	0,29	0,35	0,36	0,24	0,32	0,32	0,30	0,27	0,28	0,24	0,32	0,36	0,40	0,35	0,33	0,33
MgO	1,11	1,08	1,10	1,14	1,13	1,09	1,09	1,09	1,10	1,09	1,13	1,09	1,10	1,11	1,09	1,09	1,09
ZnO	0,01	0,03	0,01	0,01	0,00	0,00	0,00	0,02	0,01	0,00	0,01	0,00	0,00	0,00	0,01	0,02	0,02
CaO	0,02	0,02	0,03	0,02	0,00	0,00	0,00	0,01	0,01	0,00	0,02	0,01	0,01	0,04	0,00	0,03	0,03
Na2O	0,06	0,04	0,04	0,00	0,03	0,02	0,02	0,03	0,04	0,02	0,03	0,00	0,00	0,04	0,03	0,02	0,02
K2O	0,01	0,00	0,00	0,01	0,01	0,00	0,00	0,01	0,01	0,02	0,00	0,01	0,01	0,00	0,01	0,00	0,00
Total	96,44	96,18	95,51	96,27	95,91	95,79	95,79	96,62	95,76	95,18	95,78	95,58	95,76	95,64	96,24	95,67	95,67
Si	7,53	7,46	7,53	7,45	7,42	7,56	7,56	7,49	7,49	7,54	7,57	7,60	7,59	7,46	7,52	7,51	7,51
Al IV	0,47	0,55	0,47	0,55	0,58	0,44	0,44	0,51	0,51	0,46	0,43	0,41	0,41	0,54	0,48	0,49	0,49
Tot IV	8	8	8	8	8	8	8	8	8	8	8	8	8	8	8	8	8
Al VI	17,54	17,53	17,56	17,50	17,55	17,57	17,57	17,52	17,54	17,56	17,54	17,55	17,51	17,55	17,53	17,54	17,54
Ti	0,07	0,08	0,09	0,10	0,10	0,06	0,06	0,08	0,07	0,07	0,08	0,08	0,09	0,08	0,08	0,09	0,09
TotS1	17,61	17,62	17,64	17,59	17,65	17,62	17,62	17,60	17,60	17,63	17,62	17,63	17,59	17,64	17,61	17,63	17,63
Fe2+	3,23	3,26	3,16	3,27	3,22	3,22	3,22	3,28	3,27	3,21	3,20	3,19	3,21	3,19	3,23	3,21	3,21
Mn	0,07	0,07	0,08	0,09	0,06	0,08	0,08	0,07	0,07	0,07	0,06	0,08	0,09	0,10	0,08	0,08	0,08
Mg	0,47	0,46	0,47	0,48	0,48	0,46	0,46	0,46	0,46	0,47	0,48	0,46	0,47	0,47	0,46	0,46	0,46
Zn	0,00	0,01	0,00	0,00	0,00	0,00	0,00	0,00	0,00	0,00	0,00	0,00	0,00	0,00	0,00	0,00	0,00
Ca	0,01	0,01	0,01	0,01	0,00	0,00	0,00	0,00	0,00	0,00	0,01	0,00	0,00	0,01	0,00	0,01	0,01
Na	0,03	0,02	0,02	0,00	0,02	0,01	0,01	0,02	0,02	0,01	0,02	0,00	0,00	0,02	0,02	0,01	0,01
K	0,00	0,00	0,00	0,00	0,01	0,00	0,00	0,00	0,00	0,01	0,00	0,01	0,00	0,00	0,00	0,00	0,00
Tot S2	3,80	3,82	3,74	3,85	3,78	3,76	3,76	3,83	3,83	3,76	3,76	3,73	3,77	3,79	3,80	3,77	3,77
Tot Cat	29,41	29,44	29,38	29,44	29,43	29,38	29,38	29,43	29,43	29,39	29,37	29,35	29,37	29,42	29,41	29,40	29,40
ΣO	46	46	46	46	46	46	46	46	46	46	46	46	46	46	46	46	46
XMg	0,12	0,12	0,13	0,13	0,13	0,12	0,12	0,12	0,12	0,12	0,13	0,12	0,12	0,13	0,12	0,12	0,12

Table 15: continued

Sample	LL 61b1	LL 61b1	LL 61b1	LL 61b1	LL 61b1	LL 61b1	LL 61b1	LL 61b1	LL 61b1	LL 61b1	LL 61b1	LL 61b1	LL 61b1	LL 61b1	LL 61b1	LL 61b1	LL 61b1
Descrip. Prof. B-B'	Prof. B-B'	Prof. B-B'	Prof. B-B'	Prof. B-B'	Prof. B-B'	Prof. B-B'	Prof. B-B'	Prof. B-B'	Prof. B-B'	Prof. B-B'	Prof. B-B'	Prof. B-B'	Prof. B-B'	Prof. B-B'	Prof. B-B'	Prof. B-B'	Prof. B-B'
SiO ₂	26,40	26,21	26,73	26,53	26,58	26,33	26,85	26,26	26,50	26,80	26,45	26,64	26,49	26,97	26,97	26,97	26,97
TiO ₂	0,46	0,40	0,49	0,26	0,45	0,42	0,38	0,39	0,45	0,45	0,52	0,37	0,40	0,38	0,38	0,38	0,41
Al ₂ O ₃	54,17	54,30	53,86	53,81	53,62	53,15	53,85	54,05	53,56	53,70	53,56	53,60	53,76	53,53	53,53	53,53	53,48
FeO	13,65	13,83	13,49	13,88	13,48	13,72	13,54	13,64	13,55	13,71	13,64	13,60	13,66	13,27	13,27	13,27	13,51
MnO	0,35	0,33	0,24	0,33	0,43	0,32	0,31	0,30	0,22	0,25	0,36	0,35	0,24	0,34	0,34	0,34	0,37
MgO	1,10	1,12	1,07	1,12	1,08	1,07	1,07	1,09	1,05	1,12	1,06	1,03	1,06	1,06	1,06	1,06	1,08
ZnO	0,00	0,02	0,00	0,01	0,00	0,00	0,00	0,01	0,00	0,00	0,02	0,01	0,00	0,00	0,00	0,00	0,00
CaO	0,00	0,00	0,01	0,03	0,03	0,01	0,00	0,00	0,04	0,02	0,00	0,00	0,00	0,02	0,02	0,02	0,00
Na ₂ O	0,04	0,01	0,05	0,02	0,02	0,04	0,04	0,03	0,01	0,01	0,01	0,02	0,00	0,02	0,02	0,02	0,07
K ₂ O	0,03	0,00	0,00	0,00	0,02	0,01	0,02	0,00	0,02	0,00	0,01	0,01	0,00	0,00	0,00	0,00	0,00
Total	96,19	96,22	95,93	95,98	95,70	95,06	96,07	95,78	95,40	96,06	95,63	95,62	95,63	95,59	95,59	95,59	95,94
Si	7,47	7,42	7,56	7,52	7,55	7,54	7,59	7,46	7,55	7,58	7,52	7,57	7,53	7,65	7,65	7,65	7,65
Al IV	0,53	0,58	0,44	0,48	0,45	0,46	0,41	0,54	0,45	0,42	0,48	0,43	0,47	0,35	0,35	0,35	0,35
Tot IV	8	8	8	8	8	8	8	8	8	8	8	8	8	8	8	8	8
AL VI	17,52	17,53	17,53	17,51	17,50	17,48	17,53	17,55	17,53	17,49	17,48	17,53	17,54	17,55	17,55	17,55	17,49
Ti	0,10	0,08	0,11	0,06	0,10	0,09	0,08	0,08	0,10	0,10	0,11	0,08	0,09	0,08	0,08	0,09	0,09
TotS1	17,62	17,61	17,63	17,57	17,60	17,57	17,62	17,63	17,62	17,59	17,59	17,61	17,62	17,63	17,63	17,63	17,58
Fe2+	3,23	3,27	3,19	3,29	3,20	3,29	3,20	3,24	3,23	3,24	3,25	3,23	3,25	3,15	3,15	3,15	3,20
Mn	0,08	0,08	0,06	0,08	0,10	0,08	0,08	0,07	0,05	0,06	0,09	0,08	0,06	0,08	0,08	0,09	0,09
Mg	0,46	0,47	0,45	0,47	0,46	0,46	0,45	0,46	0,45	0,47	0,45	0,43	0,45	0,45	0,45	0,46	0,46
Zn	0,00	0,00	0,00	0,00	0,00	0,00	0,00	0,00	0,00	0,00	0,00	0,00	0,00	0,00	0,00	0,00	0,00
Ca	0,00	0,00	0,00	0,01	0,01	0,00	0,00	0,00	0,01	0,01	0,00	0,00	0,00	0,01	0,01	0,00	0,00
Na	0,02	0,01	0,03	0,01	0,01	0,02	0,02	0,02	0,01	0,01	0,01	0,01	0,00	0,01	0,01	0,04	0,04
K	0,01	0,00	0,00	0,00	0,01	0,01	0,01	0,00	0,01	0,00	0,00	0,01	0,00	0,00	0,00	0,00	0,00
Tot S2	3,81	3,84	3,73	3,87	3,79	3,85	3,76	3,79	3,75	3,79	3,80	3,77	3,76	3,70	3,70	3,78	3,78
Tot Cat	29,43	29,45	29,36	29,43	29,39	29,42	29,37	29,42	29,37	29,37	29,39	29,38	29,38	29,33	29,33	29,36	29,36
ΣO	46	46	46	46	46	46	46	46	46	46	46	46	46	46	46	46	46
XMg	0,12	0,12	0,12	0,12	0,12	0,12	0,12	0,12	0,12	0,12	0,12	0,12	0,12	0,12	0,12	0,12	0,12

Table 15: continued

Sample	LL 61b1	LL 61b1	LL 61b1	LL 61b1	LL 61b1	LL 61b1	LL 61b1	LL 61b1	LL 61b1	LL 61b1	LL 61b1	LL 61b1	LL 61b1	LL 61b1	LL 61b1	LL 61b1	LL 61b1
Descrip. Prof. B-B'	Prof. B-B'	Prof. B-B'	Prof. B-B'	Prof. B-B'	Prof. B-B'	Prof. B-B'	Prof. B-B'	Prof. B-B'	Prof. B-B'	Prof. B-B'	Prof. B-B'	Prof. B-B'	Prof. B-B'	Prof. B-B'	Prof. B-B'	Prof. B-B'	Prof. B-B'
SiO2	26,85	26,31	26,91	26,79	26,71	26,53	26,17	26,22	26,57	26,46	26,74	26,34	26,53	26,38	26,53	26,38	26,53
TiO2	0,42	0,47	0,37	0,51	0,42	0,38	0,35	0,43	0,38	0,41	0,39	0,45	0,40	0,45	0,45	0,45	0,45
Al2O3	53,20	53,83	53,53	53,64	53,54	53,64	53,93	53,75	53,84	53,81	53,39	53,83	53,54	53,89	53,54	53,89	54,08
FeO	13,55	13,53	13,48	13,57	13,58	13,64	13,41	14,00	13,53	13,72	13,71	13,63	13,69	13,64	13,69	13,64	13,74
MnO	0,26	0,29	0,32	0,29	0,34	0,34	0,32	0,27	0,29	0,43	0,30	0,39	0,37	0,38	0,37	0,38	0,19
MgO	1,01	1,03	1,05	0,99	1,04	1,03	0,97	1,02	1,00	0,97	0,98	0,99	1,00	0,94	1,00	0,94	0,95
ZnO	0,00	0,01	0,00	0,00	0,02	0,02	0,01	0,01	0,01	0,01	0,00	0,00	0,00	0,02	0,00	0,02	0,00
CaO	0,01	0,01	0,01	0,00	0,00	0,03	0,05	0,01	0,03	0,01	0,03	0,00	0,01	0,00	0,01	0,00	0,00
Na2O	0,00	0,02	0,03	0,02	0,02	0,05	0,03	0,04	0,03	0,02	0,03	0,03	0,02	0,03	0,02	0,03	0,05
K2O	0,00	0,01	0,03	0,02	-0,01	0,00	0,00	0,00	0,00	0,02	0,00	0,01	0,01	0,00	0,01	0,00	0,00
Total	95,29	95,50	95,72	95,83	95,65	95,67	95,25	95,75	95,68	95,86	95,56	95,68	95,57	95,73	95,57	95,73	95,97
Si	7,65	7,49	7,63	7,59	7,59	7,54	7,47	7,46	7,54	7,51	7,61	7,49	7,55	7,50	7,55	7,50	7,51
Al IV	0,35	0,51	0,37	0,41	0,41	0,46	0,53	0,54	0,46	0,49	0,39	0,51	0,45	0,50	0,45	0,50	0,49
Tot IV	8	8	8	8	8	8	8	8	8	8	8	8	8	8	8	8	8
Al VI	17,52	17,54	17,53	17,52	17,51	17,52	17,60	17,49	17,56	17,52	17,51	17,53	17,52	17,54	17,52	17,54	17,56
Ti	0,09	0,10	0,08	0,11	0,09	0,08	0,08	0,09	0,08	0,09	0,08	0,10	0,09	0,10	0,09	0,10	0,10
Tot S1	17,61	17,65	17,61	17,62	17,61	17,60	17,68	17,59	17,64	17,61	17,59	17,63	17,60	17,64	17,60	17,64	17,66
Fe2+	3,23	3,22	3,20	3,22	3,23	3,24	3,20	3,33	3,21	3,26	3,26	3,24	3,26	3,24	3,26	3,24	3,25
Mn	0,06	0,07	0,08	0,07	0,08	0,08	0,08	0,07	0,07	0,10	0,07	0,09	0,09	0,09	0,09	0,09	0,05
Mg	0,43	0,44	0,44	0,42	0,44	0,44	0,41	0,43	0,43	0,41	0,41	0,42	0,42	0,40	0,42	0,40	0,40
Zn	0,00	0,00	0,00	0,00	0,00	0,01	0,00	0,00	0,00	0,00	0,00	0,00	0,00	0,01	0,00	0,01	0,00
Ca	0,00	0,00	0,00	0,00	0,00	0,01	0,01	0,00	0,01	0,00	0,01	0,00	0,00	0,00	0,00	0,00	0,00
Na	0,00	0,01	0,02	0,01	0,01	0,03	0,02	0,02	0,02	0,01	0,02	0,02	0,01	0,02	0,01	0,02	0,03
K	0,00	0,00	0,01	0,01	0,00	0,00	0,00	0,00	0,00	0,01	0,00	0,00	0,01	0,00	0,01	0,00	0,00
Tot S2	3,72	3,75	3,75	3,73	3,76	3,81	3,72	3,86	3,73	3,80	3,77	3,78	3,79	3,75	3,79	3,75	3,72
Tot Cat	29,33	29,39	29,35	29,35	29,36	29,40	29,40	29,44	29,38	29,41	29,37	29,41	29,39	29,39	29,39	29,39	29,38
ΣO	46	46	46	46	46	46	46	46	46	46	46	46	46	46	46	46	46
XMg	0,12	0,12	0,12	0,11	0,12	0,12	0,11	0,11	0,11	0,11	0,11	0,11	0,11	0,11	0,11	0,11	0,11

Table 15: continued

[illegible]

Table 15: continued

Sample	LI61b2	LI61b2	LI61b2	LI61b2	LI61b2	LI61b2	LI61b2	LI61b2	LI61b2	LI61b2	LI61b2	LI61b2	LI61b2	LI61b2	LI61b2	LI61b2	LI61b2
Descrip.	Prof. C-C'	Prof. C-C'	Prof. C-C'	Prof. C-C'	Prof. C-C'	Prof. C-C'	Prof. C-C'	Prof. C-C'	Prof. C-C'	Prof. C-C'	Prof. C-C'	Prof. C-C'	Prof. C-C'	Prof. C-C'	Prof. C-C'	Prof. C-C'	Prof. C-C'
SiO ₂	26,74	26,42	26,99	26,22	25,68	25,94	25,24	25,63	25,81	25,92	26,21	25,72	26,32	25,85	26,64	26,64	26,64
TiO ₂	0,56	0,60	0,85	0,60	0,63	0,61	0,80	0,50	0,69	0,55	0,82	0,72	0,64	0,52	0,45	0,45	0,45
Al ₂ O ₃	55,07	54,78	54,55	55,17	55,18	54,70	54,28	53,86	54,58	54,62	54,74	54,31	54,45	54,71	54,28	54,28	54,28
FeO	13,56	13,56	13,65	13,67	13,97	13,59	13,75	14,24	13,83	13,91	14,08	13,55	13,73	13,57	14,16	14,16	14,16
MnO	0,30	0,25	0,26	0,33	0,35	0,28	0,42	0,27	0,38	0,34	0,34	0,42	0,27	0,27	0,31	0,31	0,31
MgO	1,09	1,11	1,06	1,03	1,15	1,16	1,16	1,13	1,01	1,06	1,15	1,22	1,18	1,12	1,10	1,10	1,10
ZnO	0,77	0,56	0,71	0,71	0,65	0,60	0,74	0,61	0,59	0,66	0,82	0,64	0,71	0,68	0,63	0,63	0,63
CaO	0,02	0,00	0,01	0,04	0,01	0,00	0,03	0,00	0,03	0,02	0,00	0,00	0,00	0,01	0,00	0,00	0,00
Na ₂ O	0,01	0,04	0,00	0,06	0,02	0,02	0,01	0,00	0,01	0,03	0,03	0,05	0,04	0,04	0,02	0,02	0,02
K ₂ O	0,00	0,00	0,00	0,01	0,02	0,00	0,00	0,00	0,00	0,01	0,00	0,00	0,02	0,00	0,00	0,00	0,00
Total	98,12	97,33	98,07	97,83	97,67	96,90	96,43	96,25	96,94	97,12	98,19	96,64	97,35	96,76	97,60	97,60	97,60
Si	7,43	7,40	7,50	7,32	7,20	7,31	7,18	7,30	7,28	7,30	7,31	7,28	7,39	7,30	7,47	7,47	7,47
Al IV	0,57	0,60	0,50	0,68	0,80	0,69	0,83	0,70	0,72	0,70	0,69	0,72	0,61	0,70	0,53	0,53	0,53
Tot IV	8	8	8	8	8	8	8	8	8	8	8	8	8	8	8	8	8
AL VI	17,47	17,48	17,38	17,48	17,43	17,47	17,36	17,38	17,43	17,44	17,32	17,39	17,40	17,49	17,39	17,39	17,39
Ti	0,12	0,13	0,18	0,13	0,13	0,13	0,17	0,11	0,15	0,12	0,17	0,15	0,14	0,11	0,10	0,10	0,10
Tot S1	17,59	17,61	17,56	17,60	17,56	17,60	17,53	17,49	17,58	17,56	17,49	17,54	17,53	17,60	17,49	17,49	17,49
Fe2+	3,15	3,18	3,17	3,19	3,28	3,20	3,27	3,39	3,27	3,28	3,29	3,21	3,22	3,20	3,32	3,32	3,32
Mn	0,07	0,06	0,06	0,08	0,08	0,07	0,10	0,07	0,09	0,08	0,08	0,10	0,06	0,06	0,07	0,07	0,07
Mg	0,45	0,47	0,44	0,43	0,48	0,49	0,49	0,48	0,42	0,45	0,48	0,52	0,49	0,47	0,46	0,46	0,46
Zn	0,16	0,12	0,15	0,15	0,14	0,13	0,16	0,13	0,12	0,14	0,17	0,13	0,15	0,14	0,13	0,13	0,13
Ca	0,01	0,00	0,00	0,01	0,00	0,00	0,01	0,00	0,01	0,01	0,00	0,00	0,00	0,00	0,00	0,00	0,00
Na	0,00	0,02	0,00	0,03	0,01	0,01	0,01	0,00	0,01	0,02	0,02	0,03	0,02	0,02	0,01	0,01	0,01
K	0,00	0,00	0,00	0,00	0,01	0,00	0,00	0,00	0,00	0,00	0,00	0,00	0,01	0,00	0,00	0,00	0,00
Tot S2	3,84	3,84	3,82	3,89	4,00	3,89	4,03	4,07	3,92	3,97	4,03	3,99	3,95	3,91	4,00	4,00	4,00
Tot Cat	29,43	29,45	29,38	29,49	29,56	29,49	29,57	29,55	29,50	29,52	29,52	29,53	29,49	29,51	29,48	29,48	29,48
ΣO	46	46	46	46	46	46	46	46	46	46	46	46	46	46	46	46	46
XMg	0,12	0,12	0,12	0,11	0,12	0,13	0,12	0,12	0,11	0,11	0,12	0,13	0,13	0,12	0,12	0,12	0,12

Table 15: continued

Sample	LI61b2	LI61b2	LI61b2	LI61b2	LI61b2	LI61b2	LI61b2	LI61b2	LI61b2	LI61b2	LI61b2	LI61b2	LI61b2	LI61b2	LI61b2	LI61b2	LI61b2
Descrip.	Prof. C-C'	Prof. C-C'	Prof. C-C'	Prof. C-C'	Prof. C-C'	Prof. C-C'	Prof. C-C'	Prof. C-C'	Prof. C-C'	Prof. C-C'	Prof. C-C'	Prof. C-C'	Prof. C-C'	Prof. C-C'	Prof. C-C'	Prof. C-C'	Prof. C-C'
SiO2	26,62	26,46	26,69	26,23	26,76	26,61	25,76	26,21	27,39	27,10	27,22	27,84	27,10	27,39	27,10	27,22	27,84
TiO2	0,63	0,64	0,69	0,74	0,76	0,53	0,85	0,66	0,64	0,61	0,85	0,53	0,61	0,64	0,61	0,85	0,53
Al2O3	55,10	54,76	54,77	54,81	54,73	55,06	55,28	53,43	55,22	54,23	55,35	55,41	54,23	55,22	54,23	55,35	55,41
FeO	13,69	13,42	13,79	13,54	13,46	13,59	14,28	13,10	13,44	13,64	13,58	13,25	13,64	13,44	13,64	13,58	13,25
MnO	0,23	0,32	0,23	0,31	0,39	0,31	0,23	0,18	0,13	0,34	0,39	0,34	0,34	0,13	0,34	0,39	0,34
MgO	1,06	1,10	1,07	1,04	1,13	1,19	1,05	1,09	1,14	1,05	1,16	1,05	1,05	1,14	1,05	1,16	1,05
ZnO	0,79	0,70	0,57	0,61	0,60	0,62	0,78	0,51	0,58	0,79	0,92	0,75	0,79	0,58	0,79	0,92	0,75
CaO	0,01	0,00	0,03	0,00	0,03	0,00	0,04	0,06	0,01	0,03	0,00	0,01	0,03	0,01	0,03	0,00	0,01
Na2O	0,03	0,06	0,04	0,04	0,00	0,04	0,00	0,05	0,01	0,03	0,00	0,01	0,03	0,01	0,03	0,00	0,01
K2O	0,06	0,00	0,00	0,00	0,00	0,00	0,00	0,04	0,00	0,00	0,00	0,01	0,00	0,00	0,00	0,00	0,01
Total	98,22	97,47	97,87	97,32	97,84	98,46	99,44	95,32	98,57	97,83	99,49	99,21	97,83	98,57	97,83	99,49	99,21
Si	7,40	7,40	7,44	7,35	7,45	7,50	7,41	7,48	7,55	7,56	7,47	7,63	7,56	7,55	7,56	7,47	7,63
Al IV	0,60	0,60	0,56	0,65	0,55	0,50	0,59	0,52	0,45	0,44	0,53	0,38	0,44	0,45	0,44	0,53	0,38
Tot IV	8	8	8	8	8	8	8	8	8	8	8	8	8	8	8	8	8
AL VI	17,45	17,46	17,43	17,46	17,42	17,46	17,33	17,46	17,49	17,39	17,36	17,51	17,39	17,49	17,39	17,36	17,51
Ti	0,13	0,14	0,15	0,16	0,16	0,11	0,18	0,14	0,13	0,13	0,18	0,11	0,13	0,13	0,13	0,18	0,11
Tot S1	17,58	17,60	17,57	17,62	17,58	17,57	17,51	17,61	17,62	17,52	17,54	17,62	17,52	17,62	17,52	17,54	17,62
Fe2+	3,18	3,14	3,21	3,18	3,14	3,14	3,29	3,13	3,10	3,18	3,12	3,04	3,18	3,10	3,18	3,12	3,04
Mn	0,06	0,08	0,05	0,07	0,09	0,07	0,05	0,04	0,03	0,08	0,09	0,08	0,08	0,03	0,08	0,09	0,08
Mg	0,44	0,46	0,45	0,44	0,47	0,49	0,43	0,46	0,47	0,44	0,48	0,43	0,44	0,47	0,44	0,48	0,43
Zn	0,16	0,15	0,12	0,13	0,12	0,13	0,16	0,11	0,12	0,16	0,19	0,15	0,16	0,12	0,16	0,19	0,15
Ca	0,00	0,00	0,01	0,00	0,01	0,00	0,01	0,02	0,00	0,01	0,00	0,00	0,01	0,00	0,01	0,00	0,00
Na	0,01	0,03	0,02	0,02	0,00	0,02	0,00	0,03	0,01	0,02	0,00	0,01	0,02	0,01	0,02	0,00	0,01
K	0,02	0,00	0,00	0,00	0,00	0,00	0,00	0,01	0,00	0,00	0,00	0,01	0,00	0,00	0,00	0,00	0,01
Tot S2	3,88	3,85	3,86	3,83	3,83	3,85	3,94	3,80	3,73	3,89	3,87	3,71	3,89	3,73	3,89	3,87	3,71
Tot Cat	29,46	29,45	29,43	29,45	29,41	29,42	29,45	29,40	29,35	29,41	29,41	29,33	29,41	29,35	29,41	29,41	29,33
ΣO	46	46	46	46	46	46	46	46	46	46	46	46	46	46	46	46	46
XMg	0,11	0,12	0,12	0,11	0,12	0,13	0,11	0,12	0,13	0,11	0,12	0,12	0,11	0,13	0,11	0,12	0,12

Table 15: continued

Sample	LI61b2	LI61b2	LI61b2	LI61b2	LI61b2	LI61b2	LI61b2	LI61b2	LI61b2	LI61b2	LI61b2	LI61b2	LI61b2	LI61b2	LI61b2	LI61b2	LI61b2
Descrip.	Prof. C-C'	Prof. C-C'	Prof. C-C'	Prof. C-C'	Prof. C-C'	Prof. C-C'	Prof. C-C'	Prof. C-C'	Prof. C-C'	Prof. C-C'	Prof. C-C'	Prof. C-C'	Prof. C-C'	Prof. C-C'	Prof. C-C'	Prof. C-C'	Prof. C-C'
SiO ₂	26,55	26,85	25,73	26,16	25,42	26,16	26,85	26,22	26,32	26,32	26,17	27,02	26,34	26,16	26,34	26,16	26,34
TiO ₂	0,88	0,56	0,76	0,77	0,80	0,53	0,52	0,66	0,55	0,55	0,79	0,64	0,56	0,76	0,56	0,69	0,45
Al ₂ O ₃	55,28	55,60	54,49	55,00	54,61	55,02	54,56	54,88	54,60	54,60	55,60	55,15	55,59	55,47	55,59	55,21	55,07
FeO	14,04	13,74	13,37	13,76	13,56	13,52	13,49	12,94	13,63	13,63	13,63	13,76	13,32	13,89	13,32	13,70	13,59
MnO	0,36	0,27	0,34	0,25	0,38	0,41	0,28	0,25	0,22	0,22	0,23	0,24	0,37	0,28	0,37	0,35	0,37
MgO	1,02	1,02	1,15	1,10	1,04	1,07	1,27	1,10	1,07	1,07	1,04	1,08	1,02	1,02	1,02	1,10	1,01
ZnO	0,85	0,73	0,64	0,78	0,67	0,66	0,79	0,78	0,65	0,65	0,72	0,71	0,59	0,75	0,59	0,87	0,78
CaO	0,01	0,01	0,05	0,02	0,04	0,00	0,06	0,02	0,15	0,15	0,00	0,04	0,00	0,00	0,00	0,00	0,02
Na ₂ O	0,06	0,05	0,03	0,04	0,00	0,00	0,06	0,04	0,03	0,03	0,09	0,04	0,06	0,04	0,06	0,05	0,03
K ₂ O	0,00	0,00	0,03	0,00	0,00	0,03	0,00	0,00	0,00	0,00	0,00	0,00	0,00	0,02	0,00	0,00	0,00
Total	99,05	98,83	96,59	97,88	96,52	97,41	97,87	96,89	97,20	97,20	98,28	98,69	97,85	98,40	97,85	98,55	97,67
Si	7,34	7,41	7,28	7,31	7,20	7,33	7,48	7,37	7,39	7,39	7,27	7,47	7,33	7,27	7,33	7,37	7,36
Al IV	0,66	0,59	0,72	0,69	0,80	0,67	0,52	0,64	0,61	0,61	0,73	0,53	0,67	0,73	0,67	0,63	0,64
Tot IV	8	8	8	8	8	8	8	8	8	8	8	8	8	8	8	8	8
AL VI	17,35	17,50	17,43	17,41	17,44	17,50	17,41	17,54	17,46	17,46	17,47	17,43	17,57	17,44	17,57	17,41	17,51
Ti	0,18	0,12	0,16	0,16	0,17	0,11	0,11	0,14	0,12	0,12	0,16	0,13	0,12	0,16	0,12	0,14	0,10
Tot S1	17,53	17,61	17,59	17,57	17,61	17,62	17,51	17,67	17,57	17,57	17,64	17,57	17,68	17,60	17,68	17,56	17,60
Fe ₂ +	3,25	3,17	3,16	3,21	3,21	3,17	3,14	3,04	3,20	3,20	3,17	3,18	3,10	3,23	3,10	3,18	3,18
Mn	0,09	0,06	0,08	0,06	0,09	0,10	0,07	0,06	0,05	0,05	0,05	0,06	0,09	0,07	0,09	0,08	0,09
Mg	0,42	0,42	0,49	0,46	0,44	0,45	0,53	0,46	0,45	0,45	0,43	0,44	0,42	0,42	0,42	0,46	0,42
Zn	0,17	0,15	0,13	0,16	0,14	0,14	0,16	0,16	0,14	0,14	0,15	0,15	0,12	0,16	0,12	0,18	0,16
Ca	0,00	0,00	0,02	0,01	0,01	0,00	0,02	0,01	0,05	0,05	0,00	0,01	0,00	0,00	0,00	0,00	0,01
Na	0,03	0,03	0,01	0,02	0,00	0,00	0,03	0,02	0,02	0,02	0,05	0,02	0,03	0,02	0,03	0,03	0,02
K	0,00	0,00	0,01	0,00	0,00	0,01	0,00	0,00	0,00	0,00	0,00	0,00	0,00	0,01	0,00	0,00	0,00
Tot S2	3,96	3,83	3,90	3,92	3,90	3,86	3,95	3,75	3,90	3,90	3,85	3,86	3,77	3,90	3,77	3,92	3,87
Tot Cat	29,49	29,45	29,50	29,49	29,51	29,48	29,46	29,42	29,47	29,47	29,49	29,43	29,45	29,50	29,45	29,48	29,48
ΣO	46	46	46	46	46	46	46	46	46	46	46	46	46	46	46	46	46
XMg	0,11	0,11	0,13	0,12	0,11	0,12	0,14	0,12	0,12	0,12	0,11	0,12	0,11	0,11	0,11	0,12	0,11

Table 15: continued

Sample	LI61b2	LI61b2	LI61b2	LI61b2	LI61b2	LI61b2	LI61b2	LI61b2	LI61b2	LI61b2	LI61b2	LI61b2	LI61b2	LI61b2	LI61b2	LI61b2	LI61b2
Descrip.	Prof. C-C'	Prof. C-C'	Prof. C-C'	Prof. C-C'	Prof. C-C'	Prof. C-C'	Prof. C-C'	Prof. C-C'	Prof. C-C'	Prof. C-C'	Prof. C-C'	Prof. C-C'	Prof. C-C'	Prof. C-C'	Prof. C-C'	Prof. C-C'	Prof. C-C': C
SiO ₂	26,03	26,06	26,02	26,67	26,44	26,85	26,98	26,84	26,70	26,82	26,59	26,77	26,60	26,10	26,60	26,10	25,79
TiO ₂	0,85	0,48	0,60	0,48	0,56	0,68	0,68	0,60	0,68	0,86	0,58	0,63	0,48	0,60	0,48	0,60	0,50
Al ₂ O ₃	54,80	55,13	54,55	54,63	55,04	54,91	54,57	55,38	55,43	55,48	55,32	55,22	55,64	55,80	55,64	55,80	57,29
FeO	13,41	13,53	13,12	13,69	13,61	13,42	13,58	13,45	13,43	13,35	13,50	13,35	13,73	13,53	13,73	13,53	12,81
MnO	0,14	0,36	0,36	0,25	0,42	0,27	0,20	0,25	0,29	0,25	0,38	0,25	0,41	0,21	0,41	0,21	0,38
MgO	1,06	1,08	1,16	1,01	1,03	1,20	1,15	1,08	1,06	1,12	1,08	1,00	1,07	1,05	1,07	1,05	1,02
ZnO	0,68	0,69	0,63	0,67	0,55	0,79	0,81	0,67	0,75	0,73	0,69	0,79	0,73	0,71	0,73	0,71	0,74
CaO	0,01	0,00	0,07	0,03	0,05	0,01	0,04	0,00	0,03	0,00	0,00	0,00	0,01	0,04	0,01	0,04	0,01
Na ₂ O	0,07	0,11	0,06	0,06	0,02	0,06	0,03	0,01	0,07	0,01	0,00	0,00	0,02	0,02	0,02	0,02	0,03
K ₂ O	0,01	0,00	0,02	0,04	0,01	0,03	0,00	0,00	0,00	0,03	0,00	0,02	0,03	0,02	0,03	0,02	0,02
Total	97,05	97,44	96,59	97,53	97,73	98,21	98,03	98,27	98,45	98,65	98,13	98,04	98,73	98,08	98,73	98,08	98,59
Si	7,31	7,30	7,34	7,46	7,38	7,45	7,51	7,43	7,39	7,40	7,39	7,44	7,36	7,26	7,36	7,26	7,11
Al IV	0,69	0,70	0,66	0,54	0,62	0,55	0,49	0,57	0,61	0,60	0,61	0,56	0,64	0,74	0,64	0,74	0,89
Tot IV	8	8	8	8	8	8	8	8	8	8	8	8	8	8	8	8	8
AL VI	17,46	17,51	17,49	17,48	17,49	17,42	17,40	17,52	17,48	17,45	17,50	17,52	17,50	17,55	17,50	17,55	17,74
Ti	0,18	0,10	0,13	0,10	0,12	0,14	0,14	0,12	0,14	0,18	0,12	0,13	0,10	0,13	0,10	0,13	0,10
Tot S1	17,64	17,61	17,62	17,58	17,61	17,56	17,54	17,64	17,62	17,63	17,62	17,65	17,60	17,67	17,60	17,67	17,84
Fe2+	3,15	3,17	3,10	3,20	3,18	3,12	3,16	3,12	3,11	3,08	3,14	3,10	3,18	3,15	3,18	3,15	2,96
Mn	0,03	0,09	0,09	0,06	0,10	0,06	0,05	0,06	0,07	0,06	0,09	0,06	0,10	0,05	0,10	0,05	0,09
Mg	0,44	0,45	0,49	0,42	0,43	0,50	0,48	0,45	0,44	0,46	0,45	0,42	0,44	0,44	0,44	0,44	0,42
Zn	0,14	0,14	0,13	0,14	0,11	0,16	0,17	0,14	0,15	0,15	0,14	0,16	0,15	0,15	0,15	0,15	0,15
Ca	0,00	0,00	0,02	0,01	0,02	0,00	0,01	0,00	0,01	0,00	0,00	0,00	0,00	0,01	0,00	0,01	0,00
Na	0,04	0,06	0,03	0,03	0,01	0,03	0,01	0,00	0,04	0,00	0,00	0,00	0,01	0,01	0,01	0,01	0,01
K	0,00	0,00	0,01	0,01	0,01	0,01	0,00	0,00	0,00	0,01	0,00	0,01	0,01	0,01	0,01	0,01	0,01
Tot S2	3,81	3,91	3,86	3,88	3,85	3,88	3,87	3,76	3,82	3,77	3,81	3,75	3,89	3,81	3,89	3,81	3,64
Tot Cat	29,45	29,52	29,48	29,45	29,45	29,44	29,41	29,40	29,44	29,40	29,44	29,40	29,48	29,48	29,48	29,48	29,48
ΣO	46	46	46	46	46	46	46	46	46	46	46	46	46	46	46	46	46
XMg	0,12	0,12	0,13	0,11	0,11	0,13	0,12	0,12	0,12	0,12	0,12	0,11	0,11	0,12	0,11	0,12	0,12

Table 15: continued

Sample	LL 61a2	LL 61a2	LL 61a2	LL 61a2	LL 61a2	LL 61a2	LL 61a2	LL 61a2	LL 61a2	LL 61a2	LL 61a2	LL 61b2	LL 61b2	LL 61b2	LL 61b2	LL 61b2	LL 61b2	LL 61b2	LL 61b2	LL 61b2	LL 61b2	LL 61b2	LL 61b2	LL 61b2	LL 61b2
Descrip.	Relict	Relict	Relict	Relict	Relict	Relict	Relict	Relict	Relict	Relict	Relict	Relict	Relict	Relict	Relict	Relict	Relict	Relict	Relict	Relict	Relict	Relict	Relict	Relict	Relict
SiO ₂	27,38	27,65	27,07	26,69	27,49	27,44	27,40	26,25	26,86	27,06	26,86	26,95	27,21	27,23	27,37	27,17	27,18	26,99							
TiO ₂	0,48	0,54	0,61	0,52	0,57	0,50	0,57	0,36	0,49	0,59	0,52	0,38	0,48	0,41	0,49	0,50	0,53	0,50							
Al ₂ O ₃	54,09	54,86	55,18	55,87	55,27	55,69	55,61	55,99	53,92	53,72	53,22	54,08	54,59	53,82	54,42	54,92	54,66	54,23							
FeO	13,02	12,76	12,95	12,98	13,07	13,38	13,26	13,13	13,25	13,97	13,59	13,49	13,89	13,46	13,67	13,22	12,72	13,08							
MnO	0,30	0,39	0,37	0,20	0,32	0,34	0,33	0,33	0,29	0,29	0,28	0,22	0,35	0,30	0,36	0,23	0,27	0,28							
MgO	0,70	0,69	0,62	0,61	0,65	0,63	0,68	0,78	1,04	1,08	1,08	1,09	1,10	1,05	0,74	0,66	0,82	0,93							
ZnO	0,21	1,71	0,68	1,07	0,75	0,86	1,82	0,81	0,57	0,68	0,46	0,11	0,00	0,43	0,75	0,86	0,64	0,75							
CaO	0,00	0,01	0,03	0,00	0,02	0,00	0,00	0,00	0,00	0,00	0,00	0,01	0,01	0,01	0,00	0,00	0,01	0,02							
Na ₂ O	0,03	0,03	0,01	0,05	0,08	0,05	0,01	0,03	0,03	0,01	0,05	0,07	0,05	0,04	0,00	0,02	0,05	0,00							
K ₂ O	0,00	0,00	0,00	0,01	0,00	0,00	0,01	0,00	0,00	0,00	0,02	0,00	0,00	0,00	0,00	0,03	0,00	0,01							
Total	96,21	98,64	97,53	98,00	98,22	98,89	99,70	97,68	96,45	97,39	96,07	96,40	97,68	96,74	97,80	97,61	96,91	96,78							
Si	7,70	7,64	7,54	7,41	7,60	7,55	7,51	7,31	7,57	7,59	7,62	7,59	7,57	7,65	7,63	7,57	7,60	7,58							
Al IV	0,30	0,36	0,46	0,59	0,40	0,45	0,49	0,69	0,43	0,41	0,38	0,41	0,43	0,35	0,37	0,43	0,40	0,42							
Tot IV	8	8	8	8	8	8	8	8	8	8	8	8	8	8	8	8	8	8	8						
Al VI	17,64	17,51	17,64	17,69	17,61	17,61	17,49	17,70	17,50	17,35	17,41	17,54	17,48	17,48	17,50	17,61	17,63	17,54							
Ti	0,10	0,11	0,13	0,11	0,12	0,10	0,12	0,08	0,10	0,13	0,11	0,08	0,10	0,09	0,10	0,11	0,11	0,11							
Tot S1	17,74	17,63	17,77	17,80	17,73	17,71	17,61	17,78	17,60	17,47	17,52	17,62	17,58	17,57	17,60	17,71	17,74	17,64							
Fe ₂ +	3,06	2,95	3,02	3,01	3,02	3,08	3,04	3,06	3,13	3,28	3,22	3,18	3,23	3,16	3,19	3,08	2,98	3,07							
Mn	0,07	0,09	0,09	0,05	0,07	0,08	0,08	0,08	0,07	0,07	0,07	0,05	0,08	0,07	0,08	0,05	0,06	0,07							
Mg	0,30	0,28	0,26	0,25	0,27	0,26	0,28	0,32	0,44	0,45	0,45	0,46	0,46	0,44	0,31	0,28	0,34	0,39							
Zn	0,04	0,35	0,14	0,22	0,15	0,17	0,37	0,17	0,12	0,14	0,10	0,02	0,00	0,09	0,15	0,18	0,13	0,16							
Ca	0,00	0,00	0,01	0,00	0,01	0,00	0,00	0,00	0,00	0,00	0,00	0,00	0,00	0,00	0,00	0,00	0,00	0,01							
Na	0,02	0,02	0,01	0,03	0,04	0,03	0,01	0,01	0,02	0,00	0,03	0,04	0,03	0,02	0,00	0,01	0,03	0,00							
K	0,00	0,00	0,00	0,01	0,00	0,00	0,01	0,00	0,00	0,00	0,01	0,00	0,00	0,00	0,00	0,01	0,00	0,00							
Tot S2	3,49	3,69	3,52	3,57	3,57	3,62	3,78	3,64	3,77	3,94	3,88	3,75	3,81	3,79	3,73	3,61	3,55	3,69							
Tot Cat	29,24	29,32	29,29	29,36	29,30	29,33	29,39	29,42	29,37	29,41	29,39	29,37	29,39	29,36	29,33	29,32	29,29	29,34							
ΣO	46	46	46	46	46	46	46	46	46	46	46	46	46	46	46	46	46	46							
ΣMg	0,08	0,08	0,07	0,07	0,08	0,07	0,07	0,09	0,12	0,11	0,12	0,12	0,12	0,12	0,08	0,08	0,10	0,11							

Table 15: continued

Sample	LL 61b2	LL 61b2	LL 61b2	LL 61b2	LL 61b2	LL 61b2	LL 61b2	LL 61b2	LL 61b2	LL 61c2	LL 61c2
Descrip.	Relict	Relict	Relict	Relict	Relict	Relict	Relict	Relict	Relict	Relict	Relict
SiO ₂	26,91	26,96	27,09	27,05	27,31	26,33	27,31	27,06	27,27		
TiO ₂	0,61	0,58	0,68	0,35	0,47	0,35	0,39	0,64	0,53		
Al ₂ O ₃	54,57	53,83	53,79	54,23	54,61	54,11	52,53	55,14	55,42		
FeO	12,67	12,69	12,66	13,16	13,66	13,38	13,47	11,75	12,38		
MnO	0,31	0,29	0,31	0,28	0,25	0,30	0,18	0,29	0,24		
MgO	0,96	0,83	0,93	1,11	1,10	1,00	1,10	1,09	1,08		
ZnO	1,07	0,46	1,18	0,11	0,12	0,46	0,92	3,75	3,61		
CaO	0,00	0,00	0,02	0,00	0,06	0,00	0,04	0,00	0,02		
Na ₂ O	0,03	0,05	0,06	0,01	0,02	0,02	0,04	0,08	0,08		
K ₂ O	0,00	0,00	0,00	0,01	0,00	0,01	0,00	0,00	0,04		
Total	97,11	95,70	96,72	96,32	97,60	95,94	95,99	99,80	100,67		
Si	7,53	7,64	7,62	7,61	7,60	7,47	7,76	7,45	7,46		
Al IV	0,47	0,37	0,38	0,39	0,40	0,53	0,24	0,55	0,55		
Tot IV	8	8	8	8	8	8	8	8	8		
AL VI	17,54	17,60	17,46	17,59	17,51	17,56	17,35	17,34	17,31		
Ti	0,13	0,12	0,15	0,07	0,10	0,07	0,08	0,13	0,11		
Tot S1	17,67	17,72	17,60	17,67	17,61	17,64	17,44	17,47	17,42		
Fe ₂ +	2,97	3,01	2,98	3,10	3,18	3,17	3,20	2,71	2,83		
Mn	0,07	0,07	0,07	0,07	0,06	0,07	0,04	0,07	0,05		
Mg	0,40	0,35	0,39	0,46	0,46	0,42	0,47	0,45	0,44		
Zn	0,22	0,10	0,25	0,02	0,02	0,10	0,19	0,76	0,73		
Ca	0,00	0,00	0,01	0,00	0,02	0,00	0,01	0,00	0,01		
Na	0,02	0,03	0,03	0,01	0,01	0,01	0,02	0,04	0,04		
K	0,00	0,00	0,00	0,01	0,00	0,00	0,00	0,00	0,01		
Tot S2	3,68	3,55	3,73	3,66	3,75	3,78	3,94	4,03	4,11		
Tot Cat	29,34	29,27	29,33	29,33	29,36	29,42	29,37	29,50	29,53		
ΣO	46	46	46	46	46	46	46	46	46		
XMg	0,11	0,10	0,11	0,13	0,12	0,11	0,12	0,11	0,11		

Table 15: continued

Sample	LL 61c2	LL 61c2	LL 61c2	LL 61c2	LL 61c2	LL 61c2	LL 61c1	LL 61c1	LL 61c1	LL 61c1	LL 61c1	LL 61a2	LL 61a2	LL 61b1
Descrip.	PI *	PI *	PI *	PI *	PI *	PI *	PI *	PI *	PI *	PI *	PI *	PI *	PI *	PI *
SiO ₂	62,59	59,79	61,18	63,19	62,37	63,04	63,17	61,32	62,69	63,05	62,19	62,33	62,63	61,31
TiO ₂	0,00	0,00	0,00	0,03	0,08	0,00	0,17	0,03	0,04	0,02	0,07	0,87	0,04	0,06
Al ₂ O ₃	23,67	25,28	25,44	23,38	24,81	23,81	23,06	23,94	23,09	23,26	23,27	22,37	23,07	23,63
Fe ₂ O ₃	0,46	0,34	0,39	1,06	0,51	0,61	0,80	0,25	0,69	0,53	1,01	1,70	0,56	0,80
MnO	0,11	0,00	0,07	0,14	0,00	0,06	0,09	0,01	0,06	0,03	0,13	0,15	0,10	0,00
MgO	0,01	0,00	0,00	0,03	0,00	0,00	0,00	0,00	0,00	0,00	0,01	0,03	0,00	0,01
CaO	3,94	5,97	6,07	3,63	5,43	4,10	4,28	5,91	4,76	4,79	5,02	2,51	4,65	4,82
Na ₂ O	10,18	8,53	8,56	9,98	9,19	10,04	9,58	8,62	9,34	9,66	9,31	9,56	9,50	9,02
K ₂ O	0,05	0,12	0,08	0,05	0,04	0,11	0,04	0,03	0,08	0,04	0,03	0,92	0,04	0,09
Total	101,01	100,03	101,79	101,49	102,42	101,77	101,18	100,12	100,75	101,39	101,03	100,44	100,58	99,75
Si	2,76	2,67	2,68	2,77	2,71	2,75	2,77	2,73	2,77	2,77	2,74	2,77	2,77	2,73
Al	1,23	1,33	1,31	1,21	1,27	1,23	1,19	1,25	1,20	1,20	1,21	1,17	1,20	1,24
Ti	0,00	0,00	0,00	0,00	0,00	0,00	0,01	0,00	0,00	0,00	0,00	0,03	0,00	0,00
Fe ³⁺	0,02	0,01	0,01	0,04	0,02	0,02	0,03	0,01	0,02	0,02	0,03	0,06	0,02	0,03
Mn	0,00	0,00	0,00	0,01	0,00	0,00	0,00	0,00	0,00	0,00	0,01	0,01	0,00	0,00
Mg	0,00	0,00	0,00	0,00	0,00	0,00	0,00	0,00	0,00	0,00	0,00	0,00	0,00	0,00
Ca	0,19	0,29	0,29	0,17	0,25	0,19	0,20	0,28	0,23	0,23	0,24	0,12	0,22	0,23
Na	0,87	0,74	0,73	0,85	0,77	0,85	0,82	0,74	0,80	0,82	0,80	0,82	0,81	0,78
K	0,00	0,01	0,00	0,00	0,00	0,01	0,00	0,00	0,01	0,00	0,00	0,05	0,00	0,01
Tot Cat	5,06	5,04	5,02	5,04	5,03	5,05	5,02	5,02	5,02	5,04	5,03	5,03	5,03	5,02
ΣO	8	8	8	8	8	8	8	8	8	8	8	8	8	8
Or	0,26	0,67	0,42	0,26	0,21	0,59	0,21	0,18	0,45	0,23	0,15	5,21	0,20	0,52
Ab	82,17	71,63	71,56	83,05	75,23	81,10	80,05	72,40	77,66	78,31	76,92	82,79	78,57	76,80
An	17,58	27,70	28,02	16,68	24,57	18,32	19,75	27,42	21,89	21,45	22,93	12,00	21,23	22,68

Table 16: microprobe analyses of 16 plagioclase included in garnet (PI*) and 16 syntectonic crystals of plagioclase (PI synt.). Analyses are shown in Fig. 3.13.

Sample	LL 61c1	LL 61c1	LL 61c1	LL 61c1	LL 61c1	LL 61c1	LL 61c1	LL 61c1	LL 61a2	LL 61a2	LL 61c2	LL 61c2	LL 61c2	LL 61c2	LL 61c2	LL 61c2	LL 61c2	LL 61c2
Descrip.	PI synt.	PI synt.	PI synt.	PI synt.	PI synt.	PI synt.	PI synt.	PI synt.	PI synt.	PI synt.	PI synt.	PI synt.	PI synt.	PI synt.	PI synt.	PI synt.	PI synt.	PI synt.
SiO2	63,66	63,56	63,12	62,93	62,10	62,78	62,72	64,32	63,62	63,50	63,01	64,38	63,75	63,83	64,12	62,61	62,61	62,61
TiO2	0,06	0,02	0,00	0,00	0,00	0,00	0,00	0,00	0,00	0,00	0,00	0,16	0,02	0,09	0,06	0,05	0,05	0,05
Al2O3	22,55	22,58	22,84	22,77	23,10	22,89	22,44	22,88	23,35	23,24	22,66	23,23	23,53	22,63	23,50	23,07	23,07	23,07
Fe2O3	0,11	0,02	0,18	0,07	0,00	0,19	0,19	0,07	0,04	0,03	0,00	0,09	0,09	0,13	0,05	0,10	0,10	0,10
MnO	0,00	0,02	0,00	0,00	0,07	0,00	0,02	0,02	0,00	0,08	0,10	0,00	0,01	0,00	0,00	0,01	0,01	0,01
MgO	0,00	0,00	0,00	0,00	0,01	0,01	0,00	0,00	0,00	0,00	0,00	0,01	0,00	0,01	0,02	0,00	0,00	0,00
CaO	4,28	4,29	4,34	4,20	4,70	4,24	4,26	3,67	4,31	4,24	3,78	3,77	3,82	3,67	3,85	4,17	4,17	4,17
Na2O	9,71	9,38	9,71	9,82	9,24	9,77	9,57	10,16	10,00	9,59	9,95	10,32	10,13	9,97	9,76	9,63	9,63	9,63
K2O	0,03	0,02	0,07	0,06	0,05	0,08	0,05	0,06	0,04	0,06	0,06	0,05	0,04	0,03	0,12	0,05	0,05	0,05
Total	100,39	99,90	100,25	99,85	99,27	99,95	99,25	101,18	101,36	100,73	99,56	102,01	101,38	100,36	101,47	99,70	99,70	99,70
Si	2,81	2,81	2,79	2,79	2,77	2,79	2,80	2,81	2,78	2,79	2,80	2,80	2,78	2,81	2,79	2,78	2,78	2,78
Al	1,17	1,18	1,19	1,19	1,22	1,20	1,18	1,18	1,20	1,20	1,19	1,19	1,21	1,18	1,21	1,21	1,21	1,21
Ti	0,00	0,00	0,00	0,00	0,00	0,00	0,00	0,00	0,00	0,00	0,00	0,01	0,00	0,00	0,00	0,00	0,00	0,00
Fe3+	0,00	0,00	0,01	0,00	0,00	0,01	0,01	0,00	0,00	0,00	0,00	0,00	0,00	0,00	0,00	0,00	0,00	0,00
Mn	0,00	0,00	0,00	0,00	0,00	0,00	0,00	0,00	0,00	0,00	0,00	0,00	0,00	0,00	0,00	0,00	0,00	0,00
Mg	0,00	0,00	0,00	0,00	0,00	0,00	0,00	0,00	0,00	0,00	0,00	0,00	0,00	0,00	0,00	0,00	0,00	0,00
Ca	0,20	0,20	0,21	0,20	0,23	0,20	0,20	0,17	0,20	0,20	0,18	0,18	0,18	0,17	0,18	0,20	0,20	0,20
Na	0,83	0,81	0,83	0,85	0,80	0,84	0,83	0,86	0,85	0,82	0,86	0,87	0,86	0,85	0,83	0,83	0,83	0,83
K	0,00	0,00	0,00	0,00	0,00	0,01	0,00	0,00	0,00	0,00	0,00	0,00	0,00	0,00	0,01	0,00	0,00	0,00
Tot Cat	5,02	5,00	5,03	5,04	5,02	5,04	5,02	5,03	5,04	5,02	5,04	5,04	5,04	5,02	5,02	5,03	5,03	5,03
ΣO	8	8	8	8	8	8	8	8	8	8	8	8	8	8	8	8	8	8
Or	0,14	0,12	0,36	0,34	0,27	0,43	0,27	0,30	0,22	0,34	0,32	0,28	0,21	0,16	0,64	0,27	0,27	0,27
Ab	80,31	79,73	79,90	80,61	77,84	80,31	80,03	83,12	80,58	80,10	82,40	82,99	82,58	82,96	81,58	80,48	80,48	80,48
An	19,55	20,15	19,74	19,05	21,89	19,26	19,69	16,58	19,21	19,56	17,29	16,73	17,21	16,88	17,79	19,26	19,26	19,26

Table 16: continued

Sample Descrip	LL 61b1		LL 61b1		LL 61b1		LL 61b1		LL 61b1		LL 61b1		LL 61b1		LL 61b1		LL 61b1		LL 61b1		
	Ms I	Ms I	Ms I	Ms I	Ms I	Ms I	Ms I	Ms I	Ms I	Ms I	Ms I	Ms I	Ms I	Ms I	Ms I	Ms I	Ms I	Ms I	Ms I	Ms I	
SiO2 TiO2 Al2O3 Cr2O3 Fe2O3 FeO MnO MgO CaO BaO Na2O K2O F (Cl) F-12O Cl-12O H2O Total	46,16	45,49	47,09	46,84	45,92	45,43	45,44	46,04	45,80	46,65	45,98	46,35	45,64	46,12	45,17	46,88	46,18	46,88	46,18	46,18	
	0,17	0,15	0,21	0,26	0,20	0,27	0,02	0,51	0,32	0,37	0,16	0,00	0,15	0,41	0,40	0,33	0,34	0,33	0,34	0,34	
	33,92	35,01	33,72	34,40	35,58	35,44	35,64	35,52	35,66	35,01	35,95	36,03	35,45	34,94	35,07	34,75	34,68	34,75	34,68	34,68	
	0,00	0,00	0,00	0,00	0,00	0,00	0,00	0,00	0,00	0,00	0,00	0,00	0,00	0,00	0,00	0,00	0,00	0,00	0,00		
	0,00	0,00	0,00	0,00	0,00	0,00	0,00	0,00	0,00	0,00	0,00	0,00	0,00	0,00	0,00	0,00	0,00	0,00	0,00		
	1,07	0,98	1,09	1,00	1,37	0,82	0,79	0,86	1,01	0,98	0,82	0,63	0,90	0,84	0,80	0,93	0,96	0,93	0,96	0,96	
	0,00	0,01	0,00	0,01	0,00	0,00	0,02	0,00	0,04	0,03	0,02	0,03	0,00	0,00	0,00	0,00	0,00	0,00	0,00		
	0,74	0,49	0,79	0,54	0,39	0,46	0,30	0,38	0,34	0,51	0,35	0,22	0,35	0,40	0,36	0,59	0,57	0,59	0,57	0,57	
	0,02	0,01	0,00	0,03	0,01	0,01	0,12	0,04	0,01	0,00	0,00	0,00	0,00	0,00	0,02	0,00	0,00	0,00	0,00	0,00	
	0,00	0,00	0,00	0,00	0,00	0,00	0,00	0,00	0,00	0,00	0,00	0,00	0,00	0,00	0,00	0,00	0,00	0,00	0,00	0,00	
FeO MnO MgO CaO BaO Na2O K2O F (Cl) F-12O Cl-12O H2O Total	0,88	1,05	0,97	1,07	1,04	0,92	1,34	1,16	1,21	1,12	1,23	1,58	1,28	1,15	1,10	0,98	1,05	0,98	1,05	0,98	
	9,61	9,56	9,85	9,86	9,84	10,00	9,45	9,86	9,94	9,88	9,91	9,28	9,69	9,92	9,67	9,85	9,80	9,85	9,80	9,80	
	0,06	0,06	0,18	0,09	0,09	0,04	0,01	0,13	0,16	0,04	0,17	0,04	0,19	0,06	0,13	0,06	0,15	0,06	0,15	0,15	
	0,00	0,00	0,01	0,01	0,00	0,00	0,01	0,00	0,00	0,00	0,03	0,00	0,00	0,00	0,01	0,00	0,01	0,00	0,01	0,01	
	0,03	0,03	0,11	0,05	0,05	0,03	0,01	0,07	0,09	0,03	0,10	0,03	0,11	0,04	0,08	0,03	0,09	0,03	0,09	0,09	
	0,00	0,00	0,00	0,01	0,00	0,00	0,01	0,00	0,00	0,00	0,02	0,00	0,00	0,00	0,01	0,00	0,01	0,00	0,01	0,01	
	4,38	4,38	4,37	4,42	4,43	4,41	4,42	4,42	4,40	4,47	4,40	4,47	4,35	4,43	4,33	4,46	4,37	4,46	4,37	4,37	
	96,96	97,18	98,20	98,49	98,82	97,80	97,56	98,87	98,81	99,04	98,93	98,64	97,92	98,26	97,01	98,81	98,05	98,81	98,05	98,05	
	Si Al IV Tot IV AL VI Ti Cr Fe2+ Mn Mg Tot S1 Ca Ba Na K Tot S2 Tot Cat	6,29	6,19	6,34	6,29	6,16	6,15	6,15	6,16	6,14	6,23	6,15	6,19	6,16	6,21	6,16	6,27	6,23	6,27	6,23	6,23
		1,71	1,82	1,66	1,71	1,84	1,85	1,85	1,84	1,86	1,77	1,85	1,81	1,84	1,79	1,84	1,73	1,77	1,73	1,77	1,77
8,00		8,00	8,00	8,00	8,00	8,00	8,00	8,00	8,00	8,00	8,00	8,00	8,00	8,00	8,00	8,00	8,00	8,00	8,00	8,00	
3,73		3,80	3,69	3,73	3,78	3,80	3,84	3,76	3,78	3,74	3,82	3,86	3,81	3,75	3,79	3,74	3,74	3,74	3,74	3,74	
0,02		0,02	0,02	0,03	0,02	0,03	0,00	0,05	0,03	0,04	0,02	0,00	0,02	0,04	0,04	0,03	0,04	0,03	0,04	0,04	
0,00		0,00	0,00	0,00	0,00	0,00	0,00	0,00	0,00	0,00	0,00	0,00	0,00	0,00	0,00	0,00	0,00	0,00	0,00	0,00	
0,12		0,11	0,12	0,11	0,15	0,09	0,09	0,10	0,11	0,11	0,09	0,07	0,10	0,10	0,09	0,10	0,11	0,10	0,11	0,11	
0,00		0,00	0,00	0,00	0,00	0,00	0,00	0,00	0,00	0,00	0,00	0,00	0,00	0,00	0,00	0,00	0,00	0,00	0,00	0,00	
0,15		0,10	0,16	0,11	0,08	0,09	0,06	0,08	0,07	0,10	0,07	0,05	0,07	0,08	0,07	0,12	0,11	0,12	0,11	0,11	
4,02		4,02	3,99	3,98	4,03	4,01	3,99	3,99	4,00	3,99	4,00	3,98	4,00	3,97	4,00	4,00	4,00	4,00	4,00	4,00	
F Cl OH EO	0,00	0,00	0,00	0,00	0,00	0,00	0,02	0,01	0,00	0,00	0,00	0,00	0,00	0,00	0,00	0,00	0,00	0,00	0,00	0,00	
	0,00	0,00	0,00	0,00	0,00	0,00	0,00	0,00	0,00	0,00	0,00	0,00	0,00	0,00	0,00	0,00	0,00	0,00	0,00	0,00	
	0,23	0,28	0,25	0,28	0,27	0,24	0,35	0,30	0,31	0,29	0,32	0,41	0,34	0,30	0,29	0,25	0,27	0,25	0,27	0,27	
	1,67	1,66	1,69	1,69	1,68	1,73	1,63	1,68	1,70	1,68	1,69	1,58	1,67	1,70	1,68	1,68	1,69	1,68	1,69	1,69	
	1,90	1,94	1,95	1,97	1,96	1,97	2,00	1,99	2,02	1,97	2,01	1,99	2,01	2,01	1,98	1,93	1,96	1,93	1,96	1,96	
	13,92	13,96	13,94	13,95	13,99	13,98	14,00	13,98	14,01	13,96	14,01	13,97	14,00	13,98	13,97	13,93	13,96	13,93	13,96	13,96	
	0,02	0,02	0,08	0,04	0,04	0,02	0,01	0,05	0,07	0,02	0,07	0,02	0,08	0,03	0,06	0,03	0,06	0,03	0,06	0,06	
	0,00	0,00	0,00	0,00	0,00	0,00	0,00	0,00	0,00	0,00	0,01	0,00	0,00	0,00	0,00	0,00	0,00	0,00	0,00	0,00	
	3,98	3,98	3,92	3,96	3,96	3,98	3,99	3,95	3,93	3,98	3,92	3,98	3,92	3,98	3,94	3,98	3,94	3,98	3,94	3,94	
	22	22	22	22	22	22	22	22	22	22	22	22	22	22	22	22	22	22	22	22	

Table 17: chemical analyses of white mica of the paragneisses. Analyses are shown in Fig. 3.14.

Sample Descrip	LL 61c1 Ms I	LL 61c1 Ms I	LL 61c1 Ms I	LL 61c1 Ms I	LL 61c1 Ms I	LL 61b2 Ms I	LL 61b2 Ms I	LL 61b2 Ms I	LL 61b2 Ms I	LL 61b2 Ms I	LL 61b2 Ms I	LL 61b2 Ms I	LL 61b2 Ms I	LL 61b2 Ms I
SiO2	45.09	45.79	45.71	45.34	45.19	45.26	45.04	46.22	47.29	47.25	45.58	46.63	45.60	46.90
TiO2	0.43	0.68	0.38	0.52	0.68	0.60	0.37	0.41	0.39	0.30	0.29	0.54	0.27	0.21
Al2O3	35.87	35.41	35.88	36.05	35.74	35.77	35.34	35.57	34.27	34.68	36.37	35.40	36.66	35.16
Cr2O3	0.00	0.00	0.00	0.00	0.00	0.00	0.00	0.00	0.00	0.00	0.00	0.00	0.00	0.00
Fe2O3	0.00	0.00	0.00	0.00	0.00	0.00	0.00	0.00	0.00	0.00	0.00	0.00	0.00	0.00
FeO	1.23	1.28	1.11	1.31	1.16	1.32	1.27	0.75	1.18	1.13	0.87	0.80	0.80	1.02
MnO	0.00	0.11	0.11	0.03	0.05	0.04	0.09	0.00	0.00	0.00	0.00	0.00	0.01	0.04
MgO	0.32	0.39	0.31	0.30	0.35	0.34	0.38	0.43	0.86	0.68	0.38	0.47	0.33	0.61
CaO	0.00	0.02	0.00	0.03	0.02	0.00	0.00	0.00	0.00	0.00	0.01	0.00	0.00	0.00
BaO	0.00	0.00	0.00	0.00	0.00	0.00	0.00	0.00	0.00	0.00	0.00	0.00	0.00	0.00
Na2O	1.31	1.12	1.15	1.27	1.20	1.22	1.25	1.17	1.04	1.00	1.10	1.16	1.30	1.04
K2O	9.73	9.24	9.72	9.71	9.57	9.70	9.57	8.13	7.73	7.95	7.96	7.71	7.93	8.01
(F)	0.00	0.02	0.03	0.10	0.11	0.09	0.13	0.00	0.12	0.00	0.12	0.10	0.19	0.05
(Cl)	0.00	0.01	0.00	0.01	0.01	0.01	0.00	0.00	0.01	0.00	0.01	0.03	0.01	0.00
F-12O	0.00	0.01	0.02	0.06	0.07	0.05	0.08	0.00	0.07	0.00	0.07	0.06	0.11	0.03
Cl-12O	0.00	0.01	0.00	0.01	0.01	0.01	0.00	0.00	0.01	0.00	0.01	0.02	0.01	0.00
H2O	4.45	4.46	4.46	4.42	4.40	4.42	4.36	4.46	4.41	4.48	4.39	4.42	4.37	4.45
Total	98.42	98.52	98.86	99.05	98.46	98.72	97.74	97.15	97.24	97.46	97.01	97.20	97.38	97.47
Si	6.08	6.14	6.12	6.08	6.08	6.08	6.11	6.22	6.35	6.33	6.14	6.25	6.12	6.28
Al IV	1.92	1.86	1.88	1.93	1.92	1.92	1.89	1.78	1.65	1.67	1.86	1.75	1.88	1.72
Tot IV	8.00	8.00	8.00	8.00	8.00	8.00	8.00	8.00	8.00	8.00	8.00	8.00	8.00	8.00
AL VI	3.78	3.75	3.79	3.77	3.75	3.75	3.76	3.86	3.77	3.80	3.91	3.85	3.92	3.84
Ti	0.04	0.07	0.04	0.05	0.07	0.06	0.04	0.04	0.04	0.03	0.03	0.05	0.03	0.02
Cr	0.00	0.00	0.00	0.00	0.00	0.00	0.00	0.00	0.00	0.00	0.00	0.00	0.00	0.00
Fe2+	0.14	0.14	0.13	0.15	0.13	0.15	0.14	0.08	0.13	0.13	0.10	0.09	0.09	0.12
Mn	0.00	0.01	0.01	0.00	0.01	0.00	0.01	0.00	0.00	0.00	0.00	0.00	0.00	0.00
Mg	0.06	0.08	0.06	0.06	0.07	0.07	0.08	0.09	0.17	0.14	0.08	0.09	0.07	0.12
Tot S1	4.02	4.05	4.03	4.03	4.03	4.03	4.03	4.07	4.11	4.10	4.12	4.09	4.11	4.10
Ca	0.00	0.00	0.00	0.00	0.00	0.00	0.00	0.00	0.00	0.00	0.00	0.00	0.00	0.00
Ba	0.00	0.00	0.00	0.00	0.00	0.00	0.00	0.00	0.00	0.00	0.00	0.00	0.00	0.00
Na	0.34	0.29	0.30	0.33	0.31	0.32	0.33	0.31	0.27	0.26	0.29	0.30	0.34	0.27
K	1.67	1.58	1.66	1.66	1.64	1.66	1.66	1.40	1.32	1.36	1.37	1.32	1.36	1.37
Tot S2	2.02	1.88	1.96	1.99	1.96	1.98	1.99	1.70	1.60	1.62	1.66	1.62	1.70	1.64
Tot Cat	14.04	13.92	13.99	14.02	13.99	14.01	14.02	13.77	13.70	13.71	13.77	13.71	13.80	13.74
F	0.00	0.01	0.01	0.04	0.05	0.04	0.06	0.00	0.05	0.00	0.05	0.04	0.08	0.02
Cl	0.00	0.00	0.00	0.00	0.00	0.00	0.00	0.00	0.00	0.00	0.00	0.01	0.00	0.00
OH	4.00	3.99	3.99	3.95	3.95	3.96	3.94	4.00	3.95	4.00	3.95	3.95	3.92	3.98
ΣO	22	22	22	22	22	22	22	22	22	22	22	22	22	22

Table 17: continued.

Sample Descrip	LL 61b2 Ms I	LL 61b2 Ms I	LL 61b2 Ms I	LL 61b2 Ms I	LL 61c2 Ms I	LL 61c2 Ms I	LL 61c2 Ms I	LL 61c2 Ms I	LL 61b1 Ms I	LL 61b1 Ms I	LL 61b1 Ms I	LL 61b1 Ms I	LL 61b1 Ms I	LL 61b1 Ms I	LL 61b1 Ms I	LL 61b1 Ms I	LL 61b1 Ms I	LL 61b1 Ms I
SiO2	46.33	46.25	44.98	46.31	46.80	46.54	44.78	44.85	45.79	46.68	45.48	45.68	45.57	47.24	46.08	46.70	46.92	46.27
TiO2	0.48	0.48	0.58	0.32	0.48	0.34	0.60	0.65	0.34	0.53	0.11	0.04	0.04	0.39	0.21	0.28	0.34	0.28
Al2O3	34.74	34.32	35.62	35.15	37.12	36.95	37.09	36.89	35.56	35.34	35.32	37.42	36.57	34.47	34.72	34.45	35.39	35.81
Cr2O3	0.00	0.00	0.00	0.00	0.00	0.00	0.00	0.00	0.00	0.00	0.00	0.00	0.00	0.00	0.00	0.00	0.00	0.00
Fe2O3	0.00	0.00	0.00	0.00	0.00	0.00	0.00	0.00	0.00	0.00	0.00	0.00	0.00	0.00	0.00	0.00	0.00	0.00
FeO	1.01	0.97	0.90	0.97	1.25	0.96	1.16	1.43	0.83	1.08	0.89	0.82	0.78	1.19	1.06	1.22	1.02	0.87
MnO	0.01	0.00	0.00	0.00	0.02	0.09	0.04	0.05	0.00	0.03	0.04	0.07	0.01	0.00	0.00	0.06	0.00	0.00
MgO	0.66	0.74	0.38	0.65	0.39	0.36	0.39	0.43	0.55	0.71	0.70	0.31	0.33	0.90	0.75	0.65	0.66	0.44
CaO	0.00	0.00	0.02	0.03	0.00	0.00	0.00	0.07	0.01	0.01	0.00	0.05	0.00	0.00	0.01	0.00	0.00	0.03
BaO	0.00	0.00	0.00	0.00	0.00	0.00	0.00	0.00	0.00	0.00	0.00	0.00	0.00	0.00	0.00	0.00	0.00	0.00
Na2O	1.06	0.92	1.23	1.05	1.29	1.23	1.25	1.20	1.09	1.00	1.11	1.17	1.03	0.86	0.87	0.91	0.97	0.99
K2O	8.47	8.52	8.29	8.14	9.38	9.11	9.37	9.24	9.34	8.89	9.01	8.72	9.03	9.30	9.32	9.44	9.07	9.04
(F)	0.15	0.12	0.09	0.09	0.16	0.00	0.00	0.00	0.00	0.00	0.00	0.00	0.00	0.00	0.00	0.00	0.00	0.00
(Cl)	0.02	0.00	0.00	0.01	0.00	0.01	0.00	0.03	0.00	0.00	0.00	0.00	0.00	0.00	0.00	0.00	0.00	0.00
F-12O	0.09	0.07	0.05	0.05	0.09	0.00	0.00	0.00	0.00	0.00	0.00	0.00	0.00	0.00	0.00	0.00	0.00	0.00
Cl-12O	0.02	0.00	0.00	0.00	0.00	0.01	0.00	0.02	0.00	0.00	0.00	0.00	0.00	0.00	0.00	0.00	0.00	0.00
H2O	4.37	4.36	4.36	4.41	4.53	4.56	4.49	4.49	4.46	4.51	4.42	4.51	4.46	4.50	4.43	4.46	4.51	4.48
Total	97.23	96.63	96.43	97.09	101.35	100.16	99.17	99.30	97.97	98.78	97.08	98.80	97.82	98.85	97.45	98.18	98.87	98.23
Si	6.25	6.28	6.12	6.24	6.10	6.12	5.98	5.98	6.16	6.21	6.17	6.07	6.12	6.30	6.23	6.28	6.24	6.19
Al IV	1.75	1.72	1.88	1.76	1.90	1.88	2.02	2.02	1.84	1.79	1.83	1.93	1.88	1.71	1.77	1.72	1.76	1.81
Tot IV	8.00	8.00	8.00	8.00	8.00	8.00	8.00	8.00	8.00	8.00	8.00	8.00	8.00	8.00	8.00	8.00	8.00	8.00
AL VI	3.78	3.77	3.84	3.82	3.80	3.84	3.81	3.79	3.80	3.76	3.81	3.93	3.91	3.71	3.77	3.73	3.78	3.84
Ti	0.05	0.05	0.06	0.03	0.05	0.03	0.06	0.07	0.03	0.05	0.01	0.00	0.00	0.04	0.02	0.03	0.03	0.03
Cr	0.00	0.00	0.00	0.00	0.00	0.00	0.00	0.00	0.00	0.00	0.00	0.00	0.00	0.00	0.00	0.00	0.00	0.00
Fe2+	0.11	0.11	0.10	0.11	0.14	0.11	0.13	0.16	0.09	0.12	0.10	0.09	0.09	0.13	0.12	0.14	0.11	0.10
Mn	0.00	0.00	0.00	0.00	0.00	0.01	0.01	0.01	0.00	0.00	0.01	0.01	0.00	0.00	0.00	0.01	0.00	0.00
Mg	0.13	0.15	0.08	0.13	0.08	0.07	0.08	0.09	0.11	0.14	0.14	0.06	0.07	0.18	0.15	0.13	0.13	0.09
Tot S1	4.07	4.07	4.08	4.09	4.06	4.06	4.08	4.10	4.04	4.08	4.07	4.10	4.07	4.06	4.06	4.04	4.06	4.05
Ca	0.00	0.00	0.00	0.01	0.00	0.00	0.00	0.01	0.00	0.00	0.00	0.01	0.00	0.00	0.00	0.00	0.00	0.00
Ba	0.00	0.00	0.00	0.00	0.00	0.00	0.00	0.00	0.00	0.00	0.00	0.00	0.00	0.00	0.00	0.00	0.00	0.00
Na	0.28	0.24	0.33	0.27	0.33	0.31	0.33	0.31	0.29	0.26	0.29	0.30	0.27	0.22	0.23	0.24	0.25	0.26
K	1.46	1.48	1.44	1.40	1.56	1.53	1.60	1.57	1.60	1.51	1.56	1.48	1.55	1.58	1.61	1.62	1.54	1.54
Tot S2	1.74	1.72	1.77	1.68	1.89	1.84	1.92	1.89	1.89	1.77	1.85	1.79	1.82	1.80	1.84	1.86	1.79	1.81
Tot Cat	13.81	13.79	13.84	13.77	13.95	13.91	14.00	13.99	13.93	13.85	13.92	13.89	13.89	13.86	13.90	13.89	13.85	13.86
F	0.06	0.05	0.04	0.04	0.07	0.00	0.00	0.00	0.00	0.00	0.00	0.00	0.00	0.00	0.00	0.00	0.00	0.00
Cl	0.01	0.00	0.00	0.00	0.00	0.00	0.00	0.01	0.00	0.00	0.00	0.00	0.00	0.00	0.00	0.00	0.00	0.00
OH	3.93	3.95	3.96	3.96	3.94	4.00	4.00	3.99	4.00	4.00	4.00	4.00	4.00	4.00	4.00	4.00	4.00	4.00
ΣO	22	22	22	22	22	22	22	22	22	22	22	22	22	22	22	22	22	22

Table 17: continued.

Sample Descrip	LL 61b1 Ms I	LL 61b2 Ms I	LL 61c1 Ms II	LL 61c1 Ms II	LL 61c1 Ms II	LL 61c1 Ms II	LL 61c1 Ms II	LL 61c1 Ms II	LL 61b1 Ms II	LL 61b1 Ms II	LL 61b1 Ms II	LL 61a2 Ms II	LL 61a2 Ms II	LL 61a2 Ms II	LL 61a2 Ms II
SiO2	48.39	47.11	45.37	47.39	45.78	45.41	45.50	45.80	44.99	45.49	45.18	45.26	47.37	45.20	46.38
TiO2	0.39	0.22	0.45	0.16	0.69	0.46	0.41	0.40	0.52	0.54	0.31	0.40	0.23	0.24	0.33
Al2O3	34.99	34.32	35.39	33.61	35.66	35.48	35.33	35.80	35.49	36.00	35.61	35.67	34.57	35.06	36.38
Cr2O3	0.00	0.00	0.00	0.00	0.00	0.00	0.00	0.00	0.00	0.00	0.00	0.00	0.00	0.00	0.00
Fe2O3	0.00	0.00	0.00	0.00	0.00	0.00	0.00	0.00	0.00	0.00	0.00	0.00	0.00	0.00	0.00
FeO	0.95	1.26	0.80	1.07	0.94	0.85	0.95	0.86	0.80	0.96	0.79	0.91	1.02	0.97	1.02
MnO	0.00	0.00	0.00	0.00	0.06	0.00	0.00	0.05	0.03	0.00	0.00	0.05	0.03	0.02	0.03
MgO	0.39	0.95	0.35	0.87	0.34	0.32	0.38	0.36	0.33	0.31	0.41	0.41	0.68	0.45	0.52
CaO	0.15	0.00	0.02	0.01	0.00	0.00	0.00	0.00	0.01	0.00	0.00	0.00	0.00	0.00	0.02
BaO	0.00	0.00	0.00	0.00	0.00	0.00	0.00	0.00	0.00	0.00	0.00	0.00	0.00	0.00	0.00
Na2O	1.00	0.99	1.28	0.98	1.22	1.18	1.24	1.31	1.19	1.34	1.19	1.05	1.07	1.22	1.17
K2O	8.92	8.28	9.36	9.37	9.65	10.11	9.68	9.76	10.04	9.71	9.79	10.08	9.89	9.82	9.36
(F)	0.00	0.18	0.00	0.13	0.02	0.10	0.06	0.02	0.12	0.18	0.07	0.00	0.04	0.06	0.05
(Cl)	0.00	0.00	0.00	0.00	0.00	0.00	0.01	0.02	0.00	0.00	0.00	0.00	0.00	0.00	0.00
F-12O	0.00	0.10	0.00	0.08	0.01	0.06	0.03	0.01	0.07	0.10	0.04	0.00	0.03	0.03	0.00
Cl-12O	0.00	0.00	0.00	0.00	0.00	0.00	0.01	0.01	0.00	0.00	0.00	0.00	0.00	0.00	0.00
H2O	4.56	4.38	4.43	4.40	4.47	4.40	4.41	4.47	4.37	4.39	4.39	4.45	4.49	4.38	4.51
Total	99.75	97.61	97.43	97.95	98.83	98.27	97.95	98.83	97.84	98.84	97.71	98.36	99.37	97.41	99.75
Si	6.36	6.32	6.15	6.37	6.13	6.13	6.15	6.13	6.10	6.10	6.12	6.10	6.30	6.15	6.13
Al IV	1.64	1.68	1.85	1.63	1.87	1.87	1.85	1.87	1.90	1.91	1.88	1.90	1.70	1.85	1.87
Tot IV	8.00	8.00	8.00	8.00	8.00	8.00	8.00	8.00	8.00	8.00	8.00	8.00	8.00	8.00	8.00
AL VI	3.78	3.75	3.80	3.70	3.76	3.77	3.77	3.78	3.77	3.78	3.80	3.77	3.72	3.77	3.80
Ti	0.04	0.02	0.05	0.02	0.07	0.05	0.04	0.04	0.05	0.06	0.03	0.04	0.02	0.03	0.03
Cr	0.00	0.00	0.00	0.00	0.00	0.00	0.00	0.00	0.00	0.00	0.00	0.00	0.00	0.00	0.00
Fe2+	0.10	0.14	0.09	0.12	0.11	0.10	0.11	0.10	0.09	0.11	0.09	0.10	0.11	0.11	0.11
Mn	0.00	0.00	0.00	0.00	0.01	0.00	0.00	0.01	0.00	0.00	0.00	0.01	0.00	0.00	0.00
Mg	0.08	0.19	0.07	0.17	0.07	0.06	0.08	0.07	0.07	0.06	0.08	0.08	0.14	0.09	0.10
Tot S1	4.00	4.10	4.00	4.01	4.01	3.98	4.00	4.00	3.98	4.00	4.01	4.01	3.99	4.00	4.06
Ca	0.02	0.00	0.00	0.00	0.00	0.00	0.00	0.00	0.00	0.00	0.00	0.01	0.00	0.00	0.00
Ba	0.00	0.00	0.00	0.00	0.00	0.00	0.00	0.00	0.00	0.00	0.00	0.00	0.00	0.00	0.00
Na	0.26	0.26	0.34	0.26	0.32	0.31	0.32	0.34	0.31	0.35	0.31	0.28	0.28	0.32	0.30
K	1.50	1.42	1.62	1.61	1.65	1.74	1.67	1.67	1.74	1.66	1.69	1.74	1.68	1.70	1.58
Tot S2	1.77	1.68	1.96	1.87	1.97	2.05	1.99	2.01	2.05	2.01	2.00	2.02	1.95	2.03	1.88
Tot Cat	13.77	13.78	13.96	13.88	13.97	14.03	13.99	14.01	14.04	14.01	14.01	14.03	13.94	14.03	13.94
F	0.00	0.08	0.00	0.06	0.01	0.04	0.03	0.01	0.05	0.07	0.03	0.00	0.02	0.03	0.02
Cl	0.00	0.00	0.00	0.00	0.00	0.00	0.00	0.00	0.00	0.00	0.00	0.00	0.00	0.00	0.00
OH	4.00	3.93	4.00	3.94	3.99	3.96	3.97	3.99	3.95	3.93	3.97	4.00	3.98	3.98	4.00
ΣO	22	22	22	22	22	22	22	22	22	22	22	22	22	22	22

Table 17: continued.

Sample Descrip	LL 61a2		LL 61a2		LL 61a2		LL 61c2		LL 61b2		LL 61b2		LL 61b2		LL 61b2		LL 61b2		LL 61b2	
	Ms II	Ms II	Ms II	Ms II	Ms II	Ms II	Ms II	Ms II	Ms II	Ms II	Ms II	Ms II	Ms II	Ms II	Ms II	Ms II	Ms II	Ms II	Ms II	Ms II
SiO2	46,21	45,91	46,29	45,73	46,33	46,13	46,61	47,26	45,74	45,25	46,52	45,48	46,33	45,32	45,38	45,44	45,73	45,22		
TiO2	0,36	0,24	0,19	0,18	0,38	0,19	0,46	0,36	0,32	0,31	0,49	0,47	0,28	0,45	0,69	0,53	0,13	0,30		
Al2O3	35,95	36,16	36,50	37,06	35,66	37,44	35,69	35,97	36,26	36,02	36,91	36,32	35,23	35,84	36,62	36,35	36,40	35,50		
Cr2O3	0,00	0,00	0,00	0,00	0,00	0,00	0,00	0,00	0,00	0,00	0,00	0,00	0,00	0,00	0,00	0,00	0,00	0,00		
Fe2O3	0,00	0,00	0,00	0,00	0,00	0,00	0,00	0,00	0,00	0,00	0,00	0,00	0,00	0,00	0,00	0,00	0,00	0,00		
FeO	0,90	1,05	1,00	1,04	0,86	1,15	1,01	1,04	0,93	0,84	0,84	0,82	1,14	0,73	0,85	0,90	0,78	0,80		
MnO	0,07	0,03	0,00	0,08	0,02	0,00	0,00	0,00	0,01	0,03	0,06	0,01	0,00	0,00	0,03	0,02	0,04	0,00		
MgO	0,55	0,41	0,51	0,34	0,53	0,43	0,74	0,68	0,47	0,37	0,39	0,39	0,67	0,35	0,28	0,41	0,36	0,34		
CaO	0,02	0,00	0,04	0,00	0,06	0,00	0,01	0,00	0,00	0,06	0,01	0,02	0,05	0,00	0,00	0,02	0,00	0,01		
BaO	0,00	0,00	0,00	0,00	0,00	0,00	0,00	0,00	0,00	0,00	0,00	0,00	0,00	0,00	0,00	0,00	0,00	0,00		
Na2O	1,14	1,19	1,11	1,26	1,19	1,14	1,02	1,10	1,19	1,04	1,16	1,19	1,06	1,17	1,18	1,20	1,32	1,21		
K2O	9,52	9,54	9,10	9,28	9,53	8,99	8,83	9,78	7,70	7,41	8,04	7,85	7,64	8,01	7,75	7,81	8,09	9,78		
(F)	0,00	0,20	0,13	0,09	0,13	0,08	0,12	0,04	0,04	0,12	0,11	0,35	0,13	0,13	0,00	0,29	0,15	0,06		
(Cl)	0,00	0,02	0,00	0,01	0,02	0,02	0,02	0,00	0,00	0,01	0,01	0,00	0,01	0,00	0,00	0,00	0,01	0,01		
F-120	0,00	0,11	0,08	0,05	0,08	0,05	0,07	0,02	0,02	0,07	0,07	0,20	0,07	0,08	0,00	0,17	0,09	0,03		
Cl-120	0,00	0,02	0,00	0,01	0,02	0,02	0,02	0,00	0,00	0,01	0,01	0,00	0,01	0,00	0,00	0,00	0,01	0,01		
H2O	4,51	4,39	4,46	4,48	4,43	4,51	4,45	4,56	4,44	4,35	4,49	4,29	4,39	4,35	4,46	4,32	4,39	4,39		
Total	99,23	99,05	99,27	99,55	99,08	100,04	98,90	100,76	97,08	95,76	98,98	97,03	96,87	96,31	97,23	97,17	97,32	97,60		

Table 17: continued.

Sample Descrip	LL 61c1 Ms III	LL 61b1 Ms III	LL 61b1 Ms III	LL 61b1 Ms III	LL 61c2 Ms III	LL 61b2 Ms III	LL 61b2 Ms IV	LL 61b2 Ms IV	LL 61b2 Ms IV	LL 61b2 Ms IV	LL 61b2 Ms IV	LL 61b2 Ms IV
SiO2	45,13	44,92	44,73	45,03	45,43	45,55	45,08	46,32	45,35	45,10	44,34	45,37
TiO2	0,38	0,14	0,31	0,53	0,37	0,27	0,40	0,18	0,75	0,46	0,54	0,39
Al2O3	36,01	36,01	35,31	35,43	37,49	36,06	35,89	34,34	35,96	35,98	35,02	36,08
Cr2O3	0,00	0,00	0,00	0,00	0,00	0,00	0,00	0,00	0,00	0,00	0,00	0,00
Fe2O3	0,00	0,00	0,00	0,00	0,00	0,00	0,00	0,00	0,00	0,00	0,00	0,00
FeO	0,87	0,86	0,85	1,17	0,79	0,92	0,74	0,97	0,98	0,84	0,96	1,17
MnO	0,00	-0,03	0,05	0,03	0,00	0,02	0,01	0,00	0,00	0,03	0,05	0,04
MgO	0,32	0,28	0,34	0,35	0,33	0,34	0,38	0,76	0,39	0,37	0,42	0,42
CaO	0,00	0,01	0,04	0,00	0,01	0,01	0,01	0,01	0,00	0,00	0,05	0,03
BaO	0,00	0,00	0,00	0,00	0,00	0,00	0,00	0,00	0,00	0,00	0,00	0,00
Na2O	1,19	1,23	1,27	1,14	1,16	1,18	1,18	1,00	1,16	1,14	1,02	1,07
K2O	9,97	9,87	9,89	9,68	9,07	8,35	8,38	8,40	8,56	8,64	8,77	8,44
(F)	0,00	0,10	0,07	-0,03	0,00	0,12	0,00	0,11	0,07	0,18	0,03	0,10
(Cl)	0,02	0,00	0,00	0,01	0,00	0,00	0,00	0,00	0,01	0,00	0,00	0,00
F-12O	0,00	0,06	0,04	-0,02	0,00	0,07	0,00	0,07	0,04	0,10	0,02	0,06
Cl-12O	0,01	0,00	0,01	0,01	0,00	0,00	0,00	0,00	0,01	0,00	0,00	0,00
H2O	4,45	4,38	4,36	4,44	4,52	4,39	4,41	4,36	4,41	4,34	4,33	4,40
Total	98,35	97,74	97,18	97,80	99,16	97,18	96,47	96,41	97,51	96,99	95,51	97,47
Si	6,08	6,09	6,11	6,10	6,03	6,15	6,13	6,29	6,11	6,11	6,12	6,12
Al IV	1,92	1,91	1,90	1,90	1,97	1,85	1,87	1,71	1,89	1,89	1,88	1,88
Tot IV	8,00	8,00	8,00	8,00	8,00	8,00	8,00	8,00	8,00	8,00	8,00	8,00
AL VI	3,80	3,84	3,79	3,76	3,89	3,88	3,87	3,79	3,81	3,86	3,81	3,85
Ti	0,04	0,02	0,03	0,05	0,04	0,06	0,04	0,02	0,08	0,05	0,06	0,04
Cr	0,00	0,00	0,00	0,00	0,00	0,00	0,00	0,00	0,00	0,00	0,00	0,00
Fe2+	0,10	0,10	0,10	0,13	0,09	0,10	0,08	0,11	0,11	0,10	0,11	0,13
Mn	0,00	0,00	0,01	0,00	0,00	0,00	0,00	0,00	0,00	0,00	0,01	0,01
Mg	0,07	0,06	0,07	0,07	0,07	0,07	0,08	0,15	0,08	0,08	0,09	0,08
Tot S1	4,01	4,01	3,99	4,03	4,08	4,08	4,08	4,08	4,07	4,08	4,07	4,11
Ca	0,00	0,00	0,01	0,00	0,00	0,00	0,00	0,00	0,00	0,00	0,01	0,00
Ba	0,00	0,00	0,00	0,00	0,00	0,00	0,00	0,00	0,00	0,00	0,00	0,00
Na	0,31	0,32	0,34	0,30	0,30	0,31	0,31	0,26	0,30	0,30	0,27	0,28
K	1,71	1,71	1,72	1,67	1,54	1,44	1,45	1,46	1,47	1,49	1,54	1,45
Tot S2	2,03	2,03	2,07	1,97	1,84	1,75	1,76	1,72	1,78	1,79	1,82	1,73
Tot Cat	14,03	14,04	14,05	14,00	13,92	13,83	13,84	13,80	13,85	13,87	13,89	13,84
F	0,00	0,04	0,03	-0,01	0,00	0,05	0,00	0,05	0,03	0,08	0,01	0,04
Cl	0,00	0,00	0,00	0,00	0,00	0,00	0,00	0,00	0,00	0,00	0,00	0,00
OH	4,00	3,96	3,97	4,01	4,00	3,95	4,00	3,95	3,97	3,92	3,99	3,96
ΣO	22	22	22	22	22	22	22	22	22	22	22	22

Table 17: continued.

Sample Descrip	LL 61b2 Ms IV	LL 61b2 Ms IV	LL 61b2 Ms IV	LL 61b2 Ms IV	LL 61b2 Ms IV	LL 61b2 Ms IV	LL 61b2 Ms IV	LL 61b2 Ms IV	LL 61b2 Ms IV	LL 61b2 Ms IV	LL 61b2 Ms IV	LL 61b2 Ms IV	LL 61b2 Ms IV
SiO2	44,94	45,19	45,33	45,08	44,79	46,03	45,27	45,56	44,57	44,81	44,72	44,36	44,92
TiO2	0,44	0,59	0,52	0,37	0,18	0,15	0,18	0,27	0,23	0,25	0,32	0,54	0,37
Al2O3	36,67	36,24	36,10	36,14	36,94	34,83	36,33	36,84	36,83	36,85	37,10	36,14	36,67
Cr2O3	0,00	0,00	0,00	0,00	0,00	0,00	0,00	0,00	0,00	0,00	0,00	0,00	0,00
Fe2O3	0,00	0,00	0,00	0,00	0,00	0,00	0,00	0,00	0,00	0,00	0,00	0,00	0,00
FeO	0,86	0,79	0,96	0,90	0,74	0,98	0,78	0,79	0,69	0,76	0,87	0,87	0,89
MnO	0,09	0,02	0,02	0,00	0,00	0,02	0,01	0,09	0,11	0,02	0,00	0,00	0,02
MgO	0,45	0,40	0,36	0,33	0,31	0,65	0,33	0,40	0,34	0,41	0,45	0,36	0,41
CaO	0,00	0,03	0,00	0,02	0,00	0,00	0,03	0,00	0,18	0,00	0,03	0,02	0,00
BaO	0,00	0,00	0,00	0,00	0,00	0,00	0,00	0,00	0,00	0,00	0,00	0,00	0,00
Na2O	1,11	1,10	0,88	1,02	1,03	0,99	1,12	1,04	1,18	1,16	1,10	1,22	0,92
K2O	9,10	9,42	9,37	9,20	9,54	9,36	9,11	9,02	9,22	9,35	9,12	8,89	9,16
(F)	0,00	0,00	0,00	0,00	0,00	0,00	0,00	0,00	0,00	0,00	0,00	0,00	0,00
(Cl)	0,00	0,00	0,00	0,00	0,00	0,00	0,00	0,00	0,00	0,00	0,00	0,00	0,00
F-12O	0,00	0,00	0,00	0,00	0,00	0,00	0,00	0,00	0,00	0,00	0,00	0,00	0,00
Cl-12O	0,00	0,00	0,00	0,00	0,00	0,00	0,00	0,00	0,00	0,00	0,00	0,00	0,00
H2O	4,46	4,46	4,46	4,44	4,45	4,43	4,45	4,49	4,44	4,46	4,47	4,40	4,45
Total	98,12	98,23	97,99	97,48	97,97	97,44	97,60	98,50	97,80	98,06	98,18	96,81	97,80
Si	6,04	6,07	6,10	6,10	6,03	6,23	6,11	6,08	6,02	6,03	6,01	6,04	6,05
AlIV	1,96	1,93	1,90	1,91	1,97	1,77	1,89	1,92	1,98	1,97	1,99	1,96	1,95
Tot IV	8,00	8,00	8,00	8,00	8,00	8,00	8,00	8,00	8,00	8,00	8,00	8,00	8,00
AL VI	3,85	3,81	3,83	3,85	3,90	3,78	3,88	3,88	3,87	3,87	3,88	3,84	3,87
Ti	0,04	0,06	0,05	0,04	0,02	0,02	0,02	0,03	0,02	0,03	0,03	0,06	0,04
Cr	0,00	0,00	0,00	0,00	0,00	0,00	0,00	0,00	0,00	0,00	0,00	0,00	0,00
Fe2+	0,10	0,09	0,11	0,10	0,08	0,11	0,09	0,09	0,08	0,09	0,10	0,10	0,10
Mn	0,01	0,00	0,00	0,00	0,00	0,00	0,00	0,01	0,01	0,00	0,00	0,00	0,00
Mg	0,09	0,08	0,07	0,07	0,06	0,13	0,07	0,08	0,07	0,08	0,09	0,07	0,08
Tot S1	4,09	4,04	4,06	4,06	4,06	4,04	4,05	4,09	4,06	4,07	4,10	4,07	4,09
Ca	0,00	0,00	0,00	0,00	0,00	0,00	0,00	0,00	0,03	0,00	0,01	0,00	0,00
Ba	0,00	0,00	0,00	0,00	0,00	0,00	0,00	0,00	0,00	0,00	0,00	0,00	0,00
Na	0,29	0,29	0,23	0,27	0,27	0,26	0,29	0,27	0,31	0,30	0,29	0,32	0,24
K	1,56	1,62	1,61	1,59	1,64	1,62	1,57	1,54	1,59	1,61	1,56	1,55	1,57
Tot S2	1,85	1,91	1,84	1,86	1,91	1,87	1,86	1,81	1,92	1,91	1,85	1,87	1,81
Tot Cat	13,94	13,95	13,90	13,92	13,97	13,92	13,92	13,89	13,98	13,98	13,95	13,94	13,91
F	0,00	0,00	0,00	0,00	0,00	0,00	0,00	0,00	0,00	0,00	0,00	0,00	0,00
Cl	0,00	0,00	0,00	0,00	0,00	0,00	0,00	0,00	0,00	0,00	0,00	0,00	0,00
OH	4,00	4,00	4,00	4,00	4,00	4,00	4,00	4,00	4,00	4,00	4,00	4,00	4,00
ΣO	22	22	22	22	22	22	22	22	22	22	22	22	22

Table 17: continued.

Sample Descrip	LL6'lb2		LL6'lb2		LL6'lb2		LL6'lb2		LL6'lb2		LL6'lb2		LL6'lb2		LL6'lb2		LL6'lb2		LL6'lb2	
	Pinite	Pinite	Pinite	Pinite	Pinite	Pinite	Pinite	Pinite	Pinite	Pinite	Pinite	Pinite	Pinite	Pinite	Pinite	Pinite	Pinite	Pinite	Pinite	Pinite
SiO2	41.62	41.57	41.47	41.29	41.89	41.71	41.35	42.18	42.36	41.68	41.52	42.36	42.52	41.78	41.31	42.23				
TiO2	0.00	0.00	0.00	0.03	0.00	0.08	0.07	0.02	0.13	0.05	0.03	0.00	0.08	0.00	0.00	0.00				
Al2O3	35.86	35.07	35.93	35.02	35.31	35.48	35.26	35.76	35.40	35.64	35.06	35.96	35.60	35.27	34.77	36.49				
FeO	5.87	5.65	5.47	5.90	5.95	5.60	5.22	5.91	5.58	6.01	6.14	5.66	5.67	5.44	6.17	6.60				
MnO	0.10	0.00	0.12	0.06	0.03	0.00	0.08	0.00	0.06	0.05	0.00	0.00	0.00	0.00	0.07	0.03				
MgO	1.15	1.20	1.18	1.09	1.15	1.09	1.05	1.08	1.18	1.10	1.10	1.04	1.08	1.05	1.12	1.21				
CaO	0.83	0.77	0.89	0.76	0.81	0.83	0.76	0.70	0.78	0.76	0.73	0.87	0.72	0.69	0.88	0.81				
BaO	0.00	0.00	0.00	0.00	0.00	0.00	0.00	0.00	0.00	0.00	0.00	0.00	0.00	0.00	0.00	0.00				
Na2O	0.12	0.13	0.07	0.03	0.04	0.05	0.05	0.09	0.05	0.10	0.08	0.11	0.12	0.09	0.01	0.11				
K2O	1.34	1.44	1.26	1.49	1.45	1.32	1.29	1.46	1.48	1.46	1.45	1.53	1.36	1.34	1.34	1.29				
(F)	0.00	0.00	0.00	0.00	0.00	0.00	0.00	0.00	0.00	0.00	0.00	0.00	0.00	0.00	0.00	0.00				
(Cl)	0.00	0.00	0.00	0.00	0.00	0.00	0.00	0.00	0.00	0.00	0.00	0.00	0.00	0.00	0.00	0.00				
F-1%2O	0.00	0.00	0.00	0.00	0.00	0.00	0.00	0.00	0.00	0.00	0.00	0.00	0.00	0.00	0.00	0.00				
Cl-1%2O	0.00	0.00	0.00	0.00	0.00	0.00	0.00	0.00	0.00	0.00	0.00	0.00	0.00	0.00	0.00	0.00				
H2O	4.23	4.18	4.22	4.17	4.22	4.21	4.17	4.25	4.25	4.23	4.19	4.27	4.26	4.19	4.16	4.31				
Total	91.11	90.01	90.61	89.83	90.84	90.38	89.29	91.44	91.27	91.09	90.31	91.80	91.42	89.84	89.84	93.09				
Si	5.90	5.96	5.90	5.94	5.96	5.95	5.95	5.95	5.98	5.92	5.95	5.95	5.99	5.98	5.95	5.88				
Al IV	2.10	2.04	2.10	2.06	2.05	2.06	2.05	2.05	2.02	2.08	2.06	2.05	2.01	2.02	2.05	2.12				
Tot IV	8.00	8.00	8.00	8.00	8.00	8.00	8.00	8.00	8.00	8.00	8.00	8.00	8.00	8.00	8.00	8.00				
AL VI	3.89	3.88	3.92	3.88	3.87	3.91	3.94	3.90	3.87	3.88	3.86	3.91	3.90	3.93	3.85	3.86				
Ti	0.00	0.00	0.00	0.00	0.00	0.01	0.01	0.00	0.01	0.01	0.00	0.00	0.01	0.00	0.00	0.00				
Fe2+	0.70	0.68	0.65	0.71	0.71	0.67	0.63	0.70	0.66	0.71	0.74	0.67	0.67	0.65	0.74	0.77				
Mn	0.01	0.00	0.02	0.01	0.00	0.00	0.01	0.00	0.01	0.01	0.00	0.00	0.00	0.00	0.01	0.00				
Mg	0.24	0.26	0.25	0.23	0.24	0.23	0.23	0.23	0.25	0.23	0.24	0.22	0.23	0.22	0.24	0.25				
Tot S1	4.84	4.81	4.83	4.83	4.83	4.81	4.81	4.82	4.80	4.84	4.84	4.79	4.80	4.81	4.84	4.88				
Ca	0.13	0.12	0.14	0.12	0.12	0.13	0.12	0.11	0.12	0.12	0.11	0.13	0.11	0.11	0.14	0.12				
Ba	0.00	0.00	0.00	0.00	0.00	0.00	0.00	0.00	0.00	0.00	0.00	0.00	0.00	0.00	0.00	0.00				
Na	0.03	0.04	0.02	0.01	0.01	0.02	0.02	0.03	0.02	0.03	0.02	0.03	0.03	0.02	0.00	0.03				
K	0.24	0.26	0.23	0.27	0.26	0.24	0.24	0.26	0.27	0.26	0.26	0.27	0.24	0.24	0.25	0.23				
Tot S2	0.40	0.42	0.39	0.40	0.40	0.38	0.37	0.39	0.40	0.41	0.40	0.43	0.39	0.37	0.38	0.38				
Tot Cat	13.24	13.23	13.22	13.23	13.22	13.19	13.18	13.22	13.20	13.24	13.24	13.22	13.19	13.18	13.23	13.26				
F	0.00	0.00	0.00	0.00	0.00	0.00	0.00	0.00	0.00	0.00	0.00	0.00	0.00	0.00	0.00	0.00				
Cl	0.00	0.00	0.00	0.00	0.00	0.00	0.00	0.00	0.00	0.00	0.00	0.00	0.00	0.00	0.00	0.00				
OH	4.00	4.00	4.00	4.00	4.00	4.00	4.00	4.00	4.00	4.00	4.00	4.00	4.00	4.00	4.00	4.00				
ZO	22	22	22	22	22	22	22	22	22	22	22	22	22	22	22	22				

Table 18: chemical analyses of cordierite alteration products (pinitite).

Sample Descrip	LL61b2 Pinite	LL61b2 Pinite	LL61b2 Pinite	LL61b2 Pinite	LL61b2 Pinite	LL61b2 Pinite	LL61b2 Pinite
SiO2	43,10	42,82	42,39	42,77	43,31	42,78	42,82
TiO2	0,01	0,00	0,00	0,00	0,03	0,00	0,01
Al2O3	35,47	35,47	35,84	35,43	36,86	36,32	36,45
FeO	6,44	6,39	5,96	5,33	5,94	5,76	6,02
MnO	0,05	0,00	0,05	0,00	0,02	0,03	0,03
MgO	1,26	1,21	1,15	1,01	1,21	1,21	1,26
CaO	0,92	0,92	0,79	0,75	0,94	0,85	0,87
BaO	0,00	0,00	0,00	0,00	0,00	0,00	0,00
Na2O	0,09	0,08	0,09	0,09	0,09	0,12	0,10
K2O	1,23	1,31	1,42	1,42	1,34	1,33	1,51
(F)	0,31	0,03	0,10	0,04	0,09	0,07	0,03
(Cl)	0,01	0,00	0,00	0,00	0,00	0,00	0,01
F-112O	0,18	0,02	0,06	0,02	0,05	0,04	0,02
Cl-112O	0,01	0,00	0,00	0,00	0,00	0,00	0,01
H2O	4,16	4,28	4,22	4,23	4,34	4,28	4,32
Total	92,92	92,48	91,97	91,05	94,13	92,72	93,42
Si	6,00	5,99	5,95	6,04	5,93	5,95	5,95
Al IV	2,00	2,01	2,05	1,97	2,07	2,05	2,08
Tot IV	8,00	8,00	8,00	8,00	8,00	8,00	8,00
Al VI	3,82	3,83	3,88	3,93	3,89	3,90	3,87
Ti	0,00	0,00	0,00	0,00	0,00	0,00	0,00
Fe2+	0,75	0,75	0,70	0,63	0,68	0,67	0,70
Mn	0,01	0,00	0,01	0,00	0,00	0,00	0,00
Mg	0,26	0,25	0,24	0,21	0,25	0,25	0,26
Tot S1	4,83	4,83	4,83	4,77	4,82	4,82	4,82
Ca	0,14	0,14	0,12	0,11	0,14	0,13	0,13
Ba	0,00	0,00	0,00	0,00	0,00	0,00	0,00
Na	0,03	0,02	0,03	0,02	0,03	0,03	0,03
K	0,22	0,23	0,25	0,26	0,23	0,24	0,27
Tot S2	0,38	0,39	0,40	0,39	0,40	0,40	0,42
Tot Cat	13,21	13,22	13,22	13,16	13,22	13,21	13,25
F	0,14	0,01	0,04	0,02	0,04	0,03	0,01
Cl	0,00	0,00	0,00	0,00	0,00	0,00	0,00
OH	3,86	3,99	3,96	3,98	3,96	3,97	3,99
ΣO	22	22	22	22	22	22	22

Table 18: continued.

Sample Descrip.	LL 61a2 Fe-Ti Ox	LL 61a2 Fe-Ti Ox	LL 61a2 Fe-Ti Ox	LL 61a2 Fe-Ti Ox	LL 61c1 Fe-Ti Ox	LL 61b1 Fe-Ti Ox	LL 61b1 Fe-Ti Ox	LL 61b1 Fe-Ti Ox
SiO2	0,41	0,18	0,03	0,08	0,02	0,04	0,02	0,02
TiO2	99,39	99,76	53,75	53,49	52,61	53,36	52,47	52,47
Al2O3	0,43	0,18	0,05	0,00	0,00	0,03	0,00	0,00
FeO	0,15	0,10	42,50	42,75	43,80	43,36	44,80	44,80
MnO	0,03	0,00	2,73	2,01	1,45	1,50	1,40	1,40
MgO	0,02	0,00	0,03	0,07	0,10	0,12	0,11	0,11
CaO	0,07	0,03	0,00	0,01	0,02	0,01	0,00	0,00
Na2O	0,02	0,02	0,01	0,02	0,00	0,01	0,01	0,01
K2O	0,05	0,02	0,00	0,01	0,03	0,00	0,00	0,00
Total	100,57	100,29	99,10	98,44	98,02	98,42	98,81	98,81
Si	0,01	0,00	0,00	0,00	0,00	0,00	0,00	0,00
Al	0,01	0,00	0,00	0,00	0,00	0,00	0,00	0,00
Ti	0,98	0,99	0,52	0,52	0,51	0,52	0,50	0,50
Fe2+	0,00	0,00	0,45	0,46	0,47	0,47	0,48	0,48
Mn	0,00	0,00	0,03	0,02	0,02	0,02	0,02	0,02
Mg	0,00	0,00	0,00	0,00	0,00	0,00	0,00	0,00
Ca	0,00	0,00	0,00	0,00	0,00	0,00	0,00	0,00
Na	0,00	0,00	0,00	0,00	0,00	0,00	0,00	0,00
K	0,00	0,00	0,00	0,00	0,00	0,00	0,00	0,00
Tot Cat	1,00	1,00	1,00	1,00	1,00	1,00	1,00	1,00
OΣ	1,99	2,00	1,52	1,52	1,51	1,52	1,50	1,50
XRt	1,00	1,00	0,06	0,53	0,52	0,53	0,51	0,51
XIIIm	0,00	0,00	0,94	0,47	0,48	0,47	0,49	0,49

Table 19: chemical analyses of Fe-Ti oxides

APPENDIX 4: MASS BALANCE CALCULATIONS AND COMPOSITION OF REACTION DOMAINS.

Metamorphic reactions (c.f. 4.2) have been balanced using PETROCALC 2.0 software (Godard & Chat, 1994, not published). This software uses the singular-value-decomposition techniques. Microanalyses of reactants and products have been collected in selected reaction domains. The composition of each phase used for mass balance calculations corresponds to an average of at least 10 microanalyses.

In order to model the observed reactions, it has been considered that during these reactions the chemical system was opened to some mobile components, such as Na_2O and H_2O . Moreover, for few minerals involved by the reactions, it has been considered a possible variation of the composition in terms of exchange (e.g. $\text{Mg}_{-1}\text{Fe}_{+1}$, $\text{Mn}_{-1}\text{Fe}_{+1}\dots$).

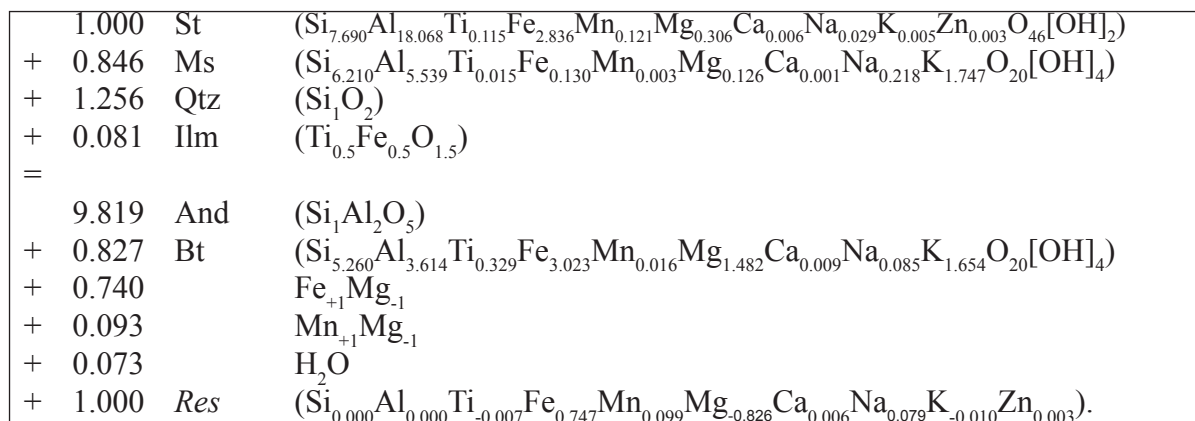
Mass balance calculations (matrix calculations) assign a stoichiometric coefficient for each phase involved by the reaction. After matrix calculations, stoichiometric coefficients of reactants and products have been used to calculate the compositions of the reaction domains.

These latter are generally expressed in a large chemical system such as the NCKFMnMASHTO. Therefore, some adjustments have been performed to reduce the effective chemical system (11 components) to a simpler one (e.g. KFMASH).

LL56a4 MICASCHIST: STAUROLITE-CONSUMING REACTION DOMAIN.

The P-T pseudosections of **Fig. 4.10** has been calculated in the KFMASH system using reactant and product compositions obtained from masse balance calculations.

Balanced reaction R3c (c.f. 4.2; 4.3.2.4.1; **Fig. 4.10**):



The compositions of the reaction domain before (reactants) and after (products) the reaction are:

	Reactants	Products
SiO ₂	14.203	14.203
AlO _{1.5}	11.378	11.378
TiO ₂	0.207	0.214
FeO	3.027	2.280
MnO	0.123	0.024
MgO	0.413	1.239
CaO	0.007	0.000
NaO _{0.5}	0.107	0.027
KO _{0.5}	0.741	0.752
ZnO	0.003	0.000

Each term of these two composition vectors has been calculated in this manner: SiO₂ of reactants (14.203)= (1*SiSt)+(0.846*SiMs)+(1.256*SiQtz).

Ten-component compositions of the reaction domain have been simplified making some assumption and/or projections, in order to obtain KFMASH compositions.

Some simply adjustments are listed below:

- ZnO and MnO have been added to FeO.
- CaO has been added to MgO
- NaO_{0.5} has been added to KO_{0.5}

Moreover, the composition of the domain before the reaction has been projected from theoretical ilmenite to eliminate Ti, whereas the composition of the domain after the reaction has been projected from theoretical Ti-biotite [K₂(Mg₄ Ti₂)Al₂Si₆O₂₄].

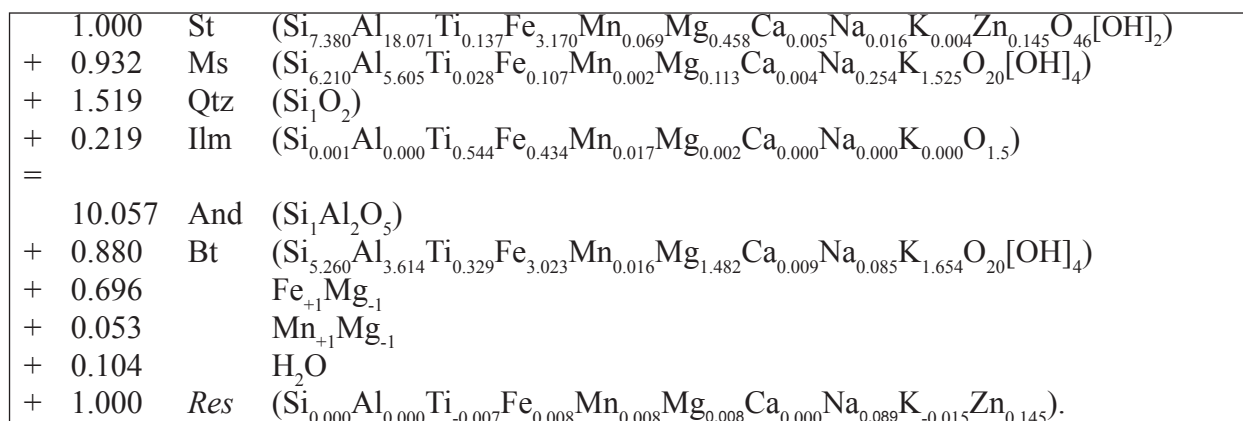
Final compositions used for pseudosection calculations are (in bold):

	Reactants	Products
K	0.848	0.672
F	2.940	2.304
M	0.420	0.810
A	11.378	11.271
S	14.203	13.559
Ilm	0.207	
Ti-Bt		0.107

**LL61b2 BIOTITE-RICH PARAGNEISS:
STAUROLITE-CONSUMING REACTION DOMAIN.**

The P-T pseudosection of **Fig. 4.12** has been calculated in the KFMASH system using reactant and product compositions obtained from masse balance calculations.

Balanced reaction R3e (c.f. 4.2; 4.3.2.4.1; **Fig. 4.12**):



Compositions of reaction domain before (reactants) and after (products) reaction

	Reactants	Products
SiO ₂	14.688	14.688
AlO _{1.5}	11.648	11.648
TiO ₂	0.282	0.289
FeO	3.365	3.357
MnO	0.076	0.068
MgO	0.564	0.556
CaO	0.009	0.008
NaO _{0.5}	0.126	0.037
KO _{0.5}	0.713	0.728
ZnO	0.145	0.000

Ten-component compositions of microdomain before and after reaction have been simplified making some assumption and/or projections in order to obtain KFMASH compositions.

Some simply adjustments are listed below:

- d) MnO have been added to FeO.
- e) ZnO and CaO have been neglected
- f) NaO_{0.5} has been added to KO_{0.5}

Moreover, the composition of domain before reaction has been projected from theoretical ilmenite to eliminate Ti, whereas Ti content of reaction domain after reaction has been neglected.

Reduced compositions are:

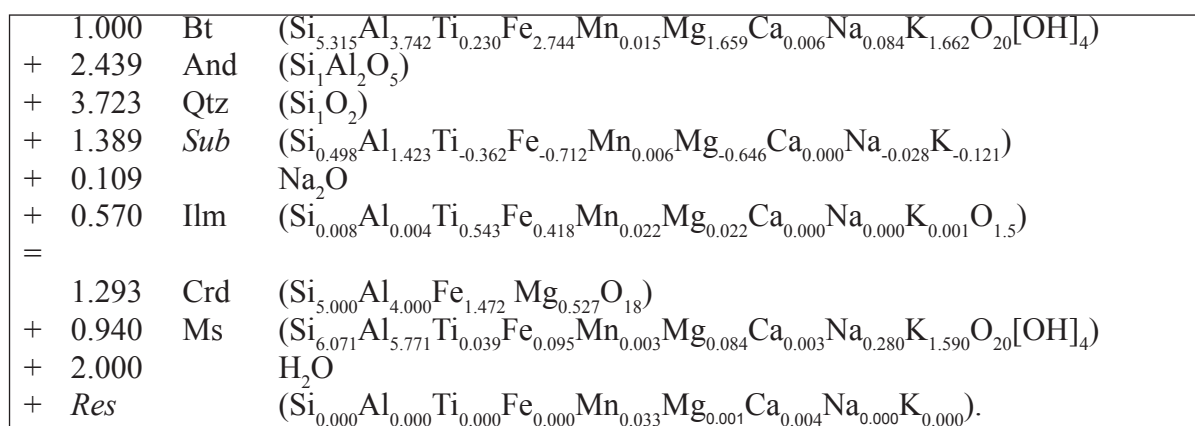
	Reactants	Products
K	0.839	0.766
F	3.207	3.424
M	0.563	0.556
A	11.648	11.648
S	14.687	14.688
Ilm	0.282	

The composition used for the pseudosection calculation (**Fig. 4.12**) corresponds to the average composition between the reactants and the products composition.

**LL61b2 BIOTITE-RICH PARAGNEISS:
CORDIERITE-FORMING REACTION DOMAIN**

The P-T pseudosection of **Fig. 4.14** has been calculated in the KFMASH system using reactant and product compositions obtained from masse balance calculations. In particular, considering that fresh cordierite has never been found, its composition is always theoretical in which only its X_{Fe} value corresponds to the measured X_{Fe} value of pinite cores.

Balanced reaction R4d (c.f. 4.2; 4.3.2.4.2; Fig. 4.14):



Compositions of reaction domain before (reactants) and after (products) reaction
System has been considered opened to $\text{NaO}_{0.5}$:

	Reactants	Products
SiO_2	12.1737	12.1739
$\text{AlO}_{1.5}$	5.2993	5.2993
TiO_2	0.0359	0.0368
FeO	1.9933	1.9939
MnO	0.0367	0.0033
MgO	0.7629	0.7614
CaO	0.0068	0.0032
$\text{KO}_{0.5}$	0.7474	0.7474

Eight-component compositions of the reaction domain before and after reaction have been simplified making some assumption and/or projections, in order to obtain KFMASH compositions.

Some simply adjustments are listed below:

- g) MnO has been added to FeO.
- h) CaO has been neglected

Moreover, the composition of the domain before the reaction has been projected from

theoretical ilmenite to eliminate Ti, whereas Ti content of reaction domain after reaction has been neglected.

Reduced compositions are:

	Reactants	Products
K	0.770	0.879
F	2.000	1.997
M	0.763	0.761
A	5.299	5.299
S	12.173	12.174
Ilm	0.036	

The composition used for the pseudosection calculation (**Fig. 4.14**) corresponds to the average composition between the reactants and the products composition.

APPENDIX 5: EFFECTIVE-BULK-COMPOSITION (EBC) CALCULATIONS.

The bulk-rock compositions used for phase diagram calculations have been obtained from XRF data (**Table 2 Appendix 2**). The XRF data have been reduced for thermodynamic calculations using simplified chemical systems, e.g. KFMASH (+H₂O). For such cases, corrections for Al₂O₃ may be required, especially when the rock contains plagioclase or other non-KFMASH minerals. For plagioclase, XRF-derived bulk rock compositions have been projected from albite and anorthite to remove Na and Ca, respectively. This correction is only an approximation, because other minerals, such as garnet and white mica, can also contain important amounts of CaO and Na₂O. Considering that in the analysed samples other Ca- and Na-bearing phases, e.g. muscovite and garnet, have low abundance Na₂O and CaO, this approximation seems to be correct. P₂O₅ and TiO₂ have been subtracted projecting XRF-bulk-rock compositions from apatite and Ti-bearing phases, such as ilmenite.

Another problem using XRF data arises from the different oxidation states of iron, which have an important influence on the effective Fe/(Fe+Mg) ratio of the rock. One approximation is that all iron is considered to be ferric iron (=FeO_{tot}), and the FeO content of the rocks has been obtained using the 0.899 conversion factor (e.g. Fe₂O₃ x 0.899).

LL56a4: calculation of the effective-bulk-rock composition.

The Effective-Bulk-Composition (EBC) of the micaschist has been calculated in order to model the garnet-growth induced fractionation.

To this end, two effective-bulk-compositions have been calculated in the KMnFMASH and the KFMASH system, respectively. The EBC calculated in the KMnFMASH system is the more appropriate in order to model the garnet growth, whereas the EBC calculated in the KFMASH system reproduce the equilibrium composition after the garnet growth.

Schematically, the XRF-composition has been projected from (a) the pre-tectonic Ca-rich garnet, in order to obtain the KMnFMASH EBC, and from (b) the whole garnet, in order to obtain the KFMASH EBC

The first step consisted in the calculation of garnet modes focusing the attention on pre-tectonic Ca-rich garnet and syn- to post-tectonic garnet.

X-ray maps have been acquired for all the garnet present in the analysed thin section. Using computer software (*e.g.* Adobe Photoshop), pixels relative to different textural generations of garnet have been calculated (see below).

Garnet	Pixel tot	Ca-rich core	Mn-rich core	Fe-rich rim
		Pre-tectonic	Syntetonic	Post-tectonic
GRT2	50457		50457	
GRT4	38413		21824	16589
GRT5	69644		55711	13933
GRT6	16568		16568	
GRT8	35581		35581	
GRT10	90529	18696	71833	
GRT11	45687		34076	11611
GRT12	70567	4866	65701	
Total	417446	23562	351751	42133

Pixel have been normalised to 100 resulting in partial totals:

Ca-rich core	Mn-rich core	Fe-rich rim
5,644	84,263	10,093

These values correspond to % volumes.

Fe-rich rims have been grouped with syntectonic Mn-rich cores (Mn+Fe rich garnet), for thermodynamic calculations.

Among garnet crystals it has been selected a representative one, which chemical profile is characterised by the following molar proportions:

	XPrp	XAlm	XSps	XGrs
Inherited Ca-rich core	0,02	0,5	0,254	0,208
Mn+Fe rich garnet	0,065	0,683	0,188	0,028

Considering the molar volume of pure pyrope (11318 cm³), almandine (11511 cm³), spessartine (11792 cm³) and grossularite (12535 cm³) it has been calculated the molar volume of the two parts of garnet:

Inherited Ca-rich core	$(0,02 \times 11318) + (0,5 \times 11511) + (0,254 \times 11792) + (0,208 \times 12535) = 11584,31$
Mn+Fe rich garnet	$(0,065 \times 11318) + (0,683 \times 11511) + (0,188 \times 11792) + (0,028 \times 12535) = 11165,56$

Moles of inherited Ca-rich garnet and remaining garnet have been calculated dividing the volumes % by molar volumes, resulting in 0,0545 and 0,9455 moles (normalised to 1), respectively.

Finally, a theoretical composition of garnet has been obtained in following manner:

1 Grt theoretic = 0,0545 Inherited Ca-rich core + 0,9455 remaining garnet.

1 Grt th. =	0,0545	3,013	Si	+	0,9455	2,988	Si	=	2,990
	0,0545	0,000	Al IV	+	0,9455	0,013	Al IV	=	0,012
	0,0545	1,948	Al VI	+	0,9455	1,920	Al VI	=	1,922
	0,0545	0,008	Ti	+	0,9455	0,004	Ti	=	0,004
	0,0545	0,036	Fe3+	+	0,9455	0,073	Fe3+	=	0,071
	0,0545	1,491	Fe2+	+	0,9455	2,056	Fe2+	=	2,025
	0,0545	0,757	Mn	+	0,9455	0,566	Mn	=	0,576
	0,0545	0,060	Mg	+	0,9455	0,197	Mg	=	0,189
	0,0545	0,673	Ca	+	0,9455	0,188	Ca	=	0,215
	0,0545	0,002	Na	+	0,9455	0,001	Na	=	0,001
	0,0545	0,000	K	+	0,9455	0,000	K	=	0,000
	0,0545	2,023	Prp	+	0,9455	6,536	Prp	=	6,291
	0,0545	50,011	Alm	+	0,9455	68,282	Alm	=	67,286
	0,0545	20,789	Grs	+	0,9455	2,775	Grs	=	3,757
	0,0545	25,383	Sps	+	0,9455	18,793	Sps	=	19,152
	0,0545	1,794	Adr	+	0,9455	3,614	Adr	=	3,515
	0,0545	0,026	XMg	+	0,9455	0,070	XMg	=	0,067
	0,0545	0,020	XPrp	+	0,9455	0,065	XPrp	=	0,063
	0,0545	0,500	XAlm	+	0,9455	0,683	XAlm	=	0,673
	0,0545	0,208	XGrs	+	0,9455	0,028	XGrs	=	0,038
	0,0545	0,254	XSps	+	0,9455	0,188	XSps	=	0,192
	0,0545	0,018	XAdr	+	0,9455	0,036	XAdr	=	0,035

Paragneisses: LL61a2 and LL61b2

Phase diagrams relative to LL61a2 and LL61b2 paragneisses have been calculated in the KFMASH system. Samples are near garnet free, consequently, garnet-growth induced fractionation has not been considered. Appropriate bulk-rock composition has been obtained projecting the XRF composition from apatite, albite, anorthite and ilmenite in order to eliminate P₂O₅, CaO, Na₂O and TiO₂, respectively. These projections led to a KMnFMASH composition. The KFMASH composition has been obtained simply adding MnO to FeO.

MULTIPLE INJECTIONS OF MAGMAS ALONG A HERCYNIAN MID-CRUSTAL SHEAR ZONE (SILA MASSIF, CALABRIA, ITALY)

Domenico Liotta^{a*}, Alfredo Caggianelli^b, Jörn Kruhl^c, Vincenzo Festa^b, Giacomo Prosser^d, Antonio Langone^e

^a *Dipartimento di Geologia e Geofisica, Università di Bari (Italy)*

^b *Dipartimento Geomineralogico, Università di Bari (Italy)*

^c *Tectonics and Material Fabrics Section, Technische Universität München, (Germany)*

^d *Dipartimento di Scienze Geologiche, Università della Basilicata, Potenza (Italy)*

^e *Dipartimento di Scienze geologiche, Università di Bologna (Italy)*

Submitted to the Journal of Structural Geology

1

1 MULTIPLE INJECTIONS OF MAGMAS
2 ALONG A HERCYNIAN MID-CRUSTAL SHEAR ZONE
(SILA MASSIF, CALABRIA, ITALY) 34

5 Domenico Liotta*, Alfredo Caggianelli, Jörn H. Kruhl,

6 Vincenzo Festi, Giacomo Prosser, Antonio Langone

78

9 a Dipartimento di Geologia e Geofisica, Università di Bari (Italy)

10 b Dipartimento Geomineralogico, Università di Bari (Italy)

11 c Tectonics and Material Fabrics Section, Technische Universität München,
12 (Germany)

13 d Dipartimento di Scienze Geologiche, Università della Basilicata, Potenza
14 (Italy)

15 e Dipartimento di Scienze della Terra e Geologico-Ambientali, Università
16 di Bologna (Italy)

17

18 * Corresponding Author

19 Dipartimento di Geologia e Geofisica

20 Campus universitario

21 Via Orabona, 4

22 70125, Bari (Italy)

23 e-mail: d.liotta@geo.uniba.it

24 tel. +390805442573

25 fax. +390805442625

26

27

28 Abstract

29 Syn-tectonic late-Hercynian granitoids, emplaced at mid-crustal level
30 through multiple dyke injections, are well-exposed in a ~1km -long
31 section, in the southern Sila Massif (Calabria, Italy). The fieldwork study
32 permitted us to reconstruct the following order of emplacement: (i)
33 granodiorites with euhedral Kfs megacrystals (Grd1, in the main text)
34 and heterogranular granodiorites with coarse rounded Pl and Kfs in a
35 fine-grained biotite-rich matrix (Grd2); (ii) granodiorites with a nearly
36 homogeneous grain size (Grd3); (iii) tonalite and, (iv) granite. Both in
37 the wall-rock, represented by migmatitic paragneisses, and in the
38 deformed granitoids the foliation attitude is substantially homogeneous,
39 striking about N140 with a dip of 50-60° to the NE. The magmatic
40 lineation is defined by the preferred alignment of euhedral feldspars,
41 parallel to the mineral lineation observed in the host rocks. Micro- and
42 meso-structural analyses indicate that foliation evolved from melt
43 present to solid-state conditions. Feldspar tiling, S/C structures, ..-type
44 structures, c-axis quartz orientations commonly suggest a top-to-the
45 west sense of shear during magma injection and deformation under
46 decreasing temperatures. Age of magma emplacement is constrained by
47 U/Pb datings at 304-300 Ma, coeval with the regional metamorphic peak.
48 Foliated granitoids and wallrock are intruded by poorly foliated Hbl
49 gabbro and, finally, by undeformed leucogranite, pegmatite and felsic

* Manuscript

50 porphyritic dykes. New U/Pb datings of the last intrusion event, indicate
51 an age of emplacement of 281 ± 8 Ma, providing a minimum estimate for
52 the end of the shear strain at mid-crustal level.

53

54 Key words: magma emplacement, shear zone, late Hercynian, Calabria

55

56

57 1. Introduction

58 Large-scale shear zones in the continental crust can easily become
59 preferred channels for the migration and ascent of granitoid magmas
60 (Hollister and Crawford, 1986; D'Lemos et al. 1992; Neves et al., 1996).
61 If the supply of magmas is continuous, thermal softening is expected,
62 enhancing ductile deformation and localization of shearing, in both
63 constrictional and extensional domains (Hutton, 1982, 1988). Other
64 factors being equal (i.e.: composition, strain rate or velocity of magma
65 supply), synkinematic granitoids record deformation if their cooling rate
66 is sufficiently slow to permit the development of deformation fabrics
67 during crystallisation (Paterson et al., 1989). Therefore, syn-kinematic
68 granitoids, cooling at mid- to lower-crust levels, are the best candidates
69 to undergo continuous deformation features, from sub-magmatic flow to
70 solid-state conditions (Tribe and D'Lemos, 1996; Vernon, 2000, with
71 references therein).

72 In these crustal environments, involvement of both mantle- and crust-
73 derived melts is common and hybrid magmas can be generated by
74 mingling/mixing processes (Neves and Vauchez, 1995; Fernandez et al.,
75 1997). By structural and petrological observations, it is possible to infer
76 the progressive involvement of magmas derived from different sources
77 into the shear zone. Then, dating of the magmatic rocks would also
78 permit to encompass the age of deformation.
79 In this paper we deal with multiple syn-kinematic injections of magmas
80 within a late-Hercynian mid-crustal shear zone cropping out in the Sila
81 Massif (Figs. 1 and 2)

82

83 Figure 1

84 Figure 2

85

86 at the boundary between high-grade metamorphic rocks and granitoids.
87 Shear-zone foliation is mainly north-east dipping and kinematic
88 indicators commonly point out a top-to-the-west sense of shear (Festa et
89 al., 2006). We studied a section of this regional shear zone, close to the
90 Mesoraca town, where the relationships between several late-
91 Carboniferous syn- to post-tectonic granitoids (Ayuso et al. 1994;
92 Graessner et al., 2000) can be clearly observed (Fig. 1). Granitoids show
93 calc-alkaline affinity and composition varying from tonalite to two-mica
94 strongly peraluminous leucogranite (Caggianelli and Prosser, 2001, with
95 references therein).
96 Our results allow to (i) unravel the sequence of intrusions, (ii) recognize
97 continuous deformation from magmatic through high-T to low-T
98 conditions, within the same kinematic framework, and (iii) discuss the

99 tectonic environment for the emplacement of the granitoids in the Sila
100 Massif.

101

102 2. Geological setting

103 The Calabria-Peloritani terrane (Bonardi et al., 2001) builds a curved
104 mountain belt, connecting the NW-SE-trending southern Apennines and
105 the E-W-trending Maghrebide chain of Sicily (Amodio-Morelli et al.,
106 1976). It is a fault-bounded terrane that was involved in the southern
107 Apennines orogeny (Fig. 1). The present structure of the Calabria-
108 Peloritani terrane derives from two main tectonic episodes. The first one
109 occurred during Eocene-Oligocene times and is connected to the collision
110 between the Adria promontory and the European plate (Borsi and
111 Dubois, 1968; Platt and Compagnoni, 1990). The stacking of the
112 Calabria-Peloritani tectonic units is related to this episode (e.g.
Amodio-

113 Morelli et al., 1976; Van Dijk et al., 2000, with references therein).
The

114 second episode (late-Oligocene to the Present) is related to the south115
eastward migration of the Calabria-Peloritani terrane, in relation to
116 retreating subduction of the Ionian oceanic lithosphere and to the
117 opening of the Tyrrhenian oceanic Basin (Dewey et al., 1989; Gueguen
118 et al., 1998, with references therein). During migration, the eastern
119 margin of the Calabria terrane experienced shortening whereas the
120 western margin underwent extension and uplift (Wallis et al., 1993;
121 Thomson 1994). A consequence of this geological evolution is a regional
122 crustal tilting of about 40-45° (Schenk 1980; Thomson, 1994;
123 Caggianelli et al., 2000; Festa et al., 2003) that favoured the outcrop
of

124 a nearly complete tilted Hercynian crustal section (Dubois, 1976;
125 Schenk, 1980, 1989, 1990). Despite post-Hercynian tectonic events, the
126 original Hercynian structural setting is still preserved in the Sila and
127 Serre massifs (Lorenzoni and Zanettin Lorenzoni, 1983; Atzori et al.,
128 1984; Caggianelli and Prosser, 2001).

129 In the Sila area (Fig. 1), the late-Hercynian continental crust is
basically

130 composed of high-grade and low-grade Palaeozoic metamorphic rocks,
131 intruded by nearly tabular late-Hercynian granitoids and minor quartz132
dioritic to gabbroic bodies (Dubois, 1976; Schenk, 1980; Caggianelli and
133 Prosser, 2001). Granitoids are located between high-grade migmatitic
134 paragneisses (bottom), cropping out to the west, and low-grade
135 metamorphic rocks (top), exposed to the east (Figs 1 and 2). Their
136 emplacement depths regionally range from 8 to 18 km, with the
137 granitoids in the surrounding of the study area injected at approximately
138 18 km depth (Caggianelli et al., 1997). Age of Sila granitoids
139 emplacement spans from 304 to 300 Ma (U-Pb method on zircon and
140 monazite), near synchronously with the peak metamorphism (Graessner
141 et al., 2000). Two peraluminous granites, cropping out in the
142 neighbourhood of the study area, provided monazite and xenotime ages
143 of 303-302 Ma by U-Pb method (Graessner et al., 2000). Datings of
144 tonalite of the study section was performed by $^{40}\text{Ar}/^{39}\text{Ar}$ method by
145 Ayuso et al. (1994) and resulted in hornblende ages of 293 Ma (Fig.1), in
146 agreement with the lower closing temperature of hornblende by this
147 geochronological method, compared to that of monazite by U-Pb method.

148 Undeformed felsic porphyritic dykes and pegmatites crosscut all previous
149 rocks and fabrics. An age of 281±8 Ma (see chapter 5) has been
150 obtained by U-Pb for zircons in a felsic porphyritic dyke cropping out
near

151 Arvo Lake (Fig. 1). A muscovite age of 265 Ma was obtained by Rb/Sr
152 method for a pegmatite (Festa et al., 2001) in a zone located directly
153 northwest of Mesoraca (Fig. 1).

154 Older ages are from the Devonian phyllites and interlayered
155 metavolcanites of the upper crust (Fig. 1). Here, three ages of the
156 regional metamorphism were estimated at 326±6 Ma (Acquafredda et
157 al., 1991), at 330±4 and 328±4 Ma (Acquafredda et al., 1992) by Rb/Sr
158 isochrons of whole-rock.

159 In the Sila Massif, from bottom to top, high-grade metamorphic rocks
160 are metagabbros, felsic granulites, and migmatitic paragneisses with
161 intervening marbles and metabasites. In the paragneisses, according to
162 Graessner and Schenk (2001), the metamorphic assemblage of biotite -
163 garnet - sillimanite - K-feldspar - cordierite - spinel, indicates peak
P-T
164 conditions of 400–600 MPa and 740–770 °C, reached simultaneously
165 with the emplacement of the granitoids. The study section is structurally
166 located at the boundary between granitoids and migmatitic paragneisses
167 (Fig. 2).

168

169 3. Petrography

170 In the study section, similarly to other Calabria areas (Rottura et al.,
171 1990), high-grade metamorphic rocks show a migmatitic zone at the
172 contact with the granitoids (Fig. 3a).

173

174 Figure 3

175

176 Away from the boundary, a wide spectrum of calc-alkaline intrusive
177 rocks crops out over about 1 km perpendicular to strike. These are
178 represented by: granodiorite with euhedral Kfs megacrystals outlining a
179 strong foliation (Grd 1, Fig. 3b); heterogranular foliated dark
180 granodiorite with coarse rounded Pl and Kfs (Fig. 3c) in a fine-grained
181 biotite-rich matrix (Grd2); granodiorite with a nearly equi-granular grain
182 size (Grd3, Fig. 3c); tonalite (Fig. 3d), granite, leucogranite (Fig. 3e),
183 hornblende gabbro, and swarms of mafic enclaves (Fig. 3f) including rare
184 norite xenoliths (Fig. 3g). Granodiorites, tonalite and granite are
strongly

185 foliated. Differently, hornblende-gabbro is poorly foliated whereas
186 leucogranite, pegmatite, (Fig. 3h) and felsic porphyritic dykes (Fig. 3i)
187 intruding the host rocks and the previously emplaced granitoids, are
188 undeformed and therefore considered post-tectonic.

189

190 3.1 - Chemical composition of intrusive rocks

191 The chemical composition of the intrusive rocks (Lioy, 2006) is
192 summarized in Table 1.

193

194 Table 1

195

196 A wide compositional range with silica content comprised between 47.49
197 wt. % and 74.56 wt. % is observed. Mafic rocks are mostly amphibole
198 gabbros and dioritic enclaves, but noritic compositions are also detected
199 in rare and small xenoliths enclosed in granodiorites.

200 Some general considerations can be made on nature and evolution of
201 magmas, by examining diagrams in Fig. 4.

202

203 Figure 4

204

205 The AFM plot outlines an arrangement of datapoints along a typical calc206
alkaline trend, except for the mafic rocks (Fig. 4a). The latter show a
207 notable scattering, beyond the boundary dividing the calc-alkaline from
208 the tholeiite suites. The diagram in Fig. 4b allows estimation of an
Alkali-

209 Lime index of 58 wt.%, typical of calc-alkaline suites and compatible with
210 late orogenic timing of magma activity (D'Amico et al., 1987).

211 Harker diagrams (Fig. 4c-f) display nearly linear trends for some oxides
212 (e.g. Fe₂O₃t diagram) or a notable dispersion of datapoints

213 representative of the more mafic rock types (e.g. Al₂O₃, MgO and Sr
214 diagram). This is possibly connected with variable accumulation of

215 pyroxenes and amphibole. Evolution from tonalitic to granodioritic
216 compositions, according to least-squares calculations, can be compatible
217 with crystal fractionation and, chiefly, of plagioclase and amphibole with
218 minor involvement of biotite and ilmenite. The transition from

219 metaluminous to peraluminous compositions, occurring around 60 wt.%

220 in silica content (Fig. 4g), can be justified if amphibole was abundant in
221 the fractionating assemblage (Cawthorn and Brown, 1976). Alternatively,

222 this suggests a significant contamination or mixing with crustal material.

223 In fact, some acidic rocks have values of the A/CNK ratio close or higher
224 than 1.1, reflecting S-type characteristics (White and Chappell, 1988)

225 and a dominant contribution from the continental crust in their genesis
226 (Caggianelli et al., 2003).

227 In synthesis, despite the different timing of emplacement (see chapter
228 4), intrusive rocks involved in the study area, share common chemical

229 affinities. Their compositional features fit well in the petrogenetic

230 scenario depicted by Rottura et al. (1990) and Ayuso et al. (1994) for

231 the late Hercynian plutonism in Calabria, on the basis of geochemical and
232 isotopic features. According to these authors, the precursor mantle

233 magmas underplated in a late- to post-collision tectonic setting,

234 undergoing crystal fractionation and contamination with crustal material,
235 acquiring progressively a hybrid nature. The presence of noritic xenoliths

236 in the studied area is in agreement with early orthopyroxene

237 crystallization favoured by contamination of mantle magmas with crustal
238 material (Campbell, 1985).

239 In following evolution, heating of the lower crust by the underplated

240 mantle magmas generated anatexic melts that mixed with the

241 contaminated magmas in the route to the final emplacement site, thus

242 producing, together with crystal fractionation, the wide spectrum of the
243 observed compositions.

244

245 4. Chronology of magmatic intrusions

246 Cross-cutting relationships detected along the study section (Fig.5)

247

248 Figure 5

249

250 led to a chronology of magmatic intrusions, that from old to young is:

K251

feldspar megacrysts- bearing granodiorite carrying mafic enclaves (Grd1)

252 and heterogranular dark granodiorite (Grd2), equigranular granodiorite

253 (Grd3), tonalite, granite. Fabric observations indicate that multiple

254 magma injections occurred when melt was still present in the magmatic

255 host-rocks. Granodiorites, tonalite and granite are followed by poorly

256 foliated amphibole-gabbro and finally by unfoliated leucogranite,

257 pegmatites and porphyritic dykes. Wall-rocks are intruded by tonalite

258 magmas, with a thickness ranging from few centimeters to 5 m, almost

259 parallel to the NE-dipping basement foliation, over about 500 m

260 perpendicular to strike. All granodiorites, tonalite and granite coexisted

261 as crystal mushes, for periods between 303-302 Ma and 281+8Ma, as

262 described in chapter 5. The reconstruction of the chronology of magmatic

263 intrusions is based on the following field observations:

264

265 4.1 Grd1 granodiorite - mafic enclaves relationship

266 Swarms of dioritic enclaves, cropping out as disrupted and disaggregated

267 dykes (Fig.3f), show margins that are partly parallel to and partly

268 intersected by the Grd1 magmatic foliation, defined by euhedral (Fig. 6)

269

270 Figure 6

271

272 K-feldspars (more arguments in section 6.1). Enclaves display variable

273 elongation and their boundaries are from saw-tooth to smooth, in

274 response to viscosity contrast among the involved magmas (Tobisch et

275 al., 1997, with ref.; Paterson et al., 2004). Within the mafic enclaves,

276 patches of Grd1 granodiorite are also observed, suggesting reciprocal

277 mingling relationships. Grd1 granodiorite carries also rare xenoliths of

278 norite (Fig.3g). Since norite is only rarely observed in the exposed

279 Calabria late Hercynian lower crust, we argue that the occurrence of

280 these xenoliths indicate magma contamination (Campbell, 1985) at

281 deeper crustal levels.

282

283

284 4.2 Grd2 - Grd3 granodiorite relationship

285 The relationship between these two magmatic rocks is shown in Fig.3c.

286 The equigranular granodiorite (Grd3) is here a dyke injecting the

287 heterogranular dark granodiorite (Grd2) obliquely to its foliation.

288 Consequently, Grd3 is younger than Grd2. The Grd3 cusped margins are

289 separated from the host-rock by a centimetre-thick pegmatite. Grd3

290 cusps indicate a minor viscosity of the Grd3 magma with respect to the

291 pegmatite.

292

293 4.3 Grd1 - Grd3 granodiorite relationship

7

294 The equigranular granodiorite (Grd3) contains Grd1 enclaves (Fig. 7),

295

296 Figure 7

297

298 which are generally rounded or show elliptical shape. The Grd3 foliation

299 does not wrap around the enclaves, suggesting that these still contained

300 melt when they were incorporated in the Grd3 magma.

301 The Grd1-Grd3 structural relationships (Fig. 8)

302

303 Figure 8

304

305 are similar to those already described in the 4.2 section: (i) the Grd3

306 margins are oblique to the host-rock foliation; (ii) a ~ 70 cm thick

307 pegmatite separates the Grd3 and Grd1 granodiorites; (iii) the cusped

308 margin indicates, first, that both rocks contained melt and, second, that

309 viscosity of Grd3 was lower than that of pegmatite; (iv) the boundary

310 between pegmatite and Grd1 is transitional suggesting that the

311 pegmatite rimming the Grd3 probably represents the interstitial melt

312 expelled from the surrounding Grd1 crystal mush.

313 Following these lines of evidence, together with the described Grd2-Grd3

314 relationship (4.2 section), the Grd3 granodiorite is interpreted as a dyke

315 injecting both the Grd1 and Grd2 granodiorites and, consequently, as

316 being younger.

317

318 4.4 Grd1- Grd2 granodiorite relationship

319 The Grd2 granodiorite outcrops in the eastern part of the study section

320 and overlies the Grd1 granodiorite (Fig.5, h-i). The boundary between

321 the two granodiorites is gradual over ~10m. Going from the Grd1 to the

322 Grd2 granodiorite, gradation is indicated by the progressive size

323 reduction of the aligned euhedral feldspars of Grd1 by the increase in

324 biotite amount and by the change from euhedral to lenticular-shape of

325 feldspars. Foliations in the Grd1 and Grd2 rocks commonly dip ~60° to

326 the NE and are parallel to the lithological boundary between Grd1 and

327 Grd2. These characteristics of the lithological boundary and the common

328 foliation suggest that the Grd1 and Grd2 granodiorites shared the same

329 kinematics starting from melt-present conditions and therefore they were

330 nearly coeval.

331

332 4.5 Tonalite - Grd1 granodiorite relationship

333 Tonalite intruded the Grd1 and wall-rock (Fig.5a-b, 5d-e, 5f-g). This

334 implies that the tonalite follows the emplacement of the Grd1-Grd2

335 granodiorites and probably also emplacement of the Grd3. The boundary

336 between tonalite and Grd1 granodiorite is parallel to the Grd1 magmatic

337 foliation (Fig.5 f-g) and dipping ~ 50° to the NE. As indicated in section

338 4.7, tonalite and Grd1 are synkinematic over a certain period of time.

339

340 4.6 Grd1 granodiorite - granite relationship

341 In the Grd1, the granite is only exposed as cm to dm thick dykes.
342 Margins of these dykes can be parallel to the Grd1 magmatic foliation or
343 transect it. In the latter case (Fig.9),

344

345 Figure 9

346

347 the magmatic foliation cross-cuts the lithological boundary without
348 changing direction. Accordingly, euhedral K-feldspars straddle obliquely

349 the Grd1-granite margin. Such features indicate that foliation developed
350 in melt-present conditions in both host-rock and dyke (Paterson et al.,
351 1989; Vernon, 2000).

352

353 4.7 Tonalite - granite relationship

354 Tonalite is intruded by at least two granite dykes. The larger one,
355 approximately 15 m thick (Fig. 5d-e and 5e-f), incorporates elongate
356 tonalite enclaves. Their flat faces are parallel to the granite magmatic
357 foliation that, in turn, is parallel to the magmatic to solid-state
tonalite

358 foliation. At the outcrop scale, the central parts of the granite dykes
are

359 characterised by a strong and pervasive magmatic to solid-state foliation
360 (Fig.10),

361

362 Figure 10

363

364 parallel to the lithological boundary and to the tonalite foliation. In
365 contrast, close to the dyke margin a planar anisotropy can be locally
366 observed at an angle of $\sim 45^\circ$ to the lithological boundary. Such
367 anisotropy is interpreted as a shear foliation, coeval with the injection
of

368 the acidic magma into the tonalite. All these observations suggest that
369 granite, tonalite and Grd1 granodiorite, coexisted as crystal mush over a
370 certain period of time.

371

372 4.8 Amphibole-gabbro - tonalite - Grd1 granodiorite relationships

373 Amphibole-gabbro intrudes tonalite and Grd1 granodiorite (Fig.5c-d, 5d374
e). The contacts of the gabbro to the host-rocks dip $\sim 70^\circ$ to the NE but
375 are not clearly exposed. In contrast to tonalite and Grd1, the
amphibole376

gabbro is weakly foliated and the orientation of foliation varies from W377
dip over sub-horizontal to E-dip. It remains open if the wall-rocks were
378 solid or crystal-mush when the gabbro intruded but the completely
379 different orientation of the magmatic foliation in the gabbro argues for
a

380 kinematic framework different from the one affecting earlier granite,
381 tonalite and granodiorites.

382

383 4.9 Leucogranite, pegmatite, porphyritic rocks

384 Basement rocks, tonalite, Grd1 and Grd2 are intruded by non-foliated
385 leucogranite, non-foliated pegmatite, felsic and mafic porphyritic rocks.
386 All these rocks are interpreted as post-kinematic with respect to the
387 magmatic foliation of their host-rocks (Fig.5).

388

389

390 5. Age of post-tectonic intrusions

391 Dated post-tectonic intrusions are represented by leucogranites and
392 pegmatites. Leucogranites cropping out in the Sila Massif, near the
393 Cecita Lake (Fig. 1) provided a Rb/Sr isochron age of 284 ± 14 Ma
394 (Caggianelli et al., 2000). An undeformed pegmatite from the Mesoraca
395 area in clear crosscutting relationships with heterogranular dark
396 granodiorites (Grd 2) gave a Rb/Sr muscovite whole rock age of 265 ± 3
397 Ma (Festa et al., 2001; Fig.1). The gap between these two ages in large
398 amount can be attributed to the adoption of diverse dating methods that
399 imply different closing temperatures. In fact, reasonable Rb/Sr closing
400 temperatures for whole rock isochron and muscovite methods are around
401 700°C (e.g. Hollister, 1982) and 500°C (Wagner et al., 1977),
402 respectively. In addition, recent data are available from a felsic
403 porphyritic dyke that was dated by U/Pb method, using LA-ICP-MS (see
404 the Appendix). The dyke is exposed close to the Arvo Lake (Fig. 1), ~40
405 km north of the study area (Langone, 2007). On cathodoluminescence
406 images zircons are euhedral and prismatic (mean aspect ratio of 2.04)
407 with concentric oscillatory zoning from core to rims, indicative of
igneous
408 origin (Fig. 11).

409

410 Figure 11

411

412 Generally, crystal luminescence is faint in cores and bright in rims (Fig.
413 11). Only few crystals show inverse luminescence intensities (D, G, H,
414 Fig. 11). In some cases we observed zircons having a core with an
415 irregular outline (M, Fig. 11) surrounded by a rim with oscillatory
zoning.

416 These probably represent former xenocrysts partially resorbed and then
417 overgrown by shells in equilibrium with the evolving acidic magma.
418 Analyses have been performed using a laser spot size of $25\text{ }\mu\text{m}$ and
419 isotopic compositions have been collected from different portions of
420 selected crystals with contrasting luminescence intensities (Fig. 11).
421 Isotopic ratios and a summary of concordant LA-ICP-MS ages are
422 reported in Table 2 and Table 3,

423 Table 2

424

425 Table 3

426 respectively, whereas a concordia diagram is shown in Fig. 12.

427

428 Figure 12

429

430 As expected, ages relative to inner portions of crystals are older than
431 those obtained from the outer parts, with an average of 293 ± 8 and
432 281 ± 8 , respectively. Undisturbed internal oscillatory zoning of zircons

433 coupled with geochronological data becoming progressively younger

434 towards the outer crystals parts, is compatible with continuous magmatic

10

435 growth. The older ages obtained in the inner zones, easily identified on
436 the basis of the contrasting luminescent properties, could be linked to
437 the early stage of crystallization in a deeper magma chamber whereas
438 the younger ages could be linked to the final stage of crystallization at
439 the shallow emplacement level of the porphyritic dykes.

440

441 6. Structures of magmatic intrusions and wall-rocks

442 In this chapter we describe meso- to microstructures of all different
443 rocks in more detail in order to demonstrate that all magmatic rocks as
444 well as the basement were affected by a common kinematic framework
445 during crystallization of the magmas and subsequent regional cooling
446 from high- to low-T conditions. Our description starts with the analysis
of

447 the common magmatic foliation and lineation and proceeds with the
448 examination of the structures produced from high-T to progressively
449 lower-T conditions in both magmatic and basement rocks. The transition
450 from magmatic to totally solid state is also discussed.

451

452 6.1 Magmatic structures

453 In the magmatic rocks of the study section and surroundings a pervasive
454 planar anisotropy with alignment of euhedral minerals (mostly
455 amphibole, biotite and feldspars), and mafic enclaves (Fig.3b,f) is
456 present. It strikes about 140° with a dip of 50° - 60° to the NE, roughly
457 parallel to the host-rock foliation (Fig. 13)

458

459 Figure 13

460

461 and to the contact with the metamorphic basement (Fig.5a-b). The bulk
462 of euhedral minerals, observed on the XZ plane, i.e., parallel to the
463 mineral lineation, do not show pressure shadows, suggesting that they
464 were aligned mostly under melt-present conditions (Vernon, 2000;
465 Vernon et al., 2004).

466 Considering that (i) the observations are structurally located close to
the

467 border of the basement, (ii) the magmatic foliation is almost parallel to
468 this border and parallel to sub-parallel to the internal boundaries of
the

469 magmatic bodies (Fig. 5), and (iii) in general the magmatic intrusions of
470 the Sila represent large-scale sills (Caggianelli and Prosser, 2001), the
471 plane of mineral alignment is interpreted as magmatic flow plane, i.e., as
472 magmatic foliation.

473 In the tonalite, the magmatic foliation is expressed by a pervasive planar
474 anisotropy marked by alignments of euhedral or subhedral biotite and
475 plagioclase (Fig.14a).

476

477 Figure 14

478

479 The latter sometimes is zoned and poikilitic, enclosing euhedral biotite
480 flakes, typically $0.3\ \mu\text{m}$ across.

481 In the granite, the occurrence of a magmatic planar anisotropy is
482 suggested by the preferred orientation of subhedral K-feldspars and of ~
483 $20\ \mu\text{m}$ long lenses made up of quartz and biotite.

11

484 Conversely, in the hornblende-gabbro magmatic foliation appears to be
485 weak in the field although, in thin section, it is well characterised by
486 alignment of large subhedral and zoned plagioclase and amphibole
487 (mostly cummingtonite).
488 However, the most striking mineral alignment is related to the K-feldspar
489 megacrysts from the Grd1 (Fig.3a). Only in this strongly foliated rock a
490 magmatic mineral lineation is well developed and represented by the
491 alignment of long axes of the centimetric tabular K-feldspar megacrysts.
492 This lineation dips with $\sim 20^\circ$ towards the E (Fig.13). Differently, the
493 matrix (of millimetre size) does not show any evident linear anisotropy.
494 Grd1 fabrics is also characterised by folds (Fig 14b). At the microscope
495 scale, rare fractures in coarse K-feldspar are sealed with quartz,
496 feldspars and biotite (Fig.14c).
497 Elongate enclaves, folds and fractures are interpreted as melt-present
498 deformation features (Bouchez et al., 1992; Tobisch et al., 1997;
499 Paterson et al., 1998) of the K-feldspar megacrystals-bearing
500 granodiorite.
501 Locally, in the K-feldspar-bearing granodiorite, tiling of feldspar
502 phenocrysts suggests that shearing was active during magmatic flow. In
503 addition, at one locality, the distribution of K-feldspar long axes is
504 asymmetric (Fig.15)

505

506 Figure 15

507

508 with respect to the magmatic foliation. From this asymmetry, together
509 with the local occurrence of tiling structures, a top-to-the-W sense of
510 shear during magmatic flow can be inferred, following criteria adopted in
511 other studies (Blumenfeld and Bouchez, 1988; Ildefonse and Fernandez,
512 1988; Vernon, 2000; Spanner and Kruhl, 2002).

513

514 6.2 Structures transitional from magmatic to solid-state

515 Here we describe structures that formed during cooling and
516 crystallization of magmas in a regional stress field that also affected
517 the

517 wall rocks.

518 In the foliated granitoids, structures testifying a continuum from HT to
519 LT

519 deformation conditions have been recognised. Deformation temperatures
520 are provided by the commonly observed chessboard pattern (Fig.16a)

521

522 Figure 16

523

524 of quartz in all the granodiorites. This type of prism- and basis-parallel
525 subgrain- boundary pattern solely develops in the stability field of
high526

quartz (Kruhl, 1996). Since the boundary between low- and high-quartz
527 is at $\sim 700^\circ\text{C}$ at ~ 5 Kbar - the approximate pressure of intrusion for the
528 sheared granitoids (Caggianelli et al., 1997) - a minimum temperature
529 of deformation of $\sim 700^\circ\text{C}$ is indicated.

530 Universal-stage measurements of quartz c-axis have been carried out on
531 samples from migmatitic paragneiss (Fig. 17b),

532

535 foliated tonalites (Fig. 17a, c and d) and granodiorites (17e-h). The
 536 crystallographic preferred orientations (CPOs) show mostly a monoclinic
 537 symmetry. Three different point maxima have been recognized: (i) a pair
 538 of point maxima with angles of $\sim 100^\circ$ - 130° across strain-Z (Fig. 17a-h);
 539 (ii) point maxima close to strain-Z (Fig. 17b-d, g and h); (iii) point
 540 maxima close to strain Y (Fig. 17a-e and g). These point maxima are
 541 generally referred to the activation of prism [c], basal <a> and prism
 542 <a> slip systems, respectively (e.g., Garbutt and Teyssier, 1991, and
 543 references therein).

544 Again, these opening angles indicate deformation temperatures of about
 545 700°C (Kruhl, 1998), in agreement with the temperatures inferred from
 546 quartz chessboard pattern.

547 A top-to-the-W shear sense both in migmatitic paragneiss and in syn548
 tectonic plutonic rocks (Fig. 17a-c, e and f) can be deduced from
 549 different densities of point maxima related to prism [c] glide system in
 550 most samples (e.g.: Schmid and Casey, 1986). This shear sense is
 551 coherent with outcrop- and micro-scale kinematic indicators.
 552 In some samples (i.e. Fig. 17a and c) orientation of point maxima
 553 located near strain-Z is coherent with top-to-the-W shear sense along
 554 the basal <a> slip system, as already deduced from maxima related to
 555 prism [c] slip system. In other samples (Fig. 17b, d and g), strong point
 556 maxima located close to strain-Z apparently suggest a contrasting shear
 557 sense. This contradiction may be explained by the fact that, starting
 558 from the initial high temperature maxima, the quartz c-axis would
 559 necessarily rotate toward strain Z, due to dominant activity of basal <a>
 560 glide during low temperature coaxial flattening (Garbutt and Teyssier,
 561 1991; Duguet and Faure, 2004).

562 Evidence of prismatic <a> slip, indicated by c-axis maxima subparallel to
 563 strain Y (Fig.17 a-e and g), is consistent with deformation at
 564 intermediate to high temperatures (Stipp et al., 2002).

565 Summing up, c-axis CPOs are coherent with solid-state deformation at
 566 high to low temperature conditions. c-axis patterns can be explained by
 567 the dominance of prism <c> glide at high temperatures or by transition
 568 from dominant prism <c> to prism <a> to basal <a> slip systems at
 569 decreasing temperatures.

570

571 6.3 Structures at medium- to low-temperature solid-state conditions

572 Deformation under decreasing temperatures is pointed out by coarse573
 grained (Fig.16b) as well as fine-grained recrystallization of feldspars,
 574 widespread occurrence of myrmekite (Fig.16c), and grain-boundary
 575 migration recrystallization in the quartz ribbons (Fig.16d), especially
 in

576 the heterogranular granodiorite (Grd2). In this rock the solid-state
 fabric

577 is defined by strong alignment of biotite plates and the flat faces of
 578 lenticular feldspars and elongate quartz aggregates (Fig. 16e). Locally,
 579 the Grd2 displays S/C fabrics (Berthé et al., 1979), pointed out by
 biotite

580 films and thin quartz-feldspar layers (Fig. 16f). Mineral lineation (about
 581 85/25) is mainly indicated by quartz and feldspar long axes. S/C fabrics,

13

582 delta- and sigma-type feldspar porphyroclasts confirm a top-to-the-west
583 sense of shear.

584

585 6.4 Structures in the wall-rocks

586 In the migmatitic paragneisses the main foliation is generally oriented
587 45/40 (Fig.13). This is defined by the compositional layering of well
588 aligned fine-grained mica, sillimanite and cordierite, alternating with
589 quartz-feldspar-rich bands. Hinges of intrafolial folds are rare, probably
590 due to the intense transposition during deformation.

591 The mineral lineation, oriented 85/25 on average (Fig.13) is defined by
592 long axes of sillimanite, cordierite, biotite, and quartz grains. This
593 peak

metamorphic mineral assemblage (Graessner and Schenk, 2001)

594 indicates that foliation as well lineation were formed during maximum
595 temperature conditions of 740°-770°C. A widespread crystallization of
596 post-kinematic white mica and fibrous sillimanite can be observed (Fig.
597 18a,b).

598

599 Figure 18

600

601 Rims of garnet porphyroblasts are replaced by cordierite, indicating
602 decompression, as well as biotite-sillimanite aggregates, indicating
603 cooling (Graessner and Schenk, 2001). The occurrence of cordierite,
604 biotite and sillimanite in garnet pressure shadows points to continuous
605 deformation during decreasing pressure and temperature. .-type garnet
606 porphyroclasts, mica-fishes and c-axis analyses (Fig.17b) indicate top
607 to-the-west sense of shear.

608

609

610 7. DISCUSSION

611 The relationships among the different magmatic rocks are sketched in
612 Fig. 19.

613

614 Figure 19

615

616 The chronology of emplacement is based on field relationships, by which

617 the Grd1 and the Grd2 are considered the first magmatic bodies to be
618 emplaced. Then, the Grd3 injected both previous granodiorites still in
619 melt-present conditions. The sequence of injections continued with the
620 tonalite magma and afterwards with the granite dykes. The emplacement
621 of the hornblende-gabbro is interpreted as a late magmatic episode with
622 respect to the deformation history in the granodiorites, tonalites and
623 granites. The injection sequence ended with the emplacement of non
624 foliated post-kinematic leucogranite, pegmatite and porphyritic dykes.
625 Meso- and micro-structural observations suggest that shearing of wall
626 rocks and magmatic intrusions occurred under the same kinematic
627 conditions during injection of Grd1, Grd2, Grd3, tonalite and granite
628 magmas and during their subsequent cooling. The period of deformation
629 can be encompassed between the age of emplacement of the syn

kinematic granitoids (granodiorites, tonalite and granite) and of the undeformed leucogranite, pegmatites and porphyritic dykes. Age of emplacement of granodiorites, tonalite and granite is regionally well constrained by U/Pb datings at 304–300 Ma; within this time range, the dates near the study section are also encompassed (Graessner et al., 2000). Shearing of the magmas therefore is considered active during emplacement. Then, since leucogranite pegmatites and porphyritic dykes intrude older foliated magmatic and wall-rocks throughout the whole Sila Massif (Ayuso et al., 1994), we reasonably assume that the age of 281±8 Ma from the porphyritic dyke located close to the Arvo Lake (Fig.1), could at least represent a minimum age for the end of shear deformation. Following this view, injection and shear strain history took place over a period of about 20 Ma although a shorter time range cannot be ruled out. Concerning the tectonic context in which the deformation and emplacement developed, the following considerations can be argued. The late-Hercynian Calabrian crust is palaeogeographically related to the French Massif Central and Sardinia Massif (Matte, 1986; 2001; Stampfli and Borel, 2002; Von Raumer et al., 2002). Petrologic, structural and kinematic data indicate that collision occurred around 350–320 Ma with pressure of 2 GPa at least in Sardinia (Giacomini et al., 2005) or of about 3 GPa in the French Massif Central (Lardeaux et al., 2001). In Sardinia and French Massif Central, ages around 300–310 Ma mark the turning point from contraction to post-collisional extension, favouring the emplacement of syn- to post-tectonic granitoids and the achievement of the metamorphic peak conditions. Then, isothermal exhumation and isobaric cooling followed (Carmignani et al., 1994; Burg et al., 1994; Faure, 1995; Ledru et al. 2001; Di Vincenzo et al., 2004, among many others). Also the late-Hercynian Calabria evolution is typified by the coexistence between magmatism and peak metamorphic conditions at ~ 300 Ma, followed by isothermal decompression and isobaric cooling. The Calabria peak metamorphism is estimated at about 4–6 kbar (Schenk, 1984; Schenk, 1989; Graessner et al., 2000; Graessner and Schenk, 2001) or at about 7 kbar (Acquafredda et al., 2006). Schenk (1984) and Graessner and Schenk (2001) suggested that emplacement of granitoids and the Calabria peak metamorphic conditions can be developed during contractional tectonics. According to these authors, compression developed in an Andean-type geodynamic context, determining crustal doubling, heating, partial melting of the overridden plate and high geothermal gradient in the upper crust (~ 60°C/km). Then, erosion was responsible for the isothermal exhumation. It implies that the thickening of the crust was occurring at about 300 Ma, almost 30–50 Ma later than the Hercynian collision in Sardinia and French Massif Central. However, the magma intrusion would postdate the age of the Palaeozoic phyllite metamorphism in the Sila massif (dated at about 330 Ma: Acquafredda et al., 1991, 1992).

Alternatively, as also indicated by Schenk and Graessner (2001), a postcollisional extensional tectonics (Caggianelli and Prosser, 2001) can be

15

679 considered. In this tectonic context, also the low- to medium-pressure
680 metamorphism characterising the Calabrian late-Hercynian mid-crust
681 could be easily framed.
682 Structural and kinematic data collected in the study area do not help to
683 constrain the geodynamic setting, in which shearing and injection
684 occurred; however, the metamorphic conditions in which shearing
685 developed and the similarities with the evolutions of Sardinia and Central
686 Massif suggest extensional tectonics during magma emplacement.
687 Furthermore, the occurrence of norite enclaves in the Grd1 rocks and the
688 broad tendency of the syn-tectonic injections towards mafic
689 compositions, account for a progressive involvement of the lithospheric
690 mantle in the melting process, as it is typical during lithospheric
thinning.
691 In this framework, magma underplating would provide an additional
692 source of heating, favouring high geothermal gradient and crustal
693 magma generation.

694

695 8. CONCLUDING REMARKS

696 Syn-tectonic and post-tectonic magmatic rocks have been recognised in
697 a mid-crustal section. Field data suggest that multiple injections of
698 magmas occurred in crystallizing granitoids while shear strain was
699 ongoing. The broad tendency toward a basic composition of magmas,
700 suggest a progressive involvement of the mantle in the melting process.
701 High-temperature deformation affected both crystallizing magmas and
702 wall rocks. Meso- and micro-structural data in the study area document
703 continuous progression of deformation under decreasing temperatures,
704 within the same kinematic framework.
705 The period of time over which magma injection and shear strain
706 coexisted is enclosed between the emplacement of the syn-kinematic
707 granitoids (304-300 Ma) and emplacement of undeformed porphyritic
708 dyke (281±8 Ma). Therefore shear strain developed over a period of ~20
709 Ma as a maximum.
710 From our data, no conclusive considerations on the tectonic context can
711 be proposed: however extension could provide a tectonic evolution
712 similar to the one characterising other sectors of the southern European
713 Hercynian belt.

714

715

716

717 APPENDIX

718

719 Geochronological method

720 Sample has been completely crushed and zircons were separated using
721 conventional heavy liquid and magnetic techniques. Crystals were
722 selected by handpicking under a binocular microscope, mounted in epoxy
723 resin and polished down to expose the major surface of crystal. The
724 selection of zircons for isotope analyses was done on the basis of
725 cathodoluminescence (CL) images acquired with a SEM at the
726 Department of Earth Science in Siena (Accelerate voltage 20-25 kv).
727 Geochronological data were performed using a LA-ICP-MS system

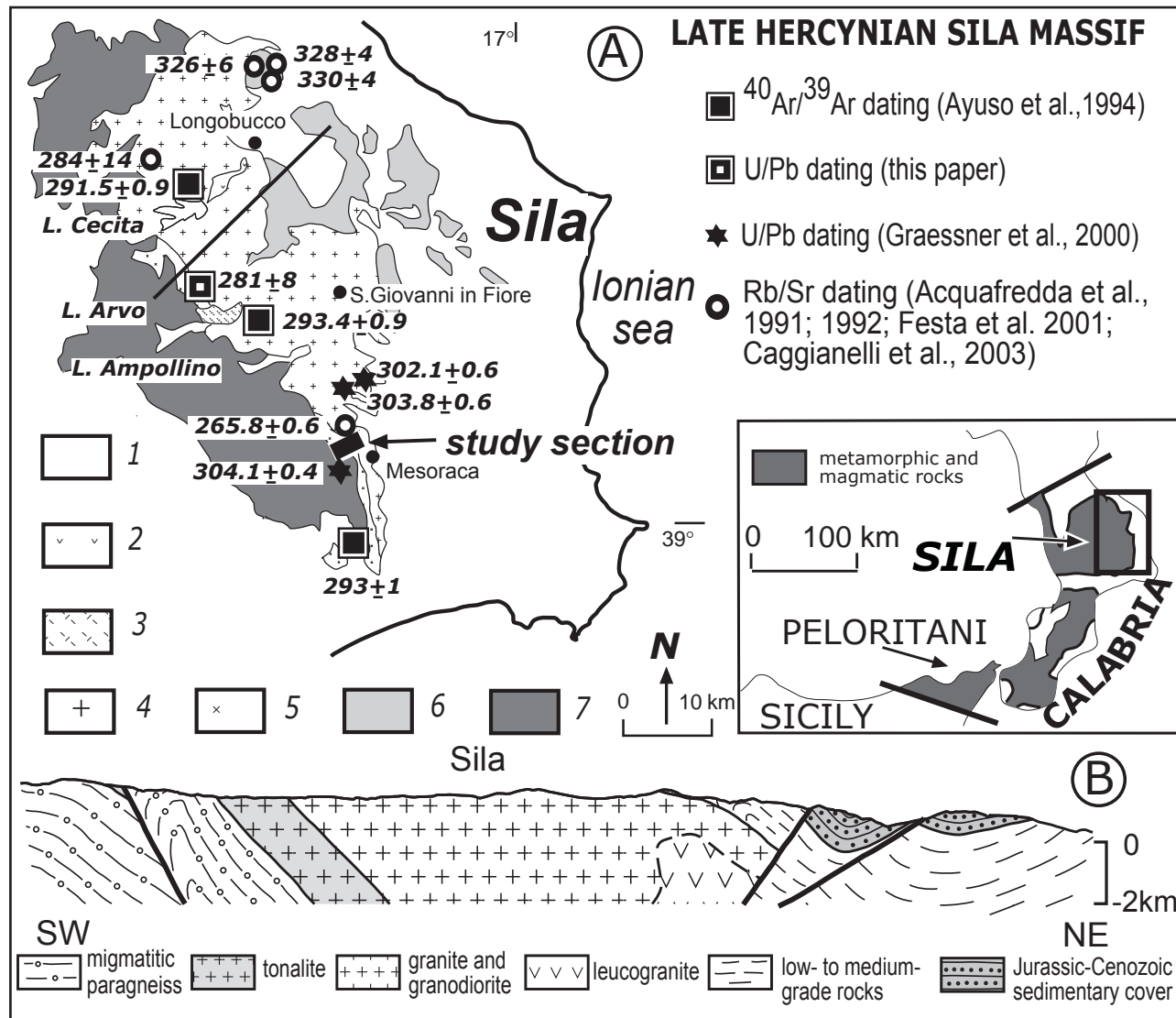


FIGURE 1 - Liotta et al.

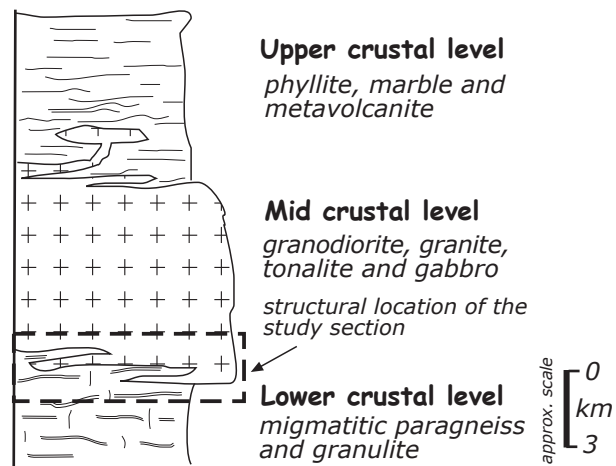


Figure 2 - Liotta et al.

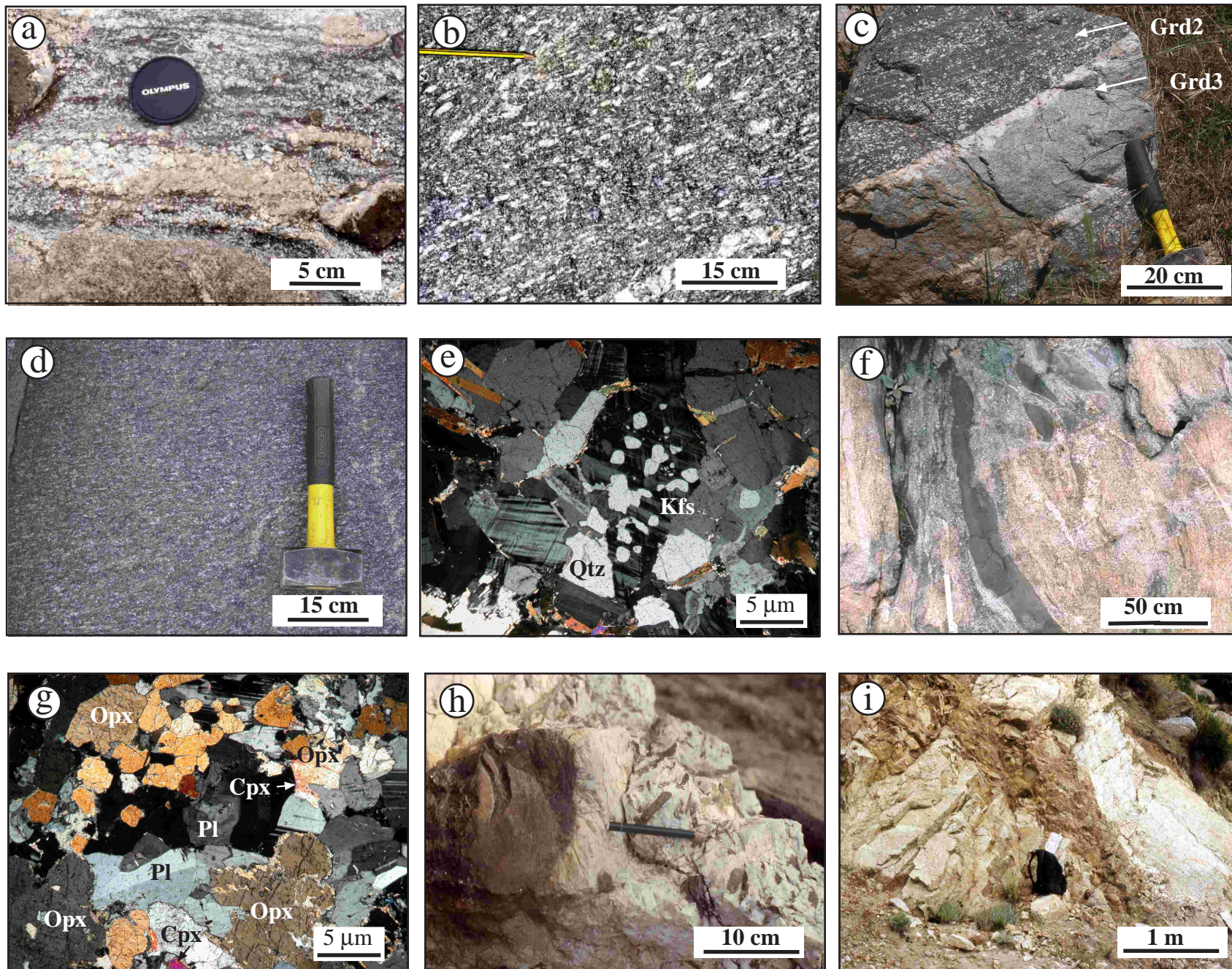


Figure 3 - Liotta et al.

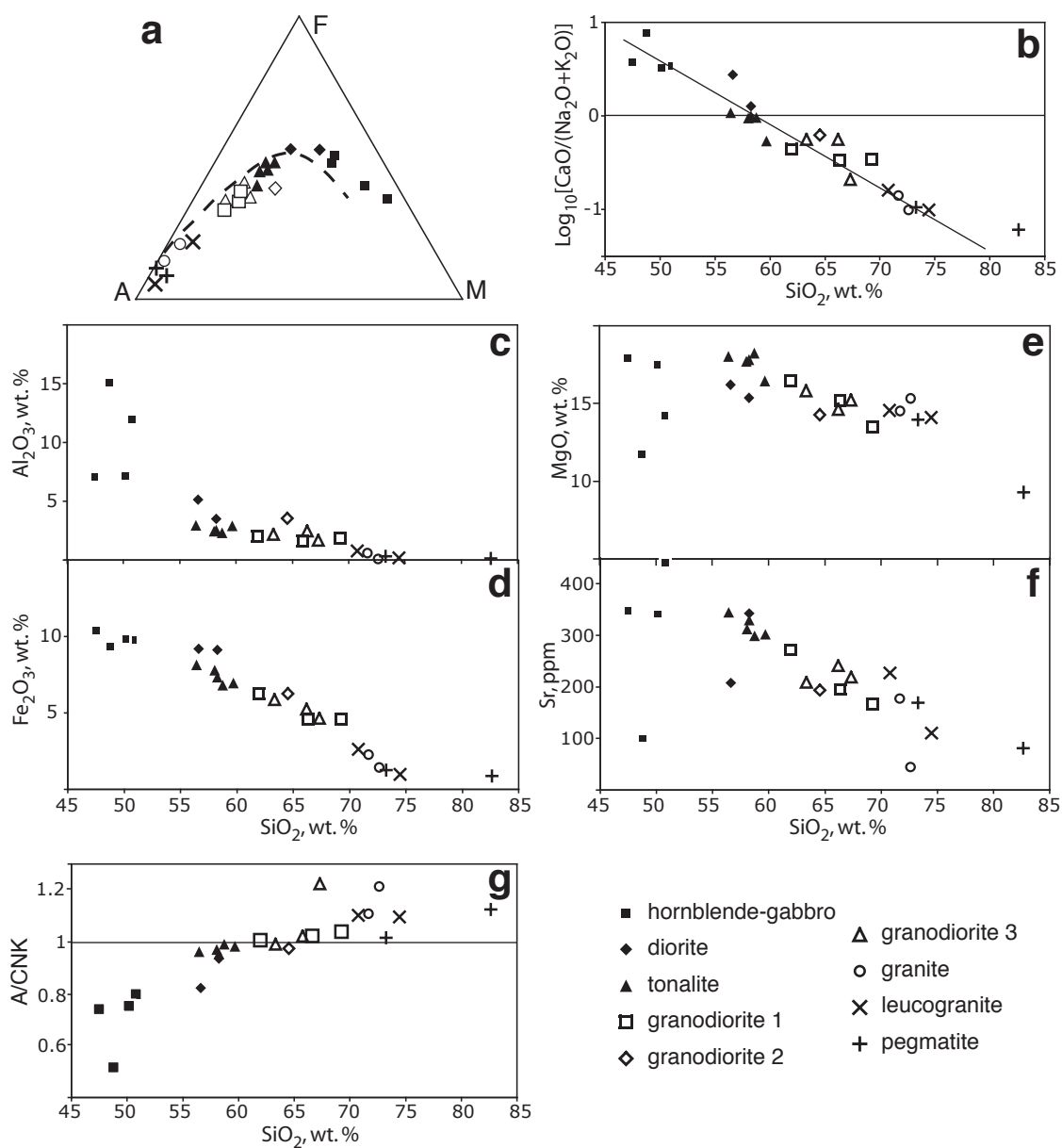


FIGURE 4 - Liotta et al.

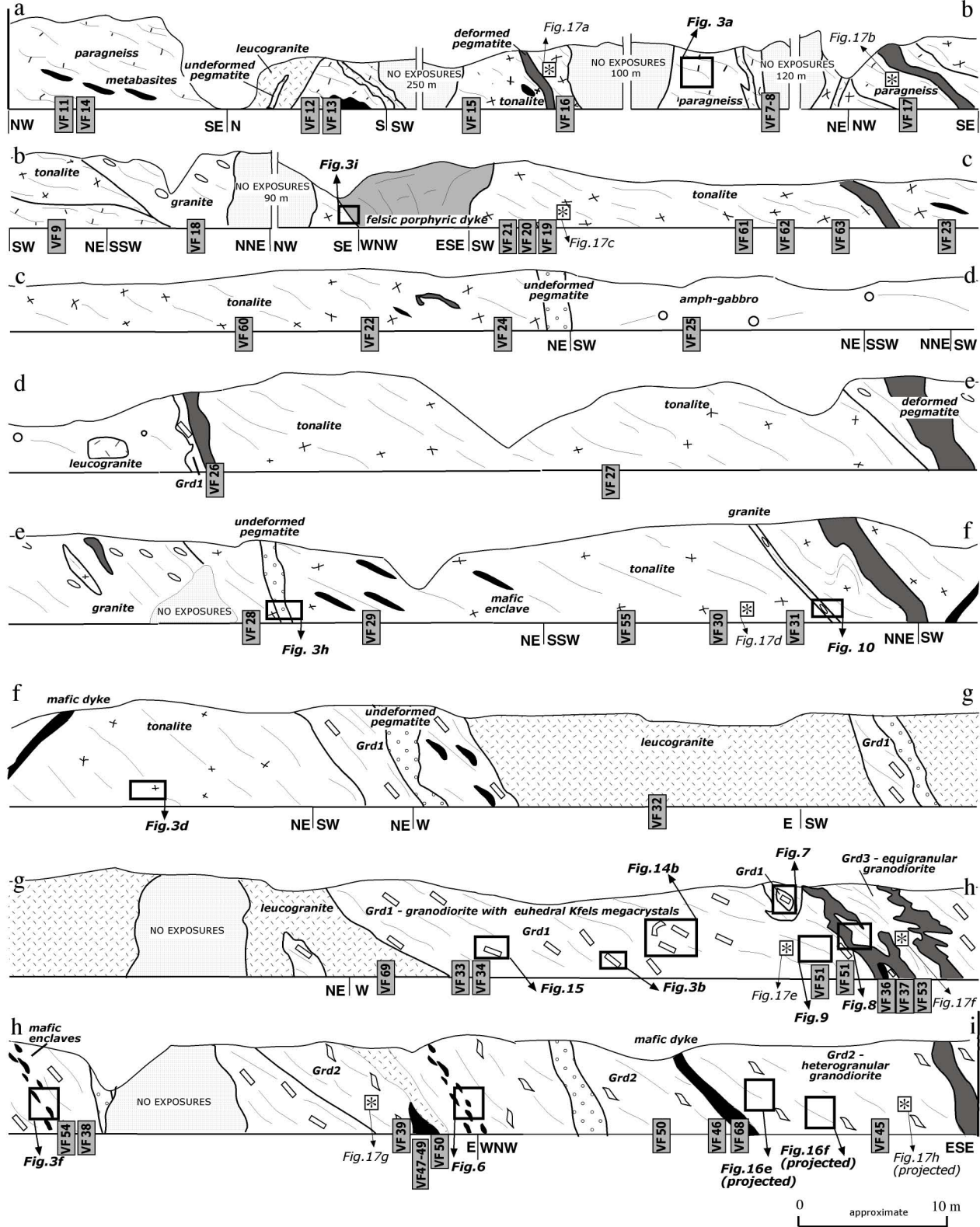


Figure 5 – Geologic profile along the study section; the structural relationships and foliation attitude are displayed. Locations of samples for thin section analysis (from VF7 to VF68), outcrop photographs (squares) and samples for the quartz c-axis orientations (stars) are indicated.



Figure 6 – (a) Disrupted mafic dyke with crenulated margins in the Grd1 granodiorite; (b) Close-up of the previous image, showing an enclave in granodiorite, dismembered from the mafic dyke: granodiorite entrapped in the mafic enclave and vice-versa, indicates mixing/mingling processes; outcrop location in Fig.5, h-i.

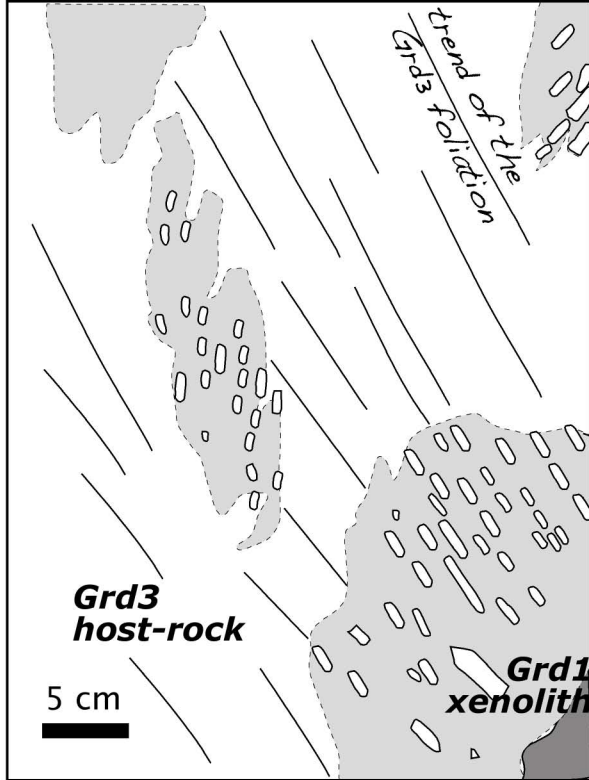


Figure 7 – Relationship between the Grd1 and Grd3 granodiorites. (a) Grd1 granodiorite enclaves in the equigranular Grd3 granodiorite and (b) structural sketch. The Grd3 foliation does not deflect around the enclaves, suggesting that the enclaves were not solid object when they were included in the Grd3 granodiorite. Outcrop location in Fig.5, g-h.

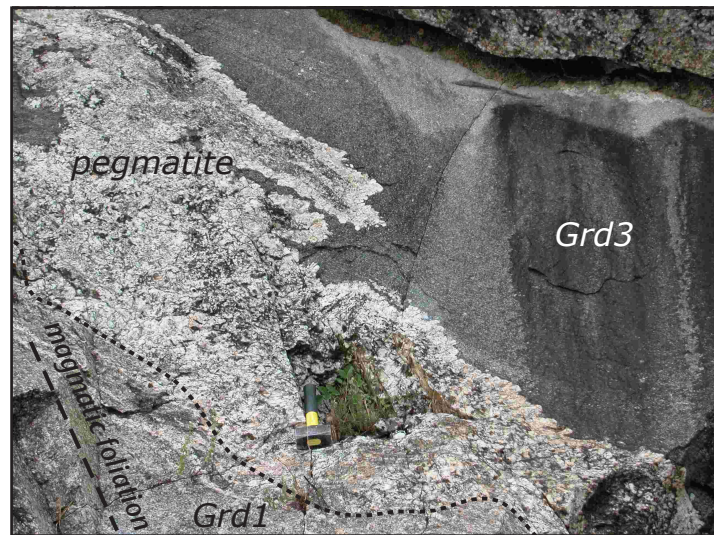


FIGURE 8 - Liotta et al.

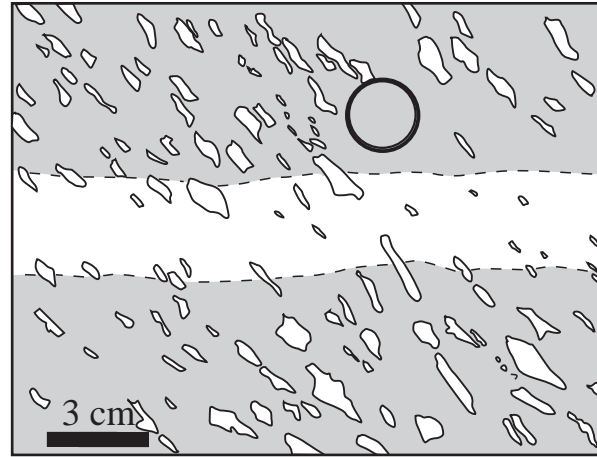
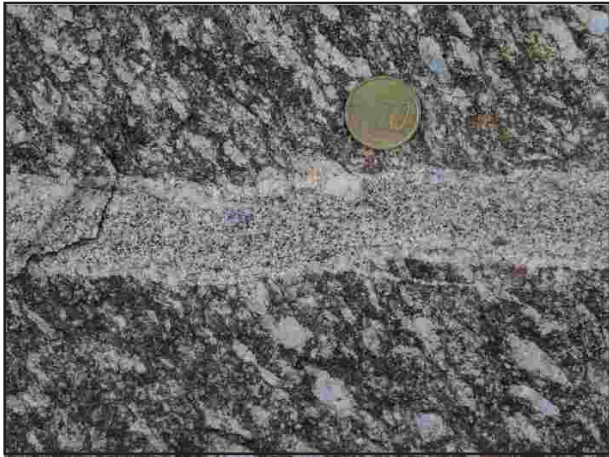


Figure 9 - Liotta et al.

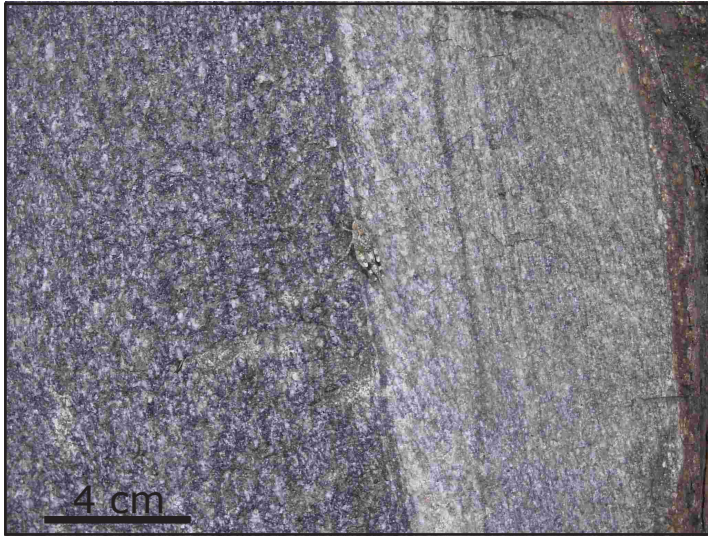


Figure 10 - Liotta et al.

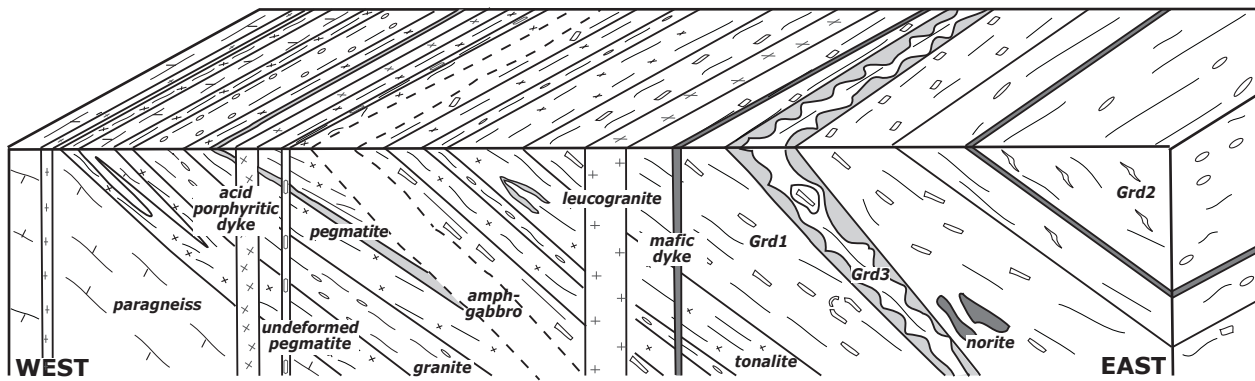


FIGURE 11 - Liotta et al.

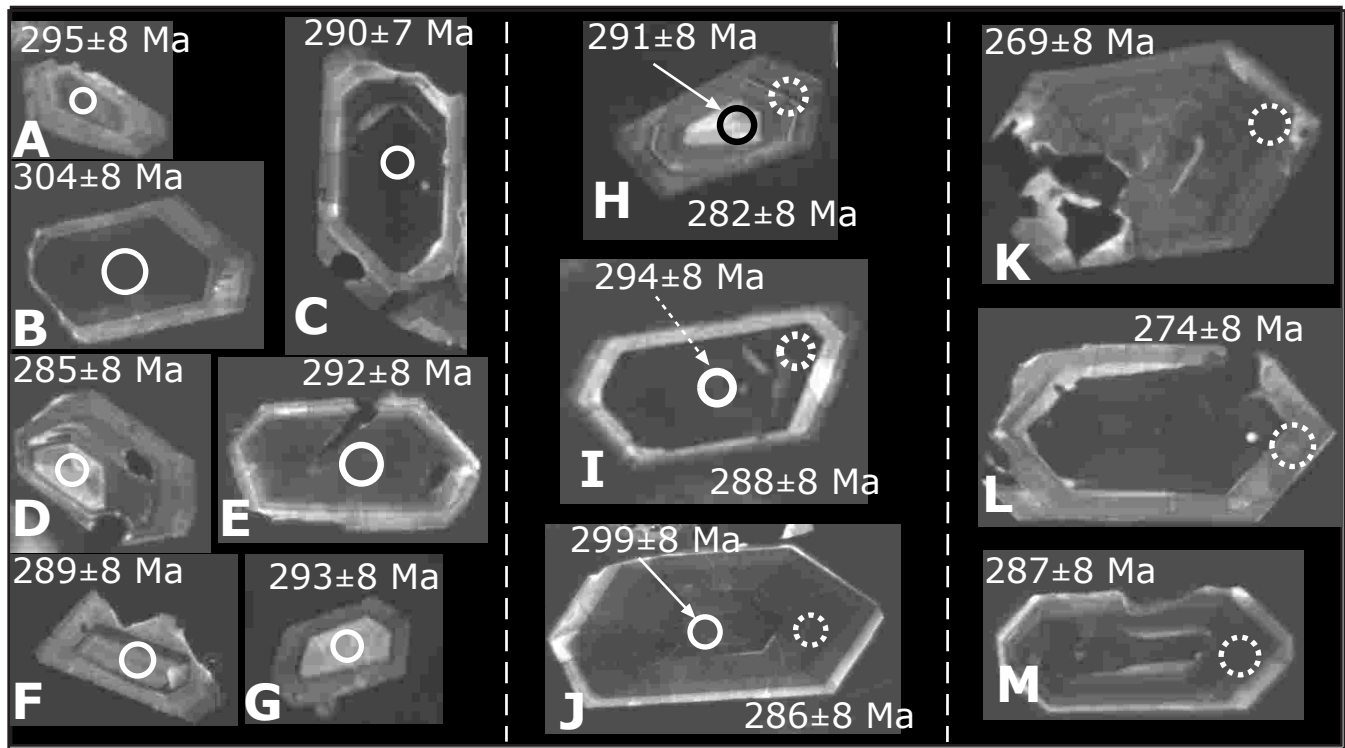


Figure 12 - Liotta et al.

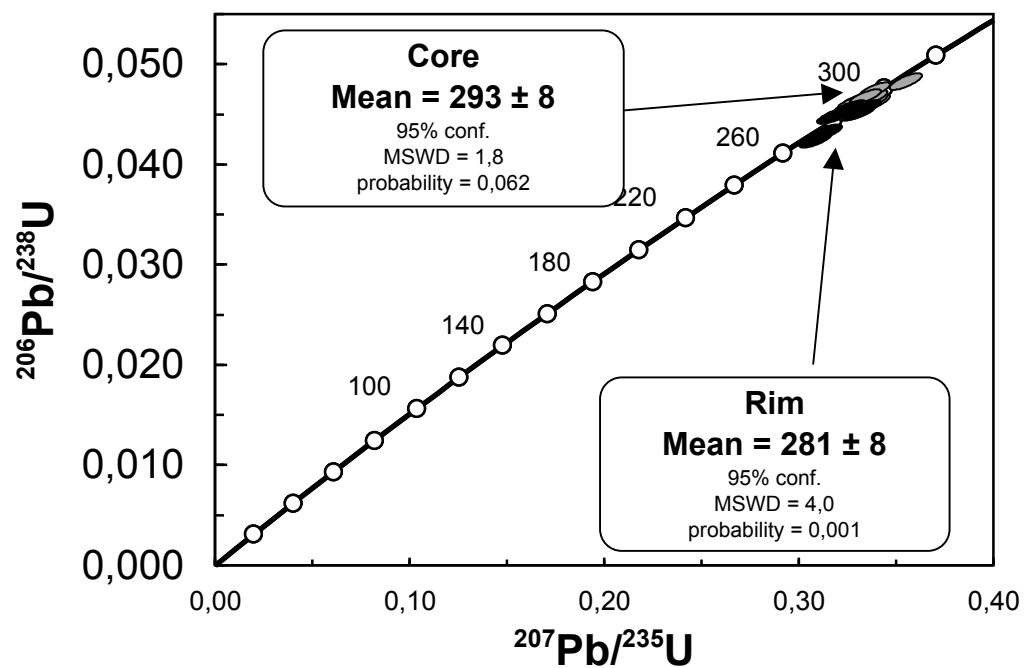


FIG. 13 - LIOTTA et al.

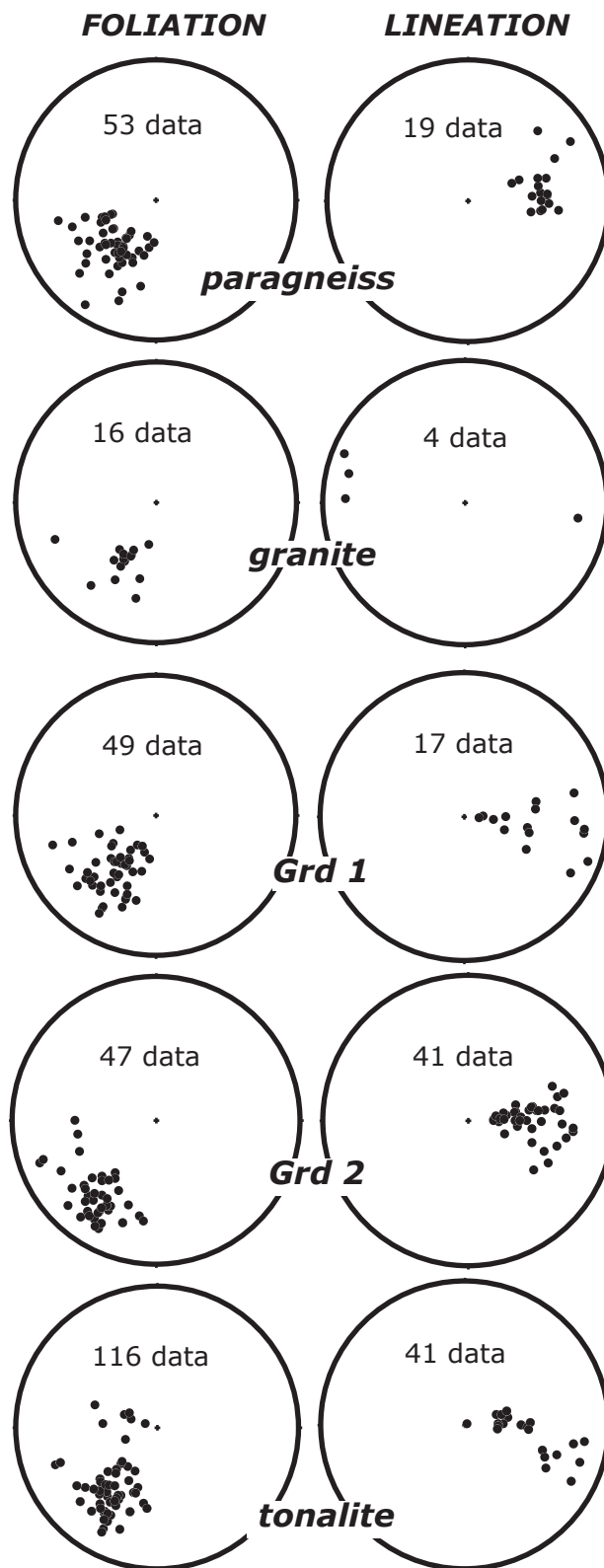


Figure 14 - Liotta et al.

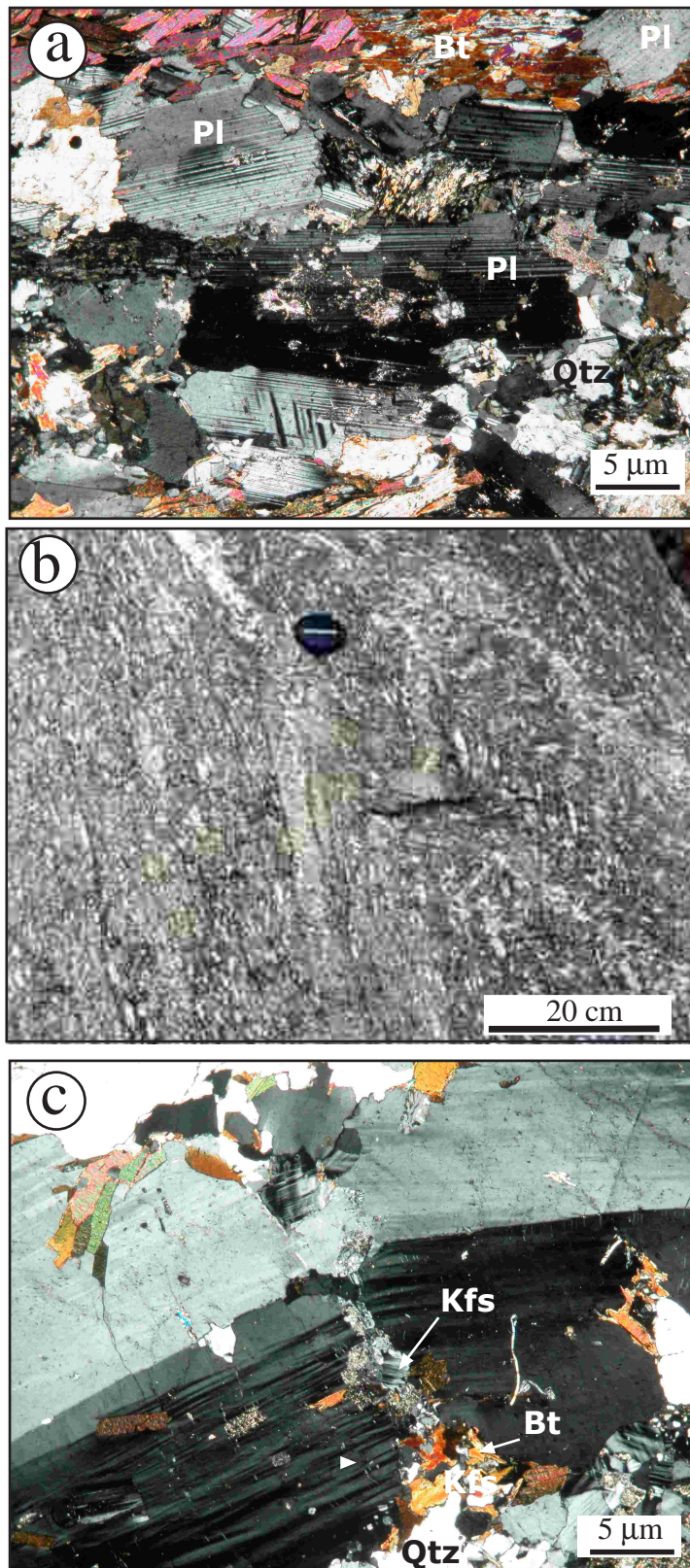


Figure 15 - Liotta et al.

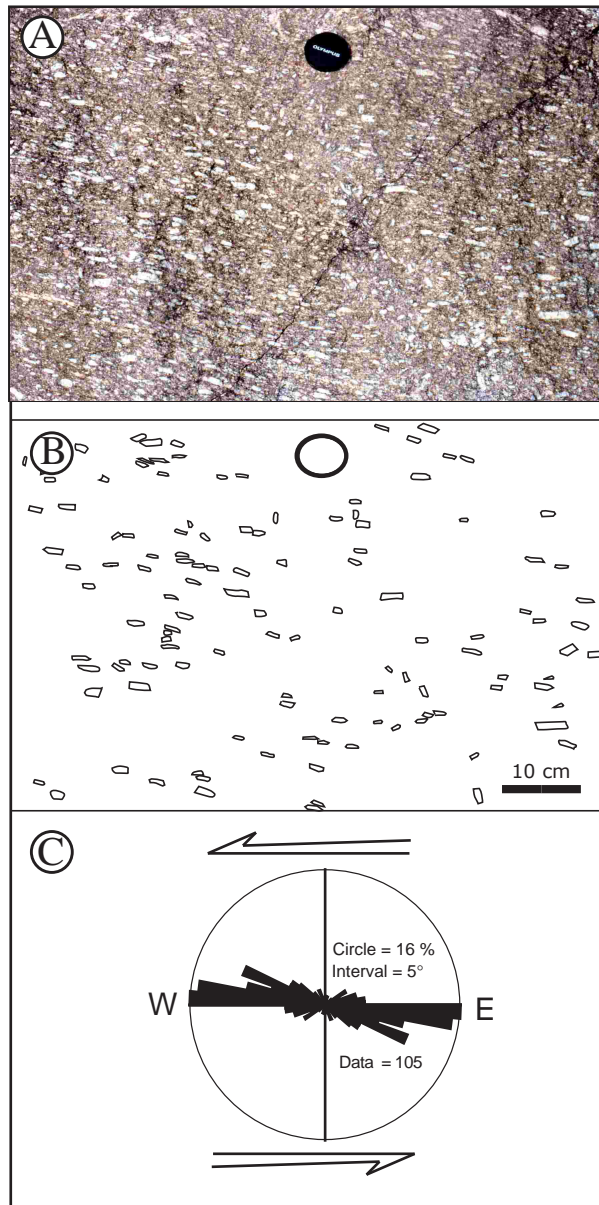


Figure 16 - Liotta et al.

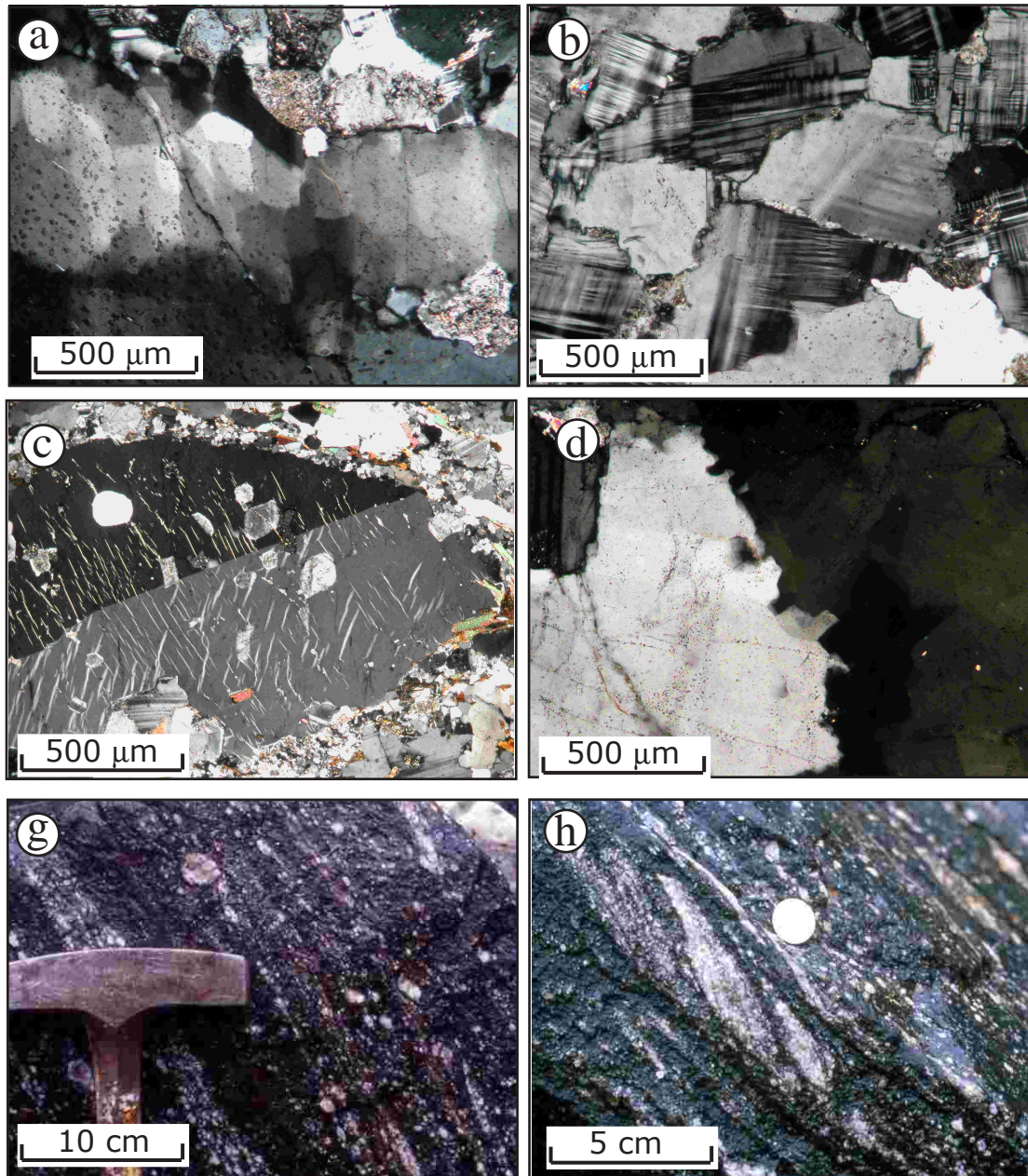


Figure 17 - Liotta et al.

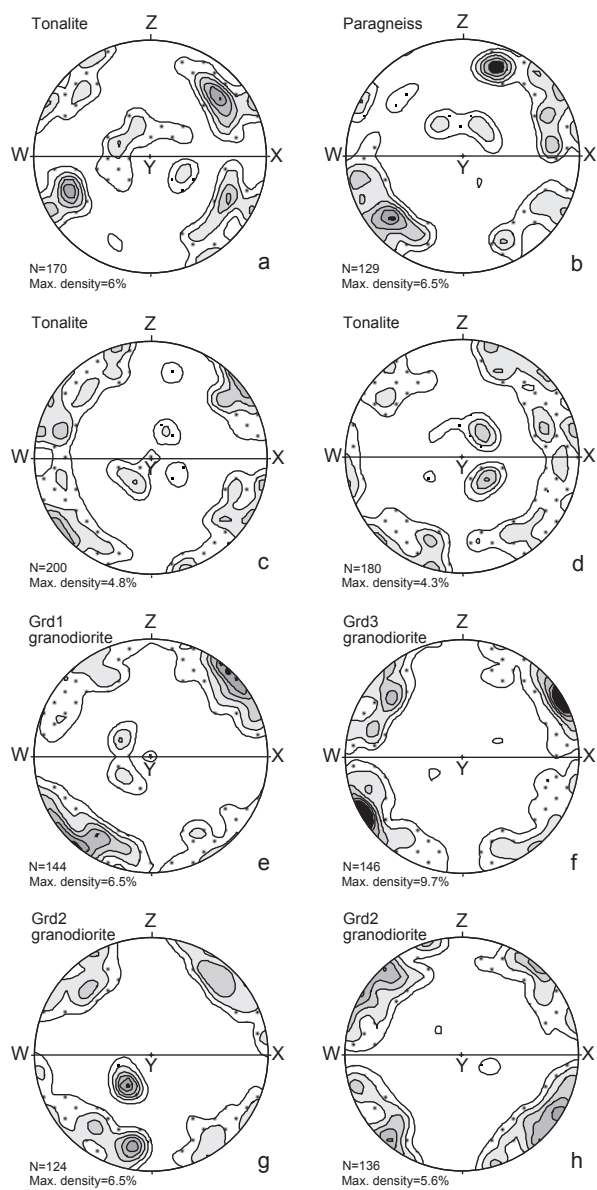


FIGURE 18 - Liotta et al.

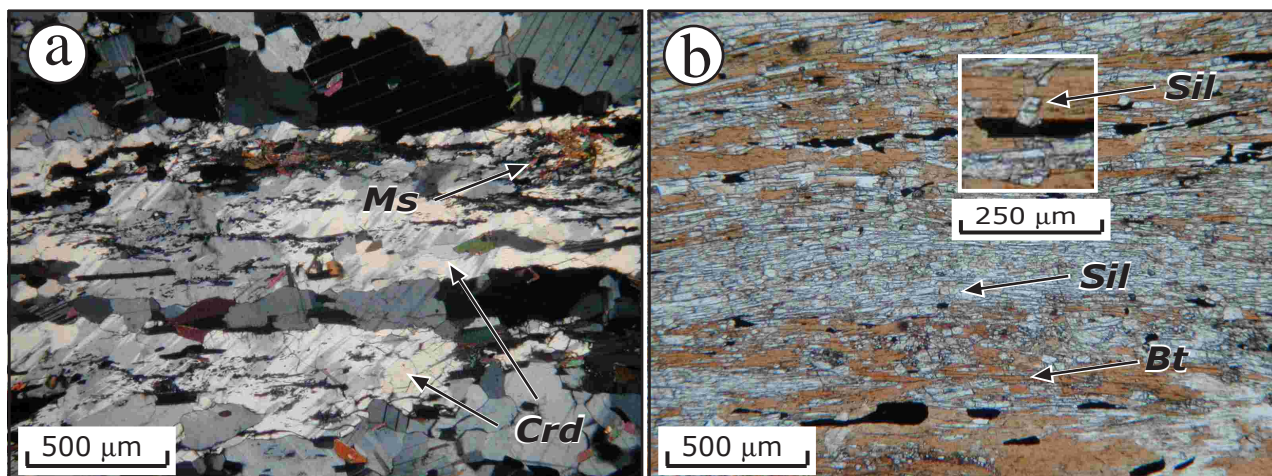


Figure 19 - Liotta et al.

	Amph - gabbro	dioritic enclave	tonalite	1	granodiorite 2	3	granite	leucogranite	pegmatite
wt. %									
SiO ₂	47.49	56.61	58.25	66.36	64.64	67.41	72.61	74.56	82.73
TiO ₂	1.11	0.94	1.21	0.77	1.24	0.83	0.10	0.13	0.03
Al ₂ O ₃	17.91	16.20	17.83	15.14	14.2	15.15	15.34	14.03	9.22
Fe ₂ O ₃	10.38	9.21	7.35	4.59	6.20	4.58	1.44	0.92	0.79
MnO	0.18	0.20	0.11	0.10	0.12	0.10	0.07	0.06	0.09
MgO	7.04	5.13	2.56	1.70	3.47	1.60	0.09	0.08	0.06
CaO	10.98	8.34	5.86	2.64	3.61	1.56	0.86	0.86	0.38
Na ₂ O	1.86	2.28	2.99	2.75	2.93	2.41	3.10	2.86	1.15
K ₂ O	1.07	0.74	2.87	5.06	3.00	5.20	5.52	6.08	5.21
P ₂ O ₄	0.13	0.16	0.41	0.40	0.24	0.17	0.21	0.16	0.11
L.O.I.	2.03	0.33	0.56	0.67	0.56	1.28	0.79	0.69	0.24
TOT	100.18	100.14	100.00	100.18	100.21	100.29	100.13	100.43	100.01
A/CNK	0.74	0.82	0.95	1.02	0.97	1.21	1.21	1.09	1.12
ppm									
Rb	47	32	136	185	120	197	179	190	92
Sr	347	208	329	194	191	217	44	108	78
Y	37	33	21	36	38	23	9	5	6
Zr	66	110	418	334	274	263	19	48	18
Nb	7	7	18	19	18	17	16	5	1

Table 1 - Liotta et al.

Table 2: LA-ICP-MS analytical results

Zircon	$^{206}\text{Pb}/^{238}\text{U}$		$^{207}\text{Pb}/^{235}\text{U}$		$^{207}\text{Pb}/^{206}\text{Pb}$		$^{208}\text{Pb}/^{232}\text{Th}$	
	Ratio	1 σ (%)	Ratio	1 σ (%)	Ratio	1 σ (%)	Ratio	1 σ (%)
Zr A core	0,047	1,40	0,334	1,91	0,052	1,51	0,015	1,88
Zr B core	0,048	1,38	0,349	1,83	0,052	1,44	0,016	1,87
Zr C core	0,046	1,31	0,325	1,84	0,051	1,49	0,014	1,83
Zr D core	0,045	1,40	0,327	1,90	0,053	1,52	0,014	1,89
Zr E core	0,046	1,47	0,336	1,89	0,053	1,45	0,014	1,88
Zr F core	0,046	1,46	0,329	1,93	0,052	1,50	0,014	1,92
Zr G core	0,046	1,46	0,334	1,99	0,052	1,58	0,014	1,92
Zr H core	0,046	1,38	0,327	1,88	0,051	1,51	0,015	1,88
Zr H rim	0,045	1,39	0,316	1,86	0,051	1,47	0,015	1,87
Zr I core	0,047	1,37	0,332	1,81	0,051	1,41	0,015	1,84
Zr I rim	0,046	1,43	0,329	1,88	0,052	1,45	0,014	1,89
Zr J core	0,048	1,34	0,336	1,80	0,051	1,43	0,016	1,84
Zr J rim	0,045	1,35	0,326	1,81	0,052	1,43	0,014	1,86
Zr K rim	0,043	1,51	0,307	2,00	0,052	1,55	0,013	1,92
Zr L rim	0,043	1,40	0,312	2,00	0,052	1,66	0,014	1,90
Zr M rim	0,046	1,46	0,322	1,88	0,051	1,44	0,014	1,90

TABLE 2 - LIOTTA et al.

Table 3: LA-ICP-MS age results

	$^{206}\text{Pb}/^{238}\text{U}$		$^{207}\text{Pb}/^{235}\text{U}$		Concordant age				$^{207}\text{Pb}/^{206}\text{Pb}$		$^{208}\text{Pb}/^{232}\text{Th}$	
	Age (Ma)	1 σ error	Age (Ma)	1 σ error	Age (Ma)	2 σ error	MSWD	Prob.	Age (Ma)	1 σ error	Age (Ma)	1 σ error
Zr A core	295	4	293	6	295	8	0.34	0.56	281	4	292	5
Zr B core	305	4	304	6	304	8	0.04	0.85	298	4	318	6
Zr C core	291	4	286	5	290	7	2.60	0.11	255	4	282	5
Zr D core	285	4	288	5	285	8	0.59	0.44	309	5	285	5
Zr E core	292	4	294	6	292	8	0.60	0.42	312	5	286	5
Zr F core	289	4	289	6	289	8	0.07	0.80	280	4	286	5
Zr G core	293	4	293	6	293	8	0.02	0.97	296	5	285	5
Zr H core	292	4	287	5	291	8	2.30	0.13	251	4	292	5
Zr H rim	283	4	279	5	282	8	2.40	0.12	242	4	293	5
Zr I core	295	4	291	5	294	8	1.90	0.17	259	4	294	5
Zr I rim	288	4	289	5	288	8	0.01	0.93	294	4	284	5
Zr J core	300	4	294	5	299	8	3.00	0.085	251	4	316	6
Zr J rim	286	4	287	5	286	8	0.20	0.65	297	4	283	5
Zr K rim	269	4	272	5	269	8	1.30	0.26	301	5	264	5
Zr L rim	273	4	275	6	274	8	0.31	0.58	287	5	278	5
Zr M rim	288	4	283	5	287	8	3.00	0.09	238	3	276	5

TABLE 3 – Liotta et al.

APPENDIX 7: GEOCHRONOLOGIC DATING

U, Th and Pb isotopic compositions analyses of zircon and monazite have been performed at the CNR-Istituto di Geoscienze e Georisorse of Pavia (Italy) using a 213 nm LAM coupled with a magnetic sector ICP-MS (Tiepolo *et al.*, 2003).

Zircons have been separated from 5-6 kg of fresh rock material using standard techniques (steel jaw-crusher, roller mill, hydrodynamic separator, Frantz magnetic separator, heavy liquids) at the Dipartimento di Scienze della Terra e Geologico-Ambientali, University of Bologna. Crystals have been selected by handpicking under a binocular microscope, mounted in epoxy resin and polished down to expose the major surface of crystal. Analytical spots of 10 and 25µm have been selected after the characterisation of zircons under transmitted light and on the basis of cathodoluminescence (CL) images. CL images have been acquired with a Philips XL30 electron microscope equipped with a cathodoluminescence (CL) detector (Dipartimento di Scienze della Terra, Università di Siena). Operating conditions for CL imaging were an accelerating voltage of 20-25 kV with a variable spot size.

Monazite crystals have been analysed directly on selected thin sections of micaschists and paragneisses. Before the isotopic analyses, monazite crystals have been characterised (dimensions, microstructural position and internal structures) using an SEM at the Dipartimento di Scienze della Terra e Geologico-Ambientali, University of Bologna. Isotopic analyses have been performed using an analytical spot of 5µm. Analytical details and results are reported in **Table 20-24**.

Spot	Isotopic ratios					Age estimates (Ma)					Concordia							
	$^{207}\text{Pb}/^{206}\text{Pb}$	$\pm 1\sigma$	$^{206}\text{Pb}/^{238}\text{U}$	$\pm 1\sigma$	$^{207}\text{Pb}/^{235}\text{U}$	$\pm 1\sigma$	$^{208}\text{Pb}/^{232}\text{Th}$	$\pm 1\sigma$	$^{207}\text{Pb}/^{206}\text{Pb} \pm 1\sigma$	$^{206}\text{Pb}/^{238}\text{U} \pm 1\sigma$	$^{207}\text{Pb}/^{235}\text{U} \pm 1\sigma$	$^{208}\text{Pb}/^{232}\text{Th} \pm 1\sigma$	Age	$\pm 2\sigma$				
26Ac	0.05585	0.00122	0.07217	0.00104	0.55812	0.01246	0.02275	0.00119	446	10	449	6	450	10	455	24	449	12
26Ar	0.05623	0.00133	0.07202	0.00098	0.55826	0.01325	0.02309	0.00128	461	11	448	6	450	11	461	26	449	12
26Bc	0.06732	0.00115	0.14545	0.00198	1.34957	0.02371	0.03944	0.00204	848	14	875	12	867	15	782	40	870	20
26Br	0.06141	0.00104	0.10811	0.00139	0.91525	0.01570	0.03820	0.00210	654	11	662	9	660	11	758	42	661	15
26Cc	0.05758	0.00157	0.08241	0.00114	0.65410	0.01762	0.02131	0.00117	513	14	511	7	511	14	426	23	511	13
27Ac	0.07380	0.00161	0.17162	0.00233	1.74577	0.03815	0.04882	0.00255	1036	23	1021	14	1026	22	964	50	1023	24
27Ar	0.07152	0.00237	0.16531	0.00261	1.62607	0.05302	0.05517	0.00306	972	32	986	16	980	32	1085	60	985	28
27Bc	0.06838	0.00126	0.14716	0.00203	1.38600	0.02622	0.04054	0.00212	880	16	885	12	883	17	803	42	884	21
28Ac	0.05575	0.00199	0.07170	0.00113	0.55243	0.01951	0.01866	0.00109	442	16	446	7	447	16	374	22	446	13
28Ar	0.05604	0.00132	0.07345	0.00099	0.56757	0.01339	0.02207	0.00120	454	11	457	6	456	11	441	24	457	12
28Bc	0.07035	0.00299	0.18020	0.00301	1.74312	0.07517	0.04626	0.00267	939	40	1068	18	1025	44	914	53	1061	32
28Cr	0.06863	0.00101	0.15079	0.00193	1.42797	0.02229	0.04221	0.00221	888	13	905	12	901	14	836	44	901	19
29Ac	0.06559	0.00275	0.13048	0.00218	1.17629	0.05022	0.05089	0.00326	793	33	791	13	790	34	1003	64	791	25
29Ar	0.06503	0.00361	0.12854	0.00246	1.16032	0.06168	0.07574	0.00539	775	43	780	15	782	42	1476	105	780	28
29Bc	0.06154	0.00116	0.10106	0.00132	0.85839	0.01662	0.02650	0.00138	658	12	621	8	629	12	529	28	623	15
29Br	0.06133	0.00198	0.10829	0.00162	0.91796	0.02996	0.03186	0.00195	651	21	663	10	661	22	634	39	663	19
29Cc	0.05824	0.00118	0.08820	0.00122	0.70762	0.01479	0.02408	0.00126	538	11	545	8	543	11	481	25	545	14
29Cr	0.05659	0.00167	0.08091	0.00107	0.62956	0.02045	0.01923	0.00120	475	14	502	7	496	16	385	24	501	13
29Dc	0.06100	0.00143	0.10306	0.00141	0.86892	0.02105	0.02634	0.00140	639	15	632	9	635	15	526	28	633	16
29Dr	0.06045	0.00263	0.10233	0.00173	0.85390	0.03655	0.02676	0.00164	620	27	628	11	627	27	534	33	628	20
34c	0.16558	0.00361	0.47399	0.00663	10.81380	0.25890	0.10773	0.00596	2513	55	2501	35	2507	60	2088	114	2506	43
34r	0.05833	0.00114	0.08698	0.00112	0.70112	0.01459	0.05725	0.00387	541	11	538	7	540	11	1125	76	538	13
33c	0.06113	0.00212	0.09864	0.00156	0.82135	0.02875	0.02909	0.00169	644	22	606	10	609	21	580	34	607	18
33r	0.05983	0.00172	0.09980	0.00141	0.82127	0.02467	0.02556	0.00143	597	17	613	9	609	18	510	29	613	16
32Ac	0.06809	0.00472	0.09860	0.00183	0.84515	0.05275	0.03798	0.00316	871	60	606	11	622	39	753	63	607	21
32Ar	0.05774	0.00110	0.08682	0.00117	0.69016	0.01399	0.02569	0.00139	520	10	537	7	533	11	513	28	536	14
32Bc	0.05622	0.00193	0.07021	0.00103	0.54466	0.01881	0.02100	0.00126	460	16	437	6	442	15	420	25	438	12
32Br	0.05544	0.00255	0.07296	0.00113	0.55754	0.02645	0.02698	0.00195	430	20	454	7	450	21	538	39	454	14
32Cc	0.07399	0.00361	0.16889	0.00301	1.66587	0.07909	0.05503	0.00371	1041	51	1006	18	996	47	1083	73	1005	33
32Dc	0.06054	0.00146	0.10046	0.00136	0.84002	0.02163	0.02611	0.00148	623	15	617	8	619	16	521	30	617	16
32Dr	0.06056	0.00256	0.09921	0.00149	0.82735	0.03590	0.04233	0.00285	624	26	610	9	612	27	838	56	610	17
31c	0.10685	0.00344	0.30209	0.00438	4.44336	0.15153	0.07160	0.00432	1746	56	1702	25	1721	59	1398	84	1707	41
31r	0.10145	0.01013	0.28920	0.00496	3.98919	0.37242	0.10940	0.01262	1651	165	1638	28	1632	152	2098	242	1637	49
37c	0.05564	0.00105	0.07652	0.00087	0.58712	0.01479	0.02164	0.00030	438	8	475	5	469	12	433	6	475	10
37r	0.05672	0.00081	0.07362	0.00081	0.57582	0.01274	0.02156	0.00029	480	7	458	5	462	10	431	6	458	9
38c	0.05647	0.00181	0.07812	0.00113	0.60439	0.02175	0.02983	0.00070	470	15	485	7	480	17	594	14	485	13
38r	0.05760	0.00121	0.07582	0.00087	0.60195	0.01606	0.02543	0.00041	514	11	471	5	479	13	508	8	471	10
39Ac	0.06728	0.00177	0.14446	0.00189	1.33794	0.04145	0.04377	0.00088	846	22	870	11	862	27	866	17	869	21
39Ar	0.05529	0.00134	0.07556	0.00096	0.57622	0.01700	0.02311	0.00051	424	10	470	6	462	14	462	10	469	11
39Bc	0.05864	0.00125	0.09451	0.00121	0.76540	0.02088	0.02777	0.00035	554	12	582	7	577	16	554	7	582	14
39Br	0.06174	0.00141	0.10252	0.00125	0.86525	0.02447	0.02515	0.00046	665	15	629	8	633	18	502	9	629	14
39Cc	0.06054	0.00158	0.09526	0.00119	0.78866	0.02431	0.02699	0.00047	623	16	587	7	590	18	538	9	587	14
39Cr	0.05841	0.00131	0.08855	0.00101	0.71505	0.01981	0.03080	0.00053	545	12	547	6	548	15	613	11	547	12
39Dc	0.11405	0.00166	0.34893	0.00381	5.50127	0.12232	0.08936	0.00100	1865	27	1930	21	1901	42	1730	19	1916	32
39Dr	0.11241	0.00154	0.33314	0.00356	5.16111	0.11201	0.08408	0.00098	1839	25	1854	20	1846	40	1632	19	1850	31

Table 20: U-Pb isotopic ratios and concordia ages of zircons from LL61b2 paragneiss.

Spot	Isotopic ratios					Age estimates (Ma)					Concordia							
	$^{207}\text{Pb}/^{206}\text{Pb}$	$\pm 1\sigma$	$^{206}\text{Pb}/^{238}\text{U}$	$\pm 1\sigma$	$^{207}\text{Pb}/^{235}\text{U}$	$\pm 1\sigma$	$^{208}\text{Pb}/^{232}\text{Th}$	$\pm 1\sigma$	$^{207}\text{Pb}/^{206}\text{Pb}$	$\pm 1\sigma$	$^{206}\text{Pb}/^{238}\text{U}$	$\pm 1\sigma$	$^{207}\text{Pb}/^{235}\text{U}$	$\pm 1\sigma$	$^{208}\text{Pb}/^{232}\text{Th}$	$\pm 1\sigma$	Age	$\pm 2\sigma$
39Ec	0.06176	0.00234	0.10829	0.00155	0.92134	0.03855	0.02516	0.00058	666	25	663	9	663	28	502	12	663	18
39Er	0.06066	0.00151	0.11101	0.00144	0.92894	0.02787	0.03193	0.00055	627	16	679	9	667	20	635	11	677	16
39Fr1	0.05842	0.00102	0.09182	0.00101	0.73848	0.01799	0.02314	0.00029	546	10	566	6	562	14	462	6	566	12
39Fr2	0.06145	0.00142	0.09497	0.00111	0.80358	0.02297	0.02427	0.00037	655	15	585	7	599	17	485	7	586	13
44c	0.07483	0.00329	0.17213	0.00243	1.73221	0.08977	0.03736	0.00154	1064	47	1024	14	1021	53	741	31	1024	26
44r	0.06793	0.00238	0.14416	0.00196	1.31666	0.05021	0.04544	0.00146	866	30	868	12	853	33	898	29	867	22
40r	0.07675	0.00125	0.18125	0.00205	1.91863	0.04512	0.05767	0.00082	1115	18	1074	12	1088	26	1133	16	1076	22
41Ac	0.05786	0.00109	0.09392	0.00107	0.74938	0.01905	0.02550	0.00035	524	10	579	7	568	14	509	7	578	12
41Bc	0.07177	0.00146	0.16363	0.00179	1.61900	0.04410	0.04894	0.00093	979	20	977	11	978	27	966	18	977	19
41Br	0.06091	0.00115	0.09946	0.00108	0.83499	0.02157	0.06348	0.00149	636	12	611	7	616	16	1244	29	612	13
41Cr	0.05837	0.00210	0.08372	0.00107	0.67180	0.03050	0.02675	0.00109	544	20	518	7	522	24	534	22	518	13
43Ar	0.05984	0.00161	0.09494	0.00109	0.78304	0.02462	0.02760	0.00071	598	16	585	7	587	18	550	14	585	13
43Bc	0.17294	0.00395	0.48639	0.00591	11.57749	0.32952	0.12516	0.00269	2586	59	2555	31	2571	73	2384	51	2562	44
43Cr	0.05461	0.00193	0.06865	0.00084	0.51967	0.02326	0.01867	0.00071	396	14	428	5	425	19	374	14	428	10
48r2	0.07188	0.00172	0.15700	0.00178	1.55729	0.04778	0.03852	0.00079	983	24	940	11	953	29	764	16	941	20
21r	0.05796	0.00386	0.08418	0.00119	0.67375	0.05016	0.02277	0.00180	528	35	521	7	523	39	455	36	521	14
99r	0.12108	0.00780	0.35260	0.00518	5.89248	0.43611	0.07545	0.00616	1972	127	1947	29	1960	145	1470	120	1948	49
98Ar	0.07403	0.00302	0.17104	0.00255	1.73767	0.08153	0.04988	0.00266	1042	42	1018	15	1023	48	984	52	1018	28
98Br	0.06088	0.00218	0.09944	0.00123	0.83579	0.03567	0.02785	0.00147	635	23	611	8	617	26	555	29	611	14
98Cr	0.11661	0.00415	0.33626	0.00437	5.35756	0.22796	0.07716	0.00404	1905	68	1869	24	1878	80	1502	79	1870	41
97Ar	0.06099	0.00304	0.09988	0.00150	0.84443	0.04619	0.02931	0.00169	639	32	614	9	622	34	584	34	614	18
97Br	0.05967	0.00461	0.09821	0.00205	0.80889	0.06427	0.02563	0.00149	592	46	604	13	602	48	511	30	604	24
97Dr	0.06144	0.00254	0.11539	0.00163	0.97915	0.04639	0.03682	0.00204	655	27	704	10	693	33	731	40	703	19
94r	0.06220	0.00221	0.10490	0.00137	0.90097	0.03839	0.02788	0.00147	681	24	643	8	652	28	556	29	643	16
92A2	0.05899	0.00273	0.09898	0.00143	0.81051	0.04161	0.03597	0.00199	567	26	608	9	603	31	714	39	608	17
92Br	0.05993	0.00217	0.09856	0.00131	0.81561	0.03528	0.07885	0.00494	601	22	606	8	606	26	1534	96	606	15
92Cr	0.06176	0.00238	0.10548	0.00138	0.89853	0.04039	0.02811	0.00148	666	26	646	8	651	29	560	30	647	16
92Dr	0.06118	0.00331	0.10278	0.00164	0.86631	0.05045	0.03045	0.00181	645	35	631	10	634	37	606	36	631	19

Table 20: continued.

Spot	Isotopic ratios					Age estimates (Ma)					Concordia				
	$^{207}\text{Pb}/^{206}\text{Pb}$	$\pm 1\sigma$	$^{206}\text{Pb}/^{238}\text{U}$	$\pm 1\sigma$	$^{207}\text{Pb}/^{235}\text{U}$	$\pm 1\sigma$	$^{208}\text{Pb}/^{232}\text{Th}$	$\pm 1\sigma$	$^{206}\text{Pb}/^{238}\text{U}$	$\pm 1\sigma$	$^{207}\text{Pb}/^{235}\text{U}$	$\pm 1\sigma$	$^{208}\text{Pb}/^{232}\text{Th}$	$\pm 1\sigma$	Age $\pm 2\sigma$
Zr_1c	0,05398	0,00156	0,05510	0,00084	0,41070	0,01092	0,01570	0,00035	370	11	346	5	315	9	346
Zr_3c	0,05283	0,00118	0,05523	0,00067	0,40209	0,00722	0,01933	0,00038	322	7	347	4	387	6	346
Zr_4c	0,05294	0,00120	0,04476	0,00058	0,32680	0,00616	0,01422	0,00028	326	7	282	4	286	5	283
Zr_4r	0,05174	0,00129	0,04352	0,00057	0,31075	0,00659	0,01304	0,00027	274	7	275	4	262	6	275
Zr_15c	0,05950	0,00153	0,09290	0,00128	0,76251	0,01714	0,02756	0,00058	585	15	573	8	550	13	573
Zr_21r	0,06866	0,00390	0,05513	0,00113	0,52217	0,02810	0,01448	0,00202	889	50	346	7	291	23	333
Zr_20c	0,04660	0,00843	0,05315	0,00174	0,34156	0,06085	0,02132	0,00131	29	5	334	11	426	53	351
Zr_20r	0,05556	0,00916	0,05593	0,00202	0,42543	0,06873	0,01999	0,00219	434	72	351	13	400	58	462
Zr_22r	0,07063	0,00458	0,06626	0,00146	0,64520	0,03996	0,02050	0,00103	947	61	414	9	410	31	399
Zr_18c	0,05639	0,00255	0,06374	0,00113	0,49550	0,02087	0,02278	0,00068	467	21	398	7	455	17	328
Zr_18r	0,05428	0,00249	0,05220	0,00088	0,39046	0,01661	0,01787	0,00061	383	18	328	6	358	14	458
Zr_16r	0,09765	0,03347	0,05064	0,00422	0,68794	0,22951	0,03084	0,00952	1580	541	318	27	614	177	352
Zr_17r	0,06246	0,00214	0,05399	0,00090	0,46401	0,01441	0,01828	0,00050	690	24	339	6	366	12	318
Zr_14r	0,06255	0,00231	0,04646	0,00082	0,40076	0,01365	0,02419	0,00106	693	26	293	5	483	12	248
Zr_7c	0,06440	0,00367	0,04698	0,00088	0,41757	0,02342	0,01931	0,00100	755	43	296	6	387	20	299
Zr_2Br	0,07316	0,00182	0,17475	0,00227	1,76567	0,04748	0,04447	0,00191	1019	25	1038	14	880	28	1037
Zr_3r_07	0,05891	0,00143	0,09554	0,00120	0,78234	0,02075	0,05688	0,00374	564	14	588	7	1118	16	588
Zr_5Ar	0,05512	0,00163	0,05467	0,00073	0,41530	0,01297	0,01988	0,00091	417	12	343	5	398	11	343
Zr_6Ar	0,07287	0,00190	0,16807	0,00227	1,68603	0,04750	0,04259	0,00188	1010	26	1002	14	843	28	1002
Zr_6Br	0,06253	0,00279	0,10784	0,00171	0,92863	0,04192	0,04558	0,00234	692	31	660	10	901	30	661
Zr_11Ar	0,05848	0,00172	0,06852	0,00091	0,55283	0,01724	0,02146	0,00094	548	16	427	6	429	14	428

Table 21: U-Pb isotopic ratios and concordia ages of zircons from LL42c basic meta-sill.

Spot	Isotopic ratios					Age estimates (Ma)					Concordia				
	$^{207}\text{Pb}/^{206}\text{Pb}$	$\pm 1\sigma$	$^{206}\text{Pb}/^{238}\text{U}$	$\pm 1\sigma$	$^{207}\text{Pb}/^{235}\text{U}$	$\pm 1\sigma$	$^{208}\text{Pb}/^{232}\text{Th}$	$\pm 1\sigma$	$^{206}\text{Pb}/^{238}\text{U}$	$\pm 1\sigma$	$^{207}\text{Pb}/^{235}\text{U}$	$\pm 1\sigma$	$^{208}\text{Pb}/^{232}\text{Th}$	$\pm 1\sigma$	Age $\pm 1\sigma$
Zr 40B c	0,05254	0,01517	0,04521	0,01400	0,32738	0,01904	0,01419	0,01887	285	4	285	5	309	5	285
Zr 41B r	0,05292	0,01471	0,04882	0,01368	0,35581	0,01848	0,01522	0,01857	307	4	326	5	305	6	308
Zr 37A c	0,05190	0,01513	0,04681	0,01404	0,33445	0,01909	0,01454	0,01876	295	4	281	4	292	5	295
Zr 37B c	0,05140	0,01411	0,04689	0,01369	0,33216	0,01812	0,01465	0,01841	295	4	259	4	294	5	294
Zr 37B r	0,05219	0,01454	0,04572	0,01425	0,32856	0,01884	0,01415	0,01888	288	4	294	4	284	5	288
Zr 36 c	0,05224	0,01578	0,04646	0,01462	0,33436	0,01991	0,01420	0,01921	293	4	296	5	285	5	293
Zr 33 c	0,05131	0,01494	0,04619	0,01315	0,32521	0,01839	0,01405	0,01826	291	4	255	4	282	5	290
Zr 27 c	0,05123	0,01509	0,04631	0,01379	0,32653	0,01883	0,01457	0,01875	292	4	251	4	292	5	291
Zr 27 r	0,05103	0,01470	0,04492	0,01388	0,31555	0,01861	0,01462	0,01874	283	4	242	4	293	5	282
Zr 20 c	0,05123	0,01427	0,04760	0,01341	0,33634	0,01802	0,01573	0,01845	300	4	251	4	316	6	299
Zr 20 r	0,05227	0,01426	0,04528	0,01347	0,32645	0,01809	0,01410	0,01856	286	4	297	4	283	5	286
Zr 16 c	0,05188	0,01499	0,04590	0,01456	0,32856	0,01928	0,01423	0,01920	289	4	280	4	286	5	289
Zr 15 c	0,05261	0,01448	0,04627	0,01466	0,33596	0,01893	0,01425	0,01885	292	4	312	5	286	5	292
Zr 12 c	0,05229	0,01439	0,04838	0,01376	0,34897	0,01833	0,01585	0,01871	305	4	298	4	318	6	304
Zr 10 r	0,05203	0,01656	0,04333	0,01402	0,31154	0,02001	0,01383	0,01898	273	4	287	5	278	5	274
Zr 2 c	0,05081	0,01774	0,04232	0,01518	0,29671	0,02161	0,01353	0,02029	267	4	232	4	272	6	267
Zr 4 c	0,05249	0,01617	0,04194	0,01528	0,30377	0,02044	0,01339	0,01953	265	4	307	5	269	5	265
Zr 4 r	0,05236	0,01548	0,04254	0,01513	0,30730	0,01998	0,01316	0,01922	269	4	301	5	264	5	269
Zr 5 r	0,05095	0,01444	0,04576	0,01459	0,32182	0,01882	0,01377	0,01900	288	4	238	5	276	5	287

Table 22: U-Pb isotopic ratios and concordia ages of zircons from LL134 porphyritic dyke.

Thin sec.	Analyses	Mnz/spot	Grain position	Isotopic ratios $^{206}\text{Pb}/^{238}\text{U}$	$\pm 1\sigma$	$^{207}\text{Pb}/^{235}\text{U}$	$\pm 1\sigma$	$^{206}\text{Pb}/^{232}\text{Th}$	$\pm 1\sigma$	Age estimates (Ma) $^{206}\text{Pb}/^{238}\text{U}$	$\pm 1\sigma$	$^{207}\text{Pb}/^{235}\text{U}$	$\pm 1\sigma$	U-Pb Concordia Age	$\pm 2\sigma$
LL61b2	Ja17a005	09A-1	Into Bt	0.04825	0.00095	0.36675	0.01896	0.01536	0.00023	304	6	308	5	317	16
LL61b2	Ja17a006	09A-2	Into Bt	0.04696	0.00094	0.35847	0.01889	0.01526	0.00023	296	6	306	5	311	16
LL61b2	Ja17a007	12A-1	Into Bt	0.04742	0.00093	0.35299	0.01820	0.01414	0.00021	299	6	284	4	307	16
LL61b2	Ja17a008	12A-2	Into Bt	0.04516	0.00089	0.38127	0.01954	0.01408	0.00021	285	6	283	4	328	17
LL61b2	Ja17a009	12A-3	Into Bt	0.04747	0.00093	0.38636	0.01979	0.01385	0.00020	299	6	278	4	332	17
LL61b2	Ja17a010	19-1	Along S2	0.04909	0.00096	0.49382	0.02490	0.01570	0.00023	309	6	315	5	408	21
LL61b2	Ja17a011	19-2	Along S2	0.04680	0.00096	0.43666	0.02320	0.01433	0.00022	295	6	288	4	368	20
LL61b2	Ja17a012	18-1	Along S2	0.04497	0.00091	0.33119	0.01753	0.01388	0.00022	284	6	279	4	291	15
LL61b2	Ja17a013	16-1	Along S2	0.04887	0.00107	0.58169	0.03501	0.01433	0.00022	308	7	288	4	466	28
LL61b2	Ja17a014	16-2	Along S2	0.04796	0.00099	0.39007	0.02108	0.01467	0.00023	302	6	294	5	334	18
LL61b2	Ja17a015	15-1	Into Bt	0.04604	0.00092	0.36745	0.01919	0.01429	0.00021	290	6	287	4	318	17
LL61b2	Ja17a016	15-2	Into Bt	0.04635	0.00098	0.31696	0.01802	0.01491	0.00023	292	6	299	5	280	16
LL61b2	Ja17a017	13-1	Along S2	0.04668	0.00096	0.37577	0.02035	0.01486	0.00023	294	6	298	5	324	18
LL61b2	Ja17a018	7-1	Into Bt	0.04615	0.00094	0.33063	0.01779	0.01484	0.00023	291	6	298	5	290	16
LL61b2	Ja17a019	7-2	Into Bt	0.04673	0.00096	0.43149	0.02361	0.01465	0.00022	294	6	294	4	364	20
LL61b2	Ja17a020	8-1	Into Bt	0.04840	0.00096	0.39674	0.02050	0.01507	0.00023	305	6	302	5	339	18
LL61b2	Ja17a021	8-2	Into Bt	0.04825	0.00096	0.39051	0.02021	0.01500	0.00022	304	6	301	4	335	17
LL61b2	Ja17a022	10-1	Into Bt	0.04855	0.00097	0.36651	0.01900	0.01551	0.00023	306	6	311	5	317	16
LL61b2	Ja17a023	1-1	Along S2	0.04596	0.00093	0.31492	0.01659	0.01418	0.00022	290	6	285	4	278	15
LL61b2	Ja17a024	1-2	Along S2	0.04538	0.00092	0.32971	0.01743	0.01447	0.00022	286	6	290	4	289	15
LL61b2	Ja17a027	8A-1	Into Bt	0.04699	0.00093	0.34612	0.01770	0.01375	0.00020	296	6	276	4	302	15
LL61b2	Ja17a028	8A-2	Into Bt	0.04975	0.00099	0.35009	0.01835	0.01442	0.00022	313	6	289	4	305	16
LL61b2	Ja17a029	7A-1	Along S2	0.04971	0.00099	0.36388	0.01893	0.01550	0.00023	313	6	311	5	316	16
LL61b2	Ja17a030	7A-2	Along S2	0.04744	0.00103	0.40589	0.02432	0.01457	0.00023	299	6	292	5	346	21
LL61b2	Ja17a031	6A-1	Along S2	0.04738	0.00100	0.37995	0.02175	0.01458	0.00022	298	6	293	4	327	19
LL61b2	Ja17a032	13A-1	Into Bt	0.04660	0.00093	0.37241	0.01925	0.01434	0.00021	294	6	288	4	321	17
LL61b2	Ja17a033	13A-2	Into Bt	0.04850	0.00097	0.36324	0.01902	0.01469	0.00022	305	6	295	5	315	16
LL61b2	Ja17a034	14A-1	Into Bt	0.04623	0.00095	0.33348	0.01813	0.01485	0.00023	291	6	298	5	292	16
LL61b2	Ja17a035	14A-2	Into Bt	0.04881	0.00097	0.35201	0.01855	0.01492	0.00023	307	6	299	5	306	16
LL61b2	Ja17a036	14A-3	Into Bt	0.05055	0.00101	0.37268	0.01972	0.01433	0.00021	318	6	288	4	322	17
LL61b2a	Ja17b005	6-1	Along S2	0.04345	0.00129	0.29101	0.01196	0.01360	0.00016	274	8	273	3	259	11
LL61b2a	Ja17b006	6-2	Along S2	0.04478	0.00133	0.28130	0.01163	0.01419	0.00017	282	8	285	3	252	10
LL61b2a	Ja17b007	4-1	Along S2	0.04551	0.00136	0.31484	0.01296	0.01357	0.00016	287	9	273	3	278	11
LL61b2a	Ja17b008	3-1	Along S2	0.04551	0.00136	0.30506	0.01253	0.01455	0.00018	287	9	292	4	270	11
LL61b2a	Ja17b009	3-2	Along S2	0.04725	0.00141	0.31796	0.01316	0.01432	0.00017	298	9	288	3	280	12
LL61b2a	Ja17b010	2-1	Along S2	0.04885	0.00146	0.34143	0.01394	0.01475	0.00018	307	9	296	4	298	12
LL61b2a	Ja17b011	2-2	Along S2	0.04368	0.00130	0.28065	0.01145	0.01425	0.00017	276	8	286	3	251	10
LL61b2a	Ja17b012	1-1	Along S2	0.04607	0.00137	0.32178	0.01324	0.01466	0.00018	290	9	294	4	283	12
LL61b2a	Ja17b013	1-2	Along S2	0.04795	0.00143	0.33493	0.01384	0.01430	0.00017	302	9	287	3	293	12
LL61b2a	Ja17b014	7-1	Along S2	0.04709	0.00141	0.32735	0.01370	0.01489	0.00018	297	9	299	4	288	12
LL61b2a	Ja17b015	7-2	Along S2	0.04830	0.00144	0.33580	0.01393	0.01487	0.00018	304	9	298	4	294	12
LL61b2a	Ja17b018	9-1	Into Bt	0.04928	0.00150	0.36263	0.01671	0.01457	0.00018	310	9	292	4	314	14
LL61b2a	Ja17b019	9-2	Into Bt	0.04713	0.00144	0.37695	0.01726	0.01526	0.00019	297	9	306	4	325	15
LL61b2a	Ja17b020	9-3	Into Bt	0.04752	0.00146	0.34375	0.01701	0.01696	0.00021	299	9	340	4	300	15
LL61b2a	Ja17b021	13-1	Along S2	0.04860	0.00148	0.33399	0.01539	0.01445	0.00018	306	9	290	4	293	13
LL61b2a	Ja17b022	13-2	Along S2	0.04729	0.00142	0.33670	0.01465	0.01538	0.00018	298	9	308	4	295	13
LL61b2a	Ja17b023	12-1	Along S2	0.04691	0.00142	0.35464	0.01550	0.01485	0.00018	296	9	288	4	308	13
LL61b2a	Ja17b024	12-2	Along S2	0.04655	0.00143	0.39721	0.01819	0.01420	0.00018	293	9	285	4	340	16
LL61b2a	Ja17b025	15-1	Along S2	0.04832	0.00148	0.35057	0.01660	0.01448	0.00019	304	9	291	4	305	14
LL61b2a	Ja17b026	21-1	Into Bt	0.04785	0.00146	0.34640	0.01721	0.01498	0.00018	301	9	301	4	302	15
LL61b2a	Ja17b027	21-2	Into Bt	0.04618	0.00139	0.35024	0.01579	0.01476	0.00017	291	9	296	3	305	14
LL61b2a	Ja17b028	21-3	Into Bt	0.04679	0.00142	0.35020	0.01641	0.01560	0.00018	295	9	313	4	305	14

Table 23: U-Pb isotopic ratios and ages of monazites from LL61b2 paragneiss

Thin sec.	Analyses	Mnz-spot	Grain position	Isotopic ratios		Age estimates (Ma)				U-Pb Concordia						
				$^{206}\text{Pb}/^{238}\text{U}$	$\pm 1\sigma$	$^{207}\text{Pb}/^{235}\text{U}$	$\pm 1\sigma$	$^{208}\text{Pb}/^{232}\text{Th}$	$\pm 1\sigma$	$^{206}\text{Pb}/^{238}\text{U}$	$\pm 1\sigma$	$^{207}\text{Pb}/^{235}\text{U}$	$\pm 1\sigma$	Age	$\pm 2\sigma$	
LL56a4	Ja17c005	Mnz1-1	Into Bt	0,04558	0,00051	0,24856	0,02243	0,01586	0,00035	287	3	318	7	225	20	
LL56a4	Ja17c006	Mnz1-2	Into Bt	0,04449	0,00049	0,25554	0,02310	0,01422	0,00031	281	3	285	6	231	21	
LL56a4	Ja17c007	Mnz2-1	Into Bt	0,04656	0,00053	0,25653	0,02328	0,01388	0,00031	293	3	279	6	232	21	
LL56a4	Ja17c008	Mnz2-2	Into Bt	0,04804	0,00056	0,29107	0,02672	0,01539	0,00034	303	4	309	7	259	24	
LL56a4	Ja17c009	Mnz3-1	Along S2	0,04199	0,00046	0,23549	0,02122	0,01513	0,00033	265	3	304	7	215	19	308
LL56a4	Ja17c010	Mnz3-2	Along S2	0,04893	0,00056	0,31126	0,02836	0,01516	0,00034	308	4	304	7	275	25	
LL56a4	Ja17c011	Mnz5-1	Along S2	0,04668	0,00051	0,25580	0,02305	0,01368	0,00030	294	3	275	6	231	21	287
LL56a4	Ja17c012	Mnz4-1	Along S2	0,04546	0,00051	0,29554	0,02666	0,01372	0,00030	287	3	276	6	263	24	289
LL56a4	Ja17c013	Mnz8-1	Along S2	0,04585	0,00071	0,30533	0,03027	0,01325	0,00031	289	4	266	6	271	27	
LL56a4	Ja17c014	Mnz8-2	Along S2	0,04705	0,00069	0,26108	0,02583	0,01424	0,00033	296	4	286	7	236	23	
LL56a4	Ja17c015	Mnz8-3	Along S2	0,04978	0,00058	0,29772	0,02728	0,01535	0,00034	313	4	308	7	265	24	
LL56a4	Ja17c016	Mnz9-1	Along S2	0,04386	0,00050	0,28137	0,02570	0,01396	0,00031	277	3	280	6	252	23	290
LL56a4	Ja17c017	Mnz9-2	Along S2	0,04601	0,00053	0,31389	0,02866	0,01455	0,00032	290	3	292	6	277	25	
LL56a4	Ja17c018	Mnz10-1	Into Bt	0,04660	0,00049	0,26022	0,02360	0,01379	0,00030	294	3	277	6	235	21	286
LL56a4	Ja17c019	Mnz10-2	Into Bt	0,04533	0,00047	0,29405	0,02647	0,01471	0,00032	286	3	295	6	262	24	293
LL56a4	Ja17c020	Mnz10-3	Into Bt	0,04655	0,00056	0,31670	0,02923	0,01399	0,00031	293	4	281	6	279	26	
LL56a4	Ja17c021	Mnz11-1	Along S2	0,04831	0,00056	0,27642	0,02523	0,01406	0,00030	304	4	282	6	248	23	286
LL56a4	Ja17c022	Mnz11-2	Along S2	0,04534	0,00053	0,29086	0,02668	0,01447	0,00032	286	3	290	6	259	24	

Table 24: U-Th-Pb isotopic ratios and ages of monazites from LL56a4 micaschist.